



Michigan Technological University
Create the Future Digital Commons @ Michigan Tech

Dissertations, Master's Theses and Master's
Reports - Open

Dissertations, Master's Theses and Master's
Reports

2011

Diesel spray mixing limited vaporization with non-ideal and multi-component fuel thermophysical property effects

Jaclyn Elyse Nesbitt
Michigan Technological University

Follow this and additional works at: <https://digitalcommons.mtu.edu/etds>

 Part of the [Mechanical Engineering Commons](#)

Copyright 2011 Jaclyn Elyse Nesbitt

Recommended Citation

Nesbitt, Jaclyn Elyse, "Diesel spray mixing limited vaporization with non-ideal and multi-component fuel thermophysical property effects", Dissertation, Michigan Technological University, 2011.
<https://doi.org/10.37099/mtu.dc.etds/390>

Follow this and additional works at: <https://digitalcommons.mtu.edu/etds>

 Part of the [Mechanical Engineering Commons](#)

DIESEL SPRAY MIXING LIMITED VAPORIZATION WITH NON-IDEAL AND
MULTI-COMPONENT FUEL THERMOPHYSICAL PROPERTY EFFECTS

By

Jaclyn Elyse Nesbitt

A DISSERTATION

Submitted in partial fulfillment of the requirements for the degree of

DOCTOR OF PHILOSOPHY

(Mechanical Engineering – Engineering Mechanics)

MICHIGAN TECHNOLOGICAL UNIVERSITY

2011

Copyright 2011 Jaclyn Elyse Nesbitt

This dissertation, “Diesel Spray Mixing Limited Vaporization with Non-Ideal and Multi-Component Fuel Thermophysical Property Effects,” is hereby approved in partial fulfillment of the requirements for the Degree of DOCTOR OF PHILOSOPHY IN MECHANICAL ENGINEERING – ENGINEERING MECHANICS.

Department of Mechanical Engineering – Engineering Mechanics

Signatures:

Dissertation Advisor

Jeffrey D. Naber

Department Chair

William W. Predebon

Date

Table of Contents

List of Figures	xv
List of Tables	xxxvii
Preface.....	xliii
Acknowledgements	xlvi
Nomenclature	xlvi
Abstract.....	li
1. Introduction	1
1.1. Overview and Motivation	1
1.2. Background	2
1.2.1. Sustainability Issues	8
1.3. Problem Statement	12
1.4. Goals and Objectives.....	12
1.5. Method of Solution	14
2. Literature Review.....	17
2.1. Experimental Apparatus.....	17
2.1.1. Preburn Procedure for Thermodynamic State Generation	20
2.2. Optical Diagnostics	21
2.3. Macroscopic Spray Characteristics	23
2.3.1. Spray Penetration.....	23
2.3.2. Liquid Length	25
2.3.3. Cone Angle.....	28

2.3.4. Lift-Off Length	30
2.3.5. Plume to Plume Variations.....	31
2.3.6. Liquid Length Fluctuations.....	32
2.4. Spray Modeling	33
2.4.1. 1-D Spray Models	34
2.4.1.1. Conservation Equation Methodology	34
2.4.1.2. Eulerian Approach – Fuel Mass Particle Tracking	48
2.5. Surrogate Fuels	51
2.6. Property Relationships – Equations of State	55
2.7. Mixing Relationships.....	58
2.8. Summary.....	59
3. Experimental Facility, Test Setup & Diagnostics.....	61
3.1. Combustion Vessel	61
3.2. Gas System	66
3.2.1. Operating Regime	68
3.3. Control, Monitoring and Data Acquisition System.....	69
3.4. Diesel Fuel System	73
3.4.1. Diesel Fuel Properties	75
3.4.2. Piezoelectric Injector.....	75
3.4.2.1. Injector Characteristics Influencing Spray Behavior	78
3.4.2.2. Piezoelectric Injector Driver	82
3.4.2.3. Rate of Injection Signal.....	88
3.4.2.4. Chiller for Fuel Temperature Control	88
3.5. Spark Ignition System	92
3.6. Optical Diagnostics.....	97
3.7. Image Processing Tools.....	98

3.8.	Chemical Kinetics Modeling Tools	99
4.	Thermodynamic State Generation Analysis.....	101
4.1.	CV Preburn Procedure for Thermodynamic State Generation	101
4.2.	Energy and Fuels Journal Publication.....	102
4.3.	‘Spray A’ Ambient Composition Analysis	121
4.3.1.	Comparison of Major Species at Injection	122
4.3.2.	Comparison of Preburn Environments.....	123
4.3.2.1.	Chemical Kinetics Preburn Modeling for Combustion Vessel Comparison	127
4.3.3.	Autoignition Modeling of n-Heptane as a Diesel Surrogate.....	131
4.3.3.1.	Constant Pressure Flow Rig and Constant Volume Combustion Vessel Comparison Considering Major Species.....	132
4.3.3.2.	Constant Volume Combustion Vessel Comparison – Major and Minor Species.....	134
4.3.4.	Conclusions from ‘Spray A’ Ambient Composition Comparison	135
4.4.	Modification to the Preburn Mixture	136
4.4.1.	0% Oxygen Mixture Analysis	136
4.4.1.1.	Mixture Sampling Setup and Test Procedures	136
4.4.1.2.	Mixture Sampling Results and Analysis	138
4.4.1.3.	Modifications to the 0% Oxygen Mixture	140
4.5.	Conclusions	141
5.	Optical Diagnostic Setup & Image Processing Methodology	143
5.1.	Mie Scattering Optical Diagnostic Imaging Setups.....	143
5.2.	Characterizing Cone Angle Definitions and Methodologies	146
5.3.	Influence of Optical Setup and Image Processing method on Spray Parameter Results	150
5.3.1.	Test Matrix.....	152
5.3.2.	Back Scattering Image Processing Methods.....	152

5.3.2.1. Baseline A – Image Processing Method 1 (BL A IP 1)	153
5.3.2.2. Baseline A – Image Processing Method 2 (BL A IP 2)	153
5.3.2.3. Baseline B (BL B)	154
5.3.2.4. Method Summary	154
5.3.3. Results & Discussion	154
5.3.3.1. Case A: 12.3 kg/m ³ Ambient Density, 914 Bar Injection Pressure ...	154
5.3.3.2. Baseline A – IP 1	156
5.3.3.3. Baseline A – IP 2	157
5.3.3.4. Baseline B	158
5.3.4. Summary on Threshold Influence on Penetration and Cone Angle...	159
5.4. Processing Methods for Mie Back Scatter Images.....	161
5.4.1. Nonvaporizing (Nitrogen Sprays)	162
5.4.2. Vaporizing (0% Oxygen Sprays)	164
5.4.3. Combusting (21% Oxygen Sprays)	165
5.4.4. Gaussian Image Processing Method	167
5.5. Summary.....	168
6. Macroscopic Spray Characteristics and Plume-to-Plume Variations	171
6.1. Non-Vaporizing Sprays	172
6.1.1. Injection Pressure Sweep - Chiller Off – 328 K Fuel Temperature ...	173
6.1.2. Charge Density Effect	176
6.1.3. Summary – Non-vaporizing Spray Results & Plume to Plume Variation Trends.....	178
6.2. Vaporizing Sprays	178
6.2.1. ILASS Paper – Temperature Sweep and Repeatability Sweep (363 K Fuel Temperature)	179
6.2.2. Fuel Pressure Sweep at 363 K Fuel Temperature.....	195
6.2.2.1. Additional Results - Fuel Pressure Sweep	197
6.2.3. Reduced Charge Density	199
6.2.4. Summary – Vaporizing Spray Results & Plume to Plume Variation Trends.....	200

6.3.	Combusting Sprays	201
6.3.1.	Injection Pressure Variation at 1100 K Bulk Gas Temperature	203
6.3.2.	Density Variation.....	206
6.3.3.	Charge Gas Temperature Variation at 2000 Bar Injection Pressure	209
6.3.4.	Summary – Combusting Spray Results & Plume to Plume Variation Trends.....	211
6.4.	Lift-off Length and Liquid Length Comparison.....	212
6.5.	Penetration and Flame Length Comparison.....	213
6.6.	Measurement Uncertainty	215
6.7.	Summary	216
7.	Liquid Length Modeling with an Equation of State Approach..	217
7.1.	Review of Siebers Liquid Length Model.....	218
7.2.	Application Limitations of Siebers Liquid Length Model.....	219
7.3.	Liquid Length Model (1999) Application – Tabulated Thermodynamic Data.....	223
7.4.	Equation of State Approach for Thermodynamic Property Evaluation.....	226
7.5.	Methodology Comparison – Tabulated Properties versus Equation of State Approach.....	236
7.6.	Comparison of Model Results to Additional Experimental Data – Single Component Fuel.....	238
7.7.	Single- and Multi-Component Surrogates	239
7.7.1.	Single Component Surrogate Application	239
7.7.2.	Multi-Component Surrogate Application	240
7.7.2.1.	Diesel Surrogate: Mixture of n-Decane and Methylnaphthalene.....	241
7.7.2.2.	Diesel Surrogate: Mixture of n-Tetradecane, n-Decane, Heptamethylnonane and 1-Methylnaphthalene.....	242

7.8.	Multi-component Diesel Surrogate for Vaporization.....	244
7.9.	Summary.....	246
8.	Fluctuations in Quasi-Steady Liquid Length.....	249
8.1.	Motivation	249
8.2.	Test Conditions.....	250
8.3.	Magnitude of Liquid Length Fluctuations.....	250
8.3.1.	Maximum Liquid Length Fluctuations	250
8.3.2.	Average Liquid Length Fluctuations.....	252
8.4.	Frequency Analysis	254
8.4.1.	Fuel Pressure Frequency	254
8.4.2.	Frequency of Liquid Penetration Fluctuations	256
8.5.	Hypotheses and Implications of Liquid Length Fluctuations	259
8.6.	Parametric Modeling Study – Liquid Length Fluctuations.....	260
8.6.1.	Charge – Gas Temperature Gradients – Boundary Layers.....	261
8.6.2.	Injector Cavitation – Nozzle Discharge Coefficient	262
8.6.3.	Internal Injector Flow and Injection Pressure – Orifice Coefficients	263
8.6.4.	Summary of Liquid Length Fluctuation Model Results & Conclusions	264
8.7.	Summary and Conclusions	265
9.	Summary and Conclusions	267
10.	Future Work.....	273
11.	References.....	277
12.	Appendices.....	297
12.1.	Copyright Permissions.....	297

12.1.1. Chapter 4.2 – Energy and Fuels.....	297
12.1.2. Chapter 6.2.1 – ILASS Conference Proceedings	297
12.1.3. Figure 3.5 Copyright Permission – Sam Johnson	298
12.1.4. Figure 3.33 Copyright Permission – Eric Kurtz.....	298
12.1.5. Figure 3.34 Copyright Permission – Chris Green	299
12.2. Supplements to Chapter 3 – Nozzle Hole Measurements.....	299
12.2.1. SEM Images – Test Set 1	300
12.2.2. SEM Images – Test Set 2	302
12.3. Supplements to Chapter 4 -Chemical Kinetics Modeling.....	305
12.3.1. EES Extent of Reaction Initial Condition Determination	305
12.3.2. n-Heptane Autoignition Model	307
12.3.3. Processing Files.....	309
12.3.3.1. Extent of Reaction Calculation Using Engineering Equation Solver (EES)	309
12.3.3.2. Premixed Burn Phase Chemical Kinetics Model Using Cantera Interfaced with Matlab	312
12.3.3.3. Cantera n-Heptane Ignition Delay Chemical Kinetics Model Using Matlab	320
12.3.3.4. ECN Modeling – Stoichiometric n-Heptane Mixtures with Major Species.....	327
12.4. Image Processing & Data Analysis Programs	332
12.4.1. Nonvaporizing (Nitrogen) Spray Image Processing Program	332
12.4.2. Vaporizing (0% Oxygen) Spray Image Processing Program.....	341
12.4.3. Combusting (21% Oxygen) Spray Image Processing Program.....	351
12.4.4. Gaussian Curve Fit Image Processing for Nonvaporizing Sprays	361
12.4.5. Data Analysis Program	374
12.4.5.1. Nonvaporizing (Nitrogen) Tests	386
12.4.5.2. Vaporizing (0% Oxygen) Tests.....	386
12.4.5.3. Combusting (21% Oxygen) Tests	388
12.5. Supplements to Chapter 5 – Optical Setup and Processing Method Influence.....	394
12.5.1. Case B: 34.8 kg/m ³ Ambient Density, 1700 Bar Injection Pressure...	394

12.5.1.1. Baseline A – IP 1	396
12.5.1.2. Baseline A – IP 2	396
12.5.1.3. Baseline B	397
12.6. Supplements to Chapter 6 – Experimental Results	399
12.6.1. Non-Vaporizing Results	399
12.6.1.1. Repeat Tests - Chiller Off – Fuel Temperature 328 K.....	399
12.6.1.2. Repeat Tests - Chiller On – Fuel Temperature 321 K	402
12.6.1.3. Combined Repeat Results	407
12.6.1.4. Injection Pressure Sweep – Chiller Off – 328 K Fuel Temperature ..	407
12.6.1.5. Injection Pressure Sweep – Chiller On – 321 K Fuel Temperature...	409
12.6.1.6. Combined Injection Pressure Sweep Results	412
12.6.1.7. Density Variation	412
12.6.2. Vaporizing Results	413
12.6.2.1. Repeat Tests – Chiller On – 355 K Fuel Temperature.....	413
12.6.2.2. Combined Repeat Results	417
12.6.2.3. Injection Pressure Sweep – Chiller Off – 363 K Fuel Temperature ..	417
12.6.2.4. Injection Pressure Sweep – Chiller On – 355 K Fuel Temperature...	419
12.6.2.5. Combined Results – Fuel Pressure Sweep	421
12.6.2.6. Charge Gas Density Variation	422
12.6.2.7. Charge Gas Temperature Sweep at 1379 Bar	423
12.6.3. Combusting Results – Plume to Plume Variations	426
12.6.3.1. Repeat Tests – Chiller Off.....	426
12.6.3.2. Injection Pressure Variation at 950 K	430
12.6.3.3. Injection Pressure Variation at 1100 K	435
12.6.3.4. Charge Gas Density Variation	437
12.6.3.5. Charge Gas Temperature Variation – 1379 Bar Injection Pressure...	438
12.6.3.6. Charge Gas Temperature Variation – 2000 Bar Injection Pressure...	441
12.7. Supplements to Chapter 7.....	441
12.7.1. Liquid Length Modeling Programs & Property Constants	441
12.7.1.1. Tabulated Thermodynamic Property Relationships.....	441

12.7.1.2. Liquid Length Modeling Program Using Tabulated Thermodynamic Property Relations	442
12.7.1.3. Equation of State Approach – Liquid Length	450
12.7.1.4. Single-Component Fuel Properties	462
12.7.1.5. Fuel Properties - Equation of State Evaluation	463
12.7.1.6. Ideal Gas Ambient Charge Gas Specific Heat Constants	463
12.7.1.7. Ideal Gas Fuel Specific Heat Constants	464
12.7.1.8. Multi-Component Surrogate Fuel Liquid Length Methodology.....	465
12.8. Supplements to Chapter 8	467
12.8.1. Frequency Analysis Matlab Programs	467
12.8.1.1. Frequency Analysis of Liquid Length Fluctuations	467
12.8.1.2. Frequency Analysis of Fuel Pressure Fluctuations	471
12.8.2. Magnitude of Liquid Length Fluctuations.....	472
12.8.2.1. Maximum Extent of Fluctuations	472
12.8.2.2. Average Extent of Fluctuations.....	477
12.8.3. Penetration and PSD Results	481

List of Figures

Figure 1.1: History of NO _x and PM emission standards from 1978 to present. In 1978, 1984, and 1987 there were no established PM standards. Data from US EPA 2010A. White text numbers denote NO _x , black text numbers denote PM standards.	4
Figure 1.2: NO _x -soot formation based on the equivalence ratio – temperature path of combustion. Adapted from (Kitamura et al. 2002; Pickett et al. 2007).	4
Figure 1.3: Schematic of liquid length and lift-off length relationship relative to soot and NO _x emissions. Adapted from Siebers and Higgins 2001.	7
Figure 2.1: Definition of macroscopic spray parameters for non-vaporizing, vaporizing and combusting sprays, including penetration, cone angle, liquid length, and lift-off length.	23
Figure 2.2: Control surface for the spray penetration model. Modified from Naber and Siebers (1996).	36
Figure 2.3: Model with discrete control volumes, adapted from Musculus and Kattke (2009).	37
Figure 2.4: Control volume schematic for the liquid length model. Modified from Siebers (1999).	39
Figure 2.5: Control volume for the Versaevel et al. liquid length and penetration model. Modified from Versaevel et al. (2000).	43
Figure 3.1: External view of the CV in the AFCL facility (Left); Internal view of the CV (Right).	62
Figure 3.2: Temperature – pressure time plot showing the preburn including premixed burn and cool down along with diesel combustion event. Temperature is that of the bulk gas conditions.	64
Figure 3.3: Preburn propagation example for a mixture yielding 2% oxygen post preburn. Time after spark dwell is given on each image showing the transition from a laminar to turbulent flame propagating through the combustion chamber. Bulk charge-gas density of 12.6 kg/m ³ , CV temperature of 453 K. Images acquired with low-speed (30 frames per second) monitoring camera, Samsung SCC-B2311.	66
Figure 3.4: Figure <i>A</i> - Gas system for mixture preparation. Figure <i>B</i> – 10 L mixing vessel.	67
Figure 3.5: CV operating regime including comparison to engine operating regions and critical fuel points. Figure reproduced with permission from Sam Johnson (Refer to appendix 12.1.3).	68
Figure 3.6: Overview of the control and data acquisition system architecture.	69

Figure 3.7: iTest low speed process control screen shot. Left panel shows gas panel layout for process control with manual control of valves with scripts for preburn mixture creation based on user inputs to the right panel. Pressure and temperature feedback is provided on this interface.	69
Figure 3.8: Facility interface cabinet and additional hardware for the data acquisition and control system.	70
Figure 3.9: Data acquisition and process control diagram.....	70
Figure 3.10: ADX logged signals of CV pressure, triggers for ignition, injection and the pulse generator, spark current, and LaVision camera gate. Ignition triggered 1 second after the procedure commences yielding the preburn pressure rise followed by cool down until the desired pressure is reached, injection is triggered (2300 ms).....	71
Figure 3.11: ADX logged signals of spark current, CV pressure, and ignition trigger. The ignition trigger is 5 TTL pulses which cause the ignition coils to charge and discharge five times to ensure ignition of the preburn mixture. The first ignition trigger is sent 1 second after the procedure begins.	71
Figure 3.12: ADX logged signals of pressure, injection and pulse generator trigger along with LaVision camera gate. The injection trigger is sent at the desired pressure during the cool down phase.	72
Figure 3.13: Timing diagram for fuel injection study including camera and flashlamp synchronization.	73
Figure 3.14: High pressure air operated diesel fuel system.	74
Figure 3.15: Low pressure fuel system providing injector back pressure.	74
Figure 3.16: Piezoelectric injector used in the current study with the nozzle tip showing the injector nozzle holes in the image on the right.	76
Figure 3.17: Injector orientation properties. Plume labeling is also provided to reference the spray plumes in all discussions.	76
Figure 3.18: Piezoelectric injector, disassembled, showing all components that comprise the injector.	77
Figure 3.19: Additional piezoelectric injector assembly pictures.....	78
Figure 3.20: Start of injection spray characteristics for repeat tests at 355 K fuel temperature, 34.8 kg/m ³ bulk charge-gas density, 1100 K bulk charge gas temperature, 2000 bar injection pressure.	79
Figure 3.21: Curve fit methodology for nozzle hole, modeled as an ellipse.	80
Figure 3.22: Ellipse curve fitting result to determine hole radius, shown for SEM image set 2, hole number 5.	80
Figure 3.23: Test 2 versus test 1 mean diameter comparison.	81
Figure 3.24: Injector fuel flow path.	82

Figure 3.25: Piezoelectric injector driver interface.....	83
Figure 3.26: Left figure: Fuel pressure trace top and current and voltage injector driver signals on bottom for the injection event. Time 0 microseconds corresponds to the start of electronic injector drive. Right figure provides a zoomed in look at the injector driver traces of current and voltage at the start of injection.	83
Figure 3.27: Actual fuel injection duration relative to the trigger duration. Time in equation is in milliseconds.....	84
Figure 3.28: Injector driver correlations for open voltage (<i>A</i>), peak current (<i>B</i>) and current slope (<i>C</i>) as a function of fuel injection pressure.	85
Figure 3.29: Fuel injector pressure transducer location relative to injector.	86
Figure 3.30: Comparison of injector driver traces for identical injection conditions, spraying into 14.7 kg/m^3 at 914 bar injection pressure, 0.6 ms trigger duration. .	86
Figure 3.31: Zoomed in comparison of injector driver traces for identical injection conditions spraying into 14.7 kg/m^3 at 914 bar injection pressure 0.6 ms trigger duration.	87
Figure 3.32: Spray images at 14.7 kg/m^3 nitrogen at 914 bar injection pressure 0.6 ms trigger duration. Image is at 0.2 ms after start of injection (0.445 ms after state of current) comparing Test 1 and Test 2 injections where Test 2 has the extra current peak and larger driver voltage.....	87
Figure 3.33: Rate of Injection signal for a 2000 bar injection using the production 8-hole injector nozzle. Rate of injection is the total for all 8 spray plumes, dividing the signal by eight provides the average injection rate for a single hole. Reproduced with permission from Eric Kurtz (appendix 12.1.4).	88
Figure 3.34: <i>A</i> - Cooled injector window model. <i>B</i> – Cross section view of injector window model near injector tip showing temperature measurement location. Window edge information is removed from the images. Reproduced with permission from Chris Green (appendix 12.1.5).	89
Figure 3.35: Thermocouple (TC) probe measurement locations.	89
Figure 3.36: Injector tip temperature measurement setup.	90
Figure 3.37: Injector tip temperature map with grayed region showing extrapolated temperature data.	92
Figure 3.38: Spark ignition system setup for dual-electrode one fan window.	93
Figure 3.39: Spark ignition system wiring.....	93
Figure 3.40: EMI box for preburn spark ignition system.	94
Figure 3.41: EMI box wiring schematic.	95
Figure 3.42: Mie back scattering and shadowgraph optical layout.	97
Figure 3.43: Mie back scatter imaging setup.	98

Figure 4.1. Pressure-time and temperature-time histories of in-chamber conditions during the premixed burn, heat transfer, diesel fuel injection, and combustion. Produced ambient conditions of 21% O ₂ , density of 14.8 kg/m ³ , and temperature of 1000 K for fuel injection and combustion. τ_{CD} denotes time constant of the cool-down. Peak pressure and temperature are 74 bar and 1750 K, respectively.....	106
Figure 4.2. Experimental conditions, 458 K and 20 bar, compared with starting simulation conditions based on extent of reaction method for 21% O ₂ and 14.8 kg/m ³ premixed burn product conditions.....	107
Figure 4.3. Temperature during the cool-down comparing experimental and simulation results with modeled heat flux. Conditions for cool-down are 21% O ₂ post preburn and a density of 14.8 kg/m ³ . Time 0s corresponds to peak temperature in the premixed burn and start of cool-down.	108
Figure 4.4. Mole fractions of O ₂ , OH, NO, NO ₂ , and CO along with temperature during cool-down. Total of the minor species is also included for comparison (53 GRI species excluding CO ₂ , H ₂ O, N ₂ , O ₂ , C ₂ H ₂ and H ₂ .) Results are for the condition of 21% oxygen post-preburn and an initial elevated temperature of 963 K corresponding to a maximum temperature of 1748 K.	110
Figure 4.5. Temperature histories with three different initial temperatures, with the time shifted to match at peak temperature. Additionally, NO mole fraction time history for the three cases with peak NO values (symbols). Peak NO for the baseline, increase, and decrease cases is 13, 31, and 7 ppm, respectively.....	111
Figure 4.6. Characteristic time for NO formation in the CV for the cases of 1, 10 and 21% oxygen at a constant density of 14.8 k/m ³ compared to that for diesel engine conditions (Heywood Correlation (1988)), including Arrhenius-type curve fits for the different percent oxygen cases:.....	112
Figure 4.7. Ignition delay for <i>n</i> -heptane combustion code validation, with simulation results compared to Ciezki and Adomeit (1993) results, for stoichiometric combustion at an initial pressure of 13.5 bar, over a range of initial temperatures from 650 to 1400 K.....	113
Figure 4.8. Ignition delays for stoichiometric <i>n</i> -heptane with dry air (circle symbol, solid line), CV gas composition of 21% O ₂ (triangle symbol, dotted line), and air with 7.6% ideal residuals (square symbol, dashed line).	114
Figure 4.9. Ignition delay as a function of percent oxygen in the premixed burn products and respective percent EGR at 1000 K for the combustion vessel, compared to that of <i>n</i> -heptane in air and EGR (CO ₂ and H ₂ O), no minor species.....	118
Figure 4.10: Experimental temperature-time trace for the four preburn environments under ‘Spray A’ conditions. Time 0 seconds corresponds to the time of spark.	125
Figure 4.11: Cool-down curve fits time shifted to 900 K occurring at 0 seconds.	127
Figure 4.12: Chemical kinetics modeling of temperature time trace in Cantera for the four different preburn environments.....	128

Figure 4.13: NO – time trace from the CV preburns.	129
Figure 4.14: NO ₂ – time trace during the preburn for the four different combustion vessels.	129
Figure 4.15: OH – time trace during the preburn environment.	130
Figure 4.16: Comparison of levels of major species of carbon dioxide and water for n-heptane autoignition study.	133
Figure 4.17: Peak temperature of n-heptane autoignition as a result of different levels of major species.	133
Figure 4.18: N-heptane ignition delay variation as a result of different levels of major species.	134
Figure 4.19: Two sampling points, pre- and post- burn of the premixture.	137
Figure 4.20: Sampling setup for use of the Semtech in the CV Laboratory for preburn sampling (draw sample directly from mixing vessel into the sample bag) and post preburn sampling (draw sample which is stored in the exhaust sample cylinder into the sample bag).	138
Figure 5.1: Mie back scatter imaging setup with head-on illumination and visualization.	144
Figure 5.2: Mie scatter setup with side illumination and side view light collection showing the top view of the diagnostic setup. Camera used is Cooke DiCam Pro ICCD with Cooke SensiFlash flashlamp.	144
Figure 5.3: Laser scattering setup. Coherent Innova 90 laser at 514.5 nm, 1 W power, with a 38.1 mm expanding lens. High speed camera is Cooke DiCam Pro ICCD in double shutter mode with 60 mm Nikon Micro-Nikkor lens, f-stop 11.	145
Figure 5.4: Laser scattering image of baseline injector. Diesel spray into nitrogen at 373 K, 34.8 kg/m ³ density, 1700 bar injection pressure, 1.6 ms electronic trigger duration.	145
Figure 5.5: Projected area isosceles triangle method for determining cone angle of the spray.	147
Figure 5.6: Top and bottom cone angle method calculated at spray edge at 50 percent penetration for determining cone angle of the spray.	147
Figure 5.7: Top and bottom cone angle curve fit method calculated by linear curve fit to the spray edge from the injector tip to 50% penetration distance.	147
Figure 5.8: Cone angle results as a function of time ASOI for different definitions and methodologies.	148
Figure 5.9: Schematic of diesel fuel spray shape, shaped as a cone with a semicircle at the tip.	149
Figure 5.10: Back scattering imaging setup – Baseline B. Cooke camera is shown in setup but reflecting mirror was only used with the Photron camera.	150

Figure 5.11: Background images for back scattering setup comparison showing improved illumination and larger region of interest in the Baseline B case yielding improved images with higher signal to noise ratio.	151
Figure 5.12: Liquid phase spray parameter definitions from back scattering images. The plume penetration parameter determined from the image (L_p) must be scaled by the cosine of 15 degrees to account for the plumes leaving the injector at an angle (refer to Figure 3.17). A zoomed in view of the injector tip is shown in the right image to provide visualization of the reference point for spray parameters as the injector hole, which is offset 1.5 mm from the central injector tip.....	152
Figure 5.13: Back scattering image processing steps.	153
Figure 5.14: Back scattering images – Top set is from Baseline A setup, Bottom set is from Baseline B setup. Time after start of injection is displayed on the image. Conditions are non-vaporizing nitrogen sprays at 373 K temperature, 12.3 kg/m ³ ambient density, 914 bar fuel injection pressure with 0.6 ms drive duration.	155
Figure 5.15: Penetration (left) and cone angle (right) as a function of Time ASOI for injection at 914 bar into an ambient environment of 12.3 kg/m ³ nitrogen. Penetration data is compared to the Naber and Siebers (1996) correlation.	155
Figure 5.16: Penetration (left) and Cone angle (Right) as a function of threshold factor for BL A IP 1 results.....	156
Figure 5.17: Spray boundary (left) and edges for cone angle determination (right) as a function of threshold factor (displayed on image) overlaid on original spray image. These images correspond to Plume 1 0.6 ms ASOI.....	157
Figure 5.18: Penetration (left) and cone angle (right) as a function of threshold factor for setup Baseline A, image processing method 2.....	158
Figure 5.19: Spray boundary (left) and edges for cone angle determination (right) as a function of threshold factor (displayed on image) overlaid on original spray image. Images correspond to 0.6 ms ASOI.	158
Figure 5.20: Penetration (left) and cone angle (right) as a function of threshold factor for setup Baseline B.....	159
Figure 5.21: Spray boundary (left) and edges for cone angle determination (right) as a function of threshold factor (displayed on image) overlaid on original spray image. These images correspond to 0.6 ms ASOI.	159
Figure 5.22: Spray penetration and cone angle definitions for nonvaporizing sprays....	162
Figure 5.23: Background subtracted, rotated, cropped, and masked nonvaporizing spray image.....	163
Figure 5.24: Black and white spray image used for boundary tracing and spray property analysis.....	163
Figure 5.25: Original masked spray image with traced boundary overlaid.....	163

Figure 5.26: Spray edge definition and linear curve fits for calculating cone angle. Green lines and symbols define the cone angle at 45d ₀ , red defines the cone angle at 60% penetration, and the magenta circle at the tip of the spray defines the determined penetration.....	163
Figure 5.27: Vaporizing spray analysis, left image shows traced spray boundary and right image shows determined cone angle (green is at 45D ₀ and red is at 60% penetration), with magenta circle at the spray tip denoting penetration.	164
Figure 5.28: Combusting parameter definitions of combusting flame length, cone angle, and lift-off length.	165
Figure 5.29: Injector tip location determination.	166
Figure 5.30: Combusting image processing methodology. Green lines show cone angle at 60% penetration (the spray edge points are not shown), yellow shows the combusting flame boundary, red circle shows the location of the nozzle hole, and the magenta line defines the location of the lift-off-length.....	166
Figure 5.31: Lift-off length methodology. Top figure shows the summed radial intensity as traversing axially along the spray, along with the lift-off length threshold. Bottom image is the combusting spray plume with the determined lift-off length denoted by the vertical yellow line.	167
Figure 5.32: Example of Gaussian curve fit to spray intensity distribution data.....	168
Figure 6.1: Diesel spray images from injection pressure sweep tests, 34.8 kg/m ³ Nitrogen, 1034, 1379 and 2000 bar injection pressures, chiller off (328 k fuel temperature).	173
Figure 6.2: Median penetration as a function of time ASOI for three different injection pressures, chiller off.....	174
Figure 6.3: Median cone angle as a function of time ASOI for three different injection pressures, chiller off.....	174
Figure 6.4: Penetration at 0.1 ms ASOI for the injection pressure sweep with the chiller off.....	175
Figure 6.5: Penetration at 0.5 ms ASOI for the injection pressure sweep with the chiller off.....	175
Figure 6.6: Diesel spray images from density sweep tests, 2000 bar injection pressures, chiller off.....	176
Figure 6.7: Median penetration (left) and cone angle (right) as a function of time ASOI for the density variation, chiller off, 2000 bar injection pressure.	177
Figure 6.8: Penetration at 0.1 ms ASOI (left) and 0.5 ms ASOI (right) for the density variation with the chiller off.	177
Figure 6.9: Michigan Tech optically accessible combustion vessel with gas panels for mixture creation (Top). Internal view of combustion chamber and external view of diesel injector window (Bottom).	181

Figure 6.10: Back scattering imaging setup (Top). Injector orientation and spray plume angles (Bottom).....	182
Figure 6.11: Pressure trace showing CV premixed burn, cool down, and timing of diesel fuel injection	183
Figure 6.12: Left - Spray plume labeling, yellow dot denotes injector tip location. Right – picture of injector nozzle with select holes labeled, holes circle the entire nozzle tip in 45° increments.	184
Figure 6.13: Liquid penetration definition.....	185
Figure 6.14: Background subtracted spray images showing steady state spray characteristics for the three repeat tests at varying times ASOI. Physical scale is shown on the image.	186
Figure 6.15: Median liquid penetration as a function of time ASOI for three repeat tests.	186
Figure 6.16: Polar plots of penetration for three repeat tests, each spoke of the polar plot corresponds to physical spray plume placement.....	187
Figure 6.17: Mean steady state liquid length for three repeat tests over eight spray plumes.	188
Figure 6.18: Background subtracted spray images displayed during steady state liquid penetration stage for the charge temperatures investigated. Time ASOI and scaling is displayed.	189
Figure 6.19: Median liquid penetration as a function of time ASOI for charge gas bulk temperature sweep tests.	189
Figure 6.20: Mean experimental liquid length during steady state as a function of bulk gas temperature including error bars representing one standard deviation of liquid length. Data is compared to an expected temperature trend (Payri et al. 2008 [16]; Sandia ECN 2011 [17]) and experimental data (Siebers 1998 [8]; Sandia ECN 2011 [17]).....	190
Figure 6.21: Polar plots of plume penetration for various times ASOI (for spray development and steady state), charge temperatures 800 to 1300 K.....	191
Figure 6.22: Mean steady state liquid length (over 1 to 2 ms ASOI) for the charge temperature sweep, normalized by the mean liquid length to isolate plume influences from temperature effects.....	192
Figure 6.23: Images during the early injection portion of the three repeat tests, time ASOI displayed on image showing uneven SOI due to eccentric needle motion.....	193
Figure 6.24: Background subtracted spray images. Injection pressure sweep test: 34.8 kg/m ³ density, 0% O ₂ , 1100 K, chiller off.	196
Figure 6.25: Median penetration (liquid) as a function of time ASOI for the injection pressure sweep at 34.8 kg/m ³ density, 1100 K, 0% O ₂ , chiller off.....	196

Figure 6.26: Polar plot of normalized liquid length during steady state (1 to 2 ms ASOI), 34.8 kg/m ³ 0% O ₂ , 1100 K, chiller off.....	197
Figure 6.27: Spray images for 0% oxygen environment, 5.7 kg/m ³ bulk charge gas density, 900 K bulk charge gas temperature, 363 K fuel temperature.....	198
Figure 6.28: Median liquid penetration versus time ASOI for a sweep in injection pressure.	198
Figure 6.29: Background subtracted spray images. Charge density influence, 1100 K, 0% O ₂ , 2000 bar injection pressure.	199
Figure 6.30: Median liquid penetration as a function of time ASOI for the charge density sweep, 1100 K 0% O ₂ , 2000 bar injection pressure.....	199
Figure 6.31: Polar plot of normalized liquid length during steady state (1 to 2 ms ASOI), 0% O ₂ , 1100 K, chiller off, 2000 bar injection pressure.....	200
Figure 6.32: Ignition delay definition and determination procedure.	202
Figure 6.33: Heat release rate analysis for combusting spray tests.	203
Figure 6.34: Combusting spray images from injection pressure sweep tests, 1100 K bulk gas temperature, 34.8 kg/m ³ density.	204
Figure 6.35: Median flame length versus time ASOI for combusting spray tests, 1100 K bulk gas temperature, 34.8 kg/m ³ density. Ignition delay from pressure measurement of 0.79, 0.59 & 0.52 ms; injection pressures 1034, 1379 & 2000 bar.	204
Figure 6.36: Median cone angle versus time ASOI for combusting spray tests, 1100 K bulk gas temperature, 34.8 kg/m ³ density.	205
Figure 6.37: Median lift-off length versus time ASOI for combusting spray tests, 1100 K bulk gas temperature, 34.8 kg/m ³ density.....	205
Figure 6.38: Median combusting plume intensity versus time ASOI for combusting spray tests, 1100 K bulk gas temperature, 34.8 kg/m ³ density.....	206
Figure 6.39: Combusting spray images from tests at 2000 bar injection pressures, 1100 K bulk gas temperature, density variation.	207
Figure 6.40: Median flame length versus time ASOI for combusting spray tests, 1100 K bulk gas temperature, 2000 bar injection pressure.....	207
Figure 6.41: Median cone angle versus time ASOI for combusting spray tests, 1100 K bulk gas temperature, 2000 bar injection pressure.....	207
Figure 6.42: Median lift-off length versus time ASOI for combusting spray tests, 1100 K bulk gas temperature, 2000 bar injection pressure.....	208
Figure 6.43: Median combusting plume intensity versus time ASOI for combusting spray tests, 1100 K bulk gas temperature, 2000 bar injection pressure.....	208
Figure 6.44: Combusting spray images from tests at 2000 bar injection pressure, 34.8 kg/m ³ density.....	209

Figure 6.45: Median flame length versus time ASOI for combustng spray tests, 34.8 kg/m ³ density, 2000 bar injection pressure. Ignition delay as determined from pressure is 0.81 ms and 0.52 ms for the 950 and 1100 K charge-gas temperature cases, respectively.....	210
Figure 6.46: Median cone angle versus time ASOI for combustng spray tests, 34.8 kg/m ³ density, 2000 bar injection pressure.....	210
Figure 6.47: Median lift-off length versus time ASOI for combustng spray tests, 34.8 kg/m ³ density, 2000 bar injection pressure.	211
Figure 6.48: Median combustng plume intensity versus time ASOI for combustng spray tests, 34.8 kg/m ³ density, 2000 bar injection pressure.....	211
Figure 6.49: Mean steady state liquid length compared to the mean lift-off length for the matching 0% and 21% oxygen conditions, as labeled in the plot.....	213
Figure 6.50: Comparison of median penetration and flame length for conditions of 34.8 kg/m ³ density 1034 bar injection pressure.	214
Figure 6.51: Comparison of median penetration and flame length for conditions of 34.8 kg/m ³ density 1379 bar injection pressure.	214
Figure 6.52: Comparison of median penetration and flame length for conditions of 34.8 kg/m ³ density 2000 bar injection pressure.	214
Figure 6.53: Comparison of median penetration and flame length for conditions of 17.4 kg/m ³ density 2000 bar injection pressure.	215
Figure 7.1: Overview of the fuel and charge-gas mixing schematic for the liquid length model.....	218
Figure 7.2: Liquid length solution methodology.	219
Figure 7.3: Ratio of penetration at transition time to liquid length for conditions in Table 7.3.....	222
Figure 7.4: Liquid length versus core-gas temperature comparing model and experimental results. 34.8 kg/m ³ core charge-gas density, 2000 bar injection pressure.	225
Figure 7.5: LL model method comparison, with comparison to experimental results. Conditions corresponding to the test numbers are defined in Table 7.4 and Table 7.6.....	237
Figure 7.6: Liquid length versus core gas density with Cetane as the fuel, comparing Sandia experimental data to liquid length predictions using the Siebers model with an equation of state approach. Core gas temperatures are defined in the legend.....	238
Figure 7.7: Liquid length model results, using the equation of state approach, for various diesel single-component surrogates compared to experimental results. Bulk gas-density of 34.8 kg/m ³ , 2000 bar injection pressure, 363 K fuel temperature.	239
Figure 7.8: Liquid length results for model application using a multi-component surrogate proposed by Farrell et al. 2007 (mixture of n-decane and methylnaphthalene).	

Conditions are a charge-gas temperature sweep for 34.8 kg/m^3 bulk gas density, 2000 bar injection pressure, and 363 K fuel temperature.	242
Figure 7.9: Liquid length versus core charge-gas density for Sandia experimental data and three proposed diesel fuel surrogates (Liang et al. 2010).	243
Figure 7.10: Liquid length versus core charge-gas temperature for model surrogate to match boiling point to 90% distillation of diesel. 34.8 kg/m^3 bulk charge-gas density, 2000 bar injection pressure, and 363 K fuel temperature.	245
Figure 7.11: Liquid length versus core charge-gas density for Sandia experimental data. Conditions are a core gas temperature of 700 K, injection pressure of 130 MPa, fuel temperature of 436 K, and nozzle orifice diameter of 0.246 mm.	245
Figure 8.1: Mean steady state liquid length with error bars showing the magnitude of the maximum fluctuations in liquid length, for 34.8 kg/m^3 density, 0% oxygen, 2000 bar injection pressure, 1100 K temperature, fuel temperature 363 K.	251
Figure 8.2: Histogram of steady state liquid length. Results are for Plume 8 of a diesel spray into 0% Oxygen at 34.8 kg/m^3 bulk gas density and 1100 K bulk gas temperature, at 2000 bar injection pressure.	252
Figure 8.3: Mean steady state liquid length with error bars showing the magnitude of the average fluctuations in liquid length, for 34.8 kg/m^3 density, 0% oxygen, 2000 bar injection pressure, 1100 K temperature, 363 K fuel temperature.	253
Figure 8.4: Fuel pressure trace before, during, and after the fuel injection event, zoomed in on the injection region of interest in the right portion of the figure.	254
Figure 8.5: Fuel pressure region of interest for the FFT (left), along with FFT results (right), zoomed in to visualize the frequency peaks.	255
Figure 8.6: Tukey window with a tapering factor of 0.5, used in the current FFT analysis.	256
Figure 8.7: FFT analysis of liquid length fluctuations, including liquid penetration offset, windowing of the data, and the resultant PSD.	257
Figure 8.8: Quasi-steady penetration versus time ASOI (left) for all eight spray plumes, PSD versus frequency (right) for all eight sprays plumes. Test conditions of 2000 bar, 363 K fuel temperature, 34.8 kg/m^3 , 1100 K 0% O_2 Environment. Bottom figure provides information on the dominant mean frequencies for the mean liquid length fluctuations.	258
Figure 8.9: Influence of core charge-gas temperature on liquid length results.	262
Figure 8.10: Modeled liquid length as a result of the area contraction coefficient sweep.	263
Figure 12.1: Hole number 1, test set 1.	300
Figure 12.2: Hole number 2, test set 1.	300
Figure 12.3: Hole number 3, test set 1.	300

Figure 12.4: Hole number 4, test set 1.....	301
Figure 12.5: Hole number 5, test set 1.....	301
Figure 12.6: Hole number 6, test set 1.....	301
Figure 12.7: Hole number 7, test set 1.....	302
Figure 12.8: Hole number 8, test set 1.....	302
Figure 12.9: Hole number 1, test set 2.....	303
Figure 12.10: Hole number 2, test set 2.....	303
Figure 12.11: Hole number 3, test set 2.....	303
Figure 12.12: Hole number 4, test set 2.....	304
Figure 12.13: Hole number 5, test set 2.....	304
Figure 12.14: Hole number 6, test set 2.....	304
Figure 12.15: Hole number 7, test set 2.....	305
Figure 12.16: Hole number 8, test set 2.....	305
Figure 12.17: Preburn chemical kinetics modeling procedure.....	306
Figure 12.18: EES extent of reaction methodology.....	306
Figure 12.19: n-Heptane ignition delay modeling flow chart.....	308
Figure 12.20: Ignition delay definition used in modeling.....	309
Figure 12.21: Back scattering images for Baseline A setup (Top) and Baseline B setup (bottom) for the 34.8 kg/m ³ density case, 1700 bar injection pressure.....	395
Figure 12.22: Image processing results for penetration (left) and cone angle (right) as a function of time ASOI for the three result sets, for 34.8 kg/m ³ ambient density, 1700 bar injection pressure. Penetration correlation of the Naber and Siebers (1996) is also included in the figure.....	395
Figure 12.23: Penetration (left) and cone angle (right) as a function of threshold factor for Baseline A image processing method 1 results.....	396
Figure 12.24: Spray images showing threshold influence on penetration (left) and cone angle (right) results for BL A IP 1.....	396
Figure 12.25: Penetration (left) and cone angle (right) as a function of threshold factor for BL A IP 2 results.....	397
Figure 12.26: Spray images showing threshold influence on penetration (Top) and cone angle (Bottom) results for baseline A IP 2.....	397
Figure 12.27: Penetration (left) and cone angle (right) as a function of threshold factor for Baseline B image setup & processing method.....	398
Figure 12.28: Spray images showing threshold influence on penetration (top) and cone angle (bottom) results for Baseline B.....	398

Figure 12.29: Spray images from repeat tests, 34.8 kg/m ³ Nitrogen, 2000 bar injection pressure, chiller off.	399
Figure 12.30: Median penetration as a function of time ASOI for the three repeatability tests with the chiller off, 34.8 kg/m ³ density, 2000 bar injection pressure.	400
Figure 12.31: Median cone angle as a function of time ASOI for repeat tests, chiller off.	400
Figure 12.32: Repeat tests, chiller off, nitrogen spray penetration (left) and cone angle at 60% penetration (right) as a function of time ASOI for all 8 spray plumes, Test 1.	401
Figure 12.33: Repeat tests, chiller off, nitrogen spray penetration (left) and cone angle at 60% penetration (right) as a function of time ASOI for all 8 spray plumes, Test 2.	401
Figure 12.34: Repeat tests, chiller off, nitrogen spray penetration (left) and cone angle at 60% penetration (right) as a function of time ASOI for all 8 spray plumes, Test 3.	401
Figure 12.35: Repeat tests, chiller off, diesel spray penetration compared to the average value over all eight plumes for tests 1 and 3, 0.1 ms ASOI left figure; 0.5 ms ASOI right figure.	402
Figure 12.36: Diesel spray images from repeatability tests, 34.8 kg/m ³ nitrogen, 2000 bar injection pressure, chiller on (reduced fuel temperature).	403
Figure 12.37: Median penetration as a function of time ASOI for the three repeat tests, chiller on.	403
Figure 12.38: Median cone angle as a function of time ASOI for three repeat tests, chiller on.	404
Figure 12.39: Repeat tests, chiller on, nitrogen spray penetration (left) and cone angle at 60% penetration (right) as a function of time ASOI for all 8 spray plumes, Test 1.	404
Figure 12.40: Repeat tests, chiller on, nitrogen spray penetration (left) and cone angle at 60% penetration (right) as a function of time ASOI for all 8 spray plumes, Test 2.	405
Figure 12.41: Repeat tests, chiller on, nitrogen spray penetration (left) and cone angle at 60% penetration (right) as a function of time ASOI for all 8 spray plumes, Test 3.	405
Figure 12.42: Repeat tests, chiller off, diesel spray penetration compared to the average value over all eight plumes for tests 1 through 3, 0.1 ms ASOI in left figure; 0.5 ms ASOI in right figure.	406
Figure 12.43: Test 1, 2, and 3 at 0.5 ms ASOI comparing the individual plume values to the mean value over all eight plumes for the given test, chiller on repeat tests..	406

Figure 12.44: Repeat tests, chiller on and chiller off median penetration comparison on left, median cone angle comparison on right.	407
Figure 12.45: Chiller off, nitrogen spray penetration(left) and cone angle at 60% penetration (right) as a function of time ASOI for all 8 spray plumes, 1034 bar.	408
Figure 12.46: Chiller off, nitrogen spray penetration (left) and cone angle at 60% penetration (right) as a function of time ASOI for all 8 spray plumes, 1379 bar.	408
Figure 12.47: Chiller off, nitrogen spray penetration(left) and cone angle at 60% penetration (right) as a function of time ASOI for all 8 spray plumes, 2000 bar.	408
Figure 12.48: Diesel spray images from injection pressure sweep tests, 34.8 kg/m ³ and 373 K Nitrogen, 1034, 1379 and 2000 bar injection pressures, chiller on (reduced fuel temperature).	409
Figure 12.49: Median penetration in left figure, cone angle in right figure, as a function of time ASOI for three different injection pressures, chiller on.	410
Figure 12.50: Chiller on, nitrogen spray penetration (left) and cone angle at 60% penetration (right) as a function of time ASOI for all 8 spray plumes, 1034 bar.	410
Figure 12.51: Chiller on, nitrogen spray penetration (left) and cone angle at 60% penetration (right) as a function of time ASOI for all 8 spray plumes, 1379 bar.	411
Figure 12.52: Chiller on, nitrogen spray penetration (left) and cone angle at 60% penetration (right) as a function of time ASOI for all 8 spray plumes, 2000 bar.	411
Figure 12.53: Penetration at 0.1 ms ASOI (left) and 0.5 ms ASOI (right) for the injection pressure sweep with the chiller on.	411
Figure 12.54: Median penetration as a function of time ASOI for the injection pressure sweeps, with chiller on and chiller off.	412
Figure 12.55: Chiller off, nitrogen spray penetration as a function of time ASOI for all 8 spray plumes, 17.4 kg/m ³ , 2000 bar injection pressure.	413
Figure 12.56: Chiller off, nitrogen spray penetration as a function of time ASOI for all 8 spray plumes, 34.8 kg/m ³ , 2000 bar injection pressure.	413
Figure 12.57: Background subtracted spray images. Repeat tests: 34.8 kg/m ³ density, 0% O ₂ , 1100 K, 2000 bar injection pressure, chiller on. Scaling is preserved between images.	414
Figure 12.58: Median liquid penetration versus time ASOI for the three repeat tests at reduced fuel temperature, chiller on. 34.8 kg/m ³ , 0% O ₂ , 1100 K temperature, 2000 bar injection pressure.	415

Figure 12.59: Polar plot of liquid penetration as a function of various times ASOI, 34.8 kg/m ³ , 0% O ₂ , 2000 bar injection pressure, 1100 K, Test 1.	415
Figure 12.60: Polar plot of liquid penetration as a function of various times ASOI, 34.8 kg/m ³ , 0% O ₂ , 2000 bar injection pressure, 1100 K, Test 2.	416
Figure 12.61: Polar plot of liquid penetration as a function of various times ASOI, 34.8 kg/m ³ , 0% O ₂ , 2000 bar injection pressure, 1100 K, Test 3.	416
Figure 12.62: Polar plot of normalized liquid length during steady state (1 to 2 ms ASOI), 34.8 kg/m ³ , 0% O ₂ , 1100 K, Repeat Tests, Chiller On.	417
Figure 12.63: Combined vaporizing spray repeat results, chiller on (355 K injector temperature) and chiller off (363 K injector temperature).	417
Figure 12.64: Polar plot of liquid penetration as a function of various times ASOI, 34.8 kg/m ³ 0% O ₂ , 1034 bar injection pressure, 1100 K, chiller off.	418
Figure 12.65: Polar plot of liquid penetration as a function of various times ASOI, 34.8 kg/m ³ 0% O ₂ , 1379 bar injection pressure, 1100 K, chiller off.	418
Figure 12.66: Polar plot of liquid penetration as a function of various times ASOI, 34.8 kg/m ³ 0% O ₂ , 2000 bar injection pressure, 1100 K, chiller off.	418
Figure 12.67: Background subtracted spray images. Injection pressure sweep test: 34.8 kg/m ³ density, 0% O ₂ , 1100 K, chiller on.	419
Figure 12.68: Median penetration (liquid) as a function of time ASOI for the injection pressure sweep at 34.8 kg/m ³ density, 1100 K, 0% O ₂ , fuel chiller on.	420
Figure 12.69: Polar plot of liquid penetration as a function of various times ASOI, 34.8 kg/m ³ 0% O ₂ , 1034 bar injection pressure, 1100 K, chiller on.	420
Figure 12.70: Polar plot of liquid penetration as a function of various times ASOI, 34.8 kg/m ³ 0% O ₂ , 1379 bar injection pressure, 1100 K, chiller on.	420
Figure 12.71: Polar plot of liquid penetration as a function of various times ASOI, 34.8 kg/m ³ 0% O ₂ , 2000 bar injection pressure, 1100 K, chiller on.	421
Figure 12.72: Polar plot of normalized liquid length during steady state (1 to 2 ms ASOI), 34.8 kg/m ³ 0% O ₂ , 1100 K, chiller on.	421
Figure 12.73: Median liquid penetration as a function of time ASOI for the injection pressure sweep with both the chiller off and chiller on. 0% O ₂ , 1100 K, 34.8 kg/m ³ density.	422
Figure 12.74: Polar plot of liquid penetration as a function of various times ASOI, 17.4 kg/m ³ 0% O ₂ , 2000 bar injection pressure, 1100 K, chiller off.	422
Figure 12.75: Polar plot of liquid penetration as a function of various times ASOI, 34.8 kg/m ³ 0% O ₂ , 2000 bar injection pressure, 1100 K, chiller off.	423
Figure 12.76: Background subtracted spray images. Charge temperature sweep, 0% O ₂ , 1379 bar injection pressure, 34.8 kg/m ³ density.	424

Figure 12.77: Median liquid penetration as a function of time ASOI for the temperature sweep, 950 to 1200 K, 0% O ₂ , 34.8 kg/m ³ , 1379 bar injection pressure.	424
Figure 12.78: Polar plot of liquid penetration as a function of various times ASOI, 34.8 kg/m ³ 0% O ₂ , 1379 bar injection pressure, 950 K, chiller off.	425
Figure 12.79: Polar plot of liquid penetration as a function of various times ASOI, 34.8 kg/m ³ 0% O ₂ , 1379 bar injection pressure, 1100 K, chiller off.	425
Figure 12.80: Polar plot of liquid penetration as a function of various times ASOI, 34.8 kg/m ³ 0% O ₂ , 1379 bar injection pressure, 1200 K, chiller off.	425
Figure 12.81: Polar plot of normalized liquid length during steady state (1 to 2 ms ASOI), 34.8 kg/m ³ charge-gas density, 0% O ₂ , charge gas temperature sweep, chiller off, 1379 bar injection pressure.	426
Figure 12.82: Combusting spray images from repeat tests, 2000 bar injection pressures, 1100 K bulk gas temperature, 34.8 kg/m ³ density.	427
Figure 12.83: Median flame length versus time ASOI for combusting spray repeat tests, 2000 bar injection pressure, 1100 K bulk gas temperature, 34.8 kg/m ³ density. Computed ignition delay from pressure was an average 0.51 ms.	427
Figure 12.84: Median cone angle versus time ASOI for combusting spray repeat tests, 2000 bar injection pressure, 1100 K bulk gas temperature, 34.8 kg/m ³ density.	428
Figure 12.85: Median lift-off length versus time ASOI for combusting spray repeat tests, 2000 bar injection pressure, 1100 K bulk gas temperature, 34.8 kg/m ³ density.	428
Figure 12.86: Median combusting plume intensity versus time ASOI for combusting spray repeat tests, 2000 bar injection pressure, 1100 K bulk gas temperature, 34.8 kg/m ³ density.	428
Figure 12.87: Polar plots for Test 1 of the repeats considering plume to plume variations in flame length, cone angle, lift-off length, and total combusting intensity for 2000 bar injection pressure, 1100 K bulk gas temperature, 34.8 kg/m ³ density.	429
Figure 12.88: Polar plots for Test 2 of the repeats considering plume to plume variations in flame length, cone angle, lift-off length, and total combusting intensity for 2000 bar injection pressure, 1100 K bulk gas temperature, 34.8 kg/m ³ density.	430
Figure 12.89: Combusting spray images from injection pressure variation, 950 K bulk gas temperature, 34.8 kg/m ³ density. Computed ignition delay from pressure was 0.93 ms at 1379 bar, and 0.81 ms at 2000 bar.	431
Figure 12.90: Median flame length versus time ASOI for combusting spray tests, 950 K bulk gas temperature, 34.8 kg/m ³ density.	432
Figure 12.91: Median cone angle versus time ASOI for combusting spray tests, 950 K bulk gas temperature, 34.8 kg/m ³ density.	432
Figure 12.92: Median lift-off length versus time ASOI for combusting spray tests, 950 K bulk gas temperature, 34.8 kg/m ³ density.	433

Figure 12.93: Median combusting plume intensity versus time ASOI for combusting spray tests, 950 K bulk gas temperature, 34.8 kg/m ³ density.	433
Figure 12.94: Polar plots for 1379 bar injection pressure considering plume to plume variations in flame length, cone angle, lift-off length, and total combusting intensity for 950 K bulk gas temperature, 34.8 kg/m ³ density.....	434
Figure 12.95: Polar plots for 2000 bar injection pressure considering plume to plume variations in flame length, cone angle, lift-off length, and total combusting intensity for 950 K bulk gas temperature, 34.8 kg/m ³ density.....	435
Figure 12.96: Polar plots for 1034 bar injection pressure considering plume to plume variations in flame length, cone angle, lift-off length, and total combusting intensity for 1100 K bulk gas temperature, 34.8 kg/m ³ density.....	436
Figure 12.97: Polar plots for 1379 bar injection pressure considering plume to plume variations in flame length, cone angle, lift-off length, and total combusting intensity for 1100 K bulk gas temperature, 34.8 kg/m ³ density.....	437
Figure 12.98: Polar plots for 2000 bar injection pressure considering plume to plume variations in flame length, cone angle, lift-off length, and total combusting intensity for 1100 K bulk gas temperature, 17.4 kg/m ³ density.....	438
Figure 12.99: Combusting spray images from tests at 1379 bar injection pressure, 34.8 kg/m ³ Density, Charge gas temperature variation.	439
Figure 12.100: Median flame length versus time ASOI for combusting spray tests, 34.8 kg/m ³ density, 1379 bar injection pressure. Computed ignition delay from pressure measurements of 0.93 ms and 0.59 ms for 950 and 1100 K charge-gas temperatures, respectively.....	439
Figure 12.101: Median cone angle versus time ASOI for combusting spray tests, 34.8 kg/m ³ density, 1379 bar injection pressure.	440
Figure 12.102: Median lift-off length versus time ASOI for combusting spray tests, 34.8 kg/m ³ density, 1379 bar injection pressure.	440
Figure 12.103: Median combusting plume intensity versus time ASOI for combusting spray tests, 34.8 kg/m ³ density, 1379 bar injection pressure.	440
Figure 12.104: Mean quasi-steady liquid length with error bars showing the maximum magnitude of the fluctuations in liquid length, for 34.8 kg/m ³ density, 0% oxygen, 1034 bar injection pressure, 355 K fuel temperature, 1100 K charge gas temperature.	472
Figure 12.105: Mean quasi-steady liquid length with error bars showing the maximum magnitude of the fluctuations in liquid length, for 34.8 kg/m ³ density, 0% oxygen, 1379 bar injection pressure, 355 K fuel temperature, 1100 K charge gas temperature.	473
Figure 12.106: Mean quasi-steady liquid length with error bars showing the maximum magnitude of the fluctuations in liquid length, for 34.8 kg/m ³ density, 0% oxygen,	

2000 bar injection pressure, 355 K fuel temperature, 1100 K charge gas temperature, repeat test 1.	473
Figure 12.107: Mean quasi-steady liquid length with error bars showing the maximum magnitude of the fluctuations in liquid length, for 34.8 kg/m ³ density, 0% oxygen, 1034 bar injection pressure, 355 K fuel temperature, 1100 K charge gas temperature, repeat test 2.	473
Figure 12.108: Mean quasi-steady liquid length with error bars showing the maximum magnitude of the fluctuations in liquid length, for 34.8 kg/m ³ density, 0% oxygen, 1034 bar injection pressure, 355 K fuel temperature, 1100 K charge gas temperature, repeat test 3.	473
Figure 12.109: Mean quasi-steady liquid length with error bars showing the maximum magnitude of the fluctuations in liquid length, for 34.8 kg/m ³ density, 0% oxygen, 2000 bar injection pressure, 363 K fuel temperature, 800 K charge gas temperature.	474
Figure 12.110: Mean quasi-steady liquid length with error bars showing the maximum magnitude of the fluctuations in liquid length, for 34.8 kg/m ³ density, 0% oxygen, 2000 bar injection pressure, 363 K fuel temperature, 950 K charge gas temperature.	474
Figure 12.111: Mean quasi-steady liquid length with error bars showing the maximum magnitude of the fluctuations in liquid length, for 34.8 kg/m ³ density, 0% oxygen, 2000 bar injection pressure, 363 K fuel temperature, 1100 K charge gas temperature, repeat test 2.	474
Figure 12.112: Mean quasi-steady liquid length with error bars showing the maximum magnitude of the fluctuations in liquid length, for 34.8 kg/m ³ density, 0% oxygen, 2000 bar injection pressure, 363 K fuel temperature, 1100 K charge gas temperature, repeat test 3.	474
Figure 12.113: Mean quasi-steady liquid length with error bars showing the maximum magnitude of the fluctuations in liquid length, for 34.8 kg/m ³ density, 0% oxygen, 2000 bar injection pressure, 363 K fuel temperature, 1200 K charge gas temperature.	475
Figure 12.114: Mean quasi-steady liquid length with error bars showing the maximum magnitude of the fluctuations in liquid length, for 34.8 kg/m ³ density, 0% oxygen, 2000 bar injection pressure, 363 K fuel temperature, 1300 K charge gas temperature.	475
Figure 12.115: Mean quasi-steady liquid length with error bars showing the maximum magnitude of the fluctuations in liquid length, for 17.4 kg/m ³ density, 0% oxygen, 2000 bar injection pressure, 363 K fuel temperature, 1100 K charge gas temperature.	475
Figure 12.116: Mean quasi-steady liquid length with error bars showing the maximum magnitude of the fluctuations in liquid length, for 34.8 kg/m ³ density, 0% oxygen,	

1034 bar injection pressure, 363 K fuel temperature, 1100 K charge gas temperature.	476
Figure 12.117: Mean quasi-steady liquid length with error bars showing the maximum magnitude of the fluctuations in liquid length, for 34.8 kg/m ³ density, 0% oxygen, 1379 bar injection pressure, 363 K fuel temperature, 950 K charge gas temperature.	476
Figure 12.118: Mean quasi-steady liquid length with error bars showing the maximum magnitude of the fluctuations in liquid length, for 34.8 kg/m ³ density, 0% oxygen, 1379 bar injection pressure, 363 K fuel temperature, 1100 K charge gas temperature.	476
Figure 12.119: Mean quasi-steady liquid length with error bars showing the maximum magnitude of the fluctuations in liquid length, for 34.8 kg/m ³ density, 0% oxygen, 1379 bar injection pressure, 363 K fuel temperature, 1200 K charge gas temperature.	476
Figure 12.120: Mean quasi-steady liquid length with error bars showing the average magnitude of the fluctuations in liquid length, for 34.8 kg/m ³ density, 0% oxygen, 1034 bar injection pressure, 355 K fuel temperature, 1100 K charge gas temperature.	477
Figure 12.121: Mean quasi-steady liquid length with error bars showing the average magnitude of the fluctuations in liquid length, for 34.8 kg/m ³ density, 0% oxygen, 1379 bar injection pressure, 355 K fuel temperature, 1100 K charge gas temperature.	477
Figure 12.122: Mean quasi-steady liquid length with error bars showing the average magnitude of the fluctuations in liquid length, for 34.8 kg/m ³ density, 0% oxygen, 2000 bar injection pressure, 355 K fuel temperature, 1100 K charge gas temperature, repeat test 1.	478
Figure 12.123: Mean quasi-steady liquid length with error bars showing the average magnitude of the fluctuations in liquid length, for 34.8 kg/m ³ density, 0% oxygen, 1034 bar injection pressure, 355 K fuel temperature, 1100 K charge gas temperature, repeat test 2.	478
Figure 12.124: Mean quasi-steady liquid length with error bars showing the average magnitude of the fluctuations in liquid length, for 34.8 kg/m ³ density, 0% oxygen, 1034 bar injection pressure, 355 K fuel temperature, 1100 K charge gas temperature, repeat test 3.	478
Figure 12.125: Mean quasi-steady liquid length with error bars showing the average magnitude of the fluctuations in liquid length, for 34.8 kg/m ³ density, 0% oxygen, 2000 bar injection pressure, 363 K fuel temperature, 800 K charge gas temperature.	478
Figure 12.126: Mean quasi-steady liquid length with error bars showing the average magnitude of the fluctuations in liquid length, for 34.8 kg/m ³ density, 0% oxygen,	

2000 bar injection pressure, 363 K fuel temperature, 950 K charge gas temperature.	479
Figure 12.127: Mean quasi-steady liquid length with error bars showing the average magnitude of the fluctuations in liquid length, for 34.8 kg/m ³ density, 0% oxygen, 2000 bar injection pressure, 363 K fuel temperature, 1100 K charge gas temperature, repeat test 2.	479
Figure 12.128: Mean quasi-steady liquid length with error bars showing the average magnitude of the fluctuations in liquid length, for 34.8 kg/m ³ density, 0% oxygen, 2000 bar injection pressure, 363 K fuel temperature, 1100 K charge gas temperature, repeat test 3.	479
Figure 12.129: Mean quasi-steady liquid length with error bars showing the average magnitude of the fluctuations in liquid length, for 34.8 kg/m ³ density, 0% oxygen, 2000 bar injection pressure, 363 K fuel temperature, 1200 K charge gas temperature.	479
Figure 12.130: Mean quasi-steady liquid length with error bars showing the average magnitude of the fluctuations in liquid length, for 34.8 kg/m ³ density, 0% oxygen, 2000 bar injection pressure, 363 K fuel temperature, 1300 K charge gas temperature.	480
Figure 12.131: Mean quasi-steady liquid length with error bars showing the average magnitude of the fluctuations in liquid length, for 17.4 kg/m ³ density, 0% oxygen, 2000 bar injection pressure, 363 K fuel temperature, 1100 K charge gas temperature.	480
Figure 12.132: Mean quasi-steady liquid length with error bars showing the average magnitude of the fluctuations in liquid length, for 34.8 kg/m ³ density, 0% oxygen, 1034 bar injection pressure, 363 K fuel temperature, 1100 K charge gas temperature.	480
Figure 12.133: Mean quasi-steady liquid length with error bars showing the average magnitude of the fluctuations in liquid length, for 34.8 kg/m ³ density, 0% oxygen, 1379 bar injection pressure, 363 K fuel temperature, 950 K charge gas temperature.	481
Figure 12.134: Mean quasi-steady liquid length with error bars showing the average magnitude of the fluctuations in liquid length, for 34.8 kg/m ³ density, 0% oxygen, 1379 bar injection pressure, 363 K fuel temperature, 1100 K charge gas temperature.	481
Figure 12.135: Mean quasi-steady liquid length with error bars showing the average magnitude of the fluctuations in liquid length, for 34.8 kg/m ³ density, 0% oxygen, 1379 bar injection pressure, 363 K fuel temperature, 1200 K charge gas temperature.	481
Figure 12.136: Quasi-steady penetration versus time ASOI (Left) for all eight spray plumes, PSD versus frequency (Right) for all eight sprays plumes. Test conditions of 1034 Bar, 355 K fuel temperature, 34.8 kg/m ³ , 1100 K 0% O ₂ environment.	

Bottom figure provides information on the dominant mean frequencies for the mean liquid length fluctuations.....	482
Figure 12.137: Quasi-steady penetration versus time ASOI (Left) for all eight spray plumes, PSD versus frequency (Right) for all eight sprays plumes. Test conditions of 1379 Bar, 355 K fuel temperature, 34.8 kg/m ³ , 1100 K 0% O ₂ environment. Bottom figure provides information on the dominant mean frequencies for the mean liquid length fluctuations.....	483
Figure 12.138: Quasi-steady penetration versus time ASOI (Left) for all eight spray plumes, PSD versus frequency (Right) for all eight sprays plumes. Test conditions of 2000 Bar, 355 K fuel temperature, 34.8 kg/m ³ , 1100 K 0% O ₂ environment, Repeat test 1. Bottom figure provides information on the dominant mean frequencies for the mean liquid length fluctuations.....	484
Figure 12.139: Quasi-steady penetration versus time ASOI (Left) for all eight spray plumes, PSD versus frequency (Right) for all eight sprays plumes. Test conditions of 2000 Bar, 355 K fuel temperature, 34.8 kg/m ³ , 1100 K 0% O ₂ environment, Repeat test 2. Bottom figure provides information on the dominant mean frequencies for the mean liquid length fluctuations.....	485
Figure 12.140: Quasi-steady penetration versus time ASOI (Left) for all eight spray plumes, PSD versus frequency (Right) for all eight sprays plumes. Test conditions of 2000 Bar, 355 K fuel temperature, 34.8 kg/m ³ , 1100 K 0% O ₂ environment, Repeat test 3. Bottom figure provides information on the dominant mean frequencies for the mean liquid length fluctuations.....	486
Figure 12.141: Quasi-steady penetration versus time ASOI (Left) for all eight spray plumes, PSD versus frequency (Right) for the first spray plume. Test conditions of 2000 Bar, 355K fuel temperature, 34.8 kg/m ³ , 1100 K 0% O ₂ environment, high frame rate (216,000 fps frame rate).	487
Figure 12.142: Quasi-steady penetration versus time ASOI (Left) for all eight spray plumes, PSD versus frequency (Right) for all eight sprays plumes. Test conditions of 2000 Bar, 363 K fuel temperature, 34.8 kg/m ³ , 800 K 0% O ₂ environment. Bottom figure provides information on the dominant mean frequencies for the mean liquid length fluctuations.....	487
Figure 12.143: Quasi-steady penetration versus time ASOI (Left) for all eight spray plumes, PSD versus frequency (Right) for all eight sprays plumes. Test conditions of 2000 Bar, 363 K fuel temperature, 34.8 kg/m ³ , 950 K 0% O ₂ environment. Bottom figure provides information on the dominant mean frequencies for the mean liquid length fluctuations.....	488
Figure 12.144: Quasi-steady penetration versus time ASOI (Left) for all eight spray plumes, PSD versus frequency (Right) for all eight sprays plumes. Test conditions of 2000 Bar, 363 K fuel temperature, 34.8 kg/m ³ , 1100 K 0% O ₂ environment, Repeat test 1. Bottom figure provides information on the dominant mean frequencies for the mean liquid length fluctuations.....	489

- Figure 12.145: Quasi-steady penetration versus time ASOI (Left) for all eight spray plumes, PSD versus frequency (Right) for all eight sprays plumes. Test conditions of 2000 Bar, 363 K fuel temperature, 34.8 kg/m^3 , 1100 K 0% O_2 environment, Repeat test 2. Bottom figure provides information on the dominant mean frequencies for the mean liquid length fluctuations..... 490
- Figure 12.146: Quasi-steady penetration versus time ASOI (Left) for all eight spray plumes, PSD versus frequency (Right) for all eight sprays plumes. Test conditions of 2000 Bar, 363 K fuel temperature, 34.8 kg/m^3 , 1100 K 0% O_2 environment, Repeat test 3. Bottom figure provides information on the dominant mean frequencies for the mean liquid length fluctuations..... 491
- Figure 12.147: Quasi-steady penetration versus time ASOI (Left) for all eight spray plumes, PSD versus frequency (Right) for all eight sprays plumes. Test conditions of 2000 Bar, 363 K fuel temperature, 34.8 kg/m^3 , 1200 K 0% O_2 environment. Bottom figure provides information on the dominant mean frequencies for the mean liquid length fluctuations..... 492
- Figure 12.148: Quasi-steady penetration versus time ASOI (Left) for all eight spray plumes, PSD versus frequency (Right) for all eight sprays plumes. Test conditions of 2000 Bar, 363 K fuel temperature, 34.8 kg/m^3 , 1300 K 0% O_2 environment. Bottom figure provides information on the dominant mean frequencies for the mean liquid length fluctuations..... 493
- Figure 12.149: Quasi-steady penetration versus time ASOI (Left) for all eight spray plumes, PSD versus frequency (Right) for all eight sprays plumes. Test conditions of 2000 Bar, 363 K fuel temperature, 17.4 kg/m^3 , 1100 K 0% O_2 environment. 494
- Figure 12.150: Quasi-steady penetration versus time ASOI (Left) for all eight spray plumes, PSD versus frequency (Right) for all eight sprays plumes. Test conditions of 1034 Bar, 363 K fuel temperature, 34.8 kg/m^3 , 1100 K 0% O_2 environment. 495
- Figure 12.151: Quasi-steady penetration versus time ASOI (Left) for all eight spray plumes, PSD versus frequency (Right) for all eight sprays plumes. Test conditions of 1379 Bar, 363 K fuel temperature, 34.8 kg/m^3 , 950 K 0% O_2 environment.. 496
- Figure 12.152: Quasi-steady penetration versus time ASOI (Left) for all eight spray plumes, PSD versus frequency (Right) for all eight sprays plumes. Test conditions of 1379 Bar, 363 K fuel temperature, 34.8 kg/m^3 , 1100 K 0% O_2 environment. 497
- Figure 12.153: Quasi-steady penetration versus time ASOI (Left) for all eight spray plumes, PSD versus frequency (Right) for all eight sprays plumes. Test conditions of 1379 Bar, 363 K fuel temperature, 34.8 kg/m^3 , 1200 K 0% O_2 environment. 498

List of Tables

Table 1.1 Liquid length and lift-off length trends.....	7
Table 2.1 Evaluation of different apparatuses for studying fundamental spray and combustion. Scale: + signifies a benefit, - signifies a disadvantage, 0 signifies no definite advantage or disadvantage.	20
Table 2.2 Spray penetration correlations.	24
Table 2.3 Penetration parameter influence (Arregle et al. 1999; Martinez-Martinez et al. 2010).	24
Table 2.4 Select liquid length correlations.	26
Table 2.5 Liquid length parameter influence (Siebers 2008; Kook et al. 2009; Martinez-Martinez et al. 2010).	26
Table 2.6 Correlations for cone angle.	29
Table 2.7 Cone angle parameter influence (Arregle et al. 1999; Martinez-Martinez et al. 2010).	30
Table 2.8 Lift-off length parameter influence (Higgins and Siebers 2001; Siebers and Higgins 2001).	30
Table 2.9 Comparison of CFD and 1-D spray models (Aneja and Abraham 1998; Pastor et al. 2008; Kook et al. 2009).	34
Table 2.10 Overview of conservation equation methodology spray models.	35
Table 2.11 Chemical formula and structure groups of suggested diesel surrogate components.	53
Table 2.12 Select diesel surrogate fuel recommendations.	54
Table 2.13 Equations of state (Martin 1979; Wei and Sadus 2000; Slavinskaya et al. 2010).	56
Table 2.14 Mixing rules for determining a and b from cubic equation of state (generalized).	58
Table 3.1 Fuel property specifications as obtained from experimental testing. ^a Paragon Laboratories Inc. Fuel Testing, December 2010, Report ID: 176559-861958. ^b Cummins Fuel Property Testing, September 2010.	75
Table 3.2 SEM image analysis results for hole diameter, test set 1 and 2.	81
Table 3.3 Injector driver settings used in testing.	85
Table 3.4 Temperature mapping data.	91
Table 3.5 Components for EMI box ignition system.	95

Table 3.6 Spark ignition system troubleshooting modifications and observations, using the new EMI box.....	96
Table 3.7 Image acquisition settings for different ambient environments.....	98
Table 4.1 NO and NO ₂ levels during cool-down in comparison to equilibrium mole fractions at peak temperature. ^a <i>Peak NO₂ corresponds to the end of the simulation.</i>	111
Table 4.2 Mole fractions of carbon dioxide, water, and nitrogen for the given percent oxygen cases used to investigate the characteristic time scales for NO formation.	112
Table 4.3 Ignition delay of stoichiometric mixtures of <i>n</i> -heptane with ambient gases for 21% O ₂ at 1000 K and 42 bar, along with percent deviation of ignition delay relative to dry air baseline. <i>*Baseline CV Case.</i>	115
Table 4.4 Ignition delay of stoichiometric mixtures of <i>n</i> -heptane with CV ambient gases for 19% O ₂ at 1000 K and 42 bar, along with percent deviation of ignition delay relative to air with 7.6% ideal residuals (CO ₂ and H ₂ O, 19% O ₂) as the baseline. <i>*Baseline CV Case.</i>	115
Table 4.5 Stoichiometric <i>n</i> -heptane ignition delay relative to minor species concentrations over the temperature range of 850 - 1200 K with 21% O ₂ in comparison to dry-air. ^a CV mixtures have a baseline steady-state level of 12 ppm NO and 2 ppm NO ₂ . ^b Minor species of OH, NO, and NO ₂ are adjusted by 1/10 and 10X, respectively, for sensitivity analysis. ^c Changes in ignition delay are relative to the CV baseline mixture (CV-BL).	116
Table 4.6 Impact of minor species concentrations on <i>n</i> -heptane ignition delay in comparison to baseline equal to 0.77 ms. Temperature is 1000 K for a 21% oxygen combustion vessel post-preburn environment.....	116
Table 4.7 Volume percent EGR (representing the total of EGR and internal residual gases) at time of diesel combustion at an excess air ratio, $\lambda = 1.372$, over a range of percent O ₂ cases	117
Table 4.8 Ignition delay for stoichiometric mixtures of <i>n</i> -heptane in the combustion vessel for the 9- 21% oxygen cases investigated in Figure 4.9, along with CO ₂ , H ₂ O, NO _x and OH mole fractions, to characterize the influence of minor species mole fractions for different percent oxygen cases on ignition delay. The combustion vessel case is compared to that of <i>n</i> -heptane plus air and ideal EGR, with no minor species present (NO _x and OH are zero). The ambient gas temperature is 1000 K.	119
Table 4.9 ‘Spray A’ environment of institutions post preburn, 15% oxygen environment at spray injection.	123
Table 4.10 ‘Spray A’ institution preburn mixture composition comparison	124
Table 4.11 CV fan speed comparisons.	125

Table 4.12 Cool-down curve fit parameters and decay times. *The experimental time from spark to peak temperature is estimated based on 0% and 21% O ₂ data at 17.4 and 34.8 kg/m ³ density.....	126
Table 4.13 EES initial conditions from extent of reaction calculation. <i>X</i> is species mole fraction.	127
Table 4.14 Equilibrium levels of minor species of interest formed during the preburn event. Calculated at the initial CV heated temperature.....	130
Table 4.15 Preburn kinetics modeling output results for conditions at injection. Temperature of 900 K, density of 22.8 kg/m ³	131
Table 4.16 Ignition delay of stoichiometric n-heptane and peak n-heptane combustion temperature for constant pressure and enthalpy reactor modeling at ‘Spray A’ conditions (15% O ₂ , 900 K, 60 Bar – 22.8 kg/m ³ Density).	132
Table 4.17 Comparison of the autoignition modeling results considering the influence of major species.....	135
Table 4.18 Gas sampling mixture composition for the original 0% oxygen mixture.....	138
Table 4.19 Ideal, complete, combustion products of the 0% oxygen mixture.....	139
Table 4.20 Mixture composition testing, pre and post preburn, for a 0% oxygen mixture.	139
Table 4.21 Comparison of original and modified 0% oxygen mixtures.....	141
Table 5.1 Back scattering imaging setup and processing specifications. Differences are underlined. *Although Baseline B injector images were acquired with a 0.1 ms inter-frame time, results presented here are typically only shown in 0.2 ms increments to match Baseline A image timings.....	151
Table 5.2 Set-point test conditions. *Injector electronic drive duration for baseline B was reduced from 1.6 to 1.0 ms to minimize fuel spray impingement on windows..	152
Table 5.3 Key method differences of the three image processing methods.	154
Table 5.4 Summary of the impact of threshold factor on penetration and cone angle results, for 12.3 kg/m ³ ambient density.	160
Table 5.5 Summary of the impact of threshold factor on penetration and cone angle results, for 34.8 kg/m ³ ambient density, injection pressure of 1700 bar.....	160
Table 6.1 Non-vaporizing sprays test matrix.....	172
Table 6.2 Injection pressure sweep test conditions, chiller off.....	173
Table 6.3 Charge density sweep conditions – chiller off.....	176
Table 6.4 Vaporizing sprays test matrix.	179
Table 6.5 Test matrix with experimental conditions for bulk and core charge density and temperature, as well as injection pressure.....	183
Table 6.6 Ambient conditions at injection – fuel pressure sweep, chiller off.	195

Table 6.7 Ambient conditions at injection – ambient density variation.	199
Table 6.8 Test matrix for combustng spray tests.	203
Table 6.9 Combusting test conditions for injection pressure sweep at 1100 K bulk gas temperature	204
Table 6.10 Combusting test conditions for density variation at 1100 K bulk gas temperature and 2000 bar injection pressure.	206
Table 6.11 Combusting test conditions for charge gas temperature variation at 2000 bar injection pressure and 34.8 kg/m ³ charge gas bulk density.	209
Table 7.1 Constants used in transition time evaluation.	220
Table 7.2 Transition time for various conditions. *Calculated using the long-time scale relationship (equation (71)).....	221
Table 7.3 Comparing penetration at transition to the mean liquid length over a range of conditions.....	221
Table 7.4 Liquid length as determined from evaluation of Siebers (1999) model using cetane as a surrogate for diesel fuel.	224
Table 7.5 Critical properties of the species composing the ambient charge gas (Reid et al. 1987).	230
Table 7.6 Liquid length as determined from evaluation of Siebers (1999) model using cetane as a surrogate for diesel fuel, equation of state approach.	235
Table 7.7 Additional properties determined from evaluation of Siebers (1999) model using cetane as a surrogate for diesel fuel, equation of state approach.	236
Table 7.8 Single-component surrogate fuel properties of boiling point (Schihl et al. 2006) and latent heat of vaporization from EES model evaluation.	240
Table 7.9 Multi-component surrogate fuels as proposed by Liang et al. 2010. Boiling point data from Reid et al. 1987.....	243
Table 8.1 Maximum quasi-steady liquid length increase and decrease relative to the mean value, in % terms, for all vaporizing spray tests. High FPS indicates the higher frame rate of 216,000 frames per second, R indicates repeat tests.	251
Table 8.2 Average quasi-steady liquid length increase and decrease relative to the mean value, in % terms, for all vaporizing spray tests.	253
Table 8.3 Fuel pressure FFT results.....	255
Table 8.4 Dominant frequency components resulting from PSD analysis, Mean Results.	259
Table 8.5 Liquid length fluctuation hypotheses, model results, and conclusions.....	265
Table 12.1 Repeatability test conditions, chiller off.	399
Table 12.2 Repeatability test conditions, chiller on.....	403

Table 12.3 Injection pressure sweep test conditions – chiller on, 373 K Nitrogen charge-gas conditions.....	409
Table 12.4 Ambient conditions at injection.....	414
Table 12.5 Ambient conditions at injection – injection pressure sweep – chiller on.	419
Table 12.6 Ambient conditions at injection – charge temperature sweep at 1379 Bar. .	423
Table 12.7 Combusting repeat tests.....	426
Table 12.8 Combusting test conditions for injection pressure variation at 950 K bulk gas temperature.	431
Table 12.9 Combusting test conditions for charge gas temperature variation at 1379 bar injection pressure and 34.8 kg/m ³ charge gas bulk density.	438
Table 12.10 Variable guesses, units, and lower and upper limits for the LL model evaluation, using tabulated thermodynamic properties.	449
Table 12.11 Variable guesses, units, and lower and upper limits for the LL model evaluation, using tabulated thermodynamic properties.	461
Table 12.12 General fuel properties (Reid et al. 1987). *Data from Poling et al. 2001. Diesel fuel properties from AFDC 2010a.....	463
Table 12.13 Fuel properties for Equation of State Modeling (Reid et al. 1987). n/a signifies data not available / tabulated. *Data from Poling et al. 2001. ^Data from Schihl et al. 2006.....	463
Table 12.14 Ideal gas constant pressure specific heat capacity polynomial constants (McBride et al. 1993, Smith 1999).	464
Table 12.14 Ideal gas constant pressure specific heat capacity polynomial constants for fuels (Reid et al. 1987). *Data from LLNL heptamethylnonae mechanism.....	464
Table 12.16 Dominant frequency components resulting from PSD analysis, Plume 1..	499
Table 12.17 Dominant frequency components resulting from PSD analysis, Plume 2..	499
Table 12.18 Dominant frequency components resulting from PSD analysis, Plume 3..	500
Table 12.19 Dominant frequency components resulting from PSD analysis, Plume 4..	500
Table 12.20 Dominant frequency components resulting from PSD analysis, Plume 5..	501
Table 12.21 Dominant frequency components resulting from PSD analysis, Plume 6..	501
Table 12.22 Dominant frequency components resulting from PSD analysis, Plume 7..	502
Table 12.23 Dominant frequency components resulting from PSD analysis, Plume 7..	502

Preface

Included in Chapter 4 and Chapter 6 are a journal article and conference proceeding, respectively, reproduced in their entirety. Both of these are multi-author papers, for which I have been the lead contributor and author. In the *Energy and Fuels* journal paper provided in Chapter 4.2, I was responsible for developing and running all model simulations. Furthermore, I wrote the journal paper which presented and discussed the modeling results, with co-authors providing feedback and suggestions on the paper including both grammar and theory. In Chapter 6.2.1, a paper I presented at the *ILASS 2011 Conference* is included. For this paper I performed the experimental testing in conjunction with other graduate students, wrote the image processing code and undertook all data analysis independently. I also authored the paper, incorporating comments from other co-authors on grammar and theory. Additional publications are in progress as the result of this work, with one discussed briefly in Chapter 5.4.4, to be presented at the ASME Internal Combustion Engine Division Fall Technical Conference in October 2011. I am the lead author on this paper, for which I performed the experimental testing in conjunction with other graduate students and undertook all analysis and processing methodology development, independently. I also wrote the paper with feedback from coauthors.

Acknowledgements

Acknowledgement is provided to Ford Motor Company for their funding of portions of this experimental work. Additional acknowledgement is provided to Motion Engineering for the loan of a high speed camera used in this study. Further acknowledgement is given to the National Science Foundation (NSF) for the funding of Major Research Instrumentation (MRI) grant number 0619585 for the development of this optically accessible combustion vessel laboratory. Acknowledgement is also given to A&D Technology for their assistance in providing the data acquisition system.

I would also like to give acknowledgement to the funding I received for my graduate education at Michigan Technological University in pursuance of my doctoral degree. This includes funding from the National Science Foundation (NSF) Integrative Graduate Education and Research Traineeship (IGERT) as an associate, grant number DGE 0333401, in conjunction with the MTU Sustainable Futures Institute (SFI), funding through a graduate fellowship from Chrysler, funding from research programs through Dr. Jeffrey Naber, and funding from the Michigan Technological University Winnikow Fellowship.

I would like to thank my research advisor, Dr. Jeffrey Naber, for all of his support and guidance while pursuing my graduate education. I learned so much during this time and am largely successful because of your guidance and encouragement. You have been a great and understanding research advisor, and your support has been instrumental in my research success.

I would also like to acknowledge my committee members, Dr. Lee, Dr. Miers, and Dr. Shonnard, for taking the time to serve on my committee and be involved in my graduate education. I would also like to thank fellow members of the Advanced Internal Combustion Engines (AICE) research group for their support through the years, and fellow combustion vessel laboratory members, both past and present.

I would also like to acknowledge my family, including my parents Mark and Barbara, sister Danielle and brother Jason, for their support throughout the years. You have always been there for me when things have become frustrating and overwhelming, and I really appreciate your faith in me succeeding at all of my endeavors. A special thank you to my mom for proofreading all of my writings, I sincerely appreciate it.

Finally I would like to acknowledge my husband, Jack, your support has been instrumental in my success. Thank you for putting up with my constant expressions of frustrations, and being patient as I have worked to complete this dissertation. I am really grateful of your support and encouragement, even though I may not have always showed it. Without you, I would not be completing this dissertation as I am today.

Nomenclature

Included in nomenclature definitions are the dimensional units, L for length, M for mass, T for time, and Q for temperature.

α	Velocity (LT^{-1}) or fuel volume fraction profile factor Full cone angle of the model spray Gaussian distribution shape factor Extent of reaction variable Equation of state parameter Cubic Equation of State Parameters
$\alpha(T), \beta, \delta(T), \gamma, \varepsilon, a,$ b, η	
Δ	Air-fuel mass ratio (equivalent to 1/B Siebers 1999)
γ	Gamma, ratio of specific heats, assumed 1.35 for diesel conditions
κ	Equation of state parameter, function of acentric factor
λ	Lambda – excess air ratio
μ	Absolute viscosity ($ML^{-1}T^{-1}$) Mean of the Gaussian Curve Fit – Location of the Peak Intensity
ρ	Density (ML^{-3})
$\bar{\rho}$	Mean axial density (ML^{-3})
φ	Fugacity ($ML^{-1}T^{-2}$)
ξ	Non-dimensional radial coordinate, ratio of radial coordinate to jet width
Σ	Standard deviation of the Gaussian Curve fit intensity distribution
τ_{ID}	Ignition delay (ms)
θ	Cone / Spray angle
ω	Acentric factor
ζ	Self-similar axial velocity profile
a	Parameter for determining core to bulk gas temperature relationship Equation of state constant Heat transfer curve fit coefficient Constant in Siebers LL model, 0.66
a_i	Polynomial constants for ambient ideal gas constant pressure specific heat capacity
ac	Model Constant
a, b, m, n	Cone angle correlation superscript constants
A	Area (L^2) Equation of State Constant (Cubic in compressibility) Matrix used in curve fit temperature mapping Peak magnitude of the Gaussian Curve Fit Intensity Distribution
$A_{Cpf}, B_{Cpf}, C_{Cpf}, D_{Cpf}$	Polynomial constants for fuel ideal gas constant pressure specific heat capacity
ASOC	Time after start of driver current (T)
ASOI	Time after start of injection (fuel) (T)
b	Constant for determining core to bulk gas temperature relationship, 0.026 Equation of state constant Constant in Siebers LL model: 0.41 Heat transfer curve fit coefficient

B	Evaporation coefficient Equation of State Constant (Cubic in compressibility) Matrix used in curve fit temperature mapping
c	Heat transfer curve fit coefficient
B, C, D	Virial equation of state coefficients
C	Curve fit constant for temperature mapping, combustion vessel temperature parameter
C1	Experimental constant
C2	Constant for nonvaporizing or vaporizing jets
C _a	Area contraction coefficient, ratio of actual fuel stream area to nozzle hole area.
C _d	Discharge coefficient, ratio of actual mass injected to ideal mass injected (Bernoulli)
C _p	Constant pressure specific heat capacity ($ML^2T^{-2}Q^{-1}$)
C _v	Velocity coefficient, ratio of actual injection velocity to ideal (Bernoulli) injection velocity
Constant	Constant in heat transfer, represents convective heat transfer coefficient
d _e	Equivalent diameter (L)
d _f	Effective nozzle diameter (L)
d _h	Injector hydraulic diameter (L)
d _o	Injector Nozzle Hole Diameter (L)
D	Curve fit constant for temperature mapping, heater set-point parameter Sack chamber diameter of the nozzle (L)
E	Curve fit constant for temperature mapping Energy ($ML^2T^{-2}Q^{-1}$)
ECN	Engine Combustion Network
EGR	Exhaust Gas Recirculation
f	Fuel mass fraction Fugacity ($ML^{-1}T^{-2}$)
f _e	Enhancement factor
g	Gravity (LT^{-2})
h	Enthalpy (ML^2T^{-2})
Δh _v	Enthalpy of vaporization (ML^2T^{-2})
H	Energy (ML^2T^{-2})
I	Intensity distribution along spray cross section
I _{offset}	Offset of the Gaussian curve fit intensity distribution from intensity equal zero.
K	Spray constant
L	Hole length (L)
L _v	Heat of vaporization (L^2T^{-2})
LL	Liquid length (L)
m	Mass or void fraction
\dot{m}	Mass flowrate (MT^{-1})
M	Momentum (MLT^{-1}) Matrix used in curve fit temperature mapping
\dot{M}	Momentum flowrate (MLT^{-2})
MW	Molecular weight

n or N	Moles
P	Pressure ($\text{ML}^{-1}\text{T}^{-2}$)
ΔP	Injection pressure to back pressure differential ($\text{ML}^{-1}\text{T}^{-2}$)
P_{O_2}	Desired percent oxygen post preburn (%)
Q	Heat transfer
\dot{Q}	Combust heat release ($\text{ML}^2\text{T}^{-2}\text{Q}^{-1}$)
\dot{Q}	Heat flux (MT^{-3})
r	Radial location along the spray jet (L)
R	Radius of spray – jet width (L)
	Ideal Gas Constant
	Ratio of hydrogen to carbon atoms in the fuel
Re	Reynolds number
S	Penetration (L)
t	Time (T)
T	Temperature (Q)
T_{bulk}	CV bulk gas temperature (Q)
T_{core}	CV core gas temperature (Q)
T_{CV}	Combustion vessel heated temperature (Q)
T_{setpoint}	Heater setpoint temperature (Q)
T_{tip}	CV tip temperature (Q)
T_{wall}	CV wall (heated) temperature (Q)
\bar{u}	Mean axial velocity (LT^{-1})
$\bar{\bar{u}}$	Cross-sectionally averaged turbulent mean axial velocity (LT^{-1})
U	Velocity (LT^{-1})
	Internal Energy (ML^2T^{-2})
v	Specific volume (L^3M^{-1})
	Velocity (LT^{-1})
V	Volume (L^3)
	CV Volume, 1.1 L
\dot{W}	Work (ML^2T^{-2})
We	Weber number
x	Number of carbon atoms in the fuel
	Axial location along spray (L)
Δx	Spray cross section thickness (L)
x^+	Spray penetration length scale (L)
\tilde{x}	Dimensionless axial distance
X	Matrix used in curve fit temperature mapping
	Mass fraction
X_f	Fuel volume fraction
Y	Mole fraction
	Distance across radial spray profile
Y_{fg}	Vapor fuel mass fraction in the gas phase
z	Axial location along spray (L) or height for potential energy conservation (L)
z'	Axial location along spray from virtual jet origin (L)
Z	Compressibility
Z_{ra}	Rackett parameter

Subscripts

a	Ambient
Actual	Actual properties
Ad	Adiabatic conditions
b	Break-up (Transition time between fuel to charge gas medium dominance)
	Boiling point property
	Bernoulli (Ideal)
c	Centerline or Critical Property
cv	Control volume
CV	Combustion Vessel Conditions
e	Entrainment or exit conditions
Elevated	Elevated temperature / pressure / partially reacted conditions
evap	Conditions at evaporation
f	Fuel (liquid)
fl	Fuel in the liquid phase
fg	Fuel in the vapor phase
g	Gas phase
i, j	Species index
	Inlet conditions
	Cross section region
l	Liquid
in	Inlet
m / mix	Mixture
out	Outlet
o	Initial
Products / p	Product species (post preburn)
Reactants / r	Reactant species (before preburn)
r	Reduced properties
	Transition time
Ref	Reference Conditions, T = 298.15 K
s	Saturation
sl	Saturated Liquid
sv	Saturated Vapor
tr	Transition
Total	Total property
v	Vapor
∞	Surroundings conditions

Superscripts

*	Ideal gas conditions
Overbar (-)	Average conditions
T	Transpose of matrix

Abstract

Internal combustion engines are, and will continue to be, a primary mode of power generation for ground transportation. Challenges exist in meeting fuel consumption regulations and emission standards while upholding performance, as fuel prices rise, and resource depletion and environmental impacts are of increasing concern. Diesel engines are advantageous due to their inherent efficiency advantage over spark ignition engines; however, their NO_x and soot emissions can be difficult to control and reduce due to an inherent tradeoff. Diesel combustion is spray and mixing controlled providing an intrinsic link between spray and emissions, motivating detailed, fundamental studies on spray, vaporization, mixing, and combustion characteristics under engine relevant conditions. An optical combustion vessel facility has been developed at Michigan Technological University for these studies, with detailed tests and analysis being conducted.

In this combustion vessel facility a preburn procedure for thermodynamic state generation is used, and validated using chemical kinetics modeling both for the MTU vessel, and institutions comprising the Engine Combustion Network international collaborative research initiative. It is shown that minor species produced are representative of modern diesel engines running exhaust gas recirculation and do not impact the autoignition of n-heptane.

Diesel spray testing of a high-pressure (2000 bar) multi-hole injector is undertaken including non-vaporizing, vaporizing, and combusting tests, with sprays characterized using Mie back scatter imaging diagnostics. Liquid phase spray parameter trends agree with literature. Fluctuations in liquid length about a quasi-steady value are quantified, along with plume to plume variations. Hypotheses are developed for their causes including fuel pressure fluctuations, nozzle cavitation, internal injector flow and geometry, chamber temperature gradients, and turbulence. These are explored using a mixing limited vaporization model with an equation of state approach for thermophysical properties. This model is also applied to single and multi-component surrogates.

Results include the development of the combustion research facility and validated thermodynamic state generation procedure. The developed equation of state approach provides application for improving surrogate fuels, both single and multi-component, in terms of diesel spray liquid length, with knowledge of only critical fuel properties. Experimental studies are coupled with modeling incorporating improved thermodynamic non-ideal gas and fuel properties.

1. Introduction

1.1. Overview and Motivation

Transportation is a necessity in society which can be achieved through various modes using a range of energies, with one key method being personal vehicles conventionally powered by internal combustion engines. The practicality, versatility, and success of the internal combustion engine developed over 125 years ago (Pischinger et al. 2006), along with its continued adoption in developing nations, make the internal combustion engine the primary mode of power generation for both personal and commercial land transportation vehicles (Pischinger et al. 2006). Conventional internal combustion engine powered vehicles are projected to decrease at an annual rate of 0.5% over the next 25 years in the US, with gasoline internal combustion engines decreasing at an annual rate of 0.7%, and diesel combustion engines actually increasing at an annual rate of 4.7% in the U.S. for light-duty vehicles (used in personal transportation) (EIA 2011). Furthermore, alternative fuel-vehicles, including flex-fuel, hybrids, natural gas, electric, liquefied petroleum gas and fuel cells are expected to grow at an annual rate of 7.3% over the next 25 years (EIA 2011). Although transition to alternative vehicles is occurring, the rate of this changeover is slow and therefore internal combustion engine powered vehicles will continue as a popular transportation source.

Although the trend for fuel efficiency is increasing, by 70% from 1975 to 2010, along with increasing acceptance of hybrid or electrified vehicles (4% of production in 2010 for light duty vehicles), the sheer magnitude of liquid-fueled vehicles continues to increase, thereby increasing fuel consumption (US EPA 2010c). Transportation fuel usage continues to increase in the US with transportation accounting for almost 30% of the total global energy used in 2007 making up more than 50% of global liquid fuel consumed (EIA 2010). Although the transportation energy sector consumption is projected to grow 0.6% annually over the next 25 years, this rate is slower relative to historic trends, including an average annual rate of 1.2% from 1975 to 2009 (EIA 2011). The US in particular is a large consumer of transportation energy with nearly 30% of all its energy consumed for transportation (EIA 2010). Putting this into perspective, if the petroleum used in the United States in one day was put into 55 gallon drums these would form a line from New York to Los Angeles passing through Detroit and Houston (Nesbitt et al. 2011b). Transportation energy is currently supplied mostly by petroleum, being 97% of the total consumption, with 65% for gasoline and 20% for diesel engines (McIllroy et al. 2006), with only 3.4% being renewable energy (Davis et al. 2010). Despite this low percentage of diesel fueled transportation vehicles, they are continuing to rise at a projected growth rate of 1.6% compared to gasoline with a projected 0% average growth rate over the next 25 years for all engine types (light-duty, heavy-duty, etc.) as these engines are becoming increasingly accepted based on engine improvements in noise and emissions (EIA 2011).

Rising fuel consumption has numerous detrimental impacts including emissions, reliance on imported oil which negatively impacts the US economy and national security due to high oil prices and shortages, consumption of a non-renewable resource, and

carbon dioxide production which may contribute to global warming (EIA 2009). To combat these trends research is needed to improve engine technologies to enable the reduction of fuel consumption and emissions while avoiding negative impacts on engine power, performance, and drivability. It is expected that advancement in fuels and engine technologies and components could provide 25-50% improvements in efficiency, a need that is vital for economic and environmental reasons (McIllroy et al. 2006).

Although these engine technologies are well accepted and established, there still exist large areas for improvement in regards to emissions and thermal fuel efficiency. Engine performance is linked to the physical, thermodynamic, and chemical properties of the fuel including the effects that these properties have on fuel and charge-gas preparation and mixing, combustion including initiation and rates, and emissions formation in a diesel engine. It is this injected fuel, which is mixed with the charge-gas that subsequently combusts providing the useful work output based on the input fuel energy. Therefore fundamental combustion and spray research and knowledge is imperative for these improvements.

1.2. Background

There are various types of internal combustion engines currently used which differ based on how fuel is introduced, ignited and combusted. Two primary internal combustion engines are gasoline (spark ignition) and diesel (compression ignition). Spark ignition (SI) engines are typically fueled with gasoline and ethanol blends and used in light duty passenger vehicles, whereas compression ignition (CI) engines are conventionally diesel fueled and used in on-road medium- and heavy- duty and off-highway equipment applications. In the United States the major reliance is on spark ignition engines for light-duty vehicles, whereas in other countries the main mover is diesel engines. Diesel engines are advantageous and have the potential to comprise a larger percentage of light-duty vehicles in the United States, as is typical in Europe, due to their higher thermal fuel efficiency with a peak at forty-five percent in comparison to gasoline engines which peak at thirty-five percent (US DOE 2010), along with increased durability and higher low-end torque (Jones 2008).

The higher efficiency of diesels relative to SI engines is attributed to several factors including a higher compression ratio (not limited by combustion knock as in SI engines) which yields improved efficiency based on the thermodynamic cycle, and their load control mechanism with CI engines using fuel control (SI engines control load by air flow restrictions) limiting energy wasted by not requiring a throttling restriction. There are also options to further change combustion and engine operating strategies to improve CI engine efficiency, including injection pressure increases (Jones 2008) which can promote fuel air mixing. As such, injection pressures over the last 30 years have increased from 800 to 2000 bar (Mahr 2002). Higher injection pressures, to 2400 bar, have been realized in 2010 using common rail systems with advanced (small hole) nozzle designs, with expected advancements to 3000 bar by 2015 and 4000 bar by 2020. When these pressure increases harness even more advancements including supercritical injection or variable spray nozzles, there are expected improvements of up to 4% in fuel efficiency (NAP 2010).

As a result of their efficiency, diesel engines exhibit a fuel economy advantage. Fuel economy is inherently linked to carbon dioxide emissions, a greenhouse gas which is thought to contribute to global warming. CO₂ is produced in combustion since as the fuel reacts with the charge gas it produces CO₂ and H₂O while converting the fuel chemical energy to thermal or sensible energy, heating the product gases to enable the engine to extract energy from the working fluid. Carbon dioxide production is directly proportional to fuel consumption with every carbon atom in the hydrocarbon fuel yielding one carbon dioxide molecule so consequently minimizing fuel consumption provides reductions in CO₂. In the United States there are standard targets defined for CO₂ emissions and fuel efficiency including for example the CAFE fuel economy standard, which regulates fuel consumption for light duty vehicles (Sissine 2007). Greenhouse gases are also being regulated through the US EPA, in particular CO₂ emissions for light-duty and medium-duty passenger vehicles, starting with model year 2012 (US EPA 2010d). Standards are also currently being proposed to regulate greenhouse gas emissions, more specifically CO₂ and N₂O, for medium and heavy duty vehicles to complement the long-existing standards for light duty vehicles. These standards propose a 9% reduction by 2016 for light heavy-duty vehicles (large pick-up trucks) (US EPA 2010b; Johnson 2011).

Current limitations of diesel engines are their high particulate matter (PM) (composed of dry soot, soot which does not oxidize during combustion and exits the tailpipe is termed particulate matter, and soluble organic compounds) and oxides of nitrogen (NO_x) emissions which require complex after-treatment systems to meet increasingly stringent emission standards (Bennett 2009). Diesel engines operate using mixing-controlled combustion where fuel is directly injected into the chamber which autoignites to form a diffusion flame at close to stoichiometric conditions, which has implications in NO_x and soot emissions (Pickett et al. 2004). NO_x emissions are detrimental as they can lead to ozone production, with PM being a potential carcinogen (Knight et al. 2011). The recent on-road heavy duty diesel engine standards in 2007 and 2010 require a factor of 10 reduction in PM (from 0.1 to 0.01 g/bhp-hr) and NO_x (from 2.0 to 0.2 g/bhp-hr) respectively (US EPA 2010a). These standards have reduced emissions levels drastically from the first established levels in 1978, as summarized in Figure 1.1.

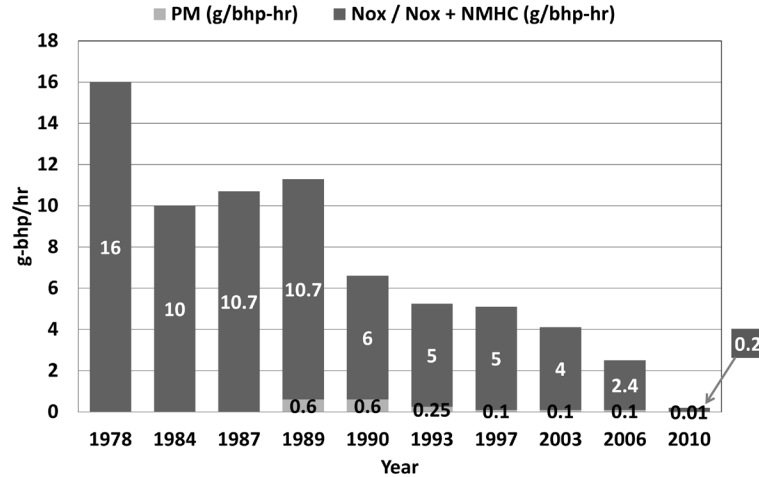


Figure 1.1: History of NO_x and PM emission standards from 1978 to present. In 1978, 1984, and 1987 there were no established PM standards. Data from US EPA 2010A. White text numbers denote NO_x, black text numbers denote PM standards.

Achieving these reductions is complicated as there exists an inherent NO_x – soot trade-off based on the temperature-equivalence ratio path which fuel-air mixing and combustion follows. Equivalence ratio is defined as the ratio of the actual fuel to air ratio of the mixture to the stoichiometric fuel to air ratio, with stoichiometric conditions being defined as the exact amount of air required to consume all of the fuel. NO_x is formed in higher-temperature, near-stoichiometric combustion regions with soot forming in the lower temperature, fuel-rich regions of the combustion zone (Kitamura et al. 2002; Pickett et al. 2007), as defined in Figure 1.2.

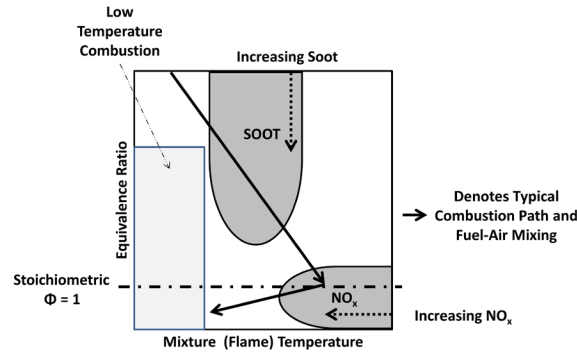


Figure 1.2: NO_x-soot formation based on the equivalence ratio – temperature path of combustion. Adapted from (Kitamura et al. 2002; Pickett et al. 2007).

Figure 1.2 outlines that current combustion / sprays in diesel engines follow a path which travels through both regions of soot and NO_x formation. Reducing the combustion temperatures will alter the equivalence ratio – temperature path shifting its trajectory to reduce residence times and traverse through lower soot and NO_x regions to assist with emission reduction. Improvements in fuel-air mixing provides a reduction in rich zones which can reduce levels of soot formed (Akihama et al. 2001).

This path and regions of soot and NO_x formation are inherently linked to the combusting spray plume. The liquid portion of the plume penetrates to a quasi-steady value, with the vapor phase continuing to penetrate forming a rich fuel-charge gas mixture, which at the tip provides the initial region of soot formation. The equivalence

ratio is decreasing as the fuel and charge-gas mix, with temperatures increasing, leading to this region being surrounded by a lifted, diffusion flame at achievement of a near stoichiometric mixture. Varying levels of soot are formed inside this flame as a function of equivalence ratio and temperature, including maximum levels towards the tip, with thermal NO_x produced on the outer edges of the diffusion flame (high temperature zones, near stoichiometric combustion as defined in Figure 1.2) (Dec 1997).

There are several proposed methods to overcome or minimize the NO_x – soot tradeoff relationship which is inherent to conventional diesel combustion, including engine operational strategies and after-treatment systems. Operational strategies consist of changes to the operating environment including charge-gas conditions via low temperature combustion or mixture dilution with exhaust gas recirculation (EGR), and injection strategy changes for example elevated injection pressures or multi-pulse injection strategies (Matthews et al. 2004). Low temperature combustion reduces flame temperatures inhibiting NO_x formation, while eliminating fuel-rich combustion zones to reduce soot formation, by up to 90% and 70% respectively, however, this application is limited due to carbon monoxide emissions, hydrocarbon emissions, penalties in fuel efficiency, and its limitation under full-load conditions (Knight et al. 2011). Low temperature combustion can be achieved via the use of EGR to provide a dilute fuel-air mixture to reduce NO_x and increasing fuel injection pressure which enables reduction in spray hole diameters to improve mixture formation providing low PM (Pischinger et al. 2006; Knight et al. 2011). Other strategies are the use of small orifice diameters (with increased injection pressures required to match combustion rates), either under high dilution (high EGR levels) at typical diesel combustion temperatures which reduces flame temperatures while still providing complete combustion with minimal soot because of sufficient fuel-air mixing before the lift-off length (location of the stabilized combusting flame relative to the injector tip) is reached, or through the use of a reduced flame temperature and elevated oxygen levels (i.e. no dilution) (Pickett and Siebers 2004). Another strategy involves the use of conventional sized orifice diameters with an oxygenated fuel under high dilution (EGR) conditions to provide cool temperatures to limit soot inception and NO_x formation (Pickett and Siebers 2004). Furthermore, diesel-fueled homogeneous charge compression ignition (HCCI) combustion can also be used, which relies on volumetric autoignition and combustion of lean or dilute charge mixtures to yield low flame temperature (low NO_x) and less rich (leaner) mixtures for low soot levels, which can be achieved by premixed early direct-injection strategies, or late injection strategies, with the requirement that fuel injection is complete before autoignition to ensure high levels of fuel-air mixing (Kimura et al. 2001; Dec 2003; Klingbeil et al. 2003). Currently, HCCI combustion is limited by control strategies and is restricted to low load applications (Pickett et al. 2004). High load applications are a current limitation for HCCI engines based on the high levels of exhaust gas recirculation needed to adequately control the start of combustion, which is required to limit combustion knock (Wimmer et al. 2006). Furthermore, HCCI limitations are apparent based on the control difficulty, which is increasingly compounded with fuel variability as the process of HCCI combustion is largely kinetically controlled.

Additional methods to minimize soot and NO_x emissions involve complex after-treatment hardware to meet emission standards. This hardware includes an oxidation

catalyst (hydrocarbon and carbon monoxide reduction), continuously regenerating PM trap, and lean NO_x reduction system or a selective-catalyst-reduction / urea system for NO_x reduction. Although successful, these systems are costly emission reduction methodologies.

The NO_x-soot tradeoff is largely tied to the mixing controlled methodology of diesel combustion and fuel efficiency. Improvements in combustion and fuel efficiency typically lead to increases in NO_x formation, whereas unburnt hydrocarbons, carbon monoxide and soot emissions are increased under incomplete combustion conditions due to poor mixing (Yanowitz et al. 2000). Diesel combustion and emission formation is inherently linked to the spray (injection) vaporization and fuel-air mixing processes. This process involves liquid fuel being injected into the combustion chamber at high pressure (injection velocity) conditions, after which the fuel spray atomizes and subsequently mixes and penetrates across the chamber. As the fuel penetrates, there is a liquid core of fuel (liquid length) led by a fuel-charge gas vapor mixture, which is combusting at the leading edge under the correct conditions, as a lifted diffusion flame. This fuel progression across the chamber includes the entrainment of charge gases into the spray. This entrainment of hot charge gases increases the temperature of the fuel-charge gas mixture, resulting in vaporization and subsequent autoignition when the fuel and air mixture reach correct proportions and temperature. Injection parameters and charge gas conditions strongly control the resulting fuel-air mixing, autoignition, and combustion, along with the interaction between vaporization and combustion. The entire diesel engine process involves fuel spray penetration and subsequent mixing with charge-gas in the combustion chamber, which directly governs flame formation at combustion, meaning that momentum flux, penetration, mixture composition and temperature are all interrelated in diesel processes (Pastor et al. 2008).

The process of the fuel vaporization in the charge gas (air or air plus recirculated exhaust) directly controls combustion. One key parameter defining the efficiency of this air-fuel mixing is liquid length. The liquid length is the location from the injector to the leading edge of the liquid core of the spray, which reaches a quasi-steady value during portions of the injection, while the vapor phase continues to penetrate. At the liquid length the rate of fuel injection is equal to the rate of fuel vaporization, and past this region only vapor fuel exists and fuel vapor continues to mix with the charge gases. A reduction in liquid length indicates an improvement or more efficient fuel-air mixing (Payri et al 2011c). Liquid length is inherently linked to injection and charge gas conditions, increasing as orifice diameter increases, charge gas temperature and density decrease, fuel volatility decreases, or fuel temperature decreases, with no influence from injection pressure (Canaan et al. 1998; Siebers 1998; Siebers and Higgins 2001).

Another parameter controlling diesel combustion is lift-off length, which defines the location relative to the injector tip that the lifted diffusion flame stabilizes at. Lift-off length increases for a reduction in charge-gas density and charge gas temperature, and an increase in nozzle orifice diameter or injection pressure (Siebers and Higgins 2001). The parameter influences for liquid length and lift-off length are summarized in Table 1.1.

Table 1.1
Liquid length and lift-off length trends.

Increase in Parameter	Liquid Length	Lift-Off Length
Orifice Diameter	+	+
Charge Gas Temperature	-	-
Charge Gas Density	-	-
Fuel Volatility	-	Unknown
Injection Pressure	No Change	-
Fuel Temperature	-	Unknown

The relationship between these two parameters, lift-off length and liquid length, for a given operating condition influences levels of soot formed in the combustion process (Siebers and Higgins 2001; Siebers 2008). For conditions where the lift-off length is less than the liquid length, all of the fuel has not yet vaporized by the onset of combustion, which results in a fuel rich diffusion flame and increased levels of soot formation (Siebers and Higgins 2001; Siebers 2008). In contrast, for conditions where the lift-off length exceeds the liquid length, the fuel has fully vaporized by the onset of combustion with sufficient fuel-air mixing which reduces rich-combustion zones thereby decreasing soot (Siebers and Higgins 2001; Siebers 2008). This ideal combustion regime (of liquid length less than lift-off length) can be achieved by reductions in orifice nozzle diameters which reduces both liquid length and lift-off length, albeit with a reduced influence for lift-off length; increases in injection pressure which increases lift-off length without a change in liquid length; or reductions in charge gas temperatures and densities achieved using exhaust gas recirculation and charge-gas cooling to also reduce NO_x (Siebers and Higgins 2001). This operational strategy is shown schematically in Figure 1.3.

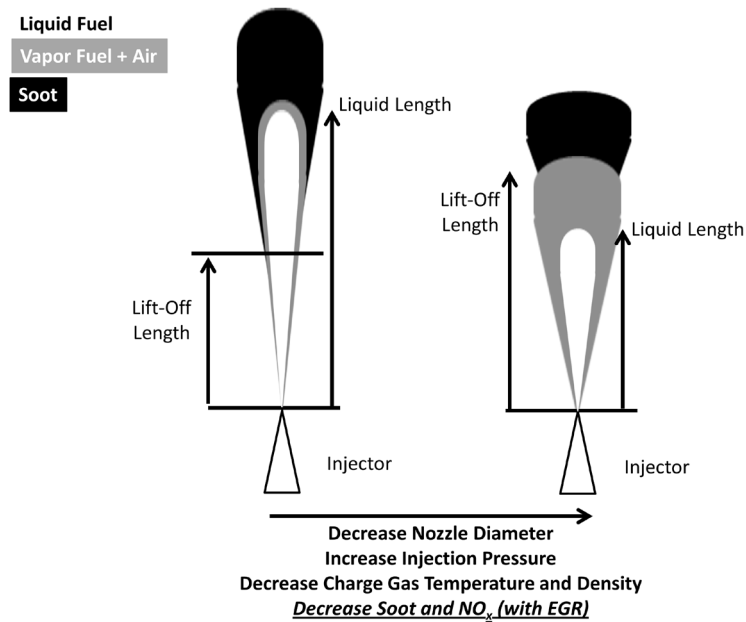


Figure 1.3: Schematic of liquid length and lift-off length relationship relative to soot and NO_x emissions. Adapted from Siebers and Higgins 2001.

By optimizing fuel air mixing with improved atomization and vaporization, the liquid length reduces which can provide reductions in soot emissions. To ensure liquid

length is optimally minimized (to ensure optimal vaporization without hindering combustion or efficiency), an improved understanding of the interaction of parameters including injection processes, spray structure, and behavior under a range of ambient conditions is required. Current injection strategies lie in between the two regimes shown in Figure 1.3 with operation at moderate injection pressures and nozzle diameters (Siebers and Higgins 2001; Siebers 2008), however, with an improved understanding of property dependent liquid length to enhance fuel vaporization, along with the use of advanced piezoelectric injectors, this transition will become increasingly adopted.

Although there is a great deal of knowledge of spray and combustion characteristics under conventional operating conditions, it is important to extend this boundary to consider advanced combustion and injection strategies, such as elevated injection pressures and reduced nozzle diameters, along with the use of advanced injectors including piezoelectric in place of solenoid for improved fuel control (Payri et al. 2011c). Not only are experimental studies important, modeling studies including simplified 1-D correlation models based on conservation principles are also useful. For example, thermophysical property modeling including the use of surrogate (simplified model) fuels provides the ability to develop computational tools. Ideally, these tools are predictive and an efficient means to improve designs for high combustion and fuel efficiency, low emission, engines through modeling as opposed to time-intensive experimental testing (Farrell et al. 2007).

1.2.1. Sustainability Issues

Assessing the sustainability and impacts of a concept or material object is essential when implementing a new technology or product into society. A sustainability assessment will ensure that the new technology or product provides significant long-term benefits compared to the current infrastructure which it is replacing or improving. This is a difficult concept based on the lack of a concise, accepted definition of sustainability. A commonly held definition for sustainability is that from the Brundtland Report (Brundtland et al. 1987) which defines sustainable development as meeting the needs of present generations, while still reserving sufficient resources for future generations to meet their own needs. Based on this definition diesel fuel from petroleum is not a truly sustainable fuel source as it is non-renewable in nature, thereby motivating not only increasingly fuel efficient technologies using diesel fuel, but also the development, and integration of alternative fuels into conventional engines.

Alternative fuels for diesel engines can include biodiesel, green-diesel, e-diesel, and dimethyl ether, as examples. It is important to consider the sustainability of these fuels since biofuels offer the potential to transform the transportation infrastructure into a more sustainable operation, based on their renewable nature and feedstock availability. In 2005 the Department of Energy (DOE) projected that there are 1.3 billion dry tons of sustainable biomass, including agricultural land and forestland, available annually in the US for the production of renewable fuels (Perlack et al. 2005). With the expected process improvements, the 1.3 billion dry tons of biomass converted to biofuels could replace 30% of the US 2005 petroleum consumption (Perlack et al. 2005).

Biodiesel, a biomass-derived fuel, is promising in that it is renewable, domestically produced, biodegradable, and provides beneficial reductions in emissions

including soot (Szybist et al. 2007). Biodiesel is a natural, energy alternative to diesel, and hence is a clean fuel (Bozbas 2008). It is designed for use in diesel engines, either in blends, for example 20% biodiesel (B20) or as 100% pure biodiesel (B100). This blending with conventional diesel fuel exploits the unique characteristics of biodiesel which enhance sustainability, while minimizing the negative aspects of the fuel, in regards to for example reduced engine performance associated with 100% pure biodiesel.

Biodiesel can reduce atmospheric CO₂ since it decreases fossil fuel consumption, with the CO₂ combustion emissions also being biologically cycled by plants using them for photosynthesis (Sheehan et al. 1998). Due to the oxygen content in the fuel, biodiesel decreases emissions of PM, CO, and HC, but causes a slight increase in NO_x emissions. However this trend in NO_x emissions is inconclusive and inconsistent since NO_x emissions decrease under certain engine and fuel-blend conditions (US EPA 2002; Demirbas 2007). Greenhouse gas emissions are decreased by approximately 41 to 54 percent when compared with diesel fuel (Hill et al. 2006; Koh and Ghazoul 2008). This reduction is partially attributed to the decreased carbon dioxide emissions with biodiesel combustion than with conventional fuels (Bozbas 2008). Sulfur dioxide emissions are reduced due to the minimal sulfur content in the fuel (Bozbas 2008). There is also a reduction in unburned hydrocarbon emissions, carbon monoxide, polycyclic aromatic hydrocarbons, nitrated polycyclic aromatic hydrocarbons and particulate matter (Groom et al. 2008; Murugesan et al. 2009).

There are several advantages to using biodiesel as a replacement transportation fuel for conventional diesel. It is easily portable, readily available, renewable, exhibits enhanced combustion efficiency, has decreased sulfur and aromatic content, and promotes decreased petroleum importation (Demirbas 2007). Using biodiesel enhances combustion efficiency based on the oxygen content in the fuel with the 11% oxygen content by weight reducing hydrocarbon, carbon monoxide and particulate emissions, based on its improved combustion (Radich 1998; Demirbas 2007). The oxygen in the fuel also promotes complete combustion and hence fuller conversion to carbon dioxide products thereby reducing the solid carbon fraction of particulate matter when compared to conventional diesel fuel combustion (Bozbas 2008).

Despite these numerous advantages, there are still disadvantages to the use of biodiesel as a transportation fuel. This includes reduced energy content in the fuel, potentially enhanced nitrogen oxides emissions, decreased engine power, issues with engine compatibility, increased price, and amplified engine wear (Demirbas 2007). Issues with power and torque are also prevalent, including an average 5% reduction in power when using biodiesel as compared with petroleum derived diesel fuel (Demirbas 2007). Additionally, the decreased energy content and heating value of biodiesel results in an increased specific fuel consumption when compared with diesel, with vehicles requiring approximately 10% more biodiesel than conventional fossil derived diesel to travel the same distance (Demirbas 2007; Frondel and Peters 2007). This fuel consumption increase results in a predicted fuel economy reduction of 0.9 to 2.1% miles per gallon when using B20 fuel blends, and 4.6 to 10.6% when using B100 fuel blends (Demirbas 2007). Biodiesel does not fare extremely well as a cost-effective transportation fuel, being up to double the cost of conventional diesel fuel (Demirbas 2007).

Despite increased costs, there do exist several economic benefits of biodiesel as a transportation fuel. These include value added to the feedstock used for biodiesel production, increased job availability especially in regards to rural manufacturing, along with raised investments in equipment and plants (Demirbas 2007). There is also reduced reliance on crude oil imports with increased agricultural support thereby yielding enhanced labor and market opportunities for domestic crops (Demirbas 2007).

Other alternative fuel sources for diesel engines include green diesel, a deoxygenated diesel fuel produced from biomass (Kalnes et al. 2009) and e-diesel, a blend of diesel with 15% ethanol to yield a low cost, reduced emissions fuel source (NREL 2002), both of which are in the early stages of development and are not commercially available. Green diesel is unique due to its high cetane number with reduced emissions attributed to the lower aromatic and sulfur content in the fuel (Kalnes et al. 2009). Another promising alternative fuel is Dimethyl-Ether (DME) which can be derived from natural gas or biomass and is very clean burning with essentially zero soot emissions (Semelsberger et al. 2006).

The implementation of biofuels will assist in reducing society's dependence on foreign oil sources resulting in a favorable economic impact by minimizing the current trade imbalance attributed to petroleum. Biofuels take advantage of natural resources, including biomass, thereby improving the sustainability of the fuel and the accompanying combustion technologies when successfully employed. To assess the sustainability of biofuels several factors must be considered. These include the fuel being technically achievable, economically competitive in comparison to conventional fuels, environmentally beneficial, and easily accessible (Demirbas 2007). Furthermore, alternative fuels need to yield net energy gains and be mass-producible without having detrimental impacts on the food supply (Hill et al. 2006). This expansion in alternative fuel use is being promoted via several initiatives including the Renewable Fuels Standard which requires 36 billion gallons of renewable fuels used for transportation by 2022 (US Congress 2007).

The United States in particular has developed several policies promoting renewable energy and energy conservation. One of the first developed policies was the 1978 National Energy Act which produced the Public Utility Regulatory Policies Act encouraging facilities to utilize renewable energy sources for electricity (Duffield and Collins 2006). This act has provided a solid basis for the development and incorporation of renewable energy sources as a whole. In 1998 the Energy Conservation Reauthorization Act was implemented to facilitate biodiesel tax and fuel use credits, providing alternative fuel vehicle credits for using a certain amount of biodiesel to satisfy the requirement of alternative fueled vehicles being used in governmental vehicle fleets (Duffield and Collins 2006; MIIQC 2006). In 2001 the Department of Energy (DOE) created a Biomass Research and Development Initiative, administered by the National Biomass Coordination Office providing grants for research, development, and demonstration projects for biomass derived energy sources, including biodiesel (Yacobucci 2008). The 2004 American Jobs Creation act provided fuel tax credits up to one dollar per gallon of biodiesel based on the feedstock used for manufacturing, including oil crops, animal fats, and recycled oils and fats (Duffield and Collins 2006). One objective of this act and tax credit was to provide biodiesel cost reductions for

consumers (MIIFQC 2006). This tax credit motivated an almost four-fold increase in biodiesel production between 2004 to 2005, contributed by 53 biodiesel production plants in the US, leading to the planning of another 40 plants to meet the increased demand (Duffield and Collins 2006).

The United States Department of Agriculture (USDA) also developed policies and regulatory agencies, including the Commodity Credit Corporation (CCC) which stimulates demand and reduces crop surpluses, encouraging the production of biodiesel (Duffield and Collins 2006). The CCC administered a USDA bioenergy program beginning in 2001 which reimbursed biodiesel producers for expanding their production capacity, promoting biodiesel growth (Yacobucci 2008). In 2005 the Internal Revenue Service (IRS) established a biodiesel tax credit as part of the American Jobs Creation act of 2004, extended by the Energy Policy Act of 2005, which enables biodiesel producers to claim a one dollar per gallon tax credit for agri-biodiesel, which is fuel produced from virgin agricultural products, and a credit of fifty cents per gallon for biodiesel manufactured from previously used agricultural products, including for example recycled fryer grease (Yacobucci 2008). The Energy Policy Act of 2005 implemented a Renewable Fuels Standard which requires incorporating set quantities of biofuels each year to slowly introduce these fuels, with this act also extending the biodiesel fuel excise tax credit and granting small-scale biodiesel producers an income tax credit (Duffield and Collins 2006). This renewable fuels standard is administered by the Environmental Protection Agency (EPA) and was expanded by the Energy Independence and Security Act of 2007, having quotas for biomass-based diesel fuel use (Yacobucci 2008). A new renewable fuels standard was developed, the Biofuels Security Act of 2007, which further expands the renewable fuels standards developed in the Energy Policy Act of 2005 (De La Torre et al. 2007).

Various policies are in place to promote the integration of alternative renewable and biomass derived fuel sources into society, in a sustainable manner. These fuel sources however must still be thoroughly researched and investigated both considering combustion and emissions formation, but also using detailed life-cycle assessments. This is necessary to ensure the fuel is providing a benefit to society when integrated, in terms of not only financial costs, but also environmental costs including greenhouse gas and other emissions. These assessments must consider the full life-cycle of the fuel, from production through combustion, to provide the most accurate understanding of its sustainability. For example, a well-to-wheel analysis of petroleum diesel fuel, soybean based biodiesel, and renewable diesel fuels from hydrogenation using a life-cycle analysis approach provides key information on energy and greenhouse gas emissions. The production of and burning of soybean based biofuels (biodiesel and renewable diesel) will yield increases in energy use, however, fossil and petroleum energy use is reduced, in excess of 52% and 88% respectively, along with an excess of 57% reduction in greenhouse gas emissions, relative to petroleum based diesel fuels, for one particular study (Huo et al. 2009). Therefore, the effects of total energy and greenhouse gas emissions must be considered in a full cycle analysis to ensure alternative fuels are sustainably integrated. The experimental methods, techniques, and model developed in this current work will provide tools needed for a more thorough study on these alternative diesel fuels to facilitate their sustainable integration.

1.3. Problem Statement

There are several key challenges in liquid-fuel combustion especially with the incorporation of new engine technologies for emission reductions coupled with the integration of novel, sustainable fuel sources (McIllroy et al. 2006). This requires providing an understanding of vaporization and mixing processes for these novel fuel sources, which may be best accomplished by advanced spray models (McIllroy et al. 2006). As discussed, diesel combustion and emissions formation is largely controlled by the fuel spray and subsequent fuel-air mixing and vaporization. Improving the understanding, or knowledge, of spray mixing including vaporization and liquid phase spray behavior under engine-relevant and advanced combustion and injection strategy conditions is imperative to comprehend the fundamental governing behavior of these processes. This includes quantifying the quasi-steady nature of liquid length, and the underlying causes and implications of this behavior, for conventional and alternative fuels. To achieve this, research tools are needed that enable independent isolation and control of parameters to understand the contributing behavior of injection properties including pressure, nozzle design, or fuel type, and ambient conditions including oxygen concentration or exhaust gas recirculation (EGR) level, density, or temperature. By optimizing fuel-air mixing, fuel consumption (and correspondingly CO₂ emissions) along with NO_x and soot emissions will be reduced to facilitate meeting stringent emission standards while maintaining high efficiency. This research is conducted to quantify and understand the influence of injection and combustion strategies including varying charge-gas conditions on the resulting spray behavior from a multi-hole injector, which directly correlates to emissions and fuel economy. By better understanding spray characteristics and fuel air mixing, hardware methodologies and strategies can be implemented to enhance this mixing which can assist in fuel economy improvements and hence carbon dioxide reductions. This knowledge is required for multi-hole production injector nozzles where current research is limited.

1.4. Goals and Objectives

This research consists of two key goals which are achieved through several objectives. The first goal is to improve the understanding of non-vaporizing, vaporizing, and combusting spray characteristics under various fuel injection and ambient states at conditions relevant to diesel engines using an optically accessible combustion vessel with Mie Scatter imaging. This includes liquid length, penetration, cone angle, lift-off length, and flame length of diesel sprays along with the plume-to-plume variations from a multi-hole injector, and in particular focus is on the fluctuations around a quasi-steady liquid length. Achievement of this goal will contribute to the diesel spray community based on an extensive study expanding knowledge on spray characteristics from a multi-hole injector, as well as by providing detailed exploration of, and knowledge on, liquid length fluctuations and their hypothesized causes, along with plume to plume spray variations. The second goal is the development of a generalized equation of state thermophysical property methodology with application to single component and multi-component surrogate fuels to compare to experimental results and to quantify property dependent liquid length using a 1-D model under conditions relevant to diesel engines. Use of this

equation of state method advances the knowledge of thermophysical fuel properties and model application based on the requirements of only hydrocarbon fuel property constants which are readily available in place of tabulated properties. These goals will be achieved through a series of objectives, as outlined below:

- Develop the combustion vessel research facility for diesel spray studies including thermodynamic state generation capability for replicating diesel engine conditions and necessary subsystems.
- Apply chemical kinetics modeling to the combustion vessel preburn procedure for thermodynamic state generation to quantify the influence of mixture properties, and the procedure, on the resulting fuel autoignition.
- Integrate optical diagnostics to quantify the macroscopic spray structure and characteristics of penetration, liquid length, cone angle, and lift-off length.
- Develop robust image processing methodologies and techniques to quantify spray characteristics.
- Use the combustion vessel to characterize diesel sprays over a range of conditions pertinent to current and advanced technology diesel engines including charge gas temperature and density, fuel injection pressure, and temperature.
- Quantify diesel spray plume to plume variations in liquid length and fluctuations about a quasi-steady value.
- Examine the validity of an existing spray correlation for vaporizing (liquid length) sprays in comparison to experimental data.
- Develop an equation of state dependent set of property relations to evaluate enthalpy, saturation pressure / temperature and fuel compressibility properties using fuel critical properties.
- Integrate thermophysical property relationships from an equation of state to evaluate the existing liquid length correlation providing a robust methodology for property-dependent characterization to facilitate parametric studies and surrogate fuel development for matching vaporization characteristics.
- Compare results from the liquid length correlation to experimental results considering both diesel sprays in the Michigan Technological University Combustion Vessel and data tabulated in the Sandia Engine Combustion Network database, which includes liquid length for fuels of cetane and diesel.
- Use liquid length models with single and multi-component surrogates to identify the relationships between boiling point matching diesel distillation properties to accurately predict diesel spray liquid length and vaporization characteristics.
- Use diesel spray experimental results in conjunction with liquid length models to evaluate property dependent liquid length including parametric modeling for hypotheses on the cause of liquid length fluctuations including vessel temperature gradients, fuel pressure fluctuations due to cavitation and eccentric needle lift, and injector design parameters influencing discharge, velocity and area contraction coefficients.

Through achievement of the above objectives, a fully functional research laboratory will be developed, with thermodynamic state generation capability for fundamental studies of conventional and advanced diesel combustion strategies including those to minimize the NO_x -soot tradeoff, under well-controlled conditions. Furthermore,

experimental results will be used to verify an existing liquid length correlation, with application to diesel and alternative fuel surrogates, which will provide insight into the causes of the quasi-steady liquid length behavior, which has implications for soot formation. The developed equation of state approach for thermophysical property determination provides a tool, which considers non-ideal effects, for surrogate fuel development and application for matching fuel vaporization characteristics. Furthermore, this tool helps to fill the void which exists between surrogate fuels and chemical kinetics which are well developed, and thermophysical property analysis and impacts for which focus has been lacking, during surrogate fuel development.

1.5. Method of Solution

Clearly, understanding diesel spray behavior is important to determine methods for improved fuel-air mixing to provide fuel efficiency improvements and emission reductions. The following work provides a contribution to knowledge of diesel fuel sprays over a wide range of conditions, with particular application on liquid length spray behavior including for example fuel effects and hypotheses on liquid length fluctuation causes. A literature review is provided in Chapter 2, with discussion on optically accessible experimental apparatuses and thermodynamic state generation procedures, macroscopic spray characteristics, diesel spray modeling, surrogate fuels, and equations of state for determining property relationships, in conjunction with mixing relationships for multicomponent fuels.

Chapter 3 discusses the development and validation of an optically accessible constant volume combustion vessel experimental facility for these studies, including facility features and applications. In Chapter 4, results from modeling of the procedure used for thermodynamic state generation are reviewed, supporting the use of this procedure despite the minor species generated. Modeling is applied to both the Michigan Technological University combustion vessel, and to the vessels comprising the Sandia National Laboratory Engine Combustion Network international research initiative.

In Chapter 5, the optical Mie scattering imaging diagnostic setup is discussed along with image processing methodologies which will be used to characterize diesel fuel spray behavior of a baseline multi-hole injector.

In Chapter 6, results from the experimental studies of diesel fuel sprays over a range of ambient and injection conditions are discussed, comparing these results with past literature and to quantify the governing parameters and the fundamentals of these processes. The aforementioned diesel spray parameters are characterized for the sprays under vaporizing, combusting and non-vaporizing conditions. Results are also included of the plume-to-plume variations between spray plumes from this multi-hole injector to facilitate understanding of the variations between spray plumes under a range of conditions, which influences combustion and emissions.

In Chapter 7, the experimental results from this work will be used in conjunction with data from the Sandia Engine Combustion Network (ECN, <http://www.sandia.gov/ecn/index.php>) for cetane as a single-component fuel and diesel, for liquid length correlation application. The model used is from Siebers (1998) and based on mixing – limited vaporization. In order to apply this model to a wide-range of hydrocarbon fuels an equation of state approach is undertaken to facilitate calculation of

the thermophysical properties as required. This approach enables determination of the evaporation coefficient necessary for model evaluation, with knowledge of only critical temperature and pressure, and acentric factor, along with ideal gas specific heat polynomial constants. This ‘program’ of equation of state for thermophysical property determination improves the application of these models by facilitating application to hydrocarbon fuels and blends, whose property data may not be readily available, which is important as new alternative fuels are considered. Furthermore, this will assist with surrogate fuel development by enabling application of both single and multicomponent mixtures to best match and predict liquid length behavior to that of conventional, and alternative, diesel fuels including understanding the influence of distillation or boiling point matching on accurate prediction of diesel spray behavior. This approach and application is reviewed, and application is provided to various single and multi-component surrogates. Investigation is also undertaken to define the lower limit of this model on predicting liquid length based on atomization limited regimes, achieved by evaluating the penetration at the transition time to a charge-gas entrainment dominated regime.

Chapter 8 quantifies the fluctuations of the diesel spray liquid length about a quasi-steady value and the influence of operating parameters on these trends. Results are also included for higher frame-rate images to better understand the frequency content of the diesel spray liquid length fluctuations. Hypotheses are presented as to the cause of these fluctuations including chamber temperature gradients, injection pressure variations attributed to eccentric needle movement and cavitation, along with variations in injector coefficients based on flow and geometry. These hypotheses are investigated using parametric modeling with the Siebers liquid length model in conjunction with the equation of state approach for thermophysical property modeling.

Summary and key conclusions are presented in Chapter 9. Chapter 10 discusses future work which includes experimental study of diesel spray liquid length for single and multi-component surrogate fuels, additional model improvements, and updates to the combustion vessel research laboratory. Additional work will also be undertaken to further explore the proposed hypotheses for liquid length fluctuations. Appendices (Chapter 12) include data and image processing programs, along with chemical kinetics modeling and equation of state thermophysical property modeling programs for liquid length. Additional supplementary data and further details for methods of solution will also be provided in the appendices.

The results from this dissertation contribute to the understanding of diesel spray liquid length including the quasi-steady spray fluctuations using both an experimental along with a thermophysical modeling approach with a mixing limited vaporization model. The developed equation of state approach for thermophysical property modeling provides application for selecting and quantifying surrogate fuels, both single and multi-component, for diesel spray studies, yielding fundamental knowledge and application for alternative fuel development and integration. Surrogate fuels do exist, along with 1-D correlation models for liquid length, however, there is a need for a methodology to evaluate these models for surrogate fuels, with knowledge of only critical fuel properties, for the cases where tabulated property data is not readily available. This equation of state

method with the 1-D mixing limited vaporization model provides an advanced tool and process for these applications.

2. Literature Review

This chapter includes a review of literature relevant to the current research. Review is included on experimental apparatuses and in particular optically accessible instruments, along with the preburn procedure for thermodynamic state generation. Discussion is also included on macroscopic spray characteristics including spray penetration, liquid length, cone angle and lift-off length, along with plume to plume variations and liquid length fluctuations. Diesel spray modeling is also discussed with a focus on 1-D spray models for characterizing spray parameters and trends. Review is also provided on surrogate fuels, commonly used in diesel spray modeling, along with the use of equations of state for determining property relationships in conjunction with mixing rules for multicomponent fuels. This literature review sets the stage for the scope and application of this work relative to existing research.

2.1. Experimental Apparatus

The study of combustion and sprays can be undertaken with the use of various experimental apparatuses. All setups have advantages and disadvantages and are useful for certain types of study. The main techniques include conventional diesel engines, modified engines for optical accessibility, constant volume combustion vessels using heating or preburn procedures which could be sequential or premixed, constant pressure flow rigs, and rapid compression machines. For fundamental and detailed research on diesel sprays and the ensuing combustion and emissions formation, in conjunction with injection into a well-controlled environment, the use of optical diagnostics are imperative.

Using a conventional diesel engine is advantageous for combustion and sprays research as conditions are those of the actual engine environment, however, research applications are limited as the engines do not provide the optical access needed for visualization. This visualization is advantageous to understand the fundamental underlying behaviors. Furthermore, in conventional engines it can be difficult to control and study advanced combustion strategies based on limitations of the engine in regards to operating conditions, injection strategies, and fuel compatibility, as examples. This lends to the development of optically accessible apparatuses that emulate or reproduce conventional engine conditions while enabling the application of optical and laser diagnostics for spray and combustion studies.

Diesel engines can and have been modified to provide optical access to the combustion chamber to enable visualization of processes which occur in an actual engine. This optical access can be achieved in various ways; replacing an exhaust valve with a window in the cylinder head with additional windows around the cylinder top (Bradsley et al. 1988; Espey et al. 1997), installing a fused silica piston top with retained bowl geometry and valve cutouts in addition to other side windows (Matthews et al. 2002) or installing windows in the piston, with supplemental access through windows in the liner near the cylinder head (Baert et al. 2009). Other methods include replacing the piston with a flat fused silica piston crown window or with an exhaust valve being replaced by a window along with windows being added around the upper portion of the cylinder wall

to provide more optical access (Kokjohn et al. 2011). Or, the use of a modified single-cylinder Caterpillar engine for optical experiments, however, it must be noted that this optical version provides more crevice volumes than production based on the requirements for optical accessibility with a window in the piston and five additional windows around the upper cylinder wall (Mueller and Musculus 2001). Others use multi-cylinder engines with one cylinder modified for optical accessibility with fused silica windows in the piston, cylinder wall and cylinder head (Verbiezen et al. 2007). Despite having this optical access for realistic engine flow conditions, it is still difficult to accurately quantify and control the ambient environment for study, and conditions can be limited in regards to achieving and analyzing advanced combustion and injection strategies. Furthermore, because of the optical access, there are reduced pressure limits and resulting compression ratios which can be used, reducing some applicability in comparison to conventional engines (Mueller and Musculus 2001; Baert et al. 2008). Engine flows can also be altered due to these optical modifications limiting applicability.

Another apparatus, constant volume combustion vessels, are a well-known and extremely utilized tool for characterizing fundamental spray and combustion characteristics including studies on spray mixing (Naber and Siebers 1996), vaporization and liquid penetration (Siebers 1998, 1999; Bougie et al. 2005; Pickett et al. 2009), flame standoff length (Higgins and Siebers 2001; Ito et al. 2003), and diesel soot emissions (Pickett and Siebers 2002; Ito et al. 2004), as examples. There are two main types of constant volume combustion vessels, heated vessels and pre-combustion vessels, for reaching ambient conditions. Heated combustion vessels have lower temperature and pressure limits compared to that of the pre-combustion vessels and have reduced applicability for future advanced combustion strategies since they are constrained by electric heater capabilities (Fujimoto and Sato 1979; Baert 1989; Labs et al. 2005; Nishida et al. 2007; Baert et al. 2008; Pawlowski et al. 2008). Pre-combustion vessels can achieve a wider range of conditions, enabling study at conditions not currently attainable or used in existing technology engines, permitting the study of advanced combustion strategies. These conditions are achieved with a fuel-lean, oxygen-enriched spark ignited combustion event, after which cool-down due to heat transfer occurs, at a rate more than an order of magnitude longer in comparison to diesel injection and combustion. Preburn vessels typically use either sequential direct CV filling or premixed mixing vessel filling. The premixed filling is time consuming, but that of sequential filling risks mixtures that are not uniform and also have the potential for repeatability issues test to test.

These apparatuses are advantageous in that they allow high levels of optical access for a wide range of laser and optical based diagnostics while also providing the ability to quickly change environmental operating conditions to study a range of phenomena with good control over the conditions including temperature, density, and pressure along with simulated dilution and EGR via different premixtures (Hurn and Hughes 1951; Oren et al. 1984; Naber and Siebers 1996; Siebers 1998; Verhoeven et al. 1998; Johnson et al. 2009). Different mixtures are used including gaseous hydrocarbons, hydrogen, carbon monoxide, argon, nitrogen and oxygen, with additional modifications to match engine specific conditions including water levels or carbon dioxide for EGR conditions (Hurn and Hughes 1951; Dyer 1979; Oren et al. 1984; Naber and Siebers 1996; Siebers 1998; Verhoeven et al. 1998; Azetsu and Ito 2007; Kim et al. 2008;

Nguyen et al. 2008; Baert et al. 2009). Despite these advantages, constant volume combustion vessel devices have difficulty providing environments with realistic engine flows. Typically preburn procedures are required to provide the thermodynamic state for diesel engine study which produces reactive minor species, and engine geometry and cycling rates cannot be replicated for direct comparisons (Oren et al. 1984). An additional application of these vessels is that their conditions are well-controlled, and well-characterized, providing use for Computational Fluid Dynamics (CFD) modeling including development, validation and calibration, which in synergy with experimental engine studies, can provide insight and knowledge for diesel engine advancements (Hurn and Hughes 1951; Reitz and Rutland 1995; Labs et al. 2005; Vishwanathan et al. 2009).

Constant pressure flow rigs are another optically accessible apparatus similar to a constant volume vessel. However, in contrast to a constant volume device, there is a continuous flow of gas through the rig to enable achievement of thermodynamic conditions representative of diesel engines providing a constant pressure environment. These flow rigs provide significant optical access for the application of laser and optical based diagnostics. However, constant pressure flow rigs typically have lower limitations in regards to the maximum temperatures (1000 K) and pressures (150 bar) which can be achieved as they rely on gas flow for thermodynamic state generation along with heaters for achieving elevated temperatures representative of diesel engines (Baert et al. 2008; Payri et al. 2011a). The utilization of these rigs requires substantial time in order to meet new test conditions based on the required heating and flow variations (Baert et al. 2008).

Rapid compression machines (RCM) are one other optically accessible combustion apparatus used to study spray and combustion behavior. Rapid compression machines work by compressing a uniform mixture of fuel and oxidizer to conventional engine conditions, with the piston kept in compression so that the conditions are constant volume (Kistopanidis and Cheng 2006). Despite their optical access, rapid compression machines can be difficult to build and control, experience vibration issues, exhibit differences in cycling rates and cylinder geometry, and characterizing in-chamber conditions and replicating realistic diesel engine flows is complicated (Baert et al. 2008). Based on the requirements for hardware of the RCM, there are limitations on the pressure and charge densities achieved and they are typically reduced relative to conventional engine operation (Baert et al. 2008).

These aforementioned apparatuses are compared and evaluated in regards to ranked advantages and disadvantages as shown in Table 2.1.

Table 2.1
Evaluation of different apparatuses for studying fundamental spray and combustion. Scale: + signifies a benefit, - signifies a disadvantage, 0 signifies no definite advantage or disadvantage.

Apparatus Type → Characteristic ↓	Engine	Optical Engine	Constant Volume CV: Preburn	Constant Volume CV: Heated	Constant Pressure Flow Rig	Rapid Compression Machine
Optical access	-	+	+	+	+	+
Engine flows	+	+	-	-	-	-
Geometry	+	+	-	-	-	-
Condition Characterization	-	-	+	+	+	0
Condition Control	-	-	+	+	+	0
Range of Achieved Conditions	-	-	+	0	0	0

Combustion vessels are a well-accepted and consistently used apparatus, as they provide a tool to acquire fundamental spray and combustion knowledge under well-controlled conditions. The results from these spray and combustion studies can be applied to diesel engines for validation and confirmation of results in regards to fuel efficiency and emissions reduction.

2.1.1. Preburn Procedure for Thermodynamic State Generation

Constant volume combustion vessels can use a preburn procedure to reach the elevated pressures and temperatures and generate the thermodynamic state representative of diesel engines, including air and air plus EGR. Different mixtures result in different specific heat capacities of the charge gas which is important in vaporization and combustion (Baert et al. 2009), different temperature and pressure levels, and also different charge gas compositions for injection in regards to major and minor species levels for simulating engine EGR. The main procedure used in the vessels is similar, a gaseous mixture is produced either in an exterior mixing vessel (Pickett et al. 2010; Nesbitt et al. 2011a), or is sequentially filled into the CV chamber (Meijer et al. 2011). Gaseous mixtures used vary between institutions, not only in the gases used in the mixture but also in the composition. Typically, gases used consist of gaseous hydrocarbons, hydrogen, carbon monoxide, argon, nitrogen, and oxygen (Azetsu and Ito 2007; Pickett et al. 2010; Meijer et al. 2011; Nesbitt et al. 2011c). Different mixtures used are derived for various reasons, for example to reach a desired level of oxygen in the products (Naber and Siebers 1996), to match the specific heat capacity of air with the use of argon (Baert et al. 2009), to match the oxygen ratio to other gases after combustion of 1:3.76 (oxygen to nitrogen) to be similar to air (Kim et al. 2007), or to match the water and carbon dioxide levels found in an engine as the result of EGR (Johnson et al. 2009), as examples. Other mixtures can be used such as a CO, Air and O₂ mixture which yields a mixture with CO₂ levels different than typical in a diesel engine except for high EGR conditions (Nguyen and Honnery 2008).

There are pros and cons to the different gases utilized which also lead to differences in achieved conditions. For example, acetylene is proposed to be preferred over hydrogen as acetylene will produce less water than the pre-combustion of hydrogen minimizing condensation inside the vessel on the windows (Oren 1984) or on the injector tip which can lead to rusting. Different fuels are used in the gaseous mixture, typically acetylene, hydrogen or ethylene, as these gaseous fuels are known to ignite easily in lean mixtures which is required for this thermodynamic state generation (Baert et al. 2008). Originally at Sandia National Laboratory, the composition for gaseous fuel was ethylene and hydrogen in a ratio of approximately 1:4 (Siebers 1985), however, that mixture has since been modified to a ratio of 1:6 of hydrogen to acetylene which is currently in use (Naber and Siebers 1996; Siebers 1998; Nesbitt et al. 2011c). Other institutions use higher levels of hydrogen relative to the hydrocarbons, for example a ratio of approximately 1:11 of ethylene to hydrogen (Verhoeven et al. 1998), whereas others just rely on hydrocarbons, for example straight acetylene without any hydrogen (Fujimoto et al. 2005).

Argon is also added to some pre-combustion mixtures with acetylene in an effort to match the specific heat capacity of air. To ensure mixture accuracy, small partial pressures in the gas mixture should be avoided as these small additions can compound errors in the procedure (Baert et al. 2009). The order of the mixture creation is typically governed by the properties of the gases added. For example, fuels are typically added first (to account for the low pressure stability limit of acetylene), followed by dilution gases such as nitrogen, and finally the oxidizer (typically oxygen) is added to avoid passing through a spontaneous combustion regime for safety (Baert et al. 2009). The literature shows there is not one preferred mixture for the pre-combustion process, rather, there are a range of mixtures in use to reach the desired temperature and pressure conditions, all exhibiting pros and cons in regards to peak temperatures, minor species produced, and species at injection in comparison to that of air or EGR in a diesel engine. The details of the mixtures, including composition and minor species produced, are not well characterized. Research is limited into the minor species produced from the differing mixtures, including their levels relative to those in conventional engines, and their influence on the spray, ignition and combustion processes. This fundamental knowledge-gap will be explored in the current work including the effect of mixture composition on ambient composition, and autoignition characteristics.

2.2. Optical Diagnostics

Various optical and laser based diagnostics are used to characterize diesel spray and combustion behavior. High speed imaging is a technique which is as advantageous as it is simple, relatively low cost, and can provide information on spray and combustion structure, and geometry, including penetration and cone angle as examples, that cannot always be achieved from laser or particle sizing techniques (Chigier 1983). Key optical based diagnostics are Schlieren or shadowgraph imaging, and Mie scattering. Shadowgraph diagnostics provides information on the vapor phase of fuel sprays as this diagnostic detects density gradients by collecting the collimated light which passed through the region of interest, and Mie scattering is used to quantify the liquid phase of the spray based on scattering principles.

Shadowgraph diagnostics work by passing collimated light through the sample region of interest, and collecting the shadows of the light using an imaging device. These diagnostics enable visualization of density gradients caused by changes in refractive indices, which correspond to vapor phase fuel spray behavior as an example. Various configurations of optics and acquisition can be applied, with one common form being a z-type system. This includes the use of two mirrors, one which collimates the light, with the other collecting the light after it passes through the test region, which is subsequently imaged (Settles 2001). To provide a Schlieren image, a knife edge is placed after the collecting optics but before the camera to block out a portion of the light, enabling visualization of density gradients which are not blocked based on knife edge orientation (Settles 2001).

Scattering diagnostics rely on removing energy from an incident light wave with a portion of this energy re-emitted, and therefore these diagnostics require a light source to provide the energy for scattering and a collection medium (Hecht 1987). Depending on the particle size, different types of scattering occur. Mie scattering is an elastic scattering technique which is dependent on spherical particles larger than the wavelength of light (Martinez-Martinez et al. 2010). Other diagnostics include Rayleigh scattering which is light scattering by particles that are small relative to the light wavelength to determine vapor and liquid concentration phases along with temperature and species measures as a combustion diagnostic (Hecht 1987; Martinez-Martinez et al. 2010).

Diagnostics are also being developed which enable almost simultaneous image acquisition, with consistent line-of-sight imaging, including visualization of both liquid and vapor spray characteristics (Parrish and Zink 2011). This involves the use of one camera with frame straddling, to visualize both the Schlieren and Mie signal, with illumination provided by high-speed light emitting diodes (LED's) timed such that they provide illumination for the diagnostic at staggered timings for image capture (Parrish and Zink 2011). This diagnostic provides information on the vapor and liquid phase of the spray characteristics, without differences in camera location, which removes the spatial camera location influence from the image results.

Laser based diagnostics are also applicable to spray and combustion studies. Laser diagnostics work by the interaction of electromagnetic radiation with sprays and combustion flames enabling the measurement of temperature, velocity, and constituent concentrations, using for example scattering, absorption, or emission techniques (Kohse-Hoinghaus et al. 2005). Various diagnostics can be used including laser induced incandescence (LII) for soot formation, light extinction which is a line of sight method for soot optical thickness, laser scattering similar to Mie scattering with the use of a laser sheet for illumination and scattering, laser induced exciplex fluorescence (LIEF) for characterizing fuel-air mixing formation and evaporation phenomenon, and others, depending on the desired areas of interest. There are several unique optical and laser based diagnostics which can provide a wide range of information on spray and combustion processes. Phase doppler anemometry (PDA) enables measurement of diameters and velocities of fuel droplets (Martinez-Martinez et al. 2010). Particle image velocimetry (PIV) is used to measure velocity fields which is related to air entrainment and is important in fuel-air mixing, which relates to fuel efficiency and emissions.

2.3. Macroscopic Spray Characteristics

There are several parameters of sprays that can be studied, including macroscopic (large-scale) and microscopic (small scale, i.e. droplet) characteristics. Of interest in the current work are macroscopic spray characteristics which will be defined here. Macroscopic spray characteristics consist of penetration (flame length for combusting conditions), liquid length, cone or spray angle, and lift-off length. A schematic defining these macroscopic spray characteristics is provided in Figure 2.1.

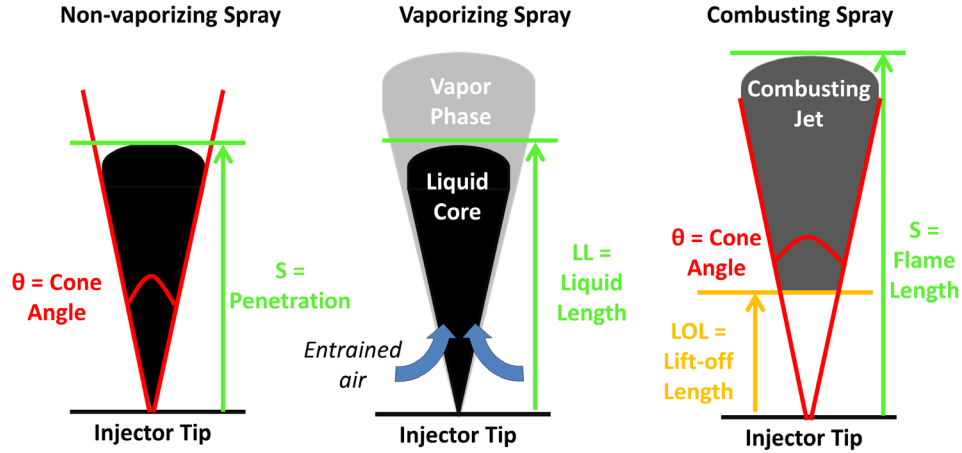


Figure 2.1: Definition of macroscopic spray parameters for non-vaporizing, vaporizing and combusting sprays, including penetration, cone angle, liquid length, and lift-off length.

The fuel spray is injected into the combustion chamber at high velocity based on the injection pressure, and the fuel propagates across the chamber where it experiences drag forces causing it to decelerate and at the same time there is momentum transfer based on ambient gas entrainment in the spray (Sazhin et al. 2003). As the fuel jet is injected and propagates it breaks-up into ligaments and atomizes, with these processes being essential to ensure efficient fuel-air mixing (Bae and Kang 2006). The first drops transfer energy to the surrounding charge gas which provides less resistance to further drops allowing them to penetrate further, sustaining the fuel propagation (Lefebvre 1989). Therefore, there are competing factors during this process which compensate each other including air entrainment attributed to momentum transfer, and conversely, the spray break up processes (Sazhin et al. 2003). Results suggest, and correlations show, that the momentum transfer occurs very quickly, after which the spray is entrainment dominated, as will be discussed. Spray and combustion properties are interrelated with quasi-steady flame lift-off location typically in the vicinity of the liquid length in reacting sprays for engine relevant conditions (Siebers and Higgins 2001; Hottenbach et al. 2010).

2.3.1. Spray Penetration

Penetration is a spray phenomenon which defines how far a fuel jet traverses the combustion chamber with respect to time and its corresponding air entrainment which is required for fuel-air mixing and efficient and complete combustion. Penetration can be defined for non-vaporizing sprays defining the entire spray. For vaporizing sprays it defines the distance the vapor portion travels, and for combusting sprays, termed the

flame length, it defines the distance the tip of the combusting flame travels relative to the injector as determined from natural luminosity images. The location of the leading edge of the spray is essentially a trade-off and balance between two opposing factors, first the momentum (kinetic energy) with which the fuel is injected, and second, the entrainment provided by the ambient charge gas (Lefebvre 1989; Martinez-Martinez et al. 2010). Various correlations have been developed for spray penetration with some examples provided in Table 2.2.

Table 2.2
Spray penetration correlations.

Author	Correlation	Notes
Dent 1971	$S(t) = 3.07 \left(\frac{\Delta P}{\rho_a} \right)^{0.25} \left(\frac{294}{T_a} \right)^{0.25} \sqrt{d_o t}$	Developed from theory of gaseous sprays and from experimental data
Hiroyasu and Arai 1990	$S(t) = 0.39 \sqrt{\frac{2\Delta P}{\rho_f}} t; t < t_b$ $S(t) = 2.39 \left(\frac{\Delta P}{\rho_a} \right)^{0.25} \sqrt{d_o t}; t > t_b$ $t_b = 28.65 * \frac{\rho_f * d_o}{\sqrt{\Delta P * \rho_a}}$	t_b is the time to droplet breakup after injection, before breakup the fuel is a continuous liquid spray
Jimenez et al. 2000	$S(t) = 0.6^{-3} U_o t^{0.9} \left(\frac{\rho_a}{\rho_f} \right)^{-0.163}$	Empirical Relation
Jawad et al. 1999	$S(t) = C_1 \Delta P^{0.25} \sqrt{\rho_f^{0.25} t \rho_a^{-0.14}}$	C_1 experimental constant

This list is not all inclusive as some relationships are discussed in more detail in later sections. It is solely meant to represent the breadth and variation of penetration relationships. The above relationships have numerous similarities in regards to parameter dependencies including injection pressure (injection velocity), fuel and charge gas densities, with some including orifice properties (nozzle diameter). The weighting of the parameter however varies with the differing correlations, for example injection pressure to the 0.25 power, whereas a linear dependence on injection velocity (Jimenez et al. 2000) represents a square-root injection pressure dependence. The Dent (1971) and Jawad et al. (1999) correlations do not include the impacts of fuel density directly, along with Hiroyasu and Arai (1990) in their long time-scale correlation, even though different fuels are known to yield different penetrations (Wang et al. 2010).

Various parameters impact fuel spray penetration as summarized in Table 2.3.

Table 2.3
Penetration parameter influence (Arregle et al. 1999; Martinez-Martinez et al. 2010).

Parameter	Penetration Trend for an Increase in Parameter
Injection Pressure	↑
Ambient Density	↓
Ambient Temperature	Can ↓, but not conclusively
Nozzle Orifice Diameter	↑

When fuel vaporization is occurring penetration is slowed relative to the non-vaporizing fuel jets which is likely caused by the cooling of the entrained air due to vaporization (Siebers 2008). In combusting cases, the fuel jet penetration (before ignition), is initially reduced due to vaporization, and after ignition and combustion has started, the fuel jet then begins penetrating faster than the non-vaporizing case (Siebers 2008). This is attributed to conservation of momentum, with a reduction in fuel jet density as combustion (heat release) progresses, with this combustion also decreasing air entrainment thereby increasing penetration (Siebers 2008).

It is ideal to match fuel spray penetration to the combustion chamber design, meaning over-penetration should be avoided to prevent impingement on the chamber walls due to increases in emissions, but under-penetration should also be prevented to ensure maximum fuel and charge gas utilization in the entire chamber for optimum combustion efficiency (Lefebvre 1989).

The diagnostic commonly used for characterizing spray penetration is Mie scattering (under non-vaporizing conditions) or Schlieren or Shadowgraph imaging, applicable under both vaporizing and non-vaporizing conditions based on visualization of density gradients.

2.3.2. Liquid Length

Liquid length (LL) is another macroscopic spray characteristic which is defined as the distance from the nozzle exit to the farthest location the liquid phase of the spray travels to while the vapor phase continues to penetrate across the chamber (Martinez-Martinez et al. 2010). Liquid length is typically characterized under vaporizing (0% oxygen), non-combusting conditions for ease of study, but is representative of behavior under combusting conditions, before ignition, as well. At the liquid length, the rate of fuel injection balances with the fuel evaporation rate which causes the diesel spray to reach a quasi-steady position (Siebers 1998). The charge-gas and fuel mixture has reached saturated conditions which thereby defines the rate of evaporation and the liquid length. Liquid length characterizes the atomization and evaporation processes of the fuel directly relating to the fuel / charge-gas mixing rates (Canaan et al. 1998).

Liquid length is governed by the fuel mass fraction which is controlled by fuel-air mixing. This dependency on the fuel-mass fraction enables definition of an evaporation rate coefficient, B , which is the fuel mass fraction over 1 minus the fuel mass fraction. Liquid length is proportional to the square root of $B + 1$ over B based on Siebers (1999) liquid length model. This yields a proportionality relationship for the liquid length as defined by equation (1).

$$LL = \frac{\sqrt{1 - Y_f}}{Y_f} \quad (1)$$

Time-dependent liquid length is directly related to jet breakup. The first break-up regime timing is estimated by equation (2), and is a function of various parameters (Hiroyasu and Arai 1990).

$$t_b = \frac{15.8\rho_f d_o}{C_d \sqrt{2\rho_a \Delta P}} \quad (2)$$

Liquid length increases proportional to the square root of time until the break-up regime with this break-up time defined by the above relationship, after which, liquid length becomes essentially constant when considered macroscopically. This break-up regime characterizes the transition from fuel injection dependent behavior to that governed by atomization and vaporization as characterized by the ambient gas surroundings.

Various correlations have been proposed for liquid length based on experimental and empirical relationships, as summarized in Table 2.4. Liquid length is established and fluctuates about a mean value; these relationships define the quasi-steady state properties.

Table 2.4
Select liquid length correlations.

Author	Correlation
Bracco 1983	$LL = 7.15 \left(\frac{\rho_f}{\rho_a} \right)^{0.5}$
Yule and Salters 1995	$LL = 2.65 * 10^3 * d_o We_a^{-0.1} Re_f^{-0.3} \left(\frac{\rho_f}{\rho_a} \right)^{0.08}$

There exist several liquid length relationships or correlations, which will be discussed in more detail in future sections. Of those presented here both show a fuel and ambient density influence, albeit of differing magnitudes. Furthermore, the Yule and Salters (1995) correlation also includes the influence of orifice diameter which is known to linearly influence liquid length (Siebers 1998), along with other fluid properties through the Weber and Reynolds number. As seen in the above table, liquid length is dependent on various parameters including nozzle and injection parameters, ambient gas conditions, and fuel properties, as further defined in Table 2.5.

Table 2.5
Liquid length parameter influence (Siebers 2008; Kook et al. 2009; Martinez-Martinez et al. 2010).

Parameter	Liquid Length Trend for an Increase in Parameter
Fuel temperature	↓
Ambient density	↓
Ambient temperature	↓
Nozzle orifice diameter	↑
Fuel boiling point	↑
Fuel volatility	↓ for diesel like fuels
Injection pressure	No effect

Several of these trends are intuitive, for example increasing temperature of the charge gas will increase vaporization and reduce the LL of the fuel, and an increase in ambient density will cause increased entrainment to the fuel, with saturation conditions being achieved at a shorter distance, thereby decreasing the LL. Other trends are not as innate including injection pressure as this is known to influence penetration, however, an increase in injection pressure does not change liquid length. An increase in the ambient entrainment which occurs with an increase in injection pressure or velocity is offset by the fueling rate as it maintains the same fuel-air mixture at an axial location (Kook et al. 2009). Conservation of mass is required, and an increase in fuel flow rate provided with

an elevation in injection pressure, proportional to the injection velocity, will be met with the same magnitude increase in vaporization rate (also proportional to the injection velocity) in regards to entrained charge-gas mass flow rate, which signifies that injection pressure does not have an impact on diesel spray liquid length (Siebers 1998). This negligible influence of injection pressure on liquid length supports the use of elevated injection pressures to improve fuel-air mixing which assists with emission reductions while still avoiding liquid fuel impingement on the cylinder wall to minimize unburnt hydrocarbon emissions.

Other trends are not well defined including that for fuel volatility in regards to governing and correlating parameter. It is agreed that as volatility is increased liquid length decreases (Fisher and Mueller 2010), however, the correlating volatility point is conflicting. More specifically, Siebers (1998) reports that liquid length increases with T90 (90% distillation point) of the fuel, whereas Higgins et al. (1999) have proposed that for alternative fuels T90 is not valid due to the high latent heat of vaporization of the fuels. Canaan et al. (1998) proposed that the T50 (50% distillation point) point is the controlling factor in liquid length. With these inconsistencies, there is much to learn about the controlling factors in fuel characteristics, be it 50 or 90% distillation point, or others, which is information that is important in surrogate fuel definition and application.

There have been observations of recession of liquid length after the end of injection meaning there is a decrease in the maximum liquid length. This is attributed to the entrainment wave traveling downstream with the entrainment wave characteristics depending on various properties including fuel and fuel rate of injection (ROI) along with ambient conditions (Kook et al. 2009). The entrainment wave is a representation of the mixing behavior which occurs after the end of injection, traveling through the combustion chamber. The entrainment must reach the quasi-steady liquid length before vaporization is complete in order to cause the liquid length to recede which is not the case in low temperature or density ambient conditions (Kook et al. 2009).

Various diagnostics have been applied to characterize diesel spray liquid length behavior for both conventional diesel fuels and single or multi-component mixtures (Siebers 1998, 1999; Fisher and Mueller 2010; Pickett et al. 2010, 2011) along with studies for alternative diesel fuels and their blends including biodiesel (Genzale et al. 2010). One common underlying characteristic of this and many other past liquid length studies is the use of single hole nozzles for spray characterization as opposed to multi-hole nozzles which are representative of production diesel engines. This leads to a fundamental knowledge gap due to the presence of plume to plume variations from multi-hole injectors which can translate to changes in fuel and charge-gas mixing resulting in combustion or emissions differences. These variations can be attributed to the small tolerances in manufacturing, geometry, flow cavitation or other phenomenon as will be discussed. There is a lack of reliable information on these plume-to-plume variations because of researchers overlooking the importance of different spray plume hole characteristics on spray characteristics.

Methods to study liquid length include Mie scattering which relies on light scattering off of fuel droplets along with laser based techniques of absorption and extinction. Mie scattering is the commonly used diagnostic for studying liquid length (Pickett et al. 2011). Despite being well accepted, Mie scattering application is limited

since the illumination method and method of light collection is known to influence the experimental results making direct comparison of findings between facilities difficult (Pickett et al. 2011). In Mie scattering, typical illumination methods are volume illumination (Zhang et al. 1997; Siebers 1998; Higgins et al. 1999) to visualize all droplets, or laser-sheet illumination, on the spray axis to visualize a portion of the spray (Baert et al. 2009; Fisher and Mueller 2010). In addition to these illumination methodologies, the orientation of the illumination can vary being side (Siebers 1998; Fisher and Mueller 2010), head on (Zhang et al. 1997), or back illumination with a diffuser (Desantes et al. 2006). The results vary as each setup including methodology, orientations of illumination, and collection, likely possesses variations in optical response depending on the concentration of droplets in the region of illumination. The influence of optical setup on liquid length was investigated by Pickett et al. (2011) by consideration of nine optical setups including Mie scatter imaging with different light source setups (orientation, light source, and other parameters) and extinction based measurements, using both continuous-wave light sources with a high speed camera or photodiode and the use of a short laser pulse to image the spray. Key conclusions from this work was that light extinction diagnostics may be better than traditional light scattering diagnostics as it is essentially self-calibrating, however, these limitations can be short-lived due to beam-steering effects. Regardless, the limitations of conventional Mie scatter diagnostics need to be acknowledged in regards to its sensitivity to the light source illumination yielding differences in scattering intensity causing variations in spray shape and measured liquid length properties. Different diagnostics have pros and cons and the limitations of the diagnostic must be considered and acknowledged when interpreting and presenting the results.

2.3.3. Cone Angle

Cone angle is a macroscopic spray characteristic representing the dispersion or spreading of the spray. It is the angle of a single plume and can be defined for vaporizing, non-vaporizing and combusting conditions, but it is difficult to characterize under vaporizing conditions due to the narrow spray width of the liquid phase. Ideally, good dispersion is desired (large cone angle) to ensure fast mixing of the liquid and gas phase with a high evaporation rate for optimum combustion (Lefebvre 1989). As the cone angle increases, there is increased air entrainment which can enhance fuel-air mixing. Consistent measures of cone angle are difficult to achieve as there is no single accepted definition or measurement technique for cone angle (Lefebvre 1989; Siebers 2008). This is largely attributed to the fact that the cone angle depends on the imaging diagnostic with Mie scattering only recording light in a small solid angle as scattered by the liquid phase whereas shadowgraph imaging records significantly more scattering and absorption yielding variations in cone angle measurements (Klein-Douwel et al. 2007).

Various correlations have been proposed to explain cone angle trends, as summarized in Table 2.6.

Table 2.6
Correlations for cone angle.

Authors	Correlation	Terminology / Restrictions
Martinez-Martinez et al. 2010	$\tan \frac{\theta}{2} = 0.13 * \left(1 + \frac{\rho_a}{\rho_f}\right)$	Ambient density < 15 kg/m ³
Hiroyasu et al. 1980	$\theta = 0.05 \left(\frac{d_o^2 \rho_a \Delta p}{\mu_a^2} \right)^{0.25}$	Radians
Hiroyasu and Arai 1990	$\theta = 83.5 \left(\frac{1}{d_o} \right)^{-0.22} \left(\frac{d_o}{D} \right)^{0.15} \left(\frac{\rho_a}{\rho_f} \right)^{0.26}$	
Delacourt et al. 2005	$\theta = 114.6 * \arctan \left(0.31 * \left(\frac{\rho_a}{\rho_f} \right)^{0.2} \right)$	
Siebers 1999	$\tan \frac{\theta}{2} = C_1 \left(\left(\frac{\rho_a}{\rho_f} \right)^{0.19} - C_2 \sqrt{\frac{\rho_f}{\rho_a}} \right)$	C1 constant 0.26, orifice dependent; C2 is 0 for non-vaporizing fuel jets, 0.0043 for vaporizing fuel jets

As detailed in the table, not only are there various correlations for cone angle, there are varying parameter influences, including parameters considered and the weight or relationship for this parameter relative to cone angle. This could be attributed to the differing, non-uniformly accepted definitions for cone angle. All correlations show an ambient gas density effect, albeit of different magnitudes, with most also including an orifice parameter effect either directly through orifice diameter or indirectly through constants, with the exception of Martinez-Martinez et al. (2010) and Delacourt et al. (2005.) Klein-Douwel et al. (2009) have proposed a common relationship for cone angle as summarized in equation (3).

$$\tan \left(\frac{\theta}{2} \right) \propto \rho_a^m P_f^n d_h^a t^B \quad (3)$$

In the above relationship, the exponents vary significantly, for example m , the density dependence ranges from 0.1 to 0.5, injection pressure dependence n , ranges from -0.115 to 0.35 power, hydraulic nozzle diameter a , ranges from 0.15 to 0.508 power, and the time dependence is presented as -0.40 for one condition while others are at steady state (Klein-Douwel et al. 2009). Therefore, although cone angle is known to depend on various parameters, the consistency is not well defined which most likely is largely impacted by inconsistencies in cone angle definition, being for example the angle at 60 nozzle diameters (Lefebvre 1989) or at 60% penetration (Pastor et al. 2001), as will be discussed in more detail in future chapters. Additionally, it is known that fuel spray cone angle can also be considerably influenced by needle lift and when the needle is at full lift, the cone angle has typically reached a constant value (Tomohisa et al. 1997).

Parameter influence is better understood by the comparison provided in Table 2.7.

Table 2.7**Cone angle parameter influence (Arregle et al. 1999; Martinez-Martinez et al. 2010).**

Parameter	Cone Angle Trend for an Increase in Parameter
Injection pressure	No influence
Fuel to ambient density	↑ unless ratio is >0.04 then independent
Ambient temperature	↓
L/d ratio	↓
Nozzle diameter	No influence
Ambient density	↑

As discussed, cone angle is influence by various ambient conditions with some inconsistencies in trends related to definitions of cone angle and large influence of cone angle on the processing methodology.

2.3.4. Lift-Off Length

Diesel sprays are a lifted flame phenomenon requiring definition of the lift-off length parameter to understand the spatial onset of combustion. Flame lift-off length is defined as the most upstream location of the combusting spray, which is a lifted turbulent diffusion flame (Siebers and Higgins 2001). This lift-off length is defined as a quasi-steady location (fluctuations due to turbulence) where reaction of the mixed fuel and air is occurring (Higgins and Siebers 2001). Lift-off length is influenced by various ambient and injection parameters as defined in Table 2.8.

Table 2.8**Lift-off length parameter influence (Higgins and Siebers 2001; Siebers and Higgins 2001).**

Parameter	Lift-Off Length Trend for an increase in parameter
Ambient density	↓
Ambient temperature	↓
Nozzle orifice diameter	↑
Injection pressure	↑
Oxygen concentration	↓

The lift-off length is important in understanding combustion and emissions formation. There is a link between fuel-air mixing upstream of the lift-off length and the resulting soot formation with soot decreasing as the fuel-air premixing upstream of the lift-off length increased since as the air entrainment increases, the average equivalence ratio at the lift-off length is reduced to a value which minimizes soot formation (Siebers and Higgins 2001).

A diagnostic commonly used to quantify diesel spray lift-off length is OH chemiluminescence imaging (310 nm) which is line-of-sight and time-averaged, since OH occurs under high temperature, stoichiometric combustion conditions at flame-stabilization locations providing an indication of high heat release regions (Higgins and Siebers 2001). Additionally, natural combusting luminosity images can be used to provide a qualitative indication of spatial soot distributions (Kook et al. 2005) along with an indication of lift-off length.

There is a relationship between liquid length and lift-off length, and in particular fuel vaporization and combustion which is governed by the ambient gas and injector properties (Siebers and Higgins 2001). Two sets of conditions can occur. The first

condition is that with a liquid length shorter than the lift-off length, meaning that fuel vaporization is complete before combustion zones are reached, and therefore there is no interaction between vaporization and combustion processes. The second condition is a liquid length longer than the lift-off length, which causes the spray to have a cool-core which has vaporized fuel that is surrounded by a rich reaction zone and vaporization cooling can influence the combustion rate, yielding a reduction in laminar flame speed and an increase in lift-off length (Siebers and Higgins 2001). For the case of a shorter liquid length relative to the lift-off length, there may be less soot formed due to a more intense central reaction zone based on enhanced fuel-air mixing before the lift-off length (Siebers and Higgins 2001).

2.3.5. Plume to Plume Variations

As discussed previously, many spray and combustion studies focus on single hole nozzles and therefore do not provide sufficient information to fully understand production multi-hole nozzles based on the potential for plume-to-plume spray interactions. Multi-hole nozzles are used in production diesel engines as required for fuel and charge-gas mixing in the cylinder, providing more efficient combustion while lowering particulate emissions (Ramirez et al. 2009). Single hole nozzles do have advantages for fundamental spray and combustion research in that there is not interference in optical diagnostics from adjacent spray plumes making diagnostic application easier, and single hole nozzles are shown to be fairly representative of multi-hole nozzles providing the necessary fundamental information in a simplified manner, being limited in regards to the influence of the number of nozzle holes and their placement and plume interactions (Prashanth et al. 2006). Multi- and single-hole injectors have different rates of injection which can translate to spray characteristics hence provide different results, which are likely attributed to the different internal flow characteristics of the nozzle (Ramirez et al. 2009). There are limitations in applying single hole nozzles to characterize multi-hole behavior based on differences in the end of injection ramp down rate which can be up to four times slower for multi-hole injectors relative to single-hole injectors (Kook et al. 2009). Furthermore, cavitation onset is asymmetrical which can translate to spray characteristics having a different influence on a multi-hole injector (Soteriou et al. 1995), and turbulence levels in multi- versus single hole nozzles are also different (Chaves et al. 1995).

Research on plume to plume variations is limited. Even in work that characterizes multi-hole spray behavior, plumes are typically grouped to provide a common result for all plumes as opposed to quantifying the individual plume to plume variations and limited work tries to understand the causes and reasoning for these variations. Manufacturing differences, along with other internal flow geometry variations and eccentric needle movement can yield differences in plume to plume spray behavior (Powell et al. 2011) and understanding the plume-to plume variations is important since hole to hole behavior is not always repeatable (Pickett et al. 2011). Differences in nozzle hole diameters, attributed to manufacturing tolerances, can result in uneven fuel pressure distribution once the needle begins to lift off of its seat, and hence the spray plume variations are most prevalent at start of injection and are reduced once the needle has reached full lift,

but transversal and vertical needle oscillations can still occur while the injector is in its energized, fully open, state (Karimi 2004; Karimi 2007).

Different injector technologies are used including valve-covered orifices (VCO's) and sac-type nozzles which have a sac that is filled with fuel for providing fuel to the holes, with the influence of injector type being important in downstream spray characteristics. This sac-type nozzle can help provide more uniform and symmetric feeding of the holes, in particular during the transient needle lift which is advantageous, however, a limitation is that the residual fuel in the sac volume can cause the release of large fuel droplets at the end of injection which yields high soot levels (De Risi et al. 2000). It has also been proposed that spray asymmetry is the result of cavitation which can be more prevalent in certain holes from a multi-hole injector being more customary in VCO nozzles, however, after engine operation of a mini-sac injector, carbon particles can be deposited which alters nozzle hole properties yielding higher hole to hole spray variation in this type of injector as well (De Risi et al. 2000). De Risi et al. (2000) found that despite differences in nozzle geometries and imperfections due to machining, there was no correlation to spray asymmetries except under engine fatigue tests, signifying that some other phenomenon is at work, for example cavitation. Spray symmetry is improved by the use of double-guide needle geometry, however, the plume-to-plume variations are not eliminated (De Risi et al. 2000).

2.3.6. Liquid Length Fluctuations

Liquid length reaches a quasi-steady value during injection, being quasi-steady due to fluctuations which exist about the mean liquid length value at steady state. These fluctuations are evident in liquid length spray characterizations; however, the underlying reasons for these fluctuations are not conclusive. Many researchers attribute these fluctuations to turbulence (Higgins et al. 1999; Kurvers and Luijten 2010; Som and Longman 2011). There is high frequency content in the force signal (for fuel momentum measurements used in mass flow rate determinations) during injection signifying pressure vibrations in the high pressure fuel line to the injector, on the order of 3-5 kHz, with these fluctuations also being present in the injector needle which can translate to downstream spray characteristics (Peters 2007). After the end of injection, the oscillation in needle lift and low frequency mechanical vibrations can cause fluctuations in liquid length with frequencies between 10 to 15 kHz with a fluctuation of $\pm 15\%$ of the mean value (Peters 2007). Siebers (1998) found a quasi-steady liquid length with $\pm 11\%$ fluctuation with frequencies in excess of 2 kHz, and attributed this to turbulence.

Another potential cause of the fluctuations in liquid length is due to slugs of concentrated liquid fuel breaking away from the main core of the spray, with these slugs being due to the fluctuation of the sprays structure due to either air entrainment or needle oscillation (Crua 2002). Pickett et al. (2009) attributed liquid length fluctuations to the large scale structures evolving at the jet tip, which can lead to a break in the connected liquid region. This causes a cluster of droplets to become isolated from the spray which subsequently evaporate resulting in a decrease in penetration, which they attribute to turbulence in the spray and not experimental uncertainty as the fluctuations are larger than the test-to-test repeatability.

2.4. Spray Modeling

Diesel spray and combustion are difficult to accurately model especially in the predictive sense. This requires a model which can not only quantify the physical phenomena, but also the detailed chemical and thermodynamic processes which occur. These phenomena include the chemical reaction processes, turbulence, thermodynamics, mixing, vaporization, entrainment, spray dynamics and combustion, along with others (Manely et al. 2008). Diesel sprays are a high velocity phenomena which result in small temporal and spatial scales further complicated by their two-phase nature (Pastor et al. 2008), and the length and time scales of the combustion and engine processes. To accurately span this wide range of length scales, various approaches are required including quantum mechanics, molecular dynamics, Kinetic Monte Carlo, Direct Numerical Simulation (DNS), Large Eddy Simulation (LES), and Reynolds-Averaged Simulations (RAN) (Manley et al. 2008). Developing modeling capabilities which incorporate all of these phenomena that is predictive and can be validated with experimental data would facilitate the development of engines to harness technological advancements and new strategies to not only reduce emissions, but also increase fuel efficiency. Modeling can also be used to understand spray penetration and liquid length over a range of conditions to minimize wall impingement (Lefebvre 1989). There are various levels of spray modeling in regards to complexity ranging from simple models for spray penetration or liquid length, to more complex computational fluid dynamics models. These CFD models themselves have different levels of complexity in regards to the sub-models which are incorporated and used, including ligament formation and subsequent breakup, droplet break-up and evaporation, turbulence effects on the spray, and air entrainment during the injection event, all which must be accurately modeled for the CFD model to be valid (Sazhin et al. 2003).

Various simplifications can be applied in the diesel spray modeling which when done correctly, still uphold the model validity. For example, sprays can be modeled and studied assuming a continuous model of a gas jet based on the inherent similarity of these two phenomenon, with this assumption having been used in several models and studies (Adler and Lyn 1969; Musculus and Kattke 2009; Desantes et al. 2011). This simplification to gas jet modeling is acceptable when the same momentum and mass flow rate is applied (Pickett et al. 2011). It is especially valid under the high boost and injection pressure conditions along with small orifice diameter injectors representative of conventional engines due to complete atomization inside the spray close to the nozzle exit (Smallwood and Gulder 2000) resulting in fast dynamic equilibrium between the droplets and the surrounding ambient charge (Pastor et al. 2008). Models can also be simplified to a spatial dimension, while considering time-varying boundary conditions. For example with variables averaged over the entire cross-section of the spray to predict evolution for both vaporizing and non-vaporizing conditions providing this simplification while still revealing information on spray tip penetration along with property evolution along the spray (Wan and Peters 1999).

There are pros and cons to each of the different modeling procedures based on the desired application as outlined in Table 2.9.

Table 2.9
Comparison of CFD and 1-D spray models (Aneja and Abraham 1998; Pastor et al. 2008; Kook et al. 2009)

Modeling Type	1-D Phenomenological Spray Models	CFD
Methodology	Control volume analysis	Conservation equations with mesh and solver
Pros	Provides the basic physics to solve the problem of spray characterization	More accurate representation of real spray behaviors
	Enables straight forward identification of the influence of boundary parameters on results	Multidimensional model
	Guide spray models with CFD applications	Predict details of fuel-ambient mixing under complex in-cylinder flow conditions
	Aid interpretation of combustion measurements	
Cons	Simplified model, usually requiring several assumptions to enable simple solutions	Hinders identifying the link between macroscopic spray results and boundary conditions of the problem
	Rarely predictive in nature	Requires large computational time to solve small cells
		Typically sensitive to numerical resolution and grid or mesh size, and mesh refinement is essential for accurate results
		Limitations for atomization in regards to grid resolution
		Model validation is imperative
		Currently limited by spray modeling uncertainty

For a first order simplified macroscopic approximation to a spray problem, 1-D phenomenological or multi-zone models are typically sufficient. However, the continued improvement to CFD models, along with the incorporation of increasingly accurate sub-models, will improve CFD model applicability to assist with predictive model development to advance the state of internal combustion engines. Overviews of some of the relevant 1-D spray models for spray penetration and liquid length will be discussed next.

2.4.1. 1-D Spray Models

There are two key classes of 1-D spray models which will be discussed, those focusing on conservation equations applied to control volumes or surfaces, and those based on tracking fuel mass particles using a Eulerian approach.

2.4.1.1. Conservation Equation Methodology

There are various one-dimensional spray models for understanding spray characteristics, some of which are summarized below. These spray models are typically based on two different vaporization limitations, that which is droplet limited (Abramzon and Sirigano 1989) meaning that the vaporization rate is restricted by droplet surface

inter-phase transport with the other, the more accepted and commonly used phenomena, being mixing limited vaporization which assumes that local processes including mass, momentum, and energy transport are faster than the global fuel-air mixing rate so that droplets are always in thermodynamic equilibrium with the ambient (Siebers 2008; Luijten and Kurvers 2010). Before discussion in detail, a summary table reviewing the models discussed is provided in Table 2.10.

Table 2.10
Overview of conservation equation methodology spray models.

Reference	Model	Rate of Injection Profile	Solution
Naber and Siebers (1996)	Penetration of non-vaporizing isothermal fuel jet	Top-hat	Conservation of mass; Conservation of momentum; Integral control surface
Musculus and Kattke (2009)	Spray and mixing behavior after end of injection – entrainment wave	Input rate of injection profile, can be variable	Expansion of Naber and Siebers 1996; Discretize spray into multiple control volumes
Siebers (1999)	Liquid length based on mixing limited vaporization	Top-hat	Based on Naber and Siebers 1996; Addition of conservation of energy equation; Control volume analysis
Versaavel et al. (2000)	Liquid length, assuming thermodynamic equilibrium at every axial position in the spray	Top-hat	Based on Naber and Siebers 1996 and Siebers 1999 models; Integral control surface with conservation of fuel mass flow rate, momentum and enthalpy
Luijten and Kurvers (2010)	Liquid length, incorporating real gas effects	Top-hat	Incorporated real gas effects into Siebers 1999 and Versaavel et al. 2000 models through an enhancement factor
Desantes et al. (2009)	Liquid length, mixing limited spray evaporation	Top-hat	Mass and energy balance, fuel mass fraction determination of evaporated fuel, energy conservation

The majority of the models to be discussed build upon that originally developed by Naber and Siebers (1996) in some form, with the exception of the Desantes et al. (2009) model. All of the models, with the exception of Musculus and Kattke (2009) rely on a top-hat rate of injection profile, which presents with reasonable accuracy the actual injection profile, however, this is a limiting factor in these models. These models will now be reviewed in more detail.

One well known and accepted scaling model is that of Naber and Siebers (1996). This model is a scaling law for the penetration of a non-vaporizing (isothermal) fuel jet under quiescent conditions assuming a top-hat injection rate and an idealized diesel fuel jet which can be applied to the entire spray behavior over time. This model is based on the fuel jet penetration analysis of Wakuri et al. (1960), with some modifications. These modifications include (Naber and Siebers 1996):

- Non-dimensionalization of the analysis including ambient gas and fuel density orifice parameters.
- Estimate for an arbitrary constant in the correlation based on fuel concentration and velocity profiles as applied to turbulent two-phase jets.
- Development of an inverse relationship for time versus penetration distance correlation.
- Derivation of mean equivalence ratio as a function of axial distance.

This scaling model is developed with the application of mass and momentum conservation principles with this model fuel jet defined such that its characteristics represent that of a real fuel jet. Derivation is based on the use of integral control surface techniques being applied to idealized, isothermal, incompressible fuel jets, as applied to the control surface shown in Figure 2.2.

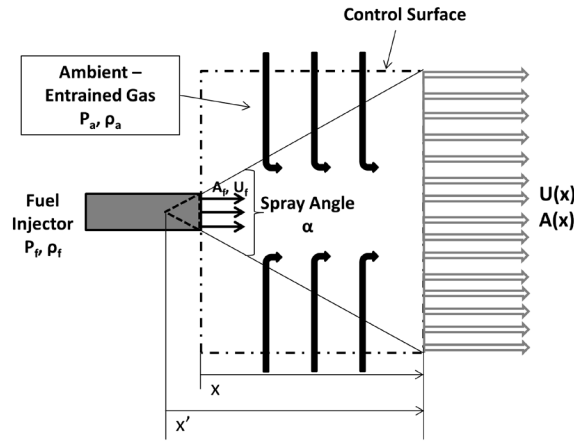


Figure 2.2: Control surface for the spray penetration model. Modified from Naber and Siebers (1996).

The mass and momentum balances applied to the above control surface are provided in equation (4).

$$\begin{aligned} \text{Mass:} \quad & \rho_f A_f(0) U_f = \rho_f A_f(x) U_f(x) \\ \text{Momentum:} \quad & \rho_f A_f(0) U_f^2 = \rho_f A_f(x) U(x)^2 + \rho_a A(x) U(x)^2 \end{aligned} \quad (4)$$

These mass and momentum relationships are solved taking into consideration these simplifying assumptions (Naber and Siebers 1996):

- Radially uniform velocity and fuel concentration profiles.
- Instantaneous start of injection.
- Constant injection velocity.
- Modeled fuel spray has the same mass and momentum fluxes as the equivalent real spray.
- No velocity slip between the fuel and entrained air implying dynamic equilibrium between the liquid and gas phases.
- Quasi-steady flow with uniform growth rate meaning constant spray spreading angle.
- Minimal azimuthal flow at the orifice exit.

The final dimensional penetration relationships developed by Naber and Siebers (1996) are defined in equation (5).

$$\begin{aligned}
S &= C_v \cdot \sqrt{2 \frac{(P_f - P_a)}{\rho_a}} t, \text{ Valid for } t < t_r \\
S &= \frac{\sqrt{C_v \cdot \sqrt{2 C_a}}}{a \cdot \tan(\theta/2)} \cdot \sqrt{\frac{(P_f - P_a)}{\rho_a}} \cdot d_o \cdot t, \text{ Valid for } t > t_r \\
t_r &= \frac{\sqrt{\frac{C_a}{2}}}{C_v \tan(\frac{\theta}{2})} \frac{d_f \cdot \sqrt{\bar{\rho}}}{\sqrt{\frac{P_f - P_a}{\rho_f}}} \\
d_f &= \sqrt{C_a} \cdot d_o \\
\bar{\rho} &= \frac{\rho_f}{\rho_a}
\end{aligned} \tag{5}$$

As the Naber and Siebers liquid length model is a simplified model enabling parametric studies of spray penetration, it has several limitations. These include the use of a single control volume requiring the injection rate to be steady, and transient effects cannot be considered.

The Naber and Siebers penetration model was further improved upon by Musculus and Kattke (2009) by dividing the spray into multiple discrete control volumes axially along the jet as shown in Figure 2.3.

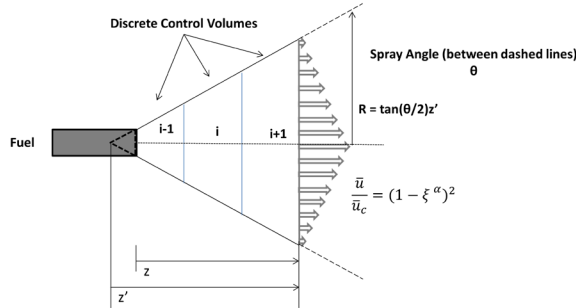


Figure 2.3: Model with discrete control volumes, adapted from Musculus and Kattke (2009).

The goal of this model was to look at spray and mixing behavior after the end of injection to understand the entrainment wave. This wave is shown to travel downstream at twice the initial jet propagation rate subsequently increasing mixing by up to a factor of three. This increase in mixing can help to reduce soot formation but can also yield incomplete combustion and high levels of unburnt hydrocarbons due to the creation of lean mixtures near the injector. Between control volumes, mass and momentum transport is solved numerically to provide information on fuel mass, entrained ambient mass, and the ratio of fuel to entrained ambient mass. Other improvements are a polynomial radial profile for mixing and velocity that approximates a real jet distribution as opposed to the uniform profiles used previously. With this multiple control volume approach, variable injection rates can also be included to better approximate real diesel sprays. Assumptions are as follows:

- Non-vaporizing jet.

- Incompressible flow.
- Turbulent and molecular viscous forces acting on each control volume are neglected.
- Neglect axial mixing of momentum due to molecular and turbulent diffusion.
- Neglect net force due to axial pressure gradient.
- Constant jet spreading angle during injection and after the end of injection transient. This constant jet spreading angle is a known limitation since researchers have found that there is a transition where spreading angle increases with axial distance, i.e. the model doesn't capture the transition from narrow jet angle upstream to a wider jet angle downstream (Pickett et al. 2011). This transition in spreading angle is especially important for modeling of the liquid phase region.
- Normalized radial profile of mean axial velocity is unchanged during the end of injection transient.
- Neglect density variations across the jet.

Inputs to the model are mass and momentum rate shapes, with the output of the model being the fuel to ambient ratio throughout the jet, which is used to define the spray conditions based on the expected fuel to ambient ratio for different characteristics.

Model development is undertaken by defining the transient transport equations for fuel mass and total jet momentum for each control volume as shown in equation (6).

$$\frac{\partial \dot{m}_f}{\partial t} = \dot{m}_{f,in} - \dot{m}_{f,out} \quad (6)$$

$$\frac{\partial \dot{M}}{\partial t} = \dot{M}_{in} - \dot{M}_{out}$$

Where the 'dots' on the mass and momentum define integral fluxes crossing the upstream and downstream faces of each control volume. These are defined by equation (7).

$$\begin{aligned} \dot{m}_f &= \rho_f \int \bar{X}_f \bar{u} dA \\ \dot{M} &= \int \bar{\rho} (\bar{u})^2 dA \end{aligned} \quad (7)$$

The over-bars on the parameters define the turbulent, transient, components of the spray. The jet cross sectional area is defined in equation (8).

$$A = \pi (\tan(\theta/2) z')^2 \quad (8)$$

Where z' is the distance from the virtual jet origin to the control volume of interest. The model assumptions rely on non-uniform profiles for velocity and fuel volume fraction (a modification from the Naber and Siebers (1996) model) and these are defined in equation (9), resembling a Gaussian error function.

$$\begin{aligned} \frac{\bar{X}_f}{\bar{X}_{f,c}} &= (1 - \xi^\alpha)^2 \\ \frac{\bar{u}}{\bar{u}_c} &= (1 - \xi^\alpha)^2 \end{aligned} \quad (9)$$

Where ξ is the ratio of the radial coordinate r to the jet width R , which is defined as $\tan(\theta/2) z'$. The exponent, alpha, is variable, and is chosen to fit the evolving radial velocity profile as the flow exits the nozzle. Downstream of the nozzle the radial profile

becomes self-similar leading alpha to be defined as 1.5, representing a fully developed profile. The entrainment rate is defined in equation (10).

$$\frac{\partial \dot{m}_e}{\partial z} = \rho_a \frac{\partial}{\partial z} (\bar{u}A) \quad (10)$$

The model predicts the cross-sectionally averaged turbulent mean velocity, \bar{u} . Even though the Musculus and Kattke (2009) model was developed for nonvaporizing sprays it can be used to estimate the extent of fuel vaporization based on the predicted mixture distribution. This model however does not provide an explicit solution for penetration. A steady state penetration solution can be developed but this requires various steps and numerical integration including solving mass flux and momentum flux, along with the entrainment rate relationship, and spatially integrating the momentum over the length of the jet (Musculus and Kattke 2009).

Models have also been developed for characterizing the liquid length of the vaporizing spray. This includes a model from Siebers (1999) which is based on mixing limited vaporization, i.e. atomization and interphase transport are not the limiting factor, rather, mixing is the limiting factor in controlling the liquid length. This requires that the ambient gas mixture in the vaporization region be saturated (Siebers 2008), a key factor in model development. Siebers (1999) liquid length scaling model is developed based on the Naber and Siebers (1996) spray model which defines mass and momentum conservation equations, and with the inclusion of the energy equation, can be extended to liquid phase spray behavior with liquid length being defined as the axial distance along the spray where saturation occurs. These conservation equations are applied to the control volume shown in Figure 2.4.

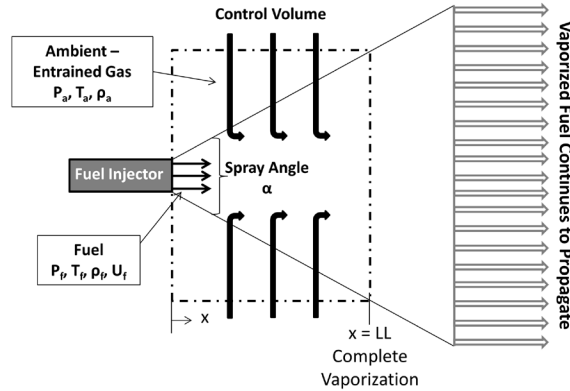


Figure 2.4: Control volume schematic for the liquid length model. Modified from Siebers (1999).

The definition for liquid length in the model is the location along the spray centerline where the mixture fraction is equal to the mixture fraction for saturated liquid-vapor equilibrium where just enough hot ambient gas has been mixed with fuel to fully vaporize the fuel (Siebers 1999). Siebers liquid length model has limited application for low gas densities and temperatures because in these regions droplet transport processes begin to drive the vaporization processes in place of mixing. Model assumptions are similar to that of Naber and Siebers (1996) and are listed here (Siebers 1999):

- Quasi-steady flow with constant spray spreading the result of air entrainment. This spreading angle is governed by injector properties and fuel and ambient gas

densities defining turbulent momentum transport from the injected fuel to the entrained gases.

- Perfect mixing, achieved by uniform velocity, temperature and fuel concentration profiles.
- No velocity slip between entrained ambient gas and the injected fuel.
- Fuel flow is locally homogeneous, i.e. neglect atomization processes and droplets, due to fast transport processes at droplet surfaces in comparison to the rates of the spray mixing processes.
- Vapor phase fuel is saturated and in thermodynamic equilibrium with liquid phase fuel and the entrained ambient gas.
- Neglect gas absorption in the liquid phase and recovery of kinetic energy in the region of fuel vaporization.
- Idealized phase equilibrium:
 - **Raoult's rule applies** (Cengel and Boles 2008): This rule states that the partial vapor pressure of a component in a mixture is equal to the vapor pressure of the pure component, multiplied by its mole fraction in the mixture), as defined by equation (11).

$$P_{i,a} = Y_{i,a} * P_{Total} = y_{i,f} * P_{i,s}(T) \quad (11)$$

Where the saturation pressure is the pressure at the interface temperature, T , and P_{Total} is the total pressure on the gas phase side (i.e. outside of the fuel-entrained gas mixture).

- **Dalton's rule applies** (Cengel and Boles 2008): This rule applies to gases and defines the pressure of the mixture P_m as given by equation (12).

$$P_m = \sum_{i=1}^k P_i(T_m, v_m) \quad (12)$$

Where P_i is the pressure of each gas at the mixture temperature, T_m , and mixture volume, v_m , essentially meaning that the total mixture pressure is a sum of the individual gas pressures at the mixture temperature and volume.

To develop the liquid length model, conservation of mass, momentum and energy must be applied at the injector inlet and at the location of complete fuel vaporization, the liquid length. This derivation is a multistep process that begins first with applying conservation of mass and energy to the control surface for complete vaporization due to fuel-gas mixing as provided in equation (13).

$$\begin{aligned} \dot{m}_f(LL) &= \rho_f(LL) * A(LL) * U(LL) \\ \dot{m}_a(LL) &= \rho_a(LL) * A(LL) * U(LL) \end{aligned} \quad (13)$$

At the liquid length, gas and fuel densities are dependent on their partial pressures.

Next, conservation of energy is applied to the control surface. This starts with the generic form of conservation of energy as provided in equation (14).

$$\frac{dE_{cv}}{dt} = \dot{Q}_{cv} - \dot{W}_{cv} + \sum_i \dot{m}_i \left(h_i + \frac{v_i^2}{2} + gz_i \right) - \sum_e \dot{m}_e \left(h_e + \frac{v_e^2}{2} + gz_e \right) \quad (14)$$

Kinetic and potential energy are neglected along with work and heat on the control volume. As the flow is assumed to be quasi-steady, the time derivative is zero, simplifying the conservation of energy relationship to equation (15).

$$\sum_i \dot{m}_i h_i = \sum_e \dot{m}_e h_e \quad (15)$$

This simplified conservation of energy relationship is applied to the control volume. Inlet conditions are relative to the injected fuel and entrained ambient gas; exit conditions are defined by the mixed and vaporized saturated fuel. Applying these concepts to the conservation of energy relationship yields equation (16).

$$\begin{aligned} \dot{m}_f(LL) * h_f(T_f, P_a) + \dot{m}_a(LL) * h_a(T_a, P_a) \\ = \dot{m}_f(LL) * h_f(T_s) + \dot{m}_a(LL) * h_a(T_s, P_a - P_s) \end{aligned} \quad (16)$$

Based on conservation of mass, the mass flow rate of the injected fuel is equal to the mass flow rate of the fuel at the liquid length, with the same reasoning applied to the ambient gas mass flow rate.

The evaporation coefficient, B , is defined by determining the fuel to ambient gas mass flow rates from both conservation of mass and conservation of energy, as provided in equation (17).

$$\frac{\dot{m}_f(LL)}{\dot{m}_a(LL)} = \frac{\rho_f(LL) * A(LL) * U(LL)}{\rho_a(LL) * A(LL) * U(LL)} = \frac{\rho_f(LL)}{\rho_a(LL)} \quad (17)$$

Applying a real gas equation of state to the above relationship which includes compressibility, provides the final fuel to ambient mass flow rate relationship, as determined from the conservation of mass and shown in equation (18).

$$\begin{aligned} \frac{\dot{m}_f(LL)}{\dot{m}_a(LL)} &= \frac{\rho_f(LL)}{\rho_a(LL)} = \frac{P_s * MW_f}{Z_f(T_s, P_s) * R * T_s} * \frac{Z_a(T_s, P_a - P_s) * R * T_s}{(P_a - P_s) * MW_a} \\ &= \frac{P_s * MW_f * Z_a(T_s, P_a - P_s)}{Z_f(T_s, P_s) * (P_a - P_s) * MW_a} \end{aligned} \quad (18)$$

At the liquid length the ambient gas is saturated since the vapor phase fuel is in thermodynamic equilibrium with the ambient gas per an earlier assumption. The same relationship for fuel to ambient mass flow rate is derived using the conservation of energy relationship as shown in equation (19).

$$\frac{\dot{m}_f(LL)}{\dot{m}_a(LL)} = \frac{h_a(T_a, P_a) - h_a(T_s, P_a - P_s)}{h_f(T_s) - h_f(T_f, P_a)} \quad (19)$$

Using these two ratios of fuel mass flow rate to ambient mass flow rate, the evaporation coefficient, B , is defined in equation (20).

$$\begin{aligned} B = \frac{\dot{m}_f(LL)}{\dot{m}_a(LL)} &= \frac{P_s * MW_f * Z_a(T_s, P_a - P_s)}{Z_f(T_s, P_s) * (P_a - P_s) * MW_a} \\ &= \frac{h_a(T_a, P_a) - h_a(T_s, P_a - P_s)}{h_f(T_s) - h_f(T_f, P_a)} \end{aligned} \quad (20)$$

To calculate the evaporation coefficient which is used in the liquid length determination, the saturation temperature must be determined. Once this is known all other terms can be evaluated as saturation pressure is governed by saturation temperature which then permits the evaluation of compressibility and enthalpies which together with known parameters enable calculation of the evaporation coefficient. Solving for the

saturation temperature requires an iterative solution of the two right-hand terms in the above equation.

The outcome of the conservation of mass and energy application is an expression for the evaporation coefficient which is a key component of the liquid length model. The next step is to characterize the axial variation of the fuel to ambient gas ratio based on mass and momentum conservation which originates from the Naber and Siebers (1996) model. In this definition, it is assumed that characteristics for the vaporizing sprays considered are similar to non-vaporizing isothermal sprays which equates to having locally homogeneous flow with the requirement that temperature effects do not change the mean fuel to ambient gas mass flow rate ratio significantly over any axial spray location. This assumption has been validated by Naber and Siebers (1996). Conservation of mass and momentum are defined in equation (21).

$$\begin{array}{ll}
 \text{Mass} & \dot{m}_f(x) = \rho_f * A_f * U_f \\
 & \dot{m}_a(x) = \rho_a * A(x) * U(x) \\
 \text{Momentum} & \dot{m}_f U_f = \dot{m}_f(x) \cdot U(x) + \dot{m}_a(x) \cdot U(x)
 \end{array} \quad (21)$$

These above relationships are used in conjunction with several other intermediate relationships as defined in equation (22) which stem from the Naber and Siebers (1996) spray penetration analysis.

$$\begin{aligned}
 A(x) &= \pi * (x * \tan\left(\frac{\alpha}{2}\right))^2 \\
 A_f &= \frac{\pi}{4} d_f^2 \\
 d_f &= \sqrt{C_a} * d \\
 x^+ &= \sqrt{\frac{\rho_f}{\rho_a} * \frac{d_f}{\tan\left(\frac{\alpha}{2}\right)}} \\
 \tilde{x} &= \frac{x}{x^+} \\
 \tan\left(\frac{\alpha}{2}\right) &= \text{atan}\left(\frac{\theta}{2}\right)
 \end{aligned} \quad (22)$$

Typically, x^+ is defined without the tangent angle term; however, this term is necessary as it takes into effect the density different between ambient gas and injected fluid, required based on the exchange between the two fluids. The last relationship in the above equation defines the idealized spray angle (α) relative to that of the measured spray angle (θ). The axial variation of fuel and ambient gas mass flow rates is defined by combining equations (21) and (22) as provided in equation (23).

$$\frac{\dot{m}_f(x)}{\dot{m}_a(x)} = \frac{2}{\sqrt{1 + 16 \cdot (x/x^+)^2} - 1} \quad (23)$$

Taking the axial variation of the fuel to ambient gas mass flow rate as provided in the above equation and evaluating at x equal to the liquid length defines the mass flow rate ratio as B and hence a relationship for liquid length is provided in equation (24), where B was defined in equation (20).

$$LL = \frac{b}{a} \sqrt{\frac{\rho_f}{\rho_a} \frac{\sqrt{C_a} d_o}{\tan(\theta/2)}} \sqrt{\left(\frac{2}{B} + 1\right)^2 - 1} \quad (24)$$

There are limitations in Siebers model as discussed, the first being the assumption of uniform velocity profile. Second, this model decouples the fuel and ambient gas at the liquid length which is not appropriate based on the fuel and gas interaction, rather, the fuel and ambient gas should be treated as one medium, characterized using the saturated mole fraction of fuel in the gas (vapor) phase (Luijten and Kurvers 2010).

Another spray model for liquid length is that of Versaavel et al. (2000) which is derived using both the Naber and Siebers (1996) and Siebers (1999) spray models, being a 1D model coupled with a 3D code. This model is quite similar to that of Siebers (1999) with the major modification being that thermodynamic equilibrium is assumed at every axial position (x) in the spray which provides additional information about spray formation upstream of the liquid length location. Assumptions in this model are as follows:

- No velocity slip between gas and liquid phases.
- Constant pressure for the whole system.
- Velocity, density and temperature profiles are top hat.
- Constant jet angle.
- System is at thermodynamic equilibrium.
- Assumes that velocity is equal to the velocity of the spray tip to enable determination of the time-dependent penetration length.
- Assumes radially uniform velocity and concentration profiles across the spray.
- Only valid for vaporizing sprays under mixing-limited vaporization assumption and under conditions where liquid impingement on the wall is avoided.
- Real gas effects are neglected.

Integral control surface techniques are used on the idealized quasi-steady diesel spray to solve conservation of fuel mass flow rate, momentum, and enthalpy applied to the control volume shown in Figure 2.5.

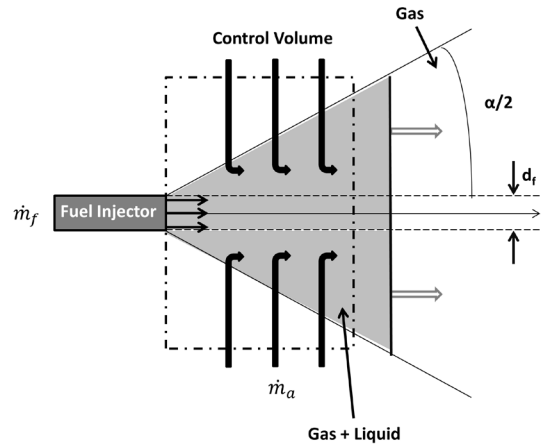


Figure 2.5: Control volume for the Versaavel et al. liquid length and penetration model. Modified from Versaavel et al. (2000).

For the fuel mass balance, the liquid fuel mass flow rate at the injector hole is equated to the remaining liquid fuel mass flow rate at x in addition to the gaseous evaporated fuel mass flow rate at x as defined in equation (25).

$$\rho_{fo}A_oU_{fo} = \rho_f(1 - m)AU + Y_{fg}\rho_g mAU \quad (25)$$

Where m is the void fraction, Y_{fg} is the vapor fuel mass fraction in the gas phase and U is the gas and liquid velocity at any axial location. Evaluating the above equation for the two velocity definitions results in the air-fuel mass ratio, Δ , is defined in equation (26). In comparison to the Siebers (1999) model, this air-fuel mass ratio is equivalent to $1/B$.

$$\Delta = \frac{\dot{m}_a}{\dot{m}_f} = \frac{m(1 - Y_{fg})\rho_g}{\rho_f(1 - m) + mY_{fg}\rho_g} \quad (26)$$

For the momentum balance, the liquid fuel momentum flow rate at the injector hole along x is equated to the remaining liquid fuel momentum flow rate at x in addition to the gaseous mixture momentum flow rate at x as defined in equation (27).

$$\rho_{fo}A_oU_{fo}^2 = \rho_f(1 - m)AU^2 + \rho_g mAU^2 \quad (27)$$

This momentum balance is combined with the previously discussed mass conservation principles to yield a new relationship for the air-fuel mass ratio along with other supplemental equations as provided in equation (28).

$$\Delta^2 = \frac{m^2(1 - Y_{fg})^2\rho_g^2 A}{A_o\rho_{fo}(\rho_f(1 - m) + m\rho_a)}$$

$$A = \pi(d_f/2 + x\tan(\alpha/2))^2$$

$$\tan\left(\frac{\alpha}{2}\right) = ac \left[\left(\frac{\rho_a}{\rho_f}\right)^{0.19} - 0.0043 \sqrt{\frac{\rho_f}{\rho_a}} \right]$$

$$\tan\left(\frac{\alpha}{2}\right) = a \tan\left(\frac{\theta}{2}\right) \quad (28)$$

The constant ac is given the value of 0.105 for liquid length.

The energy balance is defined by equating the liquid fuel enthalpy flow rate at the injector hole and the entrained air enthalpy flow rate, to the liquid fuel enthalpy flow rate at x in addition to the fuel vapor enthalpy flow rate at x plus air enthalpy flow rate at x as defined in equation (29), which is rewritten in terms of specific heats.

$$\begin{aligned} \dot{m}_{fo}h_{fl}(T_{fl}) + \dot{m}_a h_a(T_a) &= \rho_f(1 - m)AUh_{fl}(T) + Y_{fg}\rho_g mAvh_{fg}(T) \\ &+ \dot{m}_a h_a(T) \end{aligned} \quad (29)$$

$$\Delta \int_T^{T_a} c_{pa}(s)ds = \left(\frac{Y_{fg}\Delta}{1 - Y_{fg}} - 1 \right) L_v(T) + L_v(T_f) + \int_{T_f}^T c_{pfg}(s)ds$$

Where A is the spray area at the axial coordinate x , subscript fl represents the fuel in the liquid phase, a corresponds to ambient, and fg represents the fuel in the vapor phase.

Penetration or liquid length is solved for by using a Newton-Raphson method on the three nonlinear conservation equations of mass, momentum, and energy. The equations are solved for the air-fuel mass ratio, void fraction, gas phase density, mass fraction of fuel in the gaseous phase, and temperature of the gas-vapor mixture at x . This

is a set of three equations in five unknowns so additional information is required to close and solve the problem. This includes developing relations for the mass fraction of the fuel in the gaseous phase and the density of the gas phase, as provided in equation (30), determined based on the fundamental definitions for liquid length behavior. Up to the liquid length, due to thermodynamic equilibrium, the fuel partial pressure equals the fuel saturated vapor pressure which defines the saturated mole fraction of the fuel in the gas phase which can then be converted to mass fraction as defined.

$$Y_{fg} = \frac{1}{\left[\frac{P_a}{P_s(T)} - 1 \right] \frac{MW_a}{MW_f} + 1} \quad (30)$$

This first relationship is used for axial locations less than the liquid length where there is some liquid fuel left. The second required relationship is based on the uniform pressure assumption which enables developing a relationship between the gas phase density, temperature and mass fraction of the fuel in the gas phase as shown in equation (31).

$$\rho_g = \rho_a \frac{T_a}{T} \frac{1}{Y_{fg} \frac{MW_a}{MW_f} + (1 - Y_{fg})} \quad (31)$$

This equation is valid for an axial location greater than the liquid length where all liquid has disappeared so the void fraction is 1. Together, these equations close the problem to provide results for liquid length spray behavior.

Versaavel et al. (2000) did not provide an explicit relationship for liquid length, rather they state that the mass, momentum and energy conservation equations are iteratively solved at each axial location (x) in the spray, and the liquid length is then defined as the location (x) where the void fraction (m) is equal to 1. This led to Luijten and Kurvers (2010) taking the Versaavel et al. (2000) model to develop an explicit relationship for liquid length, using the definition of void fraction being 1. This involves simplifying the above set of equations starting with equation (27) using the knowledge that the gas phase density is the sum of the fuel (vapor) and ambient densities at the liquid length. Using definitions of mass flow rate to eliminate velocity terms and area definitions, a relationship is provided for the liquid length with a definition for the evaporation coefficient, B , as provided in equation (32).

$$LL = \frac{1}{4a} * \sqrt{\frac{\rho_{fo}}{\rho_a(LL)}} \frac{\sqrt{C_a}d}{\tan\left(\frac{\theta}{2}\right)} \sqrt{\left(\frac{2}{B} + 1\right)^2 - 1} - \frac{1}{2a} \frac{\sqrt{C_a}d}{\tan\left(\frac{\theta}{2}\right)} \quad (32)$$

$$B = \sqrt{\frac{\rho_{fo}}{\rho_a(LL)}} \frac{0.5d_e}{0.5d_e + LL \tan(\alpha/2)} \sqrt{B + 1}$$

$$d_e = \sqrt{C_a}d$$

The second group of terms on the right hand side of the equation takes into account that the spray actually starts from within the nozzle which is important at high temperature and density conditions. This explicit relationship for liquid length enables comparison to that defined by Siebers (1999).

Both the Siebers (1999) and Versaavel et al. (2000) model neglect most real gas effects. Luijten and Kurvers (2010) modified these two models to include real gas effects which are important under the conditions of study here, asserting that Siebers does not correctly account for real gas effects and that Versaavel et al. (2000) neglects them all together. Fuel injection occurs at high pressure which could alter the phase equilibrium due to non-ideal gas effects which is significant at ambient densities relevant for diesel combustion (Luijten and Kurvers 2010).

Siebers (1999) model does incorporate real gas effects based on the compressibility factor, Z , however, this is done in such a way that fuel and ambient gas at the liquid length are decoupled which is not valid due to the interaction of the fuel and ambient. Luijten and Kurvers (2010) have proposed a modification to the Siebers (1999) mass conservation relationship to incorporate these real gas effects as shown in equation (33).

$$\frac{\rho_f(LL)}{\rho_g(LL)} = \frac{Y_{fg}\rho_g}{(1 - Y_{fg})\rho_g} = \frac{X_{fg}MW_f}{(1 - X_{fg})MW_a} \quad (33)$$

This requires determination of the saturated mole fraction of the fuel in the gas phase which is accomplished using a flash calculation with an equation of state, which is a vapor-liquid equilibrium calculation for a binary mixture (charge-gas and fuel), using mole fractions and fugacity. The Peng-Robinson equation of state is used and the fuel-ambient is modeled as a two-component binary mixture. For the flash calculation, equilibrium is defined by equation (34) using fugacity coefficients, Φ , which are computed from the equation of state.

$$\begin{aligned} X_{fg}\Phi_f^g(p_a, T_s, X_{fg}, X_{ag}) &= X_{fl}\Phi_f^l(p_a, T_s, X_{fl}, X_{al}) \\ X_{ag}\Phi_a^g(p_a, T_s, X_{fg}, X_{ag}) &= X_{al}\Phi_a^l(p_a, T_s, X_{fl}, X_{al}) \end{aligned} \quad (34)$$

In order to appreciate the deviation from ideal gas effects, Luijten and Kurvers (2010) introduced the enhancement factor f_e which is the ratio of saturated partial vapor pressure in a mixture to the saturated vapor pressure of the pure fuel as defined in equation (35).

$$f_e = \frac{X_{fg}P_a}{P_s} \quad (35)$$

At low pressure, representing an ideal gas, f_e is 1, with this factor becoming increasingly important at high pressure and low temperature conditions. This enhancement factor can be used in the mass conservation equation to mitigate the need for flash calculations which results in a new definition for the mass flow rate ratio, B , including real gas effects, as shown in equation (36).

$$B = \frac{h_a(T_a, p_a) - h_g(T_s, P_a, X_{fg})}{h_g(T_s, P_a, X_{fg}) - h_f(T_f, P_a)} = \frac{f_e P_s MW_f}{(P_a - f_e P_s) MW_a} \quad (36)$$

Comparing this relation to the original form in Siebers (1999) (equation (20)), the ratio of compressibility factors found in the Siebers equation is now replaced by the inclusion of the enhancement factor as a multiplier on the saturation pressure. Based on

the inability to decouple the fuel vapor and ambient gas, the mixture enthalpy at the liquid length (h_g) is now included as opposed to that of pure components requiring evaluation with departure functions and an equation of state. Considering these enthalpy terms, the difference between ideal gas and real gas enthalpy is small signifying that effects on liquid length will be small due to the larger effect from temperature relative to that of pressure.

Taking a similar approach to include real gas effects to the Versaevel et al. (2000) model, the fuel vapor mass fraction, equation (30), is modified to include this enhancement factor (again determined from flash calculations), as shown in equation (37).

$$Y_{fg} = \frac{1}{\left[\frac{P_a}{f_e P_s(T)} - 1 \right] \frac{MW_a}{MW_f} + 1} \quad (37)$$

One final required modification is that of the gas phase density definition as it was originally defined assuming the ideal gas law equation of state still holds. However, this must include the compressibility factor as updated in equation (38).

$$\rho_g = \rho_a \frac{Z_a(p_a, T_a)}{Z_g(p_a, T_a, X_{fg})} \frac{T_a}{T} \frac{1}{Y_{fg} \frac{MW_a}{MW_f} + (1 - Y_{fg})} \quad (38)$$

Compressibility factors are calculated using the Peng-Robinson equation of state in conjunction with Van der Waals mixing rules. It should be noted that Z_g , which is the compressibility factor of the saturated gas-vapor mixture, is a function of axial location as the composition and temperature continue to change along the spray so this compressibility factor must be included in the iterative the solution. Other real gas effects would need to be included in pressure terms, however, it was determined in the Siebers real gas analysis that pressure effects are small on the liquid length and for that reason no other changes were made.

Comparing the modified Siebers (1999) and Versaevel et al. (2000) models with real gas effects it was determined that the B term is the same for both models. The Versaevel model (with real gas effects) yields reductions in liquid lengths relative to that of Siebers. Another difference is attributed to the ambient density in the Versaevel model being evaluated at the liquid length (saturation temperature), whereas for Siebers this is evaluated at the ambient temperature which will impact the fuel mass and momentum conservation. Luijten and Kurvers (2010) recommend the use of the Siebers (1999) liquid length model in conjunction with real-gas effect modifications as a scaling model for liquid length and also support the neglecting of considering non-ideal enthalpy for liquid length models.

Desantes et al (2009) have also developed a model based on the mixing-limited spray evaporation defining liquid length as the location along the spray where the energy from the ambient air is enough to vaporize the fuel. This is computed based on a mass and energy balance along with determination of the fuel mass fraction of evaporated fuel with their scaling model presented in equation (39). In this scaling model, K is a constant of the spray. This relationship is modified with the application of energy conservation which includes enthalpy relationships applied to the fuel mass fraction of evaporated fuel.

$$LL = Kd_o \sqrt{\frac{\rho_f}{\rho_a}} * \frac{1}{Y_{f, \text{evap}}} \quad (39)$$

$$LL = Kd_o \sqrt{\frac{\rho_f}{\rho_a}} * \left[1 + \frac{\Delta h_f(T_f, T_{\text{evap}})}{\Delta h_a(T_a, T_{\text{evap}})} \right]$$

This scaling model is limited, as are the other aforementioned models, as it does not account for the changes in physical fuel properties in the liquid phase including viscosity and surface tension which govern atomization (Payri et al. 2011b, 2011c).

2.4.1.2. Eulerian Approach – Fuel Mass Particle Tracking

Another subset of models involve tracking fuel mass particles using Eulerian approaches. One such example is the 1D spray model developed by Pastor et al. (2008) which characterizes and predicts spray flow under inert and reacting conditions. This model looks at the relationship between local fuel-air mixing processes, spray dynamic evolution, and transient tip penetration. As it is based upon the mixing controlled, it can be applied for both a gas jet and a diesel spray under conventional engine conditions (Pastor et al. 2008). By assuming that the diesel spray can be represented as a turbulent gas jet, this provides an estimation of property distribution of temperature, and density within the spray, in addition to tip penetration provided with most other 1D spray models (Pastor et al. 2008). This 1D spray model is an expansion of that proposed by Desantes et al. (2007) which tracked discrete fuel mass particles along the spray axis and is restricted to inert conditions with limited application to transient injection rates. This new version of the model uses a Eulerian approach which is advantageous for transient spray evolution without the need for corrections as was done in past versions. This methodology can be extended to reacting conditions to model transient flame evolution (Pastor et al. 2008). Assumptions are as follows:

- No air swirl which provides spray axisymmetric conditions.
- Fully developed turbulent flow yields self-similar radial profiles for conserved variables (ratio of conserved variable by centerline does not depend on axial location). Assumes Gaussian radial distribution function.
- Schmidt and Prandtl numbers are 1. Schmidt number is a representation of the relative rate of momentum and mass transfer. Prandtl number represents the ratio of momentum to thermal diffusivity.
- Neglect laminar contributions to transport processes meaning that the flow is insensitive to the initial uniform radial profiles, which is only valid at the intact length (defined as the farthest location from the nozzle where the fuel mass fraction along the centerline of the spray is equal to 1). When the fuel mass fraction along the centerline is less than one, the cell has reached the fully-developed flow region.
- Spatially uniform velocity of the spray at the injector exit.
- Spray angle definition is the location where the self-similar axial velocity profile (ζ) is 0.01 which provides a relationship for a constant, k , relative to the self-similar Gaussian profiles as shown in equation (40).

$$k = \frac{\ln\left(\frac{1}{\xi}\right)}{\tan^2\left(\frac{\theta}{2}\right)} \quad (40)$$

- Locally-homogeneous flow is assumed meaning local equilibrium for thermal and velocity conditions enabling modeling of the spray as a gas jet.
- Spray is assumed to be constant pressure which allows neglecting compressibility effects.
- Ideal mixing is assumed to make possible the calculation of local density as defined by equation (41).

$$\rho(x, r) = \frac{1}{\sum_i \frac{Y_i(x, r)}{\rho_i(x, r)}} \quad (41)$$

The model is implemented by dividing the spray axially into several cells across the spray cross section of thickness Δx with conservation equations for axial momentum, fuel mass, and energy being formulated and applied to each cell to solve for axial velocity, fuel mass fraction and enthalpy as defined in equation (42).

$$\begin{aligned} \text{Axial momentum} \quad M(x_i, t) - M(x_{i+1}, t) &= \frac{d}{dt} \left[\int \rho(x, r, t) \cdot u(x, r, t) \cdot dV \right] \\ \text{Fuel mass} \quad m_f(x_i, t) - m_f(x_{i+1}, t) &= \frac{d}{dt} \left[\int \rho(x, r, t) \cdot f(x, r, t) \cdot dV \right] \\ \text{Energy} \quad H(x_i, t) - H(x_{i+1}, t) &= \frac{d}{dt} \left[\int \rho(x, r, t) \cdot (h(x, r, t) - h_{a,\infty}) \cdot dV \right] \end{aligned} \quad (42)$$

Specified boundary conditions are:

- Momentum, fuel mass, and enthalpy fluxes at the nozzle exit ($i = 0$) are constant or a function of time, with momentum and fuel mass being obtained experimentally.
- Spray cone angle is considered to be constant with time and can be considered as a fit in the model.
- Explicit relationship between local density and other unknowns is applied which requires defining a function or state relationship which governs composition and thermodynamic conditions.

To determine spray characteristics, the conservation equations are reformulated and solved for every time instant and axial position. This solution provides the on-axis velocity, fuel mass fraction, and enthalpy at the cell inlet and outlet which with the self-similar radial profile relationship enables calculation at other positions. This involves the use of state relationships to account for the different air and fuel temperatures occurring in vaporizing sprays. For vaporizing sprays, the turbulent Lewis number is assumed equal to 1 allowing fuel mass fraction to be calculated from equation (43).

$$f(x, r, t) = \frac{h(x, r, t) - h_{a,\infty}}{h_{f,0} - h_{a,\infty}} \quad (43)$$

Local conditions assume adiabatic mixing of fuel and air, and the following procedure is undertaken to solve the equations:

1. Local mixing enthalpy is calculated.
2. Inert adiabatic mixing hypotheses is applied to the two streams to obtain the local composition, $f + Y_a = 1$.
3. With enthalpy and fuel mass fraction range known the local temperature is calculated assuming an ideal mixture from $h(T, f) = \sum_i Y_i \cdot h_i(T)$.
4. Calculate density of each mixture component at this local temperature using a real gas equation of state with a compressibility factor. Calculate local mixture density for the range of the fuel mass fractions.

This model calculation enables determination of the fuel mass fraction range showing a characteristic fuel mass fraction defined as f_{evap} which is the fuel mass fraction where the last fuel droplets are seen meaning no liquid fuel but vapor is saturated. This is the fuel-mass fraction that represents maximum liquid length. These fuel mass fraction characteristics are evidenced by a change in slope of the temperature curve, and also, the leveling off of the $Y_{f,v}/f$ curve. If $f > f_{evap}$, this is the liquid spray core, and as f increases, air entrainment is increasing, enthalpy transfer to the mixture is increasing, and the spray is approaching the liquid length.

To summarize, this modeling involves using thermodynamic properties of pressure (constant), temperature, and density of the fuel at the orifice exit, and air in the ambient, in state relationships to compute density, temperature, and mole fraction as a function of fuel mixture fraction. With this information, the radial integral F is calculated and then used to solve the conservation equations for axial momentum and fuel mass to provide velocity and fuel mass fraction along the centerline which then yields output results of velocity, fuel mass fraction, temperature, and mole fraction of I as a function of x , r , and t .

Various profiles can be applied for axial velocity or other parameters to more realistically approximate spray behavior, for example, Desantes et al. (2011) applied a Gaussian based velocity profile for the axial velocity as defined in equation (44).

$$U(x, r) = U_c(x) \exp\left(-\alpha \left(\frac{r}{R}\right)^2\right) \quad (44)$$

Where r is the radial-position perpendicular to the spray axis (radial coordinate), α is the Gaussian distribution shape factor, x is the distance along the spray (axial coordinate), $U(x, r)$ is the local spray velocity, and U_c is the velocity at the sprays axis (centerline).

Other models neglect the liquid computation of the spray entirely by treating the liquid portion of the spray as a source of vapor mass, momentum, and energy, termed a Virtual Liquid Source (VLS) model which helps to overcome the unknown physics behind spray atomization processes (Abraham and Magi 1999). To achieve this, model inputs include the maximum liquid core length and the time to reach this length to overcome grid limitations. The key model assumption is that the volume of mass occupied by the liquid fuel component is small relative to the total injected fuel. The required fuel properties in these models have been defined using tabulated data typically from API handbooks (Schihl et al. 2006) and various other correlations (Gimenes 2006), avoiding the application of a generalized equation of state approach.

2.5. Surrogate Fuels

Spray modeling requires an understanding of fuel properties and behavior including thermodynamic and chemical kinetic properties of the fuel. This is complicated as these properties of real fuels are typically unknown due to the multiple components, and therefore, a simplified representation of these complex fuels are required to meet computational limits. This has led to the development of surrogate, or model, fuels with the goal of representing the thermodynamic and chemical properties of real fuels, such as diesel, to help advance the state of combustion and fuels models. Surrogate fuels are simplified versions of real fuels which can be used in spray and combustion models such as those for CFD to simplify studies of complex multi-component real fuels to better understand the underlying relationships and characteristics of fuels including vaporization, mixing, ignition and pollutant formation. These fuels can also be used in fundamental experimental tests to provide results for model validation, and better understand the underlying spray and combustion characteristics with a simpler fuel.

These fuels are typically single or multi-component mixtures of well-understood fuels that can replicate physical, thermal, and chemical properties of conventional fuels. This may require matching physical properties including density, fuel energy content, evaporation characteristics including boiling point, flash point and vapor pressure, thermal conductivity, surface tension, viscosity and others, along with the chemical properties of composition, carbon to hydrogen ratio, flame speed, ignition delay, sooting tendency and others (Slavinskaya et al. 2010). Different levels of surrogate fuels are developed including property targets to match fundamental physical and chemical fuel properties, development targets which match kinetic and fluid dynamic processes important for mixture behavior, and finally application targets including matching engine operating characteristics of combustion efficiency and emissions (Farrell et al. 2007). The best surrogate fuel uses the smallest number of components while meeting the targets of fuel properties to minimize computational complexity while upholding applicability. Certain surrogates may be best for spray characteristics whereas others may best reproduce combustion characteristics based on the overall characteristics of the fuel.

Combustion and spray models can be largely simplified through the use of surrogate fuels. This requires developing surrogates which are a combination of simple species with well-known chemistry, ideally with the same functional groups as diesel fuel, to ensure best representation. These surrogate fuels must accurately react with oxidants at the correct reaction rates participating in the correct chain reactions. Limitations with surrogates must be acknowledged in their model applications remembering that surrogates are a discrete set of components which are trying to emulate a close to continuous spectrum of components characteristic of real fuels (Battin-Leclerc 2008).

Surrogates are desired to match the chemical composition of diesel fuel, however, this is complicated as diesel fuel composition varies significantly based on production methodologies with a cetane number of 40-56, carbon numbers of C10 – C24, boiling point range of 190 – 360°C, and composition of 25-50% normal iso-paraffins, 20-40% cyclo-paraffins (naphthenes), and 15-40% aromatics. It can also include lightly branched iso-alkanes with one or two side methyl groups (Farrell et al. 2007, Pitz and Mueller 2011). This information must be considered when developing and applying surrogate

fuels. The composition variability makes the development of a single surrogate for representing diesel fuel difficult (Farrell et al. 2007). To further complicate the matter, the composition of hydrocarbon real fuels can include various additives or impurities such as sulfur, oxygenates, and anti-knock agents which must be considered in surrogate development (Tsang et al. 2003). Additionally, ignition improvers are also mixed in with standard diesel fuel to improve the cetane number, and reduce the ignition delay, such as 2-ethylhexyl nitrate, which must also be considered in surrogate development as they influence the combustion processes and emissions formation (Farrell et al. 2007).

In addition to diesel, surrogates must also be developed for alternative fuels, such as biodiesel which is composed of fatty acid esters produced via transesterification of animal fats or vegetable oils using methanol or ethanol (Radich 1998). Not only must individual surrogates be understood, but those of diesel-biodiesel blends need to be considered as blending may be phased in. Surrogate modeling of biodiesel is different when compared to diesel as it has a more homogeneous distribution of components based on its molecular structure (Farrell et al. 2007). One advantage of developing a surrogate for biodiesel is that it is typically composed of a smaller number of components, on the order of ten, which simplifies surrogate development relative to the significantly higher component quantity for diesel (Pitz and Mueller 2011). Renewable diesel, another renewable fuel, is produced by hydrotreating bio-derived oils and fats, primarily composed of n-alkanes and iso-alkanes but, details on the composition are unknown which hinders surrogate fuel development and modeling capability of this fuel (Pitz and Mueller 2011).

Surrogates can either be single-component or multi-component. As more components are added, applicability and representation of real fuels is improved, however, computational time and surrogate complexity is increased which can hinder its implementation. Multi-component surrogates are sometimes difficult to develop as the species may interact between components in a mixture, which must be considered (Pitz and Mueller 2011).

Various surrogate components are recommended depending on the fuel being replicated. Components of interest for diesel are n-decane, iso-octane, methylcyclohexane, toluene, n-hexadecane, heptamethylnonane, n-heptane, n-octadecane, n-decylbenzene, 1-methylnaphthalene, n-dodecane, decahydronaphthalene (decalin) and tetralin, (Tsang et al. 2003; Farrell et al. 2007; Anand et al. 2011). The chemical formula and structure groups of these components are provided in Table 2.11.

Table 2.11
Chemical formula and structure groups of suggested diesel surrogate components.

Surrogate Components	Chemical Formula	Structure Groups
decahydronaphthalene (decalin)	C ₁₀ H ₁₈	8 CH ₂ (Ring), 2 CH (Ring)
heptamethylnonane	C ₁₆ H ₃₄	9 CH ₃ , 3 CH ₂ , 1 CH, 1 C
Iso-octane	C ₈ H ₁₈	5 CH ₃ , 1 CH ₂ , 1 CH, 1 C
n-decane	C ₁₀ H ₂₂	2 CH ₃ , 8 CH ₂
n-decylbenzene	C ₁₆ H ₂₆	1 CH ₃ , 9 CH ₂ , 1 =C (Ring), 5 =CH (Ring)
n-dodecane	C ₁₂ H ₂₆	2 CH ₃ , 10 CH ₂
n-heptane	C ₇ H ₁₆	2 CH ₃ , 5 CH ₂
n-hexadecane	C ₁₆ H ₃₄	2 CH ₃ , 14 CH ₂
n-octadecane	C ₁₈ H ₃₈	2 CH ₃ , 16 CH ₂
methycyclohexane	C ₇ H ₁₄	1 CH ₃ , 5 CH ₂ (Ring), 1 CH (Ring)
1-methylnaphthalene	C ₁₁ H ₁₀	1 CH ₃ , 3 =C (Ring), 5 =CH (Ring)
tetralin	C ₁₀ H ₁₂	4 CH ₂ (Ring), 2 =C (Ring), 4 =CH (Ring)
toulene	C ₇ H ₈	1 CH ₃ , 5 =CH (Ring), 1 =C (Ring)

The surrogate components span a wide range of hydrogen to carbon ratios, and exhibit various structures including both ring and non-ring groups. These components, based on their differing chemical composition, will provide a range of physical and chemical properties, which when combined in varying compositions, and with other components not listed here, can produce various fuels to replicate diesel, or other alternatives, including biodiesel for example, which requires the addition of oxygenated components (Agarwal 2007).

Some examples of conventional, in-use, surrogates for diesel fuel are provided in Table 2.12.

Table 2.12
Select diesel surrogate fuel recommendations.

Reference	Proposed Surrogate	Formula	Notes
Farrell et al. 2007	n-heptane	C_7H_{16}	Limitations in ignition if mixing controlled due to the differences in fuel volatility along with the single component nature of the fuel.
Farrell et al. 2007	n-heptadecane	$C_{17}H_{36}$	Matches fuel vaporization based on matching of T90, liquid length, and density of real diesel fuel. Only matches physical properties not chemical kinetics.
Farrell et al. 2007	70% volume n-decane and 30% volume of methyl-naphthalene		Matches the diesel boiling range, hydrogen to carbon ratio, cetane number, density, ignition delay and heat release rate. Predicts emissions lower than expected, partially attributed to reductions in liquid penetration relative to that of diesel.
Natelson et al. 2008	n-decane, n-butylcyclohexane and n-butylbenzene in a 1:1:1 mixture by volume		Chosen to match complexity of three HC classes commonly found in real diesel fuel. Increased reactivity in comparison to diesel fuel.
Tsang et al. 2003	70% cetane and hexamethyl nonane mixture, 30% alpha-methylnaphthalene		Matches cetane number.
Mathieu et al. 2009	39% p-cyclohexane, 28% n-butylbenzene, and 33% 2,2,4,4,6,8,8 heptamethylnonane by mass		
Mati et al. 2007	23.5% n-hexadecane, 19% iso-octane, 26.9% n-propylcyclohexane, 22.9% n-propylbenzene and 7.7% 1-methylnaphthalene		Matches quantities of chemical classes in diesel.
Myong et al. 2006	Iso-octane, n-dodecane and n-hexadecane mixtures in varying mass levels of 6:3:1, 1:1:1 or 1:3:6		
Siebers 1999	n-heptadecane		Relevant for spray and liquid length models.
Espey and Dec 1995	Mass weight 67% heptamethylnonane and 33% cetane		Low sooting; improved optical diagnostic application.
Gustavsson & Golovitchev 2003	3:7 mixture of toluene and n-heptane		Similar cetane number and should represent soot formation, however, does not consider physical properties of the fuel.

Various surrogates have been used and experimented with, however, as mentioned in the table above, there are limitations with these surrogates. For example, several surrogates

may match certain fuel properties, such as cetane number for example, but do not match other diesel fuel properties, including physical properties, which influence spray characteristics (Gustavsson and Golovitchev 2003). Therefore although a surrogate may match diesel combustion characteristics (through chemical properties), it may have limited applicability to diesel spray or vaporization characteristics (in regards to physical properties), or vice versa. Additionally, the breadth of these surrogates in regards to composition and complexity show that the complex composition of diesel fuel is difficult to accurately match, and that one surrogate may not be the ideal solution, depending on characteristics which are attempting to be matched.

Surrogates are also being developed for alternative fuels to facilitate their modeling to ensure efficient integration into conventional diesel engines. A proposed surrogate for biodiesel is methyl deaconate (Herbinet et al. 2008). Another proposed surrogate for biodiesel fuel from rapeseed oil could be n-hexadecane (Dagaut et al. 2007; Herbinet et al. 2008). As was discussed with diesel, developing a surrogate for biodiesel is complicated due to the variation in biodiesel components as a function of production method and feedstock. Biodiesel is composed of esters of methyl palmitate, methyl stearate, methyl oleate, methyl linoleate, and methyl linoleate at varying levels dependent on the feedstock used and composition of that feedstock assuming methanol is used in the transesterification process, if not, compositions vary further (Herbinet et al. 2008).

For surrogates used to represent spray and vaporization properties, the vaporization processes in the fuel must be considered. This is further complicated as there are different theories on the control of vaporization. Certain researchers have defined the vaporization and resulting liquid length as being controlled by the high boiling point (lower volatility) component of the diesel surrogate (Siebers 1998; Myong et al. 2006). Other work has shown that vaporization is neither batch-distillation like (not controlled by volatility differences) nor onion-skin like (controlled solely by volatility differentials) but a mixed mode mechanism is more likely. Vaporization can be even further complicated by the attainment of super-critical conditions at an early time in the process (Farrell et al. 2007). Others have found that for diesel-like sprays there is no preferential evaporation of a two-component fuel representing diesel fuel sprays which is largely attributed to the rapid droplet evaporation and mixing processes not providing time for preferential evaporation (Hottenbach et al. 2011).

2.6. Property Relationships – Equations of State

Equations of state exist to represent the pressure-volume-temperature relationships of fluids exhibiting varying levels of complexity, ranging from the simple ideal gas law, to complex relationships with numerous constants, of up to 50 or more (Martin 1979). As expected, as the complexity and number of constants increases, on average, the equations become increasingly accurate in representing fluid properties, however, their application is increasingly difficult and computationally intensive. By manipulating the cubic equation of state in the general form, several equations of state can be derived which are summarized in Table 2.13 and are expressed either in terms of pressure or compressibility, with compressibility defined as $Z = PV/RT$.

Table 2.13
Equations of state (Martin 1979; Wei and Sadus 2000; Slavinskaya et al. 2010).

Name	Equation of State	Coefficients
Ideal Gas	$PV = nRT$	
Virial	$Z = 1 + \frac{B}{V} + \frac{C}{V^2} + \frac{D}{V^3} + \dots$	B, C, D are virial coefficients
General Cubic	$P = \frac{RT}{V} - \frac{\alpha(T)}{(V + \beta)(V + \gamma)} + \frac{\delta(T)}{V(V + \beta)(V + \gamma)}$	α and δ are functions of temperature, β and γ are constants
Cubic	$P = \frac{RT}{v - b} - \frac{a}{v^2 + \gamma v + \varepsilon}$	$a, b, \gamma, \varepsilon$
Lee-Edmister	$P = \frac{RT}{V - b} - \frac{a}{V(V - b)} + \frac{c}{V(V - b)(V + b)}$	$b = -\beta = \gamma$ $a = \alpha - \beta RT$ $c = \alpha\gamma + \delta$
Van der Waals – Cubic	$P = \frac{RT}{V - b} - \frac{a}{V^2}$	$a = \alpha$ $b = \beta$
Redlich Kwong	$P = \frac{RT}{V - b} - \frac{a}{V(V + b)}$	$a = \alpha$ $b = \beta$
Soave-Redlich-Kwong – Cubic	$Z = \frac{V}{V - b} - \frac{a(T)}{RT(V + b)}$	$a(T) = 0.4274 \left(\frac{R^2 T_c^2}{P_c} \right) \left(1 + m \left(1 - \left(\frac{T}{T_c} \right)^{0.5} \right)^2 \right)$ $m = 0.480 + 1.57\omega - 0.176\omega^2$ $b = 0.08664 \frac{RT_c}{P_c}$
Peng-Robinson – Cubic	$P = \frac{RT}{V - b} - \frac{a}{V(V + b) + b(V - b)}$	$a = \alpha$ $b = \beta$
Carnahan and Starling	$Z = \frac{1 + \eta + \eta^2 - \eta^3}{(1 - \eta)^3} - \frac{a}{RTV}$	$a = 0.4963 \frac{R^2 T_c^2}{P_c}$ $b = 0.18727 \frac{RT_c}{P_c}$ $\eta = \frac{b}{4V}$
Carnahan and Starling – Redlich Kwong	$Z = \frac{1 + \eta + \eta^2 - \eta^3}{(1 - \eta)^3} - \frac{a}{RT^{1.5}(V + b)}$	$a = 0.4963 \frac{R^2 T_c^2}{P_c}$ $b = 0.18727 \frac{RT_c}{P_c}$ $\eta = \frac{b}{4V}$
Benedict Webb Rubin	$Z = 1 + \frac{f_1(t)}{V} + \frac{f_2(t)}{V^2} + \frac{f_3(t)}{V^n} + f_4(t) * \left[\frac{\gamma_1 + \frac{\gamma_2}{V^2}}{V^m} \right] \exp\left(-\frac{\gamma_2}{V^2}\right)$	f_i functions with up to 30 parameters, γ_1, γ_2 additional parameters

Table 2.13, Continued

Name	Equation of State	Coefficients
Benedict Webb Rubin	$Z = 1 + \frac{B_0 RT - A_0 - C_0/T^2}{RTV} - \frac{bRT - a}{RTV^2}$ $+ \frac{\alpha a}{RTV^5}$ $+ \left(\frac{c}{RT^3 V^2} \right) \left(1 + \frac{\gamma}{V^2} \right) \exp \left(\frac{-\gamma}{V^2} \right)$	$A_0, B_0, C_0, a, b, c, \alpha, \gamma$ parameters

All equations of state have pros and cons in regards to their ease of application and accuracy. More specifically, cubic equations of state are typically simple and easy to use analytically, but are limited in application to certain mixtures or species based on molecular sizes or characteristics. The Benedict Webb Rubin equation is beneficial in its ability to treat supercritical components with good precision but is computationally intensive.

Constants in the cubic equations of state can be determined in terms of critical properties using two solution methodologies (Martin 1979). The first method is based on the fact that at the critical point, the first two pressure volume derivatives equal zero for constant temperature derivatives, as expressed in equation (45).

$$\left(\frac{dP}{dV} \right)_T = \left(\frac{d^2 P}{dV^2} \right)_T = 0 \text{ at } P_c, T_c, V_c \quad (45)$$

The second methodology considers three equal volume roots at the critical point necessitating the rearranging of the cubic equation of state to be cubic in volume on the left-hand side, and zero on the right hand side, solving for the three equal roots as defined in equation (46). Keep in mind that this solution is valid for all cubic equations of state as the general cubic equation of state is the starting point for the derivation of the aforementioned cubic equations of state.

$$V^3 + \left(\beta + \gamma - \frac{RT}{P} \right) V^2 + \left(\beta \gamma - \frac{RT}{P} (\beta + \gamma) + \frac{\alpha}{P} \right) V - \frac{\beta \gamma RT}{P} - \frac{\delta}{P} = 0 \quad (46)$$

$$(V - V_c)^3 = V^3 - 3V_c V^2 + 3V_c^2 V - V_c^3 = 0$$

Comparing these two equations the roots of volume can easily be determined, however, there are four unknowns which requires specifying one of the unknown values. More specifically, for the frequently used two-term cubic equations, δ is set to zero.

Reduced variables, based upon critical properties, are also defined for species properties including those for pressure, temperature and volume as shown in equation (47).

$$P_r = \frac{P}{P_c}$$

$$T_r = \frac{T}{T_c} \quad (47)$$

$$V_r = \frac{V}{V_c}$$

Critical points of molecules are tabulated but can also be evaluated as these points are the stability limit of the stable phase which can be determined using a Taylor series for the Helmholtz energy (Slavinskaya et al. 2010).

The choice of equation of state is largely governed by fluid properties. The Peng-Robinson equation of state is proven accurate for high pressure, non-polar systems, relevant to diesel sprays and has been used under these applications in the past (Desantes et al. 2007; Luijten and Kurvers 2010). For standard hydrocarbons the size difference of molecules is typically less than a factor of 2, with these molecules being non-polar, validating the use of a simple equation of state with simplified Van der Waals mixing rules (as will be discussed) (Slavinskaya et al. 2010).

2.7. Mixing Relationships

Many surrogates are composed of multiple components to best represent that of diesel fuel. This requires the understanding of mixing rules for evaluating properties. Standard simple mixing rules do not apply to non-ideal cases when there are large differences in molecular sizes, high polarity, and others typically representative of conventional diesel surrogates (Slavinskaya et al. 2010).

Mixing rules can be applied using various methods. One method is in determining constants for the equation of state evaluation, for example the values of a and b for the generalized cubic equation of state (Wei and Sadus 2000). This includes various rules as summarized in Table 2.14.

Table 2.14
Mixing rules for determining a and b from cubic equation of state (generalized).

Type	'a' Relationship	'b' Relationship
Simple	$a = \sum_i x_i a_i$	$b = \sum_i x_i b_i$
Van der Waals	$a = \sum_i \sum_j x_i x_j a_{ij}$	$b = \sum_i \sum_j x_i x_j b_{ij}$

Or, mixing rules can be applied for multi-component surrogates in direct relationship to the liquid length model with two differing approaches provided by Schihr et al. (2006); a Mean Evaporation Coefficient (MEC) and Mean Liquid Length (MLL) method, with the mean evaporation coefficient methodology being preferred. The relationships for the MEC method are provided in equation (48), and those for the MLL method are defined in equation (49).

$$\begin{aligned}
 B_m &= \sum_{i=1}^n x_i B_i \\
 T_{b,m} &= \sum_{i=1}^n x_i T_{b,i} \\
 1 &= \sum_{i=1}^n x_i
 \end{aligned}
 \tag{48}$$

MEC Method

$$LL_m = \sum_{i=1}^n x_i LL_i \quad (49)$$

2.8. Summary

This review has considered a wide range of topics relevant to the work discussed in this dissertation. To reiterate the goals of this current work, these include improving the understanding of multi-hole injector spray characteristics under various fuel and ambient states using a combustion vessel, and developing and integrating an equation of state thermophysical property methodology to compare to experimental results and quantify liquid length, including a parametric study for understanding liquid length fluctuations and surrogate fuel application. This literature review addresses the scope of the existing work meeting the above goals.

First focus was on different apparatuses for fundamental spray and combustion studies, including their advantages and disadvantages. Details were provided on constant volume combustion vessels used in the current work, including a review of the preburn procedure for thermodynamic state generation with focus on the different mixtures and procedures. Optical diagnostics used for these studies were then discussed, with the diagnostic used governed by the desired knowledge acquired. The next section of the literature review focused on macroscopic spray characteristics of spray penetration, liquid length, cone angle and lift-off length, along with an examination of multi-hole injector characteristics including plume to plume variations and spray fluctuations of liquid length. These characteristics are influenced by a wide range of parameters as will be further discussed, including charge-gas conditions, fuel properties, and injector characteristics. Spray modeling was also reviewed including an in-depth review of simplified 1-dimensional scaling models based on conservation relationships. This includes discussion on the Siebers (1998) liquid length model which will be applied in detail in Chapter 8 for the current work. Surrogate fuels were then examined as these can be used in models and experimental studies to emulate diesel fuel, as diesel fuel is complex and thermodynamic fuel properties are difficult to model and analyze. Finally, equation of states and mixing properties were considered to understand the different equations and their applications, including those relevant for diesel spray characteristics.

This literature shows that there are several knowledge gaps which when addressed in this work, will enhance the knowledge of the field. First, there is minimal investigation into the influence of the preburn procedure for thermodynamic state generation on the resulting ambient composition, relative to internal combustion engines. It is understood and accepted that minor species are generated, however, the influence of these species on spray and combustion characteristics, along with the composition relative to diesel engines running with exhaust gas recirculation, has not been investigated in detail. The investigation undertaken in Chapter 4 including chemical kinetics modeling of this procedure, and a comparison over differing mixtures, provides an improved understanding of this procedure including comparison to conventional diesel engines and influence on spray autoignition. Second, literature has been published discussing the fluctuations in diesel spray liquid length about a mean value. Causes of these fluctuations have been proposed, however, reasons vary and there is little agreement. This current

work will contribute to this understanding by studying these fluctuations over a range of conditions and applying a frequency analysis to better understand their characteristics (Chapter 8). This will be further studied using a developed liquid length model with an equation of state approach for thermophysical properties, enabling a parametric study on the implications of various parameters on liquid length trends and application of single and multi-component surrogate fuels. Finally, although liquid length models have been established, to accurately model the spray they require significant temperature and pressure dependent property information. While surrogate fuels and chemical kinetics models have been significantly developed, there has been substantially less focus on thermophysical property analysis and impact. As property information is not readily available for many surrogates which are proposed to match diesel or alternative fuels, and it is often presented in tabulated format making iterative calculations tedious and inefficient, thermophysical property modeling is imperative to assist in advancing the state of knowledge. With the development of an equation of state approach for modeling thermophysical properties for both single and multi-component surrogates, the application of a liquid length model is enhanced to provide an improved understanding of liquid length over a wider range of conditions, and fuels, along with the capability to perform parametric studies and predictive modeling. This work will enhance the state of the knowledge by providing an improved understanding of spray characteristics including quasi-steady liquid length behavior and thermodynamic state generation, along with contribution of an equation of state property model for thermophysical property modeling to fill existing knowledge gaps in diesel spray and combustion characteristics. The focus on thermophysical property analysis and impact of the current work has been minimally explored in the past where focus has been on surrogate fuels and chemical kinetics. This will advance the knowledgebase, providing necessary information for development of improved surrogates to maintain the transition to alternative fuels and combustion strategies to reduce emissions while upholding fuel efficiency and performance.

3. Experimental Facility, Test Setup & Diagnostics

3.1. Combustion Vessel

This experimental work has been undertaken in the Michigan Technological University Alternative Fuels Combustion Laboratory (AFCL). The main component of this laboratory is an optically accessible constant volume combustion vessel with corresponding subsystems for functionality. This vessel is based off the design used at Sandia National Laboratory which has had significant success in diesel spray and combustion studies over a wide range of conditions (Siebers 1999; Pickett et al. 2010). The basis for the functionality of the current facility is the result of collaboration on various subsystems between researchers at Michigan Technological University and Sandia National Laboratory.

A Major Research Instrumentation (MRI) grant was obtained from the National Science Foundation (NSF), grant number 0619585, in September 2006 to construct the AFCL housed in the specifically designated Alternative Energy Research Building (AERB) in Hancock. The laboratory, as will be described briefly here, was first operational in March of 2009 with additional subsystems and testing capabilities coming online as governed by testing and research project requirements. Additional details of the various laboratory subsystems during the development stages are provided in the references (Nesbitt 2008; Johnson 2009; Johnson et al. 2010; Nesbitt et al. 2010, 2011a).

The combustion vessel laboratory is a fundamental research tool which enables control and isolation of various variables known to influence spray and combustion. The combustion vessel has a 1.1 L cubical shaped combustion volume. It is equipped with eight access ports which house an intake valve, exhaust valve, and a dynamic pressure transducer (Kistler 6001 quartz dynamic transducer with a 5010B Charge Amplifier), with the remaining ports holding blank access ports for future instrumentation. There are six window ports (102 mm diameter) that contain various assemblies as required for testing including sapphire windows, injector windows including diesel both piezoelectric or solenoid based, gasoline direct injection, or urea injectors, ignition windows for spark plugs with dual fans (Nesbitt et al. 2010) or dual electrodes with a single fan, or blank plug windows. Additionally, there exists a rate of injection window fixture for quantifying injection profiles and mass flow rates (Johnson et al. 2010). The setup in this study utilized three sapphire windows to provide access for optical diagnostics, a diesel fuel injector window, a dual-electrode single fan window for thermodynamic state generation, and a blank plug window. Refer to Figure 3.1 for details on the CV components as configured for the work discussed here.

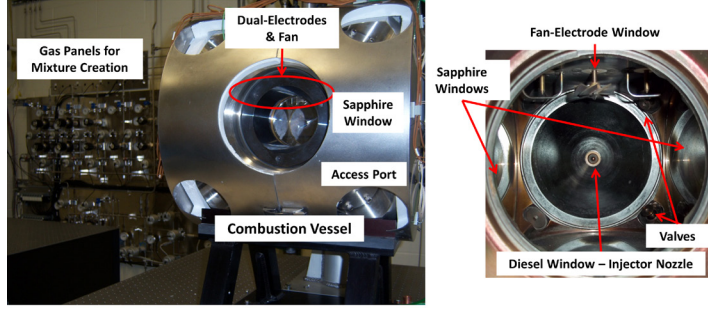


Figure 3.1: External view of the CV in the AFCL facility (Left); Internal view of the CV (Right).

Various subsystems are required for combustion vessel operation. One key system is a gas system with these panels shown in Figure 3.1, which enable production of gaseous mixtures required for the various ambient compositions under study. Other key subsystems are a spark ignition system for igniting combustible mixtures, a fuel injection system for supplying liquid fuel to the vessel including fuel system (gasoline or diesel) and injector driver (solenoid or piezoelectric), optical diagnostics to provide information on spray or combustion characteristics of interest, and a control, monitoring and data acquisition system for test operation.

The combustion vessel is electrically heated using 16 total cartridge heaters on two faces of the combustion vessel (twelve 500 W heaters, four 750 W heaters, Chromalox, controlled based on temperature feedback), to either 100 or 180°C depending on test conditions. This electrical heating of the vessel is required to ensure the vessel seals for testing, with there being seals on each window and access port, consisting of a c-seal and o-ring.

The combustion vessel can replicate the thermodynamic state (including pressure, temperature, and composition) of the charge gases in diesel engines via a preburn procedure. The preburn mixture is composed of acetylene (C_2H_2), hydrogen (H_2), oxygen (O_2) and nitrogen (N_2). By varying the initial mixture composition a wide range of ambient oxygen environments can be achieved post-preburn with oxygen concentrations of 0 to 21%, simulating vaporizing only environments (0% oxygen) to enable the study of spray characteristics to combustion in air (21% oxygen) along with a range of EGR levels characteristic of conventional internal combustion engines by varying the oxygen concentration. The general relationships for mixture composition, for oxygen concentrations greater than 0%, is provided in equation (50), defining species mole fractions, where P_{O_2} is the desired percentage of oxygen post preburn (ranging from 1 to 21) (Sandia ECN 2010).

$$\begin{aligned}
 C_2H_2 &= 0.03 + \frac{0.02 * (21 - P_{O_2})}{21} \\
 H_2 &= 0.005 \\
 O_2 &= 0.0825 + 0.0096P_{O_2} + \frac{0.001}{2100} (P_{O_2})^2 \\
 N_2 &= 0.883 - 0.0095P_{O_2} - \frac{0.001}{2100} (P_{O_2})^2
 \end{aligned} \tag{50}$$

The above equations are used for determining mixture composition for 1 to 21% oxygen mixtures. For the 0% oxygen environment, the mixture has been modified to facilitate

more complete combustion by the addition of excess hydrogen to the mixture thereby elevating the peak preburn combustion temperature. The process and support for mixture modification will be discussed in detail in Chapter 4.4. The mixture used for the creation of a 0% oxygen environment for vaporizing spray studies is 0.0309 C₂H₂, 0.0155 H₂, 0.089 O₂ and 0.865 N₂, on a mole fraction basis.

The ambient preburn mixtures are created using partial pressure mixing of component gases, with C₂H₂ first, H₂ second, N₂ third, and finally a 40% O₂ / 60% N₂ mixture to complete the fill, with the O₂/N₂ mixture being used in place of pure oxygen for safety. This mixture is produced and stored in a 10 L mixing vessel typically filled to 5.5 MPa (800 psi) yielding mixtures for tens to hundreds of tests dependent upon test (CV fill pressure / density) conditions. The mixing vessel contains a floating piston which separates the mixed gases (on the top side of the mixing vessel) from nitrogen (on the bottom side of the mixing vessel). This separation is provided to enable the use of nitrogen to push the piston up to flow gases from the mixing vessel to the combustion vessel as the mixture is consumed and the mixing vessel pressure falls below the required combustion vessel fill pressure. This is possible since there is still enough gas to fill the combustion vessel based on the volume differential between the two vessels (10 L mixing vessel, 1.1 L combustion vessel).

The creation of the mixture is handled remotely using the process control system which automatically mixes the gases and ensures gas stabilization before continuing (Nesbitt 2008). Pressures are monitored through the entire fill process, using a pressure transducer in the mixed gas line to the mixing vessel, with the mixing vessel top valve being open and therefore this transducer reads mixing vessel pressure. Thermocouples are also on the mixing vessel and gas lines to the mixing vessel (mixed gas and nitrogen) and therefore temperatures are also monitored during mixing to ensure no unintended autoignition occurs due to the flammable nature of the mixture. Stabilization is ensured by filling with the component gas to the desired partial pressure, within $\pm 2\%$, and waiting for 5 minutes with pressure being monitored to ensure there is no drop in pressure of the mixing vessel. If there was a drop in mixing vessel pressure this would signify that the piston in the mixing vessel moved (i.e. the mixing vessel mixed gas side volume was less than the expected 10 L) and this would yield an error in the mixed gas composition.

Before the start of mixing, a purge procedure is executed in the mixing vessel using acetylene in the mixed gas side of the mixing vessel with nitrogen in the bottom of the mixing vessel to ensure the mixing vessel is emptied. This purge procedure moves the floating piston in the MV to push out all leftover gases prior to filling. During acetylene filling, the nitrogen side of the MV remains open to ensure the piston is pushed completely down before proceeding with the remainder of the fill to provide the correct mixture composition. Mixing is a slow process, taking typically two hours, which is required to ensure the gases are appropriately mixed and that the piston has reached the bottom of the vessel to ensure correct gas composition.

For testing, the CV is filled with the preburn mixture to the desired fill pressure, which defines the density conditions of the study, computed via the ideal gas law as combustion vessel temperature and mixture molecular weight are also known. This initial fill process is undertaken by the control system software. This involves execution of a script, a programmed sequence of steps including valve operation, pressure monitoring,

etc., which purges the CV once with nitrogen, twice with mixed gas, and then it finally completes the fill procedure to the setpoint pressure. When the CV fill with the mixture is complete the intake valve is closed yielding a constant volume system and the chamber mixing fan (refer to Figure 3.1) is turned on to 7,000 rpm to ensure the gases are well-mixed. The mixing fan is run during the entire preburn and fuel injection event to ensure a uniform mixture; with fan velocities being orders of magnitude less than injected spray velocities. The test is initiated in the control system by spark ignition of the mixture using the dual in-chamber electrodes (refer to Figure 3.1) either half a second or one second after the intake valve is closed, depending on the user programmed test conditions. This time delay is used to ensure the mixture is well mixed at the time of ignition. Due to the premixed burn yielding a propagating flame as a result of the combustion event, the pressure and temperature rise inside the CV with the product gases then cooling due to heat transfer to the cooler vessel walls, termed the cool-down stage of the preburn. During the cool-down phase the CV pressure is monitored using a dynamic in-chamber pressure transducer (located in a CV access port, refer to Figure 3.1) and at the predetermined trigger pressure (corresponding to the desired gas temperature at injection calculated from constant density conditions) fuel injection is triggered along with corresponding diagnostics. High speed data, at 100 kHz, is logged from the time the test starts for a user defined length, which is typically three seconds. Logged analog signals include chamber pressure, fuel pressure, trigger signal timing, and others as required. This data acquisition system interfaces with the process and control software to coordinate data acquisition, and trigger signals for injection and ignition.

An example of this full test procedure, including the premixed burn, cool-down and injection event, is shown in Figure 3.2.

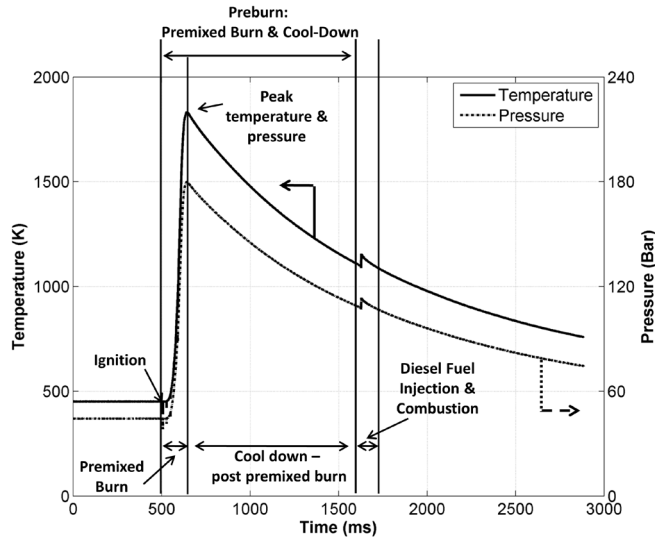


Figure 3.2: Temperature – pressure time plot showing the preburn including premixed burn and cool down along with diesel combustion event. Temperature is that of the bulk gas conditions.

For this test the CV was filled with a preburn mixture to create 21% O₂ post preburn to a pressure of 45 bar (bulk gas density of 34.8 kg/m³) reaching a peak pressure of 180 bar and bulk gas temperature of 1831 K at 0.64 seconds at the completion of the premixed

burn. As will be discussed, the combustion vessel, due to boundary layers, has temperature gradients inside leading to bulk and core gas conditions. Core gas conditions exist in the central region of the combustion vessel where fuel is injected, with the bulk gas conditions representing the entire combustion vessel considering the cooler boundary layers. The cool-down stage is next with this period behaving with a characteristic exponential decay in pressure. At the target temperature (1100 K) for fuel injection, as determined from pressure and the ideal gas law, at 1.6 seconds, the fuel injection is triggered along with image acquisition and illumination (flashlamp) to be synchronized with the fuel injection event.

The nature of the combustion vessel is such that various crevice volumes and boundary layers exist which lead to the existence of temperature gradients inside the vessel. These non-uniformities and gradients are present despite the use of a mixing fan inside the combustion vessel to mix the gases. This includes the presence of a ‘core’ central region of the combustion vessel which is the region of best temperature uniformity in regards to mean temperatures and is the location where the gases mix with the injected fuel (Naber and Siebers 1996). This core gas temperature is higher than the bulk (entire CV region) gas temperature due to the cooler and higher density gases which exist in the boundary layers and crevice volumes. A relation is provided for calculating core gas conditions from that of the bulk gas as given in equation (51) (Naber and Siebers 1996; Siebers 1998).

$$\frac{T_{\text{Core}}}{T_{\text{Bulk}}} = 1 + a * \left(1 - \frac{T_{\text{Wall}}}{T_{\text{Bulk}}}\right) + b * \left(\frac{T_{\text{Bulk}}}{T_{\text{Wall}}} - 1\right) \quad (51)$$

This relationship requires knowledge of the wall temperature, T_{wall} , which is the heated CV temperature in K (373 or 453 K depending on test conditions), the bulk gas temperature, T_{bulk} , as calculated from the chamber pressure history and initial density, and two constants, a and b , which are related to the combustion vessel and represent the boundary layers. More specifically, the constant a corresponds to the boundary layer thickness and is a function of density, and b represents the ratio of the chamber crevice volume to the total chamber volume. The precise constant relationships for the combustion vessel are unknown so they are currently approximated using relationships provided by Sandia National Laboratory as the two combustion vessels are similar in design. These relationships are defined in equation (52).

$$\begin{aligned} a &= 0.0406 * \frac{\rho_{\text{bulk}}}{20.28} \\ b &= 0.026 \end{aligned} \quad (52)$$

To undertake analysis of the bulk and core gas conditions, including application of equations (51) and (52), CV pressure data is used. CV fill pressure enables calculation of the bulk gas density via the ideal gas law as the initial wall temperature and mixture molecular weight are known. Next, this bulk gas density is used to calculate the bulk temperature at injection since pressure is known at this point and bulk gas density is assumed to be constant during the test. Core gas temperature is then calculated from equation (51). Finally, core gas density is calculated using the measured CV pressure at the time of injection in conjunction with the calculated value for the core gas temperature.

The lean preburn procedure is monitored in the control room via a low-speed thirty frames per second movie camera with a sample set of images shown in Figure 3.3.

This preburn environment is for a fill pressure of 16.5 bar at 453 K (12.6 kg/m³ density) to yield 2% oxygen post preburn with the combustion vessel mixing fan on.

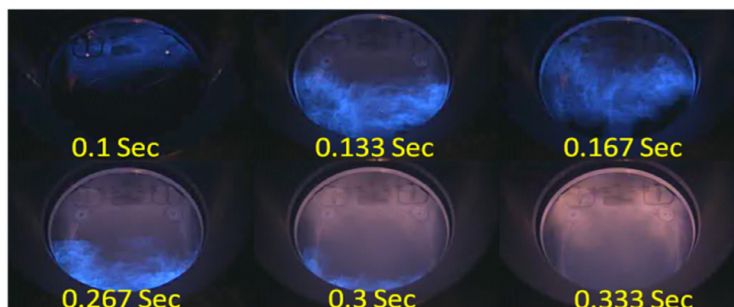


Figure 3.3: Preburn propagation example for a mixture yielding 2% oxygen post preburn. Time after spark dwell is given on each image showing the transition from a laminar to turbulent flame propagating through the combustion chamber. Bulk charge-gas density of 12.6 kg/m³, CV temperature of 453 K. Images acquired with low-speed (30 frames per second) monitoring camera, Samsung SCC-B2311.

In the first image of the figure, the spark discharge can be seen, evidenced by the two bright circles at the electrodes (refer to Figure 3.1 for electrode placement in the combustion vessel). This spark discharge initiates the combustion of the premixed charge gases, being premixed as the fuel and charge gases are mixed before entering the combustion chamber. As the time after spark dwell increases, the flame propagates through the combustion chamber, in a turbulent manner. This turbulent flow is a result of the combustion vessel fan, which yields a faster combustion event, as well as a slightly larger pressure rise (ratio of peak to fill pressure) due to better charge gas mixing and reduced heat transfer to the cooler vessel walls when compared to cases run without the mixing fan.

There are instances when the preburn procedure is not used for thermodynamic state generation for example, nonvaporizing tests at a lower temperature, below 453 K. Under these conditions nitrogen is used as the ambient gas with the CV at the electrically heated CV temperature. Fill pressure of the CV with nitrogen defines the density as calculated with the ideal gas law, with temperature and molecular weight also being known. The experimental test procedure used is modified and undertaken manually. The CV is filled with nitrogen, the intake valve is closed, and fuel injection and imaging are triggered, still in a synchronized manner. Data is logged for a three second period when started by the user. After the test is complete, two manual purges of the CV with nitrogen are performed to prepare for the next test.

3.2. Gas System

The combustion vessel relies on the aforementioned preburn procedure for thermodynamic state generation. To accomplish this gas mixing, a gas delivery and metering system is required, with gases being mixed in a 10 L mixing vessel (Autoclave Engineers) used for preburn mixture generation, as shown in Figure 3.4.

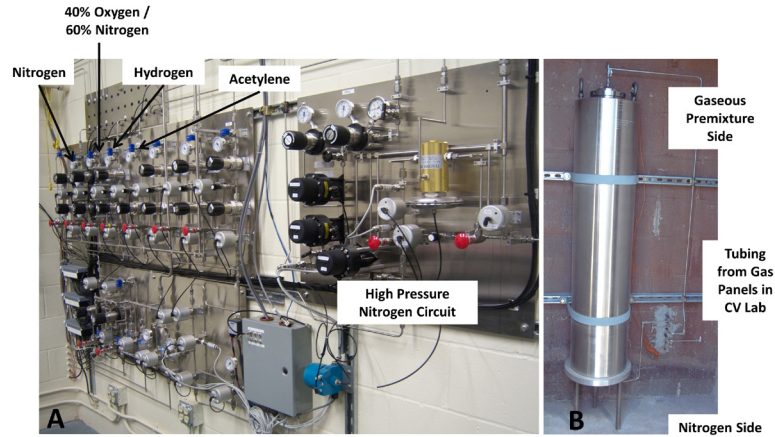


Figure 3.4: Figure A - Gas system for mixture preparation. Figure B – 10 L mixing vessel.

This system is a versatile seven-gas mixing system, developed and manufactured by Airgas, which enables switching of gases depending upon the required mixture for study. The gases used to create the preburn mixture flow from gas cylinders from the specially designed gas room into the gas mixing panel, and are then filled into the 10 L mixing vessel (Figure 3.4) via metered partial pressure filling. As acetylene and hydrogen are small quantities of fuel relative to the oxygen and nitrogen levels (refer to equation (50)), they are filled using a low pressure transducer (Wika model WU-10, 4 bar pressure limit) to ensure the most accurate filling, with an accuracy of less than 1% of the span, or 0.04 bar. The nitrogen and oxygen gases are filled using a 160 bar pressure transducer (Wika model WU-10) with an accuracy of less than 0.5% of the span, or 0.8 bar. After the mixing vessel is filled with acetylene, the required partial pressures of the remaining gases are recalculated in the software based on the actual acetylene fill pressure to ensure the most accurate mixture. The mixing vessel includes a floating piston which separates the mixture in the top portion of the mixing vessel relative to the bottom portion of nitrogen. This setup enables the use of nitrogen to pressurize the mixture to ensure the CV can be filled to a high enough pressure to match the desired density conditions for study, independent of the pressure of gases in the mixing vessel, taking advantage of the volume difference between the CV (1.1 L) and the mixing vessel (10 L).

Each gas has its own fill circuit on this panel equipped with a slow and fast fill unit to ensure controlled and regulated mixing vessel filling, which produces mixtures with a 2% accuracy based on settings in the control system for allowed partial pressure ranges. The low pressure transducer provides improved accuracy for the small quantities of fuel added to the mixing vessel, which assists in proving the correct mixture. Increasing the mixture pressure will improve the accuracy of the mixture as a larger quantity of gas is added. The upper pressure limit is constrained by the allowable pressure of acetylene based on its stability limit of 212 kPa.

In the current study, acetylene, hydrogen, oxygen, and nitrogen gases are used but the gas system is also equipped with a circuit for methane / ethylene, carbon dioxide, carbon monoxide, and others as defined by the CGA gas cylinder fittings. The system versatility and customization enables creation of various gaseous mixtures for a range of desired ambient compositions for study in the combustion vessel.

3.2.1. Operating Regime

The combustion vessel is a flexible test apparatus as it enables generation of an extremely wide range of ambient conditions replicating those found in conventional engines while also enabling achievement of conditions that incorporate technological engine advancements and alternative combustion strategies. The attainable CV operating regime is shown in Figure 3.5 and is based on the current CV preburn mixture.

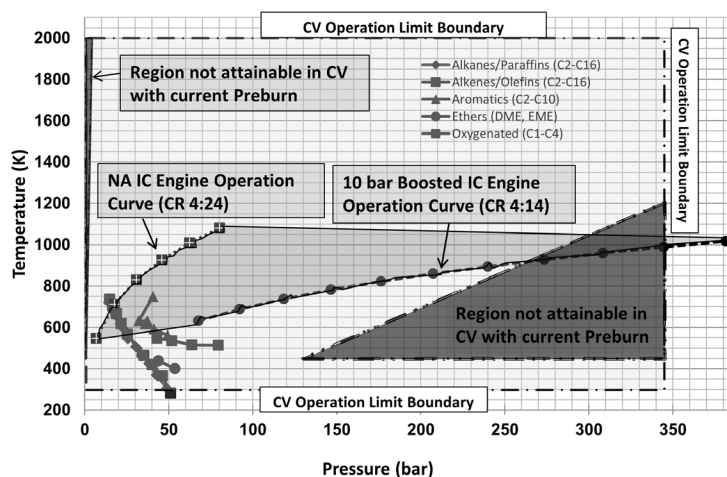


Figure 3.5: CV operating regime including comparison to engine operating regions and critical fuel points. Figure reproduced with permission from Sam Johnson (Refer to appendix 12.1.3).

Several key observations can be made from the above figure. First, the lower temperature limit is defined by the minimum heated combustion vessel temperature while still ensuring sealing of the vessel for testing. The pressure limit boundary on the upper end (350 bar) is based on mechanical design limits of the combustion vessel. The blacked out regions not attainable in the CV with the current preburn are based on system limitations in regards to maximum cartridge heater temperature (453 K) and preburn achieved temperatures and pressures. The upper temperature limit is governed by the preburn procedure. The resulting chamber pressure and temperature from the preburn are limited by the premixture composition including combustion limits of hydrogen and acetylene as well as experimental pressure and temperature conditions for the preburn. Acetylene and hydrogen levels in the mixture are kept small to stay near the lean flammability limit (equivalence ratio of 0.19 and 0.14 for acetylene and hydrogen respectively (Turns 2000)) to ensure pressure and temperature operational limits of the vessel are not exceeded, and also are used to produce carbon dioxide and water levels which are representative of engine operation. Included are curves for a naturally aspirated and a 10 bar boosted engine, showing the wide span of engine conditions that the combustion vessel can replicate using the preburn procedure. Also included in the figure are fuel critical properties of temperature and pressure. Above these conditions, the fuels will only exist in the vapor phase.

Despite these regions of limitation, the combustion vessel is able to effectively replicate a wide range of temperature and pressure conditions, including those representative of current and advanced technology engines, while exhibiting the unique ability to produce a broader set of temperature and pressure conditions which are under

study for novel technologies. This includes the transition from conventionally naturally aspirated engines to boosted engines, which run under higher pressure conditions, as shown in Figure 3.5.

3.3. Control, Monitoring and Data Acquisition System

The CV laboratory is remotely controlled and operated using a data acquisition and process control system from A&D Technology. The control, monitoring and data acquisition system (DAQ) consists of two main components. The first is the iTest software which interfaces with the hardware including relays, digital inputs and outputs, analog inputs and outputs, and temperature inputs, contained in the facility interface cabinet (FIC), which does process control of the CV laboratory. This software controls hardware and valves, runs preprogrammed user-defined scripts, which are essentially sequences of steps that perform a certain task, and monitors pressures and temperatures. The second key component is the ADX, AD5435, which is a high speed data acquisition system, acquiring analog data. These two systems communicate via Ethernet cables. An overview of the control and data acquisition system architecture is provided in Figure 3.6.

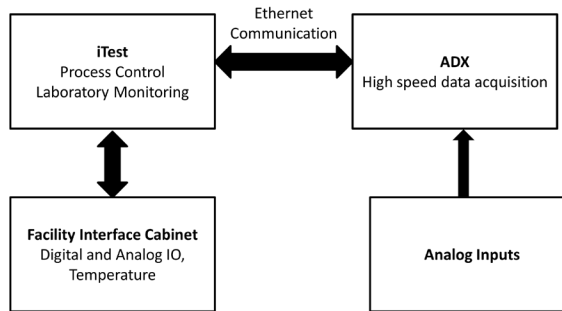


Figure 3.6: Overview of the control and data acquisition system architecture.

The individual components will be discussed in greater detail throughout this section.

The process control in iTest uses a graphical based interface, as shown in Figure 3.7.

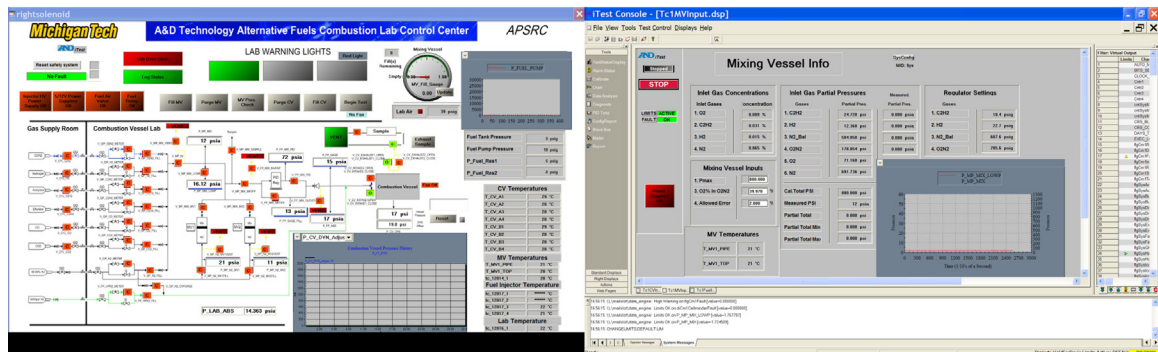


Figure 3.7: iTest low speed process control screen shot. Left panel shows gas panel layout for process control with manual control of valves with scripts for preburn mixture creation based on user inputs to the right panel. Pressure and temperature feedback is provided on this interface.

This software controls, operates, and monitors the facility using various relays, digital inputs and outputs, PWM triggers, analog inputs and outputs in the facility interface cabinet (FIC), to control air-operated solenoid valves, monitor temperatures, pressures, and valve states, as examples. The FIC is shown in Figure 3.8, along with the interface for high speed data acquisition (ADX) and triggering as will be discussed.

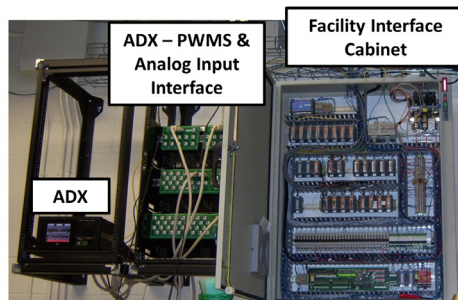


Figure 3.8: Facility interface cabinet and additional hardware for the data acquisition and control system.

The complete system consists of the process control software, iTest, which includes scripting of various procedures such as for producing preburn mixtures, filling the combustion vessel, running tests with appropriate triggers, and data acquisition. This low speed process control system is coupled with a high speed ADX software setup which sends out the necessary injection and ignition triggers, as well as logs all required data. The complete configuration for process control and data acquisition and system communication is shown in Figure 3.9, as defined for the current test setup.

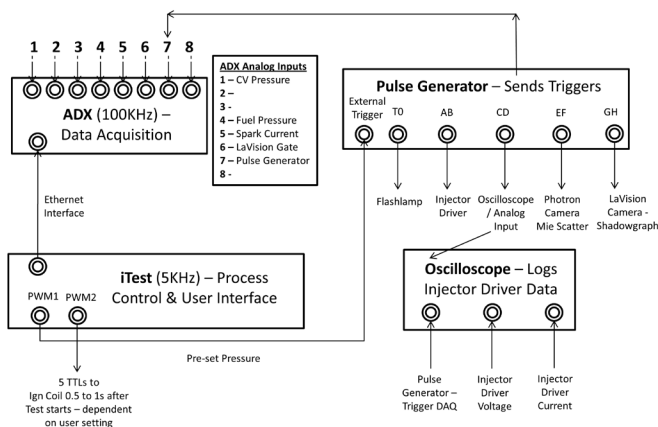


Figure 3.9: Data acquisition and process control diagram.

Logged data signals in the ADX include the CV pressure trace, trigger signals (ignition and injection, pulse generator), fuel injection pressure, spark current, and any other signals of interest, with representative experimental data from testing showing logged data and corresponding trigger signals at appropriate timings in Figure 3.10.

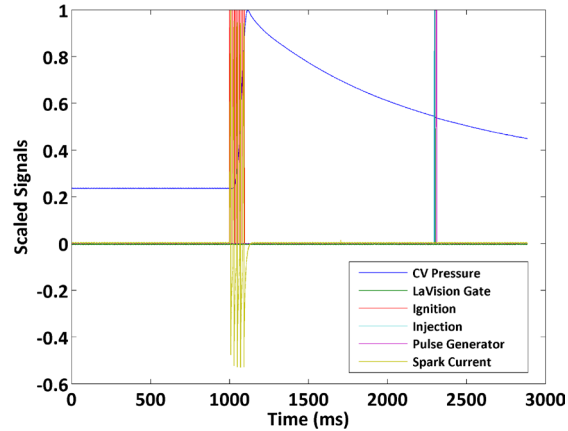


Figure 3.10: ADX logged signals of CV pressure, triggers for ignition, injection and the pulse generator, spark current, and LaVision camera gate. Ignition triggered 1 second after the procedure commences yielding the preburn pressure rise followed by cool down until the desired pressure is reached, injection is triggered (2300 ms).

The combustion vessel is filled to the desired pressure, and at 1000 ms after the start of the test, the 5 TTL pulses for ignition occur, with spark current being measured. This results in a premixed burn and subsequent cool-down phase. The pressure is monitored during the cool-down, with the injection trigger signal being sent at the predetermined set-point pressure, around 2300 ms in the above figure. This injection event is synchronized with image acquisition.

For test operation the iTest system sends the ignition trigger, 5 TTL signals of amplitude 5 volts to the spark system, which discharges 5 sparks of 5 A peak current, 6 ms dwell time (see Figure 3.11). The spark current is measured with a Fluke i200 S current clamp placed on the +12 V lead from the power supply to the ignition coil. The preburn mixture typically begins combusting on the second or third spark. This preburn combustion event results in a pressure rise to a peak pressure after which the pressure falls and the temperature cools due to heat transfer.

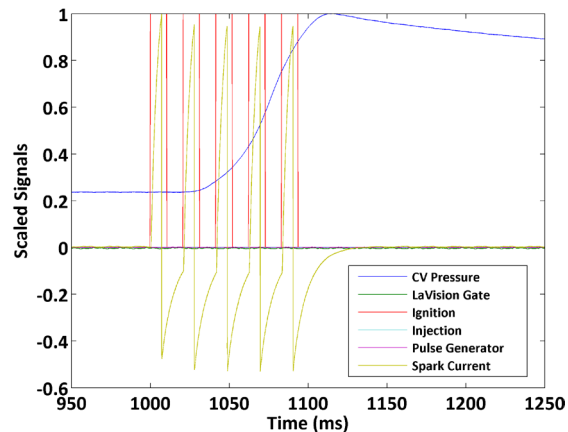


Figure 3.11: ADX logged signals of spark current, CV pressure, and ignition trigger. The ignition trigger is 5 TTL pulses which cause the ignition coils to charge and discharge five times to ensure ignition of the preburn mixture. The first ignition trigger is sent 1 second after the procedure begins.

At the desired pressure during the cool-down, which is a predetermined input into the user interface, the iTest system sends a 5 V TTL trigger signal of 1 ms duration to a pulse generator. This pressure input is determined by the user, as it corresponds to a charge gas temperature, calculated using the ideal gas law with known fill properties (and therefore known density). The control system continuously monitors pressure during the cool down, starting from a user defined enable pressure which must be 2 bar (30 psi) larger than the desired trigger pressure, sending the trigger when the setpoint pressure is reached. This pulse generator (Stanford Research Systems DG645), with nanosecond timing resolution, triggers the fuel injector, flashlamp, and cameras, as well as sends a signal to the oscilloscope and ADX DAQ for synching data logging between the ADX and the oscilloscope which logs injector driver monitoring signals, as shown in Figure 3.12.

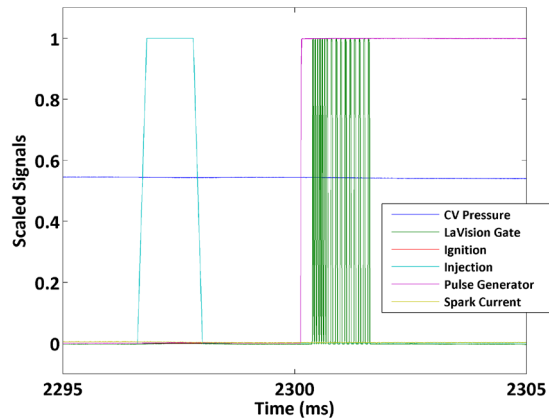


Figure 3.12: ADX logged signals of pressure, injection and pulse generator trigger along with LaVision camera gate. The injection trigger is sent at the desired pressure during the cool down phase.

The injection trigger in the figure above is the signal that is sent at the setpoint injection pressure, to trigger the pulse generator, which then triggers fuel injection and image acquisition to ensure synchronized events. The timing resolution of the PWM's are only 0.2 ms, whereas the pulse generator can provide nanosecond resolution, with this more precise time control required for synchronizing imaging with fuel injection, and therefore why the pulse generator is used for the injection triggering.

There is a delay between the trigger signal sent from iTest and the signals from the pulse generator for the cameras and injection event. The flashlamp is triggered with the pulse generator at time 0 seconds, with the injector delayed 3 ms and camera delayed 3.145 ms relative to the flashlamp to account for its warm-up time to ensure steady state illumination during the event of interest. This is depicted in the timing diagram in Figure 3.13.

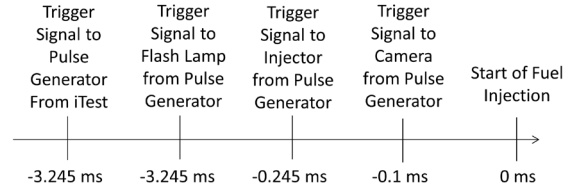


Figure 3.13: Timing diagram for fuel injection study including camera and flashlamp synchronization.

The triggers are delayed to account for not only the flashlamp rise time, but also the delay in fuel output from the injector relative to the driver receiving the trigger. The camera acquires images before fuel injection starts to provide a background image for locating the injector tip to reference spray parameters to, as will be discussed in the image processing section (Chapter 5.4).

All acquired data from the ADX and oscilloscope is post-processed using user-created Matlab processing routines. Logged data from the ADX is in a .BDF format and is converted in Matlab to a .mat file, which involves reading in the .BDF file format, converting it to array format with each channel representing its own array and deleting repeated data (every 5 ms 0.2 ms of data on the ADX is repeated). Next, based on a user defined text file which has information on channels used in the current data logging, data is deleted from channels which were not used in testing and channels are renamed based on user defined variables to facilitate data analysis and post-processing. The remaining data with correct variable names is saved into a .mat file to enable further processing and analysis to be undertaken including converting voltage signals (format of logged data) to the appropriate units for the signal such as, converting spark currents to Amps, determining preburn characteristics including pressure rise and characteristic exponential decay, and characterizing conditions at injection as examples. These processing programs are provided in the Appendix section 12.4.5.

3.4. Diesel Fuel System

The fuel system used in the current study is a high pressure system designed and manufactured by Hydraulics International Inc (Johnson 2009). This system is capable of producing output fuel pressures to 4140 bar (60,000 psi), higher than the upper limit in current production technology diesel engines and injectors. However, this high-pressure capability enables characterization of high pressure diesel sprays and combustion which are of interest as a potential solution for diesel emission control of PM and NO_x to meet stringent emission regulations. Higher injection pressures can provide improved atomization and fuel-air mixing, enabling increased EGR, to simultaneously reduce PM and NO_x (Fischer and Stein 2009). This fuel system utilizes an air operated pump which is supplied compressed air to boost fuel pressures to the desired output pressure as shown in Figure 3.14, with output fuel pressure controlled by regulation of the inlet air pressure.

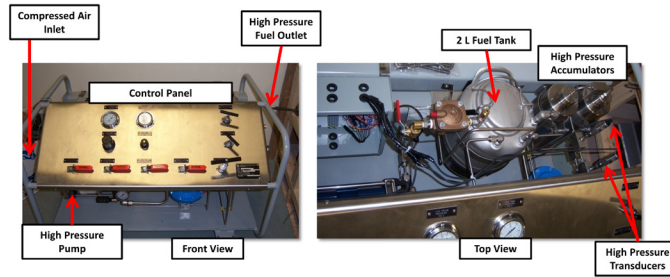


Figure 3.14: High pressure air operated diesel fuel system.

The system is multi-fuel compatible to incorporate a wide-range of fuels for study including diesel, biodiesel, gasoline, ethanol, methanol, dimethyl ether, and others. Fuel is drawn from the tank into the fuel pump, with this tank being provided a positive air pressure (2.4 bar). This fuel pump (Hydraulics International 5L-SD-600N) is air operated using compressed air and the air regulator is set at one-six hundredth of the desired output fuel pressure in psi. The high pressure fuel is stored in two 100 mL accumulators before exiting the system via the high pressure fuel line to the injector. There are two high pressure transducers which enable monitoring of the systems fuel pressure in the iTest control system to verify that injection will occur at the desired pressure conditions; a pressure transducer is also installed in a 'T' after the high pressure fuel system outlet but prior to the pressurized fuel entering the injector with this pressure logged in the high speed data acquisition system (ADX). This fuel pressure transducer is an American Sensor Technologies model AST47HPX60000P4A0123, with a 4140 bar (60,000 psig) pressure limit.

The fuel also undergoes filtering in the system to minimize contaminants reaching the injector which can cause operational problems including plugged holes or the injector being stuck open. These include filtering the fuel upon filling of the fuel tank (Mr. Funnel F1C Filter), and two additional filters in the fuel system. The first is a low-pressure 40 micron in-line filter (Swagelok B-8TF2-40) between the fuel tank and low pressure inlet to the fuel pump, with the second being a 10 micron in-line filter (High Pressure Equipment 60F-51HF4-10) between the high pressure outlet to the fuel pump and the two fuel accumulators. These filter elements can be cleaned or replaced as they become contaminated.

There is a separate low pressure fuel return system that provides the 10 bar back pressure necessary for the piezoelectric injector operation, as shown in Figure 3.15.

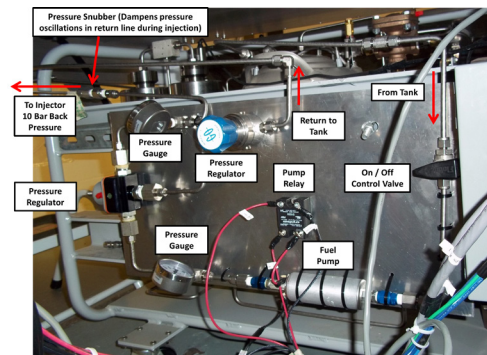


Figure 3.15: Low pressure fuel system providing injector back pressure.

This system takes fuel from the storage tank at low pressure (less than 2.4 bar) and then passes it through a 12 V operated fuel pump (Walbro GSL392), which is controlled via a solid state relay in the control software, that increases the fuel pressure to 10 bar. If desired, the fuel pressure can be regulated down to lower back pressures depending on the required back pressure for the fuel injector using a bypass regulator (Weldon Racing A2040-281-A-200). Prior to an injection event, the relay is turned on to power the pump which provides the back pressure with the relay and pump being turned off after the injection event. This low pressure system is also equipped with a return to the low pressure fuel tank from a bypass off the regulator, with this fuel being regulated down to 2.4 bar (Goreg PR11A11A3E111) before returning to the low pressure fuel tank. For the current set of studies, the injection back pressure is kept constant at 10 bar.

3.4.1. Diesel Fuel Properties

The fuel used in this testing is ultra-low sulfur diesel (ULSD) fuel, number 2. The specifications for the fuel are provided in Table 3.1. These properties are determined based on externally performed fuel property analysis.

Table 3.1
Fuel property specifications as obtained from experimental testing. ^aParagon Laboratories Inc. Fuel Testing, December 2010, Report ID: 176559-861958.
^bCummins Fuel Property Testing, September 2010.

Property (unit)	Specification
Carbon (Weight %)	86.94 ^a
Hydrogen (Weight %)	13.06 ^a
Sulfur (ppm)	7 ^b
Water (ppm)	92 ^b
API Gravity at 289 K (g/mL)	0.8457 ^a
Specific Gravity at 289 K	0.8465 ^a
Gross Heating Value (MJ/kg)	45.578 ^a
Net Heating Value (MJ/kg)	42.806 ^a
Cetane Index	40 ^b
Viscosity at 313 K (cSt)	2.3 ^b
Distillation	
Initial Boiling Point (°F)	441 ^b
0.1 (K)	468 ^b
0.5 (K)	518 ^b
0.9 (K)	576 ^b
Final Boiling Point (K)	613 ^b

3.4.2. Piezoelectric Injector

The injector used in the current study is a Bosch production (automotive application) high-pressure common rail piezoelectric fuel injector with a pressure limit of 2000 bar as shown in Figure 3.16.



Figure 3.16: Piezoelectric injector used in the current study with the nozzle tip showing the injector nozzle holes in the image on the right.

Key injector characteristics of this mini-sac hydroground nozzle are that it has 8 holes, with each hole having a mean diameter of $145\ \mu\text{m}$ and 1 mm hole length providing a length to diameter ratio of 6.9. The enclosed spray angle is 150 degrees, as shown in Figure 3.17. Plumes are also labeled in this figure, with this numbering being used for discussions on plume to plume variations in Chapter 6.

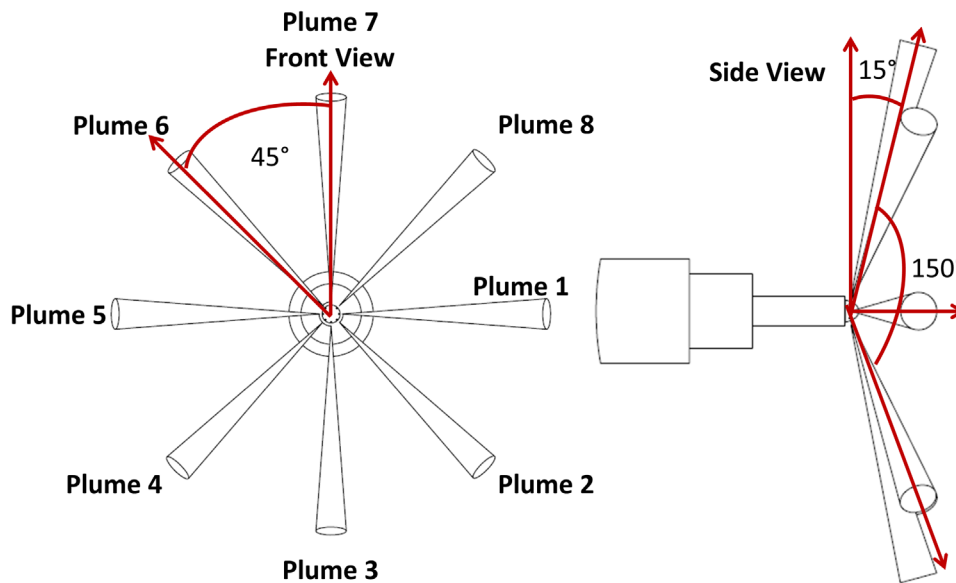


Figure 3.17: Injector orientation properties. Plume labeling is also provided to reference the spray plumes in all discussions.

These injectors (piezoelectric) are a newer technology compared to conventional solenoid diesel injectors found in current diesel engines. Solenoid injectors utilize a high current to initially open the needle to allow fuel to flow through the injector and a reduced current to keep the electromagnet open (Lee et al. 2006), defined as the peak and hold currents, respectively. Hence, current must be constantly applied during the injection event resulting in large power consumption. Piezoelectric injectors rely on an electric charge to change the dimensions of the piezoelectric crystals with current only being applied at the start of the injection event thereby reducing the overall duration of power consumption.

Piezoelectric injectors have many unique and beneficial characteristics attributed to the piezoelectric material properties, motivating their use to improve current diesel engine technology due to their fast response timings which helps to provide low smoke, NO_x , and HC emissions due to more precise fuel control (Wersing 2002). These materials exhibit the unique ability of being able to develop electrical charge as the result of

mechanical stress by converting mechanical energy into electrical energy and the converse, lending these to several applications including motors, igniters, sensors, transducers, fuel injectors, and others (Setter 2002; Wersing 2002). However, piezoelectric materials have small deformations requiring high driving fields achieved through the use of high voltage power supplies which can sometimes require voltage in excess of 200 V (Wersing 2002). By developing a multilayer ceramic, which is several very thin electrode layers, these disadvantages can be partially counteracted to enable the use of piezoelectric materials for diesel fuel injectors. To summarize the operating principle of a piezoelectric injector, an electric voltage is applied to the actuator causing the actuator to expand thereby lifting the valve off its seat. This allows fuel to flow into the low pressure drain from the control chamber resulting in a drop in pressure above the control piston. The pressure on the lower end of the nozzle is constant so the resulting hydraulic force on the needle causes the needle to be lifted off of its seat opening the nozzle outlets allowing fuel to flow into the combustion chamber at high pressures (Mock and Lubitz 2008).

Additional images of a disassembled piezoelectric injector are shown in Figure 3.18, to provide a further understanding of injector characteristics and composition.

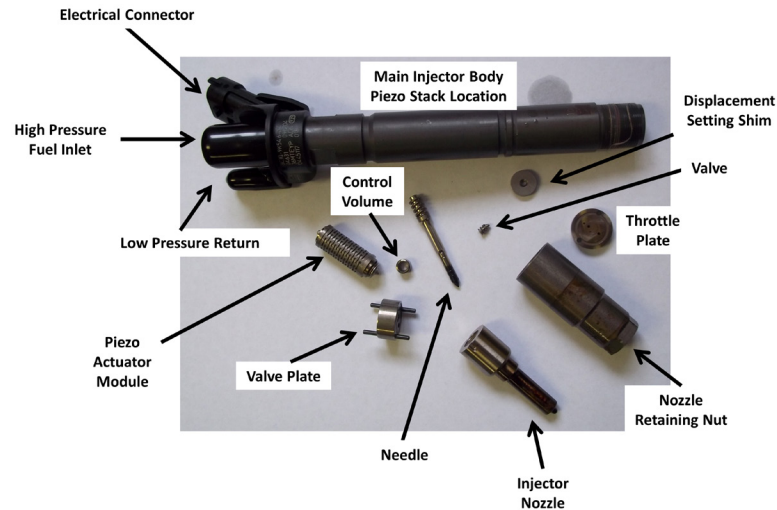


Figure 3.18: Piezoelectric injector, disassembled, showing all components that comprise the injector.

Key components are the needle which is lifted to enable fuel to flow out of the injector into the combustion chamber, the nozzle which possesses the holes for the injection event, the piezoelectric actuator which controls the control valve and needle motion, along with the fuel inlets and returns, and nozzle guide. Additional views of the components are provided in Figure 3.19.

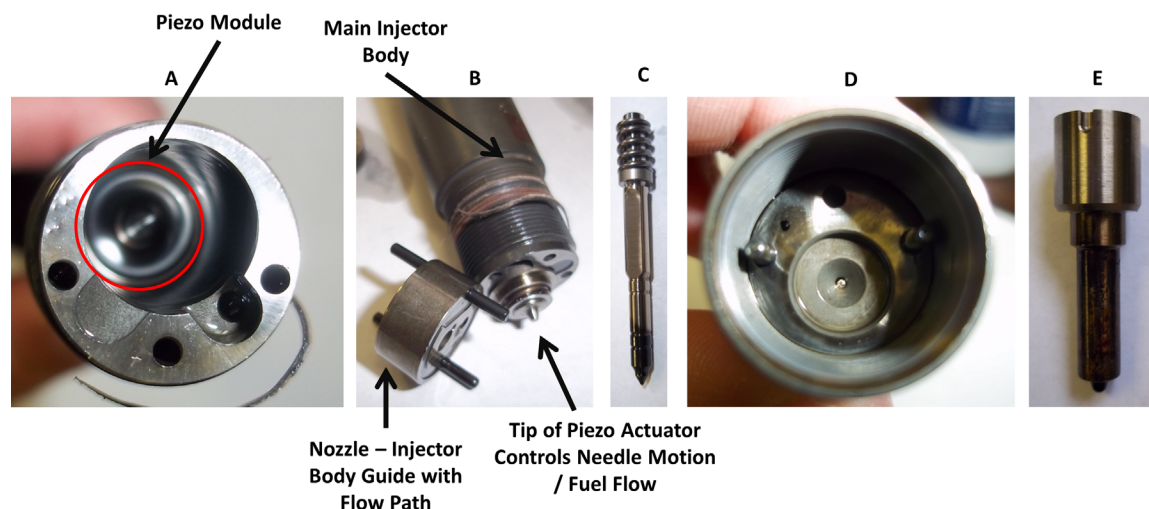


Figure 3.19: Additional piezoelectric injector assembly pictures.

Image A is a view looking down the main body of the injector towards the fuel inlet / return location, also showing the piezoelectric module. Image B provides a look at the base of the main injector body showing placement of the piezoelectric actuator and needle guide. Image C shows the injector needle and spring, along with the needle guidance, the black discoloration on the tip of the needle is due to the preburn combustion gases. Image D provides a view into the end of the injector towards the nozzle tip showing the location of the nozzle guide. Image E shows a view of the nozzle removed from the end of the injector providing indication of the location of the nozzle guides. From these images, the intricate nature of piezoelectric injectors is portrayed along with the ability to interchange nozzles of different geometries, including number of holes, hole rows, hole length, nozzle diameter, and k-factor (conicity) of the nozzle as examples, which are known to govern spray and combustion characteristics. K-factor is a nozzle property which is defined as the difference of the outer to inner diameter of the nozzle hole divided by the hole length.

3.4.2.1. Injector Characteristics Influencing Spray Behavior

As will be discussed in Chapter 6, there exist plume to plume variations of spray characteristics from the multi-hole injector, which are most pronounced and consistent in the vaporizing spray tests based on averaging over several data points to remove random noise and fluctuations. Discussed here are injector characteristics which may cause these plume to plume trends to provide background information on injector characteristics to prepare the reader for the discussions in Chapter 6.

Injectors are known to experience eccentric needle movement during the start of the injection event as the needle lifts off of its seat. This results in differences in pressure to each of the holes of the multi-hole injector, which causes the needle to lift in a non-uniform way, which is translated to downstream spray characteristics (Arcoumanis et al. 1998; Karimi 2007; Powell et al. 2011). This needle movement is observed at the start of injection and does not translate to steady state plume trends as will be shown under the repeat tests in the ILASS paper (section 6.2.1) and is also shown here in Figure 3.20 for a set of vaporizing (0% Oxygen) spray tests.

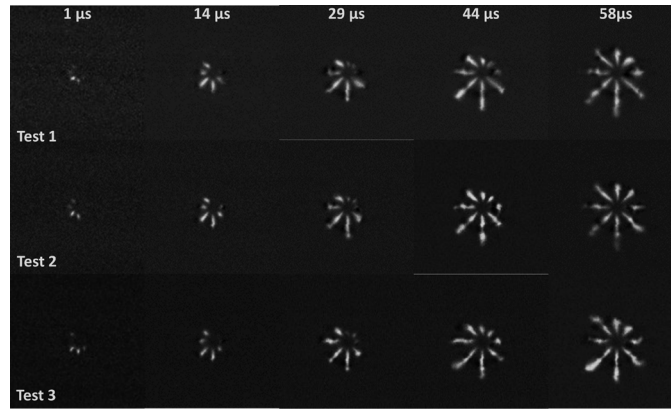


Figure 3.20: Start of injection spray characteristics for repeat tests at 355 K fuel temperature. 34.8 kg/m³ bulk charge-gas density, 1100 K bulk charge gas temperature, 2000 bar injection pressure.

Injection was delayed from holes 1, 7 and 8 (labeled per Figure 3.17) relative to the others, and had reduced initial penetration; however, as will be discussed in Chapter 6.2, this did not translate to steady state characteristics and is not an explanation for the plume to plume variations evident during that time region.

Another potential cause is of plume to plume variations in differences in nozzle hole diameter, since an increase in hole diameter leads to a direct increase in liquid length (Siebers 1998). A significant difference in hole diameter is required to explain the magnitude of plume-to-plume variations seen in Chapter 6.2. Scanning electron microscope (SEM) images of the injector nozzle were acquired to understand actual injector hole diameters to determine if this was the cause of the plume-to-plume variations. Images from these SEM measurements are provided in Appendix 12.2. Two sets of SEM images were acquired since the first set showed a significantly reduced hole diameter (on the order of 30 μm) for hole two. It was expected that hole two would actually have one of the largest hole diameters based on vaporizing spray plume trends. Tests were repeated to verify whether the reduction in hole diameter was a real phenomenon and not solely an error in SEM magnification setting. These repeat tests did not show a significant difference in hole 2 diameter relative to the others, and this reduced hole diameter in set 1 was therefore attributed to an error in magnification setting (i.e. the magnification on the SEM was set lower than the expected 400X in the imaging program).

Analysis was undertaken on the SEM images to characterize diameters of the hole using a curve fit procedure. As the SEM beam was not perfectly normal to the hole, a standard thresholding and boundary tracing procedure could not be undertaken due to differences in contrast along the spray edge, thereby requiring a modified procedure be used. Eight points of the hole edge were chosen by eye in the SEM image, in approximately 45 degree increments. These eight points were then curve fit with an ellipse (to account for the nozzle hole deviating from being perfectly circular), which defined the major and minor radii of the ellipse, as defined in Figure 3.21.

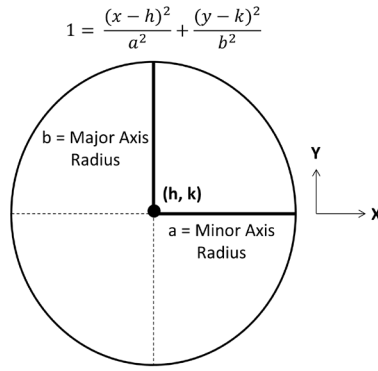


Figure 3.21: Curve fit methodology for nozzle hole, modeled as an ellipse.

The equation was solved for a and b , by curve fitting to the eight user-defined (x, y) coordinates which defined the spray edge. Hole diameters, both along the minor axis (horizontal) and major axis (vertical), were determined by multiplying the respective radii by a factor of 2. A sample result of this procedure applied to the SEM images is shown in Figure 3.22.

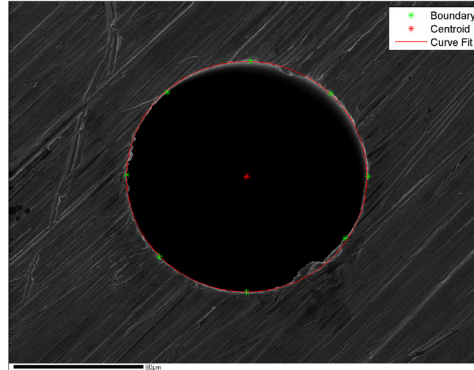


Figure 3.22: Ellipse curve fitting result to determine hole radius, shown for SEM image set 2, hole number 5.

The SEM image shows that the hole is not perfectly circular or smooth (refer to the lower right portion of the spray hole in the above SEM image) which is an artifact of the manufacturing process, which will influence the downstream spray characteristics. In the figure, boundary points are the (x,y) coordinates determined by eye based on the SEM image, centroid, and curve fit. As defined in the legend, the curve fit was based on the elliptical fit as discussed in Figure 3.21. From this particular ellipse curve fit, the horizontal diameter ($2a$) was $147.8 \mu\text{m}$, and the vertical diameter ($2b$) was $141.6 \mu\text{m}$, giving a mean diameter of $144.7 \mu\text{m}$, with an eccentricity of 0.29, defining the elliptical nature of the hole. Eccentricity is defined as $\sqrt{1 - b^2/a^2}$, and is equal to zero for a circle. Therefore, the increase in eccentricity from zero provides an indication of the extent of the non-circular nature of the nozzle hole. Tabulated results for hole diameter and eccentricity determined from image analysis for SEM images from test set 1 and 2 are provided in Table 3.2.

Table 3.2
SEM image analysis results for hole diameter, test set 1 and 2.

	Test Set 1				Test Set 2			
Plume Number	Horizontal Dia (μm)	Vertical Dia (μm)	Mean Dia (μm)	Eccentricity	Horizontal Dia (μm)	Vertical Dia (μm)	Mean Dia (μm)	Eccentricity
1	144.4	142.4	143.4	0.17	149.5	143.3	146.4	0.29
2	119.1	114.1	116.6	0.29	147.6	141.6	144.6	0.28
3	143.8	138.0	140.9	0.28	151.3	141.6	146.5	0.35
4	143.6	138.3	140.9	0.27	147.2	141.0	144.1	0.29
5	142.2	139.2	140.7	0.20	147.8	141.6	144.7	0.29
6	146.9	139.4	143.2	0.32	145.9	142.9	144.4	0.20
7	147.6	140.9	144.2	0.30	146.2	140.8	143.5	0.27
8	146.4	138.5	142.4	0.33	150.3	142.3	146.3	0.32

Test set 1 exhibits a mean diameter of 139.0 μm, including the major outlier for plume number 2 as was previously discussed, with an average eccentricity of 0.27. Neglecting the hole 2 outlier, mean diameter increased to 142.2 μm with no change in eccentricity. For test set 2, the mean diameter was 145.1 μm and mean eccentricity 0.29. These diameters are close to the manufacture reported specifications of 140 μm hole diameter.

A statistical analysis was undertaken to determine the significance of the differences between test sets and nozzle holes. There appears to be a systematic error between the two sets which could be attributed to a difference in scaling. A T-Test was undertaken to calculate the probability that two samples are from the same population, assuming they have the same mean. Data is considered for holes 1, 3-8 from test set 1 and test set 2 (neglecting the outlier hole 2 which was observed in test set 1). The T-Test is undertaken as having 2 tails (distribution), and a type 1 test is used which means it a paired or dependent test which was chosen since the same nozzle is used for the hole size measurements. The result of the T-test was 0.011 showing a statistically significant difference in the data sets because this result was less than 0.05. This statistically significant difference was likely attributed to the SEM setup measurement accuracy with the 400X resolution being within ±5% of the set magnification.

Next individual hole diameters were compared for holes 1 and 3-8, again neglecting the hole 2 outlier, as shown in Figure 3.23.

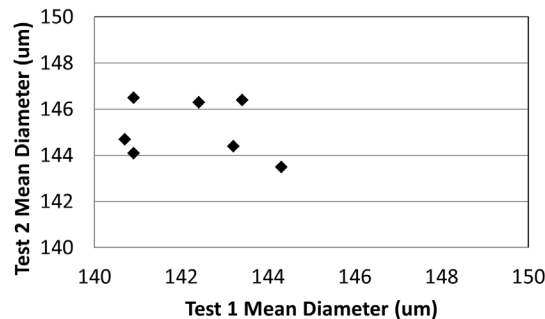


Figure 3.23: Test 2 versus test 1 mean diameter comparison.

There is no trend or relationship between test 1 and test 2 diameters. Although, overall the two tests exhibited a statistically significant difference which was likely attributed to resolution of the magnification, the individual differences between holes did not exhibit

any conclusive relationship attributed to the scatter in the data. The mean diameter of set 2 was chosen as representative of the actual hole diameter based on the lack of an outlier in this test set. This supported the conclusion that the mean diameter of all eight nozzle holes is $145.1\text{ }\mu\text{m}$, with a standard deviation of $1.2\text{ }\mu\text{m}$, which was less than the measurement repeatability since the measurement repeatability of the means for test 1 and test 2 was $2.9\text{ }\mu\text{m}$ with no significance in the diameter variations. The hole to hole variations are minimal and not of significant enough magnitude to explain the overall plume to plume variation trends discussed in Chapter 6.2.

Another potential cause of the spray plume to plume variations is hypothesized to be differences in internal fluid flow and geometry. Based on injector geometry, the flow of fuel into the injector is not symmetrically about all holes, rather, it is symmetric about holes 1 and 5 as shown in Figure 3.24.

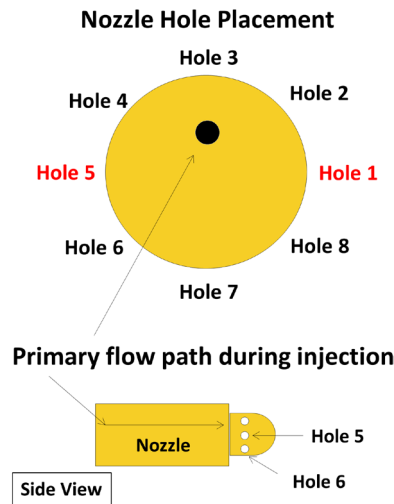


Figure 3.24: Injector fuel flow path.

The fuel fills the injector from above hole 3, but because of the filling angle, the fuel could actually flow from hole 6 through 8 in preference depending on how the fuel flows around the needle (Graham 2011). Without further studies into the nozzle flow characteristics via detailed CFD modeling or advanced diagnostics to characterize geometry and flow, the exact flow path remains unknown. Holes 1 and 5 are symmetric about the fuel filling location and these holes consistently exhibit reduced liquid lengths relative to the others, as will be discussed in Chapter 6.2. Based on this limited knowledge of fuel filling and nozzle geometry, it is hypothesized that these internal nozzle asymmetries are the cause of the steady state liquid length variations.

3.4.2.2. Piezoelectric Injector Driver

The piezoelectric injector used in the current study is driven by an EFS IPoD injector driver which provides the necessary high voltage charge to the injector to deform the crystal and initiate the injection event. The driver has three operating current modes; peak-regulation, multi-peak regulation, and constant current, based on the current profile during the injection event. The current study utilized multi-peak regulation mode providing several current peaks during the initial charging time as well as during the discharge phase in order to match production operation current profiles. Defined input

parameters to the driver included peak current, current slope, and open and closing voltage as controlled via the interface in Figure 3.25.

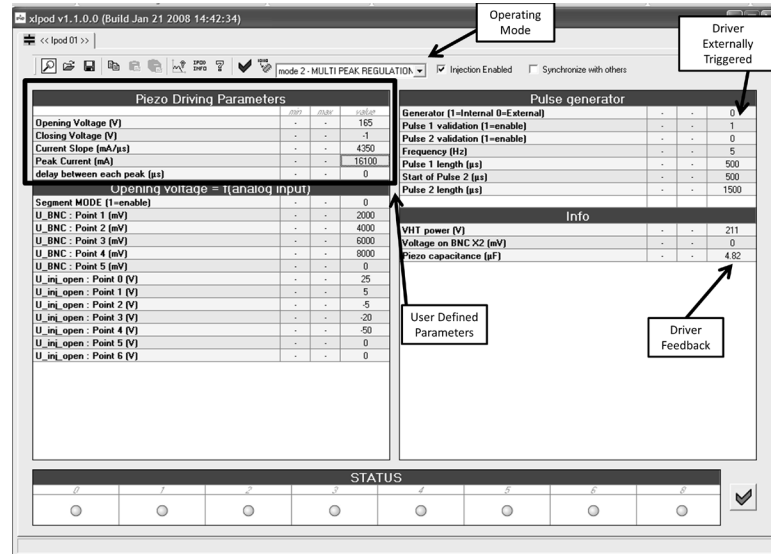


Figure 3.25: Piezoelectric injector driver interface.

In addition to the user defined parameters, the driver interface provides feedback on the level of the high voltage power supply to ensure the system is correctly powered and also on the piezoelectric capacitance. The driver provides output monitoring signals of driving current and voltage, with typical signals shown in Figure 3.26 from an injection event, along with the fuel pressure for the injection event.

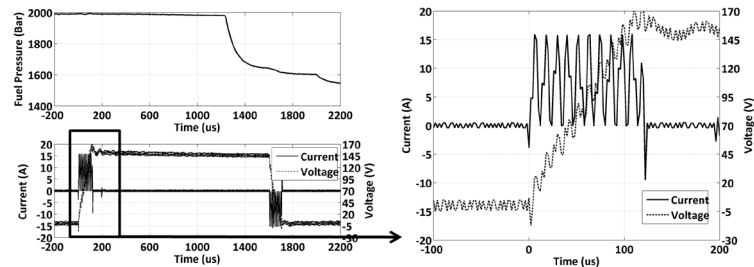


Figure 3.26: Left figure: Fuel pressure trace top and current and voltage injector driver signals on bottom for the injection event. Time 0 microseconds corresponds to the start of electronic injector drive. Right figure provides a zoomed in look at the injector driver traces of current and voltage at the start of injection.

From the figure, it is shown that the fuel injection pressure, measured at the high pressure fuel inlet to the fuel injector, does not drop until 1.2 ms after the injection event has commenced, for these particular test conditions. The driver monitoring traces show that there are multiple peaks in current, which increase the voltage, until the desired opening voltage is reached. Then the current is no longer applied until the TTL trigger is turned off at which time current is again applied in multiple peaks to deform the piezoelectric stacks and close the injector such that the voltage is set to the close voltage setpoint. This electric charge, achieved by the applied current, deforms the piezoelectric crystals to open or close the injector. Monitoring signals are recorded using a Yokogawa Oscilloscope DL 9040 at 200 μ s / division time scale. These signals are output directly

from the driver and their magnitudes are reduced internal to the driver, and therefore measured voltage signals are multiplied by twenty and current by two to receive the actual driving voltage and current profiles in volts and amperes, respectively.

The injection duration in regards to fueling is proportional to the length of the trigger signal used to fire the injector, i.e. the longer the trigger signal, the longer the fuel injection event. For the test shown in Figure 3.26, the electronic injector drive duration was 0.6 ms as defined by the length of the current signal from when the current signal first goes positive to when it first goes negative after the charging time. The actual fuel does not exit the injector until a delay after the electronic current drive starts which is 0.245 ms later and a slight function of injection pressure and charge-gas conditions. There is a small delay between the trigger signal and start of current, of 0.002 ms. The physical fuel injection is longer than the commanded duration of 0.6 ms, being actually 1.05 ms. The fuel injection duration can be related linearly to the trigger duration, as shown in Figure 3.27.

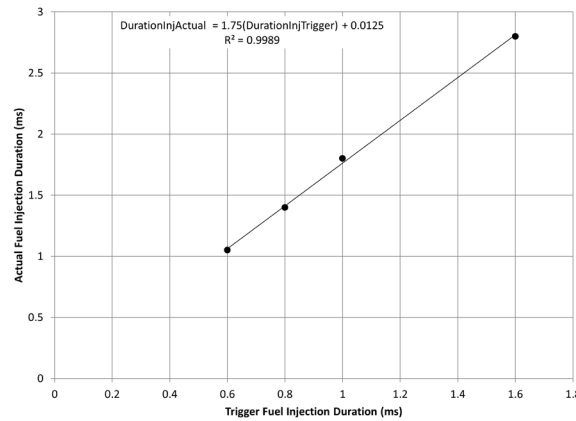


Figure 3.27: Actual fuel injection duration relative to the trigger duration. Time in equation is in milliseconds.

The linear relationship of trigger duration to actual fuel duration can be used to approximate injection durations relative to the length of the trigger signal acknowledging that actual injection duration does vary slightly due to repeatability and different ambient and injection conditions. There is a lower limit of 400 μ s on the duration for triggering fuel injection to ensure voltage reaches the operating level and fuel is injected. Shorter duration triggers can be used and fuel will be injected, down to 250 μ s, however, voltage will not reach the desired set-point for open voltage level under these shorter duration conditions.

Extensive tuning was undertaken to match driver voltage and current profiles to production voltage and current profiles. The driver settings of current and voltage are a function of the injection pressure; as injection pressure increases, parameters of open voltage, peak current, and current slope all increase. The tuning process involved matching driver traces to those production driving profiles for the injection pressure range of 400 to 2000 bar in 200 bar increments. This involved extensive trial and error with parameter sweeps of peak current, open voltage, and current slope to yield the best match between the two driver traces over a wide range of injection pressures. This iterative driver trace matching led to data trends showing the optimum relationship between MTU and production driver parameters for each injection pressure over this

range. More specifically, the required setting for peak current is equal to the peak current from the production data minus a 1.7 A offset. The current slope for the MTU driver is symmetric in the rise and fall slopes and hence this is set to the average of the positive and negative current slope for the data which is being matched as production data has asymmetric positive and negative current slopes. Current of the production driver does not return to zero as is the case with the MTU driver which makes it difficult to match traces. Opening voltage is set equal to the average steady state value of the production driver trace. The voltage first peaks, then falls off to a steady state value, at which point the average value is calculated. The closing voltage is kept as a constant -1 V for all injection pressures based on production voltage profiles. Using these determined input parameters to match production driving profiles, quadratic curve fits were developed relating open voltage, peak current, and current slope as a function of injection pressure to determine driver settings for injection pressures where matching production driver traces are not available. These fits are shown in Figure 3.28 and were used in defining injector driver parameters as a function of injection pressure.

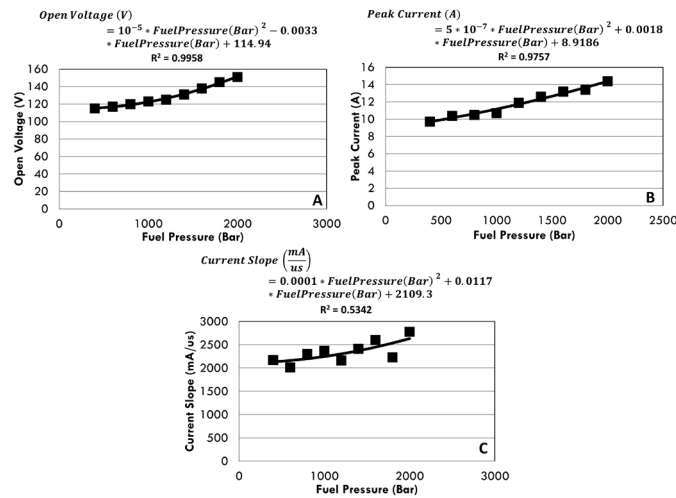


Figure 3.28: Injector driver correlations for open voltage (A), peak current (B) and current slope (C) as a function of fuel injection pressure.

The correlations are shown for fuel injection pressures up to 2000 bar since that is the pressure limit of the injector. A table of applied driver settings is provided in Table 3.3 for tests undertaken in this study.

Table 3.3
Injector driver settings used in testing.

Injection Pressure (Bar)	Current (A)	Open Voltage (V)	Close Voltage (V)	Current Peak (mA/us)
1034	11.3	122.2	-1	2228
1379	12.4	129.4	-1	2316
2000	14.5	148.3	-1	2533

Logged data signals from the fuel system into the high speed ADX include injection pressure from a high pressure transducer in a 'T' on the fuel system line (see Figure 3.29).

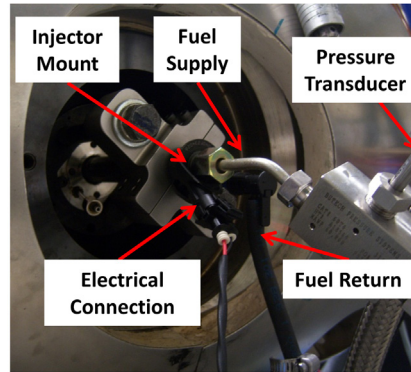


Figure 3.29: Fuel injector pressure transducer location relative to injector.

Injector driver signals of current and voltage are recorded on an oscilloscope providing indication of the drive trace parameters, as well as electronic injection duration relative to the trigger signal.

From extensive use of the driver, it is evidenced that the injector driving characteristics are not consistently repeatable. This is determined by comparison of voltage and current traces for identical driving conditions over repeated injection events. An example is shown in Figure 3.30, for injection into 14.7 kg/m^3 charge-gas density nitrogen at 914 bar injection pressure for a 0.6 ms electronic trigger duration.

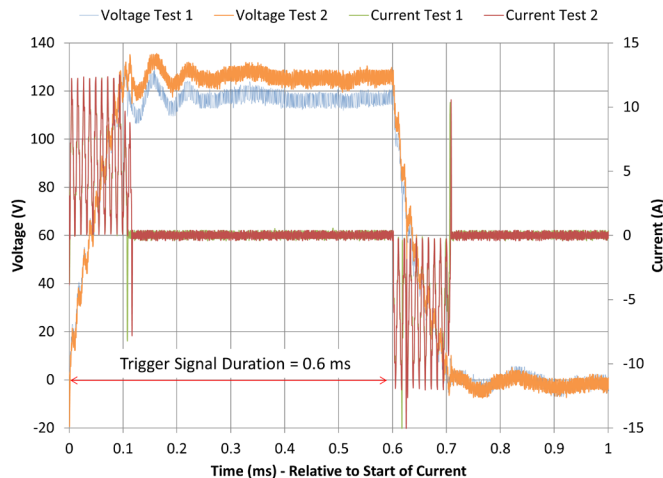


Figure 3.30: Comparison of injector driver traces for identical injection conditions, spraying into 14.7 kg/m^3 at 914 bar injection pressure, 0.6 ms trigger duration.

The trigger duration is 0.6 ms providing 0.6 ms of signal to the injector driver as evidenced by the start of current at 0 ms until the current turns on again at 0.6 ms to deform the crystals back to their original state to end the injection event. There is a noticeable difference in steady state opening voltage between Test 1 and Test 2 which is further understood when looking at a zoomed in trace of the opening multi-peak current of the driver traces, as shown in Figure 3.31.

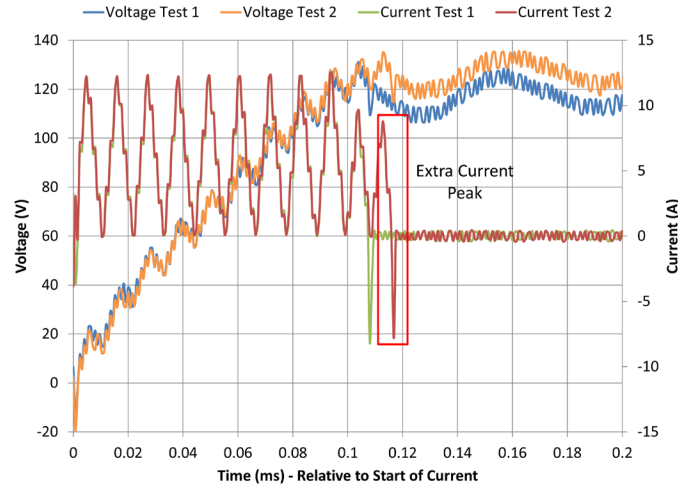


Figure 3.31: Zoomed in comparison of injector driver traces for identical injection conditions spraying into 14.7 kg/m^3 at 914 bar injection pressure 0.6 ms trigger duration.

In the zoomed-in representation of current and voltage there is an extra current peak seen for Test 2 relative to Test 1 resulting in an increase in voltage for Test 2 relative to Test 1. To determine if these differences in driver characteristics influence spray characteristics, the images acquired for each of these tests are compared as shown in Figure 3.32.

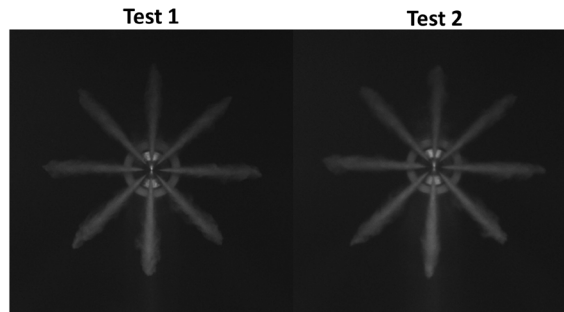


Figure 3.32: Spray images at 14.7 kg/m^3 nitrogen at 914 bar injection pressure 0.6 ms trigger duration. Image is at 0.2 ms after start of injection (0.445 ms after state of current) comparing Test 1 and Test 2 injections where Test 2 has the extra current peak and larger driver voltage.

Despite the increase in voltage and extra current peak for Test 2 there are not any substantial variations in macroscopic spray characteristics, as shown at 0.2 ms ASOI (0.445 ms after start of current (ASOC)) in the above figure, after the occurrence of the extra current peak. There are small variations in spray structure in the two images attributed to shot to shot injection variation and repeatability, but there are no significant differences in penetration or cone angle of the spray as a result of driver variations. This is further confirmed by external rate of injection (ROI) measurements which showed no significant change in injection rate shape with a change in driver voltage. Despite the variations in driver traces and the repeatability issues, these variations in current and voltage are not translated to macroscopic spray characteristics.

3.4.2.3. Rate of Injection Signal

A rate of injection signal provides an indication of the mass fuel flow rate through the injector. Furthermore, this signal, relative to the current trace, provides information on the delay for the injector to open relative to when current is first applied. A rate of injection signal for the injector used in the current study is shown in Figure 3.33, for a 2000 bar injection pressure and 1.2 ms electronic trigger duration.

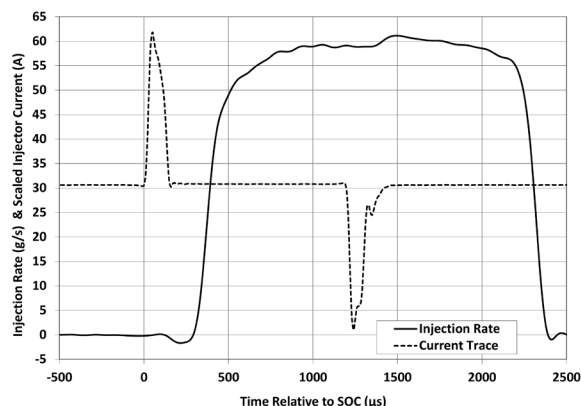


Figure 3.33: Rate of Injection signal for a 2000 bar injection using the production 8-hole injector nozzle. Rate of injection is the total for all 8 spray plumes, dividing the signal by eight provides the average injection rate for a single hole. Reproduced with permission from Eric Kurtz (appendix 12.1.4).

Shown in the above figure is the delay, of 110 μs , in the start of the injection rate, relative to the injector current. This is followed by a fast rise to the needle being fully lifted and therefore the injection rate is reaching a quasi-steady value. The injection rate does not show significant fluctuations during the entire injection event which rules out the injection rate as a cause of liquid length fluctuations (refer to Chapter 8). After the current turns off, there is a delay before the fuel spray is no longer being injected and the needle has returned back to the original position.

3.4.2.4. Chiller for Fuel Temperature Control

The combustion vessel is electrically heated via cartridge heaters to promote vessel sealing and provide an initial elevated temperature for the preburn procedure. Typically the vessel is heated to 453 K for combusting and vaporizing spray tests using the preburn procedure, but temperatures as low as 373 K were utilized for the nitrogen, nonvaporizing, spray studies. The heated combustion vessel results in elevated injector and fuel temperatures due to heat transfer from the stainless steel vessel to the injector window. However, the injector window has been designed to incorporate a cooling cup enabling cooling of the injector to lower temperatures relative to the electrically heated vessel temperatures. The cooling cup includes one-eighth inch diameter inlet and outlet lines where fluid is passed through the cooling cup to reduce the injector body temperature and the fuel temperature relative to the combustion vessel within the limits of the chiller unit. A model of the cooled injector window is shown in Figure 3.34.

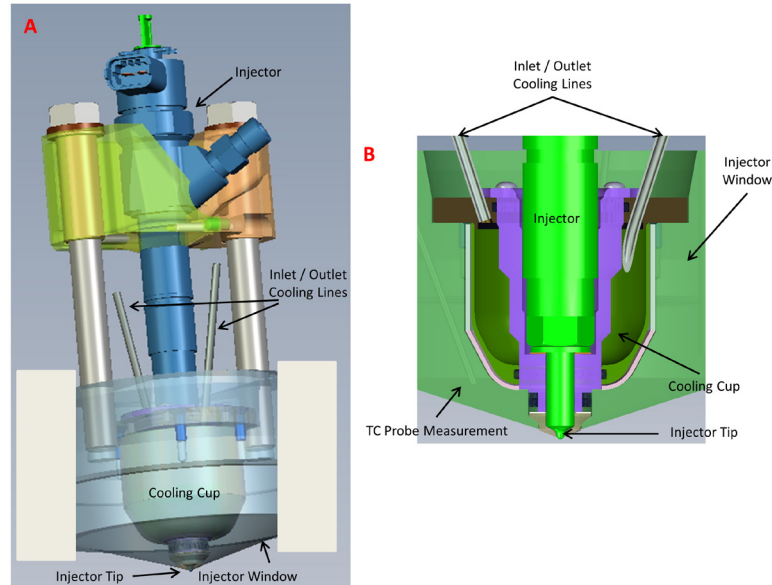


Figure 3.34: *A* - Cooled injector window model. *B* – Cross section view of injector window model near injector tip showing temperature measurement location. Window edge information is removed from the images. Reproduced with permission from Chris Green (appendix 12.1.5).

The cooled injector window also includes a hole for a thermocouple probe to enable temperature measurements of the inside of the window near the cooling cup to have an indication of achieved cooling during testing, shown in Figure 3.35. Thermocouples were also installed to measure fluid temperature on the inlet and outlet of the chiller to provide an indication of inlet fluid temperature and outlet fluid temperature and hence heat removal.

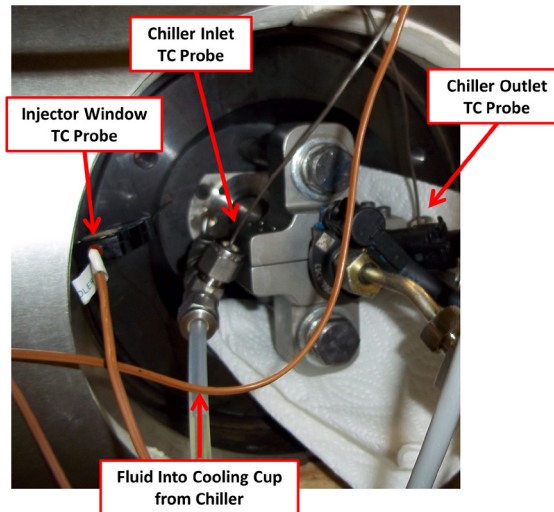


Figure 3.35: Thermocouple (TC) probe measurement locations.

The thermocouples used are Omega Type J and are monitored in the iTest control software.

The coolant used is a fifty-fifty mixture by volume of deionized water and ethylene glycol. The chiller is a Fisher Scientific IsoTemp3016D unit which has a 6L

bath, a pressure pump capable of 15 L/minute, a temperature range of -22 to 200°C, and an 800 W heater with 350 W cooling capacity at 20°C. The chiller has one-fourth inch inlet and outlet lines which pass the fluid into the injector window cooling cup and return the fluid to the chiller bath to remove heat and cool the injector. The coolant temperature is set on the chiller control unit with a minimum setpoint temperature of -22°C used to provide maximum cooling. To quantify the cooling effect on injector tip (fuel) temperature relative to the CV, temperature mapping was undertaken. This temperature mapping involves a chiller setpoint temperature sweep and monitoring of the chiller inlet and outlet temperatures at the injector coolant window inlet and outlet, injector window, and injector tip using the setup shown in Figure 3.36.

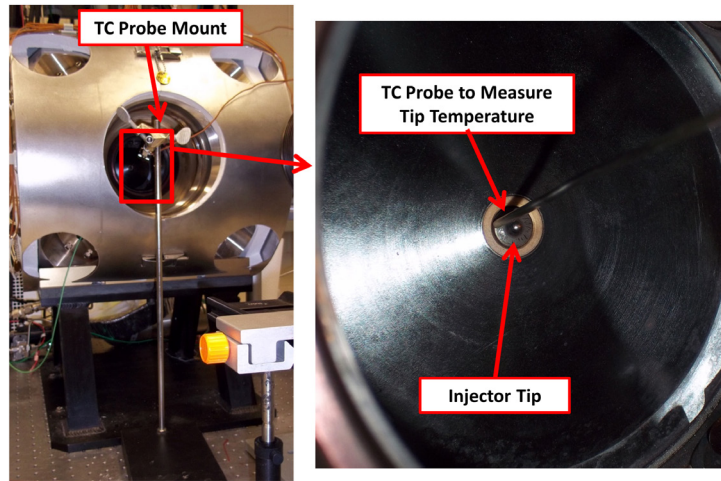


Figure 3.36: Injector tip temperature measurement setup.

To measure the injector tip temperature the CV window opposite the injector is removed and a Type J thermocouple probe is touched to the tip of the injector. This tip temperature cannot be measured during testing since a window must be removed and therefore a temperature map is prepared to predict the tip temperature under the given test conditions based on coolant setpoint and CV heated temperatures.

A temperature map is prepared by heating the combustion vessel to the desired temperature and sweeping chiller setpoint temperature in 10°C increments letting temperatures stabilize and then recording tip, window, and coolant inlet and outlet temperatures over the range from -22 to 30°C setpoint temperature. The upper limit on setpoint temperature is 35°C, since above this temperature the chiller can only operate in heating mode and therefore it will not provide the required injector cooling. This data is shown in Table 3.4 and is used to produce a temperature map with data extrapolated to a wider heated CV temperature than that measured.

Table 3.4
Temperature mapping data.

CV Temperature (°C)	Setpoint Temperature (°C)	Cooling Cup Inlet Temperature (°C)	Cooling Cup Outlet Temperature (°C)	Injector Window Temperature (°C)	Injector Tip Temperature (°C)
100	-22	-7	3	75	48
100	0	2	9	78	50
100	10	11	15	80	52
100	20	20	22	81	54
100	30	30	32	83	56
180	-22	-3	11	137	82
180	0	2	14	138	84
180	10	11	17	139	85
180	20	20	25	140	86
180	30	30	34	141	87

In order to extrapolate the data to produce a temperature map, the experimental data points are curve fit to the equation (53).

$$T_{Tip} = C * T_{CV} + D * T_{Setpoint} + E \quad (53)$$

C , D , and E are curve fit constants, and T_{CV} is combustion vessel heated temperature in °C, $T_{Setpoint}$ is the chiller setpoint in °C, and T_{Tip} is injector tip temperature in °C, determined by applying a linear algebra solution. This equation is assumed to represent the temperature behavior. The temperature is extrapolated by solving equation (54).

$$M^T * M * X = M^T * B \quad (54)$$

M is a 10 x 3 matrix composed of CV temperature data in column one and chiller setpoint temperature data in column two, from Table 3.4. The last column is a column of ones. X is a 3 x 1 matrix of unknowns, C , D , and E from the linear curve fit equation, and B is a 10 x 1 matrix with the column being the injector tip temperature data from Table 3.4. The superscript T denotes the transpose of the matrix. The right hand side of equation (54) is solved to yield a 3 x 1 matrix, B' . Combining the first two terms of the left hand side of equation (54) yields a 3 x 3 matrix, A , to give the final equation to solve, equation (55).

$$A * X = B' \quad (55)$$

Which is rearranged to provide equation (56) which is subsequently solved.

$$X = A^{-1} * B' \quad (56)$$

This solution yields the three constants for the curve fit equation, C , D , and E , determined to be 0.41, 0.13 and 9.6, respectively, which are then used in evaluating the equation at various CV temperatures and chiller setpoint temperatures.

The extrapolated temperature map is shown in Figure 3.37.

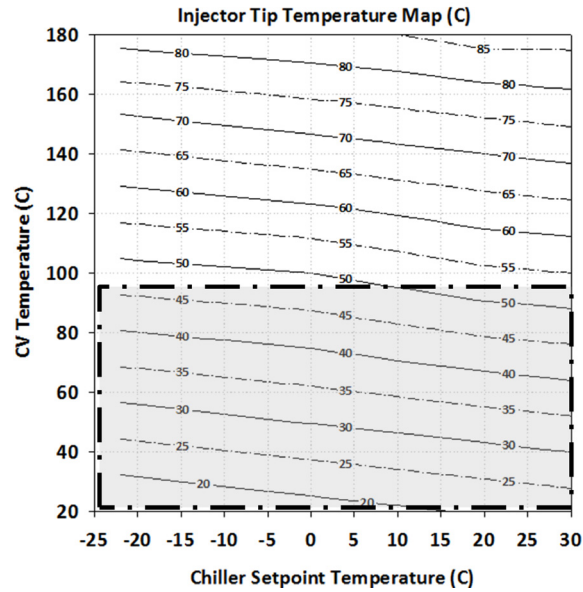


Figure 3.37: Injector tip temperature map with grayed region showing extrapolated temperature data.

As expected, as the chiller setpoint temperature decreases for a constant combustion vessel temperature, the injector tip temperature is reduced. When the chiller was used in testing the setpoint was set to the minimum value of -22°C to provide maximum cooling and therefore for testing at 100°C CV temperature the tip temperature was 48°C , and for spray testing at 180°C CV temperature, the tip temperature was 82°C . Without cooling, the temperatures are 55°C and 90°C respectively. Temperatures are not reduced significantly with the cooling, and therefore a new chiller should be integrated in the future with improved cooling capacity, along with the use of heat transfer grease on the cooling cup to facilitate fluid heat removal efficiency, to enable achievement of reduced fuel temperatures. Even without the chiller, fuel temperatures are significantly reduced relative to the CV heated temperature. The cartridge heaters are on faces 90 degrees from the injector tip window and therefore there are reductions in vessel temperature based on cartridge heater placement. The location of temperature measurement (injector tip inside the vessel) will provide a cooler temperature than the base of the window as this is where heating is occurring. Also, the measurement technique likely introduces error which will reduce the measured tip temperature as the probe is surrounded by air, and the vessel is open to the ambient, not completely enclosed, which would reduce the tip temperature due to heat transfer to the ambient environment.

3.5. Spark Ignition System

The combustion vessel utilizes two electrodes to ignite the premixture for the preburn procedure as were shown in Figure 3.1. The electrodes are connected via standard spark ignition engine wire leads to two automotive Mitsubishi coils, part number 19005218, with a secondary energy of 40 mJ, minimum secondary voltage of 35 kV, and minimum spark duration of 800 microseconds (Mitsubishi Datasheet).

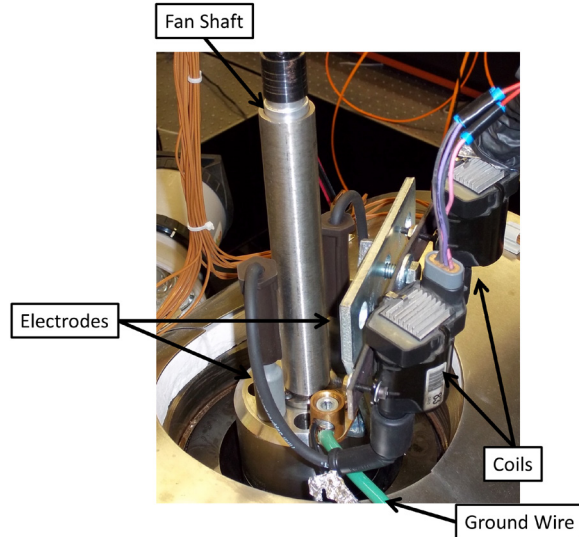


Figure 3.38: Spark ignition system setup for dual-electrode one fan window.

The spark plug wires are standard production spark ignition engine wires, Carquest WIR 35-8157. Coils are charged using a 12 V power supply which are controlled via the 5V TTL logic to the coils administered by a relay switched in the software control program, as outlined in Figure 3.39.

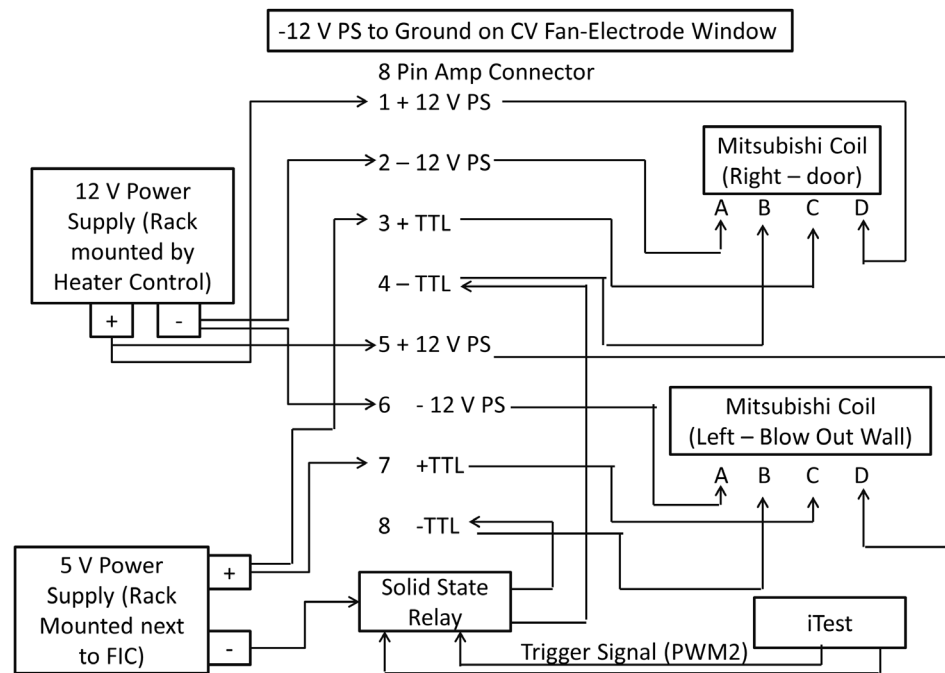


Figure 3.39: Spark ignition system wiring.

For preburn testing, the trigger signal from the control signal, PWM2 (PWM = pulse width modulated signal) is a five-pulse TTL logic signal with a 50% duty cycle and 10 ms trigger on duration. This signal charges the coil, which has a dwell time of approximately 6 ms, and then discharges to produce five sparks from each electrode, as was shown in Figure 3.11. This multi-spark event is used to facilitate mixture ignition, as mixtures typically do not ignite off of the first spark event. When the preburn mixture

ignites and combusts, it will produce the required in-chamber conditions for thermodynamic state generation. If the mixture is too lean (i.e. excess air, not enough fuel), the preburn mixture will not ignite.

In extensive testing there have been issues with conducted electrical noise as the result of the preburn spark ignition event in the chamber for pre-combustion. More specifically, during the five spark plug trigger events there are instances, particularly under high pressure conditions, where the firing of the spark plug will cause various unwanted phenomenon which can include the pulse generator triggering (even with an inhibit on the external trigger, which is a 5V signal sent from the control system to the pulse generator to prevent any output trigger signals from the pulse generator when this TTL signal is on, which is the case during the spark event), LaVision UltraSpeedStar16 (USS16) or other cameras triggering, or the Kistler pressure transducer charge amp reaching an overload condition signifying excess charge despite no pressure rise in nitrogen conditions. Troubleshooting was undertaken in an effort to remove this effect. This included, but is not limited to, cable shielding, running the spark system off a battery, changing trigger duration (dwell time), decreasing the spark gap, changing the spark plug wires, decreasing the plug wire length, and others. Despite these initial efforts, even when work-arounds were developed, there was no long term solution to the underlying problem. This led to the development of an Electromagnetic Interference (EMI) box in an effort to minimize induced noise. This setup was not used in the current testing, but discussion is included here for reference as this methodology along with other changes, has helped to contain the system in a package with minimal inputs and outputs, and reduce (but not alleviate) spark noise and false triggering issues. A picture of the modified setup is shown in Figure 3.40, and a schematic of the wiring setup is shown in Figure 3.41.

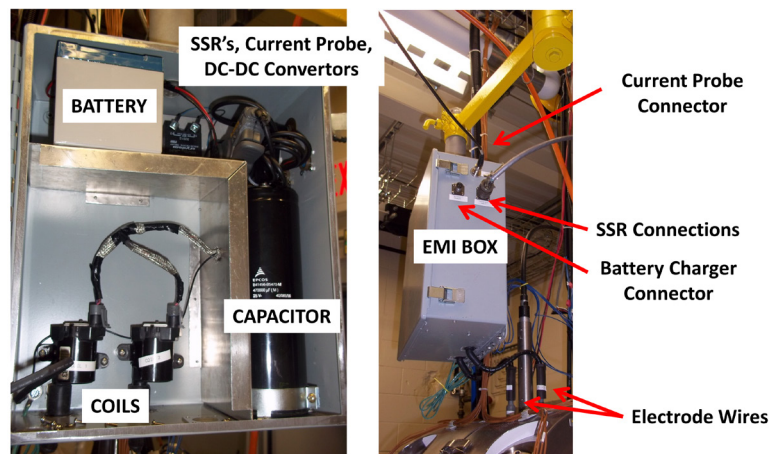


Figure 3.40: EMI box for preburn spark ignition system.

charger to the box to charge the battery overnight. The final outputs on the EMI box are two spark plug wires connected to the electrodes. This EMI box is also grounded.

During preliminary testing of the box, which involved sparking in nitrogen at 48.3 bar (700 psi), the aforementioned issues still existed. This led again to extensive troubleshooting using a differential amplifier into an oscilloscope running from the EMI box to the CV fan-electrode window ground. During a spark event, there is a jump in the ground signal level on the order of 2-3 V at approximately 10 MHz frequency. This shifting in the ground level is significant enough to false trigger devices based on the typical trigger threshold of 1.8 V. This led to additional modifications to the setup, including the removal of shields around the electrode spark plug wires as it is thought that the shielding could cause issues with electric fields, thereby reducing any of the benefits achieved with shielding. The potential exists that the noise and ground shifting could occur on the spark event before the energy could return to the ground which effectively defeats the purpose of shielding the plug wires and grounding this shield. Faraday coils were added on the charge amp charge input and the inhibit input to the pulse generator to dampen induced noise during the ground shifts. Grounding was improved with the ground from the CV top window to the table being disconnected as this was inducing ground loops (since the CV is grounded through the table and the table is still grounded to the building ground). This disconnection resulted in improved grounding between the CV EMI box to one point on the CV fan-electrode window achieved by using eight large gauge (small diameter) wires. The final modification was the grounding of the LaVision camera metal frame to the CV table which then runs to the building ground. It was observed that the LaVision camera was floating (i.e. there was infinite resistance between the camera and the table) and any variations in ground levels (as observed during the spark event) could be exaggerated and cause false triggering on the LaVision camera. These changes and modifications, along with observation improvements or issues are detailed in Table 3.6.

Table 3.6
Spark ignition system troubleshooting modifications and observations, using the new EMI box.

Modification	Observation
Removal of shields around the electrode spark plug wires.	Improved, shielding may cause electric field interference.
Faraday coil on charge amp input.	Improved, dampen induced noise during ground shifts.
Faraday coil on inhibit input to the pulse generator.	Improved, dampen induced noise during ground shifts.
Removal of CV ground strap from fan-electrode window to CV table.	Improved, this ground strap induced grounding loops.
Improved EMI box grounding using multiple large gauge (small diameter) wires.	Improved EMI box grounding.
Grounding LaVision USS16 camera metal frame to CV table.	Prevented the camera from having a floating potential.

This setup has helped to alleviate the majority of the false triggering problems which are encountered as a results of the spark ignition event.

3.6. Optical Diagnostics

Optical and laser based diagnostics enable characterization of fundamental spray and combustion parameters for tests conducted in the optically accessible combustion vessel. These diagnostics include high speed imaging of Mie back scattering and shadowgraph to image the liquid and vapor phase of the spray, respectively. Both methods can also be used to characterize combustive spray jets as well. The key diagnostic in the current work is Mie back scatter imaging with the optical setup shown in Figure 3.42.

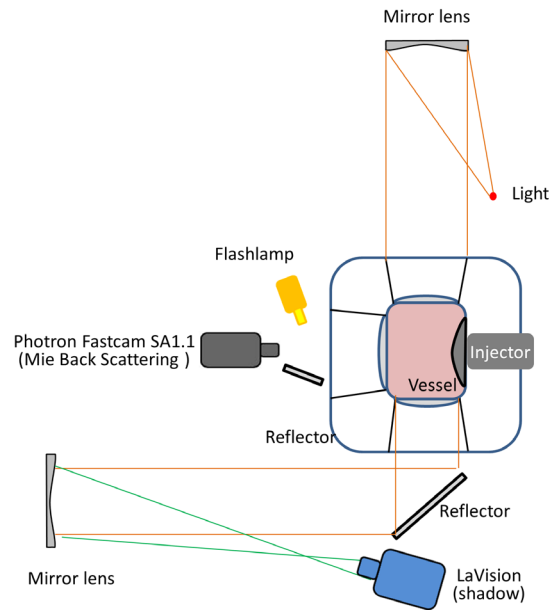


Figure 3.42: Mie back scattering and shadowgraph optical layout.

The Mie back scattering setup consists of acquiring images of the fuel spray using a flashlamp as an illumination source with images acquired with a high speed camera to capture spray movement with minimal blurring due to the high injection velocities attributed to large injection pressures. The flashlamp light scatters off the fuel droplets from the spray and this scattered signal is imaged with a high speed camera. The camera was a Photron Fastcam SA1.1 high speed streaming digital camera with a 60 mm Nikon Micro-Nikkor Lens, with f-numbers ranging from 2.8 to 32. The light source was the Cooke SensiFlash flashlamp with an 8 ms discharge duration providing illumination (maximum 1500 J) during the entire injection event with the fuel injection and image acquisition delayed to account for the flashlamp warm up time to ensure steady state luminosity during fuel injection. The light source is directed at an angle into the CV to provide uniform chamber illumination by reflecting light off the angled mirror into the CV, which enables visualization of all eight spray plumes, as shown in Figure 3.43.

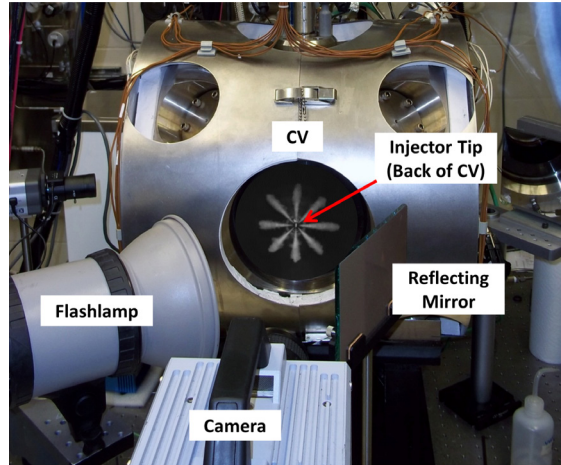


Figure 3.43: Mie back scatter imaging setup.

Different resolutions, framing rates, and exposure durations are used for the different ambient test environments as summarized in Table 3.7. These changes are made to minimize the region of interest and hence maximize the camera framing rate to yield the most information on spray characteristics.

Table 3.7
Image acquisition settings for different ambient environments.

Environment	Exposure Duration (μ s)	Frame Rate (fps)	Interframe Time (ms)	F-stop	Resolution
Nonvaporizing (N_2)	1.81	20,000	0.050	2.8	512 x 512
Vaporizing (0% O_2)	1.65	67,500	0.015	2.8	256 x 256
Combusting (21% O_2)	1.00	20,000	0.050	11	512 x 512

The shadowgraph imaging setup enables visualization of density gradients to provide information on the vapor phase of the spray by passing a collimated light sheet through the combustion vessel and collecting the shadow of the light using a high speed camera. Results from this diagnostic are not presented here based on complexity when using a multi-hole injector nozzle due to plume overlap and interference.

3.7. Image Processing Tools

Image processing is undertaken in the Mathworks MatlabTM software environment. All image processing programs, whose details will be discussed in Chapter 5.4, with the programs included in the appendix (chapter 12.4), being user-defined programs. These programs are tailored to the desired analysis including processing vaporizing liquid phase, combustng, and non-vaporizing spray parameters of cone angle and penetration, along with lift-off length and liquid length. Varying methodologies are used as a function of the different test conditions and setups. The Image Processing Toolbox coupled with the Matlab software is used extensively in the processing and analysis of images. Refer to Chapter 5.3 and Appendix section 12.4 for additional details on the image processing methodologies and documentation of the Matlab processing files.

3.8. Chemical Kinetics Modeling Tools

Chemical kinetics modeling is undertaken using two software tools. The main software is Cantera (Cantera; Goodwin 2003), which is interfaced with Mathworks MatlabTM. Cantera is a chemical kinetics modeling program which can be used to simulate chemical kinetics reactors, thermodynamic and transport processes and modeling for chemical equilibrium, simulating reactor networks, preparing reaction path diagrams, and others (Cantera).

In addition to the Cantera software for chemical kinetics modeling, Engineering Equation Solver (EES) is used to define initial conditions for the chemical kinetics modeling and also to provide basic property information for various ambient environment conditions, including specific heat, internal energy, and others. Not only is EES useful for evaluating properties of different ambient environments, it has the capability of numerically solving sets of non-linear algebraic equations, and can easily undertake iterative solutions increasing its applicability to the current work. The EES and m-file processing programs for the chemical kinetics modeling used for understanding the thermodynamic state generation procedure are provided in Appendix section 12.3.3. Not all programs are included due to the quantity of m-files used, including those for differing oxygen levels for example; however, a representative sample is included.

4. ¹Thermodynamic State Generation Analysis

This chapter details the preburn procedure used in the combustion vessel for thermodynamic state generation including the minor species generated and their impact on diesel spray autoignition behavior. A detailed study was undertaken on the Michigan Technological University and Sandia National Laboratory combustion vessel preburn procedure using chemical kinetics modeling. An additional comparison was performed on all preburn constant volume and constant pressure flow rig vessels currently contributing to the Sandia National Laboratory's Engine Combustion Network (ECN) initiative (Sandia ECN 2011). This initiative is an international collaboration effort for advancing the fundamental spray and combustion knowledgebase of internal combustion engines to promote fuel efficiency and reduce emissions. Partner institutions currently include Sandia National Laboratory, Argonne National Laboratory, Caterpillar, CMT Valencia, IFP France, Bosch, Georgia Tech University, Michigan Technological University, and Technical University of Eindhoven, with institutions continuing to join and support this effort. The chapter concludes with discussion on the preburn mixture used for 0% oxygen conditions (vaporizing spray studies) with justification for the mixture modifications.

4.1. CV Preburn Procedure for Thermodynamic State Generation

The combustion vessel preburn procedure to generate the thermodynamic state characteristic of conventional diesel engines, including temperature, pressure and gaseous composition requires spark ignition of a lean and/or dilute fuel-air mixture. This mixture can consist of oxygen, nitrogen, acetylene, and hydrogen of varying proportions to yield a range of oxygen levels post preburn. By using a range of premixtures, combustion vessels can produce well-controlled and well-characterized ambient environments over a range of temperatures, pressures, and charge-gas oxygen concentrations to enable fundamental studies on the influence of various parameters on spray, ignition and combustion (Idicheria and Pickett 2007). This supports fundamental and detailed research on sprays and the resulting combustion and emissions formation while using optical and laser diagnostics. Unanswered questions have been raised over the use of this preburn procedure in regards to the generation of minor species whose levels may differ relative to those in an engine, and their resulting influence on the subsequent spray and ignition processes, which this analysis covers. Furthermore, different initial preburn mixtures in regards to the composition of fuel and air in the mixture, yield different gas compositions post preburn including major and minor species along with peak temperatures. Chemical

¹ Section 4.2 of this chapter was previously published in *Energy and Fuels* (<http://pubs.acs.org/doi/abs/10.1021/ef101411f>). Permission for reproduction is provided in appendix 12.1.1.

kinetics modeling was undertaken to characterize the preburn procedure, the minor species produced, and the subsequent influence on autoignition of n-heptane used as a diesel surrogate to answer the fundamental questions on the impact the preburn has on the kinetics of autoignition. This analysis is motivated by the unanswered questions that this procedure has on diesel spray autoignition due to the minor species produced. Details on the modeling procedure are provided in Appendix section 12.3. It is undertaken first as a detailed analysis for the preburn used both at Sandia National Laboratory and Michigan Technological University, which is provided here as a copy of the resulting journal publication whose citation is below. The second analysis is applied to compare the different apparatuses as part of the ECN including both preburn constant volume vessels and constant pressure flow through rigs. Although this material has not been published, a collaborative paper is being developed resulting from the ECN workshop, including this work on ambient composition, in conjunction with results on nozzle and ambient temperature characterizations (Sandia ECN 2011).

Nesbitt JE, Johnson SE, Pickett LM, Siebers DL, Lee SY, Naber JD. Minor Species Production from Lean Premixed Combustion and Their Impact on the Autoignition of Diesel Surrogates. *Energy and Fuels*. 2011;25(3):926-936.

4.2. Energy and Fuels Journal Publication

Minor Species Production from Lean Premixed Combustion and their Impact on Autoignition of Diesel Surrogates

Jaclyn E. Nesbitt¹, Samuel E. Johnson¹, Lyle M. Pickett², Dennis L. Siebers², Seong-Young Lee¹, Jeffrey D. Naber^{1*§}

¹*Department of Mechanical Engineering, Michigan Technological University, Houghton, MI, United States*

²*Combustion Research Facility, Sandia National Laboratory, Livermore, California, United States*

[§]*Alternative Fuels Combustion Laboratory, Department of Mechanical Engineering, Michigan Technological University, 1011 R.L. Smith Building, 1400 Townsend Drive, Houghton, Michigan 49931, United States*

^{*}*Corresponding Author. Telephone (906) 487-1938. Fax: (906) 487-2822. E-mail: jnaber@mtu.edu.*

***Received:** October 15, 2010; **Revised:** December 31, 2010; **Published:** February 25, 2011

ABSTRACT

Formation of minor species including NO, NO₂, and OH during the premixed burn and cool-down in a constant-volume combustion vessel (CV) was modeled to investigate the effect of these species on the chemical kinetics portion of the ignition delay of *n*-heptane used as a diesel surrogate. Control parameters included ambient temperature, pressure, and diluent level (EGR) matched to typical diesel engine conditions. For the preburn model, the GRI 3.0 mechanism was used with experimentally determined heat loss from the CV. Subsequently, the cool-down premixed burn products served as reactant inputs and were mixed stoichiometrically with *n*-heptane, modeled using a reduced reaction mechanism modified to include NO and NO₂. Results computed with premixed burn constituents were compared to those using dry air and air plus ideal combustion residuals with the impact of dilution on ignition delay examined. A sensitivity analysis was performed to characterize the influence of OH and NO_x levels on ignition delay.

The preburn kinetics simulation showed OH concentrations above equilibrium; however, OH was below 100 ppb during the cool-down when fuel spray and ignition would occur. In contrast, the slow chemistry due to the low temperature (1750 K) prevents NO formation from reaching equilibrium levels; rather, levels are frozen in the 10-30 ppm range as the cool-down proceeded. This NO level is of the same order for cylinder charge concentrations in modern diesels when using 20 to 50% EGR rates producing 100-200 ppm in the exhaust. The ignition delay predictions showed that minor species of NO, NO₂ and OH shorten the ignition delay by 3% relative to dry air, while being 6% longer when compared with simulated dilution of 7.6% residuals (19% O₂), typical of internal residuals in an engine. These kinetics effects are small in comparison to changes in oxygen concentration (from 21 to 15%) associated with EGR, which show a 170% increase in ignition delay.

INTRODUCTION

Fundamental and detailed research on diesel sprays and the ensuing combustion and emissions formation using optical diagnostics requires fuel injection into a well-controlled environment at high temperature and high pressure. Although optical engines replicate conditions in their metal counterpart, including engine generated flows, they have limitations to optical access and the range of conditions that can be produced (Baert et al. 2009). Optically accessible combustion vessels, on the contrary, can provide significantly improved optical access and can vastly expand the operational ambient conditions. As the conditions in combustion vessels are well-controlled, they can also be well-characterized. These optically accessible vessels further enable the application of novel and non-intrusive optical and laser diagnostics to provide detailed information on the physical and chemical processes of high-pressure transient spray combustion, including pollutant formation (Dyer 1979; Oren et al. 1984; Naber and Siebers 1996; Bougie et al. 2005; Idicheria and Pickett 2007), which is essential for enhancing diesel combustion while simultaneously reducing emissions.

The experimental data generated from these vessels have shown to be valuable for developing a detailed understanding by parameterization of combustion characteristics, including spray mixing (Naber and Siebers 1996), vaporization and liquid penetration

(Siebers 1998, 1999; Bougie et al. 2005; Pickett et al. 2009), flame standoff length (Higgins and Siebers 2001; Ito et al. 2003), diesel soot emissions sources (Pickett and Siebers 2002; Ito et al. 2004), and so forth. Additionally these results provide excellent datasets for computational fluid dynamics (CFD) model development, calibration, and validation (Reitz and Rutland 1995; Vishwanathan et al. 2009). Combined numerical modeling and combustion vessel (CV) experimental studies have continuously provided significant insight and knowledge for the sustained advancement of diesel engines (Hurn and Hughes 1951; Labs et al. 2005).

To create the range of in-cylinder temperatures (750 to 1300 K) that are generated by compression, boosting, and exhaust gas recirculation (EGR) in a diesel engine before spray injection and combustion, the gases in the apparatus must be preheated by some means. Electrical heating is applied in many systems (Fujimoto and Sato 1979; Baert 1989; Labs et al. 2005; Nishida et al. 2007; Pawlowski et al. 2008). However, typically these systems have a limited temperature range, and it is difficult to match the composition of in-cylinder gases found in an engine. Alternatively, several investigators have utilized a fuel-lean, oxygen-enriched spark-ignited premixed burn to generate the elevated temperature. In this process, upon completion of this premixed burn, the product gases cool due to heat transfer to the chamber walls at a rate that is more than an order of magnitude longer in comparison to a diesel injection and combustion event. In these systems, a wide range of temperatures, including ambient to above 1500 K, can be generated with the density/pressure controlled by the initial fill pressure. Additionally, the premixed gases can be tailored to simulate dilution and EGR in the engine with varying oxygen concentrations (Oren et al. 1984; Naber and Siebers 1996; Siebers 1998; Verhoeven et al. 1998; Johnson et al. 2009).

The lean preburn mixture can consist of varying components, including gaseous hydrocarbons, hydrogen, carbon monoxide, argon, nitrogen, and oxygen (Hurn and Hughes 1951; Dyer 1979; Oren et al. 1984; Naber and Siebers 1996; Siebers 1998; Verhoeven et al. 1998; Azetsu and Ito 2007; Kim et al. 2007; Nguyen and Honnery 2008; Baert et al. 2009). Mixtures have been applied to control the oxygen concentration in the products (Naber and Siebers 1996), to match the specific heat capacity of air by using argon (Baert et al. 2009), and to match the water and carbon dioxide levels found in engines with EGR (Johnson et al. 2009). As a result, combustion vessels utilizing this procedure can examine a wide range of in-chamber temperature, pressure, and charge-gas oxygen concentrations simulating EGR, enabling researchers to address how these parameters independently impact the spray, ignition and combustion processes (Idicheria and Pickett 2007). However, there are unanswered questions about the use of this preburn procedure in regards to the generation of minor species and their influence on the resulting combustion process. This includes minor species, such as OH, along with oxides of nitrogen, which are set by the peak preburn temperature and cool-down, and hence, values may differ from those found in an engine.

Ignition delay is of central importance to engine performance and emissions (Higgins et al. 2000). Studies have shown that ignition delay is a function of several parameters, including temperature, pressure, fuel properties, fuel injector parameters, and charge-gas composition (Ladommatos et al. 1998; Kobori et al. 2000). In an engine, the charge-gas composition is controlled by the level of in-cylinder residuals from prior

cycles and EGR, which yields dilution by combustion products, decreasing the oxygen mole fraction and hence increasing the ignition delay. Engines can utilize variable valve timing for increasing in-cylinder residuals (US EPA 2001; Griffith 2007); however, even without this variation in valve timing, the cylinder consists of air with 4-10% combustion products (Cong et al. 2009). In addition to dilution from CO₂ and H₂O, combustion product minor species have an impact on the ignition delay. The addition of small amounts of NO and NO₂, as low as 1 ppm, to the composition was reported to reduce the ignition delay, the magnitude of which is dependent upon temperature and pressure conditions, while being most significant at temperatures less than 1200 K (Takita et al. 2007; Lee et al. 2009; Sjoberg and Dec 2009). Kinetic pathways that yield this ignition delay enhancement are believed to be through the HO₂ and RO₂ (R = alkyl group) radicals reacting with NO (Risberg et al. 2006).

In this work, a single-zone perfectly stirred reactor with heat-transfer and detailed chemistry is applied to model the premixed burn and cool-down within the CV. The ambient gas composition, including the minor species of NO, NO₂ and OH, is predicted as a function of the generated temperature and pressure. This modeling is undertaken to examine and isolate how minor species formed during this process impact autoignition of a hydrocarbon fuel injected into temperatures and pressures characteristic of diesel engines. For this, the composition predicted from this premixed burn – cool-down simulation is stoichiometrically mixed with *n*-heptane over a range of temperatures characteristic of diesel engine compression with the ignition delay predicted using a reduced kinetics mechanism. The impacts of fuel - gas mixing are not included here to isolate the kinetic impact of the minor species. Results are compared to dry air and air mixed with H₂O and CO₂ as ideal combustion residuals in the engine charge. Additional sensitivity analyses are carried out for the minor species, NO, NO₂, and OH, and for the impact of dilution with combustion products reducing the concentration of O₂. These aforementioned analyses fulfill the goals of this paper, which are to isolate and understand the chemical kinetics effect of the preburn products, including minor species, while neglecting spray dynamics, on the autoignition of *n*-heptane fuel.

CHEMICAL KINETICS MODELING

Experimental Mixture Preparation and Combustion. The preburn method for establishing the ambient conditions in the constant volume CV has been used extensively to produce a wide range of in-cylinder charge conditions characteristic of diesel engines (Johnson et al. 2009) while matching thermodynamic properties, including specific heat (Baert et al. 2009). The preburn mixture as utilized at Michigan Technological University and at Sandia National Laboratory is composed of C₂H₂, H₂, N₂, and O₂ such that, at the completion of the preburn, oxygen mole fractions from 21 to 0% can be obtained (see equation (57)). This enables the simulation of EGR with reduced oxygen concentrations, or experimentation in an inert (0% O₂), high-temperature environment for spray vaporization studies (Naber and Siebers 1996).

The CV diesel simulation experimental process is shown in Figure 4.1.

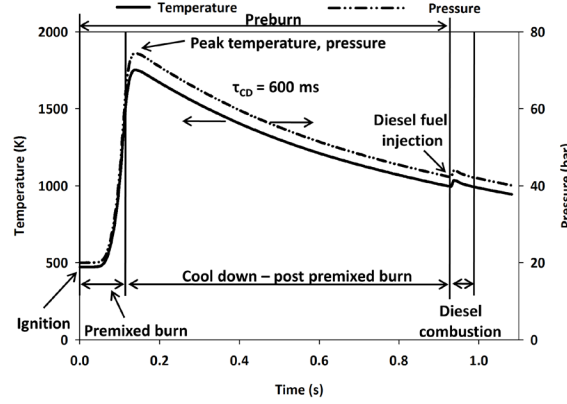
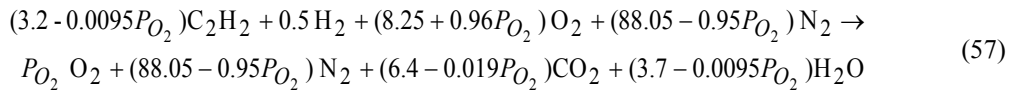


Figure 4.1. Pressure-time and temperature-time histories of in-chamber conditions during the premixed burn, heat transfer, diesel fuel injection, and combustion. Produced ambient conditions of 21% O_2 , density of 14.8 kg/m^3 , and temperature of 1000 K for fuel injection and combustion. τ_{CD} denotes time constant of the cool-down. Peak pressure and temperature are 74 bar and 1750 K, respectively.

The lean-dilute mixture is prepared in a separate 10L mixing vessel via a metered partial-pressure fill procedure that provides sufficient mixture for 10 - 100's of test runs, dependent upon conditions. Premixed gases are then metered into the CV prior to the start of the timeline shown in Figure 4.1, in this case, to a pressure of 20 bar, which corresponds to a density of 14.8 kg/m^3 , with the wall and gas temperature at 458 K. Once the target pressure is reached, valves are closed and the system becomes constant-volume. The lean-dilute preburn mixture is ignited at time zero via a spark, yielding a propagating flame, resulting in a high-temperature, high-pressure environment of ambient gases. Throughout the event, pressure is measured inside the combustion vessel to calculate the temperature-time history. A peak pressure of 74 bar and peak bulk-average temperature of 1750 K is reached 0.14 seconds at the completion of the premixed burn. After the premixed burn stage completes, the chamber pressure and temperature decrease due to heat transfer to the chamber surfaces. This is the cool-down period, which has a characteristic exponential temperature decay with a time constant of 0.6s in this test. When the target temperature of 1000 K is reached at time 0.92s, the diesel fuel injection is triggered. Autoignition of the injected fuel occurs if the chamber oxygen and temperature conditions are sufficient, resulting in a smaller pressure rise due to the spray combustion (Siebers 1998). The injected fuel may be gaseous or liquid.

Premixed Combustion and Cool-Down Simulation. To simulate the preburn process with detailed kinetics, an initial mixture whose composition is provided by equation (57), similar to past experimental mixtures (Naber and Siebers 1996) where P_{O_2} is the desired volume percent oxygen post-preburn, is reacted to produce the desired ambient in-chamber pressure, temperature, and composition.



The chemical kinetics used for simulating the combustion preburn were modeled using the Cantera software (Goodwin 2003), integrated into the Mathworks Matlab environment. A detailed reaction mechanism, GRI-Mech 3.0, which includes 53 species and 325 elementary reactions (Smith et al. 1999), was used. The simulation consists of

modeling the preburn and the subsequent cool-down phase using a single-zone, constant-volume reactor. The simulations included preburn product oxygen concentrations ranging from 21 to 1%, all at an ambient density of 14.8 kg/m^3 .

The simulation steps are described as follows and illustrated in Figure 4.2.

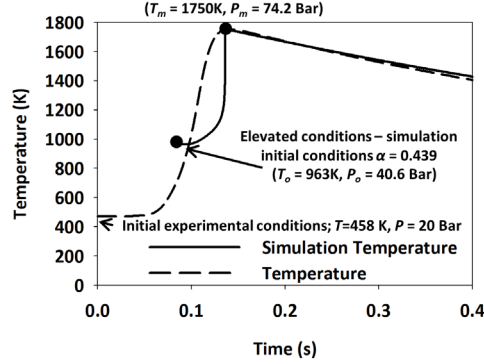
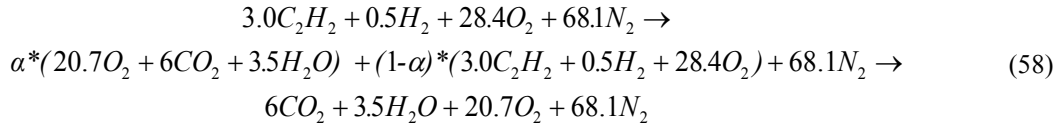


Figure 4.2. Experimental conditions, 458 K and 20 bar, compared with starting simulation conditions based on extent of reaction method for 21% O_2 and 14.8 kg/m^3 premixed burn product conditions.

To simulate the effect of premixed flame propagation while maintaining a simplified reactor, the initial conditions of the simulation are modified compared to the experimental initial conditions prior to spark ignition. The temperature and molar fractions of C_2H_2 , H_2 , N_2 , and O_2 are partially reacted to an extent of reaction (α) given by equation (58). This equation is valid for producing 21% oxygen post-preburn as required. The introduction of the extent of reaction provides an initial condition of elevated temperature and pressure to facilitate mixture ignition in the simulation via autoignition. Meanwhile, similar chemistry and temperature of the high-temperature portion of the premixed flame are mimicked.



The appropriate extent of reaction is determined by forcing the internal energy of the reactants and products to remain equal for a given initial elevated temperature, T_o . Hence, for a given extent of reaction, the concentrations of C_2H_2 , H_2 , N_2 , O_2 , CO_2 , and H_2O at an elevated temperature and pressure are the initial input conditions to the kinetics model, which correspond to the middle portion of equation (58). Figure 4.2 illustrates the technique, showing that the simulation temperature matches the experimental bulk temperature with an α of 0.439 and initial temperature (T_o) and pressure (P_o) of 963 K and 40.6 bar, respectively. This extent of reaction method, which relies on equal product and reactant internal energy by changing the “alpha” or extent of reaction, to match the experimental peak preburn temperature, is used to reduce computational time to ignite the preburn mixture and was found not impact the minor species.

The next step in the simulation process is to model the cool-down by implementation of a heat transfer loss after the completion of the premixed burn for times greater than 0.14 seconds in Figure 4.1. The heat flux is modeled from experimental temperature data for a given percent oxygen condition, with the temperature difference

between the in-chamber temperature and the CV wall ($T_w = 458$ K) computed and normalized by the maximum temperature difference. The data are fitted to determine this normalized temperature difference as a function of time. The input heat flux to the constant-volume reactor code is proportional to this normalized temperature difference function. Cool-down results are shown in Figure 4.3, where time 0s corresponds to the peak temperature of the premixed burn and start of the cool-down.

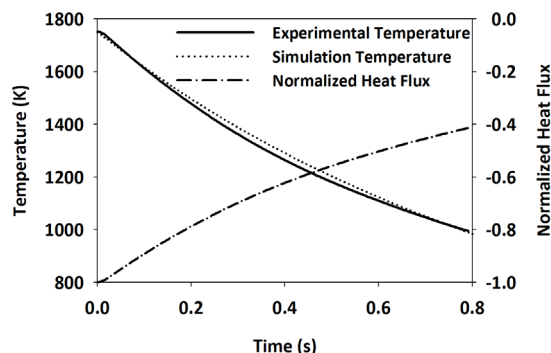


Figure 4.3. Temperature during the cool-down comparing experimental and simulation results with modeled heat flux. Conditions for cool-down are 21% O_2 post preburn and a density of 14.8 kg/m^3 . Time 0s corresponds to peak temperature in the premixed burn and start of cool-down.

The experimental and simulation data do not match exactly. The model neglects temperature inhomogeneities that exist within the CV, which cause differences between the bulk temperature, core temperature, and boundary layer temperature. However, the results provide a sufficiently accurate time history of pressure and temperature to determine species concentrations for the next simulation step, which is fuel injection autoignition. The cool-down simulation continues, applying the single-zone, perfectly stirred, reactor with heat transfer and GRI kinetics until the target pressure and temperature state for fuel injection is reached. At this point in time, the premixed burn/cool-down simulation is terminated and data for the pressure, temperature, and species mole fractions resulting from the analysis are transferred to the next stage of the simulation.

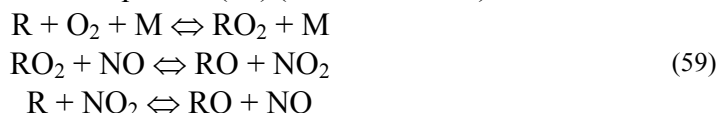
Diesel Ignition Modeling. Diesel ignition is modeled using a simple, single-component surrogate, *n*-heptane. Studies have shown that *n*-heptane has similar ignition characteristics as diesel fuel (Ranzi et al. 1995; Lu et al. 2007; Kolaitis et al. 2009). *n*-heptane has a cetane number of 56, which is at the high end for diesel fuel in the United States, but close to that in Europe. The *n*-heptane ignition modeling extracts the state of the gases in the cool-down at the target temperature, including temperature, pressure, and mole fractions of the 53 species determined from the GRI 3.0 mechanism. This is mixed with *n*-heptane in a stoichiometric mixture, holding the temperature and pressure constant. Although the temperature of the mixture is lower than that of the charge-gas, using the charge-gas temperature in this study enables comparison to fundamental data on ignition. This ideal case is used rather than modeling the complex temperature / equivalence ratio time-dependent process on a spray to isolate the kinetics of the preburn procedure. Other work studying this time-dependent mixing process includes the use of a two-stage lagrangian (TSL) model (Pickett et al. 2006). This composition is input into a

constant pressure reactor applying an *n*-heptane reduced reaction mechanism. This *n*-heptane reaction mechanism is a reduced mechanism consisting of 160 species and 770 reversible reactions (LLNL 2000), which has been modified to include NO and NO₂ species and their reactions yielding 179 total species and 823 reversible reactions, from the GRI 3.0 mechanism (Smith et al. 1999). This *n*-heptane mechanism, although reduced, has proven accurate when comparing ignition delay times in a constant volume reactor computed with the intermediate mechanism (1282 reversible reactions with 282 species) (Seiser et al. 2000).

Perfectly-stirred reactor simulations are conducted over a range of ambient temperatures and dilution conditions using the corresponding minor species mole fractions at that respective time during the cool-down. The kinetics are constrained by constant pressure and enthalpy conditions because diesel mixing is typically fast, during which time there is little change in pressure. The simulation does not include continuous evaporation and mixing processes that occur in a diesel spray as the focus of this study is to isolate the effect of minor species resulting from the preburn on diesel autoignition.

RESULTS AND DISCUSSION

Elevated levels of active radicals, including OH, O, and H, accelerate ignition processes. It is also known that NO and NO₂ promote chain-branching chemistry, and thus accelerate ignition processes of hydrocarbon combustion under low temperature (less than 1400 K) conditions (Tan et al. 1999; Takita et al. 2007). It has been demonstrated that the addition of NO and NO₂ assist in accelerating the oxidation processes of hydrocarbon fuels in low temperature chemistry (below 1200 K). The essential chemistry is shown below in equation (59) (Tan et al. 1999)



where R is an active radical and M is a third-body. This shows that the driving force to accelerate the ignition process is through the catalytic effect of NO and NO₂ chemistry to form RO radicals. These ignition-enhancing minor species, NO, NO₂, and OH, are formed during the preburn and hence are essential to characterize in this study. The following sections examine the effect these species have over a range of mixture temperatures (700 – 1450 K) and dilution levels (1-21% O₂) at a constant density (14.8 kg/m³) on the time to autoignition.

Minor Species During the Preburn. The first stage of the simulation is the adiabatic, constant-volume preburn, which is followed by the cool-down with integrated heat transfer using the modeled heat flux based on experimental temperature data, as previously described. Results for temperature and mole fraction of OH, NO, NO₂, O₂, and CO are shown versus time in Figure 4.4 for the case with 21% O₂ post preburn. In addition, the total mole fraction of minor species is shown where this total mole fraction excludes O₂, N₂, H₂O, C₂H₂, H₂, and CO₂.

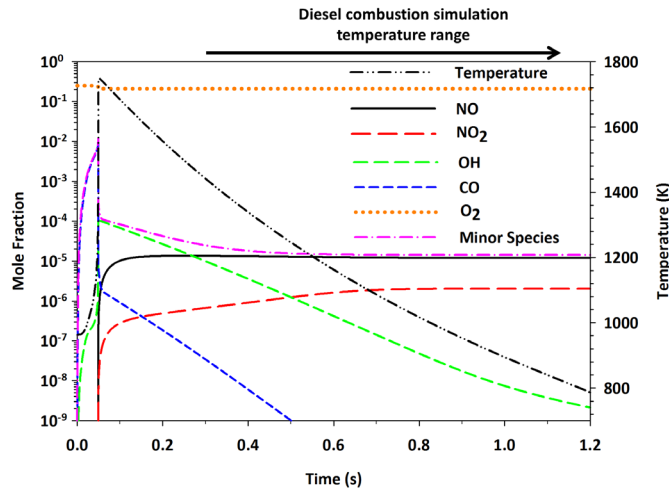


Figure 4.4. Mole fractions of O_2 , OH, NO, NO_2 , and CO along with temperature during cool-down. Total of the minor species is also included for comparison (53 GRI species excluding CO_2 , H_2O , N_2 , O_2 , C_2H_2 and H_2 .) Results are for the condition of 21% oxygen post-preburn and an initial elevated temperature of 963 K corresponding to a maximum temperature of 1748 K.

The results show that the minor species fraction increases, falling at the end of the premixed burn, which is attributed to active minor species and radicals during the combustion reaction while fuel is consumed. Once all of the fuel is consumed, the majority of the radicals and active minor species no longer exist, leading to a rapid decline in minor species fraction to match levels of the minor species of interest (NO, NO_2 and OH). The mole fractions of NO and NO_2 continue to increase after the completion of the preburn while temperatures are still high. NO_2 continues to increase as the cool-down proceeds to about 1100 K, while NO reaches steady state earlier at a temperature of 1600 K. The final ratio NO_2 (2.0 ppm) to NO (12.1 ppm) is 0.17, which falls in the range of that characteristic of diesel engines (0.11 to 0.43) (Kannan et al. 2009).

OH responds much differently to the temperature change compared to NO and NO_2 . It reaches a peak of 123 ppm, and then decays exponentially with temperature. Over the temperature range of interest, OH is 6.7 ppm at 1400 K and 0.008 ppm at 900 K. The mole fraction of CO is high initially during the premixed burn, but drops quickly and exponentially during the cool-down period. By 1400 K, the CO level is 0.0175 ppm and negligible in comparison to NO, NO_2 , and OH. The mole fraction of the total minor species is first dominated by OH, then by NO at temperatures less than 1300 K. The above confirms that NO, NO_2 and OH are the dominant minor species during the cool-down and, therefore, are the focus of the studies in the subsequent sections.

Effect of Initial Temperature on NO and NO_2 . Because NO_x is strongly temperature- and time- dependent at the temperatures under study, it is worth investigating the effect of the maximum temperature of the preburn on the formation of NO_x .

In addition to the experimental baseline with a peak temperature of 1748 K, two additional maximum temperatures of 1710 and 1795 K were examined with these peak temperatures being attained by adjusting the initial temperature. The temperature

histories for these three cases are shown in Figure 4.5 for the condition of 21% oxygen and density of 14.8 kg/m^3 . The temperature-time histories are shifted to align the peak temperatures. The corresponding time evolution of NO is also shown with peak NO levels, also shifted to match the time traces for temperature.

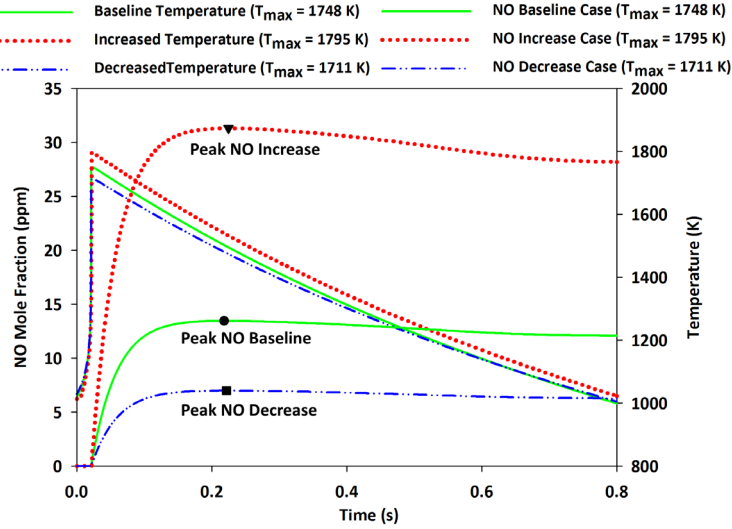


Figure 4.5. Temperature histories with three different initial temperatures, with the time shifted to match at peak temperature. Additionally, NO mole fraction time history for the three cases with peak NO values (symbols). Peak NO for the baseline, increase, and decrease cases is 13, 31, and 7 ppm, respectively.

The concentrations for NO are low, between 7 and 31 ppm, at their maxima; see Table 4.1.

Table 4.1

NO and NO₂ levels during cool-down in comparison to equilibrium mole fractions at peak temperature. ^aPeak NO₂ corresponds to the end of the simulation.

Simulation Case	Peak T (K)	NO Peak (ppm)	NO at 1000K (ppm)	NO Equil. (ppm)	NO ₂ Peak ^a (ppm)	NO ₂ at 1000K (ppm)	NO ₂ Equil. (ppm)	NO ₂ / NO at 1000K
Increased Temperature	1795	31.3	28.1	3720	4.6	4.5	82.6	0.160
Baseline Condition	1748	13.4	12.1	3200	2.0	2.0	76.8	0.165
Decreased Temperature	1711	7.0	6.3	2820	1.1	1.1	72.8	0.175

This range of NO is comparable to concentrations in the cylinder charge gases of a diesel engine operating with 10-23% EGR prior to combustion (engine out range of 150-350 ppm NO for HD 2002 on a road diesel engine (data from 2002 Cummins 10.8 L ISM HD Diesel Engine)). In comparison to their respective equilibrium values at these peak temperatures (2820 – 3720 ppm), the NO levels are more than 2 orders of magnitude lower. This is attributed to the low temperature, making the chemistry slow with respect to the limited residence time near the peak temperature. From Figure 4.5, it is seen that peak NO is not formed until after the maximum temperature because the thermal NO mechanism is controlled by the slowest reaction (Turns 2006).

Characteristic Time for NO Formation. To further quantify the impact of temperature and residence time on NO formation in the CV, the characteristic time for formation of NO under constant temperature and pressure conditions representative of the peak temperatures found in the CV was determined through a set of kinetic calculations. In these calculations the starting composition was O₂, CO₂, H₂O, and N₂, as defined in Table 4.2, with O₂ levels of 1, 10, and 21%, representing the composition post-preburn, neglecting minor species.

Table 4.2

Mole fractions of carbon dioxide, water, and nitrogen for the given percent oxygen cases used to investigate the characteristic time scales for NO formation.

O ₂ %	N ₂ %	CO ₂ %	H ₂ O %
21	69.3	6.11	3.56
10	80.0	6.32	3.67
1	88.7	6.50	3.76

The calculations were performed in a constant-temperature, perfectly stirred reactor over a temperature range of 1600 - 2200 K at a density of 14.8 kg/m³, with the composition starting with zero ppm NO. The temperature range investigated includes those for the premixed burn and cool-down phase, which are of concern for NO formation. The residence time in the calculation was then defined as the time when the mole fraction of NO reaches 63.2% of its equilibrium value. The results for the characteristic time constant are shown in Figure 4.6 in Arrhenius coordinates, compared to a diesel engine condition correlation from Heywood (1988).

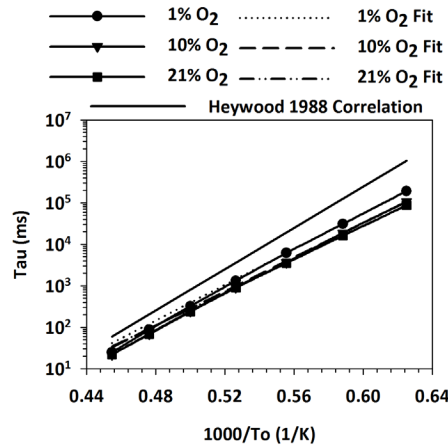


Figure 4.6. Characteristic time for NO formation in the CV for the cases of 1, 10 and 21% oxygen at a constant density of 14.8 k/m³ compared to that for diesel engine conditions (Heywood Correlation (1988)), including Arrhenius-type curve fits for the different percent oxygen cases:

$$\tau = A \exp\left(\frac{E_a}{R} * \frac{1}{T}\right)$$

The general trend is an exponentially increasing time constant with an increase in $1/T$ (decrease in temperature). The time constant increases by 2 orders of magnitude from 0.24 s at 2000 K to 16 s at 1700 K (for the case of 21% O₂). At the peak temperature of the baseline preburn ($T = 1748$ K, $1000/T = 0.572$), the time constant for NO formation

is 7.2 s, which is more than an order of magnitude longer than the cool-down time constant of 0.6 s in the combustion vessel. This further illustrates the kinetic controlled and residence time dependence of NO in the premixed burn and cool-down in the combustion vessel and confirms the low concentrations as compared to equilibrium values. Regarding the impact of O₂ percentage, the time constant for NO formation decreases with increasing O₂ level.

Diesel Ignition Delay

Modeling Validation. First, the effect of initial temperature on the ignition delay for *n*-heptane (as a surrogate for diesel) with air is examined. The ignition delay is defined as the time between the instantaneous *n*-heptane mixing with ambient gas and the maximum temperature derivative. For stoichiometric combustion of *n*-heptane at a fixed initial pressure of 13.5 bar, the ignition delay is determined over a range of initial temperatures from 650 to 1400 K. These conditions are chosen to validate the current modified *n*-heptane mechanism in comparison with the work of Ciezki and Adomeit (1993), as shown in Figure 4.7.

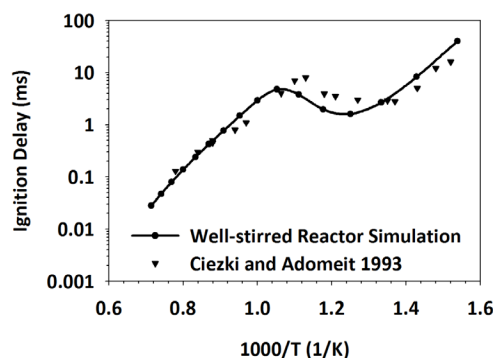


Figure 4.7. Ignition delay for *n*-heptane combustion code validation, with simulation results compared to Ciezki and Adomeit (1993) results, for stoichiometric combustion at an initial pressure of 13.5 bar, over a range of initial temperatures from 650 to 1400 K.

The model results agree well with data from Ciezki and Adomeit (1993). The ignition delay increases with decreasing temperature until 950 K, then undergoes a negative temperature dependence between the 950 and 800 K temperature region, before increasing again with decreasing temperature (Gauthier et al. 2004). The region between the maximum and minimum peaks in the ignition delay is characterized by a negative temperature coefficient (NTC) attributed to a change from a low- to high-temperature kinetic mechanism (Ciezki and Adomeit 1993). The NTC region is attributed to the cool flame endothermic CH₂O reaction.

To baseline the impact of the CV preburn, the ignition delay was examined for stoichiometric *n*-heptane mixtures with (i) dry air (21% O₂ and 79% N₂), (ii) air with 7.6% simulated ideal combustion residuals (residuals include CO₂ and H₂O, 19% O₂) to represent internal residual levels characteristic of diesel engines (Cong et al. 2009), and (iii) the CV post-preburn composition from the cool-down analysis with 21% O₂. These mixtures were examined over a range of initial temperatures from 700 to 1450 K at a constant density of 14.8 kg/m³, as shown in Figure 4.8.

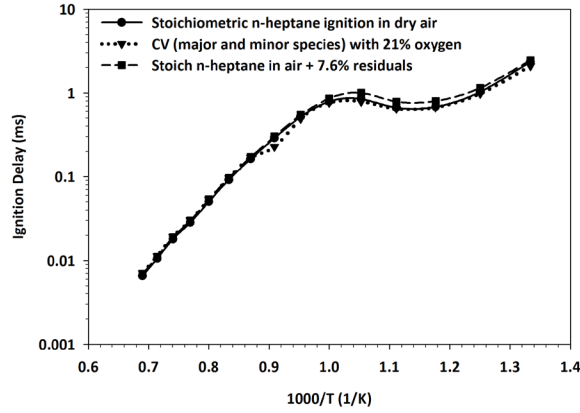


Figure 4.8. Ignition delays for stoichiometric *n*-heptane with dry air (circle symbol, solid line), CV gas composition of 21% O₂ (triangle symbol, dotted line), and air with 7.6% ideal residuals (square symbol, dashed line).

The trends in all three mixtures with temperature are similar and show a NTC region. In the temperature range of 800 -1000 K, the ignition delay for cases (i) and (iii) of dry air and the CV have similar ignition delays, being shorter than that of case (ii) with 7.6% simulated ideal internal combustion residuals. For the high temperature regime, in excess of 1000 K, ignition delays of all cases are similar. There is one outlier at 1100 K for case (iii), which is likely attributed to an issue with the kinetics mechanism during transition into the NTC zone.

Effect of Minor Species. Here, the ignition delays for stoichiometric mixtures of *n*-heptane and ambient gases produced in the products of the CV preburn for three different maximum temperatures / NO_x concentration combinations, as simulated in the manner discussed above, are compared to dry air with 21% O₂ (Table 4.3) and air with 7.6% residuals of CO₂ and H₂O, with 19% O₂ (Table 4.4). In all cases the stoichiometric *n*-heptane mixture initial conditions for the ignition delay calculations are at a temperature of 1000 K and density of 14.8 kg/m³ (pressure of 42 bar), which is chosen to be a representative condition at the time of diesel injection in an engine (Naber and Siebers 1996). These three temperature conditions, as were defined in Table 4.1, are characterized to acknowledge temperature gradients which exist as a result of the first and last mixtures to burn and to understand this influence on NO_x formation and ignition delay. Table 4.3 shows that the ignition delays for the CV mixtures decrease with increasing NO_x. In comparison to dry air, the maximum percent difference in ignition delay between dry air and CV conditions is 6%.

Similarly, Table 4.4 shows the results for 19% oxygen with the baseline being air plus 7.6% residuals. The peak preburn temperatures and NO levels are slightly higher than those for the 21% oxygen case for the CV mixtures as a result of the preburn gas properties which includes more acetylene fuel. For this reduced oxygen case, the *n*-heptane ignition delays are longer (by 8% for air plus residual baseline in comparison to dry air) for these mixtures in comparison to those in Table 4.3, which is attributed to the lower oxygen concentration. Further, opposite to the 21% findings, the ignition delays for the CV mixtures are longer by up to 7% in comparison to the air plus residuals baseline. This indicates that the sensitivity of ignition delay to ideal residuals (CO₂ and H₂O) and oxygen concentration are higher in relationship to the NO levels predicted for the CV

mixtures. The dominant major species of CO₂ and H₂O produce a trend in a different direction, relative to that of the minor species. These results show the importance of considering typical major species levels, even these caused by minimal internal residual levels. Finally, in both cases the effect of NO and NO₂ decreasing the ignition delay time is in agreement with past observations (Tan et al. 1999; Takita et al. 2007).

Table 4.3

Ignition delay of stoichiometric mixtures of *n*-heptane with ambient gases for 21% O₂ at 1000 K and 42 bar, along with percent deviation of ignition delay relative to dry air baseline. *Baseline CV Case.

Gas mixtures (21% O ₂)	NO (ppm)	NO ₂ (ppm)	H ₂ O (%)	CO ₂ (%)	Ignition Delay (ms)	Percent Change (%)
Dry Air	0.0	0.0	0.0	0.0	0.796	-
CV (Peak T = 1711 K)	6.3	1.1	3.56	6.11	0.772	-3
CV* (Peak T = 1748 K)	12.1	2.0	3.56	6.11	0.771	-3
CV (Peak T = 1795 K)	28.1	4.5	3.56	6.11	0.745	-6

Table 4.4

Ignition delay of stoichiometric mixtures of *n*-heptane with CV ambient gases for 19% O₂ at 1000 K and 42 bar, along with percent deviation of ignition delay relative to air with 7.6% ideal residuals (CO₂ and H₂O, 19% O₂) as the baseline. *Baseline CV Case.

Gas mixtures (19% O ₂)	NO (ppm)	NO ₂ (ppm)	H ₂ O (%)	CO ₂ (%)	Ignition Delay (ms)	Percent Change (%)
Air + 7.6% Residuals	0.0	0.0	1.08	0.93	0.865	-
CV (Peak T = 1724 K)	7.4	1.2	3.58	6.15	0.926	7
CV* (Peak T = 1761 K)	14.3	2.2	3.58	6.15	0.920	6
CV (Peak T = 1807 K)	33.0	5.0	3.58	6.15	0.886	2

Effects of Temperature, NO_x, and OH. Diesel fuel is typically injected into in-cylinder conditions with a temperature range of 850 - 1200 K as impacted on the engine by the initial mixture temperature, compression ratio, and injection timing. Conversely, the temperature in the CV can be varied independently from other parameters by changing the time of injection during the cool-down (see Figure 4.1). Over this range of temperatures the levels of NO and NO₂ in the CV have reached steady-state. However, OH is decreasing exponentially with temperature, as seen in Figure 4.4; thus its impact on ignition needs to be determined. The effect of these minor species over this temperature range (850 - 1200 K) on *n*-heptane ignition delay was investigated for the CV, including a 10X increase and decrease, together with dry air, all compared to the CV baseline case, Table 4.5; 10X or 1/10X represents multiplying or dividing the mole fraction of the species by a factor of 10 to achieve a new mole fraction for the simulation for this sensitivity evaluation.

Table 4.5

Stoichiometric *n*-heptane ignition delay relative to minor species concentrations over the temperature range of 850 - 1200 K with 21% O₂ in comparison to dry-air.

^aCV mixtures have a baseline steady-state level of 12 ppm NO and 2 ppm NO₂.

^bMinor species of OH, NO, and NO₂ are adjusted by 1/10 and 10X, respectively, for sensitivity analysis. ^cChanges in ignition delay are relative to the CV baseline mixture (CV-BL).

Temp.	CV Baseline Mixture ^a		Dry Air		Minor Species ^b 1/10x		Minor Species ^b (10x)	
(K)	OH (ppb)	Ignition Delay (ms)	Ignition Delay (ms)	Change CV-BL ^c (%)	Ignition Delay (ms)	Change CV-BL ^c (%)	Ignition Delay (ms)	Change CV-BL ^c (%)
850	4.1	0.67	0.68	1	0.72	7	0.59	-12
900	7.8	0.67	0.67	0	0.69	3	0.59	-12
950	16.4	0.78	0.85	9	0.81	4	0.67	-14
1000	36.7	0.77	0.80	4	0.79	3	0.67	-13
1050	79.2	0.52	0.52	0	0.53	2	0.48	-8
1100	168.0	0.23	0.22	-4	0.23	0	0.22	-4
1150	345.0	0.17	0.16	-6	0.17	0	0.16	-6
1200	676.0	0.096	0.092	-4	0.096	0	0.094	-2

Over this temperature range, the ignition delay is reduced by 2-14% with 10X increases in minor species mole fractions. The ignition delay decreases significantly, by almost 700%, for a temperature increase from 850 to 1200 K for all mixtures. When considering minor species, 10X or 1/10X changes at lower temperatures (850 - 1000 K), minor species influence the ignition delay by a maximum of 12%.

For a better understanding of the individual minor species' impact on ignition delay, individual minor species mole fractions were varied at an ambient temperature of 1000 K with the results summarized in Table 4.6, defining percent change in comparison with the baseline case (1000 K CV preburn) ignition delay being 0.77 ms. Table 4.6 considers the results of the *n*-heptane ignition delay in the baseline CV 21% oxygen post preburn case at a density of 14.8 kg/m³ and fixed temperature condition. These results are compared to the *n*-heptane ignition delay calculated when increasing and decreasing each species, NO, NO₂ and OH, by a factor of 10 at the fixed temperature condition in the baseline 21% oxygen post preburn case (which considers species of CO₂, H₂O, O₂, N₂ and baseline levels of NO, NO₂ and OH).

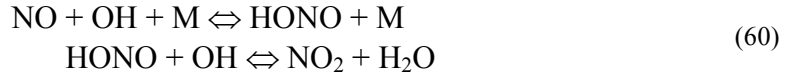
Table 4.6

Impact of minor species concentrations on *n*-heptane ignition delay in comparison to baseline equal to 0.77 ms. Temperature is 1000 K for a 21% oxygen combustion vessel post-preburn environment.

Minor Species	Increase by 10X		Decrease by 10X	
	ID (ms)	Change Relative to Baseline (%)	ID (ms)	Change Relative to Baseline (%)
NO	0.69	-10	0.79	3
NO ₂	0.78	1	0.78	1
OH	0.76	-1	0.78	1

When NO increases by 10X, there is a significant (10%) decrease in ignition delay, which is attributed to the high, 120 ppm level, of NO.

One essential NO_x chemical mechanism for ignition enhancement is $\text{RO}_2 + \text{NO} \Leftrightarrow \text{RO} + \text{NO}_2$, which yields a chemical pathway such that NO can react with the active radical RO₂ to produce the highly reactive radical, RO. In this temperature range, NO is the predominant minor species controlling the ignition delay, as shown in Table 4.6, and this trend has been demonstrated in methane and ethylene air combustion studies elsewhere (Takita et al. 2007). Overall, the increase in NO_x and OH minor species mole fraction enhances *n*-heptane ignition. Among the three minor species considered, the NO effect is most pronounced, followed by OH. This prompted further investigation using the current simulation into the sensitivity of minor species NO on the ignition delay of *n*-heptane combustion in dry air. Results showed that further increasing the levels of NO present reduces the ignition delay of *n*-heptane, with the effect on ignition delay reduction decreasing slightly as more NO is added. This is expected because, as the NO concentration increases, termination reactions become more prevalent which consume the reactive OH and hence reverse the effectiveness in enhancing the ignition delay, consisting of the following reactions in equation (60) (Risberg et al. 2006).



EGR Effect. EGR dilution is actively used to reduce NO_x formation in modern engines. The percentage EGR represented by a given percent oxygen in the intake stream is determined by the overall excess air ratio (λ) of the engine, and the hydrogen/carbon ratio of the fuel (for diesel, typically 1.85). Attempting to simulate the effect of EGR is one of the primary motivations for studies in preburn-type CVs. EGR variation results assuming a λ of 1.372 are summarized in Table 4.7.

Table 4.7
Volume percent EGR (representing the total of EGR and internal residual gases) at time of diesel combustion at an excess air ratio, $\lambda = 1.372$, over a range of percent O₂ cases

% EGR	% O ₂	% CO ₂	% H ₂ O
0.0	21	0.0	0.0
19.0	18	1.9	1.7
38.3	15	3.8	3.5
57.6	12	5.7	5.3
76.9	9	7.7	7.1

Changing EGR rate in the simulation represents a change in CO₂ and H₂O, with no change in CO or minor species. This choice of λ is characteristic of the typical operating range of diesel engines (Stone 2002; Austin 2010). Both the percent oxygen and percent EGR are volume based, with EGR percentage calculated as moles of EGR over total number of intake charge moles, which is a sum of air and EGR. In a typical engine, the operating range of EGR can approach up to 30%, with higher levels upwards of 60% being considered for advanced combustion strategies, including low-temperature combustion to facilitate emission reduction (Peng et al. 2003; Alriksson and Denbratt 2006; Eckerle et al. 2008).

To understand the EGR effect in the case of the CV preburn procedure, the results from the chemical kinetics simulation for the premixed burn at 1000 K are used as inputs into the *n*-heptane autoignition mechanism (both major and minor species), for variable oxygen concentrations, with results on *n*-heptane ignition delay shown in Figure 4.9. This study only considers the effect of chemical composition of charge gases on spray ignition; it does not include changes in temperature due to EGR addition attributed to different mixture specific heats.

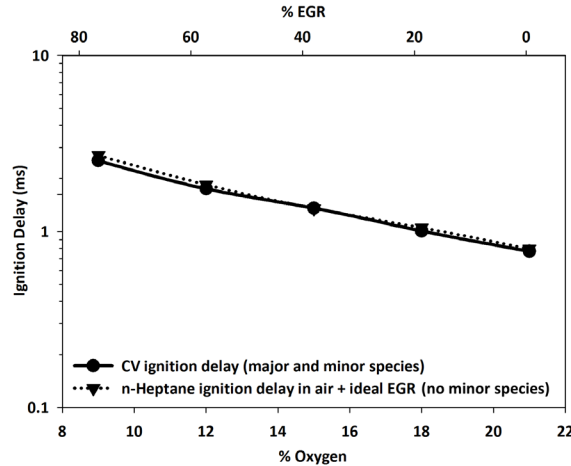


Figure 4.9. Ignition delay as a function of percent oxygen in the premixed burn products and respective percent EGR at 1000 K for the combustion vessel, compared to that of *n*-heptane in air and EGR (CO₂ and H₂O), no minor species.

The ignition delay decreases as oxygen concentration is increased, in agreement with the conclusions from Idicheria and Pickett (2007). The ignition delay decreases exponentially as a function of increasing ambient percent oxygen concentration. A reduction in oxygen concentration from 21 to 15%, which corresponds to an increase in EGR from 0 to 38%, yields a 170% increase in ignition delay. The CV results are compared to stoichiometric *n*-heptane combustion in air and ideal EGR, by changing CO₂ and H₂O levels, no minor species. These cases have a longer ignition delay for all percent oxygen cases when compared with the CV because of the NO in the combustion vessel case, which enhances ignition. Differences between the ignition delay in the CV case and that of *n*-heptane in air plus EGR are minimal, between 7-10% over the range of oxygen concentrations examined.

Understanding how minor species change with percent oxygen is needed to better comprehend the factors governing the ignition delay trends, for example, whether it is caused by changes in percent oxygen or the prevalence of minor species. As shown in Table 4.8, minor species mole fractions of NO_x and OH are compared as a function of percent oxygen, along with the computed ignition delays.

Table 4.8

Ignition delay for stoichiometric mixtures of *n*-heptane in the combustion vessel for the 9- 21% oxygen cases investigated in Figure 4.9, along with CO₂, H₂O, NO_x and OH mole fractions, to characterize the influence of minor species mole fractions for different percent oxygen cases on ignition delay. The combustion vessel case is compared to that of *n*-heptane plus air and ideal EGR, with no minor species present (NO_x and OH are zero). The ambient gas temperature is 1000 K.

% O ₂	% EGR	Combustion Vessel					n-Heptane Plus Air and Ideal EGR		
		Ignition Delay (ms)	H ₂ O (%)	CO ₂ (%)	NO _x (ppm)	OH (ppb)	Ignition Delay (ms)	H ₂ O (%)	CO ₂ (%)
9	76.9	2.5	3.68	6.33	32.2	27.3	2.7	7.1	7.7
12	57.6	1.8	3.66	6.29	27.9	29.8	1.8	5.3	5.7
15	38.3	1.4	3.62	6.23	22.6	32.4	1.4	3.5	3.8
18	19.0	1.0	3.59	6.17	18.0	34.6	1.1	1.7	1.9
21	0.0	0.8	3.56	6.11	14.1	36.6	0.8	0.0	0.0

The key observation is that the change in minor species mole fractions has minimal effect on the ignition delay; rather, the dominating trend is an increase in oxygen concentration that yields a reduction in the ignition delay. Although minor species vary slightly as oxygen concentration decreases in the simulations of the CV, the variation is minimal, on the order of 20 ppm NO_x and 12 ppb OH, for a 15% change in oxygen percentage.

CONCLUSIONS

Constant-volume vessels are versatile in that they can be used to investigate spray dynamics and combustion characteristics at temperatures, pressures, and exhaust-gas recirculation (EGR) levels representative of diesel engines. One of the methods to reach these conditions uses a preburn procedure which can lead to the generation of reactive minor species. This work investigated the formation of these minor species, including NO, NO₂, and OH, during the premixed burn and cool-down using a chemical kinetics model. The impact of these minor species on the subsequent fuel autoignition, in particular *n*-heptane, including its ignition delay was quantified.

Conclusion points from these studies are the following:

- 1) The most significant minor species formed during the cool-down is NO, which is kinetically controlled and strongly residence time dependent. NO is frozen below equilibrium values because of the low peak preburn temperatures. For a 21% oxygen case post-preburn, with a peak temperature of 1750 K, NO peaks at 13 ppm, freezing around 12 ppm, significantly less than its equilibrium value of 3200 ppm.
- 2) During the cool-down, OH tends to track equilibrium values closely.
- 3) The minor species of NO_x and OH formed during the preburn tend to shorten the autoignition delay of *n*-heptane mixtures by 3% relative to dry air, and increase it by 6% relative to air plus residuals at 1000 K ambient temperature. However, relative to the accuracy of the modeling and simulations, and experimental measures, this impact is comparatively insignificant.

- 4) Of the minor species considered (NO, NO₂, and OH), NO has the largest effect on ignition delay, with increases in NO tending to reduce the ignition delay, by 10% for a large 10X increase in NO, to 120 ppm NO, for a 1000 K 21% oxygen post preburn environment.
- 5) Ignition delay increases as EGR increases, which corresponds to a reduction in oxygen concentration. More specifically, a reduction in preburn oxygen concentration from 21 to 15% (increase in ideal EGR from 0 to 38%) yields a 170% increase in ignition delay.
- 6) Both major (CO₂, H₂O, and O₂) and minor species (NO, NO₂, and OH) influence the ignition delay. The changes in ignition delay resulting from minor species are small relative to those from major species of CO₂, H₂O, and O₂, which increase to 3.8% (CO₂) and 3.5% (H₂O), for an oxygen reduction from 21 to 15%, yielding an increase in ignition delay by 170%.
- 7) The CV is a useful tool for simulating heavy EGR use in an engine. The CV ignition delay is reduced by a maximum of 7% for a given percent oxygen case relative to that of EGR, when assuming ideal EGR with no minor species. Including minor species such as NO, in the EGR would reduce the ignition delay further, yielding closer agreement between CV and EGR cases.
- 8) The range of NO produced in the CV is not outside that representative of current technology compression ignition engines.
- 9) The CV allows users to change major species, along with minor species, by altering preburn compositions, thus enabling matching of species caused by residuals and EGR in an engine.
- 10) Change in minor species mole fractions of NO, NO₂, and OH have minimal impact on ignition delay relative to the change in oxygen concentration.

There were various simplifications used throughout these simulations; and hence, recommendations are presented to increase the complexity and application of these studies. This includes utilizing a spray and mixing model, for example the TSL model, in conjunction with a multi-zone ignition model to better incorporate the effects of equivalence ratio in the study, while improving cool-down heat transfer modeling by using a temperature convective heat transfer coefficient to predict, as opposed to experimentally fit, heat transfer. Tests should also be undertaken in the combustion vessel to validate experimental levels of minor species as predicted from the model and to also further understand the experimental influence of the minor species on *n*-heptane ignition delay, relative to results, as determined from the simulations. These results show the combustion vessel can be effectively used to study the combustion of diesel fuel over a varying set of ambient conditions without concern over reactive minor species produced by the preburn.

ACKNOWLEDGMENT

This material is based on work supported by the National Science Foundation under Grant No. 0619585. The work was supported by funding provided from Chrysler through their graduate fellowship program. Additional support was provided from the Advanced Power Systems Research Center and Sustainable Futures Institute of Michigan Technological University, as well as the NSF IGERT program under Grant No. 0333401.

Acknowledgement is also given to Sandia National Laboratory for their collaboration and support in development of the Michigan Technological University combustion vessel.

4.3. 'Spray A' Ambient Composition Analysis

Michigan Technological University is involved in an international collaboration initiative whose goal is to provide accessible spray and combustion knowledge to promote collaboration and furthering of experimental and computational research. This initiative, termed the *Engine Combustion Network (ECN)*, is led by Sandia National Laboratory. The ECN is a joint collaboration effort of institutions which have similar experimental combustion vessel facilities, whose common goal is to harness the unique capabilities and diagnostics of each facility, to advance the state of combustion and spray knowledge. A current focus of the ECN is the 'Spray A' condition, which is an experimental test condition used by all participating institutions with the same shared injector, to compare and characterize different facilities and diagnostics. The Spray A environmental conditions include fuel injection with a Bosch common rail solenoid injector equipped with a single hole nozzle 0.09 mm in diameter. The injector is supplied with n-dodecane fuel at 1500 bar through a common rail, at 90°C tip temperature. Ambient conditions include a 0% or 15% oxygen environment with 900 K gas temperature at 22.8 kg/m³ density. This condition is chosen to represent a low temperature combustion condition for engines operating on moderate levels of Exhaust Gas Recirculation (EGR). Refer to <http://www.sandia.gov/ecn/cvdata/sprayA.php> for complete details on the 'Spray A' experimental conditions.

Several institutions are contributing to the 'Spray A' study including, Sandia National Laboratory ('Sandia'), Michigan Technological University ('MTU'), Bosch, Caterpillar, CMT-Motores Termicos ('CMT'), IFP Energies Nouvelles ('IFP'), Argonne National Laboratory, Technical University of Eindhoven ('Eindhoven'), and Georgia Tech University, with others continuing to become involved as the initiative gains momentum. These contributing institutions have different vessels including both constant volume preburn vessels for thermodynamic state generation and constant pressure continuous flow rigs resulting in varying ambient compositions in regards to species used to reach the desired oxygen concentration, as will be discussed in Table 4.9. These different environments used will lead to differing levels of major and minor species produced, which motivates investigation into the influence these differences have, if any, on spray and combustion characteristics.

The comparison of ambient composition is undertaken to fulfill the goal of examining and benchmarking the test facilities charge gas compositions, and the influence the charge-gas composition has on autoignition in comparison to those in an engine through kinetics modeling. The objectives of this analysis and comparison of facilities are as follows:

- Compare major species at injection including composition and mixture specific heats.

- Compare the preburn environments used in the constant volume vessels including cool-downs and minor species produced. This includes the vessels at MTU, Sandia, Eindhoven and IFP.
- Compare n-heptane ignition delay under ‘Spray A’ conditions considering both the major species at fuel injection and also the minor species generated during the preburn procedure. n-heptane is used in place of n-dodecane (which is used in experimental ‘Spray A’ studies) based on the availability of a validated, reduced, chemical kinetic mechanism.

4.3.1. Comparison of Major Species at Injection

First, the major species at injection are compared at ‘Spray A’ conditions. These major species vary depending on the different preburn mixtures used and also the different initial compositions in the continuous flow rigs. This composition is compared in Table 4.9, along with the ambient gas composition specific heat calculated at the ‘Spray A’ temperature of 900 K. Both Caterpillar (Bazyn and Martin 2011) and CMT (Payri et al. 2011a) utilized constant pressure continuous flow rigs and their zero percent oxygen environment was achieved as a mixture of oxygen and nitrogen and as a result, for a 15% oxygen environment, the ambient composition is 15% oxygen and 85% nitrogen with heaters used to achieve the elevated temperature environment as required by the ‘Spray A’ condition. IFP (Pickett et al. 2010), MTU (Nesbitt et al. 2011a, 2011c), Sandia (Pickett et al. 2010) and Eindhoven (Meijer et al. 2011) all have constant volume combustion vessels and utilize preburn procedures of varying initial compositions to achieve the desired oxygen level for n-dodecane spray injection. Also included for comparison is a modified preburn mixture which has been proposed analytically to match the hydrogen to carbon ratio (HCR) of diesel fuel, 1.85, as opposed to the HCR of 1.17 representative of the current Sandia / MTU mixture (Johnson et al. 2009). This HCR ratio of 1.85, to match that of diesel fuel, is achieved by decreasing the C_2H_2 and O_2 in the mixture and by increasing the H_2 and N_2 to reach different CO_2 and H_2O levels in the products to match the HCR of diesel fuel. In the table below, and throughout the chapter, the term ‘ideal EGR’ is used to define the ideal engine charge gas with 38.3% EGR.

Table 4.9
‘Spray A’ environment of institutions post preburn, 15% oxygen environment at spray injection.

Institution	Vessel Configuration	Spray A Environment (Post Preburn) – Volume %					Mixture Specific Heat at 900 K (kJ/kg-K)
		O ₂ (%)	N ₂ (%)	CO ₂ (%)	H ₂ O (%)	Argon (%)	
Sandia	Preburn, Premixed	15.0	75.1	6.2	3.6	--	1.16
MTU	Preburn, Premixed	15.0	75.1	6.2	3.6	--	1.16
IFP	Preburn, Sequential	15.0	71.7	1.7	11.6	--	1.21
Eindhoven	Preburn, Sequential	15.0	71.2	6.4	3.6	4.2	1.13
CMT	Flow Pressure Vessel	15.0	85.0	--	--	--	1.13
Caterpillar	Flow Pressure Vessel	15.0	85.0	--	--	--	1.13
Ideal EGR (38.3%)	--	15.0	77.7	3.8	3.5	--	1.16
Dry Air	--	21.0	78.1	--	--	0.9	1.12
Modified HCR Match Diesel (1.85)	--	15.0	79.1	2.5	2.3	--	1.15

The Sandia / MTU and modified HCR 1.85 ratio have different levels of carbon dioxide and water. This is attributed to the different initial mixtures, with the HCR 1.85 mixture having decreased acetylene and increased hydrogen content relative to the standard Sandia / MTU mixture, with a HCR of 1.17. All mixtures considered have similar specific heats, spanning at most 0.1 kJ/kg-K (7%) at the 900 K ‘Spray A’ temperature despite the variations in the charge gas at the 15% oxygen environment. The similarities in specific heats will provide similar charge-gas environments at the time of injection. Even though these specific heats are similar, it is also interesting to compare the different ambient compositions, not just specific heat, for the ‘Spray A’ 15% oxygen condition considering the major species of CO₂, H₂O, Ar, and N₂ and their influence on the autoignition of the injected spray as will be discussed.

4.3.2. Comparison of Preburn Environments

A comparison was undertaken of the different preburn environments including, mixture used, minor species generated, and cool down history. A summary of the different initial mixture compositions utilized in these preburn vessels is provided in Table 4.10. The adiabatic flame temperature under constant volume and constant internal energy conditions was computed for each mixture composition at the initial combustion vessel heated wall temperature and corresponding pressure to achieve 22.8 kg/m³ density (‘Spray A’ condition for the Sandia mixture molecular weight).

Table 4.10
‘Spray A’ institution preburn mixture composition comparison

Institution	Preburn Mixture Composition (Volume %)						Molecular Weight Reactants (kg/kmol)	Initial CV Temp (K)	Initial Pressure (MPa)	T _{adiabatic} (U,V) (K)
	C ₂ H ₂ (%)	C ₂ H ₄ (%)	H ₂ (%)	O ₂ (%)	N ₂ (%)	Argon (%)				
Sandia	3.06	--	0.50	22.63	73.82	--	28.7	445	2.94	1927
MTU	3.06	--	0.50	22.63	73.82	--	28.7	453	2.99	1933
IFP	--	0.816	9.39	21.43	68.36	--	26.4	453	3.25	1772
Eindhoven	3.15	--	--	22.64	70.07	4.14	29.3	443	2.87	1946

The differences in mixture, including species used and composition, changed the adiabatic flame temperature and because of this, there are differences in minor species created, including NO_x which is thermally (temperature) controlled and this minor species could potentially influence the resulting spray and autoignition (refer to section 4.2). The Eindhoven mixture had the highest adiabatic flame temperature, followed by the Sandia and MTU mixture and lastly IFP. The small (6 K) difference in flame temperature between MTU and Sandia, despite identical mixtures, is due to differences in the CV heated wall temperature used (initial temperature). The highest adiabatic flame temperature is governed by the energy of the fuel in the reactants, which is controlled by acetylene, thereby resulting in Eindhoven having the highest flame temperature based on the largest amount of acetylene in their preburn mixture reactants.

Along with the varying mixture compositions used, all vessels exhibit different cool-down histories which will influence the levels of minor species produced. NO and NO₂ are largely thermally (temperature controlled), with OH, a reactive minor species, largely following the cool-down history of the combustion vessel preburn procedure. First, experimental temperature traces were compared for each CV preburn environment as shown in Figure 4.10 for 15% oxygen conditions. These temperature traces are computed from measured combustion vessel pressures. MTU has not undertaken tests at this ‘Spray A’ condition and therefore data is presented for a 0% O₂ environment at 34.8 kg/m³ ambient density to show the general MTU cool-down behavior acknowledging that peak temperatures and times will vary as a result of different mixture characteristics and density conditions.

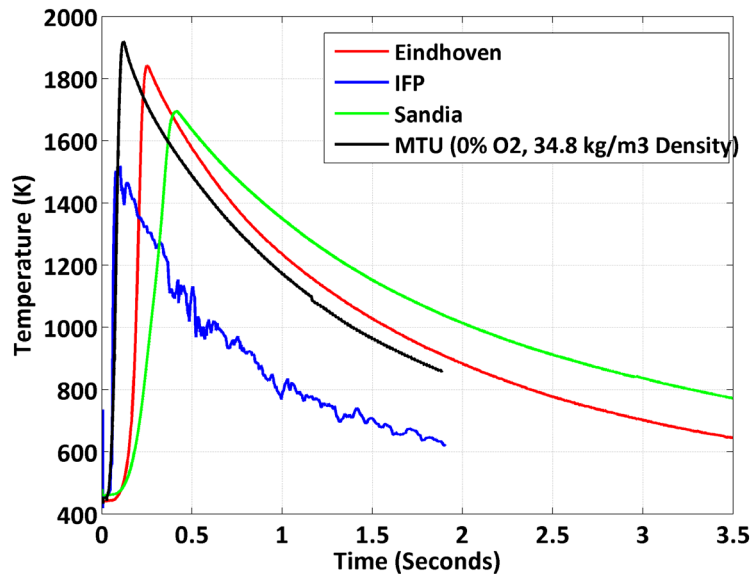


Figure 4.10: Experimental temperature-time trace for the four preburn environments under ‘Spray A’ conditions. Time 0 seconds corresponds to the time of spark.

The vessels exhibit different temperature-time traces not only in peak temperature, but also in cool-down behavior in regards to time to reach peak temperature and to reach the desired temperature at injection, 900 K. This peak temperature behavior is largely governed by initial mixture composition, the higher adiabatic flame temperature mixtures exhibit higher peak temperatures experimentally with reasons for these higher temperatures being previously discussed. Sandia exhibits a slightly different behavior in peak temperature, when compared to the other vessels, in regards to a large change between expected adiabatic flame temperature and actual peak combustion temperature, which is likely attributed to the reduced fan speed and fan placement influencing combustion. As seen, the four vessels exhibit different cool-down histories, largely attributed to fan speed variations as summarized in Table 4.11.

Table 4.11
CV fan speed comparisons.

Institution	Fan Speed (RPM)	Location
Sandia	1000	Upper Corner (opposite injector)
MTU	7000	Top Window
IFP	3140	Upper Corner (near injector)
Eindhoven	1890	Lower Corner

As the fan speed increased, the rate of cool-down increased due to increased vessel heat transfer. Additionally, the fan will generate enhanced flow motion and turbulence inside the combustion vessel which not only increases the rate of cool-down, but also enhanced combustion rates. MTU runs at the highest fan speed and has a fast cool down relative to Sandia which has the same starting mixture. Sandia runs the lowest fan speed which was evidenced in its long cool down and long time to reach the desired temperature for injection.

The cool downs can be further compared by fitting the experimental temperature decay to a modified exponential, quadratic in time, to understand both the rate and time constant of the cool down for comparison, which was also used to define the preburn heat transfer in the Cantera chemical kinetics modeling program. The cool-downs were curve fit to an equation of the form shown in equation (61).

$$T(t) = T_0 \exp(at^2 + bt) \quad (61)$$

Where a , b , and c , are constants in the curve fit, t is time in seconds, and T is CV charge gas temperature in Kelvins. Applying this curve fit to the experimental temperature-time data that was shown in Figure 4.10, cool-down curve fit constants were determined as summarized in Table 4.12. For the case of MTU, the 0% O₂ data at 34.8 kg/m³ was interpolated from data at 17.4 kg/m³, and 21% O₂ data at both 34.8 and 17.4 kg/m³ to estimate data at 15% O₂, 22.8 kg/m³ ambient density to match other experimental traces. Also included in the table is the time constant of the cool-down decay as calculated from 1000 to 800 K.

Table 4.12

Cool-down curve fit parameters and decay times. *The experimental time from spark to peak temperature is estimated based on 0% and 21% O₂ data at 17.4 and 34.8 kg/m³ density.

	Sandia	MTU	IFP	Eindhoven
Cool Down Curve Fit Parameters				
a	0.05	0.00	0.02	0.07
b	-0.41	-0.77	-0.87	-0.55
c	7.43	7.51	7.32	7.49
Experimental Time (s) from Spark to Peak Temperature	0.42	0.13*	0.100	0.25
Time Constant Cool Down Decay (s)	6.5	1.3	1.2	3.5

Sandia, IFP and Eindhoven all have a cool down curve fit parameter providing an exponential function that is quadratic in time, whereas that of MTU was only linear with time which could be caused by various factors. First, MTU runs at a significantly higher fan speed (more than double that of the next highest fan speed used by IFP). This increase in fan speed should provide more uniform mixing between the gases in the CV, promoting the cool-down to be exponential with linear temperature dependence since at peak preburn temperature, the mixture is more uniform and will yield a faster rate of cool down. The eight access ports of the combustion vessel are large crevice volumes which can be considered as pistons in conventional engines for comparison. With the higher fan speed, the flow-field will develop more quickly, yielding a true exponential decay, whereas at the lower fan speeds, it takes longer for the flow field to develop so the overall cool down is exponentially quadratic in time eventually transitioning to a true exponential decay in the longer time scales. These explanations were further confirmed by considering the value of the ' a ' parameter in the curve fit which is small for IFP as they have a higher fan speed. The trend was not completely preserved for Eindhoven and Sandia, but this could be attributed to placement of the fan in the CV and overall differences in internal vessel geometries. The curve fit results are shown in Figure 4.11 and are time shifted so that 0 seconds occurs at 900 K.

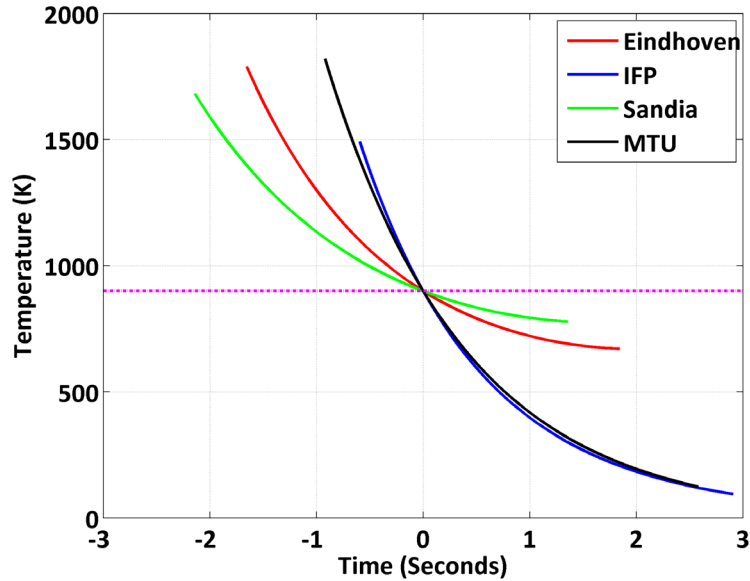


Figure 4.11: Cool-down curve fits time shifted to 900 K occurring at 0 seconds.

As shown in the figure, the cool-down curve fits are similar for IFP and MTU, which was confirmed by the time constant of the cool-down decay as calculated from 1000 to 800 K and summarized in Table 4.12.

4.3.2.1. Chemical Kinetics Preburn Modeling for Combustion Vessel Comparison

Details on the chemical kinetics preburn modeling for combustion vessel comparison are provided in Appendix section 12.3. First, initial conditions defined by the extent of reaction method must be determined, using a procedure developed with EES (refer to section 12.3.3.1). The results of the EES initial conditions from the extent of reaction calculation are shown in Table 4.13 for the four different preburn environments.

Table 4.13

EES initial conditions from extent of reaction calculation. X is species mole fraction.

	Sandia	MTU	IFP	Eindhoven
T (K)	905	1031	891	1030
Pressure (MPa)	5.93	6.75	6.24	6.61
α	0.448	0.444	0.507	0.443
X H ₂	0.003	0.003	0.047	--
X C ₂ H ₂	0.017	0.017	--	0.018
X C ₂ H ₄	--	--	0.004	--
X Ar	--	--	--	0.042
X O ₂	0.192	0.193	0.182	0.193
X N ₂	0.744	0.744	0.700	0.706
X CO ₂	0.028	0.027	0.008	0.028
X H ₂ O	0.016	0.016	0.057	0.014

Despite the same mixtures and similar starting conditions for Sandia and MTU, the elevated reaction temperatures were significantly different. This was attributed to the reduced experimental peak temperature for Sandia relative to that of MTU due to their lower fan speed.

The initial extent of reaction results were input into the Cantera chemical kinetics model which is initially set to be adiabatic to determine the ignition delay. This ignition delay must be determined as it defines when heat transfer of the cool-down will start. Once the ignition delay was determined, heat transfer was implemented starting at this ignition delay throughout the remainder of the kinetics model defining the cool-down phase. This heat transfer is modeled using an exponential decay curve fit as defined by equation (62), temperature was defined in equation (61).

$$Q = \text{Constant} * \frac{dT(t)}{dt} = \text{Constant} * T_o(b + 2at) * \exp(at^2 + bt) \quad (62)$$

Where *Constant*, in the above equation, is a representation of the convective heat transfer coefficient. In the Cantera model this constant was not defined, rather the heat flux was tuned to match the model temperature-time trace to the experimental data. This heat transfer modeling procedure is improved upon that used in the *Energy and Fuels* manuscript (Section 4.2) which included a polynomial relationship for the heat transfer modeling. Results for the temperature time trace from this model are shown in Figure 4.12.

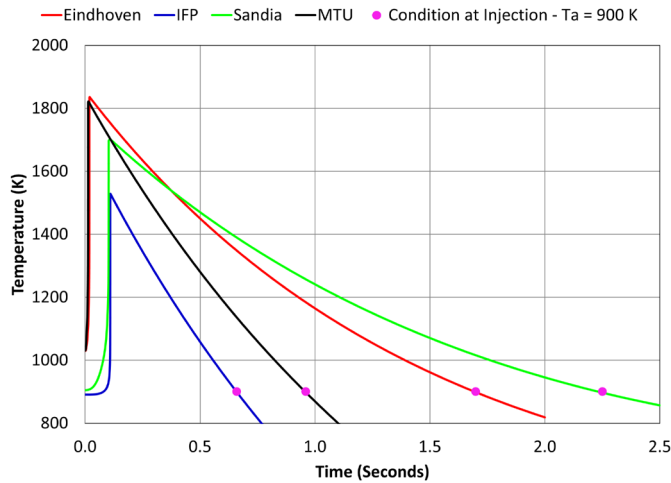


Figure 4.12: Chemical kinetics modeling of temperature time trace in Cantera for the four different preburn environments.

Peak temperature is governed by mixture properties and the differing fan speeds in the vessels.

As discussed in section 4.2, the minor species of interest are NO, NO₂, and OH. These were tracked during the premixed burn and cool-down to understand levels throughout the process and at injection. The minor species of NO is shown in Figure 4.13.

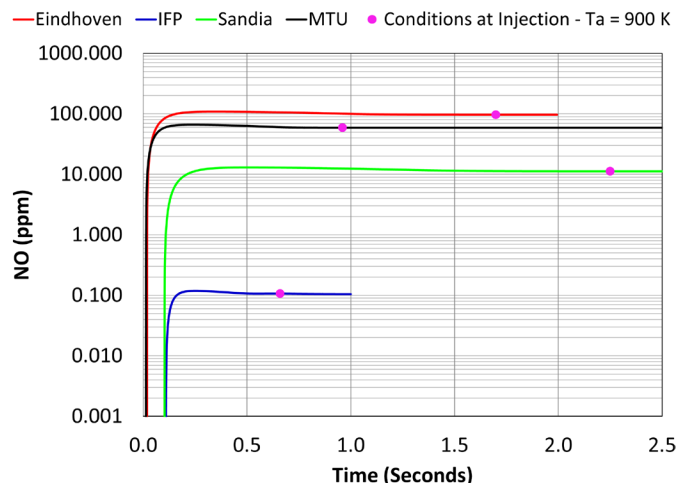


Figure 4.13: NO – time trace from the CV preburns.

NO is thermally controlled and is governed by the peak temperature of the preburn. As the peak preburn temperature increases, the NO levels increase, and therefore Eindhoven has the largest NO level, followed by MTU, Sandia and IFP. The time to reach 900 K (denoted by the magenta circle) is governed by the cool-down as was shown in Figure 4.12.

Also of interest are NO₂ levels during the preburn procedure as shown in Figure 4.14.

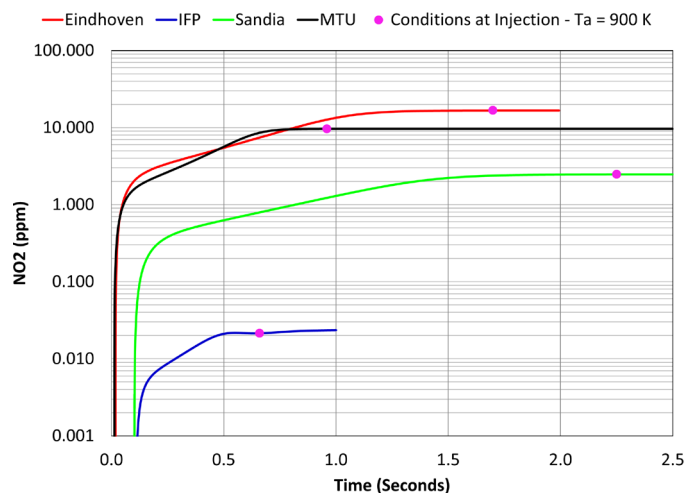


Figure 4.14: NO₂ – time trace during the preburn for the four different combustion vessels.

NO₂ levels during the preburn are similar to NO in regards to tracking peak temperature trends. Peak NO levels are reached earlier than those for NO₂, making NO₂ more residence time dependent than NO. Eindhoven has the largest value of NO₂, followed by MTU, Sandia, and finally IFP. These trends are governed by the peak temperatures of the preburn (Figure 4.12).

The last minor species of interest is OH, which tracks the preburn temperature-time trace as shown in Figure 4.15.

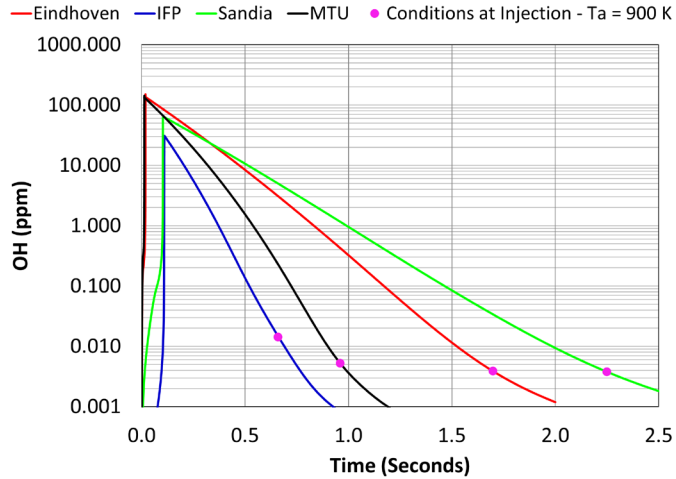


Figure 4.15: OH – time trace during the preburn environment.

OH tracks the temperature trace reaching a peak value of OH around peak temperature and then OH decreases as temperature decays. At injection, IFP has the maximum level of OH, with Sandia having minimum OH. OH levels were below equilibrium at the time of injection, by over four orders of magnitude as will be quantified.

NO levels resulting from the preburn procedure are significantly less than equilibrium. Peak OH levels occur at the time of the peak preburn temperature, and are close to equilibrium values but levels dropped sharply as cool-down proceeded with heat transfer occurring. These equilibrium levels for constant internal energy and volume are summarized in Table 4.14, calculated at the initial CV heated temperature (defined in Table 4.9 for each institution).

Table 4.14

**Equilibrium levels of minor species of interest formed during the preburn event.
Calculated at the initial CV heated temperature.**

	Sandia	MTU	IFP	Eindhoven
NO (ppm)	5098	5184	3031	5250
NO ₂ (ppm)	93.3	94.0	74.6	92.5
OH (ppm)	233	240	173	243
Peak T (K)	1927	1933	1772	1946

Equilibrium levels for NO and NO₂ were more than two orders of magnitude above what is typical of that in conventional diesel engines running moderate EGR levels.

The conditions at injection for ‘Spray A’ (900 K temperature) as determined from this preburn chemical kinetics modeling are summarized in Table 4.15.

Table 4.15
Preburn kinetics modeling output results for conditions at injection. Temperature of 900 K, density of 22.8 kg/m³.

	Sandia	MTU	IFP	Eindhoven
Time (s) at Injection Relative to Peak Temp	2.15	0.95	0.55	1.68
T (K)	900	900	900	900
Pressure (MPa)	5.81	5.82	6.13	5.71
NO (PPM)	11.24	59.14	0.11	96.72
NO ₂ (PPM)	2.47	9.64	0.02	16.66
OH (PPB)	3.78	5.24	14.34	3.87
Mole Fraction CO ₂ (-)	0.06	0.06	0.02	0.06
Mole Fraction H ₂ O(-)	0.04	0.04	0.12	0.03
Mole Fraction N ₂ (-)	0.75	0.75	0.72	0.71
Mole Fraction O ₂ (-)	0.15	0.15	0.15	0.15

At injection, Eindhoven has the largest NO and NO₂ mole fractions due to the highest peak temperature and these species are thermally controlled. OH is highest for IFP, and OH tends to track the temperature time trace of the vessel as it is a highly reactive minor species. Minor species levels of NO and NO₂ at injection are more than two orders of magnitude less than equilibrium levels and are similar to an engine running moderate EGR. The minor species of OH at injection are four orders of magnitude less than equilibrium levels.

4.3.3. Autoignition Modeling of n-Heptane as a Diesel Surrogate

The autoignition of n-heptane was modeled in a second kinetics simulation, considering first the influence of major species for all vessels and second considering the minor species produced in the preburn vessels. The autoignition was modeled using n-heptane as a diesel surrogate, using the existing validated model from that used in the *Energy and Fuels* publication. This included use of a reduced n-heptane mechanism (LLNL 2000), modified to include NO and NO₂ from the GRI 3.0 mechanism (Smith et al. 1999). The ambient gases, as defined in Table 4.9, are mixed stoichiometrically (to yield complete combustion with no excess oxygen) with n-heptane, which were used as inputs into the reactor model at 900 K ambient temperature and 22.8 kg/m³ density, which defines pressure based on the different mixture molecular weights, to match the ‘Spray A’ environment. Although the ‘Spray A’ conditions are for n-dodecane fuel injection, n-heptane is used here as the diesel surrogate as it provides insight on relative changes in ignition delay amongst institutions and vessel types, and this mechanism is well validated (Seiser et al. 2000). Furthermore, although n-dodecane mechanisms exist, they are known to have limitations, with the developers acknowledging that the current mechanism is continuously being updated and improved upon (Wang et al. 2010). Model details are provided in Appendix 12.3.2.

4.3.3.1. Constant Pressure Flow Rig and Constant Volume Combustion Vessel Comparison Considering Major Species

First, this n-heptane autoignition model was used to compare the stoichiometric n-heptane ignition delay and peak temperatures for all vessels (Sandia, MTU, IFP, Eindhoven, Caterpillar, and CMT), along with two other ambient charge gas mixtures. This includes an ideal EGR mixture (38.3% EGR to yield 15% O₂), achieved with H₂O and CO₂ dilution and a modified HCR mixture discussed previously (Johnson et al. 2009).

Table 4.16
Ignition delay of stoichiometric n-heptane and peak n-heptane combustion temperature for constant pressure and enthalpy reactor modeling at ‘Spray A’ conditions (15% O₂, 900 K, 60 Bar – 22.8 kg/m³ Density).

Institution	Mole Fractions Spray A Environment Mixed with n-Heptane						Ignition Delay (ms)	Peak Temperature (K)
	O ₂	N ₂	CO ₂	H ₂ O	Argon	n- Heptane		
Modified HCR Match Diesel (1.85)	0.148	0.780	0.024	0.023	--	0.013	0.69	2360
Dry Air	0.206	0.775	--	--	--	0.019	0.37	2708
Ideal EGR (38.3%)	0.148	0.767	0.038	0.035	--	0.013	0.71	2326
Caterpillar	0.148	0.839	--	--	--	0.013	0.69	2374
CMT	0.148	0.839	--	--	--	0.013	0.69	2374
Eindhoven	0.148	0.702	0.063	0.032	0.036	0.013	0.73	2327
IFP	0.148	0.708	0.017	0.114	--	0.013	0.65	2313
MTU	0.148	0.741	0.061	0.036	--	0.013	0.72	2308
Sandia	0.148	0.741	0.061	0.036	--	0.013	0.72	2308

There were no significant differences in n-heptane ignition delay for the 15% Oxygen conditions over the various mixtures when considering the major species in the ambient gas composition. There is a significant difference between the 15% oxygen environments and that of dry air (21% oxygen), with almost half the ignition delay. There were differences in peak temperature, spanning almost 70 K, due to the different ambient gas compositions, and when there was less ambient gas dilution by CO₂ and H₂O, the peak combustion temperature of n-heptane increased.

Comparison between the species is easier when represented as different bar charts. First, major species of H₂O and CO₂ are compared as shown in Figure 4.16.

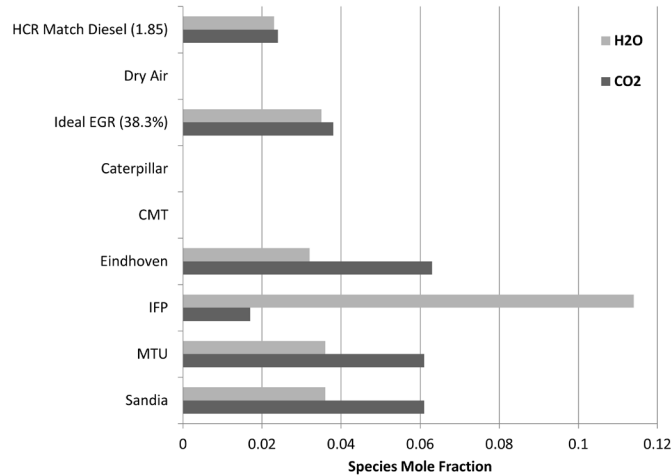


Figure 4.16: Comparison of levels of major species of carbon dioxide and water for n-heptane autoignition study.

Of note are that CMT and Caterpillar do not utilize CO₂ or H₂O dilution to achieve the 15% O₂ (refer to Table 4.17). This dilution is used by the other vessels, and is also representative of conventional diesel engines. IFP had significantly higher H₂O levels at injection which is attributed to the large amount of hydrogen in their preburn mixture. Levels of CO₂ and H₂O are similar for MTU, Sandia and IFP. These differences in major species (CO₂, H₂O, O₂, N₂ and Ar) yield variations in peak combustion temperature with n-heptane as shown in Figure 4.17.

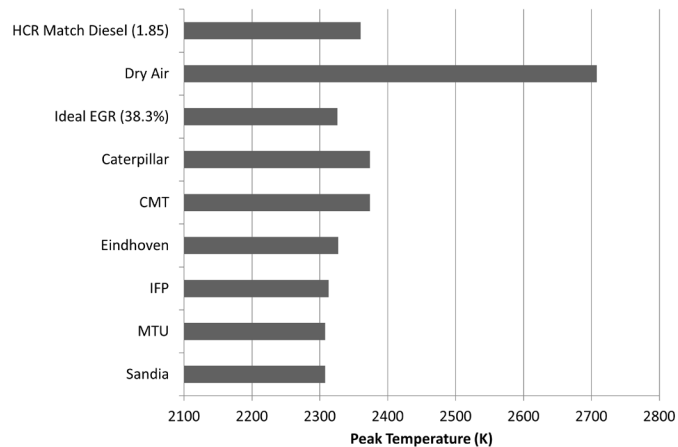


Figure 4.17: Peak temperature of n-heptane autoignition as a result of different levels of major species.

Peak combustion temperature of n-heptane combustion with lambda of 1 was largest for that of dry air which is attributed to the difference in oxygen levels. Caterpillar and CMT have the next highest peak temperature which is attributed to the lack of dilution by water and carbon dioxide. Although dilution is occurring with nitrogen, the specific heat capacity of nitrogen is less than that of both carbon dioxide and water (Turns 2000), and the reduced heat capacity of the nitrogen diluents will provide less reductions in flame temperature (Kook et al. 2005) when compared to carbon dioxide and water dilution.

Finally ignition delay was compared for the different institutions when considering solely major species as shown in Figure 4.18.

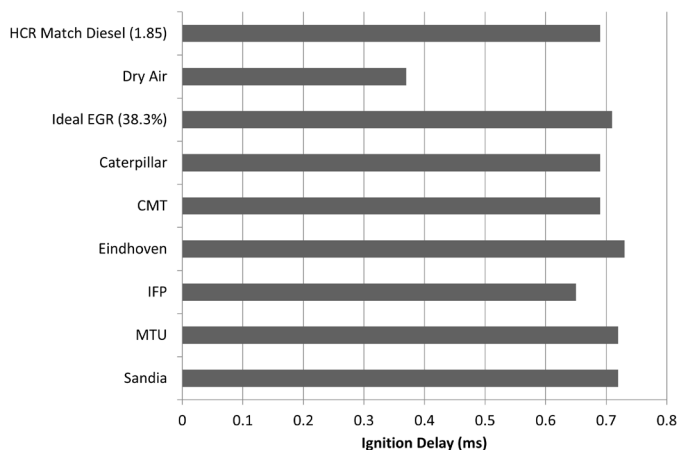


Figure 4.18: N-heptane ignition delay variation as a result of different levels of major species.

Again, the first obvious trend is the significantly reduced ignition delay for n-heptane in dry air relative to the 15% oxygen conditions, by close to 50%, due to the elevated oxygen level. Excluding this difference, there were no significant differences in ignition delay for the different vessels, having a span of 0.1 ms which is within the modeling time step of 0.1 ms and therefore the variations which do exist are within the modeling accuracy.

4.3.3.2. Constant Volume Combustion Vessel Comparison – Major and Minor Species

Although the ignition delay modeling shows no significant variations of ignition delay in n-heptane between the different ambient environments, this modeling assumed only major species levels (O_2 , CO_2 , H_2O , Ar, and N_2), however, the preburn procedure used at IFP, Eindhoven, and MTU / Sandia is known to generate reactive minor species which could influence the ignition delay (Nesbitt et al. 2011c). Therefore, complete modeling was undertaken starting with the extent of reaction method to determine elevated starting conditions. These conditions were then used to model the preburn procedure including premixed burn and cool-down. Finally, the subsequent ignition delay of fuel in a charge gas environment considering all 53 GRI species, with minor species, was undertaken. The same n-heptane autoignition modeling procedure was used as was discussed in Figure 12.19. The inputs to the n-heptane model result from the analysis undertaken in section 4.3.2. This modeling was undertaken for the CV preburn vessels including Sandia, MTU, Eindhoven, and IFP, while being compared to air plus ideal EGR at 15% oxygen and dry air. These results are shown in Table 4.17.

Table 4.17
Comparison of the autoignition modeling results considering the influence of major species.

	n-Heptane Ignition Delay (ms)	Peak Temperature (K)
Sandia	0.69	2302
MTU	0.66	2302
IFP	0.68	2307
Eindhoven	0.67	2320
Air Plus Ideal Residuals (38.3%) – 15% O ₂	0.71	2326
Dry Air	0.37	2707

The ignition delay for Sandia and MTU are different due to variations in minor species levels (Table 4.15) attributed to the cool-down histories of the two vessels (different fan speeds). Considering the influence of minor and major species resulting from the preburn, there was no significant difference in the ignition delay, less than 5% spread for the different vessels, with the exception of it being 90% longer when compared to that of dry air.

4.3.4. Conclusions from ‘Spray A’ Ambient Composition Comparison

Several key conclusions can be made from the comparison of the spray A ambient environments, as summarized below:

- Major Species Comparison – all institutions exhibited similar specific heats in the range of 1.12 to 1.21 kJ/kg-K, being within 0.1 kJ/kg-K (7%) of each other, and these specific heats matched typical levels in an engine running an EGR level of 38.3%.
- Preburn comparison
 - Different cool-down histories were seen in the different vessels which are attributed to differences in fan speed causing variations in flow fields.
 - Peak temperature, NO, and NO₂ at injection exhibit the following trend, Eindhoven, MTU > Sandia > IFP. NO and NO₂ are thermally controlled and therefore are controlled by the peak temperature. Levels of these minor species at injection are more than two orders of magnitude less than equilibrium. The peak temperature trend is controlled by both fan speed and mixture composition, with acetylene being the controlling fuel component, with the Eindhoven mixture having the largest amount of this constituent.
 - OH species trend at injection is as follows, IFP > MTU > Eindhoven > Sandia. OH levels track with the cool-down process, and are four orders of magnitude less than equilibrium at injection.
- Ignition delay comparison
 - Major species consideration – no significant variation in n-heptane ignition delay, with a less than 5% spread (0.04 ms) when considering all cases except for IFP. When considering IFP the spread was 0.1 ms which is within the model accuracy based on time step definition (0.1 ms) and model validity (refer to Figure 4.7). The smallest ignition delay for the

15% oxygen cases is seen by IFP being about 0.05 ms shorter than the other test cases.

- Preburn consideration – no variation in ignition delay due to minor species from the preburn (less than 5% spread), despite the different levels of both major and minor species from the preburn.
 - CV ignition delay is 4% shorter than Ideal EGR (15% O₂)
 - CV Ignition delay is 83% longer than dry air (21% O₂)

4.4. Modification to the Preburn Mixture

A modification has been applied to the preburn procedure in regards to premixture composition for 0% oxygen mixtures relative to that presented in section 4.2. This modified mixture was developed in an effort to improve preburn combustion and is applied in the current study.

4.4.1. 0% Oxygen Mixture Analysis

Several studies in the combustion vessel consist of injecting fuel into a 0% oxygen environment which provides ambient conditions for spray vaporization, without combustion, to enable study and characterization of spray parameters. The original 0% oxygen mixture, as used at Sandia National Laboratory (Sandia ECN 2010) consists of 3.2% acetylene, 0.50% hydrogen, 8.25% oxygen, and 88.05% nitrogen. However, using this conventional mixture under certain high temperature conditions, diesel combustion occurs. This could be attributed to various factors including for example mixture stratification when using the remnants of a premixture in the mixing vessel or incomplete combustion. This unexpected presence of diesel combustion in a 0% oxygen environment led to mixture characterization, as well as sampling of preburn exhaust gases, to understand the mixture pre- and post- burn to determine any changes which need to be made to the composition.

4.4.1.1. Mixture Sampling Setup and Test Procedures

Sampling was undertaken using a Sensors Inc Semtech DS portable emissions analyzer with the capability of measuring CO, CO₂, O₂, NO, NO₂ and total hydrocarbons (THC). For the current work, THC levels, along with O₂, CO, CO₂ and NO levels were monitored. This includes the use of a heated flame ionization detector (FID) for measuring THC, an electrochemical sensor for O₂ measurements, a non-dispersive infrared (NDIR) analyzer to measure CO and CO₂ levels, and a non-dispersive ultraviolet (NDUV) analyzer to measure NO and NO₂. NO and NO₂ were not measured in the current work as the analyzer was not calibrated for these gas species. All gases were passed through a heated sample line to the Semtech unit to ensure that the hydrocarbons were not lost or hung-up in the sample line during transport. The unit communicates wirelessly to the control computer where sampling data is logged and processed.

The THC FID unit is heated to 191°C, which includes a heated filter sample system and the FID chamber, with this heating being required to prevent condensation in the exhaust sample (Sensors Inc. 2008). The FID fuel is a mixture of hydrogen and helium, and a 10,000 PPM THC sample range was chosen based on the FID fuel

composition. The NDIR analyzer requires the sample to first be dried by passing it through a coalescing filter, followed by a thermoelectric chiller to eliminate water vapor which interferes in the infrared channels before measurement of CO and CO₂ levels (Sensors Inc. 2008). Finally, an electrochemical oxygen sensor was used to characterize oxygen levels in the sample which works by flowing the sample through a sensor that outputs a signal that is proportional to the partial pressure of oxygen in the sample (Sensors Inc. 2008). The NDUV analyzer first dries the exhaust sample with a coalescing filter followed by a thermoelectric chiller, removing heavy hydrocarbons which would contaminate it.

For testing, the analyzer must first be calibrated. This includes first zeroing the analyzer which consists of a 30 second purge and by using clean air as the sample port, the levels of CO, CO₂, NO and THC are zeroed. Next, the analyzer was spanned to ensure it was appropriately calibrated for the sample measurements. This involves the use of a quad-blend span gas which includes CO (3.95%), CO₂ (11.8%), NO (1975 ppm) and THC (1202 ppm) with the balance Nitrogen, which is connected to the span port of the analyzer. This THC range of the quad-blend span gas is small relative to the 10,000 ppm THC sample range, but was used based on limited quad-blend span gas availability, and the requirement of measuring larger levels of hydrocarbons. The span procedure included a 30 second purge and provided readings of the gas constituents which were compared to the expected bottle readings to calibrate the analyzer. The system also underwent a span for oxygen levels by using ambient air with an expected oxygen level of 20.9%.

Two different sampling procedures were used in the current work. This involves sampling the gases of the preburn mixture before combustion, and also sampling the gases after combustion, as shown in Figure 4.19.

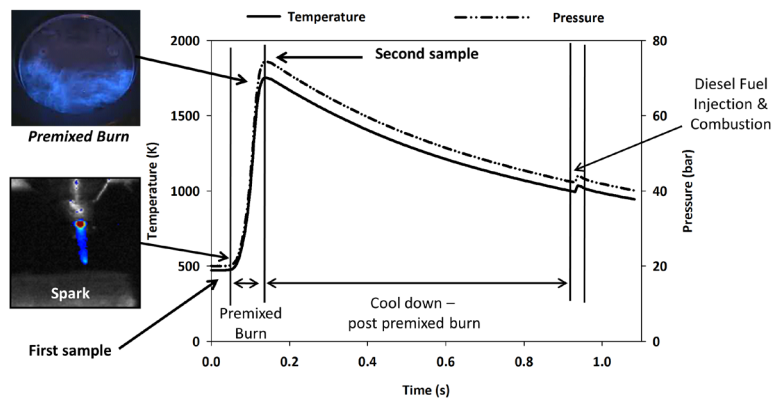


Figure 4.19: Two sampling points, pre- and post- burn of the premixture.

In both cases, a sample bag was filled with the gas mixture to be tested, with the sample bag being evacuated during gaseous sample testing by passing the gases through the heated sample line into the Semtech analyzer with this test data being logged. When sampling gases from the preburn mixture before combustion, a sample is drawn directly from the mixing vessel into the sample bag. For sampling of the gases post preburn, a different procedure is used. Two preburns are undertaken to ensure adequate sample gases, with the preburn products metered from the CV exhaust into the metal sample cylinder, as shown in Figure 4.20. After both preburns were completed, the contents of

the sample cylinder were transferred into the sample bag for metering into the Semtech analyzer via the heated sample line.

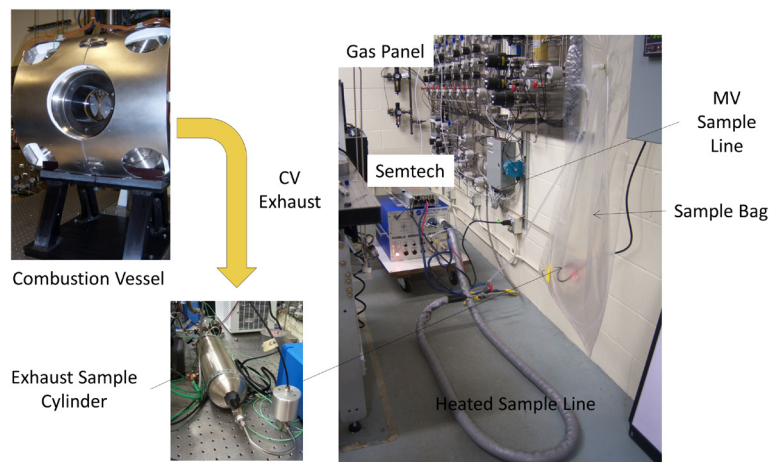


Figure 4.20: Sampling setup for use of the Semtech in the CV Laboratory for preburn sampling (draw sample directly from mixing vessel into the sample bag) and post preburn sampling (draw sample which is stored in the exhaust sample cylinder into the sample bag).

4.4.1.2. Mixture Sampling Results and Analysis

Exhaust gas sampling was undertaken of various preburn mixtures and the exhaust post preburn to understand mixture accuracy and combustion efficiency. It was with this testing that it was decided to modify the existing 0% oxygen mixture to a new mixture with more hydrogen (i.e. a richer mixture) to provide a more complete combustion event and therefore have the correct 0% oxygen environment post preburn.

Testing was undertaken on the original 0% oxygen mixture before and after a preburn. The actual mixture composition relative to that expected is summarized in Table 4.18, based on pressure transducer readings from the fill process.

Table 4.18
Gas sampling mixture composition for the original 0% oxygen mixture.

Species	Expected Mole Fractions Based on Desired Mixture (Volume %)	Actual Mole Fractions Based on Measured Partial Pressures (Volume %)
C ₂ H ₂	3.20	3.21
H ₂	0.50	0.54
O ₂	8.25	8.72
N ₂	88.1	87.5

As seen in the table, the actual mixture is 0.5% high in oxygen and correspondingly low in nitrogen by 0.5%. This mixture deviation will be translated to the actual products post-preburn, and assuming an ideal complete combustion process, these are defined in Table 4.19.

Table 4.19
Ideal, complete, combustion products of the 0% oxygen mixture.

Species	Expected Mole Fractions Based on Desired Mixture (Volume %)	Actual Mole Fractions Based on Measured Partial Pressures (Volume %)
CO ₂	6.40	6.42
H ₂ O	3.70	3.75
O ₂	0.00	0.43
N ₂	88.1	87.5

Based on the error in the initial mixture, the species levels after combustion will be almost 0.5% high in oxygen and almost 0.5% low in nitrogen.

To verify mixture characteristics before and after the preburn, the mixture was sampled using the aforementioned procedure with the Semtech emissions analyzer. Based on the measuring limits of the analyzer, only oxygen can be analyzed for the mixture before the preburn, and post preburn oxygen, carbon dioxide, carbon monoxide, and total hydrocarbons (THC, C1 basis) can be measured based on analyzer operating limits and the calibration gas used. Mixture measurements are provided in Table 4.20.

Table 4.20
Mixture composition testing, pre and post preburn, for a 0% oxygen mixture.

	Expected Levels – based on Measured Partial Pressures	Mixture Before Preburn – Test 1	Mixture Before Preburn – Test 2	Expected Levels – based on Measured Partial Pressures	Mixture Post Preburn – Test 1	Mixture Post Preburn – Test 2
Oxygen (%)	8.7	8.2	8.1	0.4	1.4	0.7
Carbon Dioxide (%)		--	--	6.4	5.4	5.1
CO (ppm)		--	--		2850	10200
THC C1 Basis (ppm)		--	--		5240	2800

Considering the results of mixture testing before the preburn, oxygen levels are reading at a minimum 0.5% lower than expected based on actual partial pressure measurements with less deviation when considering expected partial pressure measurements based on the equations for mixture definition (Table 4.19). The differences between expected and measured oxygen levels, of 0.5%, are within the Semtech measuring accuracy of $\pm 1\%$ oxygen (Sensors Inc. 2008). Looking at a carbon balance of the reactants, based on partial pressure measurements, there is 6.42 moles of carbon in the reactants. The products, based on Semtech measurements are 5.69 moles and 6.12 moles of carbon in the products for Test 1 and Test 2, respectively. As carbon does not balance this provides an indication of a combustion efficiency less than 100% as not all of the reactant carbon is converted to product carbon. This incomplete combustion results in excess oxygen in the products, as confirmed with the exhaust gas sampling.

Considering the results post preburn, there was less repeatability and larger measurement variation. In both tests, oxygen was high and carbon dioxide was low relative to what is expected for complete combustion (refer to Table 4.18). This, along with levels of THC, further supports the theory of incomplete combustion. Carbon

dioxide accuracy is $\pm 3\%$ of the reading ($\pm 0.16\%$ in this case), carbon monoxide accuracy is $\pm 3\%$ of the reading (± 86 to ± 306 ppm in this case), and THC accuracy is $\pm 2\%$ of the reading (± 105 to ± 56 ppm in this case) (Sensors Inc. 2008). The variation in measurements test to test post preburn could be attributed to various factors. First, differences in combustion repeatability attributed to ignition variations or mixture stratification of the charge-gas mixture. Second, in sampling, there could be some errors attributed to the gas analyzer in regards to mixture hang up in the sample lines or a contaminated sample cylinder or bag which would influence the readings. Third, during the preburn the gases will be compressed into the crevice volume, and some (not all) of the gases will be pulled out of the crevice volumes as the vessel is exhausted, which will influence gas sampling results. Despite these variations, it is evident that combustion was incomplete, thereby motivating hydrogen addition to raise the combustion temperature to promote combustion efficiency and more complete combustion, to achieve the correct mixture.

4.4.1.3. Modifications to the 0% Oxygen Mixture

Based on the Semtech analysis and the presence of diesel combustion under certain high temperature conditions, the 0% oxygen mixture was modified. The modification undertaken was such that this new mixture has an increase in the adiabatic flame temperature while preserving the fuel-air ratio of the original mixture, to assist in more complete combustion. The procedure taken to determine this new mixture is outlined here, using two different methods. The first method relies on adiabatic flame temperature calculations with the GRI 3.0 mechanism in Cantera, interfaced with Matlab. First, the initial adiabatic flame temperature was calculated at constant volume and internal energy for a 0% oxygen mixture (original mixture) in the combustion vessel at 6.9 bar (100 psi) and 453 K. Next, hydrogen was added to the mixture to increase the adiabatic flame temperature by 50 K, which after iterating and solving corresponds to a 2.5 kg addition of hydrogen, along with the addition of oxygen – nitrogen to keep the same fuel (acetylene and hydrogen) to air (oxygen and nitrogen) ratio as the original zero percent oxygen mixture. The new mixture mole fractions are calculated, followed by the corresponding increases in pressure, in regards to required increases in hydrogen and oxygen-nitrogen to meet these new conditions of increased flame temperature.

The second method involves standard thermodynamic relationships, acknowledging that the fuel mass multiplied by its lower heating value can be equated to the product of the total mass, specific heat, and change in temperature. The fuel is composed of acetylene and hydrogen and therefore the lower heating value is for a mixture of these constituents. The specific heat capacity is assumed to be that of air and is a limitation of the current calculation as the charge-gas composition is different than that of air. The results of the two calculation methods both yield similar results. For an original 55.2 bar (800 psi) zero percent oxygen mixture, an addition of 0.69 bar (10 psi) hydrogen and 1.5 bar (21.9 psi) oxygen / nitrogen mixture (based on a cylinder with 40% oxygen and the remainder nitrogen) achieve a 50 K increase in adiabatic peak flame temperature. This yields a final mixture mole fraction for the new zero percent oxygen mixture of 3.1% acetylene, 1.5% hydrogen, 8.9% oxygen, and 86.5% nitrogen. This mixture molar volume percent basis composition is listed in comparison to the original mixture in Table 4.21.

Table 4.21
Comparison of original and modified 0% oxygen mixtures.

Gas	Original Mixture (Volume %)	Modified Mixture (Volume %)
Acetylene	3.2	3.1
Hydrogen	0.5	1.5
Oxygen	8.25	8.9
Nitrogen	88.05	86.5

This modified mixture is used in the 0% oxygen testing undertaken for vaporizing spray conditions in this work, and does not yield diesel combustion as expected. There were no changes to the 21% oxygen mixture.

4.5. Conclusions

This chapter investigated the experimental preburn procedure used in constant volume combustion vessels for thermodynamic state generation. The procedure has been validated for diesel combustion and spray studies. Even though minor species are produced, the levels of minor species are similar to those found in a conventional internal combustion engine running 10-23% EGR prior to combustion. The reactive minor species have insignificant effects on the autoignition of n-heptane as a diesel surrogate, shortening it by 3% relative to dry air, increasing it by 6% relative to air plus residuals (within the modeling accuracy). This study supports that the combustion vessel with the preburn procedure is an effective tool for use in studying spray combustion over various ambient conditions without concern over the reactive minor species produced by the preburn. Furthermore, the differing compositions used in the preburn as part of the ECN, along with different vessel environments do not yield significant variations in specific heats, with all institutions being within 0.1 kJ/kg-K or 7% of each other, with specific heats being representative of an engine running 38.3% EGR. Additionally, the autoignition of n-heptane is similar for the different ambient environments when considering only major species, with a 6% span in ignition delay over all vessels, with the exception of IFP which has the shortest ignition delay, however, the magnitude of this is within modeling accuracy. The different preburn vessels exhibit varying cool-down histories due to fan speeds influencing the flow fields. Trends for peak temperature, NO and NO₂, show Eindhoven having the largest levels, followed by MTU, Sandia and IFP. For OH minor species, IFP has the largest value, followed by MTU, Eindhoven and Sandia. Despite differences in the minor species at injection, the influence of minor species on the ignition delay is minimal with less than 5% spread in ignition delay for the different institutions, with this ignition delay in the preburn environment matching that of ideal EGR at 15% oxygen, being only 4% shorter. Discussion was provided on the modifications which were applied to the Michigan Technological University 0% oxygen environment to improve combustion efficiency and yield more complete combustion to mitigate the presence of diesel combustion in a 0% oxygen (vaporizing) spray environment.

5. Optical Diagnostic Setup & Image Processing Methodology

The optical accessibility of the vessel enables visualization of spray and combustion processes under ambient conditions representative of current technology diesel engines. Robust and effective optical diagnostic imaging setups are required to take advantage of this accessibility. In order for these images to provide information on spray geometry, automated and efficient image processing methods are required to effectively characterize spray behavior including penetration and cone angle. The accuracy and success of image processing of geometric fuel spray characteristics are governed by selecting a method for separation of spray and background levels (Pastor et al. 2007) with this threshold being a key driver for successful image processing.

There are two goals of this chapter. The first is to demonstrate effective and efficient characterization of geometric spray properties including cone angle and penetration using automated computer based processing methods, which includes determining the best indicators for defining effective image processing programs. The second goal is to investigate imaging acquisition setup to characterize key components required to provide the most robust set of images for successful processing. These goals will be satisfied by the following objectives:

- Present and apply different methods and definitions for diesel spray cone angle determination. Provide a recommendation for the best cone angle image processing definition and method.
- Analyze back scatter imaging parameters using two different optical setups and three threshold based image processing programs to characterize optimum threshold choice and necessary characteristics of imaging setups to ensure robust results.
- Review Mie back scatter imaging setup and processing method used in the current research for non-vaporizing, vaporizing, and combusting sprays.
- Review a proposed methodology for improving non-vaporizing spray cone angle determination using Gaussian curve fits to the spray intensity distribution as an improvement to threshold based methodologies, which also has application to CFD models.

5.1. Mie Scattering Optical Diagnostic Imaging Setups

Mie scattering is a useful optical diagnostic for visualizing the liquid portion of the diesel fuel spray. This diagnostic involves illuminating the spray region with a high intensity light source and using a high speed camera to image the light scatter off of the fuel droplets. As this methodology relies on imaging scattered light, it enables visualization of the liquid portion of the spray. To visualize the vapor phase portion of the spray under vaporizing conditions a Shadowgraph or Schlieren technique can be used which relies on density gradients (Settles 2001).

In Mie scatter imaging, various setups can be utilized including a range of light sources, orientations, and cameras. Light sources can include laser sheets or flashlamps depending on the desired wavelength and intensity of light. The main requirement is that the light source be able to effectively scatter off the fuel droplets with enough intensity to provide a high signal to noise ratio (SNR) when imaged with high-speed cameras.

Depending on injector and camera relative orientation, different spray properties from the image can be acquired. In the case of back scattering, as shown in Figure 5.1, which provides a view of the spray looking down the axis of the spray, as the camera and flashlamp are both pointed at the injector tip from the front, this enables determination of parameters of single plumes from a multihole injector including penetration (or liquid length) and cone angle.

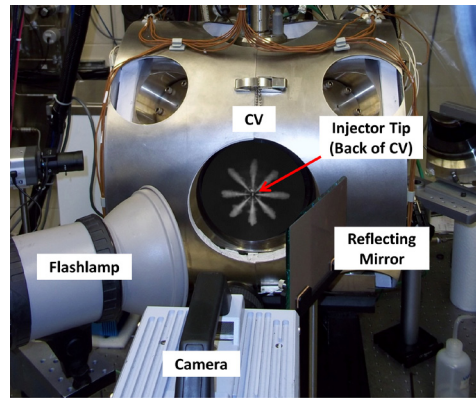


Figure 5.1: Mie back scatter imaging setup with head-on illumination and visualization.

Details on the components used and camera settings for this image acquisition method were provided in Chapter 3.6. A sample image is shown inside the combustion vessel in Figure 5.1.

Mie scattering from the side will yield images with plume overlap from a multi-hole injector, or if used with a single hole injector, spray penetration and cone angle can be resolved as shown in Figure 5.2.

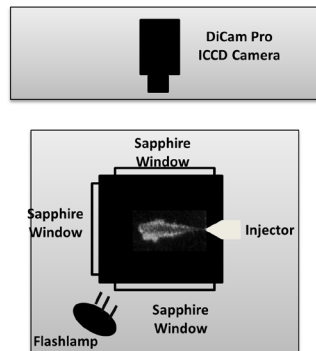


Figure 5.2: Mie scatter setup with side illumination and side view light collection showing the top view of the diagnostic setup. Camera used is Cooke DiCam Pro ICCD with Cooke SensiFlash flashlamp.

A sample image of the fuel spray when visualized using this setup is shown in Figure 5.2.

Another illumination method is the use of a laser sheet or volume to provide the light for scattering. Again, the scattered light intensity from a laser, in this case an Argon ion laser, is collected using a high-speed camera as shown in Figure 5.3. The argon ion laser is a Coherent Innova 90 used at a wavelength of 514.5 nm at 1 W power, with a 38.1 mm biconvex expansion lens. The laser beam is expanded to cover the entire region of the CV optical access, providing illumination for scattering.

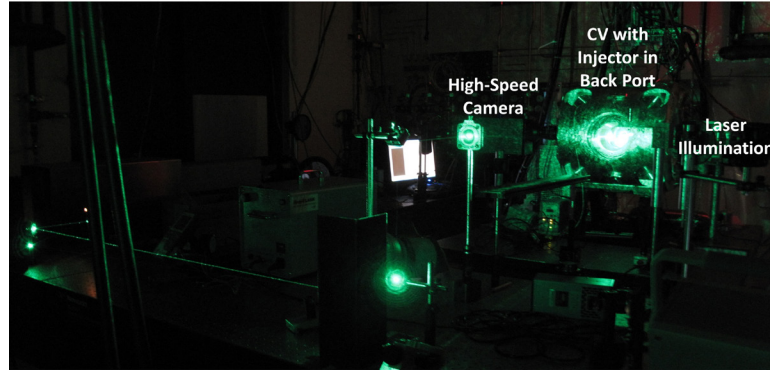


Figure 5.3: Laser scattering setup. Coherent Innova 90 laser at 514.5 nm, 1 W power, with a 38.1 mm expanding lens. High speed camera is Cooke DiCam Pro ICCD in double shutter mode with 60 mm Nikon Micro-Nikkor lens, f-stop 11. A sample image acquired using the laser scattering setup is provided in Figure 5.4.

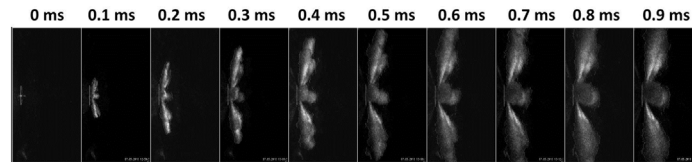


Figure 5.4: Laser scattering image of baseline injector. Diesel spray into nitrogen at 373 K, 34.8 kg/m^3 density, 1700 bar injection pressure, 1.6 ms electronic trigger duration.

This visualization acquires a side view of the spray pattern and therefore plume overlap prevents visualization of all eight plumes individually. This prevents determination of individual spray characteristics, but provides information on the full spray angle.

In addition to the laser volume illumination shown in the above figure, light sheets can also be utilized to highlight and enable visualization of certain spray plumes based on sheet location and orientation. Although different setups are possible, that provided in Figure 5.1 is used in this work based on setup simplicity, component availability, and robustness, along with the ability to resolve each plume of the multi-hole injector. As typical of any optical diagnostic tool, correct and optimal setup of the diagnostic is essential to provide high-quality results enabling the application of robust and versatile processing tools to not only provide efficient solutions, but also yield the most consistent and accurate results.

5.2. Characterizing Cone Angle Definitions and Methodologies

Diesel spray cone angle is an important parameter since as the spray propagates downstream from the injector tip; it entrains air resulting in the spray spreading. This rate of air entrainment and fuel air mixing governs vaporization, combustion and emissions formation and therefore characterizing and accurately qualifying cone angle to understand condition dependency is essential. There are various methods which can be utilized to characterize cone angle, however, there is no one commonly accepted method or definition (Klein-Douwel et al. 2007). Methods include, for example, the angle formed by an isosceles triangle which has the same area and height of the spray or the upstream half of the spray (Naber and Siebers 1996), an angle formed by the spray width at a function of the penetration distance such as one-third penetration (He et al. 2008), 50% penetration (Morgan et al. 2001), or 60% penetration (Pastor et al. 2001). Cone angle can also be defined as the angle formed by the spray width at a distance from the nozzle tip which is a function of the hole diameter for example 60 nozzle diameters (Lefebvre 1989), or the angle formed by an isosceles triangle at the maximum spray width (Senda et al. 2004), or curve fit a line through the upstream contour, or the angle formed by a tangent of the contour, but, the length to which the contour is considered is ambiguous (Klein-Douwel et al. 2007). There are marked differences in the method used for determining the cone angle in regards to choosing to compute the angle at a function of the penetration distance, or at a fixed distance relative to the injector tip location.

The ambiguity and variation in cone angle methods makes comparison amongst literature results and the definitions and values used in models difficult and inconsistent. By using different locations, cone angle results and physical meanings will be different. When considering a constant distance for the location of cone angle calculation there is consistency in location even as the time after start of injection (ASOI) varies, but, the steady region of the spray will move as the spray penetrates. In contrast, when considering the distance for the location of the cone angle as a function of the penetration distance, this location will change as time ASOI changes and can even change for each plume of a multi-hole injector at a constant time ASOI. However, there is the potential to look at the same region of the spray even as time ASOI is changed. In addition to defining this location to where cone angle will be determined, there is also the choice of calculation method which will be used. This can include applying a linear curve fit to the determined spray edge and using the curve fit parameters in angle calculation, or only using end points in the definition of cone angle, as examples. Potential methods for cone angle are now considered. The first option is the calculation of the cone angle based on the projected area of an isosceles triangle formed by the spray width at the given penetration distance (for example 50% penetration as shown here), as defined in Figure 5.5

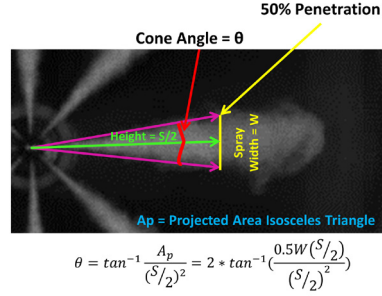


Figure 5.5: Projected area isosceles triangle method for determining cone angle of the spray.

A second option for determining cone angle is similar to the triangle method in that two lines are drawn from the injector tip to the top and bottom of the spray edge respectively at a given distance along the spray. The top and bottom angle formed by these lines from the injector tip to the spray edge are calculated and summed to give total cone angle as outlined in Figure 5.6.

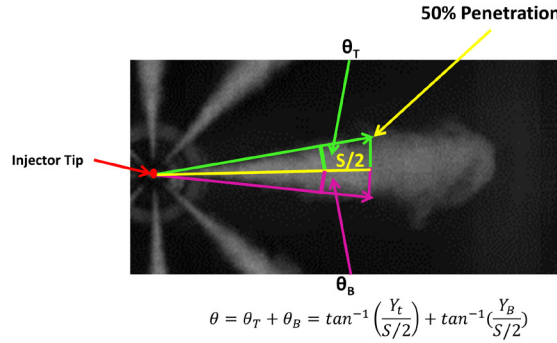


Figure 5.6: Top and bottom cone angle method calculated at spray edge at 50 percent penetration for determining cone angle of the spray.

An additional method for determining cone angle, which is an improvement to that defined in Figure 5.6, is to determine the spray edge from the injector tip to a given downstream distance, 50% penetration in this example, for both the top and bottom of the spray in 1 pixel increments axially along the spray. Two linear curve fits are then applied to the determined spray edge points, top and bottom respectively. The angle formed by these linear curve fits is calculated to define the spray cone angle. This calculation of angle is from the injector tip to the evaluated linear curve fit at the 50% penetration distance, as outlined in Figure 5.7.

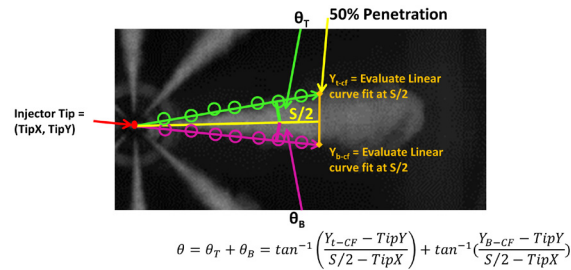


Figure 5.7: Top and bottom cone angle curve fit method calculated by linear curve fit to the spray edge from the injector tip to 50% penetration distance.

The edge of the spray is shown in Figure 5.7 as the spray is traversed axially, as denoted by the circles on the image. In actual processing the edge locations are calculated in 1 pixel increments; only a set of the determined spray edges are shown in the figure for ease of visualization. All three methods considered require definition of the location at which to calculate the cone angle, in this case it was chosen as 50% penetration, but other options are valid including 60% penetration or 60 nozzle diameters as examples.

In order to determine the preferred method, different methods were applied to one set of diesel spray data in Nitrogen to compare results. This analysis is undertaken for sprays at 373 K into 34.8 kg/m³ nitrogen, with a 2000 bar injection pressure and 0.6 ms injection trigger duration, from an 8-hole multi-hole injector nozzle. Images were acquired with a back scattering setup using the Photron SA1.1 high speed camera at 20,000 frames per second, with 1.8 microsecond exposure duration, using the setup shown in Figure 5.1.

From the previous set of cone angle definitions and methodologies, thirteen total methods were chosen and results compared (for the average of all 8 spray plumes), as shown in Figure 5.8. Methods considered include calculating the cone angle using both the curve fit method with the fit being forced through the injector tip location (denoted by CF in the legend) or using the projected area of an isosceles triangle (denoted as Triangle in legend). This is done at various distances including, 30, 45 and 60 nozzle diameters from the injector tip (30Do = 4.2 mm, 45 Do = 6.3 mm, and 60Do = 8.4 mm, respectively), along with at 1/3rd, 50% and 60% of the penetration location. A final method is to calculate the spray cone angle as the angle formed by an isosceles triangle at the maximum width of the spray (Max Width Triangle).

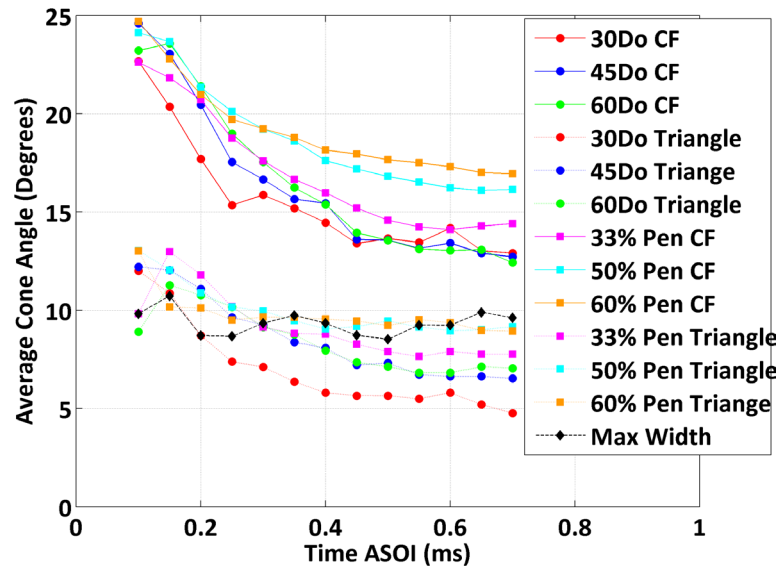


Figure 5.8: Cone angle results as a function of time ASOI for different definitions and methodologies.

As shown in the figure, cone angle results are largely influenced by the method and definition used. Overall, the trend in cone angle is a decrease to a steady-state value. Results are similar, within 0.5 degrees, for the different locations defined as a function of the nozzle diameter (i.e. 30, 45 and 60 D_o) as the spray does not change significantly

close to the nozzle. As the percent penetration distance is increased, from 33 to 60%, the cone angle is increased by 2.5 degrees. This can be explained since as the distance along the spray increases, the cone angle will also increase downstream from the injector tip, due to the progression of air entrainment as the spray propagates. An exception to this is the maximum width methodology whose trend varies attributed to the location at which the spray angle is calculated not being consistent, meaning it is not consistently increasing (percent penetration) nor is it at a fixed value (nozzle diameter location). The method of calculating the angle of a triangle at the maximum width is ideally used to characterize the large scale vortex structures at the spray periphery while assuming that the spray is shaped like an ice cream cone or an isosceles triangle for the cone with a semicircle 'scoop of ice cream' on the top (Senda et al. 2004), as shown schematically in Figure 5.9.



Figure 5.9: Schematic of diesel fuel spray shape, shaped as a cone with a semicircle at the tip.

Although this shape is representative of the majority of the sprays, there are instances where the spray width is larger at regions closer to the nozzle location due to extraneous spray drops causing variations in the representation of this method due to random inconsistencies in spray geometry.

Some key conclusions can be made in regards to the chosen cone angle definition. The triangle method for calculating cone angle typically yields a larger value than the curve fit methodology. The triangle method only considers one set of spray edge points in calculating the cone angle, and the points at this location could be representative of extraneous spray droplets or fluctuations in spray shape, which are not truly representative of the overall geometry, therefore over- or under- estimating the actual overall spray shape. By using the curve fit methodology, the full spray contour is used to calculate the cone angle which minimizes the influence of extraneous data points yielding a more representative value of the mean spray cone angle.

Two methods are chosen for the path forward in calculating spray cone angle both utilizing the linear curve fitting with the maximum location used in the curve fitting being to 60% penetration or 45D₀ curve fitting. The 45D₀ distance is chosen since when the spray just starts and for the case of the liquid core of the vaporizing spray, penetration is reduced so the larger the factor of the nozzle diameter, the further downstream the spray the angle is characterized. This 45D₀ distance of 6.3 mm is far enough from the injector tip where there is background interference, and the spray has also had a 6.3 mm distance to develop. A function of the penetration distance is also chosen for calculating spray angle to understand how the spray cone angle changes as it traverses the chamber, versus that at a fixed distance from the injector hole. Both methods provide different results for cone angle, however, both are useful based on the different physics and characteristics of the spray which they represent. The 45D₀ method characterizes the initial spray development and the gas entrainment processes near the nozzle exit, whereas the 60% penetration distance cone angle is used to characterize the steady state cone angle of the jet.

5.3. Influence of Optical Setup and Image Processing method on Spray Parameter Results

This section discusses the influence of the optical imaging setup and image processing method on the determined spray characteristics of penetration and cone angle for non-vaporizing sprays. The back scattering imaging setup is prepared such that the injector is imaged to provide information on all eight plumes of the injector without plume overlap or interference, with the final setup used being discussed in Chapter 3.6. Here, the influence of optical setup and image processing method on the spray parameter results is studied, using two different image setups in an effort to validate the importance of high intensity and uniform illumination on imaging results and robustness of processing. The main difference between these two setups is the camera which yields variations in imaging conditions and resolution, along with differences in illumination techniques. The light source for scattering was the Cooke SensiFlash, setpoint 8 ms discharge duration, flashlamp. This light source provides illumination for 6 ms which covers the entire injection event, with the injection and imaging delayed relative to the flashlamp (3 ms) to account for the previously characterized and quantified warm-up time of the flashlamp, yielding a steady state luminosity level during fuel injection (Nesbitt 2008).

The first Mie back scattering setup, referred to as *Baseline A* (BL A), involved the Cooke Sensicam QE camera, which acquires 1 frame per image acquisition event. This camera was coupled with a 60 mm Nikon Micro-Nikkor lens, f-stop setting of 5.6. Images were acquired with an exposure duration of 2 microseconds, using a 0.2 ms inter-frame time for each image, at 1376 x 1040 resolution. The second setup, referred to as *Baseline B* (BL B), used the Photron Ultima APX RS high speed camera, with a 60 mm Nikon Micro-Nikkor lens, f-stop setting of 2.8. Images were acquired with an exposure duration of 3.98 microseconds, with a streaming movie acquired for each test condition using a 0.1 ms interframe rate with 512 x 512 pixel resolution. In addition to the camera change, this setup also added a mirror to reflect the flashlamp light to provide more uniform and complete illumination into the CV, as depicted in Figure 5.10.

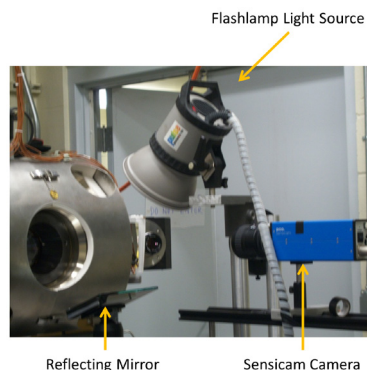


Figure 5.10: Back scattering imaging setup – Baseline B. Cooke camera is shown in setup but reflecting mirror was only used with the Photron camera.

The reflection mirror provides more uniform illumination and ensures more of the flashlamp light is passed into the chamber providing enhanced signal to noise ratio (SNR) and contrast making image processing less threshold dependent. The SNR of spray to background between the two setups was significantly different, having direct influence on the results, with the SNR being improved from an average of 2.3 for the Baseline A setup to 4.4 for the Baseline B setup. SNR is calculated by selecting pixels in the image, both from the background (noise) and the spray (signal) and dividing the signal by the noise pixels. This improvement in illumination uniformity is most evidenced in the spray images, and is also shown here in Figure 5.11 in the background images.

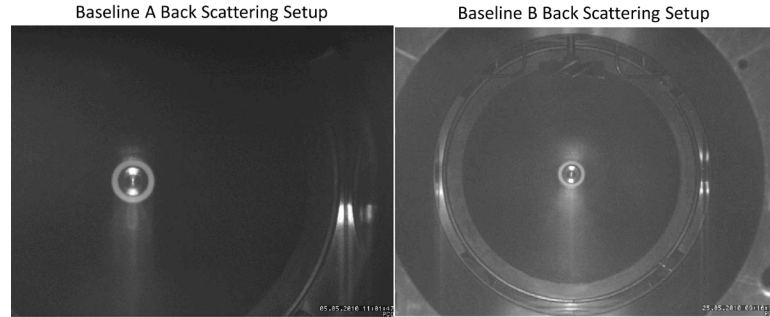


Figure 5.11: Background images for back scattering setup comparison showing improved illumination and larger region of interest in the Baseline B case yielding improved images with higher signal to noise ratio.

In addition to the setup differences already discussed, the image resolution was also different between the Baseline A and B cases with these image processing and setup specifications summarized in Table 5.1.

Table 5.1

Back scattering imaging setup and processing specifications. Differences are underlined>. *Although Baseline B injector images were acquired with a 0.1 ms inter-frame time, results presented here are typically only shown in 0.2 ms increments to match Baseline A image timings.

	Baseline A	Baseline B
Camera	Sensicam – 1 image	Photron – streaming
Camera Lens	60 mm Nikon Nikkor	60 mm Nikon Nikkor
Camera Pixel Resolution	1376 x 1040	512 x 512
Exposure Duration	2 us	3.98 us
F-Stop Used	5.6	2.8
Image Scaling (mm/pixel)	0.13	0.21
Flashlamp Setup	No mirror	Mirror for reflection
Flashlamp	Cooke Senisflash 8 ms discharge	Cooke Senisflash 8 ms discharge
Interframe Time (ms)	0.2	0.1*

Additionally, the Baseline B case captured all 8 plumes of the spray with that of the Baseline A setup only seeing one plume fully in the spray area based on the image region of interest and illumination as shown in Figure 5.11.

5.3.1. Test Matrix

Tests for this imaging setup and processing method study were undertaken at two density and injection pressure conditions for non-vaporizing (nitrogen charge-gas) spray studies, as summarized in Table 5.2. These are the set-point test conditions with the experimental values of density and injection pressure defined in the corresponding sections. The CV was electrically heated to 373 K for all tests using cartridge heaters in two of the window faces. Under this low ambient temperature (373 K) condition, there was minimal vaporization due to the initial boiling point of diesel being 441 K (section 3.4.1), and as a result, this back scattering technique captures all of the spray.

Table 5.2

Set-point test conditions. *Injector electronic drive duration for baseline B was reduced from 1.6 to 1.0 ms to minimize fuel spray impingement on windows.

Density (kg/m ³)	Fill Pressure (bar)	Injection Pressure (Bar)	Injector Drive Duration (ms)
12.3	14	914	0.6
34.8	39	1700	1.0 (BL B)/1.6 (BL A)*

Results are shown in this chapter for the 12.3 kg/m³ density condition, with the 34.8 kg/m³ density results presented in Appendix 12.5.

5.3.2. Back Scattering Image Processing Methods

All images were post-processed in Mathworks MatlabTM to determine parameters of liquid phase penetration and cone angle for the spray, as defined in Figure 5.12. Penetration is defined as the distance from the injector hole (offset 1.5 mm from the center injector tip) to the leading edge of the spray; refer to the right image in Figure 5.12. Cone angle is defined as the angle of an individual spray plume, at 60% penetration distance, using the linear curve fit to the spray edge method.

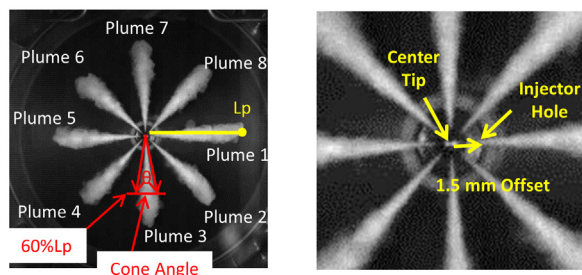


Figure 5.12: Liquid phase spray parameter definitions from back scattering images. The plume penetration parameter determined from the image (L_p) must be scaled by the cosine of 15 degrees to account for the plumes leaving the injector at an angle (refer to Figure 3.17). A zoomed in view of the injector tip is shown in the right image to provide visualization of the reference point for spray parameters as the injector hole, which is offset 1.5 mm from the central injector tip.

For this back scattering imaging since the spray exits the injector at a 15 degree angle relative to the plane through the injector tip (refer to Chapter 3.4.2), the penetration as determined in the image must be scaled accordingly.

The image processing procedure used is outlined in Figure 5.13 with small variations made to this general program for the different methods and imaging setups. This procedure was applied to each image, corresponding to the different times after start of injection (ASOI). Results were determined for each plume of the 8 hole nozzle with presented results representing the average of all 8 plumes. The exception to this is for the Baseline A case in which results are only shown for plume 1 since all other spray plumes cannot be tracked completely due to image resolution and low contrast based on poor illumination without the reflecting mirror. At the start of each test day, and after any major setup changes, a background image is acquired using the same imaging setup but without fuel injection, in the case of baseline A. For the baseline B injector, the background image is frame one of the movie as this corresponds to no spray based on triggering timings.

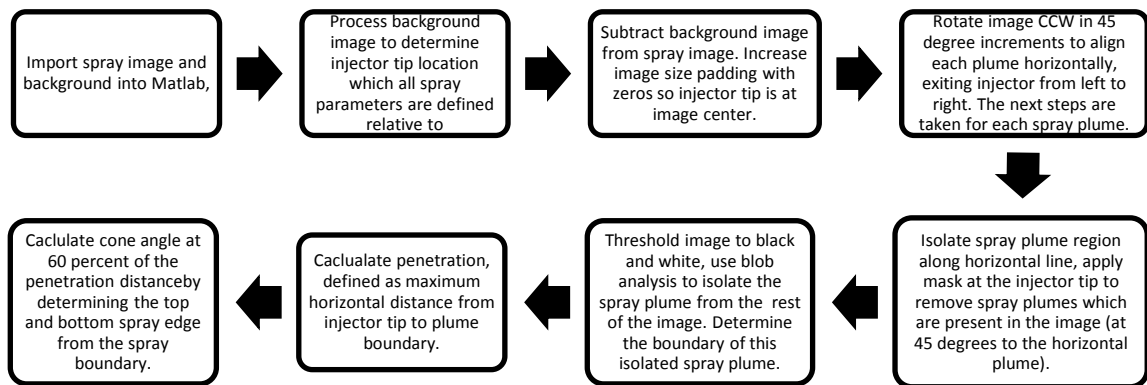


Figure 5.13: Back scattering image processing steps.

Key differences between the *Baseline A* and *Baseline B* methods are the order of the background subtraction and application of a Gaussian filter in the *Baseline A* case for conversion to a black and white image as will be discussed in subsequent sections.

5.3.2.1. Baseline A – Image Processing Method 1 (BL A IP 1)

For Baseline A, Method 1, images were resized first to have the injector tip at the center and then rotated for each spray plume to have the correct orientation. The spray plumes were isolated into rectangular sections with this smaller image having the background image subtracted using a method opposite to that provided in the figure above. An intensity scaling factor was applied to the background image during this subtraction to help normalize the intensity range. The second difference from the aforementioned method is the conversion to black and white. Gaussian filtering was applied to the image, using a 3x3 rotationally symmetric filter with standard deviation of 0.5 to reduce pixel noise, and then the image was converted to black and white using a constant 0.5 threshold, with the final steps to determine spray geometry the same as those presented in the flow diagram.

5.3.2.2. Baseline A – Image Processing Method 2 (BL A IP 2)

Procedure Baseline A, Method 2, followed the same general procedure as Method 1. The Gaussian filter was still applied, however, during thresholding to black and white, the Matlab function `graythresh` was utilized which automatically defines the threshold as

a function of image intensity as opposed to using a constant threshold. This graythresh function chooses a threshold to separate the two classes of pixels in the image, in this case spray and background, which minimizes their intra-class variance (Otsu 1979). The remainder of the processing was identical to method BL A IP 1.

5.3.2.3. Baseline B (BL B)

In the Baseline B image processing method, the procedure used was outlined in Figure 5.13. The image was converted to black and white using the Matlab function graythresh to define the threshold factor as a function of image intensity. No filtering is applied to the image.

5.3.2.4. Method Summary

Key component differences of the three processing methods, BL A IP1, BL A IP 2, and BL B are provided in Table 5.3.

Table 5.3

Key method differences of the three image processing methods.

Method	Key Method Differences
BL A IP 1	Gaussian Filtering, 0.5 Constant Threshold Black and White
BL A IP 2	Gaussian Filtering, Graythresh Threshold Black and White
BL B	No filtering, Graythresh Threshold Black and White

5.3.3. Results & Discussion

Results are presented in the next sections for the 12.3 kg/m^3 ambient density case for these non-vaporizing nitrogen tests using different optical setups and image processing methods. Results for the 34.8 kg/m^3 density case are provided in Appendix 12.5. Results include those from Baseline A image processing method 1 and 2, and from Baseline B, for each density condition, 12.3 kg/m^3 (Case A) and 34.8 kg/m^3 (Case B). Results are then compared to a penetration correlation. Discussion is provided on quantifying the success of the imaging setup and processing method. The BL A image processing methods were not applied to the BL B setups and vice-versa.

5.3.3.1. Case A: 12.3 kg/m^3 Ambient Density, 914 Bar Injection Pressure

The first set of tests involved injection into a 12.3 kg/m^3 ambient nitrogen environment achieved by heating the CV to 373 K and pressurizing to 14 bar, case A. For the Baseline A case the average fill pressure was 14.3 bar and fuel pressure was 924 bar. For the Baseline B case fill pressure was 14.2 bar and fuel pressure was 901 bar. Images from both setups are shown in Figure 5.14, with time ASOI displayed on each image. Scaling and intensity are not preserved in the images.

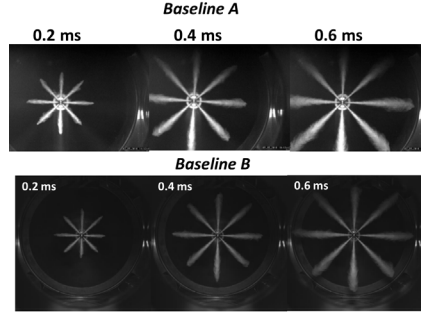


Figure 5.14: Back scattering images – Top set is from Baseline A setup, Bottom set is from Baseline B setup. Time after start of injection is displayed on the image. Conditions are non-vaporizing nitrogen sprays at 373 K temperature, 12.3 kg/m³ ambient density, 914 bar fuel injection pressure with 0.6 ms drive duration.

Results for penetration and cone angle at 60% penetration are presented in Figure 5.15, using the optimum value of threshold choice for each processing method – setup combination. The choice of these optimum thresholds will be discussed in subsequent sections but include a 40% increase in threshold value for Baseline A, Method 1, a 20% decrease in threshold value for Baseline A, Method 2, and a baseline threshold value for the Baseline B case (1.0 factor). The penetration results are compared to the correlation proposed by Naber and Siebers (1996) to predict diesel spray penetration of the spray plume as a function of time ASOI over a wide range of conditions as was discussed in Chapter 2.4.1.1 and is provided here in equation (63).

$$S = \sqrt{\frac{C_v * \sqrt{2} * C_a}{a * \tan(\frac{\theta}{2})}} * \sqrt{\sqrt{\frac{P_f - P_a}{\rho_a}} * d_o * t} \quad (63)$$

The first term in the equation is approximated as a constant with value 2.9 (Naber and Siebers 1996) as injector parameters of velocity and area contraction coefficient are unknown in the current study.

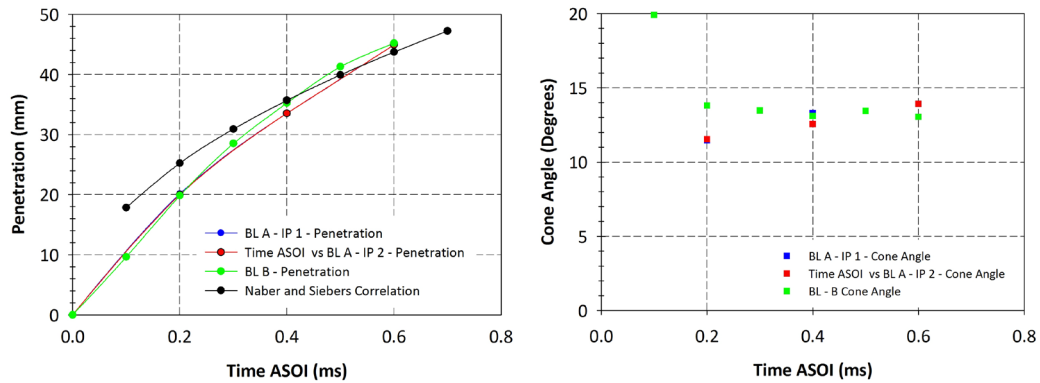


Figure 5.15: Penetration (left) and cone angle (right) as a function of Time ASOI for injection at 914 bar into an ambient environment of 12.3 kg/m³ nitrogen. Penetration data is compared to the Naber and Siebers (1996) correlation.

Choosing the optimum combination of image processing and image acquisition setup for all three test conditions yields similar trends in penetration and cone angle. There is

deviation in penetration results from 0.3 to 0.5 ms ASOI which will be investigated further in subsequent sections. A sensitivity analysis was undertaken on each image setup and processing method combination to understand optimum parameters for data processing, as will be discussed.

In the early times ASOI the fuel spray plume is still being dominated by the liquid being injected, and the above correlation is not yet valid (a linear time dependent correlation does exist however for this region) until there is a transition in the long time limit to the spray being dominated by entrained gas yielding this square root time dependence of the correlation (Naber and Siebers 1996). At this lower injection pressure (914 bar), the break-up time is longer and hence the transition is longer to a square root time dependence as evidenced by entrained gas domination. This time to break-up explains the mismatched trends in the early times ASOI. Additionally, the first term in equation (63) was approximated as a constant per the recommendation of Naber and Siebers (1996), however, the injector used in the current study has a smaller orifice diameter which will influence the velocity and area contraction coefficient parameters yielding changes in the magnitude of the correlation results. Experimental results also show that the cone angle is slightly time dependent (Figure 5.15), and therefore if a non-constant value was used for the first term in equation (63), the magnitude of this term would change as a function of time which would vary the correlations predicted penetration and may provide better agreement between the experimental results and correlation.

5.3.3.2. Baseline A – IP 1

First, the threshold for Baseline A image processing method 1 case (refer to Table 5.3) was increased by 0 to 50% and decreased by 0 to 40% in increments of 10% to understand changes in penetration and cone angle. This threshold was applied in defining the characteristics of the Gaussian filter applied to the image with this image being converted to black and white using a constant 0.5 threshold. Plots were prepared to understand the influence of threshold factor on penetration and cone angle to determine the best choice in threshold for characterizing spray parameters, as shown in Figure 5.16.

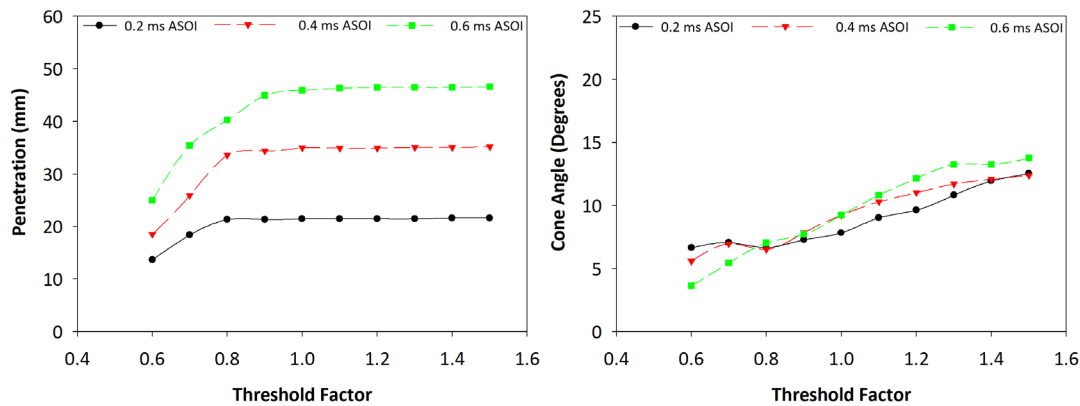


Figure 5.16: Penetration (left) and Cone angle (Right) as a function of threshold factor for BL A IP 1 results.

The choice of threshold is more influential in determining liquid phase cone angle. For penetration, any threshold factor 0.9 or above gives consistent values. However, for cone angle increasing the threshold by 30 to 50% provides more

representative values of cone angle, showing less influence on the choice of threshold. This is also evident in Figure 5.17, illustrating the determined boundary and edges for cone angle as a function of threshold choice, showing that the lower threshold factors miss some of the spray edge, and these larger factors provide a better outline of the entire fuel spray.

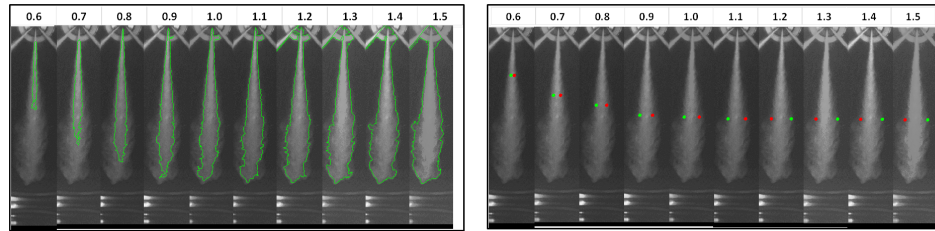


Figure 5.17: Spray boundary (left) and edges for cone angle determination (right) as a function of threshold factor (displayed on image) overlaid on original spray image. These images correspond to Plume 1 0.6 ms ASOI.

The trend of the boundary missing more spray as threshold factor is decreased is counterintuitive but can be explained. In this case, the threshold factor was applied to the Gaussian low-pass 3x3 filter, with the factor changing the filter parameters thereby influencing the image intensity distribution. An increase in threshold factor causes an increase in the magnitude of the 3x3 filter parameters, which results in better noise removal and improved intensity separation between the spray and background. This better separation of spray and background using an increase in threshold factor will yield a smaller portion of scaled intensities less than 0.5, and when applying the standard 0.5 threshold value to convert to black and white (after Gaussian filter application to the image), only small portions of the spray are mistaken to be the boundary when thresholded. Reducing the threshold factor changes the filter parameters such that the intensity distribution range is smaller. The images confirmed that reductions in the threshold factor cause spray to be missed, whereas increasing the threshold factor by 30 to 50% permits the entire spray boundary to be found providing more accurate penetration and cone angle results. A 40% increase in threshold factor was chosen at the optimum for this combined best setup and image processing method.

5.3.3.3. Baseline A – IP 2

Further investigation was undertaken for the Baseline A setup by modifying the image processing method to utilize a threshold value determined automatically as a function of image intensity levels as opposed to a constant value threshold which accommodates test to test intensity and signal to noise ratio variations. This included modifying the processing program such that the factor was applied to the choice of threshold, based on Matlab's `graythresh` function, to convert an image to black and white as opposed to being applied to the Gaussian filter used to prepare the image for thresholding. Plots are provided in Figure 5.18 to understand the influence of threshold on penetration and cone angle to see if there was a leveling off in threshold factor signifying the best choice in threshold for determining these results.

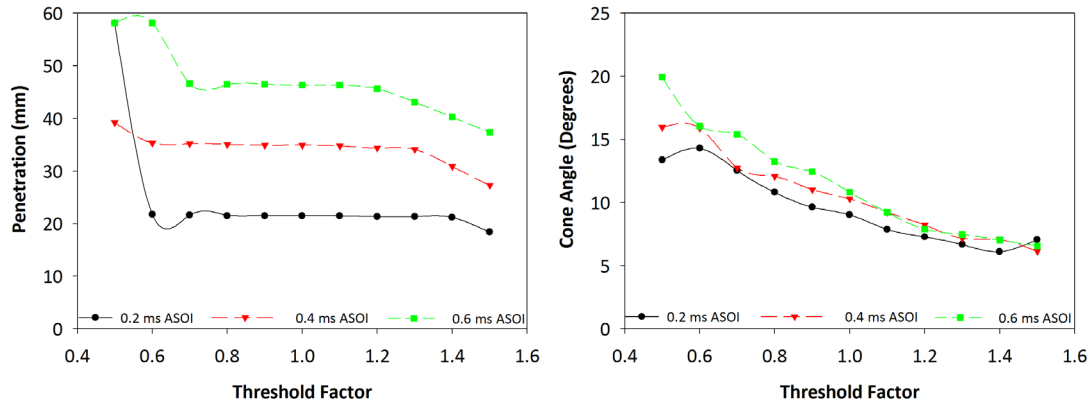


Figure 5.18: Penetration (left) and cone angle (right) as a function of threshold factor for setup Baseline A, image processing method 2.

Penetration is constant as a function of threshold factor with the exception of the extreme cases of 40 - 50% decrease or increase in threshold factor showing that penetration is minimally influenced by the threshold choice. However, variation was more significant when considering cone angle results, similar to BL A IP 1. At the largest decrease cases there was significant error as the spray was largely overestimated, mistaking the background for the spray for the 40 - 50% (0.6 - 0.5) decrease cases. This is confirmed by images in Figure 5.19 which show the fuel spray plume for 0.6 ms ASOI with the background and cone angle edges overlaid.

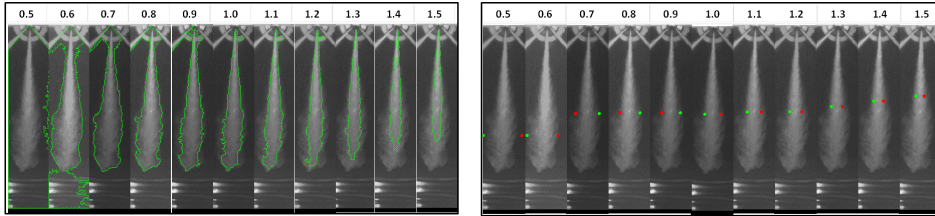


Figure 5.19: Spray boundary (left) and edges for cone angle determination (right) as a function of threshold factor (displayed on image) overlaid on original spray image. Images correspond to 0.6 ms ASOI.

For increases in threshold, namely 30 to 50% (1.3 - 1.5) increases in threshold choice, the values fall off for penetration and cone angle as a function of threshold factor showing that spray was being missed in these images. The optimum value was seen at a leveling in penetration which occurred for the 10 to 20% (0.9 - 0.8) decrease in threshold range. Consequently, the 20% (0.8) decrease case was chosen as optimum for this combination of image setup and processing method.

5.3.3.4. Baseline B

For the Baseline B case the threshold used to convert the image to black and white was increased and decreased by 0 to 50% in 10% increments. This factor was applied to the threshold determined using the graythresh function in Matlab. Plots in Figure 5.20 are shown to characterize the influence of threshold on penetration and cone angle to determine if there is a leveling point in threshold which would signify the optimum threshold for studying these geometric spray characteristics.

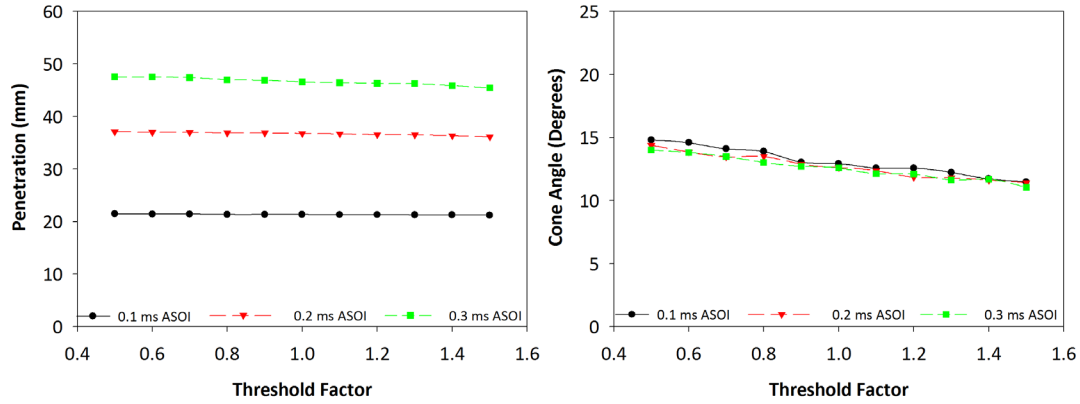


Figure 5.20: Penetration (left) and cone angle (right) as a function of threshold factor for setup Baseline B.

For penetration, the full range of threshold factors gave consistent results. At the highest factors of 40 to 50% increase, penetration decreased slightly but this change was within the resolution and accuracy limits of the system. These plots show that Baseline B penetration results were insensitive to choice of threshold over a wide range. This was further confirmed by the images in Figure 5.21 which show that all thresholds consistently caught the entire spray region, which was possible based on the high quality and SNR of the images. Cone angle decreases slightly as the threshold factor is increased, however, the change is minimal compared to the other methodologies.

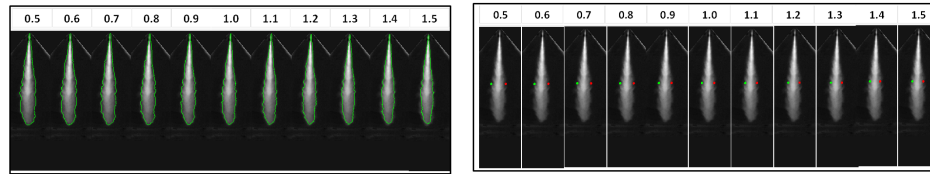


Figure 5.21: Spray boundary (left) and edges for cone angle determination (right) as a function of threshold factor (displayed on image) overlaid on original spray image. These images correspond to 0.6 ms ASOI.

There was close agreement in penetration between all threshold factors showing the minimal sensitivity of results to imaging thresholding. The Baseline B case showed an improved image setup and processing method, due to higher image contrast and SNR, which was less sensitive to image threshold. The choice of threshold was the baseline threshold factor of 1.0 in this case as results were largely insensitive to threshold.

5.3.4. Summary on Threshold Influence on Penetration and Cone Angle

The objective of this study was to characterize three different combinations of imaging setup and processing methods to understand the preferred and most robust setup and processing method for spray characterization. The combined results are shown in Table 5.4 and Table 5.5, for tests at 12.3 kg/m^3 and 34.8 kg/m^3 ambient density, respectively. These results include the magnitude of a change in penetration and cone angle for a corresponding percentage increase or decrease in threshold, as specified.

Table 5.4
Summary of the impact of threshold factor on penetration and cone angle results,
for 12.3 kg/m³ ambient density.

	Threshold Change (%)	Magnitude of Penetration Change (mm)			Magnitude of Cone Angle Change (Degrees)		
Time ASOI (ms)		0.2 ms	0.4 ms	0.6 ms	0.2 ms	0.4 ms	0.6 ms
BL A, IP 1	40% ↓	7.8	16.4	20.9	1.2	3.6	5.6
	50% ↑	0.1	0.2	0.7	4.7	3.2	4.5
BL A, IP 2	40% ↓	0.3	0.4	11.8	5.3	5.6	5.2
	50% ↑	3.1	7.6	9.0	2.0	4.1	4.3
BL B	40% ↓	0.1	0.2	0.9	1.7	1.2	1.2
	50% ↑	0.1	0.7	1.1	1.4	1.2	1.5

Table 5.5
Summary of the impact of threshold factor on penetration and cone angle results,
for 34.8 kg/m³ ambient density, injection pressure of 1700 bar.

	Threshold Change (%)	Magnitude of Pen. Change (mm)					Magnitude of Cone Angle Change (Degrees)				
Time ASOI (ms)		0.2 ms	0.4 ms	0.6 ms	0.8 ms	1.0 ms	0.2 ms	0.4 ms	0.6 ms	0.8 ms	1.0 ms
BL A, IP 1	40% ↓	3.8	8.9	14.4	18.1	21.9	5.7	8.1	7.0	7.2	8.3
	50% ↑	0.3	0.3	0.5	0.3	3.0	2.9	6.2	2.8	2.7	3.4
BL A, IP 2	40% ↓	0.4	0.3	0.5	13.3	5.4	3.9	5.3	4.1	5.7	1.2
	50% ↑	1.6	1.7	6.2	7.0	14.1	4.0	8.0	2.0	3.1	5.8
BL B	40% ↓	0.1	0.1	0.1	0.4	0.2	1.4	1.2	1.3	1.6	2.1
	50% ↑	0.1	0.3	0.5	1.1	2.0	1.4	1.8	1.7	1.9	1.4

The magnitude of penetration and cone angle change were consistently smallest for the Baseline B injector setup and image processing method, relative to that of the Baseline A IP 1 and IP 2 setups and processing methods. As shown in Table 5.4, the average change in penetration was 0.4 mm for the 40% decrease and 0.6 mm for the 50% increase case for the BL B method. Similarly, cone angle changed on average 1.4 mm for either a 40% decrease or 50% increase for the BL B method. This is small compared to the change in penetration of an average 4.2 mm for a 40% decrease and 6.6 mm for an increase of 50% for the BL A IP 2 case, being 5.4 degrees and 3.5 degrees for a 40% decrease and 50% increase in threshold factor, for cone angle. For the BL A IP 1 case, the change in penetration is an average 15 mm for a 40% decrease, and 0.2 mm for a 50% increase, and a change in average cone angle or 4.3 degrees for a 40% decrease and 4.1 degrees for a 50% increase. Similar magnitude of changes in cone angle and penetration are seen in Table 5.5 for the 34.8 kg/m³ density case. Cone angle is more largely influenced by threshold as expected based on the axial variation of intensity at the spray edge. This signifies that both the setup and image processing method for BL B is improved and more robust, and will be used in all testing.

Key conclusions are:

- Liquid phase cone angle results are largely dependent on imaging setup and processing method.

- Optimum thresholding parameters are a 40% increase for BL A IP 1, 20% decrease for BL A IP 2, and a baseline threshold factor of 1.0 for the BL B setup. To reiterate, the BL A image setup did not include a reflective mirror, with both image processing methods using a Gaussian filter, with the IP 1 method using a constant 0.5 factor for thresholding to black and white, and the IP 2 method using Matlab's graythresh method for determining the black and white threshold. The BL B method includes the reflecting mirror in the image acquisition method, and used no filtering and Matlab's graythresh to define the black and white threshold factor.
- Liquid phase penetration results are less dependent on imaging setup and processing method, showing smaller magnitude changes, relative to cone angle, when considering threshold dependence.
- High SNR optical setups, that provided by the Baseline B setup here including the reflecting mirror, yield more robust images improving image processing methods by making them less threshold dependent. The SNR for the BL B setup was 4.4 compared to a SNR of 2.3 for the BL A setup.
- Sensitivity analyses on image processing thresholds are a good indicator of the success of the processing method and help define a robust threshold choice.
- The optimum and most robust setup and processing method is one with a high SNR, uniform illumination, using an automatically chosen threshold value based on image intensity distribution without any prefiltering to the raw image. This is defined based on the results from the BL B injector.

Liquid phase spray parameters are influenced by the optical setup and image processing method and hence developing robust, threshold-independent image processing methods although challenging is imperative to ensure accurate determination of spray parameters. Based on the above analysis, the final image acquisition setup and processing methodologies were developed. The chosen image acquisition setup of Mie back scattering was previously discussed in Chapter 3.6, which is based on the BL B setup. Note that relative to the BL B setup here, the mirror position has been changed, with no detrimental influence on imaging quality or SNR. This change was undertaken based on the use of a different camera and hence different constraints on optics placement. Specifics on the image processing methods used for the three ambient environments will now be discussed, with slight modifications relative to the original BL B processing methodology.

5.4. Processing Methods for Mie Back Scatter Images

The image processing methodology is similar to that which was used in the BL B method and over the three ambient environments, with small modifications, as will be discussed. Parameters of interest include spray penetration and cone angle at both 60% penetration and 45D₀ for nonvaporizing sprays, along with penetration and mean quasi-steady liquid length for vaporizing sprays, and for combusting sprays parameters include flame length, lift-off length, cone angle, and total plume intensity. The spray parameters are determined in pixels, and are converted to millimeters using the known scaling of

0.18 mm per pixel, further scaled by the cosine of 15 degrees to account for the off-axis orientation of the spray plumes relative to the injector plane. All image processing was undertaken in MathworksTM Matlab, version 7.10.0 (R2010A).

5.4.1. Nonvaporizing (Nitrogen Sprays)

Non-vaporizing sprays are sprays in nitrogen, and with the minimal vaporization at the 373 K temperature, the Mie back scattering diagnostic enables visualization of the full spray plume. Spray parameters of interest are penetration and cone angle as defined in Figure 5.22.

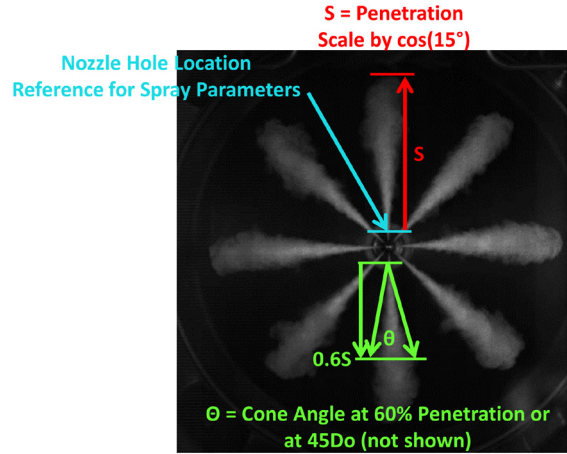


Figure 5.22: Spray penetration and cone angle definitions for nonvaporizing sprays.

The image processing procedure to determine these parameters involves several steps, with this procedure being applied to all spray frames from the movie, and parameters determined for each plume of the 8 plumes from the spray. Select tests were undertaken at higher frame rates and reduced regions of interest, which then looked at just one of the spray plumes. For these cases, spray parameters are determined only for the 1 plume, but the same overall methodology is used.

Image processing first involves reading in the movie into Matlab, and converting it from a .avi to a .mat file. The first frame of the movie is the background image which is used to define the location of the injector tip, with all spray parameters referenced to the nozzle hole, offset 1.5 mm from the injector tip. The background image is normalized so intensity spans the range from 0 to 1, and the intensity contrast is adjusted by using Matlab's *imadjust* procedure by mapping the image intensity values to the full range of available intensities based on image bit count (256 counts). The image is then converted to black and white using Matlab's *graythresh* procedure, with blob analysis undertaken to define properties of the regions of interest to effectively find the location of the central injector tip. With known injector tip location, the spray images are subsequently processed.

First, the background is subtracted from the spray images to yield images of the spray isolated from the background. For each frame, the image is first resized so that the injector tip is at the center of the image, and rotation occurs next in 45 degree increments so that the spray plume exits the injector from left to right. The rotated image region of

interest of the spray is isolated, and further masked to remove the adjacent spray plumes as shown in Figure 5.23.

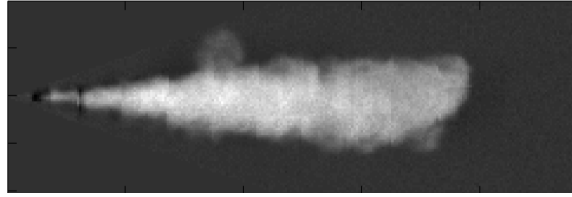


Figure 5.23: Background subtracted, rotated, cropped, and masked nonvaporizing spray image.

Next, the masked spray image is normalized by the maximum intensity so the intensity ranges from zero to one, and this normalized image is converted to black and white by Matlab's *graythresh*, with any extra noise being removed as shown in Figure 5.24.



Figure 5.24: Black and white spray image used for boundary tracing and spray property analysis.

The boundary of the black and white spray is traced, which is used to define the spray properties as shown in Figure 5.25.

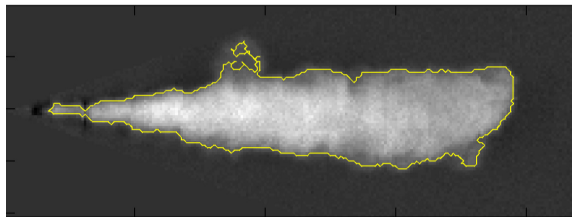


Figure 5.25: Original masked spray image with traced boundary overlaid.

Penetration is defined as the leading edge of the boundary. The spray width is determined from the boundary over the region of interest, which is used to calculate the spray cone angle, as shown in Figure 5.26.

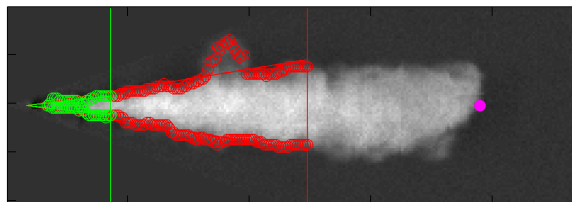


Figure 5.26: Spray edge definition and linear curve fits for calculating cone angle. Green lines and symbols define the cone angle at $45d_0$, red defines the cone angle at 60% penetration, and the magenta circle at the tip of the spray defines the determined penetration.

Figure 5.26 shows the determined penetration and spray edge used in the curve fit for calculating the cone angle.

The example figures shown here are those for one plume from one spray, however, the same procedure is applied to the other plumes in each frame by applying 45 degree image rotation to process each spray plume exiting the injector horizontally from left to right, and the same procedure applied for each frame of the entire movie to understand spray properties as a function of time ASOI.

5.4.2. Vaporizing (0% Oxygen Sprays)

Processing of the 0% oxygen (vaporizing sprays) is similar to that of the nonvaporizing sprays, with the parameter of mean steady state liquid length being determined. The cone angle and liquid penetration are defined identical to those shown in Figure 5.22. Although cone angle is processed, results are not presented here based on the difficulty in accurately resolving the cone angle based on the small spray width due to vaporization.

The image movies are read into Matlab in .avi format, and converted to .mat format. The background image (frame 1) is first processed to determine the location of the central injector tip. This involves normalizing and improving contrast of this image (using functions discussed in section 5.4.1), and converting it to black and white. Using blob processing, the location of the central injector tip is calculated. Next, background subtraction is applied to each frame of the spray image. The background subtracted spray frame image sizes are increased such that the injector tip is in the center of the image, and the image is subsequently rotated so that each plume exits the injector from left to right. The plume is further isolated and masking is applied to remove adjacent spray plumes to prevent interference. The image is normalized and subsequently thresholded to black and white, with blob analysis being undertaken to isolate the spray region from any background noise. The spray boundary is traced which is then used in defining penetration and cone angle of the spray as shown in Figure 5.27.

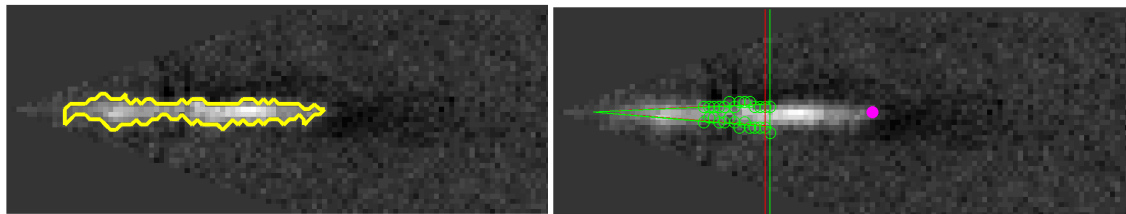


Figure 5.27: Vaporizing spray analysis, left image shows traced spray boundary and right image shows determined cone angle (green is at 45° , and red is at 60% penetration), with magenta circle at the spray tip denoting penetration.

It must be noted that as will be shown in images in Chapter 6.2, there are slugs of fuel which detach from the leading edge of the liquid spray under these vaporizing conditions. These are not considered in the image processing as the fuel spray being processed is defined as the continuous portion of fuel propagating from the injector tip.

Also of interest is the determination of the mean steady state liquid length. The liquid length in this case is the same as the penetration as the liquid portion is all that is being imaged with the Mie back scatter imaging diagnostic technique. Of interest, however, is the mean steady state liquid length (actually quasi-steady based on fluctuations). This is determined during the middle of the injection event, 1 to 2 ms

ASOI for the vaporizing spray cases (as injection duration was constant), and is the mean of the determined liquid length during this interval.

5.4.3. Combusting (21% Oxygen Sprays)

The 21% oxygen combusting spray cases were processed in a similar manner as the nonvaporizing and vaporizing spray cases. Parameters of interest, however, are different. This includes flame length (similar to penetration in the nonvaporizing spray), lift-off length (distance from the injector tip to the lifted flame), cone angle of the flame, and total combusting flame intensity. These parameters are defined in Figure 5.28.

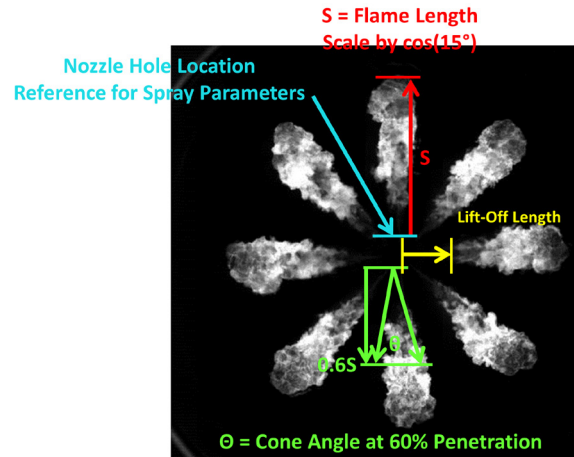


Figure 5.28: Combusting parameter definitions of combusting flame length, cone angle, and lift-off length.

The movie is first read into Matlab in the .avi format and converted to the .mat format. The method to determine the injector tip location is different in these combusting cases since the light intensity without combustion is significantly reduced based on a change in f-stop to avoid camera saturation during the high-intensity combustion luminosity. As opposed to using the background the image, a frame where the combusting spray has developed is chosen, and is normalized and thresholded to black and white. Blob analysis is undertaken to determine the centroid location of each of the eight plumes. Lines are then drawn from centroid to centroid of opposing spray plumes, with the midpoint being determined in regards to both X and Y coordinates. The X and Y location of the injector tip is then defined as the mean of all the X midpoints, and the mean of all the Y midpoints. This procedure including lines from plume midpoints and the intersections is shown in Figure 5.29.

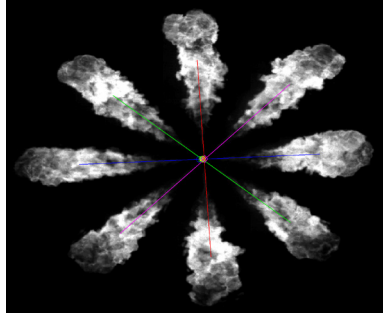


Figure 5.29: Injector tip location determination.

With the injector tip location known, the injector hole location, which is the reference for all parameters is determined based on a 1.5 mm offset from the central tip.

Subsequent frames of the movie are processed to determine the combustng spray parameters of interest. This includes first resizing the image so that the injector tip is in the center followed by image rotation in 45 degree increments for the correct plume orientation. The plume of interest is isolated and masks are applied to adjacent combustng plumes, with this image normalized and thresholded to black and white for further processing. Blob analysis is undertaken to locate the region of the combustng plume, over which the boundary is traced and the leading edge of the boundary relative to the injector nozzle hole defines the flame length. The boundary of the combustng spray is also used to define the spray edge to 60% penetration, which is then curve fit to define the combustng flame cone angle as shown in Figure 5.30.

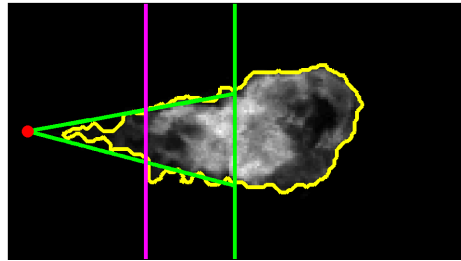


Figure 5.30: Combusting image processing methodology. Green lines show cone angle at 60% penetration (the spray edge points are not shown), yellow shows the combustng flame boundary, red circle shows the location of the nozzle hole, and the magenta line defines the location of the lift-off-length.

Cone angle at $45D_0$ is not considered in this case as the $45D_0$ distance, 6.3 mm, is typically less than the lift-off length (LOL) and therefore cannot be determined. Another parameter included in the figure above is the lift-off length (magenta vertical line), which is the location of the lifted flame from the injector nozzle hole. This is determined by calculating the intensity radially across the spray in 1 pixel increments traversing the spray axially. A threshold total radial intensity is defined, which is 10% of the maximum radial intensity, and the first axial location where the summed radial intensity exceeds this threshold is the defined lift-off length, as shown in Figure 5.31.

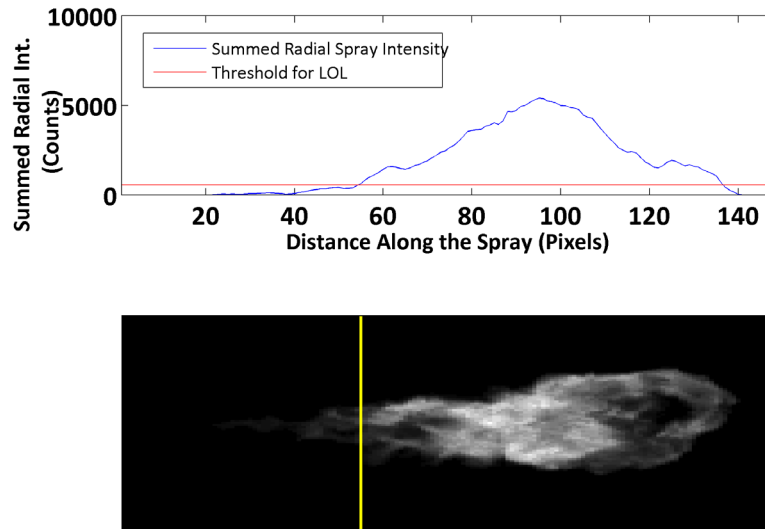


Figure 5.31: Lift-off length methodology. Top figure shows the summed radial intensity as traversing axially along the spray, along with the lift-off length threshold. Bottom image is the combustive spray plume with the determined lift-off length denoted by the vertical yellow line.

The final parameter of interest is the total intensity of the combustive spray plume. As camera saturation is minimized, and camera settings are kept identical in regards to exposure duration, location, and f-stop, this total intensity can be used to provide an indication of relative levels of soot oxidation between test conditions and spray plumes. This is determined by summing the intensity of all pixels which are determined to be inside the calculated spray boundary, providing a total intensity value in counts.

5.4.4. Gaussian Image Processing Method

A novel image processing methodology has been proposed which involves fitting Gaussian curves to the spray intensity distribution at radial cross-sections, using curve fit parameters to define the spray edge, which are then used in calculating the spray cone angle. This method has been shown to be more robust than conventional thresholding methodologies. A sample application is provided here for non-vaporizing sprays, with the full application accepted for publishing in the ASME ICED Fall Technical Conference Proceedings, after paper presentation at the October 2011 conference (Paper Title: Characterizing Diesel Fuel Spray Cone Angle from Back-Scattered Imaging by Fitting Gaussian Profiles to Radial Spray Intensity Distributions; Co-Authors: Jeffrey D. Naber and Seong-Young Lee; Paper number 60034).

Images are processed using the same method discussed in 5.4.1, with a change being applied to the cone angle method. At each pixel axially along the background subtracted spray, from 12 to 45 nozzle diameters relative to the injector tip, the intensity distribution of the spray cross section is determined. The intensity data from the cross section is curve fit to a Gaussian function, as defined in equation (64). Only intensity data greater than zero, for which the intensity is always decreasing relative to the centerline, is included in the curve fit to ensure accurate results.

$$I = A \cdot \exp\left(-\frac{(Y - \mu)^2}{2\sigma^2}\right) + I_{\text{Offset}} \quad (64)$$

This curve fit is applied in 1 pixel increments along the spray axis, with curve fit parameters being defined. An example of the curve fit applied to spray intensity distribution data is provided in Figure 5.32.

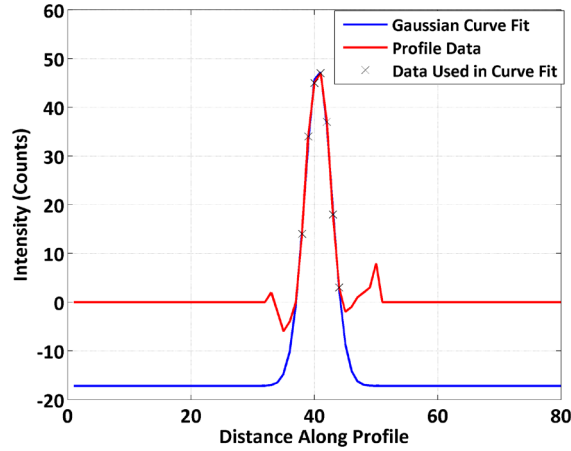


Figure 5.32: Example of Gaussian curve fit to spray intensity distribution data.

The curve fit parameters are used, in conjunction with the intersection of the curve fit with intensity equal to zero, to define the sigma which corresponds to the intensity zero condition, which effectively defines the spray edge. The sigma of the curve fit in equation (64) cannot be used directly because of the intensity offset in the equation. These parameters, along with the location of the centerline, define the spray edge. The determined spray edges from the Gaussian curve fit are curve fit using a linear fit (as was discussed in section 5.4.1) to define the cone angle of the spray. In this curve fitting, only parameters determined from acceptable Gaussian curve fits, as defined by a normalized root-mean square error less than 5%, are included in the cone angle curve fit. This method is successful in defining the spray edge based on the total spray intensity distribution as opposed to considering the spray edge at the low SNR outskirts.

5.5. Summary

This chapter reviewed different Mie scatter optical setups, and discussed the importance of high signal to noise ratio and optimum setup to yield the most robust results with minimal influence on the results due to image processing. Also reviewed were various image processing methodologies, with again the most robust method being defined, including sensitivity studies undertaken to define a metric for optimum procedure of both image acquisition and processing. To summarize, the best image acquisition setup involves using a flashlamp which is directed partially onto a mirror, with the remaining directed into the chamber. The mirror will reflect the light to illuminate the remainder of the chamber, which will provide uniform illumination, and also high signal to noise ratio. In regards to processing methods, the most robust program involves no filtering (acceptable because of the high SNR images), and thresholding to black and white using Matlab's graythresh function, which defines the threshold based on image intensity distribution. The image processing methodologies used on the current set

of non-vaporizing, vaporizing, and combusting charge-gas environments in the current work were also reviewed and key parameters of interest defined. Finally, a Gaussian based curve fitting methodology was presented for cone angle calculations, which is shown to be more robust and less subjective than standard methodologies in determining cone angle.

6. [†]Macroscopic Spray Characteristics and Plume-to-Plume Variations

Diesel fuel injectors in production engines consist of multiple holes to provide multiple spray plumes enhancing the in-chamber fuel distribution. Each fuel spray plume will: mix with the charge-gas, vaporize, and combust converting fuel energy to useful power, working to propel the vehicle while also producing detrimental emissions. The fuel-air mixing largely governs the resulting combustion and emissions formation making understanding spray behavior imperative, especially the plume to plume variations and trends. These variations were investigated using the optical setup discussed in Chapter 3.6 with the image processing methods discussed in Chapter 5.4.

Understanding diesel spray and combustion characteristics is important to enhance the fundamental knowledgebase of these behaviors, including parameter dependencies. In particular, studies using multi-hole nozzles are imperative as a large portion of diesel spray studies consider only single-hole nozzles and therefore lose vital information on spray plume variations and interactions, as touched on in Chapter 2.3.5. Furthermore, the knowledge gained from these experimental studies is used to provide data for computational fluid dynamics (CFD) model development, along with tuning and validation. This work is also part of a larger experimental study, coupled with CFD modeling, to investigate the influence of nozzle characteristics on spray, combustion, and soot characteristics.

The goals of this chapter are to characterize diesel spray behavior, including plume to plume variation and trends in spray and combusting flame characteristics, and to provide hypotheses for this behavior. These characteristics include penetration and cone angle for non-vaporizing sprays; penetration and mean steady state liquid length (mean SS LL) for vaporizing sprays; and flame length, cone angle, lift off length and total intensity for combusting spray flames. Cone angle was not characterized for vaporizing sprays due to the reduced width of the vaporizing liquid portion of the spray and limits in image resolution. These goals will be achieved through various objectives:

- Characterize non-vaporizing (nitrogen) diesel sprays plume to plume variations for:
 - Three repeat tests to understand the consistency of plume to plume variations.
 - A fuel injection pressure sweep of 1034 to 2000 bar.
 - A reduced fuel temperature (321 to 328 K).
 - A reduction in charge density (34.8 kg/m^3 to 17.4 kg/m^3).
- Characterize vaporizing (0% oxygen) diesel sprays plume to plume variations for:
 - Inclusion of ILASS conference paper which includes discussion of:
 - Three repeat tests to understand the consistency of plume to plume variations.

[†]Section 6.2.1 of this chapter was previously published in the *ILASS 2011 Conference Proceedings*. Permission for reproduction is provided in appendix 12.1.2.

- A charge temperature sweep of 800 to 1300 K.
 - A fuel pressure sweep of 1034 to 2000 bar.
 - A reduced fuel temperature (355 to 363 K).
 - A reduced charge density (34.8 kg/m^3 to 17.4 kg/m^3).
- Characterize combusting (21% oxygen) diesel sprays plume to plume variations for:
 - Two repeat tests to understand the consistency of plume to plume variations.
 - A charge temperature variation of 950 to 1100 K.
 - A fuel pressure sweep of 1034 to 2000 bar.
 - A reduced charge density (34.8 kg/m^3 to 17.4 kg/m^3).

Not all results from the above objectives are included in this Chapter. The results which are not included in Chapter 6 are provided in Appendix 12.6.1 for non-vaporizing sprays, Appendix 12.6.2 for vaporizing sprays, and Appendix 12.6.3 for combusting sprays.

6.1. Non-Vaporizing Sprays

Non-vaporizing spray studies consist of injecting diesel fuel into 373 K nitrogen. Various tests were undertaken in nitrogen including three repeatability tests, a fuel injection pressure sweep (1034, 1379 and 2000 bar), a reduced fuel temperature (achieved by the injector chiller) and a variation in charge density (34.8 kg/m^3 to 17.4 kg/m^3). Understanding plume to plume variations of non-vaporizing diesel fuel sprays is important as it assists in characterizing the behavior of the spray as a whole as there is no vaporization. This implies that the full spray is present in the image, i.e. all of the sprays momentum as a result of fuel injection. The complete test matrix used for these tests is provided in Table 6.1.

Table 6.1
Non-vaporizing sprays test matrix.

Ambient Density (kg/m^3)	Fuel Pressure (bar)	Injection Trigger Duration (ms)	Fuel Temperature ($^{\circ}\text{C}$)	Temperature at Injection (K)
34.8	1034	0.8	90	373
34.8	1379	0.8	90	373
34.8	2000	0.8	90	373
34.8	2000	0.8	90	373
17.4	2000	0.6	90	373
34.8	2000	0.8	82	373
34.8	1379	0.8	82	373
34.8	1034	0.8	82	373

Select results are provided in the main body of the chapter, with the remainder, along with discussion on plume-to-plume variations as a function of time ASOI for each test, provided in Appendix 12.6.1.

6.1.1. Injection Pressure Sweep - Chiller Off – 328 K Fuel Temperature

Test conditions for the injection pressure sweep test with the chiller off are summarized in Table 6.2. Injection was for 0.8 ms trigger duration (1.4 ms fuel injection duration).

Table 6.2
Injection pressure sweep test conditions, chiller off.

	Injection Pressure (Bar)	Density (kg/m ³)	Ambient Pressure (Bar)
1034 Bar	990	34.9	38.6
1379 Bar	1370	34.7	38.5
2000 Bar	1975	34.8	38.6

Variation in test conditions of ambient pressure and density were minimal and therefore the images will depict solely the influence of injection pressure, as shown in Figure 6.1.

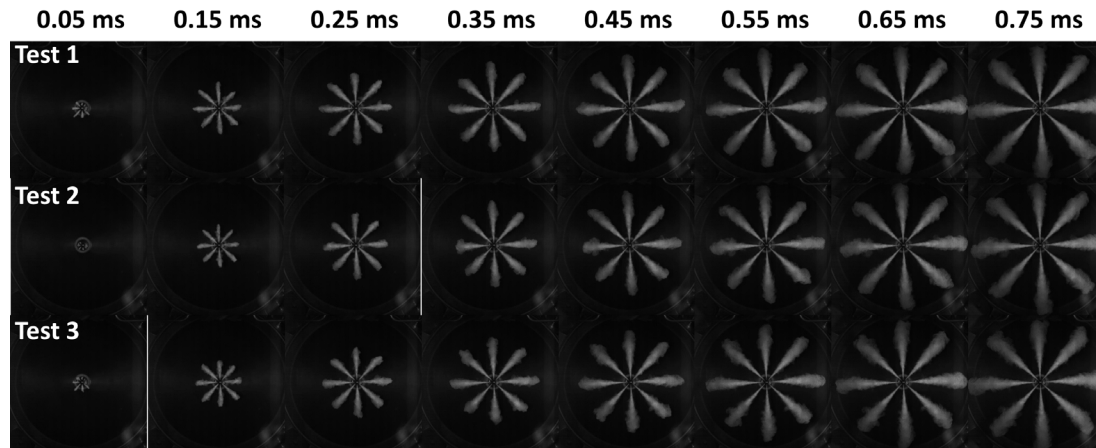


Figure 6.1: Diesel spray images from injection pressure sweep tests, 34.8 kg/m³ Nitrogen, 1034, 1379 and 2000 bar injection pressures, chiller off (328 k fuel temperature).

As injection pressure increased, spray penetration increased, with cone angle trends being difficult to deduce from the images. The magnitude of the influence of injection pressure on cone angle was quantified by image processing of the spray images. Median penetration over all 8 plumes for the three injection pressures investigated with the chiller off is shown in Figure 6.2.

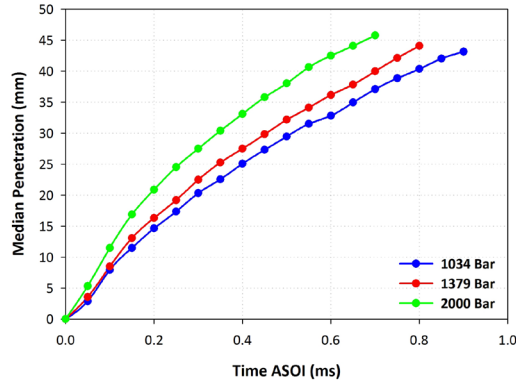


Figure 6.2: Median penetration as a function of time ASOI for three different injection pressures, chiller off.

As the time ASOI increased, medium penetration increased as the spray is into nitrogen and conditions are nonvaporizing. As injection pressure increased, penetration increased, expected based on literature (Naber and Siebers 1996). The increase in penetration is an average of 10% for an injection pressure increase from 1034 to 1379 bar, and 40% for an increase in injection pressure from 1034 to 2000 bar. This is an expected trend and is attributed to the increase in fuel velocity and the ability for the fuel to travel farther in a given time under the same density and nozzle conditions (consistent aerodynamic resistance and droplet size). Also compared was median cone angle as a function of time ASOI, shown in Figure 6.3.

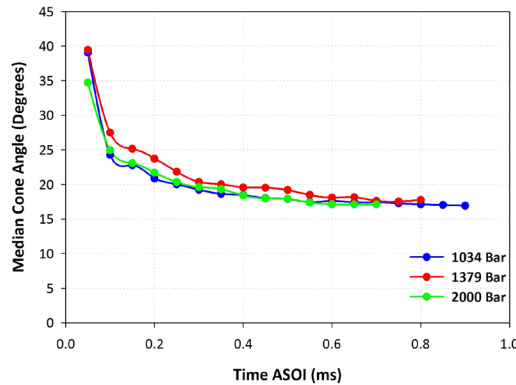


Figure 6.3: Median cone angle as a function of time ASOI for three different injection pressures, chiller off.

The middle injection pressure has a wider cone angle by a few degrees during the transient early start of injection but, during steady state, cone angles over the three injection pressures at 60% penetration were similar. Cone angle increased by an average of 6% for an injection pressure increase from 1034 to 1379 bar, with no change for an injection pressure increase from 1034 to 2000 bar.

Also of interest is a more detailed comparison of individual spray plume trends, as shown in Figure 6.4 for 0.1 ms ASOI. Penetration for each of the three injection pressures is shown and compared to the mean value for that given injection pressure and time ASOI.

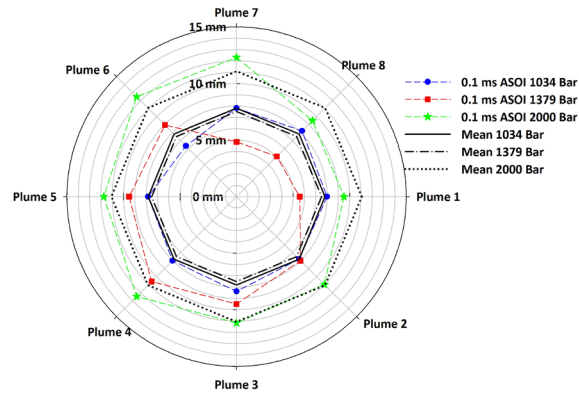


Figure 6.4: Penetration at 0.1 ms ASOI for the injection pressure sweep with the chiller off.

Eccentric needle lift was largely apparent for the 1379 bar injection pressure case based on the reduced penetration for holes 1, 7 and 8 relative to the others. This eccentric needle lift was also apparent for the 2000 bar injection pressure case, although it was not as significant. As injection pressure increased, the penetration should increase, however, there were exceptions to this as shown in the figure below which can be explained by the following. The presence of transient spray phenomenon including needle lift can cause uneven fuel pressure to different injector holes thereby changing the apparent injection pressure.

Also of interest is a comparison of plume trends during a more steady state injection period at 0.5 ms ASOI as shown in Figure 6.5.

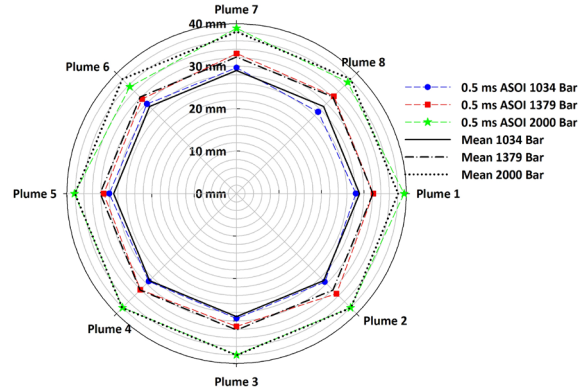


Figure 6.5: Penetration at 0.5 ms ASOI for the injection pressure sweep with the chiller off.

As injection pressure increased, the liquid penetration increased as expected. Each spray plume at a given injection pressure was compared to the mean value over all eight plumes, and trends from the mean value were apparent. Some trends were similar for the different injection pressures, such as plumes 2 and 7 always having a penetration larger than the mean value with plume 4 penetration always being approximately the mean value. Other trends were not consistent between injection pressure tests. This leads to the explanation that the trends in spray plume to plume penetration behavior may be injection pressure dependent as it is known to change internal flow characteristics such as cavitation, which would translate to downstream spray characteristics. Furthermore,

injection pressure is known to have a direct influence on diesel spray penetration as shown in Figure 6.2 which may also be manifested in plume to plume trends.

6.1.2. Charge Density Effect

Test conditions for the charge density sweep tests with the chiller off are summarized in Table 6.3. Injection was at 0.6 ms trigger duration for the 17.4 kg/m³ density case and 0.8 ms trigger duration for the 34.8 kg/m³ density case corresponding to 1.1 and 1.4 ms fuel duration, respectively. Injection duration for the reduced density case was decreased to minimize fuel spray impinging on the CV windows.

Table 6.3
Charge density sweep conditions – chiller off.

	Injection Pressure (Bar)	Density (kg/m ³)	Ambient Pressure (Bar)
17.4 kg/m ³	1975	34.8	38.6
34.8 kg/m ³	1987	17.5	19.4

As there was minimal variation in injection pressure, the influence of the ambient charge-gas density on injection pressure can be quantified from these images, which are shown for the density sweep tests in Figure 6.6.

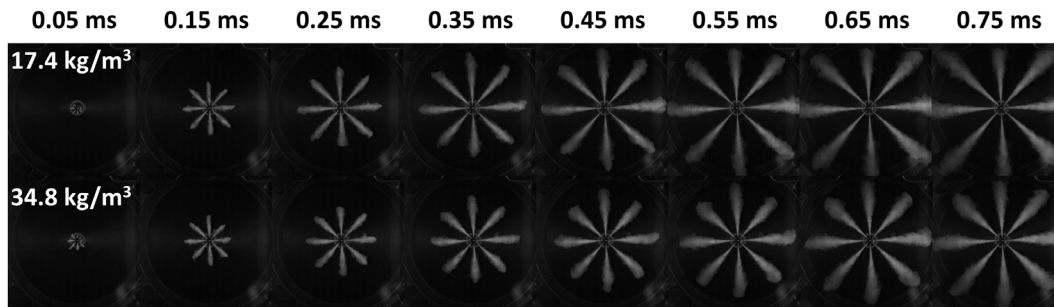


Figure 6.6: Diesel spray images from density sweep tests, 2000 bar injection pressures, chiller off.

When density increased, spray penetration reduced due to increased resistance of the fuel traversing through the ambient gas. The magnitude of the influence of ambient density on penetration and cone angle (Figure 6.7) was quantified by image processing of the spray images.

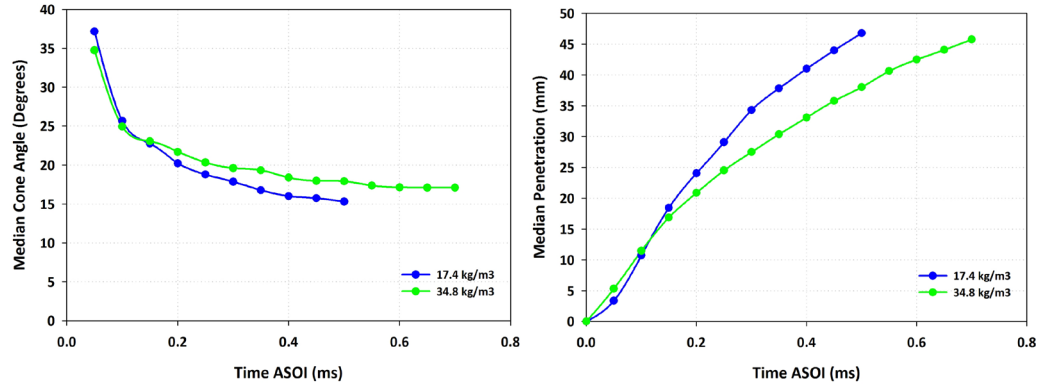


Figure 6.7: Median penetration (left) and cone angle (right) as a function of time ASOI for the density variation, chiller off, 2000 bar injection pressure.

As ambient charge-gas density reduced, the penetration increased by 20% and cone angle decreased by 9%. The charge gas density has a greater momentum under higher density conditions, which provides greater resistance to the fuel spray forcing the spray to spread wider due to the increased charge-gas momentum and resistance.

Also of interest was a comparison of the plume to plume variations for the penetration relative to the mean value, as shown in Figure 6.8 for 0.1 ms ASOI and 0.5 ms ASOI.

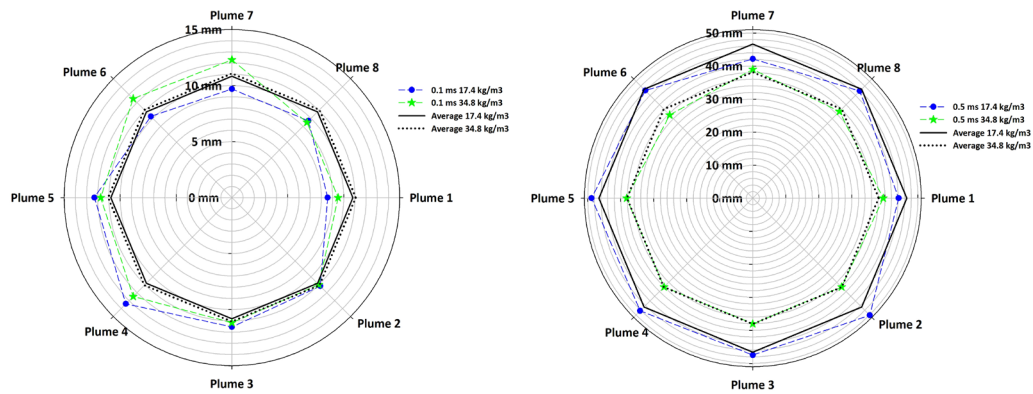


Figure 6.8: Penetration at 0.1 ms ASOI (left) and 0.5 ms ASOI (right) for the density variation with the chiller off.

At 0.1 ms ASOI, the transient start of injection behavior was largely evident, consistent with other tests. By 0.5 ms ASOI, the penetration established more consistent trends over all of the spray plumes; however, these plume trends were not consistent over the two density tests. For the lower density case, a part load condition, penetration was greater than the mean for tests 2, 3, 4, and 5, less than the mean for tests 1, 7 and 8, and equal to the mean for test 6. On contrary, for the high density, full load condition, mean penetration was greater than the mean for tests 1 and 7, less than the mean for tests 6 and 8, and equal to the mean for tests 2, 3, 4 and 5. Even though the overall trends were preserved in regards to the influence of density on penetration, the plume to plume variations were inconsistent.

6.1.3. Summary – Non-vaporizing Spray Results & Plume to Plume Variation Trends

Non-vaporizing sprays were studied over a wide range of conditions, including repeat tests, two fuel temperatures, two densities, and a sweep of injection pressure. Results were presented in this section (6.1) and also in Appendix 12.6.1. Key observations in regards to parameter influence on macroscopic spray characteristics are:

- There is a 4% spread in penetration and 5% spread in cone angle over the repeat test conditions.
- There is a 4% increase in penetration and 3% decrease in cone angle for a fuel temperature increase from 321 to 328 K, which is negligible relative to the spread in the penetration and cone angle results for the repeat tests.
- As injection pressure increased at the elevated fuel temperature of 328 K, penetration increased with no change in cone angle at 60% penetration. From 1034 to 1379 bar penetration increased by an average of 10%, from 1034 to 2000 bar penetration increased by an average of 40%. Cone angle increased by an average of 6% for an injection pressure increase from 1034 to 1379 bar, with no change for an injection pressure increase from 1034 to 2000 bar.
- An increase in injection pressure at the fuel temperature of 321 K resulted in similar increases in penetration of 40% for injection pressure increasing from 1034 to 2000 bar, however, for the smaller increase in injection pressure from 1034 to 1379 bar, penetration increased an average of 25%. Cone angle showed a 4% increase from 1034 to 1379 bar and a 7% increase from 1034 to 2000 bar, which is seen at the SOI, with levels after development showing no relative change between injection pressures.
- As charge-gas density increased, penetration decreased and cone angle increased at 60% penetration. For a charge gas density reduction from 34.8 kg/m³ to 17.4 kg/m³, penetration increased by an average of 20% and cone angle decreased by an average of 9%.
- As fuel temperature increased, there was no change in penetration or cone angle at 60% penetration.

In regards to plume to plume variations, there were no test to test consistencies in regards to certain plumes always being smaller or larger than a mean value, however, there were noticeable variations in spray characteristics over the different plumes. By removing the camera timing jitter and undertaking several more repeat tests at higher framing rates to provide additional data, these trends may become more evident.

6.2. Vaporizing Sprays

Several tests were undertaken in a vaporizing, 0% oxygen environment, achieved using the thermodynamic state generation procedure. Liquid length will be quantified to understand parameter influences and also the plume to plume spray variations. Test conditions are summarized in Table 6.4 including targets of charge-gas density, fuel temperature, fuel injection trigger duration, fuel injection pressure, and charge-gas temperature. This matrix does not show repeat tests, it solely includes the test conditions used in the current study.

Table 6.4
Vaporizing sprays test matrix.

Ambient Density (kg/m ³)	Fuel Pressure (bar)	Injection Trigger Duration (ms)	Fuel Temperature (°C)	Temperature at Injection (K)
34.8	1034	1.6	82	1100
34.8	1379	1.6	82	1100
34.8	2000	1.6	82	1100
34.8	2000	1.6	90	800
34.8	2000	1.6	90	950
34.8	2000	1.6	90	1100
34.8	2000	1.6	90	1200
34.8	2000	1.6	90	1300
17.4	2000	1.6	90	1100
34.8	1034	1.6	90	1100
34.8	1379	1.6	90	950
34.8	1379	1.6	90	1100
34.8	1379	1.6	90	1200

Results are provided in subsequent sections, with additional results provided in Appendix 12.6.2. This section starts with presentation of a paper published in the ILASS conference proceedings, and subsequently considers additional test conditions to fully quantify vaporizing spray characteristics over a range of ambient and injection conditions.

6.2.1. ILASS Paper – Temperature Sweep and Repeatability Sweep (363 K Fuel Temperature)

This paper was originally published in the May 15-18, 2011 conference proceedings for the ILASS Americas 23rd Annual Conference on Liquid Atomization and Spray Systems in Ventura California. Copyright permission provided in Appendix 12.1.2.

Investigation of Vaporizing Diesel Liquid Spray Plume to Plume Penetration Variations

Jaclyn E. Nesbitt^{*1}, Jeffrey D. Naber¹, Seong-Young Lee¹, Eric Kurtz², Hai-Wen Ge³,
and Nan Robarge²

¹Department of Mechanical Engineering – Engineering Mechanics
Michigan Technological University
Houghton, MI 49931 USA

²Ford Motor Company
Dearborn, MI 48121 USA

³ESI Mindware Inc
Farmington Hills, MI 48334 USA

Abstract

Diesel combustion and emissions formation is spray and mixing controlled. The injection event is transient and injectors consist of multiple holes and hence understanding the dynamics and variations in plume behavior is important. This includes plume-to-plume variations along with spray evolution during the injection event. In this study, an eight-hole common rail piezoelectric diesel injector was examined in an

optically accessible constant volume combustion vessel under vaporizing, non-combusting 0% oxygen conditions. Charge temperatures of 800 to 1300 K at a density of 34.8 kg/m^3 were investigated. The liquid phase spray penetration was characterized for all plumes via processing of images acquired from a high speed camera with images taken at 67,500 frames per second with back scattering illumination. Plume-to-plume differences in penetration were observed during both the initial transient and after the steady state liquid length had been established. Hypothesis and assessment on the basis of these plume-to-plume variations are presented and discussed.

Introduction

Diesel engines exhibit numerous benefits including high efficiency, optimum torque and drivability, and fuel economy advantages (Zhao and Ladommatos 1998; Stone 2002; Tree and Svensson 2007). However, they exhibit high emissions including NO_x and particulate matter (Tree and Svensson 2007). These emissions are largely governed by spray behavior as the resulting fuel-air mixing and vaporization governs the combustion processes (Aneja and Abraham 1998; Jawad et al. 2005; Lee et al. 2005). Therefore understanding spray penetration and spreading as determined from cone angle and liquid and vapor spray measurements is important to provide a fundamental understanding of fuel-spray mixing for combustion and emissions. Furthermore, diesel engines utilize multi-hole injectors which can exhibit non-uniformities in spray behavior during an injection event. By better understanding the fundamentals of injection, spray processes, and spray dynamics including plume-to-plume variations, fuel injection systems and engine operating parameters can be better optimized to take full advantage of spray properties to reduce emissions and fuel consumption. These results and observations may also be used to validate and improve spray models for more reliable computer prediction.

The goals of this paper are to characterize the liquid phase of vaporizing diesel sprays from an eight-hole injector using back scatter imaging. Tests are conducted in an optically accessible constant volume combustion vessel which enables visualization of spray processes under charge conditions representative of current and advanced technology diesel engines. Tests including repeats were conducted over a charge temperature range of 800 to 1300 K. A charge density of 34.8 kg/m^3 is selected as representative of a diesel engine under high load and boost conditions (Naber and Siebers 1996; Siebers 1998; Pastor et al. 2001; Ramierz et al. 2009). Liquid penetration is determined on an individual plume basis and variations between plumes are characterized and analyzed to provide insight into plume-to-plume variations and the implications.

Experimental Setup

The tests were conducted in the optically accessible constant volume chamber shown in Figure 6.9. The vessel has an approximately 1 liter internal volume with six face-ports housing three sapphire windows, a spark plug – dual fan port, a diesel fuel injector port (Figure 6.9), and one blank port. Additionally, there are eight access ports on the combustion vessel (CV) cube vertices containing a pressure transducer, inlet and exhaust valves, and blank ports. Numerous studies have detailed the operation and characteristics of the procedures used for studying vaporizing and combusting sprays in

this and similar laboratories (Naber and Siebers 1996; Siebers 1998, 1999; Ito et al. 2003; Baert et al. 2009; Pickett et al. 2009)

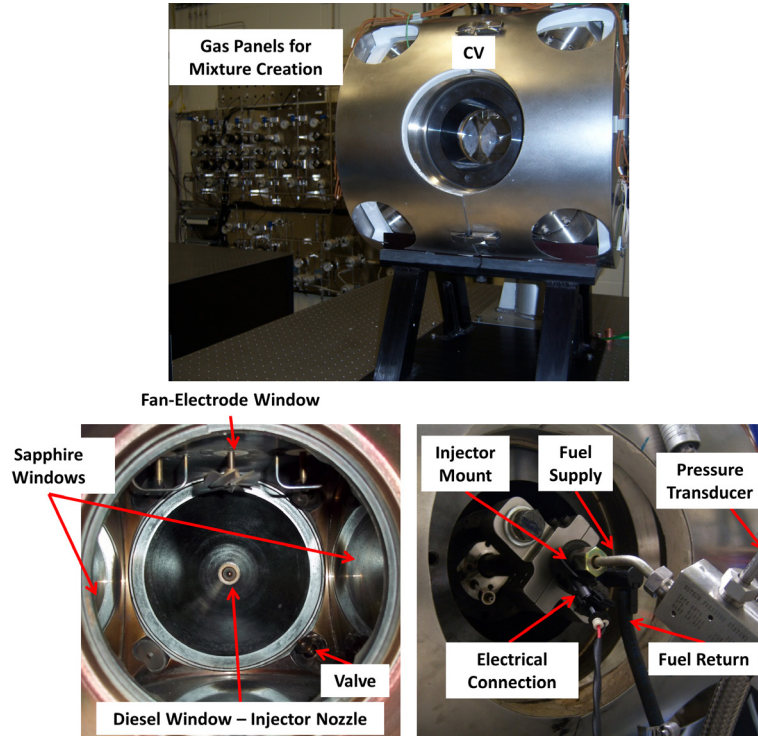


Figure 6.9: Michigan Tech optically accessible combustion vessel with gas panels for mixture creation (Top). Internal view of combustion chamber and external view of diesel injector window (Bottom).

The injector used in the current study is a Bosch Generation III piezoelectric common rail fuel injector (external view of mounting in CV shown in Figure 6.9). The injector is equipped with a sac-type nozzle, with eight holes arranged equally spaced 45° from each other azimuthally. The included angle of these holes is 150° . Each hole is nominally 1.0 mm long and 0.145 mm in diameter, with a length to diameter (L/D) ratio of 6.9.

This injector is driven by an EFS IPoD piezoelectric injector driver in multi-peak regulation mode, which requires setting peak current, open and close voltage, and current slope levels. Drive characteristics were set to match production operation. The electronic trigger injection duration was set to 1.6 ms, and the resulting spray was 2.8 ms in duration. The fuel supply system is a high pressure system from Hydraulics International capable of injection pressures to 4140 bar, compatible with multiple fuels including diesel, biodiesel, gasoline, ethanol and others, with ultra-low sulfur diesel (ULSD) fuel used in the current study.

Back scattering imaging is used to visualize the liquid phase spray in the combustion vessel. Back, or Mie, scattering imaging involves capturing the spray image via scattering light off the fuel droplets and hence this diagnostic enables visualization of the liquid portion of the spray in a vaporizing (0% oxygen) environment. The imaging setup used is shown in Figure 6.10, along with injector orientation.

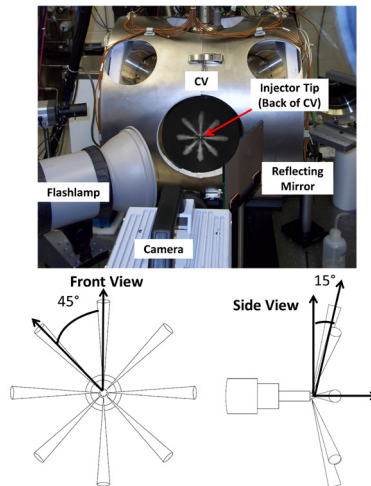


Figure 6.10: Back scattering imaging setup (Top). Injector orientation and spray plume angles (Bottom).

A Photron Fastcam SA1 streaming high speed digital camera was used. The camera was equipped with a 60 mm Nikon Micro-Nikkor lens with an f-stop of 2.8. Image resolution was 256 x 256 pixels to capture the spray region of interest with a 67,500 frames per second frame rate (15 μ s inter-frame time) and a 1.65 μ s exposure duration. The light source for scattering was a Cooke SensiFLASH flash-lamp with an 8 ms discharge duration. This light source provides illumination during the entire injection event, with the injection and imaging delayed relative to the flash-lamp to account for the warm-up time of the flash-lamp, thereby yielding a steady state illumination during the 2.8 ms liquid fuel injection. The light source as shown in the figure is directed at an angle into the CV to provide uniform illumination of the entire chamber by reflecting the light off an angled mirror. The camera and flash-lamp are remotely triggered by a pulse generator (SRS DG645) which also controls the injector to ensure synchronized fuel injection, image acquisition and illumination. This optical setup enables visualization of all eight spray plumes from the injector as shown in Figure 6.10 with the spray plumes oriented 15° off the plane of the injector.

Test Procedure

This work considers vaporizing sprays in a zero percent oxygen environment. To achieve the zero percent oxygen environment in the combustion vessel a premixed burn procedure is used (Naber and Siebers 1996; Siebers 1998). The procedure involves spark igniting via two electrodes (see Figure 6.9), a mixture of acetylene, hydrogen, oxygen and nitrogen to yield zero percent oxygen post premixed burn. The mixture is prepared via partial pressure mixing in a 10 L mixing vessel. The initial fill pressure of the CV governs the density at the time of fuel injection as determined via the ideal gas law, with the combustion vessel being electrically heated via cartridge heaters to 180°C. Fill pressure and the pressure throughout the premixed burn and injection event is monitored via a Kistler 6001 pressure transducer located in a port of the CV coupled to a Kistler 5010B charge amplifier.

The mixing fan in the top of the CV (refer to Figure 6.9) remains on during the premixed burn and fuel injection event to ensure uniform temperature distribution inside the chamber. See Figure 6.11 for a graphical description of this premixed burn process.

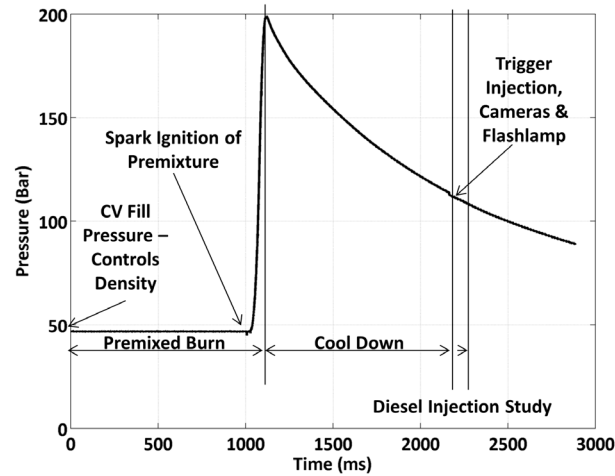


Figure 6.11: Pressure trace showing CV premixed burn, cool down, and timing of diesel fuel injection

After the peak temperature and pressure inside the CV is reached upon completion of the premixed burn, the combustion products then undergo a cool-down period due to heat transfer to the CV walls. At the desired time during this cool-down which corresponds to the predetermined temperature of study, the control system sends a trigger to the pulse generator which outputs the necessary triggers for injection, image acquisition and flash-lamp illumination. Data is logged throughout the entire premixed burn and spray event, including fuel pressure, spark current of the electrodes for the premixed burn, trigger signals, and voltage and current of the injector driver. Further information on the process is covered in numerous publications (Naber and Siebers 1996; Siebers 1998, 1999; Pickett et al. 2009).

Vaporizing ULSD spray test conditions investigated in the current work consisted of three repeat tests and a charge temperature sweep, with actual experimental conditions defined in Table 6.5.

Table 6.5

Test matrix with experimental conditions for bulk and core charge density and temperature, as well as injection pressure.

Test Set	ρ_{Bulk} (kg/m ³)	ρ_{Core} (kg/m ³)	T_{Bulk} at Inj. (K)	T_{Core} at Inj. (K)	$P_{\text{Inj.}}$ (Bar)
Repeat 1	34.7	32.2	1100	1190	1990
Repeat 2	34.5	32.0	1110	1190	2000
Repeat 3	34.5	32.0	1110	1200	2010
Charge Temp. Sweep	34.5	32.9	810	850	1990
	34.8	32.7	950	1010	2020
	34.7	32.2	1100	1190	1990
	34.8	32.0	1200	1300	2010
	34.6	31.7	1300	1430	2000

Fuel pressure was held constant at 2000 ± 20 bar, with a targeted charge bulk density of 34.8 kg/m^3 . Repeat tests were at 1100 K bulk temperature, with temperature sweep conditions targeting 800, 950, 1100, 1200 and 1300 K charge bulk temperature.

There exist boundary layers in the CV and hence temperature gradients which leads to the definition of core and bulk temperatures. The mixing fan in the CV helps to provide temperature uniformity with there being optimum uniformity in the core region of the vessel. This corresponds to the location of the gases that mix with the spray during injection where the mean temperatures are uniform but there does still exist temperature fluctuations (Naber and Siebers 1996). The core temperature is higher than the bulk temperature due to cooler, higher density gases which exist in CV boundary layers, and can be calculated from bulk gas conditions via equation (65) (Naber and Siebers 1996; Siebers 1998).

$$\frac{T_{\text{Core}}}{T_{\text{Bulk}}} = 1 + a * \left(1 - \frac{T_{\text{Wall}}}{T_{\text{Bulk}}}\right) + b * \left(\frac{T_{\text{Bulk}}}{T_{\text{Wall}}} - 1\right) \quad (65)$$

The second and third terms on the right hand side consider gases in the boundary layers and crevices, with constant a corresponding to the boundary layer thickness (and is a function of density), and constant b representing the ratio of chamber crevice volume to chamber volume (Naber and Siebers 1996; Siebers 1998). The CV fill pressure measurement enables calculation of bulk gas density, which is used to determine the bulk temperature at injection as bulk density is constant during the test. Bulk temperature is used to calculate core temperature per the above equation, which is subsequently used in the core density calculation again using measured CV pressure at the time of injection.

Image Processing

Image sets acquired at each test condition were processed in Mathworks Matlab™ to determine penetration for each spray of the eight-plume injector, as a function of time after start of injection (ASOI), which corresponds to the start of liquid fuel. Plume labeling is provided in Figure 6.12.

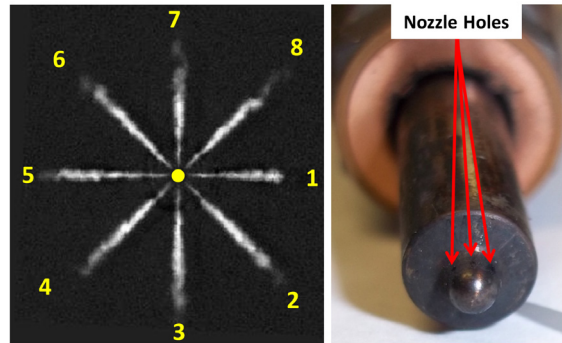


Figure 6.12: Left - Spray plume labeling, yellow dot denotes injector tip location. Right – picture of injector nozzle with select holes labeled, holes circle the entire nozzle tip in 45° increments.

Image sets were read into arrays with frame 1 prior to injection used as the background image. The center injector tip location is determined, which enables calculation of the injector hole locations which are offset from the center of the nozzle based on injector configuration (Figure 6.12). Penetration is referenced relative to the individual injector hole locations.

The image processing of each movie frame is composed of the following steps. First, the background image was subtracted from the spray image to avoid interference

from the injector tip in image processing. To process each plume in a given image frame the image was rotated in 45° increments such that each plume was aligned exiting the injector tip from left to right. The spray region of interest was isolated along a line from the injector tip to the image edge along the spray centerline, and perpendicularly relative to this line to visualize the entire width of the spray plume. Masking was applied to the adjacent spray plumes to avoid interference. The image was normalized by the maximum intensity in the image to yield an intensity scale from 0 to 1.

With the spray plume isolated from the background, injector tip, and adjacent spray plumes, the image is thresholded to black and white. The threshold is determined for each spray plume based on Matlab'sTM "graythresh" operator which relies on Otsu's method, choosing a threshold to separate the two classes of pixels in the image, in this case spray and background, by minimizing their intraclass variance (Otsu 1979). The spray is further isolated from noise in the black and white image by finding the largest connected region of the spray via blob analysis. The black and white spray image next has its boundary traced, and the leading edge of the boundary along either the spray axis or at an angle from the axis is defined as the tip penetration, relative to the injector nozzle hole. This penetration is defined as the maximum length of the continuous portion of the spray as observed from the back scattering imaging as defined in Figure 6.13.

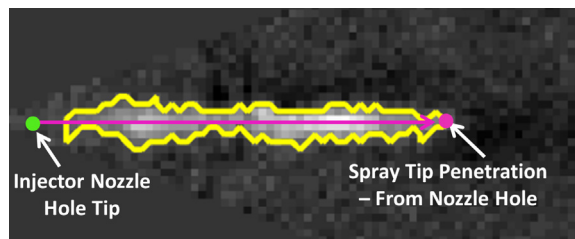


Figure 6.13: Liquid penetration definition.

Penetration is converted to millimeters using the known image scaling of 0.18 mm/pixel, and is also scaled by the cosine of 15° to account for the angled spray based on injector orientation, refer to Figure 6.10.

Results & Discussion

This section will be broken up into two parts. First, results from three repeat tests at 1100 K will be analyzed to determine the variation in individual spray plumes. Next, results will be presented on the plume-to-plume variation for the bulk charge temperature sweep from 800 to 1300 K.

Repeatability Tests

Three repeat tests were undertaken for vaporizing sprays (0% oxygen), at a bulk charge density of 34.8 kg/m^3 , 1100 K bulk charge gas temperature, and 2000 bar injection pressure with a 1.6 ms electronic injector drive duration (2.8 ms liquid fuel injection event). Actual test conditions were provided in Table 6.5, with the mean injection pressure being 2000 bar (10 bar standard deviation), mean bulk charge gas temperature of 1110 K (6 K standard deviation), and mean bulk charge gas density of 34.6 kg/m^3 (0.1 kg/m^3 standard deviation). By characterizing the plume-to-plume trends over the repeat tests it can be determined if plume-to-plume variations are a result of system repeatability or if they are an inherent phenomenon of the injector and spray.

Background subtracted images for these test conditions are shown in Figure 6.14. There are plume to plume variations at each time ASOI, as well as fluctuations in liquid length of a single plume as time ASOI progresses. This paper focuses on the plume-to-plume variations including potential causes and implications, not on the fluctuations of a single plume.

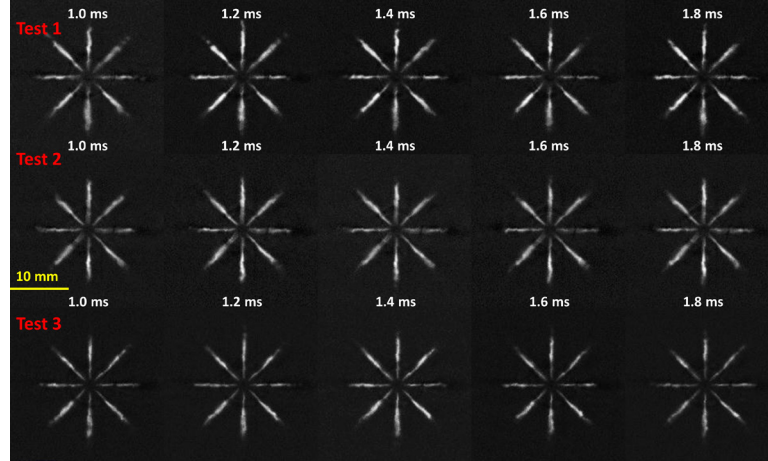


Figure 6.14: Background subtracted spray images showing steady state spray characteristics for the three repeat tests at varying times ASOI. Physical scale is shown on the image.

The median penetration for the eight plumes is plotted in Figure 6.15 as a function of time ASOI for the three tests. The median value is used as this does not weight outliers in the data and therefore provides a representative value of the combined spray characteristics.

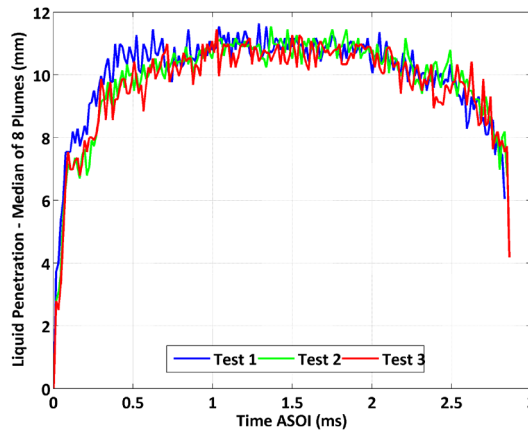


Figure 6.15: Median liquid penetration as a function of time ASOI for three repeat tests.

From Figure 6.15 it is observed that the liquid penetration is consistent between tests, with the largest deviation of 2.1 mm in early times ASOI for test 1 relative to test 2 and 3. This is the transient state of the spray during development and hence deviations are more prevalent when compared to the steady state spray in the longer times ASOI. The penetration increases until 0.75 ms ASOI at which a steady state value is reached, termed the liquid length. After this time the penetration fluctuates around this value until the end

of injection when penetration falls off following similar observations from reference Naber and Siebers (1996). Comparing the average median liquid length over the steady state period (0.75 through 2 ms ASOI), the steady state liquid length for all three tests are within 0.2 mm of each other when using the average value over steady state, but the instantaneous variation during the same steady state period can exceed 1 mm.

Polar plots of liquid penetration for each test are given in Figure 6.16 to compare plume behavior as a function of time ASOI.

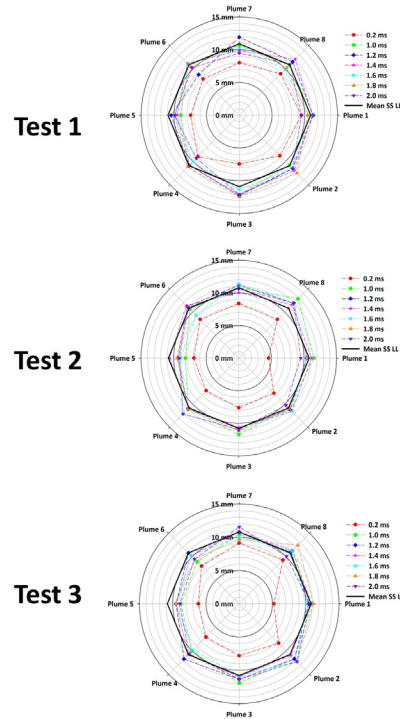


Figure 6.16: Polar plots of penetration for three repeat tests, each spoke of the polar plot corresponds to physical spray plume placement.

The eight individual spray plume penetrations are shown in the polar plots in 45° increments, with plume 1 at 0°, plume 2 at 45°, etc., (as was defined in Figure 6.10). The 0.2 ms ASOI condition represents transient spray development, but the remaining times (1.0 to 2.0 ms) correspond to steady state spray conditions when the liquid length has been established (refer to Figure 6.15). Considering the standard deviation of the penetration as a function of time ASOI, it decreases from SOI to 1.0 ms ASOI where it reaches a minimum until 2.0 ms ASOI at which the standard deviation increases due to end of injection transients. Hence the 1.0 to 2.0 ms region is chosen to represent steady state due to the decreased variation in standard deviation. Also included in the polar plots is the mean steady state liquid length (mean SS LL) over all eight plumes during steady state.

Considering each polar plot in Figure 6.16 for a given test, the variation in plume-to-plume penetration is evidenced by different radial extensions of the plume along each spoke, at various times ASOI during steady state and looking at the circular radii created for each time ASOI which represent the liquid length. The plume-to-plume variation is

most prominent at 0.2 ms ASOI, as expected as this is the transient start of injection and spray development.

To further compare plume-to-plume variations and trends over the three repeat tests, the mean liquid length was determined from 1 to 2 ms ASOI for each test (which consists of 68 data points) and compared to the mean steady state liquid length (mean SS LL) for all plumes over the three repeat tests as shown in Figure 6.17.

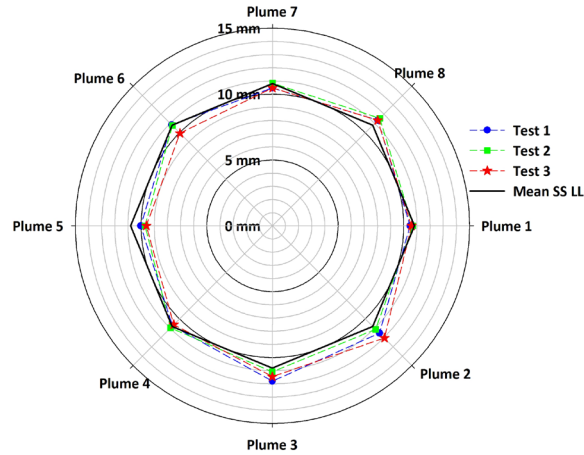


Figure 6.17: Mean steady state liquid length for three repeat tests over eight spray plumes.

Considering each plume independently and looking at the liquid length for each test, the results are similar showing there is minimal test to test variation and high repeatability. There is however plume-to-plume variation in liquid length, with certain plumes consistently having longer, or shorter, liquid lengths. Plumes 1, 4, 5, 6, and 7 are typically shorter than the mean, with plumes 2, 3, and 8 being longer than the mean, with the mean liquid length being 10.8 mm. The trends for the repeats are as follows; plume 5 has the shortest liquid length being almost 11% less than the mean, followed by plume 7 which is over 3% less than the mean, and then plume 1 which is more than 2% shorter than the mean. Plume 4 and 6 have similar liquid lengths being around 0.5% shorter than the mean, with plume 8 being almost 5% larger than the mean, and plumes 2 and 3 having similar liquid lengths and the largest of all plumes, over 6% larger than the mean.

Charge Temperature Sweep

A charge bulk-gas temperature sweep was undertaken from 800 to 1300 K to understand its influence on plume-to-plume liquid length variations. Conditions were vaporizing sprays at 34.8 kg/m^3 bulk charge density, 2000 bar injection pressure, 2.8 ms liquid injection duration. Background subtracted images during steady state are compared for temperatures investigated, as shown in Figure 6.18.

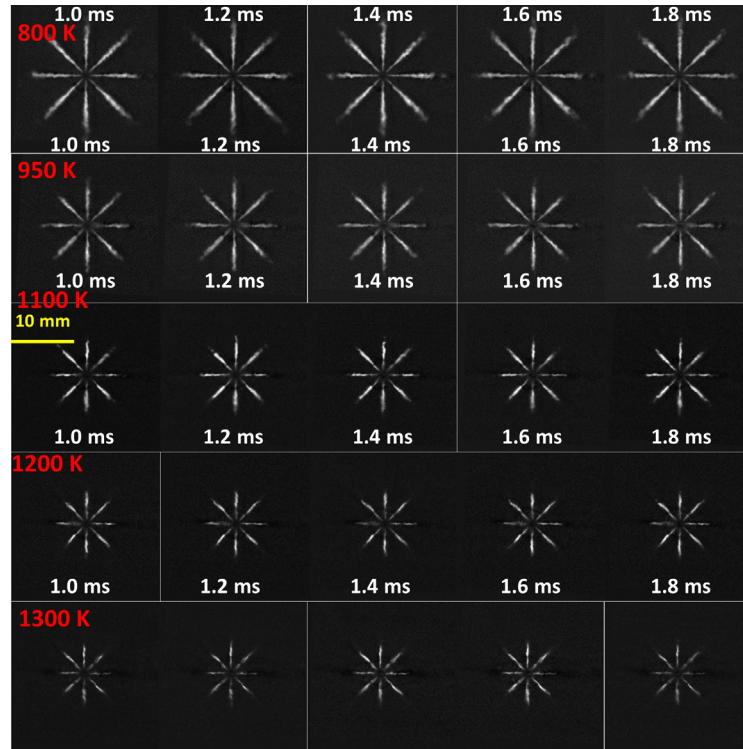


Figure 6.18: Background subtracted spray images displayed during steady state liquid penetration stage for the charge temperatures investigated. Time ASOI and scaling is displayed.

Median penetration over the eight plumes at each test condition was compared to understand temperature trends, as shown in Figure 6.19.

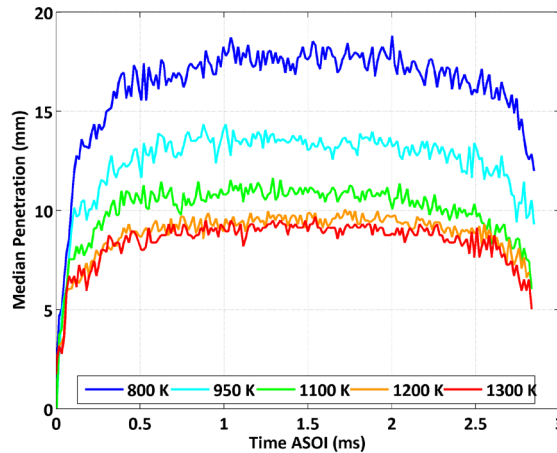


Figure 6.19: Median liquid penetration as a function of time ASOI for charge gas bulk temperature sweep tests.

Considering each temperature case independently, over a range of times ASOI, there is evidence of plume- to-plume variations in liquid length amongst all temperatures. These plume-to-plume variations are quantified to understand plume trends and characteristics. As temperature increases, plume penetration (liquid length) decreases as

expected due to increased vaporization, with the sensitivity of liquid length to temperature decreasing at higher temperatures (Siebers 1998).

The penetration change with temperature is further understood by considering the mean liquid length during steady state as a function of gas temperature, as shown in Figure 6.20. Error bars represent the average standard deviation of the mean liquid length during steady state over all eight plumes. The gas temperature at the location of the liquid spray varies between the vessel wall temperature of 453K to the core temperature (Table 6.5) due to temperature gradients near the wall. Here the liquid penetration is plotted versus the bulk temperature. The experimental mean liquid length data is compared to the expected temperature dependence, temperature to the -1.73 power, as proposed by Payri et al. 2008 and interpolated from experimental data (Sandia ECN 2011). This data is also compared to experimental data from Siebers and Sandia Engine Combustion Network (ECN) (Siebers 1998; Sandia ECN 2011) for a bulk gas density of 31.1 kg/m^3 , injection pressure of 140 MPa, hole diameter of 0.246 mm, using Heptamethylnonane (HMN) fuel to compare bulk gas temperature trends.

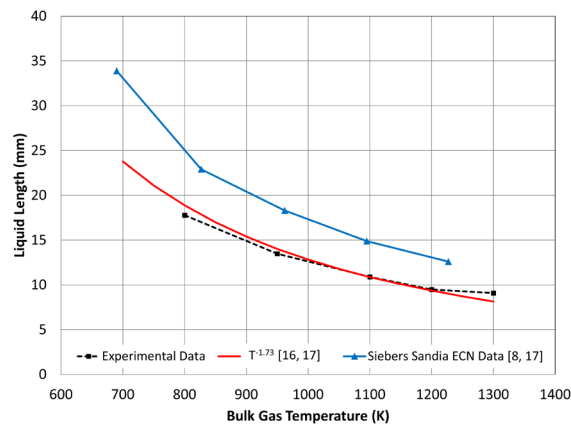


Figure 6.20: Mean experimental liquid length during steady state as a function of bulk gas temperature including error bars representing one standard deviation of liquid length. Data is compared to an expected temperature trend (Payri et al. 2008 [16]; Sandia ECN 2011 [17]) and experimental data (Siebers 1998 [8]; Sandia ECN 2011 [17]).

The mean liquid length during steady state decreases 49% as temperature increases from 800 to 1300 K. This variation in liquid length is nonlinear with temperature in agreement with literature (Siebers 1998). As temperature increases from 800 to 950 K, liquid length decreases 24%, for 950 to 1100 K temperature increase liquid length decreases 19%, for a temperature increase of 1100 to 1200 K liquid length decreases 13%, and for a temperature increase from 1200 to 1300 K liquid length decreases 4%. The experimental and published temperature trends agree within one standard deviation of the experimental mean liquid length data. The experimental data does not agree with Siebers Sandia ECN data due to the different conditions, injector geometry and fuel type, however, the temperature trends for liquid length are preserved in the current experimental data relative to that shown by Siebers.

Figure 6.21 shows the liquid penetration for each plume from the injector for each of the bulk charge gas temperatures investigated. These polar plots consider transient

spray development (0.2 ms ASOI) as well as steady state spray penetration (liquid length). Also included is the mean steady state liquid length (mean SS LL) over all eight plumes during steady state. The variation in plume-to-plume penetration is evidenced by different radial extensions of the plume along each spoke at various times during steady state. During steady state (1 to 2 ms ASOI) plume penetration should be identical as the liquid length has been established, however, not only are there fluctuations in penetration (refer to Figure 6.19), there are plume-to-plume variations in penetration for a given time ASOI. Again, plume-to-plume variation is most prominent at 0.2 ms ASOI, as expected as this is the transient start of injection and spray development.

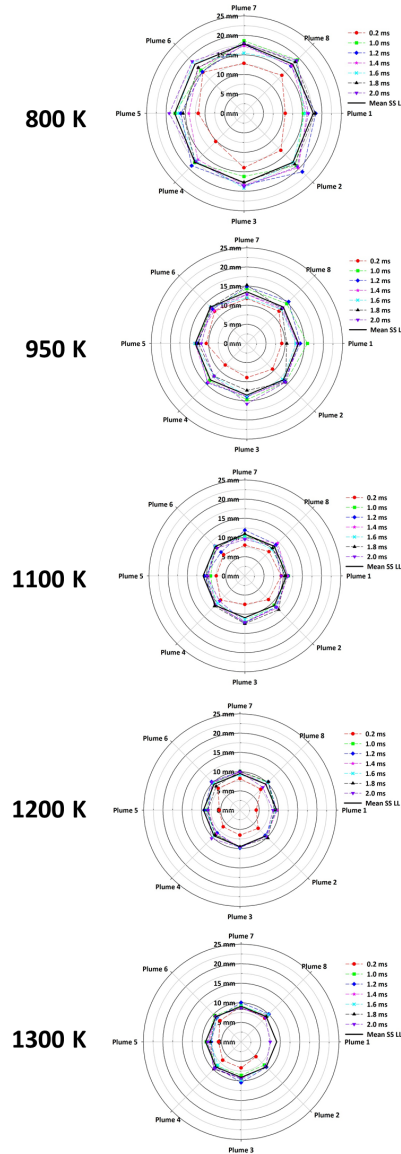


Figure 6.21: Polar plots of plume penetration for various times ASOI (for spray development and steady state), charge temperatures 800 to 1300 K.

To examine if there are plumes that consistently have longer or shorter liquid penetration over this range of charge temperatures the individual plume liquid lengths for

each charge temperature are normalized by the mean value over all eight plumes. The results are shown in Figure 6.22.

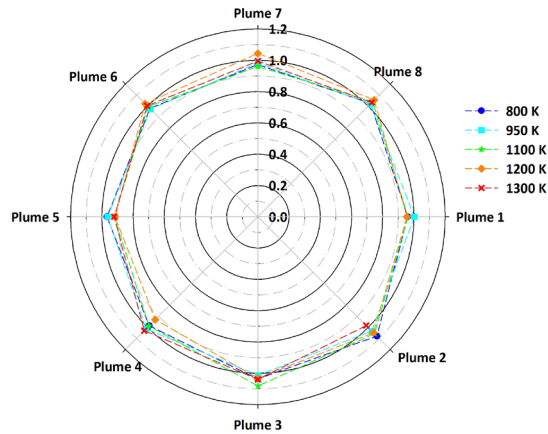


Figure 6.22: Mean steady state liquid length (over 1 to 2 ms ASOI) for the charge temperature sweep, normalized by the mean liquid length to isolate plume influences from temperature effects.

As the figure shows, plume-to-plume variations are evident as was the case for repeat tests. These plume-to-plume variations exhibit similar trends to those observed in the repeat tests, with plume 5 having the shortest liquid length on average almost 7% shorter than the mean, followed by plumes 1, 4, 6, and 7 which are up to 3% shorter than the mean. Plumes 2, 3, and 8 are almost 4% longer than the mean value, considering the average temperature trends.

Discussions on Plume-to-Plume Variations

The plume-to-plume variations in liquid length can yield differences in fuel air mixing and emissions, and therefore understanding their causes is essential. There are various potential explanations for the plume-to-plume variations. These include nozzle configuration, eccentric needle movement, nozzle manufacturing smoothness, and variations in nozzle dimensions as discussed in the literature (Arcoumanis et al. 1998; Desantes et al. 2005; Karimi 2007; Powell et al. 2011). There is the potential for eccentric needle movement, which could cause uneven needle lift and hence yield plume-to-plume variations. There is uneven needle lift evidenced in early times ASOI images as shown in Figure 6.23 which includes background subtracted images from repeat tests, during the start of injection (SOI) where certain holes start injecting fuel before others.

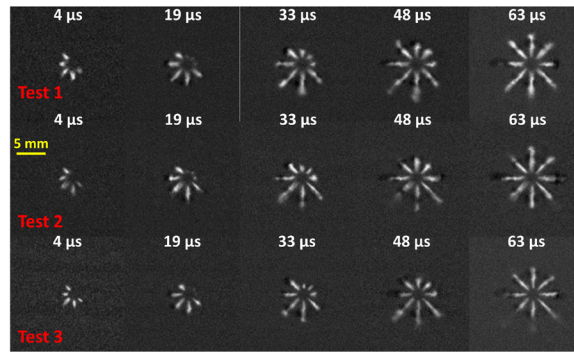


Figure 6.23: Images during the early injection portion of the three repeat tests, time ASOI displayed on image showing uneven SOI due to eccentric needle motion.

As shown in Figure 6.23, plumes 1, 7 and 8 consistently inject 0.019 ms after the other plumes. However, this change in SOI proposed as a result of uneven needle lift does not translate to variations observed during steady state when plume 8 has one of the largest liquid lengths, with plumes 1 and 7 having shorter liquid lengths. Hence the eccentric needle motion only impacts the plume dynamics during the transient state. The needle lift, even though it is double-guided, is likely dependent on the exerted pressure from the fuel, which could vary due to differences in internal nozzle geometry. During steady state the needle is relatively far away from the nozzle hole entrance as it is fully lifted, and therefore it is no longer an influencing factor on the fuel flow, and thus is likely not the cause of the observed plume-to-plume variations during steady state.

Hole-to-hole differences introduced during nozzle manufacturing could potentially explain the plume-to-plume variation trends. The nozzle was hydro-ground but there could be differences in the smoothness of each hole which would cause turbulence or cavitation differences, and this could translate into downstream spray characteristics (Arcoumanis et al. 1998). As fluid flows through the nozzle, the flow can be two-phase and cavitating both in the sac volume and holes, which changes flow characteristics and hence hole-to-hole variations in spray characteristics (Arcoumanis et al. 1999). Furthermore, there could be differences in hole diameters relative to manufacturer specifications (Desantes et al. 2005). Observations of liquid length have shown it increases linearly with orifice diameter (Siebers 1999), and therefore the 1.8 mm (19%) increase in liquid length observed between plume 5 and plumes 2 and 3 would require a 19% increase in orifice diameter. To examine this, diameters of all eight holes were measured using a scanning electron microscope (SEM, model JEOL JSM-6400). The test results showed a mean hole diameter of 145.1 μm , with a standard deviation of 1.2 μm (with this standard deviation being less than the measurement repeatability). The maximum hole diameter of 146.5 μm was observed for hole 3, with a minimum hole diameter of 143.5 μm for hole 7. Hence this variation in hole diameter is not of large enough or of significant magnitude to explain the liquid length hole-to-hole variations.

Instead it is hypothesized that internal flow geometry and conditions in the injector are a contributing factor to the observed differences in steady state liquid penetration. In this injector design it is known that the internal injector geometry results in the fuel filling the sac from one side of the injector. This geometry can increase fuel pressure to certain injector holes which could change internal nozzle flow characteristics and translate to spray variations as seen currently. Based on the orientation

of fuel filling, holes one and five are symmetric about the fuel filling location and hence the reduction in liquid length as seen with these plumes could be attributed to the internal flow geometry.

Future Work

Hypothesis on the causes of the differences in plume to plume variation have been proposed. Future work is proposed to evaluate a set of injectors to see whether trends support the proposed hypothesis. Additionally, detailed studies using CFD or advanced diagnostics to study the flow in the injector would provide insight to the causes. With respect to spray studies, future work will include the characterization of plume-to-plume variations as a function of injection pressure, gas density, and fuel temperature. Similar analyses will be undertaken on non-vaporizing sprays and on combustive sprays to understand consistencies and trends in plume behavior and determine impacts on ignition and soot formation. The time varying fluctuations in vaporizing sprays liquid penetration will also be characterized including frequency analyses to understand the phenomenon and causes.

Conclusions

Diesel combustion and emissions formation is largely spray and mixing controlled and hence understanding liquid phase spray characteristics is important to determine methods to enhance and optimize combustion while minimizing emissions. The current work aimed to understand and characterize plume-to-plume variations of the eight spray plumes from a multi-hole injector under repeat test conditions and for a charge temperature sweep. Using an optically accessible constant volume combustion vessel with Mie back scattering diagnostics liquid penetration and mean steady state liquid lengths were characterized. Key conclusions are as follows:

- Liquid penetration increases as time ASOI increases before reaching a steady state value where the liquid phase reaches a steady state. Under the conditions of this test this takes 0.75 ms.
- As charge gas temperature increases from 800 to 1300 K mean liquid length of all plumes decreases by 49% due to increased vaporization. This decrease in liquid length is nonlinear with ambient temperature agreeing with previous published studies in the literature.
- Liquid penetration is initially shorter for plumes 1, 7 and 8 as injection starts; however, this difference diminishes over time and is not observed in steady state measurements.
- Under steady state, results show that plumes 2, 3, and 8 consistently have larger liquid lengths than plumes 1, 4, 6, and 7, followed by the smallest liquid length of plume 5, both under repeat test conditions and over the charge temperature sweep. For repeat test conditions, the span in liquid length from shortest to longest is in excess of 18%. For the temperature sweep tests, the largest span in liquid length from shortest to longest considering all temperature tests is 15%.
- Measurements of the individual hole diameters indicate that this is not the primary factor in the differences in liquid penetration.

- Differences in the initial versus steady state liquid penetrations indicate that there are two factors controlling the differences in liquid length. It is hypothesized that the initial differences are driven by eccentric needle movement. Additionally it is hypothesized that the steady state differences are the result of internal flows and geometry in the injector.

Acknowledgements

Acknowledgements and thanks go to Terrence Graham from Robert Bosch LLC for his technical insight on injector characteristics. Additional acknowledgement is provided to Motion Engineering Company Inc. for use of the high-speed camera in this study. Further acknowledgement is given to the National Science Foundation for the funding of MRI grant number 0619585 for the development of this optically accessible combustion vessel laboratory. Acknowledgement is also given to A&D Technology for their assistance in providing the data acquisition system for the laboratory.

Nomenclature

a	Empirical Constant
ASOI	After start of injection of liquid fuel
b	Empirical Constant
D	Nozzle hole diameter
L	Nozzle hole length
P	Pressure
T	Temperature
ρ	Density

Subscripts

Bulk	Bulk gas conditions
Core	Core gas conditions
i	Nozzle inlet
Inj	Injection conditions
o	Nozzle outlet
Wall	CV wall conditions

6.2.2. Fuel Pressure Sweep at 363 K Fuel Temperature

An injection pressure sweep of 1034 to 1379 to 2000 bar was undertaken with the chiller off to yield a fuel temperature of approximately 363 K, with the influence on liquid length being quantified. Ambient conditions are summarized in Table 6.6.

Table 6.6
Ambient conditions at injection – fuel pressure sweep, chiller off.

Test Set	ρ_{Bulk} (kg/m ³)	ρ_{Core} (kg/m ³)	T _{Bulk} at Inj. (K)	T _{Core} at Inj. (K)	P _{Inj.} (Bar)
1034 Bar	34.6	32.1	1100	1190	1020
1379 Bar	34.7	32.1	1100	1190	1380
2000 Bar	34.7	32.2	1100	1190	1990

Ambient conditions at injection were similar amongst the injection pressure sweep, with small reductions in injection pressure relative to the expected set-point values. In all figures and discussion, the expected injection pressures were used to reference the tests.

Spray images are shown in Figure 6.24 for the injection pressure sweep with the chiller off which provides 363 K fuel temperature.

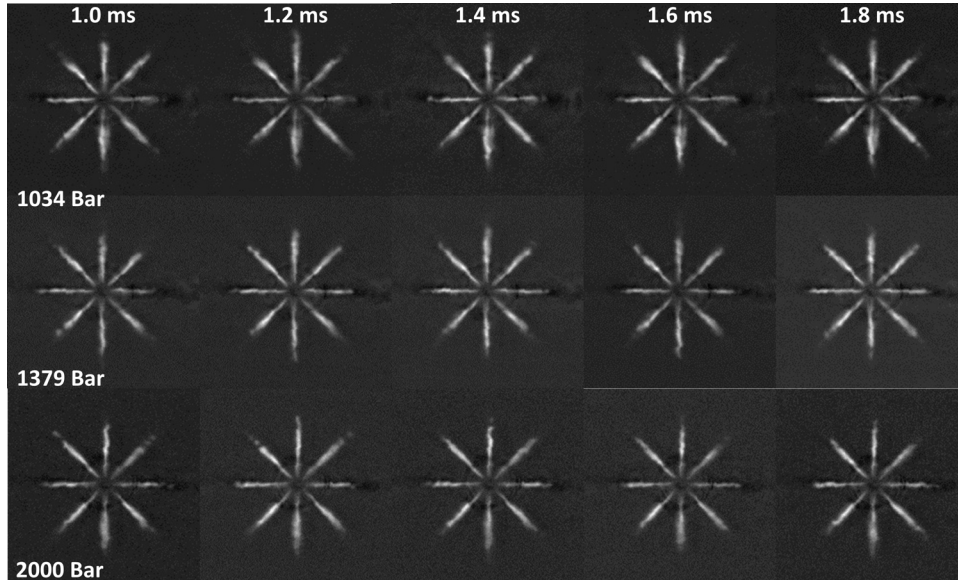


Figure 6.24: Background subtracted spray images. Injection pressure sweep test: 34.8 kg/m^3 density, 0% O_2 , 1100 K, chiller off.

From the background subtracted spray images it was evident that injection pressure did not have a significant impact on fuel spray liquid length during steady state, agreeing with literature (Siebers 1999). This was further confirmed by comparing results from the image processing shown in Figure 6.25.

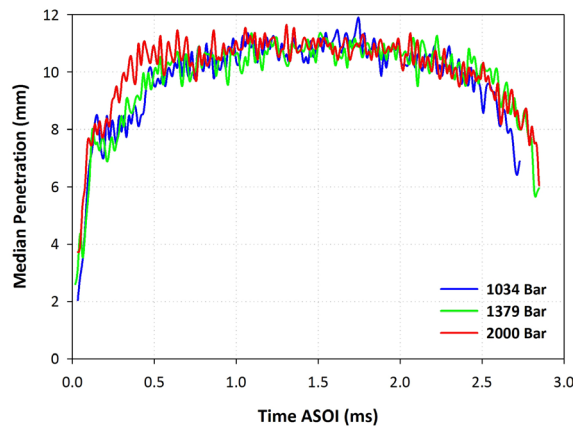


Figure 6.25: Median penetration (liquid) as a function of time ASOI for the injection pressure sweep at 34.8 kg/m^3 density, 1100 K, 0% O_2 , chiller off.

As injection pressure increased liquid penetration remained similar with negligible differences ($<1\%$) in steady state liquid length agreeing with literature trends (Siebers 1998). This independence of liquid length from injection pressure enables increased injection pressures to be used without the worry of liquid cylinder wall impingement. Furthermore, this independence showed that increased fuel injection pressures which provide increased fuel velocity and fuel flow rate must be the same as the change in the overall fuel evaporation rate for different injection pressures, for this independent

behavior trend to hold (Siebers 1998). For the 2000 bar injection pressure case steady state liquid length is reached earlier which is attributed to a rise in injection velocity of the fuel due to an increase in injection pressure and the ability for the fuel droplets to penetrate faster to their steady state region where the fuel becomes completely vaporized.

There exist distinct plume trends as further evidenced in Figure 6.26. Steady state liquid length from 1 to 2 ms ASOI for each plume was determined and normalized by the mean steady state liquid length over all eight plumes. Normalization was used to minimize any injection pressure influence in the comparison. If the normalized liquid length was greater than 1 it exceeded the mean, less than one, it was less than the mean value.

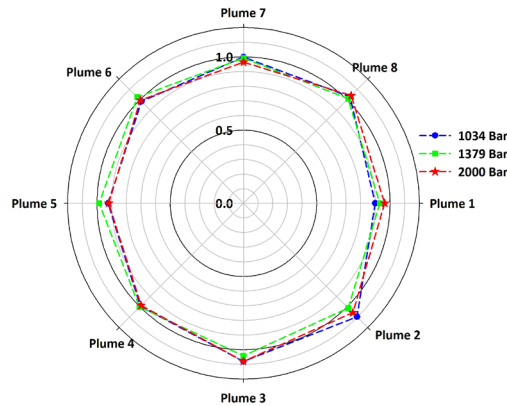


Figure 6.26: Polar plot of normalized liquid length during steady state (1 to 2 ms ASOI), 34.8 kg/m^3 0% O_2 , 1100 K, chiller off.

Looking at trends for the three injection pressures it is seen that plumes 1, 4, 5 and 7 always were less than the mean value by up to 7%, with that also being the case for plume 6 with the exception of the 1379 bar injection pressure case. Plumes 2, 3, and 8 always exceeded the mean value by approximately 5%. These trends agreed with those from both the charge temperature sweep and repeat tests discussed previously (Section 6.2.1).

6.2.2.1. Additional Results - Fuel Pressure Sweep

To further confirm that liquid length is minimally influenced by injection pressure, additional tests were performed using this multi-hole injector. Conditions were a charge-gas density (bulk) of 5.7 kg/m^3 , temperature of 900 K (bulk), fuel temperature of 363 K (no chiller), with a 1.6 ms electronic injection trigger duration. Images are shown in Figure 6.27. Framing rates are reduced to 10,000 fps since at this low density condition diesel spray liquid length is increased and therefore the region of interest, or resolution required, is increased which is achieved by a frame rate reduction.

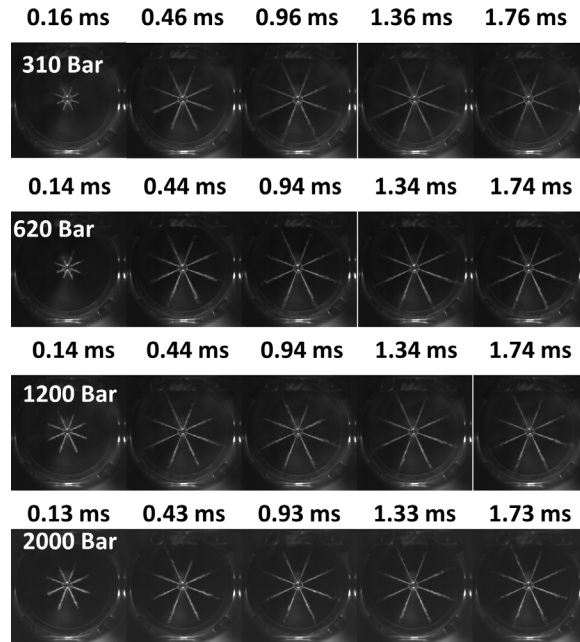


Figure 6.27: Spray images for 0% oxygen environment, 5.7 kg/m^3 bulk charge gas density, 900 K bulk charge gas temperature, 363 K fuel temperature.

There are no noticeable differences in the images for the influence of injection pressure on diesel spray liquid length. Processed results for median penetration over all 8 of the spray plumes are shown in Figure 6.28.

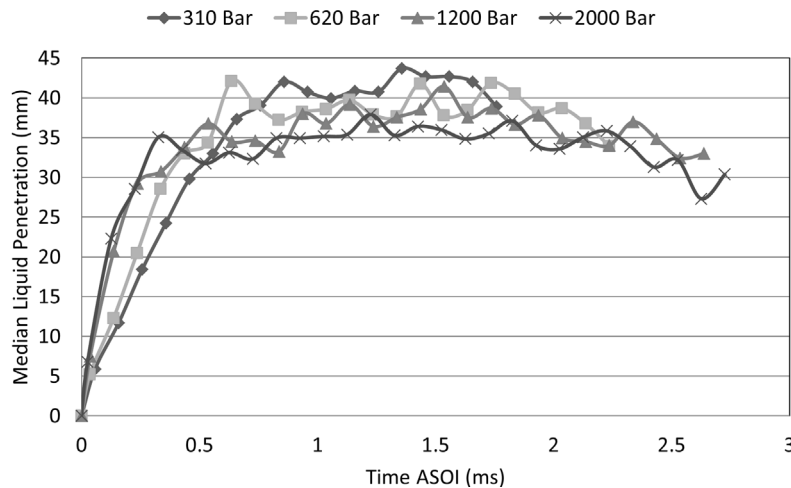


Figure 6.28: Median liquid penetration versus time ASOI for a sweep in injection pressure.

As injection pressure increases, there is a faster initial ramp up rate in liquid penetration. During the quasi-steady period of 1-2 ms ASOI, injection pressure is slightly larger for the 310 Bar case, however, the differences are minimal, at most 5 mm. These small reductions in liquid length for an increase in injection pressure is attributed to a change in the spray spreading angle which occurs under some test conditions, and will change the ambient entrainment characteristics and thereby influence the liquid length (Siebers 1998).

6.2.3. Reduced Charge Density

Charge-gas density is known to influence spray characteristics as increased density results in increased aerodynamic drag of the spray restricting liquid phase fuel penetration. Experimental test data is shown in Table 6.7.

Table 6.7
Ambient conditions at injection – ambient density variation.

Test Set	ρ_{Bulk} (kg/m ³)	ρ_{Core} (kg/m ³)	T _{Bulk} at Inj. (K)	T _{Core} at Inj. (K)	P _{Inj.} (Bar)
17.4 kg/m ³	17.3	16.3	1110	1170	2010
34.8 kg/m ³	34.7	32.2	1100	1190	1990

Small, insignificant, variations in ambient conditions between the two charge densities existed in regards to temperature and injection pressure, but these will not influence spray characteristics. Background subtracted spray images for the two charge densities are compared in Figure 6.29.

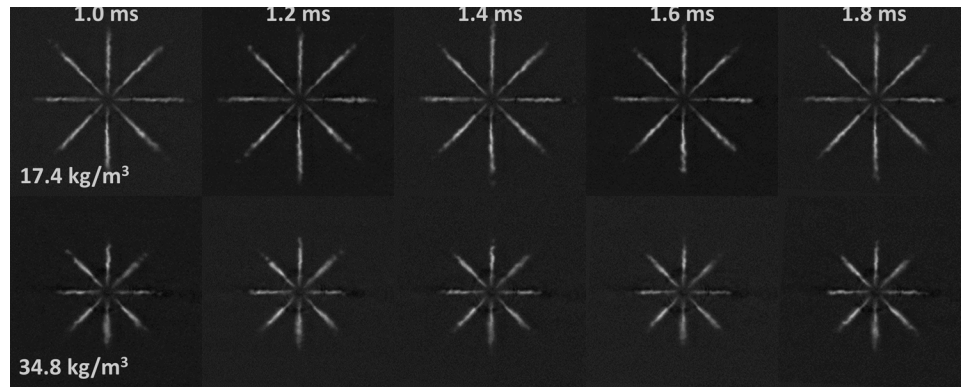


Figure 6.29: Background subtracted spray images. Charge density influence, 1100 K, 0% O₂, 2000 bar injection pressure.

As the charge gas density decreased spray liquid penetration was noticeably reduced for all spray plumes as confirmed in the median liquid penetration plot shown in Figure 6.30.

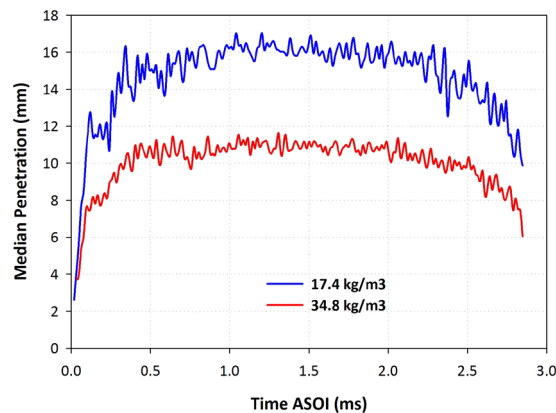


Figure 6.30: Median liquid penetration as a function of time ASOI for the charge density sweep, 1100 K 0% O₂, 2000 bar injection pressure.

As density increased from 17.4 to 34.8 kg/m³, median liquid penetration reduced 34%. Steady state liquid length was reached for both charge gas density cases around 0.75 ms ASOI.

Again, it is of interest to compare the normalized mean liquid lengths under both charge-gas conditions to understand the plume to plume trends, as shown in Figure 6.31.

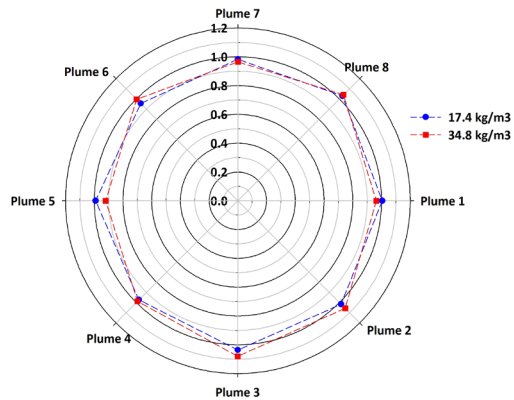


Figure 6.31: Polar plot of normalized liquid length during steady state (1 to 2 ms ASOI), 0% O₂, 1100 K, chiller off, 2000 bar injection pressure.

The mean steady state liquid length for each charge gas density sweep was normalized by the mean value over all 8 plumes to remove the density influence and solely compare the plume to plume trends. Plumes 1, 4, 5, 6 and 7 had normalized liquid lengths less than the mean (less than one) by 2 to 5%, whereas plumes 2, 3, and 8 had normalized liquid lengths larger than the mean (greater than one) by at least 4%, agreeing with prior trends. These plume dependencies and consistencies amongst a range of ambient and injection conditions confirmed the hypothesis that the plume-to-plume steady state differences are likely a result of flow and internal geometry.

6.2.4. Summary – Vaporizing Spray Results & Plume to Plume Variation Trends

This section looked at vaporizing spray liquid length behavior and trends in plume to plume variations as a function of a wide range of conditions including charge density, charge temperature, injection pressure, fuel temperature, and repeated conditions. Over all conditions distinct and consistent trends emerged in regards to the plume to plume variations. Plumes 1, 4, 5, 6 and 7 exhibited liquid lengths less than the mean by an average of 5%, and plumes 2, 3, and 8 exhibited liquid lengths in excess of the mean by an average of 5%. The consistency in plume to plume variations over all the conditions confirmed that the variations were repeatable and not inherent to the specific condition. These variations in steady state plume trends are likely the result of injector internal geometry and flow conditions, as hypothesized earlier. In addition to the plume to plume variations, several general liquid length trends were evidenced, agreeing with literature observations in regards to parameter influence on liquid length as discussed in Chapter 2.3.2. Conclusions are provided for the results presented here in section 6.2 and those presented in Appendix 12.6.2.

- For repeat tests (both chiller off and chiller on) the mean steady state liquid length varied by at most 0.3 mm.
- As charge gas temperature increased, liquid length decreased nonlinearly.

- At 1379 bar injection pressure for a 250 K charge gas temperature increase from 950 to 1200 K, liquid length decreased 30%.
- At 2000 bar injection pressure for a 500 K charge gas temperature increase from 800 to 1300 K, liquid length decreased 49%.
- As fuel temperature increased from 355 to 363 K, liquid length decreased 12%.
- As charge gas density doubled from 17.4 to 34.4 kg/m³, liquid length decreased 34%.
- As injection pressure increased from 1034 to 2000 bar, there was no significant impact on liquid length, less than a 1% increase which is within the system repeatability and accuracy.

6.3. Combusting Sprays

All combusting spray tests were undertaken in a 21% oxygen environment to emulate air, achieved by a pre-combustion event. The preburn procedure produces species of CO₂, H₂O, N₂, and O₂, in addition to levels of minor species yielding composition differences relative to that of dry air. All combusting spray tests were conducted at the elevated fuel temperature with the chiller off, 363 K.

The combustion luminosity images were used to characterize flame length (distance from the nozzle hole to the leading edge of the flame, similar to penetration in other tests), combusting cone angle (angle of a single combusting spray plume), and flame lift off length was approximated as detailed in Chapter 5.4.3. Typically, OH chemiluminescence diagnostics are used for flame lift off length as OH is known to be an indicator for ignition. However, by using natural combustion luminosity an indication of lift-off length could be determined and a relative comparison made between tests acknowledging that the actual lift-off length reported in literature for OH will be different than that provided here. Combusting luminosity images were also characterized in terms of spray plume intensities to provide an indication of relative levels of soot oxidation again acknowledging that actual soot levels will vary significantly, but this method can provide an approximate indication and method of comparison between test conditions. Understanding regions and distribution of intensity in combusting spray flames is important as differences in intensity can be related to regions of soot formation in the spray as these are natural combusting luminosity images.

Combusting spray tests quantified ignition delay from the pressure measurement with pressure traces also used to determine the net heat release from combustion. This procedure is outlined in Figure 6.32. To define the ignition delay, the pressure trace starting from the peak pressure of the preburn (initiation of the cool-down) to the end of the pressure trace was isolated. This pressure trace was then filtered using a low-pass Butterworth filter at 2000 Hz with a digital zero-phase filter. The region of the cool down was further isolated from the start of the cool-down to the location of the injector driver trigger defining the decay stage of the pressure trace. The decay phase of the pressure trace was low-pass filtered with a 2000 Hz Butterworth filter and was offset by the ending pressure value of the entire pressure trace (not just the cool-down). Offset pressure data, along with the time data from the cool-down decay, was fit to an exponential function using a linear curve fit by taking the logarithm of the pressure decay

data. The fit of the cool down was evaluated over the entire time region of interest from the start of the cool-down to the end of the data with the last value of the pressure (at the end of the data) added into this evaluated fit to provide fitted data to the cool down trace, assuming no fuel injection or combustion. The evaluated curve fit was subtracted from the filtered pressure data from the start of the cool-down to the end of the data trace and used to define the ignition delay. Definition of a time vector was required from the start of the cool down to the end of the pressure trace, offset by the time of the injector driver trigger. Ignition delay was defined as the time, relative to the injector driver trigger, when the subtracted pressure trace (data minus the fitted pressure trace) is greater than 0, subtracting the delay between the injector driver trigger and start of current (0.002 ms) along with the 0.245 ms delay between for the start of fuel relative to the driver start of current.

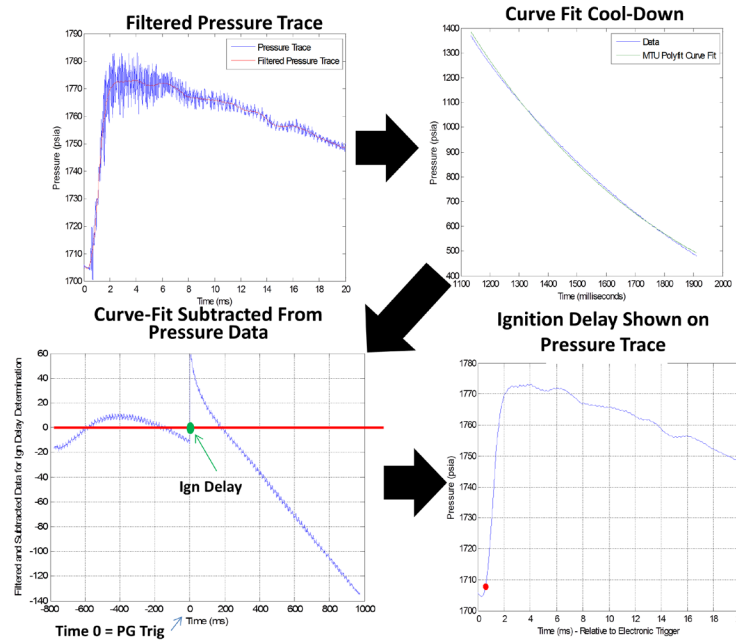


Figure 6.32: Ignition delay definition and determination procedure.

The pressure trace was also used to estimate the net heat release from the combustion event of the diesel fuel. The data region of interest was from the injector driver trigger to the peak pressure of the diesel combustion event. This pressure data was then filtered using a built-in Matlab smoothing function to facilitate ease of analysis by removing extraneous signal noise. The pressure differential (change in pressure) for each time step (10 microseconds) was determined over the entire filtered pressure region of interest during the diesel combustion event and used in the net heat release rate relationship provided by Heywood (1988) shown in equation (66).

$$\frac{dQ}{dt} = \frac{\gamma}{\gamma - 1} p \frac{dV}{dt} + \frac{1}{\gamma - 1} V \frac{dP}{dt} = \frac{1}{\gamma - 1} V \frac{dP}{dt} \quad (66)$$

This equation was simplified from the generic equation since the combustion vessel is constant volume, so the volume – time derivative can be neglected. The pressure – time derivative was calculated as previously mentioned using the pressure trace data, volume

was constant at 1.1 L which is the internal CV volume, and gamma is a constant representing the ratio of specific heats of the charge-gas environment, approximated as 1.35 for these tests. This equation provided the net heat release rate, with the total heat released being the sum of the heat release rate over the entire region of interest. This heat release analysis is shown in Figure 6.33.

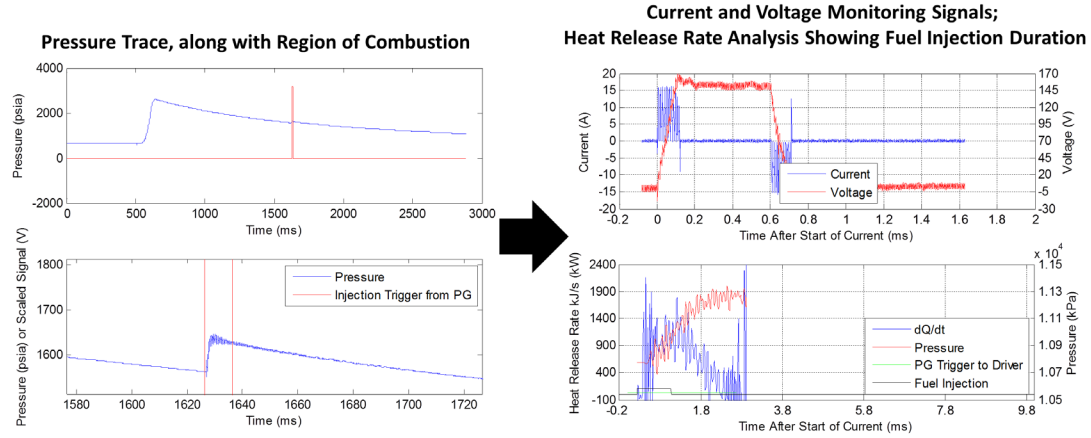


Figure 6.33: Heat release rate analysis for combustive spray tests.

The test matrix for the combustive spray tests is provided in Table 6.8.

Table 6.8
Test matrix for combustive spray tests.

Ambient Density (kg/m ³)	Fuel Pressure (bar)	Injection Trigger Duration (ms)	Fuel Temperature (°C)	Temperature at Injection (K)
34.8	1034	0.6	90	1100
34.8	1379	0.6	90	950
34.8	1379	0.6	90	1100
34.8	2000	0.6	90	950
34.8	2000	0.6	90	1100
17.4	2000	0.6	90	1100

In the combustive spray tests, plume 7 (which exits the injector and travels upward) will be obscured by the fan when it is about 10 mm from the top of the window, or 40 mm from the central injector tip, therefore, these results were not included in the median values or in the plume-to-plume variation under these obstructed conditions. Additionally, as the injector tip was not perfectly centered in the camera region of interest, data for plume 1 must be ignored after the combustive plume exits the region of interest as the full spray plume could no longer be seen. Experimental results are presented in subsequent sections, with additional results provided in Appendix 12.6.3.

6.3.1. Injection Pressure Variation at 1100 K Bulk Gas Temperature

An injection pressure sweep was undertaken at 1100 K bulk gas temperature, considering injection pressures of 1034, 1379 and 2000 bar. Charge gas density was kept constant at 34.8 kg/m³. Actual test conditions are defined in Table 6.9.

Table 6.9
Combusting test conditions for injection pressure sweep at 1100 K bulk gas temperature

	Injection Pressure (Bar)	Bulk Gas Density (kg/m ³)	Bulk Gas Temperature (K)	Core Gas Density (kg/m ³)	Core Gas Temperature (K)	Ignition Delay (ms)	Net Heat Release (kJ)
1034 Bar	1030	34.0	1100	31.5	1185	0.79	0.79
1379 Bar	1370	33.9	1100	31.4	1190	0.59	1.09
2000 Bar	2000	33.9	1100	31.5	1190	0.52	1.52

Density and temperature conditions were similar to the target values with the only significant variation being injection pressure. Heat release decreased by 48% as injection pressure decreased due to less fuel being injected with the same injection duration. Ignition delay decreased by 34% as injection pressure increased from 1034 to 2000 bar. Images from these tests are shown in Figure 6.34.

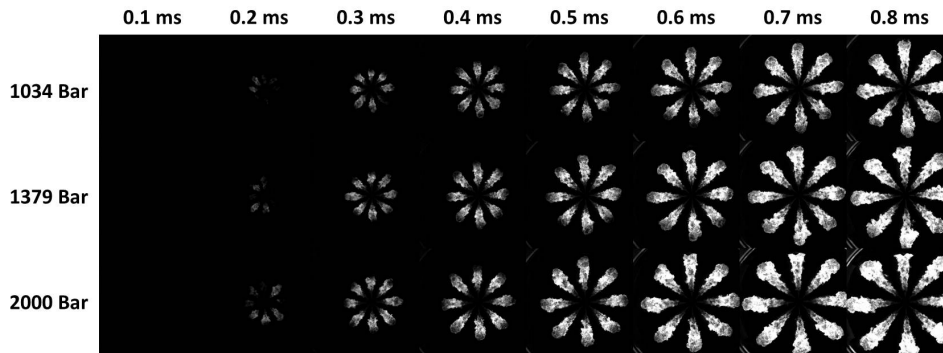


Figure 6.34: Combusting spray images from injection pressure sweep tests, 1100 K bulk gas temperature, 34.8 kg/m³ density.

The images show that as injection pressure increased, the flame length increased and ignition delay reduced. These parameters, and others, are quantified using image processing with results shown in the following set of figures, including flame length (Figure 6.35), cone angle (Figure 6.36), lift-off length (Figure 6.37) and combustor plume intensity (Figure 6.38).

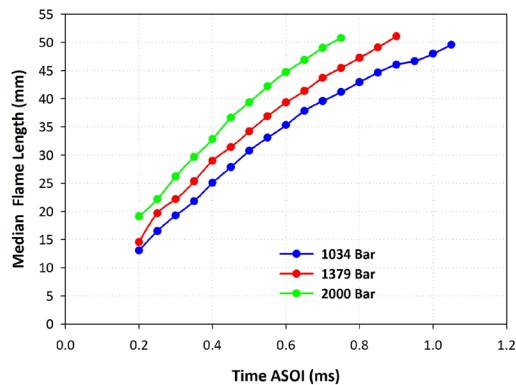


Figure 6.35: Median flame length versus time ASOI for combustor spray tests, 1100 K bulk gas temperature, 34.8 kg/m³ density. Ignition delay from pressure measurement of 0.79, 0.59 & 0.52 ms; injection pressures 1034, 1379 & 2000 bar.

As injection pressure increased at 1100 K, the flame length increased by 31% due to faster penetration because of increased momentum from the fuel.

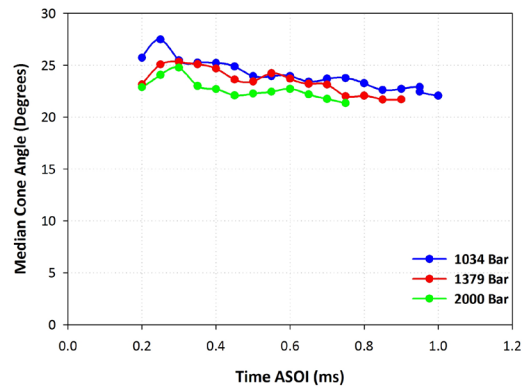


Figure 6.36: Median cone angle versus time ASOI for combustng spray tests, 1100 K bulk gas temperature, 34.8 kg/m³ density.

With injection pressure increases, there were no significant changes in the quasi-steady combustng spray flame cone angle for the 1034 and 1379 bar injection pressure cases. The 2000 bar injection pressure case had a slight reduction in cone angle, by about 2 degrees or 8%, relative to the 1034 and 1379 bar cases which exhibit similar cone angles.

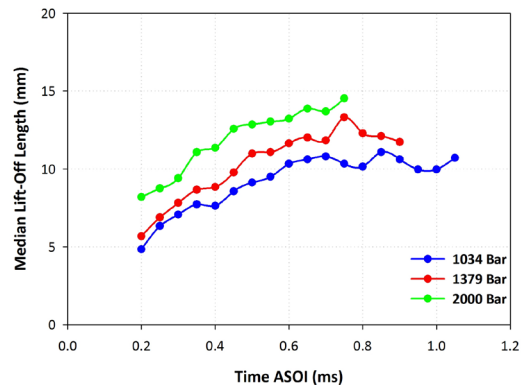


Figure 6.37: Median lift-off length versus time ASOI for combustng spray tests, 1100 K bulk gas temperature, 34.8 kg/m³ density.

An increase in injection pressure yielded an increase in the combustng flame lift-off length by close to 40%.

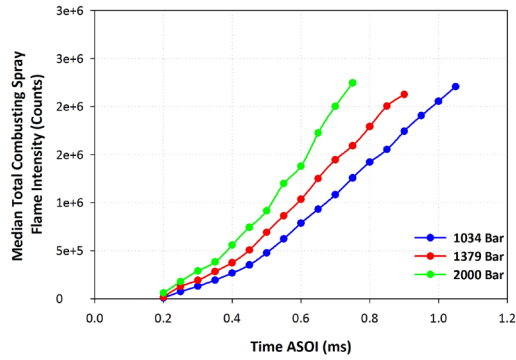


Figure 6.38: Median combusting plume intensity versus time ASOI for combusting spray tests, 1100 K bulk gas temperature, 34.8 kg/m³ density.

As injection pressure increased, the combusting spray flame intensity increased signifying an increase in soot oxidation. Actually soot produced may be higher or lower, with images showing only oxidized levels of soot. This trend was opposite to that seen at the 950 K temperature condition implying that increases in injection pressure may be more useful in controlling soot under lower temperature combustion conditions.

6.3.2. Density Variation

Also of interest was the influence of density on combusting spray parameters. This was undertaken at 2000 bar injection pressure and 1100 K charge gas temperature. Ambient charge gas density of 17.4 and 34.8 kg/m³ were considered, with actual test conditions defined in Table 6.10.

Table 6.10
Combusting test conditions for density variation at 1100 K bulk gas temperature and 2000 bar injection pressure.

	Injection Pressure (Bar)	Bulk Gas Density (kg/m ³)	Bulk Gas Temperature (K)	Core Gas Density (kg/m ³)	Core Gas Temperature (K)	Net Heat Release (kJ)
17.4 kg/m ³	1990	16.9	1110	15.9	1170	1.38
34.8 kg/m ³	2000	33.9	1100	31.5	1190	1.52

Injection pressure and temperatures were similar between the two tests, with density being increased by about a factor of two. Ignition delays could not be quantified from the pressure measurement at the low density case (17.4 kg/m³), and therefore were not included here. However, it is known that the lower density case has an increased ignition delay relative to the 34.8 kg/m³ density case, as seen in the images in Figure 6.39. Net heat release was similar between the two tests, being 10% larger in the full-load (high density) case due to improved fuel air mixing and combustion.

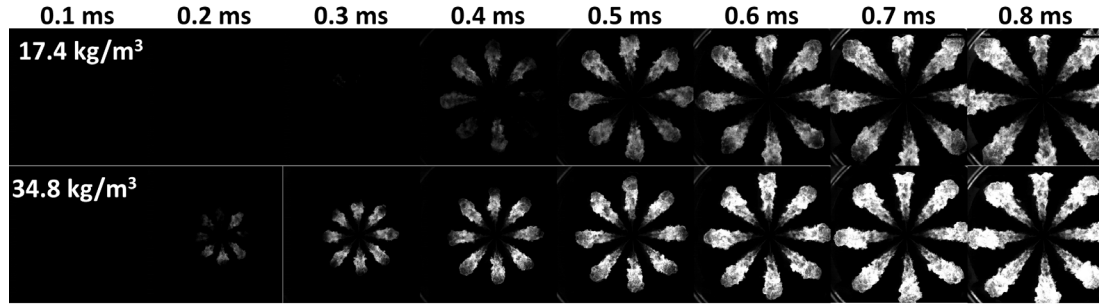


Figure 6.39: Combusting spray images from tests at 2000 bar injection pressures, 1100 K bulk gas temperature, density variation.

An increase in density reduced the ignition delay and provided increased intensity combusting spray flame images, with combusting flame penetration however being reduced under these conditions. These results are better understood by quantifying median flame length (Figure 6.40), median cone angle (Figure 6.41), median lift-off length (Figure 6.42), and median combusting plume intensity (Figure 6.43).

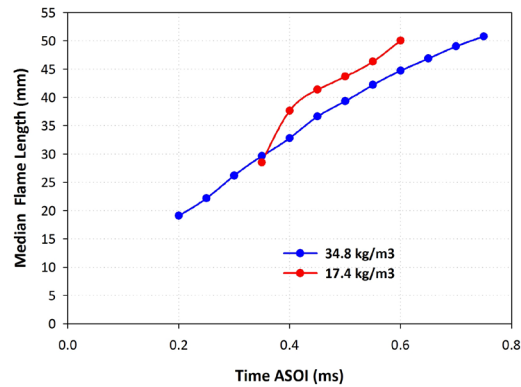


Figure 6.40: Median flame length versus time ASOI for combusting spray tests, 1100 K bulk gas temperature, 2000 bar injection pressure.

Increased aerodynamic drag on the spray is observed due to the charge-gas density increasing, which results in a flame length reduction of 11% magnitude.

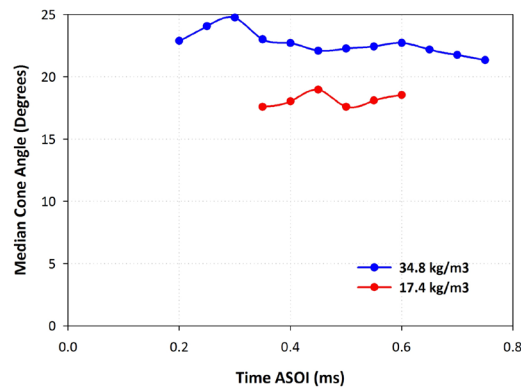


Figure 6.41: Median cone angle versus time ASOI for combusting spray tests, 1100 K bulk gas temperature, 2000 bar injection pressure.

As density increased, cone angle increased by 23% resulting in increased spray spreading and air entrainment.

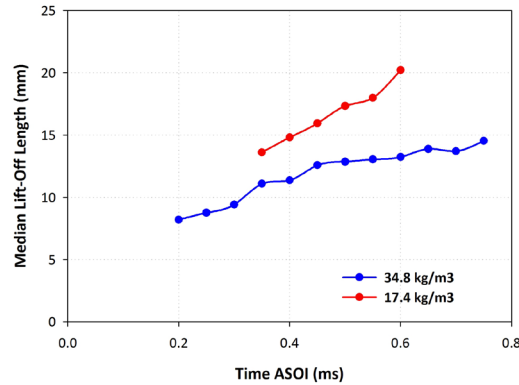


Figure 6.42: Median lift-off length versus time ASOI for combustng spray tests, 1100 K bulk gas temperature, 2000 bar injection pressure.

An increase in density yielded a reduction in lift-off length by 25% which was expected since flame length reduced due to the increased aerodynamic resistance, which limits the penetration of the spray and combustng flame. This restriction causes a reduction in lift-off length since fuel-air mixing will occur, but over a wider region based on the increased spray cone angle and reduced penetration, and as a result, the location of the onset of combustng will be closer to the injection tip.

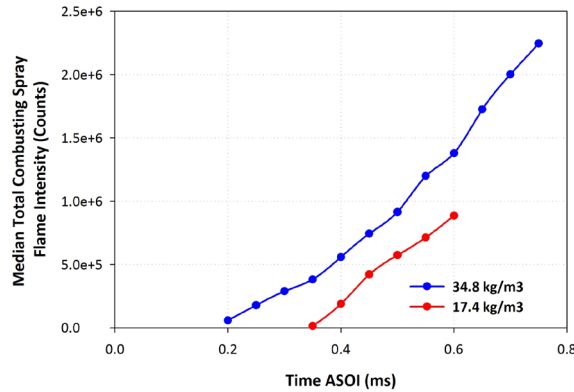


Figure 6.43: Median combustng plume intensity versus time ASOI for combustng spray tests, 1100 K bulk gas temperature, 2000 bar injection pressure.

Combustng plume intensity increased for the larger density condition by close to 90%. This indicated that relative soot oxidation levels will be larger for the increased density condition, which is expected based on full-load engine operation (higher density condition) where there are higher demands on the engine for increased power with emission levels increasing. As density increases, pressure is increased in the chamber, and all other test conditions are the same, which would provide increases in soot as soot formation is known to increase with charge-gas pressure increases (Tree and Svensson 2007).

6.3.3. Charge Gas Temperature Variation at 2000 Bar Injection Pressure

A charge gas temperature variation was undertaken at the elevated injection pressure of 2000 bar at 34.8 kg/m^3 charge gas density with the test conditions fully defined in Table 6.11.

Table 6.11
Combusting test conditions for charge gas temperature variation at 2000 bar injection pressure and 34.8 kg/m^3 charge gas bulk density.

	Injection Pressure (Bar)	Bulk Gas Density (kg/m^3)	Bulk Gas Temperature (K)	Core Gas Density (kg/m^3)	Core Gas Temperature (K)	Ignition Delay (ms)	Net Heat Release (kJ)
950 K	2030	33.7	960	31.7	1020	0.81	1.61
1100 K	2000	33.9	1100	31.5	1190	0.52	1.52

As the charge gas temperature was increased the ignition delay reduced by 36% agreeing with expected literature trends (Kobori et al. 2000). Heat release was similar with 5% decrease as temperature increased, due to the same injection pressure with a similar amount of fuel being injected. Images from the test are shown in Figure 6.44.

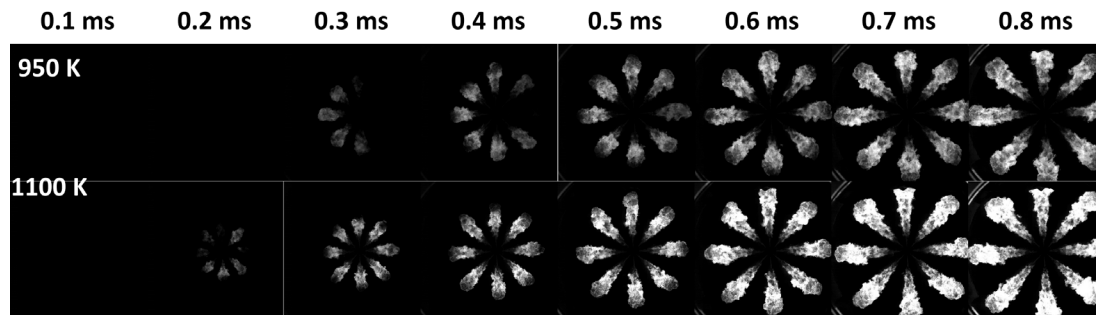


Figure 6.44: Combusting spray images from tests at 2000 bar injection pressure, 34.8 kg/m^3 density.

As charge-gas temperature increased, ignition delay reduced and combusting plume intensity increased. To provide a better understanding of the influence of charge gas temperature on combusting spray characteristics at this elevated injection pressure, results from image processing are presented in Figure 6.45, Figure 6.46, Figure 6.47, and Figure 6.48, for flame length, cone angle, lift-off length, and combusting intensity, respectively.

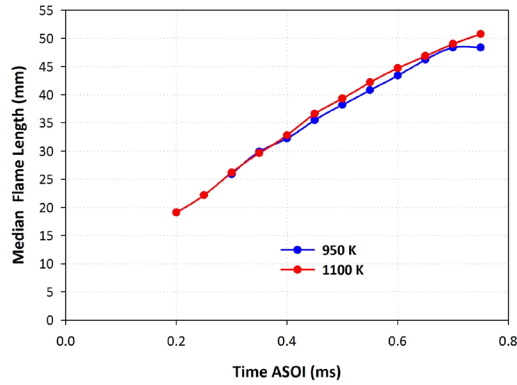


Figure 6.45: Median flame length versus time ASOI for combustng spray tests, 34.8 kg/m³ density, 2000 bar injection pressure. Ignition delay as determined from pressure is 0.81 ms and 0.52 ms for the 950 and 1100 K charge-gas temperature cases, respectively.

Median flame length was similar for the two test conditions as charge-gas temperature increased, within 2%, as was the case at the lower (1379 bar) injection pressure case reconfirming that injection pressure is more of a governing factor in flame length as opposed to charge-gas temperature.

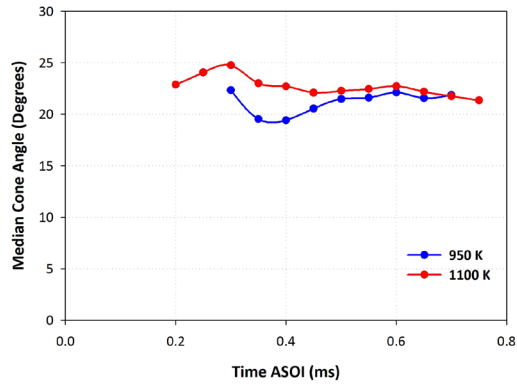


Figure 6.46: Median cone angle versus time ASOI for combustng spray tests, 34.8 kg/m³ density, 2000 bar injection pressure.

Cone angle was similar for both charge- gas temperatures and although the cone angle was larger for the 1100 K case the variation was small at steady state.

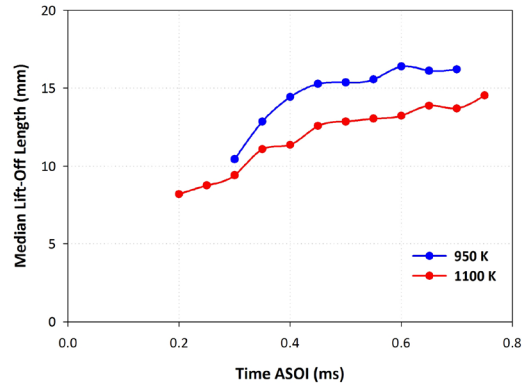


Figure 6.47: Median lift-off length versus time ASOI for combustive spray tests, 34.8 kg/m^3 density, 2000 bar injection pressure.

An increase in charge-gas temperature provided a reduction in lift-off length by 16% for this 2000 bar injection pressure case. This trend is more pronounced than that of the 1379 bar injection pressure case (refer to Appendix 12.6.3.5), with this being the expected trend based on literature (Higgins and Siebers 2001; Siebers and Higgins 2001).

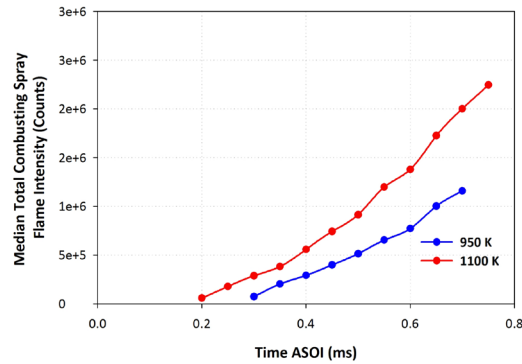


Figure 6.48: Median combustive plume intensity versus time ASOI for combustive spray tests, 34.8 kg/m^3 density, 2000 bar injection pressure.

An opposite trend to that seen at 1379 bar injection pressure case (refer to Appendix 12.6.3.5) was apparent for combustion luminosity, when the charge-gas temperature increased the combustive plume intensity increased, which indicates higher relative levels of soot oxidation, as expected for an increase in temperature.

6.3.4. Summary – Combustive Spray Results & Plume to Plume Variation Trends

A summary of combustive spray results is provided here, discussing tests presented in Section 6.3 and in Appendix 12.6.3.

- Two repeat tests showed high repeatability with minimal shot-to-shot variation, with less than a 5% variation in flame length, 1% variation in cone angle, and 6% variation in lift-off length between the two tests.
- As injection pressure increased, flame length and lift-off length increased, cone angle and total combustive spray plume intensity decreased, for the 950 K case and 1100 K case. The only exception to the 1100 K case was that as injection pressure increased, the total combustive spray plume intensity decreased. More

tests are needed to understand if this was a real effect due the different ambient charge gas temperature, or, if it was an artifact of the imaging diagnostic. Although the diagnostic was unchanged for all tests, the Mie scattering technique may not be the optimum diagnostic for these combustng intensity studies.

- An injection pressure increase from 1379 to 2000 bar at 950 K results in an increased flame length by 17% and lift-off length by 40%, with reductions in cone angle of close to 13%.
- An injection pressure increase from 1034 to 1379 bar at 1100 K increased flame length by an average of 12%, decreased cone angle by 4%, and increased lift-off length by 15%.
- An injection pressure increase from 1034 to 2000 bar at 1100 K increased flame length by an average of 31%, decreased cone angle by 8%, and increased lift-off length by 40%.
- As charge-gas density increased from 17.4 to 34.8 kg/m³, flame length and lift-off length were reduced by 11% and 25%, respectively, and cone angle and total combustng plume intensity were increased by 23% and 90%, respectively.
- As charge-gas temperature increased, there were negligible differences in flame length (less than 2%) and no consistent trends in cone angle. Lift-off length decreased as the charge-gas temperature increased by 16%, being more pronounced at the higher injection pressure (2000 bar). Trends with the combustng plume intensity were opposite with temperature for the two injection pressures providing no conclusive results without additional repeat tests.
- Heat release rate is largely driven by injection pressure as this controls the amount of fuel injected which contains the energy for combustion.
- Magnitude of plume to plume variations (as presented in Appendix 12.6.3) with the combustng spray tests were more pronounced relative to non-vaporizing or vaporizing spray tests. This is attributed to no averaging of parameters as was undertaken on the vaporizing spray tests and the combustion variation which influenced the repeatability and consistency of the parameters. This also implies that the combustng parameters were not as significantly influenced by the injector properties which govern the plume-to-plume variations in the non-vaporizing and vaporizing spray conditions.

6.4. Lift-off Length and Liquid Length Comparison

A comparison is also undertaken of lift-off length and liquid length under similar test conditions (same injection pressure, density, and bulk-gas temperature at injection), with differing oxygen environments based on the measurement, 0% or 21% oxygen. The mean steady state liquid length was determined from 1 to 2 ms ASOI for all eight spray plumes. This was compared to the mean value of the lift-off length (LOL) over all 8 spray plumes during the entire injection event. Results are shown in Figure 6.49 for the matching conditions at 0 and 21% oxygen, chiller off for all test conditions.

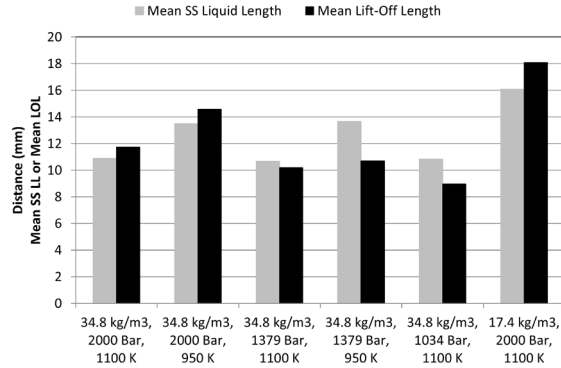


Figure 6.49: Mean steady state liquid length compared to the mean lift-off length for the matching 0% and 21% oxygen conditions, as labeled in the plot.

For the majority of the test conditions the lift-off length exceeded the liquid length by at least 8%, which implies that fuel vaporization was complete before reaching the combustion zone. Under these conditions, less soot is typically formed based on enhanced fuel-air mixing before combustion (Siebers and Higgins 2001). Current technology diesel engines are running at higher injection pressures and under these conditions, the liquid length is typically reduced relative to the lift-off length to enhance fuel air mixing and provide emission reductions. For three test conditions, 34.8 kg/m³ density at 1100 K 1034 bar injection pressure, and 950 and 1100 K 1379 bar injection pressure, the liquid length exceeded the lift-off length by at up to 20%, which implies that vaporization cooling can influence combustion rates and emission formation.

6.5. Penetration and Flame Length Comparison

A comparison is also made between non-vaporizing penetration and flame length. These conditions were at different ambient conditions, namely 373 K nitrogen for non-vaporizing tests, and 950 or 1100 K 21% oxygen for combusting tests which defines flame length. As discussed and determined previously, the charge-gas temperature does not influence the flame length. A comparison cannot be made for vaporizing conditions as only the liquid phase was visualized for these conditions. Of interest is the influence of combustion on the flame length relative to that of a non-vaporizing test condition. This comparison was undertaken for four different conditions, first for 34.8 kg/m³ density 1034 bar injection pressure, second for 34.8 kg/m³ density 1379 bar injection pressure, third for 34.8 kg/m³ density 2000 bar injection pressure and last for 17.4 kg/m³ density 2000 bar injection pressure, as shown in Figure 6.50, Figure 6.51, Figure 6.52, Figure 6.53, respectively.

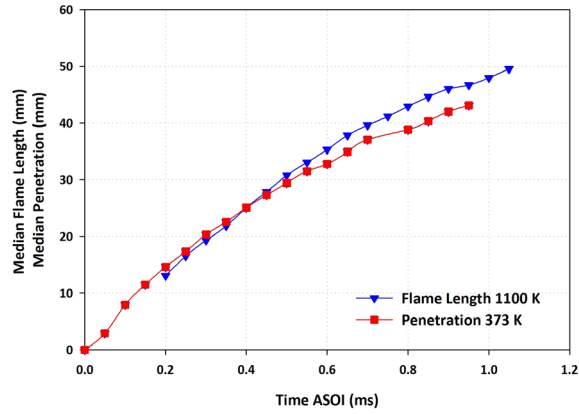


Figure 6.50: Comparison of median penetration and flame length for conditions of 34.8 kg/m³ density 1034 bar injection pressure.

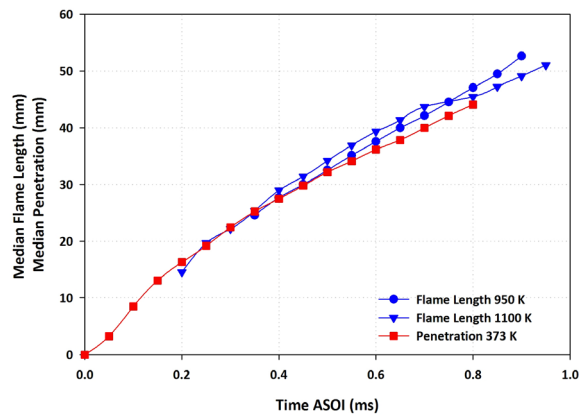


Figure 6.51: Comparison of median penetration and flame length for conditions of 34.8 kg/m³ density 1379 bar injection pressure.

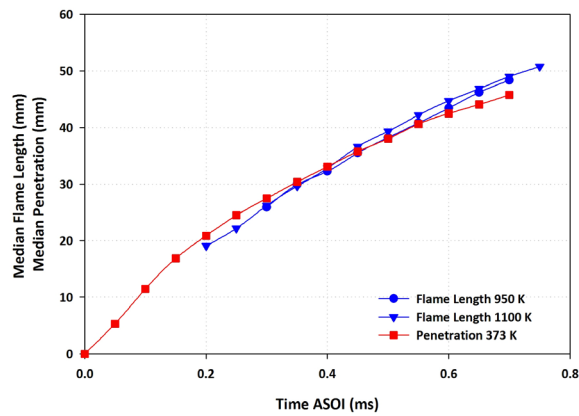


Figure 6.52: Comparison of median penetration and flame length for conditions of 34.8 kg/m³ density 2000 bar injection pressure.

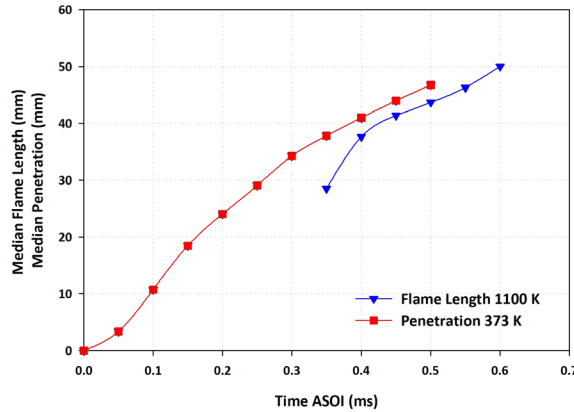


Figure 6.53: Comparison of median penetration and flame length for conditions of 17.4 kg/m³ density 2000 bar injection pressure.

Initially, penetration and flame length trends were very similar for all four cases considered. Around 0.4 ms ASOI, penetration became reduced relative to the flame length for the full load (34.8 kg/m³ density) condition by close to 7%, however, this trend was not observed for the part load (17.4 kg/m³ density) condition. As combustion occurs the hot products expand as the spray continues to propagate which could enhance the spray propagation rate. The exception to this was at the part load condition. This could be attributed to slower combustion rates at part load conditions, or camera time jitter in the non-vaporizing spray tests which was seen based on the non-linear trend from 0 to 0.1 ms ASOI.

6.6. Measurement Uncertainty

There exists uncertainties in the experimental spray measurement characteristics. These uncertainties have been quantified through the use of repeat tests and are both a function of image acquisition setup and method including scattering efficiency, as well as a function of the image processing.

Under nonvaporizing spray conditions, the maximum uncertainty or deviation in liquid phase penetration is 2 mm, with the average uncertainty being less than 1 mm. For cone angle, maximum uncertainty is 3 degrees with the average uncertainty being 1 degree, as determined over three repeat tests. For the vaporizing spray tests, the uncertainty is maximized for liquid penetration at 2.1 mm based on the largest deviation over three repeat tests. However, when considering the mean steady state liquid length the uncertainty is reduced to 0.2 mm. Under combusting spray conditions two repeat tests were undertaken, the maximum uncertainty in flame length is 2.2 mm, with the average uncertainty being 1.3 mm, and for combusting cone angle this maximum deviation is 2.3 degrees with an average deviation being 1 degree. Lift-off length shows an average uncertainty of 0.5 mm, with the maximum uncertainty being 0.9 mm.

Levels of uncertainty are small as defined by the repeat tests, relative to the spray parameters of interest. The change in spray parameters as a function of different conditions is significantly larger than the levels of uncertainty. Additionally, these uncertainties as defined by the repeat tests are in reality of lower magnitude based on the fluctuations seen in the sprays (as will be discussed in Chapter 8), as these fluctuations are random in nature. This randomness leads to differences in spray characteristics test to

test which are not the sole result of the image processing method and image acquisition setup but are inherently tied to the random nature of the spray.

6.7. Summary

This chapter provides experimental results for non-vaporizing, vaporizing and combusting spray tests. Tests were undertaken for diesel fuel sprays using a multi-hole injector, for which there are minimal quantified results in the literature due to the increased complexity in imaging. This subset of results is part of a larger study which includes CFD model development and validation, along with engine testing, for a range of injectors based on a project with an industrial partner. Results presented here are from one of the tested injectors, which is a production injector, with all others in the larger study being prototype injectors with different nozzle characteristics. Quantified parameters included; spray penetration and cone angle at 60% penetration for the non-vaporizing spray tests; penetration and quasi-steady liquid length for vaporizing tests; and flame length, lift-off length, cone angle, and total combusting plume intensity for combusting tests. Literature trends were confirmed for the various spray parameters, including the influence of fuel temperature, injection pressure, charge-gas density and charge-gas temperature. Also of interest was a comparison of the plume to plume variations. Trends were not consistent for non-vaporizing or combusting spray tests which was likely attributed to the consideration of minimal data points, whereas for the vaporizing spray tests parameters were averaged over the entire steady state portion, 1 ms, which included in excess of 50 data points to better isolate and understand the trends in the plume variations which were occurring. This resulted in observation of consistent variation trends over the spray plumes attributed to the internal injector flow geometry in the steady state, and eccentric needle motion in the initial start of injection period. This eccentric needle motion at start of injection was also evidenced in non-vaporizing spray tests.

7. Liquid Length Modeling with an Equation of State Approach

The goal of this chapter is to develop an approach for non-ideal thermophysical property evaluation using an equation of state which is integrated into Siebers liquid length model (1999). In this model, thermophysical property information is required. Siebers (1999) used tabulated property data in their model application, with Schihr et al. (2006) using piece-wave curve fits to tabulated property data. These methodologies are not readily applied to a wide range of hydrocarbon fuels due to limited availability of tabulated property data. Therefore, the development of this equation of approach will enable study of liquid length characteristics for both single and multi-component surrogate fuels, and will assist in evaluating proposed hypotheses on liquid length fluctuations, using readily available fuel property data. This is achieved via several objectives. First, it is required to understand the limitations of application of the Siebers (1999) liquid length 1-D scaling model relative to the break-up transition time. This limit is based on validity of the mixing limited hypothesis which becomes void when the injected fuel and not the ambient charge gas is the dominant medium, meaning that the break-up stage is complete. This is the case since mixing limited vaporization assumes that the local droplet interphase transport is quicker than the global fuel-air mixing rates (Siebers 1999; Lujten and Kurvers 2010). Furthermore, this model is utilized to predict liquid length, using cetane as a representative fuel for diesel, to provide a first order approximation based on readily available thermodynamic properties. Cetane is not the optimum choice as a diesel surrogate in regards to matching vaporization characteristics, based on its boiling point (560 K) difference relative to the 90% distillation point of diesel fuel (580 K) (Schihr et al. 2006), however, it is still effective at providing a good representation of diesel spray liquid length (Siebers 1999). The model results will be compared to experimental results presented in Chapter 6.2 to verify expected liquid length trends are preserved, and the accuracy of cetane as a surrogate for diesel vaporization characteristics.

Next, an equation of state approach is developed for thermophysical property evaluation used in the Siebers (1999) liquid length model to predict liquid length for various single and multi-component diesel surrogates. Fuel property data is tabulated in Appendix 12.7.1.4 for select components in comparison to diesel. The results of this approach (equation of state property determination coupled with 1-D liquid length model) using cetane as a fuel is compared to experimental results, and also to the tabulated property method results. This 1-D liquid length model and equation of state method is further compared to single-component cetane fuel experimental data from the Sandia National Laboratory Engine Combustion Network (ECN) to validate the equation of state approach and model applicability. This model is next used to compare results for various single component surrogates, with application also provided for proposed multicomponent surrogates relative to diesel experimental data from Michigan Technological University and Sandia National Laboratory. This model coupled with the equation of state approach provides a detailed tool for studying thermophysical property

characteristics, which are important in understanding diesel, and alternative fuels, spray and combustion characteristics.

7.1. Review of Siebers Liquid Length Model

Liquid length can be determined using the scaling law presented by Siebers (1999), as was previously discussed in Chapter 2.4.1.1. Fuel is injected into the ambient charge gas with the fuel and this charge gas mixing and forming a saturated state at the liquid length, as shown in Figure 7.1.

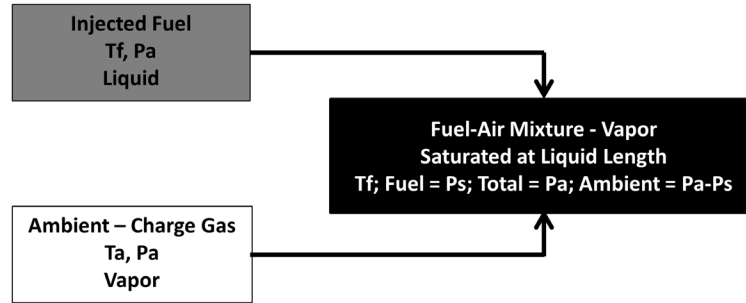


Figure 7.1: Overview of the fuel and charge-gas mixing schematic for the liquid length model.

This scaling law is presented again in equation (67) for ease of discussion, with the definition for the evaporation coefficient in equation (68).

$$LL = \frac{b}{a} \sqrt{\frac{\rho_f}{\rho_a} \frac{\sqrt{C_a} d_o}{\tan(\theta/2)}} \sqrt{\left(\frac{2}{B} + 1\right)^2 - 1} \quad (67)$$

$$B = \frac{\dot{m}_f(LL)}{\dot{m}_a(LL)} = \frac{P_s * MW_f * Z_a(T_s, P_a - P_s)}{Z_f(T_s, P_s) * (P_a - P_s) * MW_a} = \frac{h_a(T_a, P_a) - h_a(T_s, P_a - P_s)}{h_f(T_s) - h_f(T_f, P_a)} \quad (68)$$

Evaluating this relationship for liquid length provides an improved understanding on the influence of various parameters on liquid length, as well as providing use for parametric and predictive modeling studies. The solution to the liquid length model requires an iterative solution to calculate the saturation temperature, which is used to evaluate the evaporation coefficient, B. With this term evaluated the liquid length can be determined based on constants, and fuel and ambient charge-gas test conditions as shown schematically in Figure 7.2.

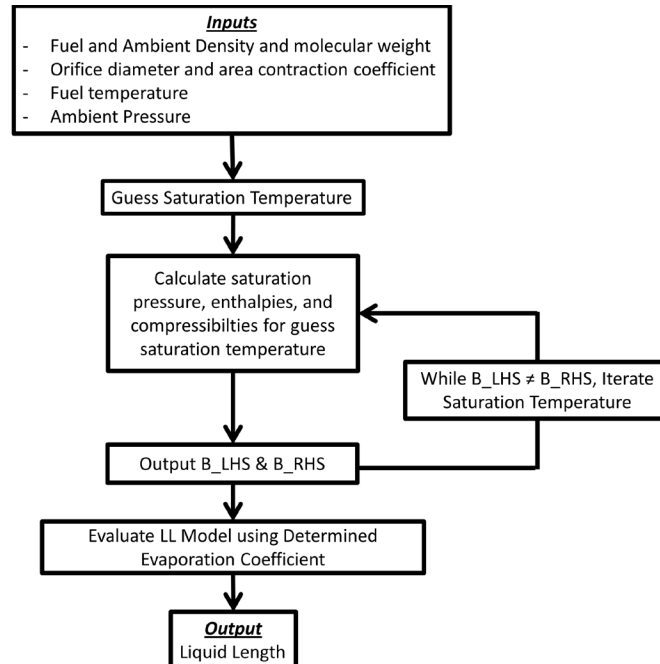


Figure 7.2: Liquid length solution methodology.

Details will be provided in subsequent sections on how these thermodynamic parameters, including saturation pressure, compressibility, and evaporation are determined for the fuel of interest.

7.2. Application Limitations of Siebers Liquid Length Model

First, it is important to understand limitations on validity of the mixing-limited hypothesis, which is the fundamental premise of this model. These limitations are determined by consideration of the transition time when the dominant controlling medium changes from injected fuel to charge gas entrainment. This relationship is based off an earlier scaling law derived by Naber and Siebers (1996) for the full gas phase penetration of vaporizing and non-vaporizing diesel sprays. In this relationship, a definition for the transition time where the dominant medium controlling the gas phase penetration switched, from that of the injected fuel to that of the ambient gas entrained, was determined (Naber and Siebers 1996). Penetration is linear with time up to the transition time, and square root in time after this period. This transition time provides an indication of the region of validity of the liquid length model since the model is based on a mixing limited vaporization assumption and is therefore valid only after the dominant medium has changed to that of the ambient gas, which is defined by liquid lengths larger than the corresponding penetration value at the transition time.

The definition for transition time is provided in equation (69), and is a function of injector and fuel properties, determined via conservation of mass and momentum relationships (Naber and Siebers 1996).

$$t_r = \frac{\sqrt{C_a/2}}{C_v \tan(\theta/2)} \frac{d_f \cdot \sqrt{\bar{\rho}}}{\sqrt{\frac{P_f - P_a}{\rho_f}}} \quad (69)$$

$$d_f = \sqrt{C_a} \cdot d_o$$

$$\bar{\rho} = \frac{\rho_f}{\rho_a}$$

Using this relationship and calculating the transition time for the conditions of interest in the current work provides an understanding of the limitation of application of the Siebers (1999) liquid length model. Values used in the calculation are provided in Table 7.1 with these being defined based on literature as parameters were not available for the injector used (Naber and Siebers 1996; Siebers 1999).

Table 7.1
Constants used in transition time evaluation.

Parameter	Value
a	0.66
C_a	0.8
C_d	0.75
C_v	Calculated from $C_d = C_v \cdot C_a$, 0.94

Fuel density is a constant 847 kg/m³ based on diesel fuel properties (Chapter 3.4.1), nozzle diameter is known to be 0.145 mm based on scanning electron microscope measurements (Chapter 3.4.2.1). Also required is knowledge of the cone angle of the spray which is determined using the correlation (equation (70)) provided by Siebers (1998).

$$\tan\left(\frac{\theta}{2}\right) = 0.26 * \left(\left(\frac{\rho_a}{\rho_f} \right)^{0.19} - 0.0043 \sqrt{\frac{\rho_f}{\rho_a}} \right) \quad (70)$$

Fuel pressure, ambient pressure, and ambient density all vary as a function of test conditions with core values used in the evaluation of the transition time (as provided in Table 7.2). The results for the transition time, and the evaluated penetration at the transition time calculated with the long-time scale penetration correlation (presented in equation (71) for ease of understanding) are provided in Table 7.2 for the test conditions currently under study.

$$S = \sqrt{\frac{C_v \cdot \sqrt{2C_a}}{a \cdot \tan(\theta/2)}} \cdot \sqrt{\frac{P_f - P_a}{\rho_f}} * d_o t \quad (71)$$

Table 7.2
Transition time for various conditions. *Calculated using the long-time scale relationship (equation (71)).

Bulk Gas Density (kg/m ³)	Bulk Gas Temperature (K)	Core Gas Density (kg/m ³)	Ambient Pressure (MPa)	Injection Pressure (MPa)	Transition Time (μs)	Penetration at Transition Time (mm)*
17.4	1100	16.3	5.7	200	21.7	7.3
34.8	1100	32.2	11.4	103	17.5	3.4
34.8	1100	32.2	11.4	138	15.0	3.4
34.8	800	32.9	8.3	200	11.6	3.3
34.8	950	32.7	9.9	200	11.7	3.3
34.8	1100	32.2	11.4	200	11.9	3.3
34.8	1200	32.0	12.4	200	12.0	3.4
34.8	1300	31.7	13.5	200	12.5	3.5

The maximum transition time occurs for the lowest density case, being 21.7 microseconds, with the minimum being reached at the low temperature, high density condition. Large differences are evident when comparing the penetration at the transition time to the mean liquid length, as shown in Table 7.3. These differences are expected, and confirm the validity of the mixing limited hypothesis. This comparison (of liquid length to penetration of the full spray at the transition time) is valid because the liquid core of the fuel spray continues to penetrate until reaching the quasi-steady liquid length, and at this transition time the quasi-steady liquid length has not yet been reached.

Table 7.3
Comparing penetration at transition to the mean liquid length over a range of conditions.

Bulk Gas Density (kg/m ³)	Bulk Gas Temperature (K)	Injection Pressure (Bar)	Mean Liquid Length (mm)	Penetration at Transition Time (mm)*
17.4	1100	2000	16.1	7.3
34.8	1100	1034	10.8	3.4
34.8	1100	1379	10.7	3.4
34.8	800	2000	17.8	3.3
34.8	950	2000	13.5	3.3
34.8	1100	2000	10.9	3.3
34.8	1200	2000	9.5	3.4
34.8	1300	2000	9.1	3.5

The penetration at the transition time is consistently less than that at the liquid length, by at least 50 percent. Therefore for the conditions in the current work the Siebers liquid length model will consistently be valid. This is further evidenced when considering the ratio of the penetration at the transition time to the mean liquid length as shown in Figure 7.3, for the conditions in Table 7.3.

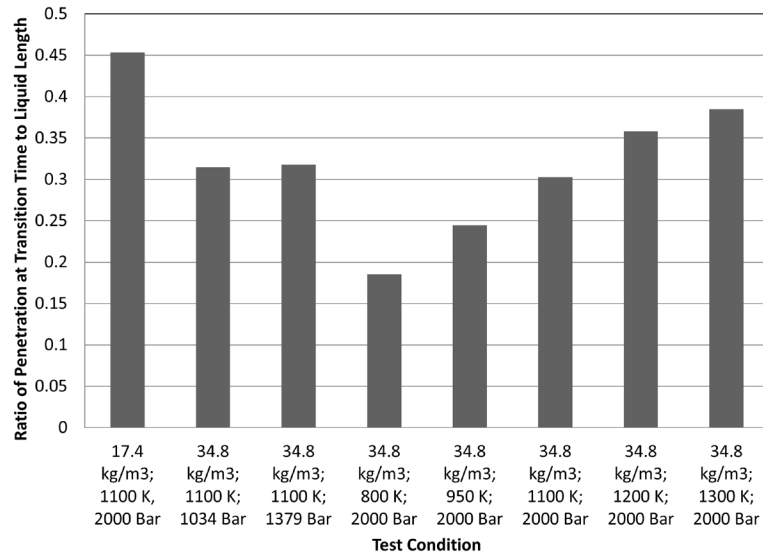


Figure 7.3: Ratio of penetration at transition time to liquid length for conditions in Table 7.3.

As density is reduced and charge-gas temperature and injection pressure are held constant, the ratio of penetration at transition time to the liquid length increases from 0.3 to 0.45. This is attributed to the longer transition time due to the reduction in aerodynamic resistance (charge gas entrainment) which enables the fuel to be the more dominant medium for a longer duration. The influence of injection pressure on this ratio is minimal, with the ratio changing by only 0.01 for an almost doubling of injection pressure. As temperature is increased, for constant density and injection pressure, the ratio is increased, by 100% for a 500 K increase in charge-gas temperature. As temperature increases, liquid length decreases, with the transition time increasing by less than 1 microsecond for this temperature increase (refer to Table 7.2), which results in minimal changes in the transition time and therefore this trend in the ratios is expected.

The validity limit in regards to mixing-limited conditions will be reached under low density and temperature conditions. This signifies therefore that as density (or temperature) is reduced (which results in increases in liquid length and the relative difference with penetration will be increasingly reduced), that the mixing limited vaporization assumption validity comes into question. At these lower density and temperature conditions, the droplet transport process rates (mass and energy) decrease relative to the mixing rates, and therefore a transition occurs from mixing limited vaporization (dominated by mass of entrained gas) to that of the processes at the droplet, where the fuel-gas mixture strays from saturated conditions thereby limiting the validity of this model (Siebers 1999). Although these conditions are not encountered here, this discussion provides an understanding on limitations of model applicability which will occur under part-load (low density), low temperature combustion conditions. Future work will include development of a dimensionless parameter for this ratio, to fully understand parameter dependency on the validity of this mixing limited hypothesis.

7.3. Liquid Length Model (1999) Application – Tabulated Thermodynamic Data

To evaluate the liquid length using Siebers model various steps are required. First the evaporation coefficient value must be determined, using equation (72), which requires an iterative solution for saturation temperature, refer to section 7.1. The evaporation coefficient can then be evaluated using the determined saturation temperature.

$$\frac{P_s * MW_f * Z_a(T_s, P_a - P_s)}{Z_f(T_s, P_s) * (P_a - P_s) * MW_a} = \frac{h_a(T_a, P_a) - h_a(T_s, P_a - P_s)}{h_f(T_s) - h_f(T_f, P_a)} \quad (72)$$

This evaluation requires knowledge of various thermodynamic properties including enthalpies, molecular weights, and compressibility's at various pressures (ambient and saturation) along with temperatures (ambient, saturation, and fuel). Thermodynamic properties of common species are typically tabulated, however, properties are not known for all species. An equation of state, coupled with thermodynamic property relationships, can be used to define thermodynamic properties which are unknown for certain fuels or species. This procedure will be discussed in section 7.4. Currently, a first order approximation is applied using readily available tabulated data for Cetane to evaluate the liquid length model for comparison to experimental data. The equations used for property data are provided in Appendix 12.7.1.1, including those for the determination of enthalpy, density, saturation pressure, and compressibility, using the relations set forth by Schihr et al. (2006). Schihr et al. (2006) applied piece-wise curve fits to tabulated property data to represent the data in equation format to facilitate an iterative solution. Siebers (1999) also used tabulated data for property evaluation in the original model via computer databases.

To solve for the saturation temperature, initial conditions are defined including ambient charge-gas pressure and temperature, and fuel temperature (355 K or 363 K with or without cooling, respectively), which are known experimental test conditions. The molecular weight of the fuel and molecular weight of the ambient (0% oxygen, mixture of water, carbon dioxide and nitrogen) environment are also known conditions, being 226.44 kg/kmol and 28.67 kg/kmol, respectively. Based on ambient test conditions, being close to ideal gas conditions, the ambient compressibility for this evaluation is assumed to be 1 (Schihr et al. 2006). These values, together with the property relationships, enable an iterative solution of equation (72) to define the saturation temperature. This solution is undertaken in the Engineering Equation Solver (EES) program, with code provided in Appendix 12.7.1.2. With known saturation temperature, the liquid length relationship is evaluated using the previously discussed values along with the constant b of 0.41 and fuel density is evaluated as discussed in Appendix 12.7.1.1, required in the calculation of the spray angle. Liquid length is evaluated using core gas conditions of density and temperature as injection and achieved liquid length occur in the core region of the vessel. Results are provided in Table 7.4.

Table 7.4
Liquid length as determined from evaluation of Siebers (1999) model using cetane as a surrogate for diesel fuel.

Test #	Core Gas Density (kg/m ³)	Core Gas Temp (K)	Inj. Press. (Bar)	Fuel Temp. (K)	Saturation Temp. (K)	Model Calculated LL (mm) for Cetane	Exp. LL (mm)	% Diff.
1	16.3	1170	2010	363	634.6	14.5	16.1	10.5
2	32.1	1190	1022	363	664.1	9.7	10.8	10.7
3	32.5	1015	1378	363	643.0	12.2	13.7	11.6
4	32.1	1190	1376	363	664.1	9.7	10.7	9.8
5	32.0	1300	1373	363	674.7	8.6	9.0	4.5
6	32.9	850	1990	363	616.9	16.8	17.8	5.8
7	32.7	1010	2020	363	642.5	12.2	13.5	10.1
8	32.2	1190	1990	363	664.2	9.6	10.9	12.7
9	32.0	1300	2010	363	674.7	8.6	9.5	9.9
10	31.7	1430	2000	363	664.2	7.8	8.4	7.4
11	32.2	1190	1068	355	664.8	9.7	12.7	26.8
12	32.2	1190	1369	355	664.8	9.7	12.4	24.4
13	32.0	1190	1988	355	664.6	9.8	12.4	23.4

Percent difference between model and calculate results is computed to compare the experimental and model results for liquid length. The largest differences are seen under the reduced fuel temperature conditions. Various conclusions can be made from the results in the above table, as summarized below.

- Cetane can be used as a surrogate for diesel fuel spray vaporization characteristics, however, the results for model calculated liquid length were at most 3 mm shorter than experimental results. The largest deviation occurs for the reduced fuel temperature cases. If these are excluded, the modeled liquid length is at most 1.6 mm shorter and at minimum 0.4 mm shorter than the experimental liquid lengths, providing percent differences between experimental and model results of at minimum 4.5%. Results for modeled cetane fuel are reduced relative to the experimental diesel fuel agreeing with literature, based on the reduction in boiling point of cetane (560 K) relative to that of diesel fuel at 90% distillation (580 K) (Schihi et al. 2006, Siebers 1999). Other reasons for the discrepancy between cetane and diesel could be attributed to the approximation of injector parameters for velocity or area contraction coefficients in place of measured values along with evaluation for cone angle using the correlation. Although there are differences in the magnitude of the results when using cetane as a surrogate representative fuel for diesel, the trends are preserved with model application relative to experimental results. This is shown for core-gas temperature trends in Figure 7.4.

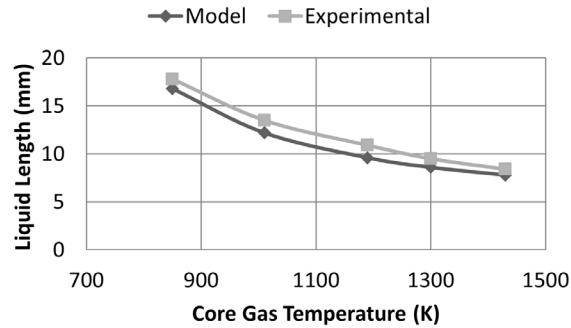


Figure 7.4: Liquid length versus core-gas temperature comparing model and experimental results. 34.8 kg/m^3 core charge-gas density, 2000 bar injection pressure.

The nonlinear influence of core charge-gas temperature on liquid length is preserved from the model using cetane as the representative fuel, matching diesel experimental results.

- Fuel injection pressure has negligible effect on liquid length in both the experimental and the modeling results as expected based on the scaling law relationship and development. This result may be considered by some to be counter-intuitive due to the influence of injection pressure on vaporizing spray penetration, but can be understood by consideration of the underlying physical processes. As injection pressure increases, the vaporization rate increases (governed by an increase in the entrained charge-gas mass flow rate), with this increase being of the same magnitude of the increase of the fuel flow rate, based on conservation of energy assuming turbulent mixing control (Siebers 1998). Conservation of mass for the ambient charge-gas entrained and that for the fuel flow rate both depend linearly on injected fuel velocity, which is proportional to the square root of injection pressure (Bernoulli's Equation), and therefore no change is seen in liquid length for a change in injection pressure. Implications of the lack of injection pressure influence on liquid length show that elevated injection pressures can be used to assist with improved fuel-air mixing and emissions reductions, without concern over fuel spray impingement on combustion chamber walls which would yield increases in unburnt hydrocarbon emissions.
- The 8 degree Kelvin reduction in fuel temperature provides a higher reduction in the liquid length in the model as compared to the experimental results. This could be attributed to uncertainties in measured fuel temperatures based on setup and measurement accuracy.

Despite these variations between model and experiment, the general trends are preserved in regards to the lack of influence of fuel injection pressure on the results, the nonlinear increase in liquid length with a reduction in charge-gas temperature, and the reduction in liquid length with an increase in charge-gas density.

This tabulated property data application provides validation of the model, with the use of cetane being valid as a first order approximation. It also serves to illustrate the method of solution in regards to the iterative nature of the saturation temperature and the evaporation coefficient determination, and solution for liquid length. This application

also shows that the use of improved surrogates that better represent diesel fuel evaporation characteristics is merited, which could be achieved through the development of an equation of state approach to account for unknown or non-readily available thermodynamic properties for both single and multi-component surrogates, as will be discussed.

7.4. Equation of State Approach for Thermodynamic Property Evaluation

There are several equations of state which can be used to describe thermodynamic behavior, as were reviewed in Chapter 2.6. The ideal gas is one such equation of state but it is limited in regards to applicability to low pressure conditions or temperatures significantly larger than the critical temperature to ensure accurate representation of real properties (Eastop and McConkey 1993). These ideal conditions are not representative of diesel engine operation. Equations of state, such as the Redlich-Kwong or Peng-Robinson as examples, require two properties, i.e. pressure and temperature, from which all others can be evaluated, i.e. compressibility and volume. The equation of state used is determined by the required application, species type considered, and conditions. Diesel sprays are known to exhibit non-ideal gas effects based on the pressure and temperature conditions they encounter in the cylinder. Fuel is injected as a compressed liquid, subsequently vaporizing into the gas state. Various equations of state have been applied to diesel sprays, with the Peng-Robinson equation of state being validated for high-pressure nonpolar systems which are pertinent to diesel sprays (Reid et al. 1987; Hohmann and Renz 2003) and will be used here.

In order to apply and utilize the scaling law of Siebers (1999) for liquid length, various fuel properties must be known to enable calculation of saturation temperature and therefore the evaporation coefficient. Tabulated properties can be used in these evaluations including those from the American Petroleum Institute (API) for example (API 1997), as were used in section 7.3, however, due to the iterative nature of the problem, tabulated properties are difficult and inefficient to use. Furthermore these properties are not readily available for all species. Therefore an approach is presented here which uses an equation of state to evaluate thermodynamic properties for known species critical properties of pressure, temperature, along with species acentric factor, ω . In the Peng-Robinson equation of state,

$$P = \frac{RT}{v-b} - \frac{a\alpha}{v^2+2bv-b^2}, \quad (73)$$

$$\alpha = (1 + (\kappa)(1 - T_r^{0.5}))^2,$$

$$\kappa = 0.37464 + 1.54226\omega - 0.26992\omega^2,$$

ω is the acentric factor which is a molecular property of the species, representing the non-spherical nature of the molecule, essentially measuring molecule complexity (both in regards to geometry and polarity) (Reid et al. 1987). R is the ideal gas constant and T_r is reduced temperature, defined as the temperature over the critical temperature, and P_r is the reduced pressure, defined as the pressure over the critical pressure. Species constants a and b will be defined and discussed shortly. With an equation of state chosen, and species properties known (as these are given, see Reid et al. 1987), the thermophysical properties must be defined and evaluated to enable application of Siebers liquid length

model, requiring use of various thermodynamic relationships and definitions as outlined below. Examples are provided here for cetane (hexadecane), $C_{16}H_{34}$ as the species of interest, to enable comparison to results provided in section 7.3. The needed properties include critical temperature, pressure, and acentric factor, which are 722 K, 14.1 bar, and 0.742, respectively (Reid et al. 1987). Also required is the Rackett parameter for density definition, and polynomial constants for constant pressure ideal gas specific heat capacity.

To determine the equation of state constants of a and b , the critical properties and acentric factor must be known and substituted into the following relationships. These relationships are defined by the use of equation (73), along with the knowledge that the partial derivative of pressure with respect to volume at the critical temperature is zero, and the second partial derivative of pressure with respect to volume at the critical temperature is also equal to zero as provided in equation (74). It should be acknowledged that these relationships are for pure substances at the critical point (the derivative is evaluated at the critical temperature).

$$\begin{aligned} \left(\frac{\partial P}{\partial V}\right)_{T_c} &= 0 \\ \left(\frac{\partial^2 P}{\partial V^2}\right)_{T_c} &= 0 \end{aligned} \quad (74)$$

Applying these derivatives yields the Peng-Robinson equation of state constants as defined in equation (75).

$$\begin{aligned} a &= 0.45724 \frac{R^2 T_c^2}{P_c} \\ b &= 0.07780 \frac{RT_c}{P_c} \end{aligned} \quad (75)$$

These constants are valid for all species by evaluation of the equations for each species critical properties.

By considering the definition of compressibility, $Z = PV/RT$, the Peng-Robinson equation of state can be written in terms of compressibility (equation (76)), where expressions are developed for new parameters, A and B , as a function of prior defined parameters.

$$\begin{aligned} Z^3 - (1 - B)Z^2 + (A - 2B - 3B^2)Z - (AB - B^2 - B^3) &= 0 \\ A &= \frac{a \propto P}{R^2 T^2} \\ B &= \frac{bP}{RT} \end{aligned} \quad (76)$$

This cubic compressibility format is required for evaluating thermophysical properties.

The first required property is a saturation pressure-temperature relationship as this information is needed for the fuel of interest based on the assumptions in the liquid length model. Saturation pressure and temperature are determined based on the vapor-liquid equilibrium assumption. For this equilibrium state, the fugacity (f) of the liquid state is equal to that of the vapor state, which occurs at the vapor, or saturation pressure. The generic fugacity relationship is given in equation (77), and will be evaluated for Peng-Robinson equation of state.

$$\ln\left(\frac{f}{P}\right) = Z - 1 - \ln(Z) + \frac{1}{RT} \int_{\infty}^V \left(\frac{RT}{V} - P\right) dV \quad (77)$$

Using the equation of state and the definition for fugacity (equation (77)), the fugacity relation for both the liquid and vapor phase of the species can be evaluated for the Peng-Robinson equation of state as shown in equation (78), where subscripts denote the vapor (gas) or liquid phase.

$$\begin{aligned} \ln\left(\frac{f_g}{P}\right) &= Z_v - 1 - \ln(Z_v - B) - \frac{A}{2^{1.5}B} \ln\left[\frac{Z_v + (2^{0.5} + 1)B}{Z_v - (2^{0.5} - 1)B}\right] \\ \ln\left(\frac{f_l}{P}\right) &= Z_l - 1 - \ln(Z_l - B) - \frac{A}{2^{1.5}B} \ln\left[\frac{Z_l + (2^{0.5} + 1)B}{Z_l - (2^{0.5} - 1)B}\right] \end{aligned} \quad (78)$$

With fugacity relationships defined, the saturation pressure–temperature relationship can now be determined using species critical properties and the solution to the cubic equation of state. This saturation condition is defined as the pressure such that the liquid and gas (vapor) phase fugacity's are equal, i.e. $f_l = f_g$.

The solution process involves first defining a temperature (saturation temperature) less than the critical temperature (as saturation conditions are vapor-liquid equilibrium and only occur under subcritical conditions based on the vapor dome), and evaluating the equation of state parameters, for a guess value of pressure (equation (76), using equations (75) and (73)). The cubic form of the equation of state in compressibility (equation (76)) is then solved which will provide three roots, the largest root representing the equilibrium vapor phase compressibility, the smallest representing the equilibrium liquid phase compressibility and the middle root is discarded as it has no physical meaning. These compressibility roots are then used to evaluate the fugacity relationships, solving for the liquid and vapor phase fugacity's, equation (78). The pressure is iterated until the fugacity of the vapor and liquid phase are equal. When this condition is achieved, the chosen temperature, and corresponding pressure, define the saturation conditions. This procedure is undertaken over a range of temperatures to provide the full saturation pressure-temperature curve for the substance, up to its critical point. This procedure only requires knowledge of critical fuel properties and acentric factors, which are tabulated for hydrocarbons and other species. This procedure is undertaken in EES as it is a program well-suited for iterative calculations, and includes a solver for determining real cubic roots, setting values to 0 if the roots are imaginary (which occurs at temperatures above the critical temperature).

Next, enthalpies must be determined for the ambient charge-gas and fuel, over temperature conditions both at saturation (liquid length) and at injection. An equation of state approach is used meaning that enthalpy departure relationships are required for determination of the enthalpy terms. Enthalpy departure is defined using the Peng Robinson equation of state, with the general relationship valid for all equations of state, $h - h^*$, provided in equation (79), where the superscript * denotes the ideal gas state (Sandler 1999). Enthalpy departure is valid when used with the vapor-phase compressibility for providing vapor phase enthalpies.

$$h(T, P) - h^*(T) = RT(Z - 1) + \int_{\infty}^V \left[T \cdot \left(\frac{\partial P}{\partial T}\right)_V - P \right] dV \quad (79)$$

The integration limit of V represents real-gas conditions and the ∞ corresponds to ideal gas conditions. For the Peng-Robinson equation of state, the enthalpy departure is defined in equation (80), based on substitution of equation (73), into equation (79). Terms of a and b were defined in equation (73) (Sandler 1999).

$$h(T, P) - h^*(T) = RT(Z - 1) + \frac{T \left(\frac{d(a\alpha)}{dT} \right) - a}{2 \cdot \sqrt{2}b} \ln \left[\frac{Z + (1 + \sqrt{2})B}{Z + (1 - \sqrt{2})B} \right] \quad (80)$$

$$\frac{d(a\alpha)}{dT} = -a\kappa \sqrt{\frac{\alpha}{TT_c}}$$

$$B = \frac{Pb}{RT}$$

To determine enthalpy of the state from the departure function, the ideal gas enthalpy must be determined. This is calculated based on the constant pressure specific heat capacity of the ideal gas, using the enthalpy definition provided in equation (81).

$$h^*(T) = \int_{T_{ref}}^T C_p^*(T) \cdot dT \quad (81)$$

To evaluate the ideal gas enthalpy, a relationship for specific heat is required as this property is temperature dependent. The relationship used in each enthalpy evaluation will be discussed, as different approaches are used for the different species / mixtures considered.

There are four enthalpies required for evaluation of the evaporation coefficient; ambient charge gas enthalpy before fuel injection (T_a, P_a), liquid fuel enthalpy at injection (T_f, P_a), saturated vapor phase fuel at the liquid length (T_s, P_s), and the saturated charge gas enthalpy at the liquid length ($T_s, P_a - P_s$) (refer to equation (72)).

The first required enthalpy is that of the ambient charge-gas, before fuel has been injected. The ambient charge-gas is that of the 0% oxygen environment, with only major species of nitrogen, carbon dioxide, and water being considered. Although not in the current ambient mixture, oxygen properties are also provided for application to other gaseous mixtures. The enthalpy departure is evaluated using equation (80), where temperature and pressure are that of the ambient charge-gas. To evaluate the enthalpy departure the compressibility of the vapor phase must be determined. This requires solving the cubic equation of state for the compressibility, equation (76), using the known pressure and temperature conditions of the ambient charge gas. To evaluate the cubic equation of state, the critical temperature and pressure of the ambient charge-gas mixture need to be determined. Critical constants of mixtures are not tabulated (they are only available for the individual species), therefore, pseudo-critical properties must be applied for determination of the ambient charge-gas enthalpy. For temperature, a simple mole fraction average of the pure component critical temperatures is used, known as Kay's rule provided in equation (82) (Reid et al. 1987).

$$T_{c,mix} = \sum_i Y_i \cdot T_{c,i} \quad (82)$$

The same approach is used for determination of the acentric factor for the mixture, equation (83).

$$\omega_{\text{mix}} = \sum_i Y_i \cdot \omega_i \quad (83)$$

For pseudo-critical pressure an alternative approach is required since the mole fraction average methodology only provides accurate results for instances where the critical pressure is similar amongst all components, which is not the case for the species of interest here as they span nearly an order of magnitude (water is 221.2 bar, carbon dioxide is 73.8 bar, nitrogen is 33.9 bar, and oxygen is 50.4 bar) (Reid et al. 1987). Therefore, the rule applied for determining mixture critical pressure is the modified Prausnitz and Gunn rule, provided in equation (84) (Reid et al. 1987).

$$P_{c,\text{mix}} = \frac{R \cdot T_{c,\text{mix}} \cdot \sum_i Y_i \cdot Z_{c,i}}{\sum_i Y_i \cdot V_{c,i}} \quad (84)$$

To determine the pseudo-critical pressure, properties of critical compressibility and critical volume are required for each species. These properties are tabulated and readily available in the literature (Reid et al. 1987), provided in Table 7.5.

Table 7.5
Critical properties of the species composing the ambient charge gas (Reid et al. 1987).

	Critical Pressure (bar)	Critical Temperature (K)	Critical Volume (cm ³ /mol)	Critical Compressibility	Acentric Factor
Water	647.3	221.2	57.1	0.235	0.344
Carbon Dioxide	304.1	72.8	93.9	0.274	0.239
Nitrogen	126.2	33.9	89.8	0.290	0.039
Oxygen	50.4	154.6	73.4	0.288	0.025

The solution to the cubic equation of state provides the vapor compressibility (largest root), which is then used to evaluate the enthalpy departure for this ambient temperature and pressure condition.

As mixture property calculations are now understood, focus returns to the evaluation of equation (80) for each of the conditions of interest. To determine the charge-gas vapor phase enthalpy from the enthalpy departure, the ideal gas enthalpy must be calculated. For this evaluation, the ideal gas specific heat capacity must be determined, as a function of temperature, which enables determination of ideal gas enthalpy based on integration. This ideal gas specific heat capacity is calculated using NASA polynomials, providing ideal gas properties (McBride et al. 1993) extracted from the GRI 3.0 mechanism (Smith 1999). The polynomial relationship is provided in equation (85), where a_i are species specific constants, with two sets of constants being provided, based on the ambient temperature range, with the midpoint for both being at 1000 K.

$$C_p^*(T) = R \cdot (a_1 + a_2 T + a_3 T^2 + a_4 T^3 + a_5 T^4) \quad (85)$$

For the ambient enthalpy, the species of interest are those in the zero percent oxygen mixture, post preburn, which include water, nitrogen, and carbon dioxide, with the required species specific constants for evaluation of the above equation provided in Appendix 12.7.1.6. Although not used in the current mixture, constants for oxygen are also included for reference. Equation (85) provides the specific heat capacity for

individual species, which, based on the definition of enthalpy and the assumption of ideal gas, when integrated from the reference temperature to the temperature of interest, provides the ideal gas enthalpy, equation (86).

$$h^*(T) = \int_{T_{\text{ref}}}^T C_p^*(T) \cdot dT = R \cdot \left[a_1 T + a_2 \frac{T^2}{2} + a_3 \frac{T^3}{3} + a_4 \frac{T^4}{4} + a_5 \frac{T^5}{5} \right] \Big|_{T_{\text{ref}}}^T \quad (86)$$

The reference temperature is defined as 298.15 K (25°C). Since there are two sets of a_i constants when evaluating this integral, care has to be taken for ambient temperatures above 1000 K (the maximum valid temperature of the lower temperature range), as there will be a transition in the constants used. Therefore, for temperatures greater than 1000 K, the following integral is used.

$$\begin{aligned} h^*(T > 1000 \text{ K}) &= \int_{T_{\text{ref}}}^{1000 \text{ K}} C_{pu}^*(T) \cdot dT + \int_{1000 \text{ K}}^T C_{pl}^*(T) \cdot dT \\ &= R \cdot \left[a_{1l} T + a_{2l} \frac{T^2}{2} + a_{3l} \frac{T^3}{3} + a_{4l} \frac{T^4}{4} + a_{5l} \frac{T^5}{5} \right] \Big|_{T_{\text{ref}}}^{1000 \text{ K}} + R \\ &\quad \cdot \left[a_{1u} T + a_{2u} \frac{T^2}{2} + a_{3u} \frac{T^3}{3} + a_{4u} \frac{T^4}{4} + a_{5u} \frac{T^5}{5} \right] \Big|_{1000 \text{ K}}^T \end{aligned} \quad (87)$$

Where the subscript l represents the lower temperature range constants, and u represents the upper temperature range constants. Equation (87) with species specific polynomials, enables calculation of the ideal gas heat capacity at the temperature of interest. As the ambient charge gas is a mixture of three species, nitrogen, carbon dioxide, and water, the enthalpy of the ideal gas mixture must be computed. This is accomplished by calculating the individual species enthalpies in conjunction with a mole fraction weighting, equation (88) (Kaminski and Jensen 2005).

$$h_{i,\text{mix}}^*(T) = \sum_i Y_i \cdot h_i^*(T) \quad (88)$$

The final ambient charge gas enthalpy at ambient temperature and pressure are calculated as defined in equation (89), where the B term is evaluated at the ambient temperature and pressure and the i species are carbon dioxide, water, and nitrogen.

$$\begin{aligned} h_a(T_a, P_a) &= RT_a(Z_v - 1) + \frac{T_a \left(\frac{da}{dT} \right) \Big|_{T_a} - a}{2 \cdot \sqrt{2}b} \ln \left[\frac{Z_v + (1 + \sqrt{2})B}{Z_v + (1 - \sqrt{2})B} \right] \\ &\quad + \sum_i \left(Y_i R \right. \\ &\quad \cdot \left[a_{1l} T + a_{2l} \frac{T^2}{2} + a_{3l} \frac{T^3}{3} + a_{4l} \frac{T^4}{4} + a_{5l} \frac{T^5}{5} \right] \Big|_{T_{\text{ref}}}^{1000 \text{ K}} + Y_i R \\ &\quad \cdot \left. \left[a_{1u} T + a_{2u} \frac{T^2}{2} + a_{3u} \frac{T^3}{3} + a_{4u} \frac{T^4}{4} + a_{5u} \frac{T^5}{5} \right] \Big|_{1000 \text{ K}}^T \right) \end{aligned} \quad (89)$$

To evaluate the second enthalpy, that of the liquid fuel, a modified approach is undertaken using equation (90), as the enthalpy departure relationship in equation (80) was derived for the vapor phase, (i.e. the vapor phase compressibility must be used and the result will be the vapor, not liquid enthalpy as required here as the fuel is not vaporized at injection) (Reid et al. 1987). Therefore, a modified expression for liquid

phase enthalpy departure is provided, by splitting the process into three terms, accounting for the transition from liquid to vapor.

$$h_f^l - h_f^* = (h_f^l - h_f^{sl}) + (h_f^{sl} - h_f^{sv}) + (h_f^{sv} - h_f^*) \quad (90)$$

Where the term, h_f^l , is the parameter of interest (liquid enthalpy at fuel temperature and charge-gas (ambient) pressure), and the sl superscript denotes saturated fuel liquid (T_f and P_f^s), and the sv superscript denotes saturated fuel vapor (T_f and P_f^s). Considering the three terms on the right-hand side of the equation, the first term is the effect of pressure on the liquid enthalpy, the second term is negative the heat of vaporization, and the third is the general enthalpy-departure relation for the saturated vapor phase, as previously discussed. The effect of pressure on liquid enthalpy is small relative to the second and third terms and is therefore neglected, attributed to the nearly incompressible nature of the liquid fuel relative to vapor conditions (Reid et al. 1987). Future work should involve further investigation into these pressure effects. To determine the heat or enthalpy of vaporization, the enthalpy difference of the saturated liquid and vapor at a constant temperature, various methods can be used based on critical properties to account for the lack of availability of tabulated data. These include the use of a vapor pressure-temperature correlation, using methodologies based on the law of corresponding states, or based on correlations using the normal boiling point (Reid et al. 1987). Based on ease of application and accuracy, the Pitzer method is used, which is based on the law of corresponding states, requiring knowledge of temperature, reduced temperature, and acentric factor, as defined in equation (91) (Reid et al. 1987).

$$\Delta h_v = RT_c \cdot (7.08 \cdot (1 - T_{r,1})^{0.354} + 10.95\omega \cdot (1 - T_{r,1})^{0.456}) \quad (91)$$

This correlation is valid for reduced temperatures between 0.6 to 1.0. Based on the conditions of the current study the reduced temperature will typically be less than 0.6, and therefore a modified approach is required to determine the enthalpy of vaporization, the Watson method, which in essence captures the variation of the latent heat of vaporization with temperature, as defined in equation (92) (Reid et al. 1987).

$$\Delta h_{v,actual} = \Delta h_v(T_{r,o}) \cdot \left(\frac{1 - T_{r,actual}}{1 - T_{r,o}} \right)^{0.38} \quad (92)$$

For consistency in the current study, the reduced temperature for the initial temperature considered is defined as 0.8, the midpoint of the Pitzer correlation validity range. Therefore, using the Pitzer & Watson combined method the enthalpy of vaporization can be determined, defined as ‘actual’, required in evaluation of the liquid phase enthalpy. The enthalpy departure of the saturated vapor fuel is evaluated, at the fuel temperature. This requires determination of the saturation pressure corresponding to the fuel temperature, evaluated based on the aforementioned fugacity assumption for vapor-liquid equilibrium. With known saturation pressure, the enthalpy departure is evaluated at T_f and $P_{f,s}$, which also requires solving the Peng-Robinson equation of state for the vapor phase compressibility at this temperature – pressure state. With enthalpy departure known for the saturated vapor phase, along with the enthalpy of vaporization known, the liquid fuel enthalpy, minus the ideal gas fuel enthalpy at the fuel temperature is known. To determine the liquid fuel enthalpy, the ideal gas enthalpy of the fuel at the fuel temperature must be determined. This is determined by integrating the temperature-dependent ideal gas constant pressure specific heat capacity of the fuel from the reference

temperature to the fuel temperature. The ideal gas constant pressure specific heat capacity of the fuel is defined based on a polynomial relationship with tabulated constants, as provided in equation (93).

$$C_{p,\text{fuel}}^*(T) = A_{Cpf} + B_{Cpf} \cdot T + C_{Cpf} \cdot T^2 + D_{Cpf} \cdot T^3 \quad (93)$$

Constants A_{Cpf} , B_{Cpf} , C_{Cpf} , and D_{Cpf} , are $-1.302\text{E}1$, 1.539 , $-8.537\text{E}-4$, and $1.85\text{E}-7$ for hexadecane, respectively (Reid et al. 1987). The constant pressure specific heat capacity is integrated for temperature, and evaluated from the reference temperature to the fuel temperature to provide the fuel ideal gas enthalpy, as defined in equation (94), which enables calculation of the liquid fuel enthalpy.

$$h_f^*(T) = \int_{T_{\text{ref}}}^{T_f} C_{p,\text{fuel}}^*(T) \cdot dT = R \cdot \left[A_{Cpf}T + B_{Cpf} \frac{T^2}{2} + C_{Cpf} \frac{T^3}{3} + D_{Cpf} \frac{T^4}{4} \right] \Big|_{T_{\text{ref}}}^{T_f} \quad (94)$$

The final liquid fuel enthalpy relationship is provided in equation (95) for evaluation at the fuel temperature and ambient pressure. Ambient pressure is not used in the calculation based on the neglecting of the term considering the effect of pressure on liquid enthalpy. The B term in the enthalpy departure portion of the relationship is a function of the fuel temperature and ambient pressure.

$$\begin{aligned} h_f(T_f, P_a) = & -RT_c \cdot (7.08 \cdot (1 - T_{r,1})^{0.354} + 10.95\omega \cdot (1 - T_{r,1})^{0.456}) \cdot \left(\frac{1 - T_{r,\text{actual}}}{1 - T_{r,1}} \right)^{0.38} \\ & + RT_f(Z_{f,v} - 1) + \frac{T_f \left(\frac{da}{dT} \right) \Big|_{T_f} - a}{2 \cdot \sqrt{2}b} \ln \left[\frac{Z_{f,v} + (1 + \sqrt{2})B}{Z_{f,v} + (1 - \sqrt{2})B} \right] + R \\ & \cdot \left[A_{Cpf}T + B_{Cpf} \frac{T^2}{2} + C_{Cpf} \frac{T^3}{3} + D_{Cpf} \frac{T^4}{4} \right] \Big|_{T_{\text{ref}}}^{T_f} \end{aligned} \quad (95)$$

The next required enthalpy is that of the saturated vapor phase fuel at the liquid length, and the temperature and pressure are those at saturation. As the fuel is in the vapor phase the standard enthalpy departure relationship provided in equation (80) is applied, using the vapor phase compressibility evaluated with the Peng-Robinson equation of state at the saturation pressure and temperature. At saturation, although mixed, the vapor enthalpy of the fuel and charge enthalpy are not treated as a mixture, rather, they are treated as two independent states, which is a limitation of the Siebers liquid length model (Siebers 1999; Luijten and Kurvers 2010). The ideal gas constant pressure specific heat capacity is integrated from the reference temperature to the saturation temperature, which defines the ideal gas enthalpy, and enables calculation of the enthalpy of the saturated fuel as defined in equation (96). The B term in the enthalpy departure portion of the relationship is a function of the saturation temperature at the liquid length.

$$\begin{aligned} h_f(T_s) = & RT_s(Z_{f,v} - 1) + \frac{T_s \left(\frac{da}{dT} \right) \Big|_{T_s} - a}{2 \cdot \sqrt{2}b} \ln \left[\frac{Z_{f,v} + (1 + \sqrt{2})B}{Z_{f,v} + (1 - \sqrt{2})B} \right] + R \\ & \cdot \left[A_{Cpf}T + B_{Cpf} \frac{T^2}{2} + C_{Cpf} \frac{T^3}{3} + D_{Cpf} \frac{T^4}{4} \right] \Big|_{T_{\text{ref}}}^{T_s} \end{aligned} \quad (96)$$

The final enthalpy required is that of the ambient charge gas at the saturation conditions of T_s for saturation temperature, and the partial pressure of the charge gas in the total ambient mixture, $P_a - P_s$, the difference between the ambient pressure and partial pressure of the fuel vapor. This ambient enthalpy term is also calculated using the

standard enthalpy departure relationship provided in equation (80), with the Peng-Robinson equation of state being evaluated for the vapor phase compressibility at the fuel saturation temperature and charge-gas partial pressure. The ideal gas enthalpy is determined by integrating the ideal gas constant pressure specific heat capacity from the reference temperature to the saturation temperature, using the procedure detailed in equations (86) and (88). The splitting of the heat capacity integral is not required for the ambient enthalpy at the saturation pressure as by definition, the saturation pressure must be less than the critical temperature of the species, which is less than 1000 K for all fuels considered. The final relationship for the ambient charge-gas enthalpy at the saturation conditions (corresponding to the liquid length) is provided in equation (97). The B term is evaluated at the saturation temperature, and partial pressure of the charge-gas at the liquid length (saturation conditions), T_s and $P_a - P_s$.

$$h_a(T_s, P_a - P_s) = RT_s(Z_v - 1) + \frac{T_s \left(\frac{da}{dT} \right) \Big|_{T_s} - a}{2 \cdot \sqrt{2}b} \ln \left[\frac{Z_v + (1 + \sqrt{2})B}{Z_v + (1 - \sqrt{2})B} \right] \quad (97)$$

$$+ \sum_i Y_i \cdot R \left[a_{1i}T + a_{2i} \frac{T^2}{2} + a_{3i} \frac{T^3}{3} + a_{4i} \frac{T^4}{4} + a_{5i} \frac{T^5}{5} \right] \Big|_{T_{ref}}^{T_s}$$

The four enthalpy relationships define the right-hand side of the evaporation coefficient (equation (72)). In order to evaluate the left-hand side of the evaporation coefficient, additional information is needed. This includes the molecular weight of the fuel, calculated from the chemical composition, and the molecular weight of the ambient charge gas. This is determined based on a mole fraction weighted average of the individual species molecular weights, as defined in equation (98).

$$MW_{mix} = \sum_i Y_i \cdot MW_i \quad (98)$$

Additional required properties are the compressibility of the ambient and the fuel at the saturation conditions, including temperature and respective partial pressures. These compressibility's are determined by solving the Peng-Robinson equation of state at the saturation partial pressure and temperature, for the fuel and ambient charge-gas respectively. The chosen root is that of the vapor phase as at the liquid length, which corresponds to saturation, the existing state is that of the vapor phase.

With all required values defined, the evaporation coefficient is determined based on iteration of the saturation temperature, until the left-hand side and right-hand side are equal. This requires re-evaluating the majority of the terms in the evaporation coefficient equation based on their dependence on the saturation temperature or pressure. When the saturation temperature, and therefore the evaporation coefficient is known, the liquid length is calculated. Required parameters in this evaluation include area contraction coefficient and orifice diameter (injector properties), along with the constants of a and b , and the defined ambient charge-gas density (core gas conditions), refer to equation (67). The two remaining parameters are the fuel density, and the spray angle. The spray angle is calculated based on equation (70), and therefore requires knowledge of the ambient charge-gas density (known based on experimental conditions), and the fuel density. The fuel density is evaluated at the fuel temperature, with a modified Rackett approach being

undertaken (Reid et al. 1987). This requires definition of the Rackett parameter, Z_{Ra} , which can be defined by equation (99), requiring knowledge of the acentric factor.

$$Z_{Ra} = 0.29056 - 0.08775 \cdot \omega \quad (99)$$

This methodology, however, introduces significant error in the calculated value of the liquid density, as the calculated Rackett parameter using equation (99) is significantly different than the tabulated value. For example, the Rackett Parameter determined for cetane with an acentric factor of 0.742 is 0.225, however, the tabulated value is 0.239 (Reid et al. 1987). If the Rackett parameter is available in tabulated literature (Reid et al. 1987), this value is used, if not, equation (99) is used acknowledging that error will be introduced. Liquid density is then calculated via equation (100), using tabulated values of the Rackett parameter.

$$\frac{1}{\rho_{f,s}} = v_{Fuel,S} = \frac{RT_c}{P_c} \cdot Z_{Ra}^{(1+(1-Trf)^{\frac{2}{7}})} \quad (100)$$

For a reduced fuel temperature of 0.5, the saturated liquid density is 719.7 kg/m³ using the tabulated Rackett value, being 799.1 kg/m³ using equation (99). The significant difference between determined density values based on the difference in Rackett parameter has led to the choice of using tabulated values for Rackett parameters, which are available in Reid et al. (1987).

Applying the equation of state approach using the developed EES program for the baseline condition (1190 K ambient core charge-gas temperature, 32.8 kg/m³ core charge-gas density, and 363 K fuel temperature) results in a liquid length of 10.9 mm when using Cetane as the fuel. This is a small increase from the experimentally determined value of 10.8 mm. The complete program is provided in Appendix 0. Results for the equation of state methodology for predicting liquid length using cetane as the fuel are provided in Table 7.6 for all of the experimental test conditions.

Table 7.6
Liquid length as determined from evaluation of Siebers (1999) model using cetane as a surrogate for diesel fuel, equation of state approach.

Test #	Bulk Gas Density (kg/m ³)	Core Gas Density (kg/m ³)	Bulk Gas Temp. (K)	Core Gas Temp. (K)	Inj Press (Bar)	Fuel Temp. (K)	Sat. Temp. (K)	Model LL (mm) for Cetane	Exp. LL (mm)
1	17.3	16.3	1110	1170	2010	363	627.1	16.5	16.1
2	34.6	32.1	1100	1190	1022	363	658.1	10.9	10.8
3	34.6	32.5	950	1015	1378	363	635.9	13.8	13.7
4	34.7	32.1	1100	1190	1376	363	658.1	10.9	10.7
5	34.8	32.0	1200	1300	1373	363	669.5	9.7	9.0
6	34.5	32.9	810	850	1990	363	608.7	19.0	17.8
7	34.8	32.7	950	1010	2020	363	635.5	13.8	13.5
8	34.7	32.2	1100	1190	1990	363	658.2	10.9	10.9
9	34.8	32.0	1200	1300	2010	363	669.5	9.7	9.5
10	34.6	31.7	1300	1430	2000	363	680.5	8.7	8.4
11	34.7	32.2	1100	1190	1068	355	659.0	10.7	12.7
12	34.5	32.2	1110	1190	1369	355	659.0	10.7	12.4
13	34.5	32.0	1110	1190	1988	355	658.7	10.8	12.4

The predicted liquid length closely matches the experimental liquid length values, over all test conditions. The largest deviation occurs at the reduced fuel temperature, as was

the case with the Schihr et al. (2006) methodology. Additional properties from the liquid length modeling with the equation of state approach are provided in Table 7.7.

Table 7.7

Additional properties determined from evaluation of Siebers (1999) model using cetane as a surrogate for diesel fuel, equation of state approach.

Test #	Saturation Pressure (kPa)	Z_a at Liquid Length	$Z_{f,v}$ at Liquid Length	Change in Ambient Enthalpy (Numerator of RHS equation (72)) (kJ/kg)	Change in Ambient Enthalpy (Denominator of RHS equation (72)) (kJ/kg)	B (Evaporation Coefficient)
1	365	1.01	0.81	648	928	0.698
2	593	1.03	0.72	643	1009	0.637
3	421	1.03	0.79	451	951	0.474
4	593	1.03	0.72	643	1009	0.637
5	701	1.03	0.68	766	1038	0.738
6	266	1.02	0.85	283	879	0.322
7	418	1.03	0.79	445	950	0.468
8	594	1.03	0.72	643	1009	0.637
9	701	1.03	0.68	766	1038	0.738
10	819	1.04	0.64	907	1066	0.851
11	601	1.03	0.72	642	1011	0.635
12	601	1.03	0.72	642	1011	0.635
13	599	1.03	0.72	642	1011	0.635

Several key conclusions can be made:

- Ambient compressibility at the liquid length is at most 1.04 and therefore the earlier assumption in section 7.3 that compressibility is 1 in the tabulated property methodology is valid.
- B, the evaporation coefficient, increases with an increase in core gas temperature. This provides an indication of evaporation requirements. As core-gas temperature increases, it is easier (higher B) to evaporate the fuel, thereby resulting in a shorter liquid length. Injection pressure does not impact the evaporation coefficient. Evaporation coefficient is also slightly higher (0.002) for the evaluated fuel temperature, again showing that it is easier to evaporate the fuel at a higher initial temperature, less energy (entrained gas) is required to raise the temperature to saturation.
- Fuel properties at saturation are clearly non-ideal as evidenced by the deviation in vapor fuel compressibility from 1. The deviation is largest at the highest ambient temperature conditions for a constant charge gas density, or at the highest charge gas density for a constant charge gas temperature.

7.5. Methodology Comparison – Tabulated Properties versus Equation of State Approach

Two methodologies have been detailed for determining the required property data for applying the Siebers (1999) liquid length model, that based on tabulated property values (section 7.3), and that based on an equation of state approach using critical

properties (section 7.4). Results from both approaches are similar, relative to the experimental results, with that of the tabulated property data yielding liquid lengths less than experimental, and that from the equation of state being close, and slightly larger than experimental data, with the exception of the reduced fuel temperature cases. This comparison is shown in Figure 7.5, with test numbers as referenced on the x-axis being defined in the earlier results tables (Table 7.4 and Table 7.6).

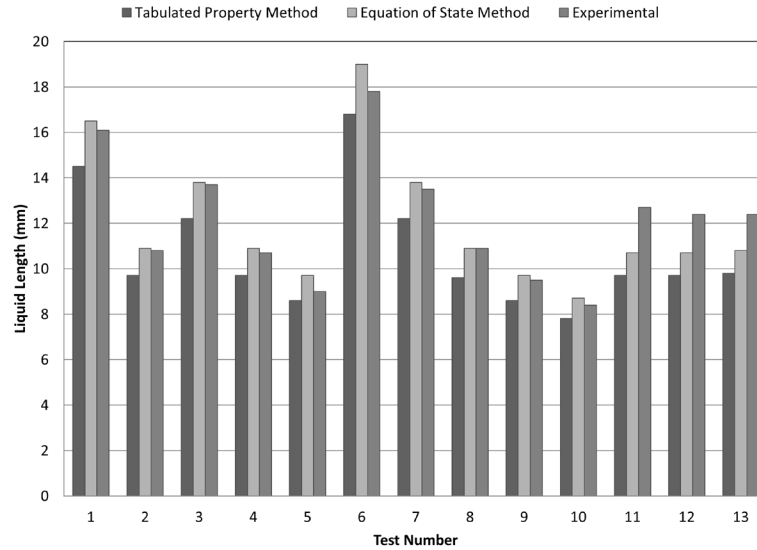


Figure 7.5: LL model method comparison, with comparison to experimental results. Conditions corresponding to the test numbers are defined in Table 7.4 and Table 7.6.

For tests 1 through 10, at the elevated fuel temperature, the liquid length predicted from the model using the Peng-Robinson equation of state method for thermophysical property evaluation typically exceeds the experimental results, or closely matches them. For the reduced fuel temperature tests, tests 11 through 13, the equation of state methodology predicts liquid lengths less than experimental results, however, the deviations are smaller relative to that of the property modeling methodology, which consistently underpredicts liquid length. The equation of state approach is advantageous as it does not require temperature dependent property data to be readily available including for example enthalpies and saturation properties, and will be used throughout the remainder of the chapter.

Differences between the two cases include an assumption of the ambient compressibility as 1 in the thermodynamic tabulated property modeling, with small deviations from this assumption seen in the equation of state approach, with the compressibility approaching 1.05. These differences however are small and will not influence the results. Additionally, the tabulated property modeling has a liquid fuel enthalpy which is a function of ambient pressure, which was not the case in the equation of state approach based on the neglecting of the pressure-dependent liquid enthalpy based on its small magnitude relative to other terms. These two differences are likely the main cause of the deviations between the results from the two methodologies.

7.6. Comparison of Model Results to Additional Experimental Data – Single Component Fuel

Data is provided by Sandia National Laboratory on the Engine Combustion Network (ECN) site (Sandia ECN 2011) with cetane, a single-component fuel. This data is used to provide a direct comparison to the model results based on an equation of state approach, using cetane as the fuel. Injection pressure was constant at 140 MPa, for a 0.246 nozzle diameter with 0.82 area contraction coefficient (Siebers 1999), and fuel temperature of 436 K. Core gas density and temperature were varied, with results shown in Figure 7.6 for both experimental and model results.

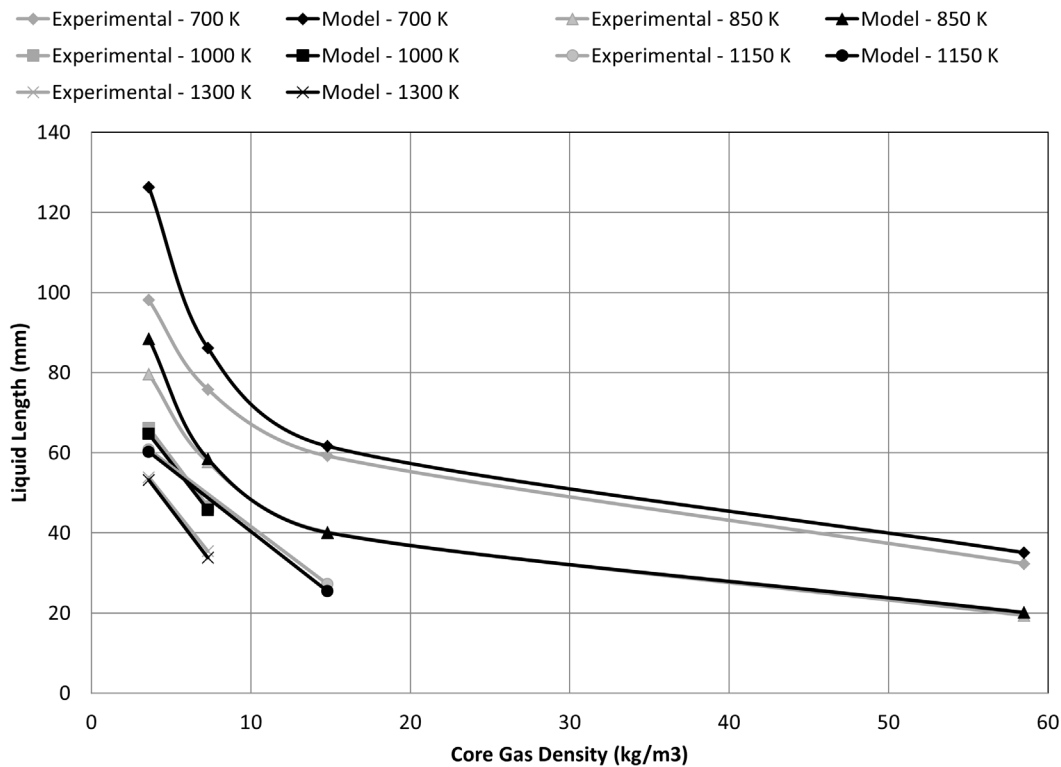


Figure 7.6: Liquid length versus core gas density with Cetane as the fuel, comparing Sandia experimental data to liquid length predictions using the Siebers model with an equation of state approach. Core gas temperatures are defined in the legend.

The model results agree with experimental results, with larger deviations occurring at lower density conditions, which is expected as the fuel will experience less charge-gas entrainment (reduced aerodynamic resistance) enabling it to be the more dominant medium, and therefore the mixing-limited assumption loses validity under these conditions, refer to discussion in section 7.2. The percent difference between experimental and model results approaches 25% at the low density conditions. As temperature increases, for 1000 K and above, the percent difference is 7% or less between experimental and model results. Overall the model and experimental results agree well for this single-component fuel comparison case, validating the developed

equation of state approach used for thermophysical property evaluation for 1-D liquid length model application.

7.7. Single- and Multi-Component Surrogates

This equation of state based thermophysical property method coupled with the 1-D liquid length model is applied to various single and multi-component surrogate fuels for an understanding of the best conditions to match diesel spray characteristics, and also to validate model applicability.

7.7.1. Single Component Surrogate Application

The model is readily applied to single component surrogates for which critical temperature and pressure, acentric factor, Rackett parameter, and polynomial constants for ideal gas constant pressure specific heat capacity are known. Results are provided for some single-component surrogate fuels in Figure 7.7. Conditions chosen are to match the test condition with a core-gas charge temperature sweep (800 to 1300 K bulk gas conditions), 2000 bar injection pressure, 34.8 kg/m^3 bulk gas density, and 363 K fuel temperature with a 0.145 mm orifice diameter and assumed area contraction coefficient of 0.8.

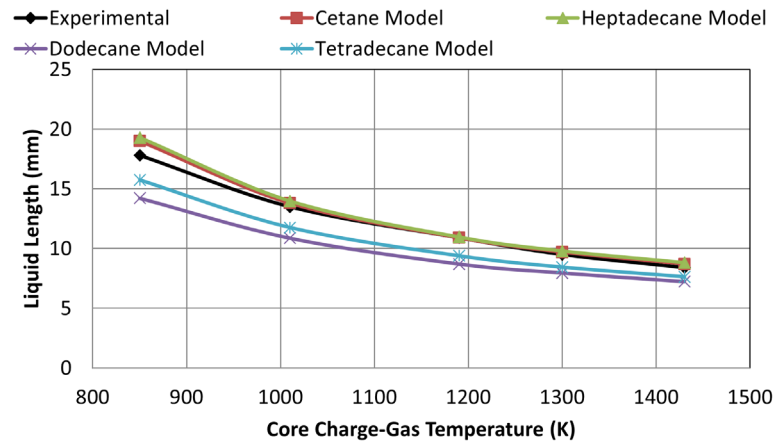


Figure 7.7: Liquid length model results, using the equation of state approach, for various diesel single-component surrogates compared to experimental results. Bulk gas-density of 34.8 kg/m^3 , 2000 bar injection pressure, 363 K fuel temperature.

As shown in Figure 7.7 the liquid length trends are similar for all of the fuels investigated, with the different magnitude of liquid length being attributed to the different fuel characteristics in regards to saturation and vaporization characteristics. At the 850 K core gas temperature, there are larger deviations, 7% difference, between the experimental data and those determined for heptadecane and cetane. This could be the result of experimental accuracy or attributed to modeling validity which reduces as temperature is decreased.

Results can be further understood by comparison of the single component surrogate fuel properties relative to diesel, as provided in Table 7.8.

Table 7.8

Single-component surrogate fuel properties of boiling point (Schihi et al. 2006) and latent heat of vaporization from EES model evaluation.

Single-Component Surrogate Fuel	Boiling Point (K)	Latent Heat of Vaporization at 289 K (kJ/kg)
Dodecane	489	334
Tetradecane	526	308
Cetane	560	318
Heptadecane	575	307

As the fuel boiling point increases, the liquid length increases, until closely matching diesel fuel for cetane and heptadecane, due to their similarity to the 90% distillation point of diesel fuel, 580 K (Schihi et al. 2006). Dodecane matches the 5% distillation point of diesel fuel, with tetradecane matching the 50% distillation point of diesel (Schihi et al. 2006). This signifies that choosing a single-component fuel with a boiling point similar to the 90% distillation point provides a better match for diesel spray evaporation characteristics, and that heptadecane and cetane are optimum single-component diesel fuel surrogates. Furthermore, considering the latent heats of vaporization, that of diesel at 289 K is 233 kJ/kg (AFDC 2010a), which is substantially less than values calculated for all of the fuels listed in the table above. However, that of tetradecane, cetane, and heptadecane exhibit latent heats of vaporization which are closest to diesel, over the four single-component surrogates considered. Therefore although heptadecane and cetane may provide a good representation of diesel spray liquid length due to a similarity of boiling point to 90% distillation, the differences in latent heat of vaporization are significant, and merit investigation into multi-component surrogates to match both parameters.

7.7.2. Multi-Component Surrogate Application

To evaluate the liquid length of multi-component surrogate fuels, properties of the fuel mixture must be known. This can be undertaken using a few methods, as discussed in Chapter 2.7, based on either equation of state evaluation for mixture properties, or using a mean evaporation coefficient. The second methodology is used here. This requires solving for the evaporation coefficient of each single component fuel, and subsequently using a mass fraction weighted average to determine the mixture evaporation coefficient for the liquid length determination (Schihi et al. 2006), as defined in equation (101).

$$\begin{aligned}
 B_{\text{mix}} &= \sum_{i=1}^n x_i B_i \\
 T_{b,\text{mix}} &= \sum_{i=1}^n x_i T_{bi} \\
 1 &= \sum_{i=1}^n x_i
 \end{aligned} \tag{101}$$

Also included in the above equation is an estimation for the boiling point of the multi-component fuel mixture, based on a mass-fraction weighting of individual species boiling points.

Along with this mixture evaporation coefficient, the fuel density for the mixed surrogate fuel, in the liquid phase, must also be determined for evaluation of the liquid length model in equation (24). The previously discussed modified Rackett approach is still used, however, it is modified to enable application for a mixture, based on each fuel components critical properties and Rackett parameters, as defined in equations (102) and (103), for mixture Rackett parameter and mixture density, respectively.

$$Z_{Ra,mix} = \sum_i X_i \cdot Z_{Ra,i} \quad (102)$$

$$\frac{1}{\rho_{f,s,mix}} = v_{Fuel,s,mix} = R \cdot \sum_i \frac{X_i T_{ci}}{P_{ci}} \cdot Z_{Ra,mix}^{(1+(1-Trf) \cdot (\frac{2}{T}))} \quad (103)$$

With the determined evaporation coefficient for each of the species and mixture fuel density in the surrogate fuel mixture, the liquid length of the mixture can be modeled as all other required properties are known. This approach is first demonstrated for a mixture of n-decane and methylnaphthalene, a proposed diesel surrogate (Farrell et al. 2007).

7.7.2.1. Diesel Surrogate: Mixture of n-Decane and Methylnaphthalene

A proposed diesel surrogate is a binary mixture which is 70% n-decane by volume and 30% methylnaphthalene by volume (Farrell et al. 2007). Tabulated properties for ideal gas constant pressure specific heat capacity constants, critical temperature and pressure, acentric factor and Rackett parameter are provided in Appendix 12.7.1.5. The Rackett parameter is not available for methylnaphthalene, and therefore is estimated using equation (99), acknowledging that error will be introduced in the determined density for this species. Mixture boiling point is calculated as 468 K using equation (101), with the boiling point of n-decane being 447 K and methylnaphthalene being 518 K (Reid et al. 1987).

The results using this multi-component proposed diesel surrogate, compared to the diesel fuel experimental results are provided in Figure 7.8. Conditions are a charge-gas temperature sweep for 34.8 kg/m³ bulk gas density, 2000 bar injection pressure, and 363 K fuel temperature.

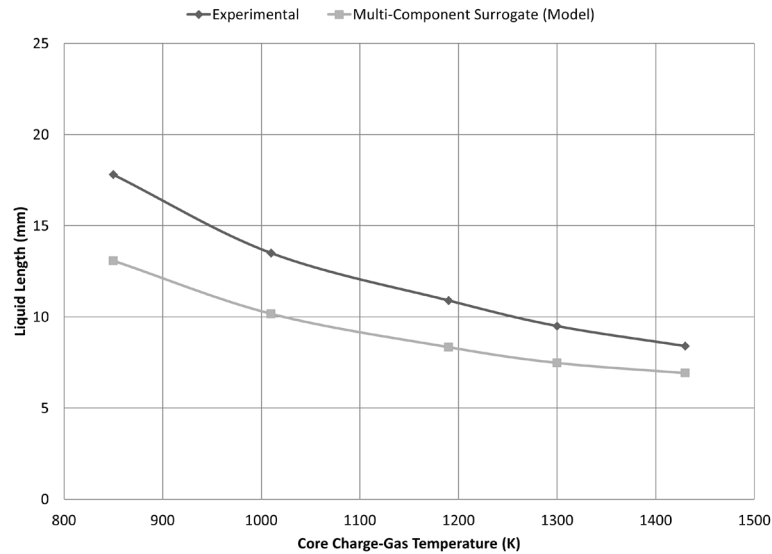


Figure 7.8: Liquid length results for model application using a multi-component surrogate proposed by Farrell et al. 2007 (mixture of n-decane and methylnaphthalene). Conditions are a charge-gas temperature sweep for 34.8 kg/m^3 bulk gas density, 2000 bar injection pressure, and 363 K fuel temperature.

The proposed surrogate was developed to match diesel boiling range, hydrogen to carbon ratio, and other combustion properties, but based on the above results, it clearly does not match vaporization characteristics. This is actually expected as this surrogate is known to underpredict liquid penetration, and therefore this surrogate is not ideal based on inconsistencies in liquid penetration, which translate to emission issues when using this in combustion models (Farrell et al. 2007). The surrogate fuel boiling point of 468 K is at the very low end of the diesel distillation curve (Schihl et al. 2006) which explains some of the difficulty in matching vaporization characteristics. Despite these issues, the multi-component surrogate methodology does yield results agreeing with trends in regards to reductions in liquid penetration with this surrogate, relative to diesel.

7.7.2.2. Diesel Surrogate: Mixture of n-Tetradecane, n-Decane, Heptamethylnonane and 1-Methylnaphthalene

Additional surrogates were modeled using the equation of state approach, using surrogates suggested by Liang et al. (2010). These are defined as surrogate 1, 2, and 3, with 1 and 2 being multi-component, and surrogate 3 being single component n-tetradecane. These surrogates have been developed to match the properties of real diesel fuel, including cetane number, carbon to hydrogen ratio by weight, lower heating value, and 50% distillation point, which is achieved by surrogate 1 (Liang et al. 2010). Surrogate 2 is further modified to better match second stage combustion heat release in model simulations (Liang et al. 2010). Surrogate properties are defined in Table 7.9.

Table 7.9
Multi-component surrogate fuels as proposed by Liang et al. 2010. Boiling point data from Reid et al. 1987.

	Surrogate 1	Surrogate 2	Surrogate 3	Diesel	Boiling Point (K)
n-Tetradecane	0.27	0.51	100.00		527
n-decane	0.22	0.34	0.00		447
Heptamethylnonane	0.30	0.00	0.00		520
1-Methylnaphthalene	0.21	0.16	0.00		518
Cetane Number	46.2	72.0	95.0	46.0	
H/C Ratio (Weight)	6.6	6.4	5.6	6.5	
Lower Heating Value (MJ/kg)	43.2	43.5	45.3	43.0	
50% Distillation Temperature (K)	513	509	526	517	

The mean evaporation coefficient method is applied for determination of the liquid length for these surrogate mixtures. Data is compared to that from Sandia (Sandia ECN 2011) for diesel fuel at a fuel temperature of 436 K, injector diameter of 0.246 mm (0.82 area contraction coefficient), injection pressure of 130 MPa. Charge-gas core temperature was constant at 700 K, core gas density was varied from 3.6 to 58.5 kg/m³ density. At the lower density / temperature combination, the model will begin to have reduced accuracy due to constraints on the mixing limited vaporization assumption. Results are provided in Figure 7.9.

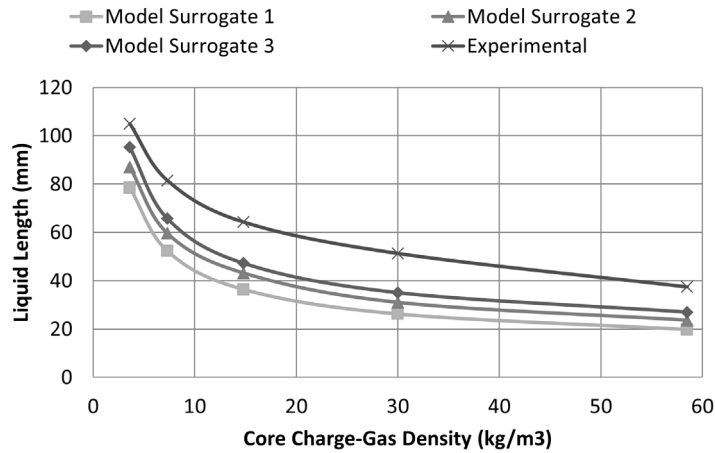


Figure 7.9: Liquid length versus core charge-gas density for Sandia experimental data and three proposed diesel fuel surrogates (Liang et al. 2010).

Several key observations can be made from the above figure:

- At the lowest density case (3.6 kg/m³), the predicted liquid length deviates from the experimental trend. This experimental trend is preserved with the model until this density condition. This is caused by the validity limit of the mixing limited vaporization hypothesis, which the liquid length model is based upon.
- The model surrogate 3, the single component tetradecane fuel, provides liquid lengths which are closest to the experimental data, however, percent difference is still in excess of an average 26%. Although the boiling point of tetradecane closely matches that of the diesel fuel 50% distillation point (within 10 K), the difference in predicted liquid lengths are significant. This concludes that for single component

fuels, matching the 90% distillation point with the distillation point provides improved matching of diesel spray vaporization characteristics, as discussed in section 7.7.1.

- As the 50% distillation temperature is reduced of the surrogate fuel relative to that of diesel, the deviation from the diesel experimental data is increased.

7.8. Multi-component Diesel Surrogate for Vaporization

Based on model results relative to diesel fuel for both single component (section 7.7.1) and multi-component (7.7.2), key conclusions can be made:

- Single component surrogates with boiling points near that of the 90% distillation point of diesel fuel, including n-heptadecane or cetane, provide a good match to diesel vaporization characteristics. Surrogates with boiling points near the 50% distillation point (tetradecane) yield a significant under prediction of diesel spray liquid length.
- Multicomponent surrogates with boiling points near the 50% distillation point of diesel fuel, surrogate 1 and 2 presented in section 7.7.2.2, significantly underpredict the diesel spray liquid length. Furthermore, the multicomponent surrogate with the boiling point near the start of the diesel distillation curve, presented in section 7.7.2.1, also underpredicts liquid length.

It is hypothesized that matching the 90% distillation point to a multi-component surrogate fuel boiling point will provide a good representation of diesel spray liquid length and vaporization characteristics, under these conditions. If this is the case, it would also signify that vaporization is not preferential or controlled by different species components, rather, it is a batch process of mixture properties as a whole.

A surrogate is proposed as a mixture of cetane, heptadecane, and octadecane, whose boiling points are all near that of diesel fuel, 560 K, 575 K, and 590 K, respectively (Reid et al. 1987). In no way is this surrogate claimed to be optimal or match all diesel spray characteristics, focus currently is on a fuel mixture with a boiling point matching the 90% distillation point of diesel. The chosen carbon range of species (C16 to C18) is within the range representative of diesel (AFDC 2010a). The composition is defined by solution of equation (101), with known individual mixture boiling points and i being the three species. For closure, it is assumed that the fuel is 50% by mass n-heptadecane, as heptadecane has the closest boiling point to the 90% distillation point of diesel fuel. This results in a surrogate with a mixture of 8.3% cetane, 50% heptadecane, and 41.7% of octadecane, by mass. This multicomponent surrogate is applied to match diesel spray conditions from the Michigan Technological University experimental tests under 0% oxygen conditions at 34.8 kg/m³ bulk charge-gas density, 2000 bar injection pressure, and 363 K fuel temperature, as shown in Figure 7.10.

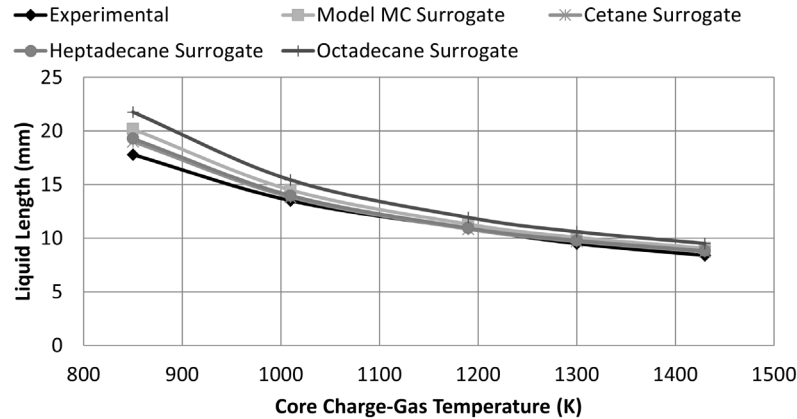


Figure 7.10: Liquid length versus core charge-gas temperature for model surrogate to match boiling point to 90% distillation of diesel. 34.8 kg/m³ bulk charge-gas density, 2000 bar injection pressure, and 363 K fuel temperature.

Matching the boiling point of the multicomponent surrogate to the 90% distillation point of diesel fuel provides a significantly improved match to experimental liquid length. As shown in the figure, the single-component surrogates of cetane and heptadecane still yield an improved match to experimental test results, however, the multicomponent surrogate mixture does provide a good match to diesel spray liquid length, with at most 12% difference occurring at the 850 K temperature. It should be noted that even the single component surrogates of heptadecane and cetane show significant deviation at this 850 K point, with up to 8% difference.

This multicomponent surrogate is also applied to diesel fuel experimental data from SNL ECN, as was used in section 7.7.2.2 to provide a comparison of results for a sweep of core charge-gas density. Results are shown in Figure 7.11. Conditions are a core gas temperature of 700 K, injection pressure of 130 MPa, fuel temperature of 436 K, and nozzle orifice diameter of 0.246 mm.

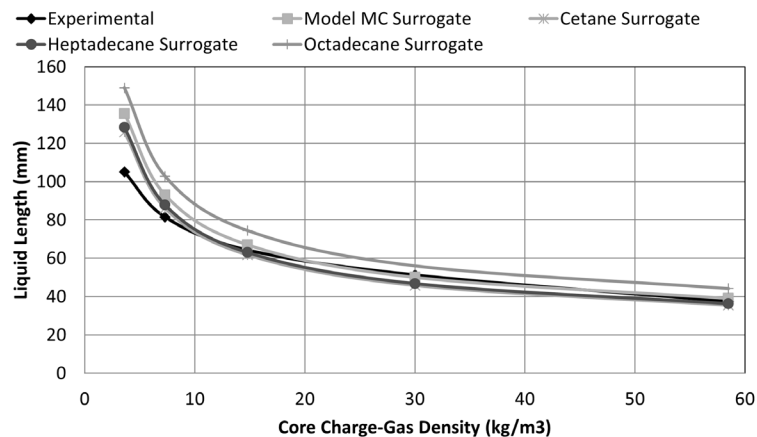


Figure 7.11: Liquid length versus core charge-gas density for Sandia experimental data. Conditions are a core gas temperature of 700 K, injection pressure of 130 MPa, fuel temperature of 436 K, and nozzle orifice diameter of 0.246 mm.

Several key observations can be made from the above figure. First, a multi-component surrogate with a mixture boiling point matching the 90% distillation point of diesel fuel provides a better match to diesel liquid length experimental results, than a mixture

matching the 50% distillation point as presented in 7.7.2.2. The multicomponent surrogate proposed provides good representation of the experimental data, with at most 4% difference over the 14.8 to 58.5 kg/m³ density range. Deviation is larger at the lower density conditions which is due to the mixing limited vaporization model assumption validity. The multi-component surrogate provides improved representation of the diesel spray trends over the full density range, compared the single-component surrogates which underpredict liquid length for the densities greater than 14.8 kg/m³, and overpredict the liquid length for densities less than 14.8 kg/m³.

Using the proposed multicomponent surrogate of heptadecane, cetane, and octadecane whose mixture boiling point matches the 90% distillation point of diesel fuel, results in modeled liquid lengths showing an improved match to diesel fuel, as compared to a multi-component surrogate fuel mixture matching the 50% distillation point of diesel fuel for both conditions of a charge gas temperature and density sweep. This signifies that to match vaporization characteristics, a surrogate must have a mixture boiling point close to that of the 90% distillation point of diesel fuel. Furthermore, this also signifies that evaporation is likely a batch process, not controlled by individual species boiling points but rather is controlled by the mixture boiling point characteristics as a whole. These model observations should be validated with additional experimental studies.

7.9. Summary

This chapter focused on applying a mixing-limited vaporization model for liquid length. First, the limits of application of the liquid length model were investigated by consideration of the transition time, where it was determined that the liquid length model is valid over the conditions currently considered and most conventional diesel engine conditions based on the significant variation between the liquid length and penetration at the transition time. The liquid length model was also evaluated using tabulated thermodynamic property values for the experimental test conditions, with cetane as a surrogate for diesel fuel to validate the model and understand its application. Cetane can predict diesel fuel liquid length, within 4.5% for the elevated fuel temperature cases, under-predicting the liquid length under all conditions, and a different surrogate would likely provide a better match to diesel experimental results, for example an improved matching of diesel 90% distillation point. Despite the variations between model and experimental results, the general trends are preserved in regards to parameter dependencies and nonlinearities between parameters and liquid length, showing that the model, and its mixing limited vaporization assumption are adequate for further use.

An equation of state thermophysical property approach was developed using the Peng-Robinson equation of state, for application of single and multi-component surrogate fuels for integration with the mixing-limited vaporization liquid length model. This methodology is a tool that can be used to explore dependencies of a range of variables on liquid length, and in particular, fuel property influence. This required definition of various thermodynamic property relationships. Also, knowledge is needed of critical temperatures and pressures, species acentric and Rackett parameters, along with polynomial constants for species ideal gas constant pressure specific heat capacities. This approach provides results for cetane as a surrogate fuel which better match those of the diesel fuel experimental results, relative to the traditional tabulated property approach.

The model is applied to a range of surrogate fuels, both single and multi-component, providing indication that surrogate fuels must match diesel vaporization characteristics, with the 90% distillation point being an important parameter to match.

Surrogates were applied, both multicomponent and single-component, and model results compared to both Michigan Technological University experimental results, and results from Sandia National Laboratory, both for diesel fuel. It is determined that single and multicomponent surrogates which match have boiling points matching the 90% distillation point of diesel fuel provide the best match to diesel liquid length characteristics, for both a charge gas temperature and density sweep. This suggests that to most effectively match vaporization characteristics of a real fuel using a surrogate fuel under these conditions it is important to consider the boiling point of the mixture, and compose the surrogate such that it matches the 90% distillation point of the fuel. Other fuel properties, such as viscosity, surface tension, chemical composition, and others which influence spray characteristics should also be considered in surrogate fuel development and matching to real fuels.

Model limitations have been discussed and will be reiterated:

- Decreased validity of the mixing limited hypothesis at low temperature and density conditions.
- The liquid length model, and equation of state evaluation, assume that the vapor fuel and ambient charge-gas are separate at the liquid length, with properties evaluated independently, when in reality the two species are intrinsically linked.
- The fuel temperature is assumed to be the measured tip temperature of the injector. This will be close to the temperature of the fuel in the sac, however, there is likely heat transfer in the form of conduction that will cause some variation in actual liquid fuel temperature. As injected, the fuel enthalpy and kinetic energy will be transferred which will cause a change in actual liquid fuel temperature at the nozzle exit, which will influence the results of liquid length. This model does not include this fuel temperature effect as a result of the exchange of kinetic energy from injection with the fuel enthalpy.

Despite these model limitations, the liquid length model, coupled with use of an equation of state approach for thermophysical property evaluation, is an effective tool for exploring liquid length parameter dependencies and surrogate fuel application and development.

8. Fluctuations in Quasi-Steady Liquid Length

The liquid phase of the spray in a vaporizing (0% oxygen) environment showed fluctuations around the steady state or quasi-steady liquid length for each plume. Understanding these fluctuations and trends, including plume to plume trends and characteristic frequency content, is important as these fluctuations influence spray and air mixing behavior translating to impacts on combustion and emissions. The goal of this chapter is to understand liquid phase fluctuations in penetration under vaporizing conditions and provide hypotheses for the causes of this behavior via image analysis, plume characterization, and frequency analysis. Evaluation of these hypotheses will also be undertaken. The goal of this chapter will be achieved via the following objectives:

- Characterize liquid length over a charge temperature sweep of 800 to 1300 K and injection pressure sweep (1034 to 2000 bar) at a constant charge density of 34.8 kg/m^3 , along with a reduced density condition (17.4 kg/m^3), reduced fuel temperature of 355 K (decreased from 363 K), and repeat tests.
- Undertake frequency analysis of the fluctuations in comparison to fuel pressure fluctuations.
- Propose hypotheses for the cause of these liquid length fluctuations.
- Evaluate the hypotheses for liquid length fluctuations via parametric sweeps of injector properties (emulating cavitation) and temperature gradients inside the chamber, using the developed liquid length model with the equation of state approach for thermophysical property modeling, as discussed in Chapter 7.

8.1. Motivation

Liquid-length is an indication of fuel-air mixing efficiency with the success of fuel-air mixing being directly correlated to soot emissions. From experimental testing, appearances of fluctuations in liquid length about a mean value are observed. These fluctuations have implications in fuel-air mixing influencing soot formation, with it being proposed that the fluctuations were attributed to slugs of fuel detaching from the core of the fuel jet and these slugs favor soot agglomeration and inhibit soot oxidation due to the local depletion of oxygen (Crua 2002).

Fluctuations in liquid length, of the magnitude seen here, could cause the liquid length to transition between being less than, to greater than, the lift-off length causing different combustion regimes leading which could lead to an increase in soot (as discussed in Chapter 1.2). Furthermore, if an engine cylinder was designed for the specified mean liquid length of the spray, liquid fuel spray impingement on the cool cylinder wall could result due to these fluctuations, which would be particularly true under low-temperature, part-load, combustion conditions where liquid length is large, which would lead to increases in un-burnt hydrocarbon emissions and reductions in fuel economy (Boot et al. 2010). Therefore, understanding the magnitude of these fluctuations, as well as providing hypotheses for the causes, is important based on the implications for fuel-air mixing and emissions.

8.2. Test Conditions

The tests discussed in this chapter were previously discussed in Chapter 6.2, including repeat tests, a charge gas temperature sweep, an injection pressure sweep, a fuel temperature variation, and a density reduction, in a 0% oxygen environment. These images were acquired at 67,500 frames per second or 0.015 ms inter-frame time. With higher frame rates used, more information was available for understanding the fluctuations in liquid length during the quasi-steady portion. An additional test was undertaken to better characterizing the fluctuations at a higher frame rate of 216,000 frames per second (0.0046 ms interframe time), for a baseline test condition (1100 K, 34.8 kg/m³ density, 2000 bar injection pressure), with the chiller on (82°C fuel temperature). Results from these tests were presented in Chapter 6.2 for median values of time-dependent liquid penetration. Of interest in this current chapter is the mean steady state liquid length, occurring during 1 to 2 ms ASOI, consisting of 68 data points for the 67,500 framing rate and 217 data points for the 216,000 framing rate, and the fluctuations about this value. These fluctuations were evident on a plume-to-plume basis.

8.3. Magnitude of Liquid Length Fluctuations

During steady state, 1 to 2 ms ASOI, there were noticeable fluctuations in liquid length, both of a single plume, and between plumes for the multi-hole injector as will be quantified. The mean quasi-steady liquid length was determined during this time period with the magnitude of the fluctuations also characterized to understand the relative fluctuations. The magnitude of these fluctuations was determined using two methodologies. This included the maximum and minimum values during the quasi-steady liquid length period, relative to the mean values, along with the magnitude of the average positive and negative deviations relative to the mean value. The magnitude of the average deviations relative to the mean value are defined using equation (104), where $S(t)$ is the time dependent liquid penetration. LL_{positive} defines the average positive fluctuation, and LL_{Negative} defines the average negative fluctuation.

$$\begin{aligned} LL_{\text{Positive}} &= \text{mean}(S(t) > LL) \\ LL_{\text{Negative}} &= \text{mean}(S(t) < LL) \end{aligned} \quad (104)$$

8.3.1. Maximum Liquid Length Fluctuations

Shown in Figure 8.1 is the mean steady state liquid length for each plume as well as the mean value over all eight plumes, with error bars denoting the minimum and maximum of the magnitude of the liquid length fluctuations relative to the mean value. This figure is for injection at 2000 bar into an 1100 K, 0% oxygen, 34.8 kg/m³ density environment, the baseline case (chiller off, fuel temperature 363 K). Figure results for the other test conditions discussed in Chapter 6.2 are provided in the Appendix 12.8.2.1.

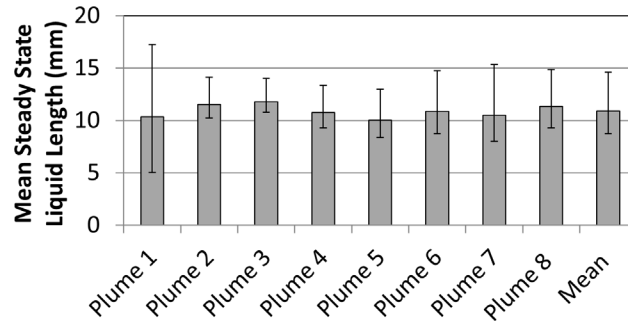


Figure 8.1: Mean steady state liquid length with error bars showing the magnitude of the maximum fluctuations in liquid length, for 34.8 kg/m³ density, 0% oxygen, 2000 bar injection pressure, 1100 K temperature, fuel temperature 363 K.

The magnitude of the maximum fluctuations in liquid length was significant being larger in the positive direction relative to the negative direction, approaching 34 to 20% of the mean liquid length, respectively. Fluctuation magnitudes were similar over the varying test conditions as presented in Appendix 12.8.2.1, with results for the mean percent change relative to the steady state value over all 8 plumes presented for the different test conditions defined here in Table 8.1 as a summary.

Table 8.1

Maximum quasi-steady liquid length increase and decrease relative to the mean value, in % terms, for all vaporizing spray tests. High FPS indicates the higher frame rate of 216,000 frames per second, R indicates repeat tests.

Ambient Density (kg/m ³)	Fuel Pressure (bar)	Fuel Temperature (K)	Temperature at Injection (K)	Maximum LL Increase Relative to Mean (%)	Maximum LL Decrease Relative to Mean (%)
34.8	1034	355	1100	34	17
34.8	1379	355	1100	32	18
34.8	2000	355	1100 (R1)	32	16
34.8	2000	355	1100 (R2)	33	18
34.8	2000	355	1100 (R3)	34	16
34.8	2000	355	1100 (High FPS)	46	23
34.8	2000	363	800	27	14
34.8	2000	363	950	30	17
34.8	2000	363	1100 (R1)	34	20
34.8	2000	363	1100 (R2)	31	18
34.8	2000	363	1100 (R3)	25	11
34.8	2000	363	1200	27	14
34.8	2000	363	1300	28	19
17.4	2000	363	1100	29	16
34.8	1034	363	1100	35	21
34.8	1379	363	950	28	14
34.8	1379	363	1100	28	15
34.8	1379	363	1300	32	21

The magnitude of the maximum fluctuations were significant, yet consistent with a typical 30% maximum increase and 18% maximum decrease, implying that they were likely not correlated to conditional variation but a different inherent phenomenon, common to all conditions. For the one plume test at the higher frame rate, the magnitude

of the fluctuations was larger. This was attributed to several factors including the fact that only one plume was considered versus the average over all eight plumes as shown in the table for other test conditions, which would work to minimize the extraneous fluctuations. Additionally, the higher frame rate data will capture more information on the fluctuations and therefore the extent of the fluctuations could in actuality be larger than those shown at the lower frame rate as there were 3 frames for the higher frame rate that fall in between those for the lower frame rate, attribute to the larger sample size. There are no consistent plume to plume trends in the magnitude of the maximum fluctuations.

It should be noted that the confidence interval for these fluctuation magnitude measurements are small and therefore a test to test comparison of the magnitude of the fluctuations is difficult due to the low sample size. This is evidenced by looking at a histogram of the liquid length distribution during steady state shown in Figure 8.2, which shows the nonsymmetrical, non-Gaussian distribution of liquid length.

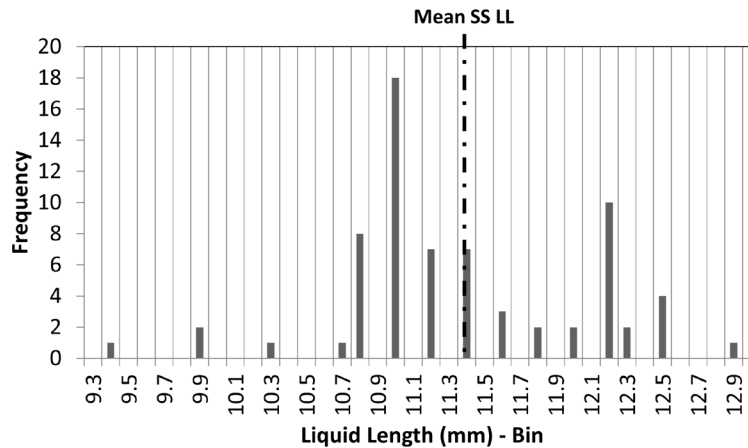


Figure 8.2: Histogram of steady state liquid length. Results are for Plume 8 of a diesel spray into 0% Oxygen at 34.8 kg/m^3 bulk gas density and 1100 K bulk gas temperature, at 2000 bar injection pressure.

The above figure shows the mean SS LL for this test, relative to the distribution of liquid lengths. The maximum and minimum fluctuations are shown at the two tails of the distribution. This distribution shows the asymmetry in liquid length fluctuations relative to the mean value.

8.3.2. Average Liquid Length Fluctuations

The average liquid length fluctuations are shown in Figure 8.3 for the baseline case of 34.8 kg/m^3 density, 1100 K charge gas temperature, 2000 bar injection pressure, and 363 K fuel temperature. The results for the remainder of the vaporizing spray tests are provided in Appendix 12.8.2.2.

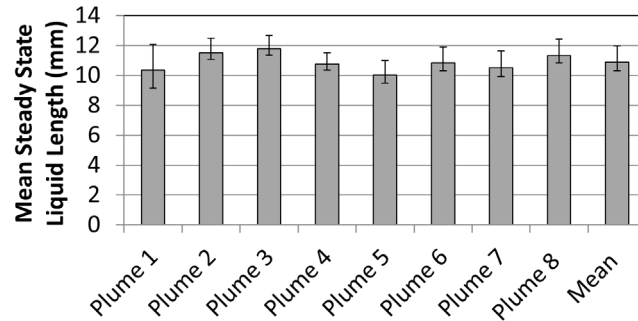


Figure 8.3: Mean steady state liquid length with error bars showing the magnitude of the average fluctuations in liquid length, for 34.8 kg/m³ density, 0% oxygen, 2000 bar injection pressure, 1100 K temperature, 363 K fuel temperature.

The average magnitude of the liquid length fluctuations was significantly reduced because of the limited sample size, relative to the maximum fluctuations. The magnitude of the fluctuations was an average increase in 10% relative to the mean value, and an average decrease of 5% relative to the mean value. The magnitude of these fluctuations are summarized in Table 8.2 for all of the vaporizing spray test conditions investigated representing the mean value over all 8 spray plumes of the multi-hole injector.

Table 8.2
Average quasi-steady liquid length increase and decrease relative to the mean value, in % terms, for all vaporizing spray tests.

Ambient Density (kg/m ³)	Fuel Pressure (bar)	Fuel Temperature (K)	Temperature at Injection (K)	Average LL Increase Relative to Mean (%)	Average LL Decrease Relative to Mean (%)
34.8	1034	355	1100	11.2	6.0
34.8	1379	355	1100	10.7	5.4
34.8	2000	355	1100 (R1)	10.3	5.3
34.8	2000	355	1100 (R2)	10.6	5.5
34.8	2000	355	1100 (R3)	11.5	5.6
34.8	2000	355	1100 (High FPS)	13.6	6.7
34.8	2000	363	800	9.4	4.7
34.8	2000	363	950	10.1	5.3
34.8	2000	363	1100 (R1)	9.8	5.3
34.8	2000	363	1100 (R2)	9.9	5.3
34.8	2000	363	1100 (R3)	9.5	4.8
34.8	2000	363	1200	9.0	4.4
34.8	2000	363	1300	9.4	4.8
17.4	2000	363	1100	9.3	4.6
34.8	1034	363	1100	10.7	5.6
34.8	1379	363	950	10.7	5.5
34.8	1379	363	1100	9.5	5.2
34.8	1379	363	1300	10.1	5.3

The magnitude of the average fluctuations was similar for all test conditions being around 10% larger and 5% shorter, than the mean value. As was the case with the maximum liquid length fluctuations discussed in the prior section, the magnitude of the average fluctuations were larger for the single hole plume test at the higher frame rate, in comparison to the average over all 8 spray plumes at the lower frame rate. The

asymmetry in the magnitude of these fluctuations signifies that the fluctuations were not consistent about the mean liquid length and that there was a grouping with the number of points above the mean value and their magnitude, relative to those falling below the mean value. There are no consistent plume to plume trends in the magnitude of the average fluctuations.

8.4. Frequency Analysis

8.4.1. Fuel Pressure Frequency

One potential explanation for the fluctuations in liquid length is due to fluctuations in the fuel pressure during injection. A pressure transducer was mounted via a ‘T’ into the fuel pressure supply line to provide a measurement of injection pressure as was shown in Chapter 3.4.2.1. The fuel pressure fluctuations were similar test to test, and are presented in Figure 8.4 for the baseline test (1100 K, 34.8 kg/m³ density, 2000 bar injection pressure, 363 K fuel temperature).

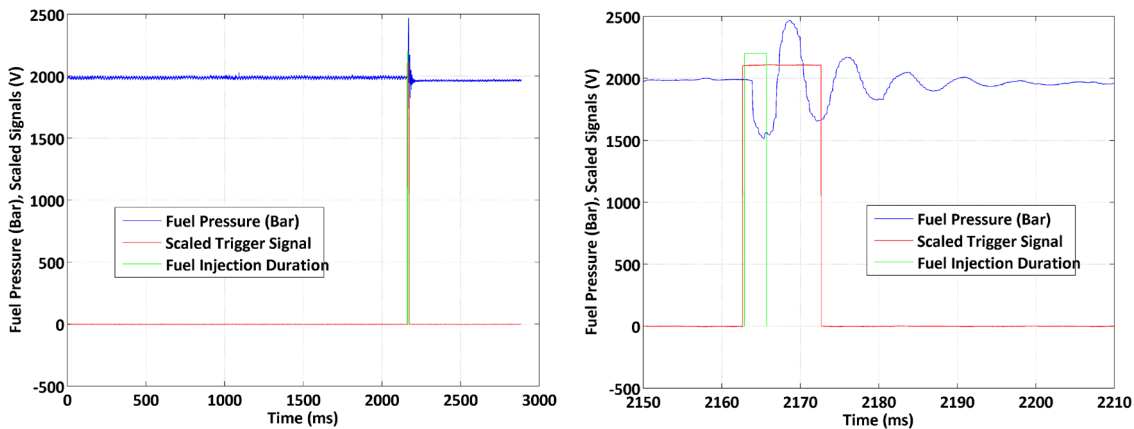


Figure 8.4: Fuel pressure trace before, during, and after the fuel injection event, zoomed in on the injection region of interest in the right portion of the figure.

The scaled trigger signal represents the electronic trigger to the driver with the fuel injection duration defining the actual time when liquid fuel was injected into the chamber, 2.8 ms in this case. The fluctuations in the fuel pressure were a result of the injection event. The relative timing of the injection pressure fluctuations relative to the fuel injection is important along with the frequencies of these pressure fluctuations, to understand if they correspond to the perturbations in liquid length. The fuel injection was delayed relative to the electronic trigger (by 0.245 ms). Fuel pressure experienced fluctuations starting 1 ms after the injection commenced. There were noticeable fluctuations in fuel pressure during the injection event and the frequency of these relative to that of the liquid length must be compared. Also, the time for the fluctuations in pressure to travel from the injector down to the pressure sensor, a distance of 11.5 inches, could cause a shift in timing and by characterizing the frequency content of the fluctuations, relative to the liquid length fluctuations, the correlations between the two, if any, will be better understood.

The frequency of the fuel pressure fluctuations was determined by applying a Fast-Fourier Transform (FFT) to the fuel pressure trace region of interest which is shown

in Figure 8.5. A FFT enables transformation of the data from the time to the frequency domain or vice-versa, to provide information on the frequency content of a signal for further analysis where attributes may be highlighted in the alternative domain (Smith 2003). The FFT was undertaken on the fuel pressure by isolating the region of interest of the injection event, from the start to the end of the fuel pressure fluctuations, with a Nyquist frequency of 50 kHz (sampling frequency of 100 kHz). The FFT results in the frequency domain will run from 0 Hz up to the Nyquist frequency and based on the mathematics of the FFT, the output of the FFT considered to half the sample size (based on the Nyquist frequency and underlying FFT mathematics), will be two times the actual output, normalized by the total number of data points (sample size, N , 4711 for this test). The result of the FFT on the region of interest is shown in Figure 8.5 with tabulated frequencies (and corresponding times) along with corresponding amplitude magnitudes, shown in Table 8.3.

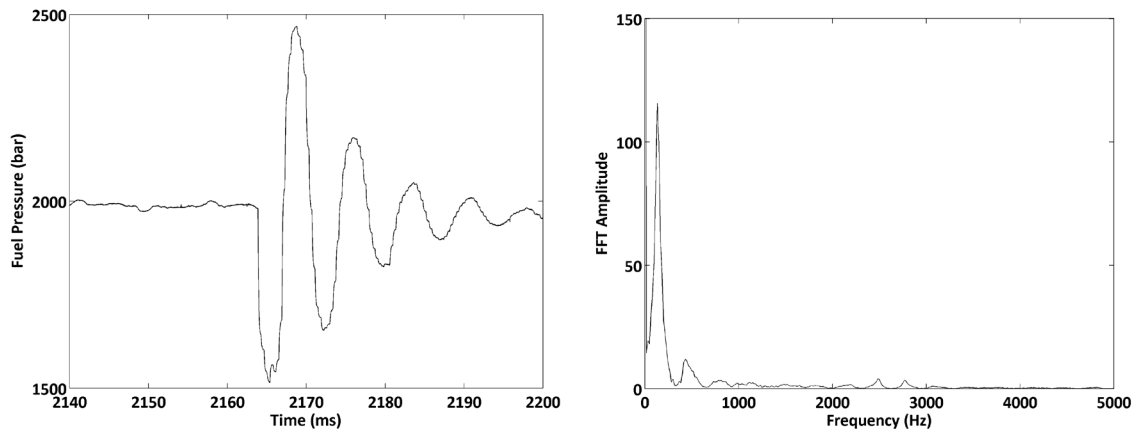


Figure 8.5: Fuel pressure region of interest for the FFT (left), along with FFT results (right), zoomed in to visualize the frequency peaks.

Table 8.3
Fuel pressure FFT results.

FFT Peak	Frequency (Hz)	Time (ms)	Amplitude
1	0		1954
2	127.4	7.85	135.3
3	424.5	2.36	15.78
4	2484	0.40	4.96
5	785.4	1.27	3.978
6	2781	0.36	3.886
7	1146	0.87	3.021
8	1486	0.67	2.22
9	2208	0.45	1.993
10	1826	0.55	1.426
11	5137	0.19	1.238

The injection duration was a 1.6 ms electronic trigger, corresponding to 2.8 ms fuel (hydraulic) injection duration, with the observed liquid length fluctuations occurring at a fraction of this injection duration with the frequency required to be significantly greater than 357 Hz. The largest frequency of measureable amplitude occurred at 5137 Hz or 0.19 ms. As the liquid length fluctuations were visible frame to frame, which occurred

over a 0.015 ms time interval, this fuel pressure frequency content is not large enough to explain the fluctuations in liquid length. This mismatch in frequency, along with the phasing of the fuel pressure perturbations relative to the liquid length fluctuations, indicates that line pressure fluctuations were not the cause of fuel spray liquid length fluctuations observed in the high speed images.

8.4.2. Frequency of Liquid Penetration Fluctuations

The frequency content of the liquid penetration fluctuations was characterized using frequency analyses with a FFT, similar to the methodology used in quantifying the characteristic frequencies of the fuel pressure fluctuations. Before undertaking the FFT to provide the key frequency components of the fluctuations, the mean quasi-steady liquid length data must be appropriately pre-processed. This included taking the penetration data for each plume and offsetting it by the mean steady state liquid length for the given plume during the quasi-steady period to provide a DC offset removing the 0 Hz frequency component. This offset penetration data was then analyzed with a window being applied to the data first to ensure that the start and end of the data return to the 0. A Tukey window was used on the data which is a tapered cosine window that sets the data at the boundaries to zero without significantly reducing the gain of the windowed transform falling between a rectangular (no window) and Hanning window (Harris 1978). The Tukey tapering factor was set at 0.5, the default value, with the window used in this analysis shown in Figure 8.6.

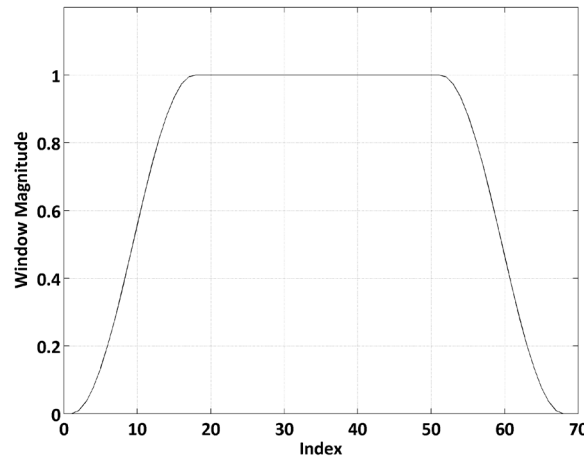


Figure 8.6: Tukey window with a tapering factor of 0.5, used in the current FFT analysis.

The windowed data then underwent a Fourier transform with an energy correction factor (ECF) being applied to account for the window application which does not conserve energy relative to the original signal, with this ECF used based on the broadband nature of the data. The auto-power of the FFT was computed next which is the result of the FFT multiplied by its complex conjugate to provide a real valued function equaling the magnitude of the FFT, squared. Finally, this autopower was normalized by the unit frequency (bandwidth of the measurement) to provide the power spectral density

(PSD) which was used to determine frequency peaks of the liquid length fluctuations. This procedure is outlined in Figure 8.7 for plume 2 of the baseline case.

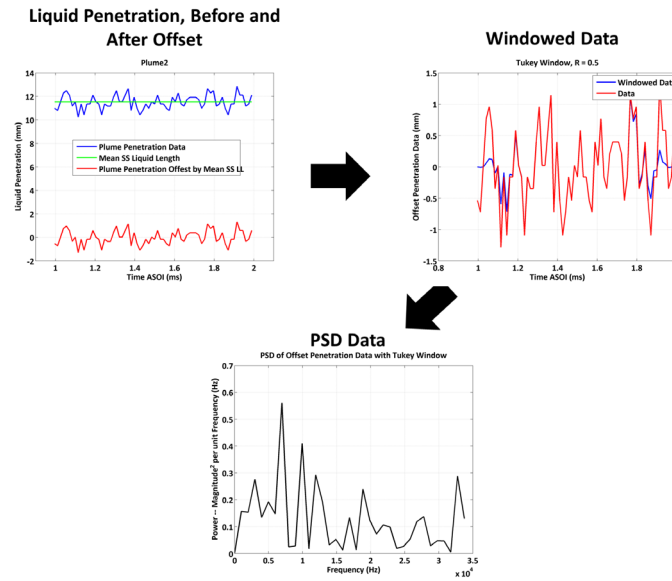


Figure 8.7: FFT analysis of liquid length fluctuations, including liquid penetration offset, windowing of the data, and the resultant PSD.

The magnitude, and corresponding frequency (and time scale) of the first five largest peaks was determined from the PSD as an indicator of the dominant frequencies in the liquid length fluctuations with these frequencies being compared for the eight plumes. Full penetration results during the quasi-steady state, along with the PSD results over all eight spray plumes, are presented for each test in Appendix 12.8.3, with figures presented here for the baseline case of 1100 K charge gas temperature, 34.8 kg/m³ density, 2000 bar injection pressure at 363 K fuel temperature (Figure 8.8).

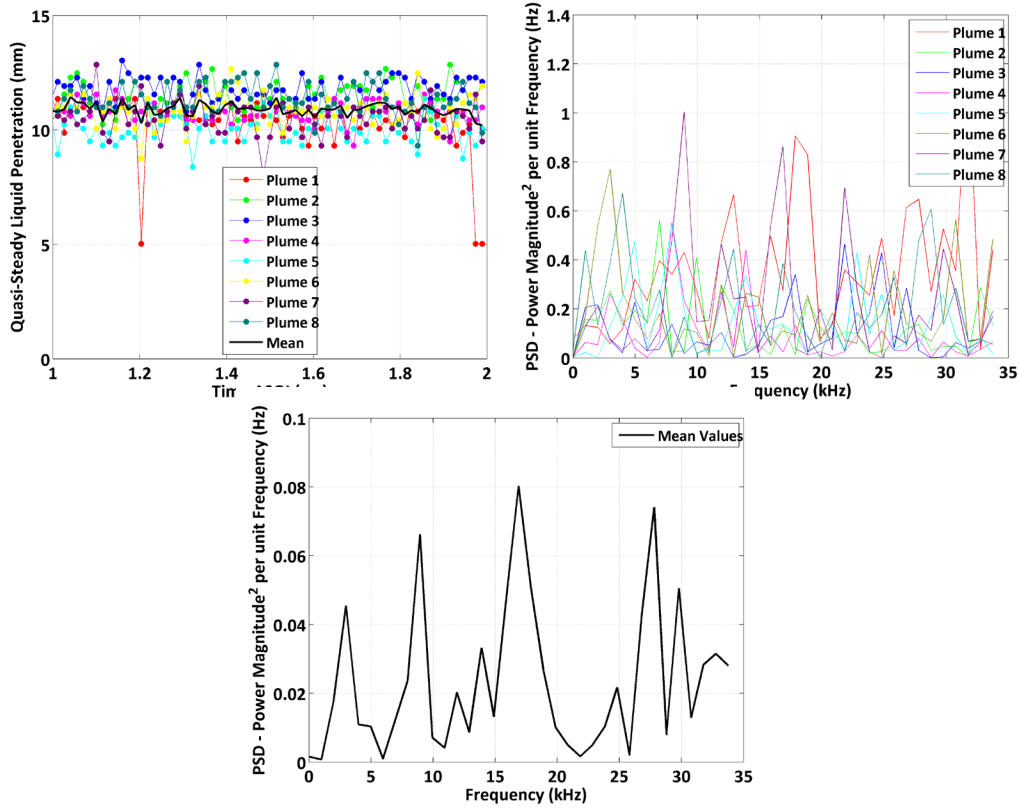


Figure 8.8: Quasi-steady penetration versus time ASOI (left) for all eight spray plumes, PSD versus frequency (right) for all eight sprays plumes. Test conditions of 2000 bar, 363 K fuel temperature, 34.8 kg/m³, 1100 K 0% O₂ Environment. Bottom figure provides information on the dominant mean frequencies for the mean liquid length fluctuations.

There were noticeable fluctuations in penetration as seen in the above figure around the nominal quasi-steady liquid length. Understanding the frequency of these fluctuations may provide insight into their causes. Information on the frequency of these fluctuations were provided in the above PSD highlighting the dominant frequencies in the figure. The dominant frequencies for the mean liquid length fluctuations are summarized in Table 8.4, over all of the vaporizing spray test conditions.

Table 8.4
Dominant frequency components resulting from PSD analysis, Mean Results.

Ambient Density (kg/m ³)	Fuel Pressure (bar)	Fuel Temp (K)	Temp. at Injection (K)	1 st Freq (Hz)	2 nd Freq (Hz)	3 rd Freq (Hz)	4 th Freq (Hz)	5 th Freq (Hz)
34.8	1034	355	1100	993	9926	25809	28787	12904
34.8	1379	355	1100	5956	993	2978	8934	10919
34.8	2000	355	1100 (R1)	1985	3971	19853	10919	22831
34.8	2000	355	1100 (R2)	993	31765	26801	6949	23824
34.8	2000	355	1100 (R3)	4963	17868	993	8934	14890
34.8	2000	355	1100 (High FPS)	16922	18912	43797	49724	12490
34.8	2000	363	800	33750	25809	3971	1985	27794
34.8	2000	363	950	993	5956	17868	10919	24816
34.8	2000	363	1100 (R1)	16875	27794	8934	29779	2978
34.8	2000	363	1100 (R2)	17868	12904	29779	10919	33750
34.8	2000	363	1100 (R3)	5956	15882	993	3971	24816
34.8	2000	363	1200	1985	3971	19853	8934	22831
34.8	2000	363	1300	10919	993	12904	8934	32757
17.4	2000	363	1100	5956	16875	3971	25809	9926
34.8	1034	363	1100	993	5956	33750	3971	25809
34.8	1379	363	950	993	2978	7941	4963	25809
34.8	1379	363	1100	993	5956	31765	9926	26801
34.8	1379	363	1200	18860	993	20846	22831	30772

There do exist repeating frequencies, however, these are not consistent test to test. The majority of the fluctuations are of frequencies which exceeded those of the fuel pressure fluctuations signifying that the fuel pressure was not the dominant contributing factor in the liquid length fluctuations. Considering the higher framing rate images, there were some dominant frequencies similar to those seen in the lower frame rate tests, in the 10 kHz range, with other frequencies being larger, in the 40 kHz range, which cannot be resolved based on the Nyquist frequency resolution limit of the low frame rate data being 33.75 kHz. Although the magnitude of the fluctuations varied, it was evident that the frequency of the perturbations were not consistent test to test or over a range of test conditions. This signified that the fluctuations are largely the result of a random nature, such as turbulence. Hypothesis and implications of these liquid length fluctuations will be discussed in the next section.

8.5. Hypotheses and Implications of Liquid Length Fluctuations

There are various potential causes for the presence of these liquid length fluctuations. As discussed in Chapter 2.3.6, these fluctuations could be attributed to turbulence, fuel pressure fluctuations, needle oscillation, slugs of concentrated fuel

breaking away from the main spray core, large scale evolving structures at the spray tip, as examples. Another potential cause of the liquid length fluctuations is temperature gradients inside the combustion vessel, as temperature is a key factor governing liquid length behavior (Siebers 1998).

As discussed in the prior section, fuel pressure has minimal influence on the liquid length fluctuations. Needle oscillation in regards to eccentric needle lift, was shown to be prevalent during the start of injection as discussed in Chapter 3.4.2.1. Needle oscillation, both axially and laterally, is known to occur during the entire injection event potentially caused by a cantilever motion of the needle with the axial fluctuations being pressure dependent, and for example at 1500 bar the frequency is 5556 Hz (Kastengren et al. 2011). Some of the liquid length fluctuations fall close to this frequency which may signify that needle lift oscillations were occurring during the quasi-steady injection period, translating to downstream spray characteristics. These oscillations would manifest themselves as differences in apparent injection pressure at the nozzle hole. However, injection pressure does not directly impact liquid length (Siebers 1999) but could result in differences in injector coefficients or spray angle which do influence liquid length. The fact that there were not dominant repeated frequencies indicates that this was not a likely cause as a structure factor such as this would have a natural frequency that would be consistent case to case.

Fuel parcels or ‘slugs’ breaking away from the main fuel jet were observed in the images and during the image processing, with the liquid length values reported resulting from image processing of the continuous portion of the liquid fuel jet. This is a contributing factor in the liquid length fluctuations as the liquid length represents the full liquid core and did not account for this detached fuel slug which yielded a reduction in liquid length from the processing relative to the prior time instant. This phenomenon was not the sole cause of the fluctuations in liquid length as fluctuations occur on a frame to frame basis but detaching slugs do not occur frame to frame as evidenced during visualization of the acquired movies, i.e. fuel slugs detach from the leading edge of the spray less often than the fluctuations are observed, but is a contributing factor.

Another phenomenon tied to downstream spray structure is cavitation within the injector nozzle hole with liquid length increasing as cavitation increased (Desantes et al. 2005), however, this role of cavitation’s influence on atomization is not well established nor is it consistent with others finding a reduction in liquid length with cavitation (Payri et al 2006). Cavitation can be defined as a change in discharge coefficient with a reduction of the dimensionless cavitation parameter, with cavitation occurring under high injection pressure conditions (Schmidt 1997). Under cavitating conditions, there is a sharp decrease in discharge coefficient based on the choking of mass flow through the nozzle (Payri et al. 2008). Cavitation can be understood as a reduction in discharge coefficient, a parameter that influences liquid length.

8.6. Parametric Modeling Study – Liquid Length Fluctuations

Hypotheses were made as to the cause of these fluctuations in Chapter 8.5 and are now reiterated:

- Fluctuations in injection pressure as a result of the injection event
- Cavitation and injector internal flow variations being manifested through injector coefficients
- Temperature gradients of the ambient charge gas.

Siebers liquid length model is applied, using heptadecane as the representative fuel based on accurately representing diesel fuel evaporation characteristics (Siebers 1999). A parametric study is undertaken in an effort to validate hypotheses as to the cause of the fluctuations. This is done using the baseline condition experimental results (1190 K core charge-gas temperature, 2000 bar injection pressure, 32.2 kg/m^3 core gas density, and 363 K fuel temperature). As presented in Chapter 8.3, the mean liquid length during the quasi-steady period, over all 8 plumes was 10.9 mm. During the quasi-steady period (1-2 ms ASOI), the difference of the liquid length computed at each time ASOI is determined relative to the mean liquid length. This difference defines the liquid length fluctuation, at each time ASOI. The average of the positive fluctuations, those which have liquid lengths above the mean value, is determined, which is a liquid length of 11.4 mm (or an average increase of 0.5 mm relative to the mean value). The same procedure is applied to the negative fluctuations, those with liquid lengths less than the mean value, with the mean negative fluctuations being 10.3 mm, or an average decrease of 0.6 mm relative to the mean value. Also considered was the maximum and minimum extent of the fluctuations, which is defined as the longest and shortest achieved liquid length during the quasi-steady period, being 12.4 mm for the maximum positive fluctuation and 8.7 mm for the maximum negative fluctuation. The liquid length model will be used, with parametric variation of different parameters in an effort to match and therefore provide evidence that the hypothesis is a possible cause of these fluctuations.

8.6.1. Charge – Gas Temperature Gradients – Boundary Layers

Boundary layers are known to exist in the combustion vessel based on the large temperature change from the cooler vessel walls (453 K) to the core region of the vessel at elevated temperature based on the preburn procedure (upwards of 800 K). These temperature gradients may be significant enough to cause variations in liquid length, as liquid length is known to decrease, nonlinearly, with increasing charge-gas temperature (Siebers 1998). The Siebers (1999) liquid length model is applied using the developed equation of state approach with n-heptadecane as the representative fuel, with charge gas temperature varied (along with core gas density based on the assumption of constant vessel pressure), to quantify this impact on penetration. Results are provided in Figure 8.9.

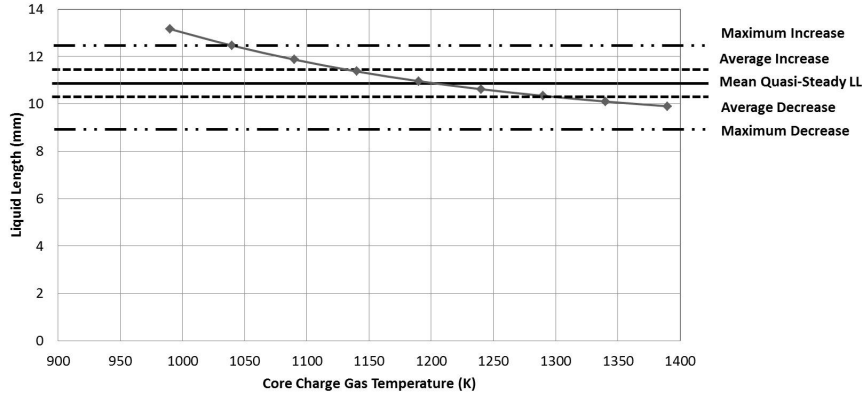


Figure 8.9: Influence of core charge-gas temperature on liquid length results.

As shown in the figure above the average increase in liquid length of 0.5 mm could be explained by a 55 K reduction in core charge-gas temperature, and the average decrease in liquid length of 0.6 mm could be explained by a 100 K increase in core charge-gas temperature, assuming all other parameters do not vary. Also, for the maximum increase of 1.5 mm over the mean steady state liquid length, this corresponds to a 150 K reduction in core charge-gas temperature. However, the temperature change representing the maximum decrease in liquid length cannot be determined from the model based on model limitations.

This variation in core charge-gas temperature is reasonable near the edges of the vessel where there are larger gradients between the heated walls and windows to the internal core charge gases, however, it is not likely to be the only controlling factor in the liquid length fluctuations. Even larger variations in liquid length are seen (when considering the maximum and minimum liquid lengths during the quasi-steady period), which require larger changes in core gas temperature (150 K decrease in temperature for the maximum liquid length increase, exceeding model limitations for the maximum liquid length decrease). Therefore, gas temperature variations and the presence of boundary layers can explain some of the liquid length fluctuations, however, they are likely not the only contributing factor. Future work acquiring data on boundary layer temperature gradients would further validate this hypothesis.

8.6.2. Injector Cavitation – Nozzle Discharge Coefficient

Cavitation inside the injector nozzle is known to influence downstream spray characteristics (Siebers 1999), with cavitation being manifested by a sharp decrease in discharge coefficient. Although discharge coefficient does not appear directly in the liquid length model, it influences the area contraction coefficient which is a parameter used in model evaluation, as defined in equation (105) (Siebers 1999).

$$C_a = 2A_f C_d^2 \frac{P_f - P_a}{\dot{M}_f} \quad (105)$$

A reduction in discharge coefficient due to the presence of cavitation will result in a decrease in the area contraction coefficient. The initial discharge coefficient and area contraction coefficient were assumed to be 0.75 and 0.8, respectively. With cavitation, the discharge coefficient typically reduces down to 0.6 (Schmidt 1997), which would

yield an area contraction coefficient of 0.65 assuming all other conditions are identical. To analyze the impact of cavitation, the area contraction coefficient is swept from 0.1 to 1.0, for the baseline condition, with results shown in Figure 8.10.

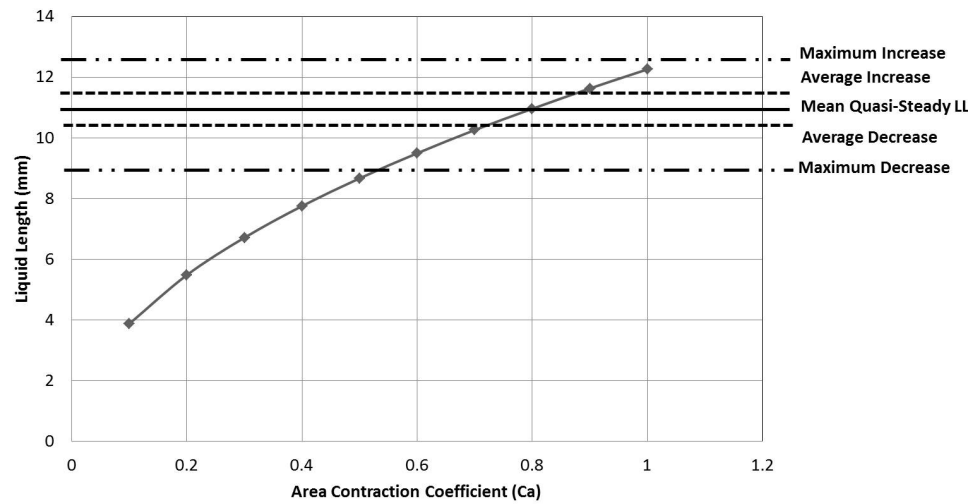


Figure 8.10: Modeled liquid length as a result of the area contraction coefficient sweep.

As shown in the figure, a reduction in the area contraction coefficient (reduction in discharge coefficient), results in a decrease in liquid length. A decrease in area coefficient by 0.08 from the starting value of 0.8 will decrease the liquid length to the magnitude of the average decrease fluctuation, and an increase of area contraction coefficient by 0.08 will increase the liquid length magnitude to the average increase representative of the fluctuations. To reach the maximum increase fluctuation of liquid length an area contraction coefficient greater than 1 is required, and to reach the maximum decrease fluctuation an area contraction coefficient of 0.5 is required, as shown in the figure. This required decrease in area contraction coefficient is reasonable based on the expected reduction in discharge coefficient attributed to the presence of cavitation, however, it is difficult to explain the required increase in area contraction coefficient (discharge coefficient) to explain the positive magnitude of the liquid length fluctuations, unless there is some transition from cavitating to non-cavitating regimes during the injection event. Therefore, cavitation may be a phenomenon which is occurring and could explain liquid length fluctuations, requiring a transition from cavitating to non-cavitating conditions during a single injection event, meaning that cavitation is occurring dynamically in the injector, which is possible and could be linked to fuel pressure fluctuations or needle lift characteristics as examples, and merits further study.

8.6.3. Internal Injector Flow and Injection Pressure – Orifice Coefficients

Internal flow and injection pressure fluctuations could be another cause of the liquid length fluctuations. Injector behavior is governed by three coefficients, area contraction, discharge, and velocity, as have been previously discussed. These coefficients are all interrelated, and provide an indication of orifice properties and

processes which are known to influence spray characteristics (Siebers 1999). Although injection pressure does not influence the quasi-steady liquid length per earlier discussions (see section 7.3), it could influence the fluctuations about this quasi-steady value, due to the fluctuations in the fuel supply line. An increase in injection pressure could manifest itself as a change in an orifice coefficient, with there being a small nonlinear decrease in C_a with an increase in injection pressure, a 10% decrease (from 0.9 to 0.8) for a 110% increase in injection pressure (80 to 170 MPa) (Siebers 1999). This change in area contraction coefficient from 0.9 to 0.8 results in a 0.7 mm reduction in liquid length, which is not of large enough magnitude to explain the liquid length fluctuations, especially since the actual variation in actual discharge coefficient would be less as the maximum change in injection pressure during the fuel line fluctuations is 95 MPa, which is less than the 110 MPa change discussed here. Therefore, from this analysis and as was previously discussed in Chapter 8.4.1 based on frequency analysis, liquid length fluctuations are minimally influenced by fuel injection pressure fluctuations.

Internal injector flow characteristics could potentially cause these liquid length fluctuations. Needle lift is likely not the case as this would manifest itself as differences in apparent injection pressure at the nozzle holes (Kastengren et al. 2011), which shows minimal influence as just discussed. If not manifested through injection pressure, these internal flow differences would be the result of differences in injector orifice coefficients (C_a , C_d , or C_v), which were considered in section 8.6.2. Liquid length, and this correlation, is for steady flow characteristics. This difference in internal flow would be unsteady momentum in regards to pulsating injection pressure, yielding different transport processes than can be predicted by this liquid length model. Liquid length fluctuations could partially be explained by differences in injector characteristics, however, the required magnitude of change of injector coefficients is significant (area contraction coefficient change of 0.5 to explain the 3.7 mm span in liquid length fluctuations).

8.6.4. Summary of Liquid Length Fluctuation Model Results & Conclusions

Various proposed hypotheses for the liquid length fluctuations are evaluated using the Siebers 1999 liquid length model coupled with an equation of state approach. Conclusions can be made from this model application to better understand the proposed causes of these fluctuations, as summarized in Table 8.5.

Table 8.5
Liquid length fluctuation hypotheses, model results, and conclusions.

Hypothesis	Model Results	Conclusion
Temperature gradients	Temperature span of 155 K required to explain 1.1 mm span in average fluctuations	Potential cause due to boundary layers but not the sole cause
Cavitation	Ca increase and decrease by 0.08 to explain 1.1 mm span in average fluctuations	Potential cause; requires dynamic transition from cavitating to noncavitating flow
Injection pressure oscillation	110 Mpa injection pressure increase, Ca decrease 0.9 to 0.8 -> 0.7 mm reduction in LL -> not significant enough	Not cause of liquid length fluctuations
Injector characteristics	0.5 change in Ca to explain 3.7 mm span in LL fluctuations	Not the sole source of fluctuations, but variations in internal flow characteristics have influence
Detaching slugs of fuel		Not the sole source of fluctuations but are a contributing factor
Turbulence		Potential cause as fluctuations are random in nature based on frequency analysis

8.7. Summary and Conclusions

Under vaporizing (0% oxygen conditions), there were noticeable fluctuations in diesel spray liquid length about a quasi-steady value. Quantifying and understanding the causes and implications of this behavior is important based on issues with wall-impingement, increased fuel consumption, un-burnt hydrocarbon and soot emissions. The average magnitude of the fluctuations seen here are an increase of 10% relative to the mean value and a decrease of 5% relative to the mean value. The fluctuations did not correlate to fuel pressure fluctuations, although these may be an influencing factor, as determined from frequency analysis of the fuel pressure fluctuations and liquid length perturbations. Overall, the fluctuations were observed in all test conditions, but the frequencies were not consistent over repeats or a range of test conditions, signifying that these fluctuations appear to be random in nature and may be caused by turbulence. Hypotheses as to the cause of the liquid length fluctuations are a combination of cavitation (manifested in the discharge coefficient), fuel line pressure fluctuations, temperature gradients in the combustion vessel, and turbulence.

The Siebers liquid length model in conjunction with the equation of state approach for thermophysical property modeling is applied, using n-heptadecane as a representative fuel based on its boiling point matching the 90% distillation point of diesel to validate proposed hypotheses on liquid length fluctuations for the baseline test condition.

Several key conclusions are made.

- The hypothesis that temperature gradients inside the combustion vessel can result in liquid length variations was evaluated. Average liquid length increase is 0.5 mm, requiring a 55 K reduction in core charge-gas temperature, and the average liquid

length decrease is 0.6 mm necessitating a 100 K increase in core charge-gas temperature, assuming all other parameters do not vary. To account for the larger maximum variations in liquid length, even larger temperature gradients are required. Variations in core charge-gas temperature are likely to exist and will influence liquid length fluctuations, however, based on the required magnitude change of temperature, it is concluded that this is not the only cause.

- The onset of cavitation, which results in a decrease in discharge coefficient and hence a decrease in area contraction coefficient, could influence liquid length behavior and fluctuations. To achieve the average increase in liquid length, the area contraction coefficient would need to increase by 0.08, and decrease by 0.08 to reach the observed average decrease in liquid length. A wider spread in area contraction coefficient would be required to explain the maximum and minimum extent of the fluctuations. For cavitation to be the explaining parameter, the flow in the injector nozzle would need to dynamically transition from cavitating to non-cavitating.
- Injection pressure variations were hypothesized as a cause of liquid length fluctuations, which was evaluated using the liquid length model. Injection pressure perturbations were evidenced in the fuel pressure traces, spanning 95 MPa. Although injection pressure is not directly in the liquid length model, there is a small reduction in area contraction coefficient (C_a) for injection pressure increase, from 0.9 to 0.8 for a 110 MPa injection pressure increase. This reduction in C_a will yield a 0.7 mm reduction in liquid length, which is not of large enough magnitude to explain the fluctuations, agreeing with characteristic frequencies as discussed in chapter 7. Therefore injection pressure perturbations are not a cause of liquid length fluctuations.
- Liquid length fluctuations could partially be explained by differences in injector characteristics, however, the required magnitude of change of injector coefficients is significant (area contraction coefficient change of 0.5 to explain the 3.7 mm span in liquid length fluctuations). Differences in injector coefficients as manifested through discharge coefficients are not the sole source of the fluctuations, but variations in internal flow characteristics could have a partial effect on liquid length.

Based on model application, it is proposed that the two main physical causes of liquid length fluctuations are that of temperature gradients inside the vessel, and differences in internal injector flow characteristics (cavitation), causing variations in nozzle orifice coefficients.

9. Summary and Conclusions

As the prime mover for transportation in society, internal combustion engines require technical advancements and improvements to continue to meet increasingly stringent emission standards while increasing performance and improving fuel efficiency. This requirement necessitates fundamental spray and combustion studies under engine-relevant conditions. This work undertook a study to provide an improved understanding of diesel spray conditions using an optically accessible combustion vessel which was subsequently linked with a thermophysical property analysis liquid length model.

The objectives of the current work are reiterated here, with key conclusions discussed. The first requirement was the development of a combustion vessel research facility for diesel spray studies which required thermodynamic state generation capability for producing internal combustion engine relevant conditions, along with other subsystems for operation. This facility has been successfully developed and subsystems integrated for initial tests in March 2009, with subsystems and diagnostics continuing to come online as dictated by research project needs based on work with industrial partners. Additional completed subsystems required for the current diesel spray testing include integration of a piezoelectric injector driver, along with the development of a low pressure return for the fuel system to provide the required back pressure for engine operation, with these upgrades being completed May 2010. Diagnostics developed and applied include high speed Mie back scattering imaging for visualizing the liquid phase of the diesel fuel spray.

To achieve the required conditions for study, replicating conventional diesel engine conditions, a preburn procedure is needed. This procedure is known to generate minor species that may influence the diesel spray and combustion process and therefore an understanding was required of the influence on mixture properties, both pre and post pre-burn, and on the resulting fuel autoignition. Using chemical kinetics modeling of the premixed burn, cool-down, and fuel autoignition, it was determined that the preburn procedure used is valid for these spray studies. Although minor species are produced, the most significant being NO, NO₂ and OH, the levels are representative of those found in conventional diesel engines running with exhaust gas recirculation (EGR). The reactive minor species had insignificant effects on the auto-ignition of n-heptane as a diesel surrogate for ignition studies, reducing the ignition delay by 3% relative to dry air, increasing it by 6% relative to air plus residuals, with these changes being within the accuracy of the modeling and simulations (0.1 ms or 10%). It is concluded that the changes in ignition delay from the minor species are small relative to those from the major species (CO₂, H₂O and O₂) which increase to 3.8% (CO₂) and 3.5% (H₂O) for a 21 to 15% oxygen reduction, yielding a 170% increase in ignition delay. The influence of different mixture composition was also investigated, which shows no significant difference in specific heats of the charge gas mixture (1.13 to 1.21 kJ/kg-K) with the mixture specific heat also closely matching an engine running 38.3% EGR (1.16 kJ/kg-K). Additionally, despite the differing cool-down histories of the vessels in the ECN due to a range of fan speeds and differences in minor species due to variations in pre-burn mixtures, there is no significant impact on the ignition delay between the vessels and the ignition delay is only 4% shorter than that of ideal EGR at 15% oxygen, which is within the modeling accuracy. The same observation is found when considering only major

species in regards to the insignificant effect of these differing mixtures on n-heptane autoignition. The preburn procedure therefore is an effective tool for state generation for these combustion vessel spray and combustion studies, and has minimal effect on autoignition.

This preburn procedure is subsequently used in the experimental studies for generating both 0% and 21% oxygen environments, for vaporizing and combusting spray tests, respectively. To quantify the spray parameters of interest including penetration, lift-off length, liquid length and cone angle, a robust optical setup and image processing methodology is required. A setup was developed which ensured uniform illumination of the chamber from the flashlamp by the use of a mirror reflector while providing a high signal to noise ratio (4.4) to ensure quality images. This methodology provides images which are minimally impacted by the choice of threshold used in edge detection for the image processing for the non-vaporizing, vaporizing, and combusting sprays. Also briefly discussed was a Gaussian based curve fitting methodology for non-vaporizing spray cone angle calculation which has application to CFD model development, being less subjective than standard methodologies. Although not applied in the current work, the methodology was reviewed as an alternative technique for cone angle definition.

Diesel spray characteristics were studied for non-vaporizing, vaporizing and combusting conditions over a range of charge gas temperatures (373 – 1300 K bulk gas conditions) and densities (17.4 and 34.8 kg/m³ bulk gas conditions), fuel injection pressures (1034 to 2000 bar), and fuel temperature, using a multi-hole injector. For the non-vaporizing sprays penetration and cone angle were quantified. For vaporizing sprays the parameters of interest were liquid length and penetration. For combusting sprays key characteristics included flame length, lift-off length, and combusting cone angle.

Under non-vaporizing conditions, a 7 K increase in fuel temperature has negligible influence on penetration or cone angle of the sprays. Injection pressure, however, shows a significant influence on penetration with it increasing 40% for an injection pressure increase from 1034 to 2000 bar, with a corresponding 6% increase in cone angle. A reduction in charge gas density, from 17.4 to 34.8 kg/m³, provided a 20% increase in penetration and 9% decrease in cone angle. Although plume to plume variations were evident under these non-vaporizing test conditions, trends could not be identified in regards to plume dependency without additional tests being conducted and an improved definition of start of injection relative to camera image acquisition.

Vaporizing spray tests showed a non-linear reduction in liquid length with an increase in charge gas temperature, with a 49% decrease for an 800 to 1300 K change in temperature. An 8 K increase in fuel temperature reduced liquid length by 12%. Increasing charge gas density by a factor of 2 provided a 34% reduction in liquid length. Injection pressure showed minimal influence on liquid length for the conditions investigated. Fluctuations of the liquid length about a quasi-steady value were apparent under all investigated test conditions. Plume to plume variations were evident with trends existing. These included plumes 1, 4, 5, 6 and 7 exhibiting liquid lengths less than the mean by an average of 5%, and plumes 2, 3, and 8 possessing liquid lengths in excess of the mean by an average of 5%. This is hypothesized to be attributed to the internal flow geometry of the injector. Eccentric needle lift and motion is ruled out as a cause of these variations, even though it is apparent at the start of injection, this motion does not

translate to the steady state plume characteristics. Similarly, with scanning electron microscope images of the injector nozzle, differences in hole diameter are eliminated as a cause of these spray plume variations.

For combusting tests in a 21% oxygen environment, an injection pressure increase from 1034 to 2000 bar results in an increase in flame lift off by 31%, decrease in cone angle by 8%, and increase in lift-off length by 40%. Charge gas-density also influences spray characteristics, showing a reduction in flame length by 11% and lift-off length by 25% for a doubling of charge-gas density from 17.4 to 34.8 kg/m³ (bulk-gas conditions), with a 23% increase in cone angle. Charge gas temperature showed no significant impact on flame length (less than 2% for a 150 K change in temperature).

A comparison of the combusting and vaporizing test results show that of the tests undertaken, three conditions exist (34.8 kg/m³ density at 1100 K 1034 bar injection pressure, and 950 and 1100 K 1379 bar injection pressure) where the liquid length exceeded the lift-off length, by up to 20%, which would likely yield increased soot production. These conditions should be avoided as it is ideal to ensure enhanced fuel-air mixing before reaching the combustion zone. Additionally, a comparison of combusting flame length and non-vaporizing penetration was undertaken (acknowledging that charge-gas temperature differences exist) and it was found that at full load (34.8 kg/m³ conditions), the penetration became reduced relative to the flame length due to hot product expansion and increased propagation as a result of combustion. This trend however was not observed under the part-load (17.4 kg/m³) condition.

The aforementioned liquid length fluctuations were further investigated in an effort to explain this behavior. Over the quasi-steady period, the magnitude of the fluctuation relative to the mean value varied. The average magnitude of these fluctuations was an increase of 10% and a decrease of 5% relative to the mean value, for all test conditions investigated. Fluctuations did not directly correlate to fuel pressure fluctuations in the high pressure fuel line as a result of injection based on frequency analysis, but, these may provide a small contribution to the behavior. Frequency analysis of the fluctuations were applied, however, there was no consistency in the determined frequencies signifying that they may in fact be random and non-systematic in nature. Hypotheses were presented as to the cause of these fluctuations including, cavitation, fuel-line pressure fluctuations, temperature gradients and turbulence (attributed to changes in mixing from steady state conditions), which were further investigated using a 1-D liquid length model.

The applied 1-D liquid length model is based on a mixing-limited vaporization assumption. Limitations of this model were investigated to ensure the conditions of the current work fall into the realm of applicability, which is confirmed. Under low temperature or density conditions the model applicability in regards to the mixing-limited vaporization, begins to come under question. The model was first evaluated using tabulated properties for cetane as a representative surrogate for diesel fuel. This application validated the model in regards to trends compared to experimental results, yielding liquid lengths at most 1.6 mm shorter from the experimental tests at the elevated fuel temperature condition, being 3 mm shorter for the reduced fuel temperature condition. An equation of state approach for thermophysical property determination was developed using the Peng Robinson equation of state to enable model application using

fuels whose thermodynamic properties are not readily available, and to evaluate fuel mixtures. This required the development of vapor-liquid equilibrium using fugacity functions for defining the saturation pressure–temperature relationship, along with various enthalpy and compressibility terms representing both conditions at injection, and those at saturation, where the liquid length is defined. Using cetane as the representative fuel, the equation of state approach for thermophysical property modeling provides results which match well with experimental results. This methodology was also applied to a range of fuels, both single and multi-component, providing indication that for fuels to match liquid length vaporization characteristics, its boiling point should closely match the 90% distillation point of diesel fuel.

This analysis and model was also used to provide a parametric evaluation of the proposed hypotheses for liquid length fluctuations, including charge-gas temperature gradients, cavitation, injection pressure fluctuations or nozzle orifice characteristics.

- To match the average magnitude of the liquid length fluctuations, of 0.5 mm increase and 0.6 mm decrease from the quasi-steady value, a 55 K reduction and 100 K increase in charge-gas temperature, respectively, is required. These charge-gas temperature gradients most likely exist due to the combustion vessel boundary layers and are a possible phenomenon influencing the liquid length fluctuations, however, they are not the only impact since even larger gradients in temperature would be required to explain the maximum extent of the fluctuations.
- The remaining hypotheses are manifested as a change in orifice coefficients, including discharge coefficient for cavitation and area contraction coefficient for injection pressure. To achieve the average increase in liquid length, the area contraction coefficient would need to increase by 0.08, and decrease by 0.08 to reach the observed average decrease in liquid length. This required decrease in area contraction coefficient is reasonable based on the expected reduction in discharge coefficient attributed to cavitation, however, it is difficult to explain the increase in the coefficient unless there is transition between conditions of cavitating to non-cavitating regimes in the flow.
- Injection pressure perturbations were evidenced in the fuel pressure traces, spanning 95 MPa, which could be manifested as a small reduction in area contraction coefficient. This reduction in C_a from 0.9 to 0.8 would yield a 0.7 mm reduction in liquid length, which is not of large enough magnitude to explain the fluctuations, agreeing with characteristic frequencies of the fuel pressure fluctuations as discussed in Chapter 7 signifying that fuel pressure fluctuations are not a governing factor in these liquid length fluctuations.
- Liquid length fluctuations could partially be explained by differences in injector orifice characteristics caused by internal flow and geometry, however, the required magnitude of change of injector coefficients is significant (area contraction coefficient change of 0.5 to explain the 3.7 mm span in liquid length fluctuations) and therefore is not the only phenomenon.

Based upon this analysis, the cause of the liquid length fluctuations is likely attributed to one, or a combination of factors including temperature gradients, internal injector flow geometry manifested in nozzle coefficients, and slugs of fuel detaching from the tip of the spray. These slugs of fuels detaching from the spray are observed in the images, and

are not evaluated in the image processing as discussed in Chapter 5.4.2 based on the spray being defined as the continuous portion of fuel from the injector.

The current work has made significant contributions to the diesel spray and combustion community through several means. This work has validated the use of a preburn procedure for thermodynamic state generation by application of the first detailed chemical kinetics modeling study. This procedure was applied for diesel spray and combustion studies from a multi-hole injector in an optically accessible constant volume combustion vessel over a range of engine-relevant conditions. This was achieved through robust optical diagnostic development and image processing methodologies. Results were quantified, including plume to plume variations and liquid length fluctuations, which have implications on emissions and fuel-air mixing. This multi-hole injector study with focus on plume to plume variations and liquid length fluctuations is the most extensive multi-hole injector study currently published. These fluctuations were characterized both using frequency analysis and a developed equation of state approach for thermophysical property modeling with an application to a 1D mixing limited vaporization model for liquid length. This equation of state approach provides a simple, but effective, method for evaluating liquid length characteristics of a wide range of surrogates over varying conditions. The thermophysical property analysis using the equation of state approach provides an advancement over past studies which focus solely on surrogate fuels and chemical kinetics. Additionally, this method is an improvement as it relies on readily available fuel property data for hydrocarbons and their mixtures, as opposed to requiring less accessible tabulated data for enthalpy and other properties. This knowledge is imperative based on the importance of liquid length in emissions, relative to lift-off length, and the avoidance of wall impingement for unburnt hydrocarbon emissions. The validated combustion vessel apparatus and equation of state 1-D liquid length model provide the necessary tools for understanding diesel spray characteristics, and the impacts of fuel, for improvements in engine design for emissions and efficiency.

10.Future Work

Numerous opportunities exist for additional experimental work and modeling to expand on the current research. One area which is a necessity for future work is temperature measurements inside the combustion vessel. This includes measurements of the ambient charge-gas temperature at various locations which could be accomplished by using a thermocouple window probe, based off that used at Sandia (Pickett et al. 2010). This would provide information on boundary layers and temperature gradients and fluctuations which do exist enabling the development of relationships for conversion of bulk gas conditions to core gas conditions for the Michigan Technological University combustion vessel, as opposed to the use of correlations developed for Sandia National Laboratories combustion vessel, as were used here. This information is imperative for a more thorough characterization of ambient composition and is essential as Michigan Technological University becomes increasingly involved with the international collaboration initiative of the Sandia National Laboratory ECN.

Also required are improved fuel temperature measurements along with improved fuel injector cooling. Several institutions use a dummy injector setup for measuring fuel temperature which could be replicated at Michigan Technological University with a moveable thermocouple included in the injector to measure temperature variations throughout the injector (Pickett et al. 2010; Bazyn and Martin 2011; Meijer et al. 2011). This would provide a more accurate understanding of the injected fuel temperature and gradients in fuel temperature at varying locations in the injector. Fuel temperature reduction capability should also be improved which could be achieved by a higher capacity chiller and the use of heat transfer grease during injection installation to facilitate more efficient heat removal.

In chapter 4 significant discussion was provided on minor species produced during the premixed burn based on modeling. Experimental testing should be undertaken to validate the reported levels of minor species, in particular NO_x , as a function of pre-mixture and test conditions. Diagnostic development would be required for in-situ sampling, which could include the use of a sampling probe coupled with a multi-component gas-analyzer. Care must be taken to minimize the effects of crevice volumes on the sampled gas results as these volumes cause elevated levels of un-burnt hydrocarbons. In addition to minor species levels, an understanding of major species produced is also beneficial, which can be achieved by verifying mixtures through exhaust gas sampling. Recommended is the installation of an oxygen (λ) sensor with feedback into the iTest control system to provide close to real-time verification of mixture properties and an indication of pre-burn combustion efficiencies by providing a reading of oxygen levels in the products. Undertaking parametric studies applying differing mixture compositions for a consistent oxygen level would be advantageous to understand minor and major species produced, coupled with fuel spray and ignition studies in these differing environments with identical experimental setup to compare the influence on spray and combustion characteristics, including ignition delay. This would enable quantification of the influence these varying mixtures have on spray characteristics. Studies should be performed to better understand the influence of fan speed on the pre-combustion event and diesel injection to determine if there is an optimal setting for pre-burn combustion efficiency and generated composition levels. The results

from this future work component will provide application and information for the advancement of the Sandia ECN by better understanding parameter influence on pre-combustion events to facilitate vessel comparison and collaboration. Exhaust gas sampling is also required to follow-up on the modified 0% oxygen mixture to verify that combustion efficiency is improved and oxygen levels provide a better representation of actual zero percent oxygen conditions.

Additional diagnostic development is required to advance the impact of the combustion vessel research efforts. This includes the development of an upgraded shadowgraph system to provide enhanced image signal to noise ratio, in particular, under conditions using the pre-burn procedure for thermodynamic state generation. This can be undertaken using a camera with increased low-light sensitivity, along with a higher intensity light source. Novel image processing techniques would also be required including for example, those used at Sandia which considers the texture of the temporal derivative for defining spray regions (Sandia ECN 2011) as opposed to standard edge detection methodologies. This shadowgraph imaging is important as it provides an understanding of vaporization characteristics which, when directly coupled with Mie scatter (liquid phase) imaging, provides an understanding of fuel-air mixing and vaporization. This may best be accomplished by development of the technique proposed by Parrish and Zink (2011) as discussed in Chapter 2 which has been successfully applied to gasoline sprays. The validity of this method for higher pressure diesel sprays is unknown, but future work should include development and integration of this imaging methodology to determine if the benefits can be realized in the Michigan Technological University combustion vessel laboratory.

In addition to imaging enhancement, it is essential to continue laser diagnostic development to enable studies on soot formation. This includes both Laser Induced Incandescence (LII) diagnostics which provide qualitative information on spatial soot distribution, which, when coupled with laser extinction, yield quantitative soot measurements in a combusting fuel jet (Musculus and Pickett 2005). This information is imperative to link the fundamentals of soot formation with spray characteristics, and better understand the influence of plume to plume variations, and liquid length fluctuations, on the levels of soot formed from production multi-hole injectors.

Although not currently used, one diagnostic that would be advantageous to increase the understanding of fuel injection profiles is a rate of injection system which provides an indication of mass fuel flowing rate (refer to Johnson 2009 for details). The existing system in the combustion vessel laboratory is only capable of measurements from an on-axis single hole nozzle under room temperature and pressure conditions. Modification to this system would enable mass fuel flow rate measurements for each plume, independently, from a multi-hole nozzle, also under pressurized and high temperature conditions, representative of the actual spray tests. Extensive updates would be required to the existing system, however, the information on fuel mass flow rate provided for the various conditions and differing fuel types would generate additional data to help understand the injection process, including any perturbations in the injected flow rate, which could tie into the observations of the spray characteristics.

Supplementary testing is proposed to compare the flame length of the combusting spray to diesel spray penetration, under varying levels of EGR (different percent oxygen

conditions). This would provide additional information on spray and combustion trends at charge-gas conditions more representative of current technology diesel engines, which consistently run EGR.

Additional experimental imaging of diesel spray liquid length, under a broader range of experimental conditions, and at enhanced frame rates, would provide additional comprehension of diesel spray fluctuations in liquid length and plume to plume variations. These behaviors have implications in emissions formation; therefore, it is essential to provide a better understanding of this minimally documented phenomenon. This could be accomplished by taking higher frame rate images which would likely require conditions of reduced liquid length to enable decreased region of interest for image acquisition to permit elevated frame rates, based on camera limitations. Furthermore, further testing is required to validate the hypotheses for liquid length fluctuations, which should include consideration of surface roughness of the nozzle holes (as indicated in the SEM images presented in Chapter 3.4.2.1 and 12.2) and this influence on downstream spray characteristics.

It is important to understand the role of fuel impact in this behavior so various single-component fuels must be tested, including hexadecane, n-dodecane, and n-heptadecane, where property and kinetics information is well known, so that experimental results could be coupled with simplified 1-D and more detailed CFD modeling to provide a better understanding of these behaviors. This model with the equation of state method for property determination should also be used in surrogate fuel development to determine optimum fuel characteristics for matching diesel spray vaporization. It was concluded that a fuel boiling point which matches the 90% distillation point of diesel fuel is appropriate as a single-component surrogate for diesel spray characteristics, whereas matching the 50% distillation point does not provide a good representation. A similar approach should be undertaken for multicomponent surrogates in regards to determining a multi-component surrogate which has a distillation curve which closely resembles that of diesel fuel to determine if this full-matching of distillation provides an improved representation of diesel spray liquid length characteristics, or if matching the mixture boiling point to the 90% distillation of diesel is sufficient as discussed here. Future work will also include development of a dimensionless parameter for this penetration at the transition time to the liquid length ratio, to fully understand parameter dependency on the validity of this mixing limited hypothesis to ensure successful model application for surrogate fuels.

Improvements can also be made in the 1-D liquid length model as used here. These include an improved method of defining conditions at saturation, which couple the fuel and ambient and treat them as a mixture, as opposed to treating them as two separate mediums as done here based on Siebers (1999) model approach. An approach of this nature, in regards to treating the fuel and ambient at saturation as a mixture, is proposed in Luijten and Kurvers (2010) through the use of an enhancement factor, which could be incorporate in the liquid length model used here, while still using the equation of state method, with some modifications, for thermophysical property modeling. Additionally it has been assumed that the pressure term for the fuel liquid enthalpy (refer to discussion in chapter 7.4) is negligible. Correlations should be developed to evaluate this term and

include it in the model to further include all non-ideal effects to enhance model applicability.

In addition to improvements on the 1-D liquid length model, this model can be coupled with a similar model for lift-off length. This application will provide a better understanding of conditions which are required to achieve the maximum separation between lift-off length and liquid length to assist with soot emission reductions without the use of aftertreatment. By using the model to determine parameters which have the largest impact on liquid length, and by determining the corresponding impact on lift-off length, a better understanding of the competing parameters and resulting trends will be seen. This has application for a wide range of advanced combustion strategies including low-temperature combustion to better understand the limits of the operating regime, in particular from an emissions standpoint, to determine the path-forward for low-temperature combustion and other advanced strategies.

The final key aspect of future work is the integration and testing of alternative diesel fuels. This could include green diesel, biodiesel and dimethyl ether which have been proposed as potential alternative fuels but require additional study on spray, combustion, and emission formation characteristics to ensure efficient and successful integration. Using the methodologies developed and integrated in the current work, these fuels could be tested experimentally with results compared to proposed surrogates or single component fuels that could provide a good representation of their behavior to provide an improved understanding of parameter influence. The alternative fuels will also be included in the equation of state model with the thermophysical property analysis to model the liquid length characteristics of these alternative fuels.

Options for future work span various sections including both experimental and modeling, as required to not only advance the research capabilities of the Michigan Technological University combustion vessel, but also to provide enhanced applicability of the tools developed currently.

11. References

- Abraham J, Magi V. A Virtual Liquid Source (VLS) Model for Vaporizing Diesel Sprays. SAE. 1999;1999-01-0911.
- Adler D, Lyn WT. The Evaporation and Mixing of a Liquid Fuel Spray in a Diesel Air Swirl. Proceedings of the Institution of Mechanical Engineers. 1969;184:171-180.
- Agarwal AK. Biofuels (Alcohols and Biodiesel) Applications as Fuels for Internal Combustion Engines. Progress in Energy and Combustion Science. 2007;33(3):233-271.
- Aguilera CAV. (Internet). Extrema.m Matlab Central File Exchange; 2006. Available from <http://www.mathworks.com/matlabcentral/fileexchange/12275>.
- Akihama K, Takatori Y, Inagaki K, Sasaki S. Mechanism of the Smokeless Rich Diesel Combustion by Reducing Temperature. SAE. 2001;2001-01-0655.
- Alriksson M, Denbratt I. Low Temperature Combustion in a Heavy Duty Diesel Engine Using High Levels of EGR. SAE. 2006;2006-01-0075.
- Alternative Fuels Data Center (AFDC) (internet). Properties of Fuels. 2010. Available from: <http://www.afdc.energy.gov/afdc/pdfs/fueltable.pdf>.
- American Petroleum Institute (API). Technical Data Book Petroleum Refining. 6th ed. 1997.
- Anand K, Ra Y, Reitz RD, Bunting B. Surrogate Model Development for Fuels for Advanced Combustion Engines. Energy and Fuels. 2011;25(4):1474-1484.
- Aneja R, Abraham J. How Far Does the Liquid Penetrate in a Diesel Engine: Computed Results vs Measurements. Combustion Science and Technology. 1998;138:233-255.
- Arcoumanis C, Gavaises M, Nouri JM, Abdul-Wahab E, Horrocks RW. Analysis of the Flow in the Nozzle of a Vertical Multi-Hole Diesel Engine Injector. SAE. 1998;980811.
- Arcomanis C, Flora H, Gavaises M, Kampanis N, Horrocks R. Investigation of Cavitation in a Vertical Multi-Hole Injector. SAE. 1999;1999-01-0524.
- Arregle J, Pastor JV, Ruiz S. The Influence of Injection Parameters on Diesel Spray Characteristics. SAE. 1999;1999-01-0200.

- Austin GT. Effects of Biodiesel Blends on Particulate Matter Oxidation in a Catalyzed Particulate Filter During Active Regeneration (master's thesis). Houghton: Michigan Technological University; 2010.
- Azetsu A, Ito H. Effects of CO₂ and N₂ Mixing into Ambient Air on Flame Temperature and Soot Formation in Intermittent Spray Combustion. SAE. 2007;2007-01-1844.
- Bae C, Kang J. The Structure of a Break-Up Zone in the Transient Diesel Spray of a Valve-Covered Orifice Nozzle. International Journal of Engine Research. 2006;7(4):319-334.
- Baert RSG. Autoignition of a Diesel Spray at High Pressures and Temperatures. SAE. 1989;890417.
- Baert R, Frijters P, Somers B, Luijten C. Design and Operation of a High Pressure, High Temperature Cell for HD Diesel Spray Diagnostics: Guidelines and Results. SAE. 2009;2009-01-0649.
- Bardsley MEA., Felton PG, Bracco FV. 2-D Visualization of liquid and Vapor Fuel in an IC Engine. SAE. 1988;880521.
- Battin-Leclerc F. Detailed Chemical Kinetic Models for the Low-Temperature Combustion of Hydrocarbons with Application to Gasoline and Diesel Fuel Surrogates. Progress in Energy and Combustion Science. 2008;34(4):440-498.
- Bazyn T, Martin GC. Spray Combustion measurements in a Flow-Through High Temperature, High Pressure Chamber. In: Proceedings of the 2011 ILASS Americas 23rd Annual Conference on Liquid Atomization and Spray Systems; 2011 May 15-18; Ventura, CA. Paper No. 177.
- Bennett S. Modern Diesel Technology: Diesel Engine. Delmar Cengage Learning; 2009.
- Boedec T, Champoussin JC, Jondeau E. Experimental Investigation on the Fluctuation Intensities in a Stationary Spray. SAE. 1998;981066.
- Boot M, Rijk R, Luijten C, Somers B, Albrecht D. Spray Impingement in the Early Direct Injection Premixed Charge Compression Ignition Regime. SAE. 2010;2010-01-1501.
- Bougie B, Tulej M, Dreier T, Dam NJ, Ter Meulen JJ, Gerber T. Optical Diagnostics of Diesel Spray Injections and Combustion in a High-Pressure High-Temperature Cell. Applied Physics B. 2005;80:1039-1045.
- Bozbas K. Biodiesel as an Alternative Motor Fuel: Production and Policies in the European Union. Renewable and Sustainable Energy Reviews. 2008;12:542-552.

- Bracco FV. Structure of High Speed Full Cone Sprays. In: Recent Advances in Gas Dynamics, NY: Plenum Publishing Corporation; 1983.
- Brundtland GH. Development and International Economic Co-Operation: Environment. United Nations General Assembly; 1987. Report of the World Commission on Environment and Development, Note by the Secretary – General, 42nd session.
- Cantera (Internet). An Object-Oriented Software Toolkit for Chemical Kinetics, Thermodynamics, and Transport Processes. Available from <http://code.google.com/p/cantera/>.
- Chaves H, Knapp M, Kubitzek A, Obermeier F, Schneider T. Experimental Study of Cavitation in the Nozzle of Diesel Injectors using Transparent Nozzles. SAE. 1995;950290.
- Chigier N. Group Combustion Models and Laser Diagnostic Methods in Sprays: A Review. Combustion and Flame. 1983;51:127-139.
- Ciezki HK, Adomeit G. Shock-Tube Investigation of Self-Ignition of *n*-Heptane-Air Mixtures Under Engine Relevant Conditions. Combustion and Flame. 1993;93:421-433.
- Cong S, McTaggart-Cowan GP, Garner CP. Measurement of Residual Gas Fraction in a Single Cylinder HSDI Diesel Engine through Skip-Firing. SAE. 2009;2009-01-1961.
- Crua C. Combustion Processes in a Diesel Engine (Doctoral dissertation on the Internet). University of Brighton; 2002. Available from: http://crua.net/research/PDFs/Crua_PhD_Thesis.pdf.
- Dagaut P, Gail S, Sahasrabudhe M. Rapeseed Oil Methyl Ester Oxidation over Extended Ranges of Pressure, Temperature and Equivalence Ratio: Experimental and Modeling Kinetic Study. Proceedings of the Combustion Institute. 2007;31:2955-2961.
- Davis SC, Diegel SW, Boundy RG. Transportation Energy Data Book: Edition 29. ORNL – 6985, US Department of Energy; 2010. Available from: http://cta.ornl.gov/data/tedb29/Edition29_Full_Doc.pdf.
- Dec JE. A Conceptual Model of DI Diesel Combustion Based on Laser Sheet Imaging. SAE. 1997;970873.
- Dec JE. Diesel Fueled HCCI Engines. In: Zhao F, editor. Homogeneous Charge Compression Ignition Engines: Key Research and Development Issues. Warrendale, PA: SAE; 2003.

- Delacourt E, Desmet B, Besson B. Characterization of Very High Pressure Diesel Sprays using Digital Imaging Techniques. *Fuel*. 2005;84:859-867.
- De La Torre Ugarte DG, English BC, Jensen K. The Promise and Challenge of Bioenergy: Sixty Billion Gallons by 2030: Economic and Agricultural Impacts of Ethanol and Biodiesel Expansion. *American Journal of Agricultural Economics*. 2007;89(5):1290-1295.
- Demirbas A. Importance of Biodiesel as Transportation Fuel. *Energy Policy*. 2007;35:4661-4670.
- Dent JC. A Basis for the Comparison of Various Experimental Methods for Studying Spray Penetration. *SAE*. 1971;710571.
- De Risi A, Colangelo G, Laforgia D. An Experimental Study of High Pressure Nozzles in Consideration of Hole-to-Hole Spray Abnormalities. *SAE*. 2000;2000-01-1250.
- Desantes JM, Lopez JJ, Garcia JM, Pastor JM. Evaporative Diesel Spray Modeling. Atomization and Sprays. 2007;17:193-231.
- Desantes JM, Pastor JV, Garcia JM, Pastor JM. A 1-D Model for the Description of Mixing Controlled Reacting Diesel Spray. *Combustion and Flame*. 2009;156(1):234-249.
- Desantes JM, Pastor JV, Payri R, Pastor JM. Experimental Characterization of Internal Nozzle Flow and Diesel Spray Behavior, Part II: Evaporative Conditions. Atomization and Sprays. 2005;15:517-543.
- Desantes JM, Payri R, Pastor JM, Gimeno J. Experimental Characterization of Internal Nozzle Flow and Diesel Spray Behavior, Part I: Non-evaporative Conditions. Atomization and Sprays. 2005;15:489-516.
- Desantes JM, Salvador FJ, Lopez JJ, De la Morena J. Study of Mass and Momentum Transfer in Diesel Sprays based on X-Ray mass Distribution Measurements and on a Theoretical Derivation. *Experiments in Fluids*. 2011;50:233-246.
- Duffield JA, Collins K. Evolution of Renewable Energy Policy. *Choices: American Agricultural Economics Association*. 2006;21(1):9-14.
- Dyer TM. Characterization of One- and Two-Dimensional Homogeneous Combustion Phenomena in a Constant Volume Bomb. *SAE*. 1979;790353.
- Eastop TD, McConkey A. *Applied Thermodynamics for Engineering Technologists*. 5th ed. England; Prentice Hall; 1993.
- Eckerle WA, Lyford-Pike EJ, Stanton DW, LaPointe LA, Whitacre SD, Wall JC. Effects of Methyl Ester Biodiesel Blends on NO_x Emissions. *SAE*. 2008; 2008-01-0078.

- EES (Internet). F-Chart Software: Engineering Equation Solver. Available from: <http://www.fchart.com/ees/>.
- Energy Information Administration (EIA) (US). Annual Energy Review. US Department of Energy, Washington, DC; 2009. DOE/EIA-0384. Available from: <http://www.eia.doe.gov/emeu/aer/pdf/aer.pdf>.
- Energy Information Administration (EIA) (US). International Energy Outlook 2010. US Department of Energy, Washington, DC; 2010. DOE/EIA-0484. Available from: <http://www.eia.doe.gov/oiaf/ieo/pdf/0484%282010%29.pdf>.
- Energy Information Administration (EIA) (US). Annual Energy Outlook. US Department of Energy, Washington, DC; 2011. DOE/EIA-0383. Available from: [http://www.eia.gov/forecasts/aeo/pdf/0383\(2011\).pdf](http://www.eia.gov/forecasts/aeo/pdf/0383(2011).pdf).
- Espey C, Dec J. The Effect of TDC Temperature and Density on the Liquid-Phase Fuel Penetration in a D.I. Diesel Engine. SAE. 1995;952456.
- Espey C, Dec JE, Litzinger TA, Santavicca DA, Planar Laser Rayleigh Scattering for Quantitative Vapor-Fuel Imaging in a Diesel Jet. Combustion and Flame. 1997;109:65-86.
- Farrell JT, Cernansky NP, Dryer FL, Friend DG, Hergart CA, Law CK, McDavid RM, Mueller CJ, Patel AK, Pitsch H. Development of an Experimental Database and Kinetic Models for Surrogate Diesel Fuels. SAE. 2007;2007-01-0201.
- Fischer S, Stein JO. Investigation on the Effect of Very High Fuel Injection Pressure on Soot-NOx Emissions at High Load in a Passenger Car Diesel Engine. SAE. 2009;2009-01-1930.
- Fisher BT, Mueller CJ. Liquid Penetration Length of Heptamethylnonane and Trimethylpentane Under Unsteady In-Cylinder Conditions. Fuel. 2010;89(10):2673-2696.
- Fronzel M, Peters J. Biodiesel: A New Oildorado? Energy Policy. 2007;35:1675-1684.
- Fujimoto HG, Higashi K, Yamahita T, Senda J. Effects of Ambient Temperature and Oxygen Concentration on Soot Behavior in Diesel Flame. SAE. 2005;2005-24-007.
- Fujimoto H, Sato GT. Investigation on Combustion in a Diesel Engine Using a Constant Volume Combustion Chamber, I. Characteristics of Flames. Bulletin Japan Society of Mechanical Engineers. 1979;7(4):309-322.
- Gauthier BM, Davidson DF, Hanson RK. Shock Tube Determination of Ignition Delay Times in Full-Blend and Surrogate Fuel Mixtures. Combustion and Flame. 2004;139:300-311.

- Genzale CL, Pickett LM, Kook S. Liquid Penetration of Diesel and Biodiesel Sprays at Late-Cycle Post-Injection Conditions. SAE. 2010;2010-01-0610.
- Gimenes T. Characterization of Diesel Sprays in the Eindhoven High Pressure Cell (final project). Eindhoven University of Technology; 2006.
- Goodwin DG. An Open-Source, Extensible Software Suite for CVD Process Simulation. In: Proceedings of CVD XVI and EuroCVD Fourteen, ECS Proceedings; 2003-08 p 155-163.
- Graham T. Private Communication. 2011.
- Griffith RC. Series Turbocharging for the Caterpillar Heavy-Duty On-Highway Truck Engines with ACERT Technology. SAE. 2007;2007-01-1561.
- Groom MJ, Gray EM, Townsend PA. Biofuels and Biodiversity: Principles for Creating Better Policies for Biofuel Production. Conservation Biology. 2008;22(3):602-609.
- Gustavsson J, Golovitchev VI. Spray Combustion Simulation Based on Detailed Chemistry Approach for Diesel Fuel Surrogate Model. SAE. 2003;2003-01-1848.
- Harris FJ. On the Use of Windows for Harmonic Analysis with the Discrete Fourier Transform. Proceedings of the Institution of Electrical and Electronics Engineers. 1978;66(1):51-83.
- He C, Ge Y, Tan J, Han X. Spray Properties of Alternative Fuels: A Comparative Analysis of Biodiesel and Diesel. International Journal of Engine Research. 2008;32:1329-1338.
- Hecht, E., Optics, 2nd Edition, Addison-Wesley, 1987.
- Herbinet O, Pitz WJ, Westbrook CK. Detailed Chemical Kinetic Oxidation Mechanism for a Biodiesel Surrogate. Combustion and Flame. 2008;154(3):507-538.
- Herbinet O, Pitz WJ, Westbrook CK. Detailed Chemical Kinetic Mechanism for the Oxidation of Biodiesel Fuels Blend Surrogate. Combustion and Flame. 2010;157(6):893-908.
- Heywood JB. Internal Combustion Engine Fundamentals. McGraw-Hill Book Company; 1988.
- Higgins BS, Mueller CJ, Siebers DL. Measurements of Fuel Effects on Liquid-Phase Penetration in DI Sprays. SAE. 1999;1999-01-0519.
- Higgins B, Siebers DL. Measurement of the Flame Lift-Off Location on DI Diesel Sprays using OH Chemiluminescence. SAE. 2001;2001-01-0918.

- Higgins B, Siebers D, Aradi A. Diesel Spray Ignition and Premixed-Burn Behavior. SAE 2000;2000-01-0940.
- Hill J, Nelson E, Tilman D, Polasky S, Tiffany D. Environmental, Economic, and Energetic Costs and Benefits of Biodiesel and Ethanol Biofuels. Proceedings of the National Academy of Sciences. 2006;103(30):11206-11210.
- Hiroyasu H, Arai M. Structures of Fuel Sprays in Diesel Engines. SAE. 1990;900475.
- Hiroyasu H, Kodata T, Arai, M. Fuel Spray Characterization in Diesel Engines. In: Mattavi and Amann, editor. Combustion Modeling in Reciprocant Engines, Plenum Press; 1980.
- Hohmann S, Renz U. Numerical Simulation of Fuel Sprays at High Ambient Pressure: the Influence of Real Gas Effects and Gas Solubility on Droplet Vaporisation. International Journal of Heat and Mass Transfer. 2003;46(16):3017-3028.
- Hottenbach P, Brands T, Grunefeld G. An Experimental Investigation on the Evaporation Characteristics of a Two-Component Fuel in Diesel-Like Sprays. SAE. 2011;2011-01-0688.
- Hottenbach P, Brands T, Grunefeld G, Janssen A, Muther M, Pischinger S. Optical and Thermodynamic Investigations of Reference Fuels for Future Combustion Systems. SAE. 2010;2010-01-2193.
- Huo H, Wang M, Bloyd C, Putsche V. Life-Cycle Assessment of Energy Use and Greenhouse Gas Emissions of Soybean-Derived Biodiesel and Renewable Fuels. Environmental Science and Technology. 2009;43(3):750-756.
- Hurn RW, Hughes KJ. Combustion Characteristics as Measured of Diesel Fuels in a Constant-Volume Bomb. SAE Quarterly Transactions. 1951;6(1):24-35.
- Idicheria CA, Pickett LM. Effect of EGR on Diesel Premixed – Burn Equivalence Ratio. Proceedings of the Combustion Institute. 2007;31:2931-2938.
- Ito T, Hosaka T, Ueda M, Senda J, Fujimoto H. Detailed Kinetic Modeling and Laser Diagnostics of Soot Formation Process in Diesel Jet Flame. SAE. 2004;2004-01-1398.
- Ito T, Kitamura T, Ueda M, Matsumoto T, Senda J, Fujimoto H. Effects of Flame Lift-Off and Flame Temperature on Soot Formation in Oxygenated Fuel Sprays. SAE. 2003;2003-01-0073.
- Iyer VA, Abraham J, Magi V. Exploring Injected Droplet Size Effects on Steady Liquid Penetration in a Diesel Spray with a Two-Fluid Model. International Journal of Heat and Mass Transfer. 2002;45:519-531.

- Jawad B, Gulari E, Heinen NA. Characteristics of Intermittent Fuel Spray. *Combustion and Flame*. 1992;88(3-4):384-396.
- Jimenez J, Castro F, Gimenez B. The Tip Evolution of an Evaporative Intermittent Fuel Spray. In: THIESEL Conference Proceedings; 2000; Valencia, Spain.
- Johnson SE. Premixed Lean Gas Combustion and HPCR Rate of Injection used with a Constant Volume Combustion Vessel (master's thesis). Houghton: Michigan Technological University; 2009.
- Johnson S, Nesbitt J, Lee SY, Naber JD. Premixed Combustion of Acetylene-Hydrogen Fuel Mixtures for Thermodynamic State Generation in a Constant Volume Combustion Vessel. *Journal of KONES Powertrain Transport*. 2009;16(2):P2-00-2.
- Johnson SE, Nesbitt JE, Naber JD Mass and Momentum Flux Measurements with a High Pressure Common Rail Diesel Fuel Injector. In: Proceedings of the ASME 2010 Internal Combustion Engine Division Fall Technical Conference; 2010; San Antonio, TX. ICEF2010-35171.
- Johnson TV. Diesel Emissions in Review. SAE. 2011;2011-01-0304.
- Jones TO. Assessment of Technologies for Improving Light Duty Vehicle Fuel Economy: Letter Report. 2010. The National Academies. Available from: <http://www.nap.edu/catalog/12163.html>.
- Kalnes TN, Koers KP, Marker T, Shonnard DR. A Technoeconomic and Environmental Life Cycle Comparison of Green Diesel to Biodiesel and Syndiesel. *Environmental Progress and Sustainable Energy*. 2009;28(1):111-120.
- Kaminski DA, Jensen MK. Introduction to Thermal and Fluids Engineering. John Wiley and Sons Inc.; 2005.
- Kannan K, Udayakumar M. Modeling of Nitric Oxide Formation in Single Cylinder Direct Injection Diesel Engine Using Diesel - Water Emulsion. *American Journal of Applied Sciences*. 2009;6:1313-1320.
- Karimi K. Multiple-Injection Diesel Spray Characterisation at Elevated Pressures and Temperatures. (MPhil / PhD transfer report on the Internet). University of Brighton. 2004. Available from: http://www.brighton.ac.uk/shrl/publications/Diesel/Karimi_PhD_Transfer.pdf.
- Karimi K. Characterisation of Multiple-Injection Diesel Sprays at Elevated Pressures and Temperatures. (PhD dissertation on the Internet). University of Brighton. 2007. Available from: http://www.bton.ac.uk/shrl/publications/Diesel/Karimi_PhD_Thesis.pdf.

- Kastengren AL, Tilocco FZ, Powell CF, Fezzaa K. Initial Evolution of Engine Combustion Network Injectors with X-Ray Diagnostics. In: Proceedings of the 2011 ILASS Americas 23rd Annual Conference on Liquid Atomization and Spray Systems; 2011 May 15-18; Ventura, CA. Paper No. 100.
- Kim Y, Lim J, Min K. A Study of the Dimetyle Ethery Spray Characteristics and Ignition Delay. *International Journal of Engine Research*. 2007;8(4):337-346.
- Kistopanidis I, Cheng WK. Soot Formation Study in a Rapid Compression Machine. *Journal of Engineering for Gas Turbines and Power*. 2006;128 (4):942-949.
- Kimura S, Aoki O, Kitahura Y, Aiyoshizawa E. Ultra-Clean Combustion Technology Combining a Low-Temperature and Premixed Combustion Concept for Meeting Future Emissions Standards. SAE. 2001;2001-01-0200.
- Kitamura T, Ito T, Senda J, Fujimoto H. Mechanism of Smokeless Diesel Combustion with Oxygenated Fuels Based on the Dependence of the Equivalence Ratio and Temperature on Soot Particle Formation. *International Journal of Engineering Research*. 2002;3(4):223-248.
- Klein-Douwel RJH, Frijters PJM, Somers LMT, de Boer WA, Baert RSG. Macroscopic Diesel Fuel Spray Shadowgraphy Using High Speed Digital Imaging in a High Pressure Cell. *Fuel*. 2007;86(12-13):1994-2007.
- Klingbeil AE, Juneja H, Ra Y, Reitz RD, Premixed Diesel Combustion Analysis in a Heavy-Duty Diesel Engine. SAE. 2003;2003-01-0341.
- Knight BM, Bittle JA, Jacobs TJ. Characterizing the Influence of EGR and Fuel Pressure on the Emissions in Low Temperature Diesel Combustion. SAE. 2001;2011-01-1354.
- Kobori S, Kamimoto T, Aradi AA. A Study of Ignition Delay of Diesel Fuel Sprays. *International Journal of Engine Research*. 2000;1(1):29-39.
- Koh LP, Ghazoul J. Biofuels, Biodiversity, and People: Understanding the Conflicts and Funding Opportunities. *Biological Conservation*. 2008;141:2450-2460.
- Kohse-Hoinghaus K, Barlow RS, Alden M, Wolfrun J. Combustion at the Focus: Laser Diagnostics and Control. *Proceedings of the Combustion Institute*. 2005;30:89-123.
- Kokjohn SL, Reitz RD, Musculus MPB. Chemiluminescence and Fuel PLIF Imaging of Reactivity Controlled Compression Ignition (RCCI) Combustion. In: Proceedings of the 2011 ILASS Americas 23rd Annual Conference on Liquid Atomization and Spray Systems; 2011 May 15-18; Ventura, CA. Paper No. 168.

- Kolaitis DI, Founti MA. On the Assumption of Using n-Heptane as a “Surrogate Fuel” For the Description of the Cool Flame Oxidation of Diesel Oil. Proceedings of the Combustion Institute. 2009;32:3197- 3205.
- Kook S, Bae C, Miles PC, Choi D, Pickett LM. The Influence of Charge Dilution and Injection Timing on Low-Temperature Diesel Combustion and Emissions. SAE. 2005;2005-01-3837.
- Kook S, Pickett LM, Musculus MPB. Influence of Diesel Injection Parameters on End-of-Injection Liquid Length Recession. SAE. 2009;2009-01-1356.
- Kurvers C, Luijten CCM. Real Gas Effects in Siebers Mixing-Limited Spray Vaporization Model. SAE. 2010;2010-01-1497.
- Labs JE, Filley J, Jepsen E, Parker TE. A Constant Volume Diesel Spray Combustion Facility and the Corresponding Experimental Diagnostics. Review of Scientific Instruments. 2005;76:035108-1 -031508-10.
- Ladommatos N, Abdelhalim SM, Zhao H, Hu Z. Effects of EGR on Heat Release in Diesel Combustion. SAE. 1998;980184.
- Lawrence Livermore National Laboratory (LLNL) (Internet). n-Heptane, Reduced Mechanism. 2000. Available from: https://www-pls.llnl.gov/?url=science_and_technology-chemistry-combustion-nc7h16_reduced_mechanism.
- Lawrence Livermore National Laboratory (LLNL) (Internet). 2,2,4,4,6,8,8-Heptamethylnonane Mechanism. 2009. Available from: https://www-pls.llnl.gov/?url=science_and_technology-chemistry-combustion-heptamethylnonane.
- Lee CS, Park SW, Kwon SI. An Experimental Study on the Atomization and Combustion Characteristics of Biodiesel-Blended Fuels. Energy and Fuels. 2005;19(5):2201-2208.
- Lee JW, Min KD, Kang KY, Bae CS, Giannadakis E, Gavaises M, Arcoumanis C. Effect of Piezo-Driven and Solenoid-Driven Needle Opening of Common-Rail Diesel Injectors on Internal Nozzle Flow and Spray Development. International Journal of Engine Research. 2006;7:489–502.
- Lee UD, Yoo CS, Chen JH, Frank JH. Effects of H₂O and NO on extinction and re-ignition of vortex-perturbed hydrogen counterflow flames. Proceedings of the Combustion Institute. 2009;32:1059-1066.
- Lefebvre AH. Atomization and Sprays. Taylor and Francis: Hemisphere Publishing Company; 1989.

- Liang L, Chitralkumar V, Naik KP, Wang C, Modak A, Meeks E, Ge HW, Reitz R, Rutland R. Efficient Simulation of Diesel Engine Combustion using Realistic Chemical Kinetics in CFD. SAE. 2010;2010-01-0718.
- Lu X, Ji L, Zu L, Hou Y, Huang C, Huang Z. Experimental Study and Chemical Analysis of n-Heptane Homogeneous Charge Compression Ignition Combustion with Port Injection of Reaction Inhibitors. Combustion and Flame. 2007;149:261-270.
- Luijten CCM, Kurvers C. Real Gas Effects in Mixing-Limited Diesel Spray Vaporization Models. Atomization and Sprays. 2010;20(7):595-609.
- Mahr B. Future and Potential of Diesel Injection Systems. In THIESEL Conference on Thermo- and Fluid-Dynamic Processes in Diesel Engines Proceedings. 2002.
- Manley DK, McIlroy A, Taatjes CA. Research Needs for Future Internal Combustion Engines. Physics Today. 2008;November Issue:47-52.
- Martin CJ. Review: Cubic Equations of State – Which? Industrial and Engineering Chemistry Fundamentals. 1979;18(2):81-97.
- Martinez-Martinez S. Sanchez-Cruz FA, Bermudez VR, Riesco-Avila JM. Liquid Spray Characteristics in Diesel Engines. In: Siano D, editor. Fuel Injection. InTech; 2010.
- Mathieu O, Djebaili-Chaumeix N, Paillard CE, Douce F. Experimental Study of Soot Formation from a Diesel Fuel Surrogate in a Shock Tube. Combustion and Flame. 2009;156:1576-1586.
- Mati K, Ristoria A, Gail S, Pengloan G, Dagaut P. The Oxidation of a Diesel Fuel at 1-10 atm: Experimental Study in a JSR and detailed Chemical Kinetic Modeling. Proceedings of the Combustion Institute. 2007;32:2939-2946.
- Matthews WS, Coverdill RE, Lee CF, White RA. Liquid and Vapor Fuel Distributions in a Small-Bore High Speed Direct-Injection Diesel Engine. SAE. 2002;2002-01-2666.
- Matthews WS, Fang T, Coverdill RE, Lee CF, White R.A. Soot Diagnostics Using Laser-Induced Incandescence within an Optically Accessible HSDI Diesel Engine. SAE. 2004;2004-01-1412.
- McBride BJ, Gordon S, Reno MA (internet). Coefficients for Calculating Thermodynamic and Transport Properties of Individual Species. NASA Technical Memorandum 4513; 1993. Available from: http://ntrs.nasa.gov/archive/nasa/casi.ntrs.nasa.gov/19940013151_1994013151.pdf.

- McIlroy A, Sick V, Westbrook CK, Taatjes C, Trouve A, Wagner AF, Rohlfing E, Manley D, Trully F, Hilderbrandt R, Green W, Marceau D, O'Neal D, Lyday M, Cebulski F, Garcia TR, Strong D. Basic Research Needs for Clean and Efficient Combustion of 21st Century Transportation Fuels. Report of the Basic Energy Sciences Workshop on Basic Research Needs for Clean and Efficient Combustion of 21st Century Transportation Fuels. 2006. Available from: http://science.energy.gov/~media/bes/pdf/reports/files/ctf_rpt.pdf.
- Meijer M, Christians RJ, van Griensven JGH, Somers LMT, de Goey LPH. Engine Combustion Network: Implementation and Analysis of Combustion Vessel Spray A Conditions. In: Proceedings of the 2011 ILASS Americas 23rd Annual Conference on Liquid Atomization and Spray Systems; 2011 May 15-18; Ventura, CA. Paper No. 151.
- Methanol Institute and International Fuel Quality Center (MIIFQC). A Biodiesel Primer: Market & Public Policy Developments, Quality, Standards & Handling. 2006. Available from: <http://www.methanol.org/pdf/BiodieselPrimer2007.pdf>.
- Mock R, Lubitz K. Piezoelectricity: Piezoelectric Injection Systems. In Springer Series in Materials Science. Vol. 114(2). Springer Berlin Heidelberg; 2008. p. 299-310.
- Morgan R, Wray J, Kennaird DA, Crua C, Heikal MR. The Influence of Injector Parameters on the Formation and Break-Up of a Diesel Spray. SAE. 2001;2001-01-0529.
- Mueller CJ, Musculus MP. Glow Plug Assisted Ignition and Combustion of Methanol in an Optical DI Diesel Engine. SAE. 2001;2001-01-2004.
- Murphy MJ, Taylor JD, McCormick R. Compendium of Experimental Cetane Number Data. Subcontractor Report NREL/SR-540-36805. 2005. Available from: <http://www.nrel.gov/vehiclesandfuels/pdfs/sr368051.pdf>.
- Murugesan A, Umarani C, Subramanian R, Nedunchezian N. Bio-Diesel as an Alternative Fuel for Diesel Engines – A Review. Renewable and Sustainable Energy Reviews. 2009;13(3):653-662.
- Musculus MPB, Kattke K. Entrainment Waves in Diesel Jets. SAE. 2009;2009-01-1355.
- Musculus MPB, Pickett LM. Diagnostic Considerations for Optical Laser-Extinction Measurements of Soot in High-Pressure Transient Combustion Environments. Combustion and Flame. 2005;141:371-391.
- Myong KJ, Suzuki H, Senda J, Fujimoto H. Evaporation Characteristics of Multi-Component Fuel. Fuel. 2006;85:2632-2639.
- Naber JD, Siebers DL. Effect of gas density and vaporization on penetration and dispersion of diesel sprays. SAE. 1996;960034.

- Natelson RH, Kurman MS, Cernansky NP, Miller DL. Experimental Investigation of Surrogates for Jet and Diesel Fuels. *Fuel*. 2008;87:2239-2342.
- National Academies Press (NAP). Technologies and Approaches to Reducing the Fuel Consumption of Medium- and Heavy-Duty Vehicles. Committee to Assess Fuel Economy Technologies for Medium- and Heavy-Duty Vehicles, Washington, DC, 2010. Available from: http://books.nap.edu/catalog.php?record_id=12845.
- National Renewable Energy Laboratory (NREL). Beyond Diesel – Renewable Diesel. Center for Transportation Technologies and Systems, NREL/FS-540-32524; 2002. Available from: <http://www.nrel.gov/docs/fy02osti/32524.pdf>.
- Nesbitt JE. Combustion Vessel Laboratory Development Focusing on Optical Diagnostic Subsystem Integration Through the Dynamic Characterization of Fuel Sprays (master's thesis). Houghton: Michigan Technological University; 2008.
- Nesbitt JE, Johnson SE, Pickett L, Siebers D, Lee SY, Naber JD. Minor Species Production from Lean Premixed Combustion and their Impact on Autoignition of Diesel Surrogates. *Energy and Fuels*. 2011c;25(3): 926-936.
- Nesbitt JE, Lee SY, Naber JD, Arora R. An Optical Study of Spark Ignition and Flame Kernel Development Near the Lean Limit at Elevated Pressure. In: Proceedings of the ASME 2010 Internal Combustion Engine Division Fall Technical Conference; 2010; San Antonio, TX. ICEF2010-35136.
- Nesbitt JE, Naber JD, Lee SY, Kurtz E, Ge HW, Robarge N. Investigation of Vaporizing Diesel Liquid Spray Plume to Plume Penetration Variations. In: Proceedings of the 2011a ILASS Americas 23rd Annual Conference on Liquid Atomization and Spray Systems; 2011 May 15-18; Ventura, CA. Paper No. 132.
- Nesbitt JE, Naber JD, Worm JJ, Miers SA. Biofuel Use from Bioenergy Crops: Internal Combustion Engines in Transportation In: Shonnard DR, Joshi S, Kole C, editors. *Bioenergy Crops Handbook*. Section 1 Chapter 10: Taylor and Francis; 2011b.
- Nguyen D, Honnery D. Combustion of Bio-Oil Ethanol Blends at Elevated Pressure. *Fuel*. 2008;87:232-243.
- Nishida K, Zhang W, Manabe T. Effects of Micro-hole and Ultra-high Injection Pressure on Mixture Properties of D.I. Spray. *SAE*. 2007;2007-01-1890.
- Oren DC, Wahiduzzaman S, Ferguson CR. A Diesel Combustion Bomb: Proof of Concept. *SAE*. 1984;841358..
- Otsu N. A Threshold Selection method from Gray-Level Histograms. *Institute of Electrical and Electronics Engineers Transactions on Systems, Man and Cybernetics*. 1979;SMC-9(1):62:66.

- Parrish SE, Zink RJ. Development and Application of an Imaging System to Evaluate the Liquid and Vapor Envelopes of Sprays from a Multi-Hole Gasoline Fuel Injector Operating under Engine-Like Conditions. In: Proceedings of the 2011 ILASS Americas 23rd Annual Conference on Liquid Atomization and Spray Systems; 2011 May 15-18; Ventura, CA. Paper No. 170.
- Pastor JV, Arregle J, Garcia JM, Zapata D. Segmentation of diesel spray images with log-likelihood ratio test algorithm for non-Gaussian distributions. *Applied Optics*. 2007;46(6):888-899.
- Pastor JV, Arrègle J, Palomares A. Diesel Spray Image Segmentation with a Likelihood Ratio Test. *Applied Optics*. 2001;40(17):2876-2885.
- Pastor JV, Lopez J, Garcia JM, Pastor JM. A 1D Model for the Description of Mixing-Controlled Inert Diesel Sprays. *Fuel*. 2008;87(13-14):2871-2885.
- Pawlowski A, Kneer R, Lippert AM, Parrish SE. Investigation of the Interaction of Sprays from Clustered Orifices under Ambient Conditions Relevant for Diesel Engines. SAE. 2008;2008-01-0928.
- Payri F, Arregle J, Lopez JJ, Hermens S. Effect of Cavitation on the Nozzle Outlet Flow, Spray and Flame Formation in a Diesel Engine. SAE. 2006;2006-01-1391.
- Payri R, Garcia-Oliver JM, Manin J, Bardi M. Fuel Temperature Influence on Diesel Sprays in Reacting Conditions. In: Proceedings of the 2011 ILASS Americas 23rd Annual Conference on Liquid Atomization and Spray Systems; 2011a May 15-18; Ventura, CA. Paper No. 163.
- Payri R, Salvador FJ, Gimeno J, Bracho G. The Effect of Temperature and Pressure on Thermodynamic Properties of Diesel and Biodiesel Fuels. *Fuel*. 2011b;90(3):1172-1180.
- Payri R, Salvador FJ, Gimeno J, De la Morena J. Influence of Injector Technology on Injection and Combustion Development – Part 2: Combustion Analysis. *Applied Energy* 2011c;88 (4):1130-1139.
- Payri R, Salvador FJ, Gimeno J, Zapata LD. Diesel Nozzle Geometry Influence on Spray Liquid-Phase Fuel Penetration in Evaporative Conditions. *Fuel*. 2008;87(7):1165-1176.
- Peng Z, Zhao H, Ladommatos N. Effects of Air/Fuel Ratios and EGR Rates on HCCI Combustion of n-heptane, a Diesel Type Fuel. SAE. 2003; 2003-01-0747.
- Perlack R D, Wright LL, Turhollow AF, Graham RL, Stokes BJ, Erbach DC. Biomass as Feedstock for a Bioenergy and Bioproducts Industry: The Technical Feasibility of a Billion-Ton Annual Supply. US Department of Energy; 2005. DOE/GO-

- 102005-2135 & ORNL/TM-2005/66. Available from: http://www1.eere.energy.gov/biomass/pdfs/final_billionton_vision_report2.pdf.
- Peters R. Penetration and Dispersion Research of Non-Reacting Evaporating Diesel Sprays (master's thesis). Eindhoven University of Technology; 2007. Available from: http://w3.wtb.tue.nl/fileadmin/wtb/ct-pdfs/Master_Theses/verslag_final_version_roel_peters.pdf.
- Pickett LM, Caton JA, Musculus MPB, Lutz AE. Evaluation of the Equivalence Ratio-Temperature Region of Diesel Soot Precursor Formation Using a Two-Stage Lagrangian Model. *International Journal of Engine Research*. 2006;7:349-370.
- Pickett LM, Genzale CL, Bruneaux G, Malbec LM, Hermant L, Christiansen C, Schramm J. Comparison of Diesel Spray Combustion in Different High-Temperature, High-Pressure Facilities. SAE. 2010;10FFL-0315.
- Pickett LM, Genzale CL, Manin J, Malbec LM, Hermant L. Measurement Uncertainty of Liquid Penetration in Evaporating Diesel Sprays. In: *Proceedings of the 2011 ILASS Americas 23rd Annual Conference on Liquid Atomization and Spray Systems*; 2011 May 15-18; Ventura, CA. Paper No. 111.
- Pickett LM, Kook S, Williams TC. Visualization of Diesel Spray Penetration, Cool-Flame, Ignition, High-Temperature Combustion, and Soot Formation Using High-Speed Imaging. SAE. 2009;2009-01-0658.
- Pickett LM, Manin J, Genzale CL, Siebers DL, Musculus MPB, Idicheria CA. Relationship Between Diesel Fuel Spray Vapor Penetration/Dispersion and Local Fuel Mixture Fraction. SAE. 2011;2011-01-0686.
- Pickett LM, Siebers DL. An Investigation of Diesel Soot Formation Processes using Micro-Orifices. *Proceedings of the Combustion Institute*. 2002;29(1):655-662.
- Pickett LM, Siebers DL. Non-Sooting, Low Flame Temperature Mixing-Controlled DI Diesel Combustion. SAE. 2004;2004-01-1399.
- Pischinger S, Rottmann M, Fricke F. Future of combustion engines. SAE. 2006;2006-21-0024.
- Pitz WJ, Mueller CJ. Review: Recent Progress in the Development of Diesel Surrogate Fuels. *Progress in Energy and Combustion Science*. 2011;37(3):330-350.
- Poling BE, Prausnitz JM, O'Connell JP. *The Properties of Gases and Liquids*. 5th ed. New York; McGraw-Hill; 2001.
- Powell CF, Kastengren AL, Liu Z, Fezzaa K. The Effects of Diesel Injector Needle Motion on Spray Structure. *Journal of Engineering for Gas Turbines and Power*. 2011;133(1):012082.

- Prashanth R, Blanchard J, Corradini M. Diesel Sprays through Multi-Hole Micro-Nozzles: Spray Dynamics and Structure. In: Proceedings of the International Conference on Liquid Atomization and Spray Systems Conference; 2006;Kyoto, Japan. Paper No. ICLASS06-222.
- Radich A (Internet). Biodiesel Performance, Costs, and Use. 1998. Available from: <http://www.eia.gov/oiaf/analysispaper/biodiesel/pdf/biodiesel.pdf>.
- Ramirez AI, Som S, Aggarwal SK, Kastengren AL, El-Hannouny EM, Longman DE, Powell CF. Quantitative X-Ray Measurements of High-Pressure Fuel Sprays from a Production Heavy Duty Diesel Injector. Experiments in Fluids. 2009;47:119-134.
- Ranzi E, Gaffuri P, Faravelli T. A Wide-Range Modeling Study of n-Heptane Oxidation. Combustion and Flame. 1995;103:91-106.
- Reid RC, Prausnitz JM, Poling BE. The Properties of Gases and Liquids. 4th ed. New York; McGraw-Hill; 1987.
- Reitz RD, Rutland C.J. Development and testing of Diesel Engine CFD Models. Progress in Energy and Combustion Science. 1995;21:173-196.
- Risberg P, Johansson D, Andrae J, Kalghatgi G, Bjornbom P, Angstrom HE. The Influence of NO on the Combustion Phasing in an HCCI Engine. SAE. 2006;2006-01-0416.
- Sandia National Laboratory (SNL) Engine Combustion Network (ECN) (Internet). Sandia CV: Constant Volume Diesel Combustion. 2010. Available from: <http://www.sandia.gov/ecn/cvdata/constantVol.php>.
- Sandia National Laboratory Engine Combustion Network (ECN) (Internet). Experimental Data Search; 2011. Available from: <http://www.sandia.gov/ecn/cvdata/dsearch.php>.
- Sandler SI. Chemical and Engineering Thermodynamics, 3rd ed. Wiley; 1999.
- Sazhin S, Crua C, Kennaird D, Heikal M. Initial Stage Fuel Spray Penetration. Fuel. 2003;82:875-885.
- Schihl P, Hoogterp L, Pangilinan H. Assessment of JP-8 and DF-2 Evaporation Rate and Cetane Number Differences on a Military Diesel Engine. SAE. 2006;2006-01-1549.
- Schmidt DP. Cavitation in Diesel Fuel Injector Nozzles (PhD dissertation). University of Wisconsin-Madison; 1997.

- Seiser R, Pitsch H, Seshadri K, Pitz WJ, Curran HJ. Extinction and Autoignition of *n*-Heptane in Counterflow Configuration. Proceedings of the Combustion Institute. 2000;28:2029-2037.
- Semelsberger TA, Borup RL, Greene HL. Dimethyl Ether (DME) as an Alternative Fuel. Journal of Power Sources. 2006;156:497-511.
- Senda J, Okui N, Suzuki T, Fujimoto H. Flame Structure and Combustion Characteristics in Diesel Combustion Fueled with Bio-Diesel. SAE. 2004;2004-01-0084.
- Sensors Inc. Semtech-DS: On Board Vehicle Emissions Analyzer User Manual Document 9510-086, Revision 1.15. 2008.
- Setter N. ABC of Piezoelectricity and Piezoelectric Materials. In Setter N, editor. Piezoelectric Materials in Devices: Extended Reviews on Current and Emerging Materials, Technology, and Applications. Switzerland: EPFL; 2002. p. 1-28.
- Settles GS. Schlieren and Shadowgraph Techniques: Visualizing Phenomena in Transparent Media. Springer Verlag; 2001.
- Siebers DL. Ignition Delay Characteristics of Alternative Diesel Fuels: Implications on Cetane Number. SAE. 1985;852102.
- Siebers DL. Liquid Phase Fuel Penetration in Diesel Sprays. SAE. 1998;980809.
- Siebers DL. Scaling Liquid-Phase Fuel Penetration in Diesel Sprays Based on Mixing Limited Vaporization. SAE. 1999;1999-01-0528.
- Siebers DL. Recent Developments on Diesel Fuel Jets Under Quiescent Conditions. In Arcoumanis C, Kamimoto T, editors. Flow and Combustion in Reciprocating Engines; 2008. Chapter 5.
- Siebers D, Higgins B. Flame Lift-Off on Direct-Injection Diesel Sprays under Quiescent Conditions. SAE. 2001;2001-01-0530.
- Sissine F. Energy Independence and Security Act of 2007: a summary of major provisions. Congressional Research Service Report for Congress, Order Code RL34294, Washington, DC; 2007.
- Sjoberg M, Dec JE. Influence of EGR Quality and Unmixedness on the High-Load limits of HCCI Engines. SAE. 2009;2009-01-0666.
- Slavinskaya NA, Zizin A, Aigner M. On Model Design of a Surrogate Fuel Formulation. Journal of Engineering for Gas Turbines and Power. 2010;132: 11501-1 – 11501-11.

- Smith GP, Golden D M, Frenklach M, Moriarty NW, Eiteneer B, Goldenberg M, Bowman CT, Hanson R, Song S, Gardiner WC, Lissianski VV, Qin Z (internet). GRI-Mech 3.0. University of California: Berkeley, CA; 1999; Available from: http://www.me.berkeley.edu/gri_mech/version30/text30.html.
- Smith SW. Digital Signal Processing: A Practical Guide for Engineers and Scientist. Newnes (Imprint of Elsevier); 2003.
- Som S, Longman DE. Numerical Study Comparing the Combustion and Emission Characteristics of Biodiesel to Petrodiesel. Energy and Fuels. 2011;25(4):1373-1386.
- Soteriou C, Andrews R, Smith M. Direct Injection Diesel Sprays and the Effect of Cavitation and Hydraulic Flip on Atomisation. SAE. 1995;950080.
- Stone R. Introduction to Internal Combustion Engines. MacMillan Press Ltd; 2002.
- Szybist JP, Song J, Alam M, Boehman AL. Biodiesel Combustion, Emissions and Emission Control. Fuel Processing Technology. 2007;88(7):679-691.
- Takita K, Abe N, Masuya G, Ju Y. Ignition Enhancement by addition of NO and NO₂ from a N₂/O₂ plasma torch in a supersonic flow. Proceedings of the Combustion Institute. 2007;31:2489-2496.
- Tan Y, Fotache C, Law C. Effects of NO on the Ignition of Hydrogen and Hydrocarbons by Heated Counterflowing Air. Combustion and Flame. 1999;119:346-355.
- Tomohisa D, Yamamoto T, Senda J, Fujimoto H. Effect of Nozzle Configurations for Characteristics of Non-Reacting Diesel Fuel Spray. SAE. 1997;970355.
- Tree DR, Svensson DR. Soot Processes in Compression Ignition Engines. Progress in Energy and Combustion Science. 2007;33:272-309.
- Tsang W, Hudgens JW, Allison TC, Burgess Jr DR, Hudgens JW, Manion JA, Matheu DM. Workshop on Combustion Simulation Databases for Real Transportation Fuels. National Institute of Standards and Technology, NISTIR 7155; 2003.
- Turns SR. An Introduction to Combustion. McGraw Hill; 2006.
- United States of America Congress. Energy Independence and Security Act of 2007. H.R.6, 110th Congress; 2007.
- US Department of Energy (DOE). Diesel Power: Clean Vehicles for Tomorrow. DOE Energy Efficiency and Renewable Energy Vehicle Technologies Program; 2010. Available from: http://www1.eere.energy.gov/vehiclesandfuels/pdfs/diesel_technical_primer.pdf.

- US Environmental Protection Agency (EPA). Nonroad Diesel Emission Standards: Staff Technical Paper. EPA420-R-01-052; 2001. Available from: <http://www.epa.gov/nonroaddiesel/r01052.pdf>.
- US Environmental Protection Agency (EPA). A Comprehensive Analysis of Biodiesel Impacts on Exhaust Emissions. Draft Technical Report EPA420-P-02-00; 2002.
- US Environmental Protection Agency (EPA). Heavy-Duty Highway Compression-Ignition Engines and Urban Busses – Exhaust Emission Standards. 2010a. Available from: <http://www.epa.gov/oms/standards/heavy-duty/hdci-exhaust.htm>.
- US Environmental Protection Agency (EPA). EPA and NHTSA Proposed First-Ever Program to Reduce Greenhouse Gas Emissions and Improve Fuel Efficiency of Medium- and Heavy-Duty Vehicles: Regulatory Announcement. EPA-420-F-10-901; 2010b. Available from: <http://www.epa.gov/oms/climate/regulations/420f10901.pdf>.
- US Environmental Protection Agency (EPA). Light-Duty Automotive Technology, Carbon Dioxide Emissions, and Fuel Economy Trends: 1975 through 2010. EPA-420-R-10-023; 2010c. Available from: <http://www.epa.gov/oms/cert/mpg/fetrends/420r10023.pdf>.
- US Environmental Protection Agency (EPA). EPA and NHTSA Finalize Historic National Program to Reduce Greenhouse Gases and Improve Fuel Economy for Cars and Trucks. EPA-420-F-10-014; 2010d. Available from: <http://www.epa.gov/oms/climate/regulations/420f10014.pdf>.
- Vasu SS, Davidson DF, Hong Z, Vasudevan V, Hanson RK. n-Dodecane Oxidation at High Pressures: Measurements of Ignition Delay Times and OH Concentration Time Histories. *Proceedings of the Combustion Institute*. 2009;32:173-180.
- Verbiezen K, Donkerbroek AJ, Klein-Douwel RJH, van Vliet AP, Frijters PJM., Seykens XLJ, Baert RSG, Meerts WL, Dam NJ, ter Meulen JJ. Diesel Combustion: In-Cylinder NO Concentrations in Relation to Injection Timing. *Combustion and Flame*. 2007;151:333-346.
- Verhoeven D, Venhemelrijck JL, Baritaud T. Macroscopic and Ignition Characteristics of High Pressure Sprays of Single-Component Fuels. *SAE*. 981069;1998.
- Versaavel P, Motte P, Wieser K. A New 3D Model for Vaporizing Diesel Sprays Based on Mixing-Limited Vaporization. *SAE*. 2000;2000-01-0949.
- Vishwanathan G, Reitz RD. Modeling Soot Formation Using Reduced Polycyclic Aromatic Hydrocarbon Chemistry in n-heptane Lifted Flames with Application to Low Temperature Combustion. *Journal of Engineering for Gas Turbines and Power*. 2009;131:032801-1 – 032801-7.

- Wan Y, Peters N. Scaling of Spray Penetration with Evaporation. *Atomization and Sprays*. 1999;9(2):111-132.
- Wang H, Dames E, Sirjean B, Sheen DA, Tangko R, Violi A, Lai JYW, Egolfopoulos FN, Davidson DF, Hanson RK, Bowman CT, Law CK, Tsang W, Cernansky NP, Miller DL, Lindstedt RP (internet). A high-temperature chemical kinetic model of *n*-alkane (up to *n*-dodecane), cyclohexane, and methyl-, ethyl-, *n*-propyl and *n*-butyl-cyclohexane oxidation at high temperatures. JetSurF version 2.0; 2010. Available from: <http://melchior.usc.edu/JetSurF/JetSurF2.0>.
- Wang X, Huang Z, Kuti OA, Zhang W, Nishida K. Experimental and Analytical Study on Biodiesel and Diesel Spray Characteristics under Ultra-High Injection Pressure. *International Journal of Heat and Fluid Flow*. 2010;31:659-666.
- Wei YS, Sadus RJ, Journal Review: Equations of State for the Calculation of Fluid-Phase Equilibria. *American Institute of Chemical Engineers Journal*. 2000;46(1):169-196.
- Wersing W. Applications of Piezoelectric materials: An Introductory Review. In Setter N, editor. *Piezoelectric Materials in Devices: Extended Reviews on Current and Emerging Materials, Technology, and Applications*. Switzerland: EPFL; 2002. p. 29-66.
- Wimmer A, Eichlseder H, Klell M, Figer G. Potential of HCCI Concepts for DI Diesel Engines. *International Journal of Vehicle Design*. 2006;41:32-48.
- Yacobucci BD. Biofuels Incentives: A Summary of Federal Programs. CRS Report for Congress, RL33572; 2008.
- Yanowitz J, McCormick RL, Graboski MS. Critical Review: In-Use Emissions from Heavy-Duty Diesel Vehicles. *Environmental Science and Technology*. 2000;34(5):729 -740.
- Yule AJ, Salters DG. The Break-Up Zone of a Diesel Sprays. Part 1: Length of Zone and Column of Unatomized Liquid. *Atomization and Sprays*. 1995;5:157-174.
- Zhang L, Tadashi T, Ueda T, Ishii Y, Itou T, Tomoyuki I, Yokota K. Measurement of Liquid Phase Penetration of Evaporating Spray in a Diesel Engine. SAE. 1997;971645.
- Zhao H, Ladommatos N. Optical Diagnostics for Soot and Temperature Measurements in Diesel Engines. *Progress in Energy and Combustion Science*. 1998;24(3):221-266.

12. Appendices

12.1. Copyright Permissions

12.1.1. Chapter 4.2 – Energy and Fuels

Jaclyn Nesbitt

From: Michael Klein <klein-office@efuels.acs.org>
Sent: Thursday, July 07, 2011 2:54 PM
To: Jaclyn Nesbitt; Michael Klein
Subject: RE: Permission to Reproduce Energy and Fuels Manuscript in Dissertation

Jaclyn,

Dr. Klein has approved this request.
Sincerely,

Elizabeth T. Klein
Journal Office Administrator
Energy and Fuels
klein-office@efuels.acs.org
Fax 202-513-8596

From: Jaclyn Nesbitt [jenesbit@mtu.edu]
Sent: Thursday, July 07, 2011 2:49 PM
To: Michael Klein
Subject: Permission to Reproduce Energy and Fuels Manuscript in Dissertation

Dr. Klein,

I have published a paper in the Energy and Fuels Journal, volume 25, issue 3, pp. 926-936, "Minor Species Production from Lean Premixed Combustion and Their Impact on Autoignition of Diesel Surrogates". I would like to reproduce this paper in my dissertation, a degree requirement for graduation from Michigan Technological University. On the journal publishing agreement it says authors may reuse the published work in a dissertation, but that written confirmation should be received from the journal editor. Can you please grant me this permission for reproduction of the above journal paper in my dissertation?

Please let me know if you require any additional information.

Thank you.
Sincerely
Jaclyn Nesbitt

12.1.2. Chapter 6.2.1 – ILASS Conference Proceedings

Jaclyn Nesbitt

From: Marcus Herrmann <marcus.herrmann@asu.edu>
Sent: Friday, July 08, 2011 5:01 PM
To: Jaclyn Nesbitt
Subject: Re: ILASS-Americas 2011 Abstract ILASS2011-132 Accepted

Hi Jaclyn,
it is my understanding that you retain all copyrights to your paper. However, you granted ILASS-Americas the right to include your paper on the proceedings CD and the ILASS website. So having it in your thesis should be no problem at all.
Please let me know if you have any further questions.

Best,
Marcus Herrmann

On Jul 7, 2011, at 8:37 PM, Jaclyn Nesbitt wrote:

Dr Herrmann,

I have a question on copyright with the ILASS conference proceedings - I am writing my dissertation currently and would like to include the paper I submitted to the ILASS 2011 conference in one of the chapters - do I need permission from someone at ILASS to do this, and if so who, or do we own the copyright of our paper and therefore we are able to reproduce it without written permission from ILASS?

Thank you
Sincerely,
Jaclyn Nesbitt

12.1.3. Figure 3.5 Copyright Permission – Sam Johnson

Jaclyn Nesbitt

From: samuel.johnson@cummins.com
Sent: Monday, July 18, 2011 8:44 AM
To: Jaclyn Nesbitt
Subject: Re: Copyright Permission

Yes, you have my permission to use said figure in your dissertation.

Good day Jaclyn,
Sam

Sam Johnson
Cummins Emissions Solutions
Performance Development Engineering
samuel.johnson@cummins.com
Columbus Engine Plant
1000 Fifth Street
Columbus, IN 47201

From: Jaclyn Nesbitt <jnesbitt@mtu.edu>
To: samuel.johnson <samuel.johnson@cummins.com>
Date: 07/17/2011 06:13 AM
Subject: Copyright Permission

Hi Sam,

I am writing to ask permission to use the figure you created, CV operating regime in my dissertation. Please reply to this email to grant me permission to use this figure in my dissertation if this is okay.

Thanks,
Jaclyn

12.1.4. Figure 3.33 Copyright Permission – Eric Kurtz

Jaclyn Nesbitt

From: Kurtz, Eric (E.) <ekurtz@ford.com>
Sent: Monday, August 01, 2011 11:21 AM
To: Jaclyn Nesbitt
Cc: Ge, Hai-Wen (H.)
Subject: RE: Inclusion of Ford Information in Dissertation

Jaclyn,
I've already spoken with Joe Lorenz at Bosch and sent him the material to take a look, so we'll see what he comes back with.

Regarding the ROI plot, no problem. Hai-Wen will support you. I assume that the longest duration injection will suffice. If you'd like something different, let Hai-Wen know.

I give Jaclyn Nesbitt permission to reproduce the rate of injection figure for her dissertation.

Hai-Wen,
Can you please support Jaclyn's request by sending her a plot of the rate of injection for the production injector at 2000 bar with the longest injection duration we have?

Best regards,
Eric Kurtz
Ford Motor Company
Diesel Combustion Systems Technical Expert
Tel: 313-323-9851
Cell: 313-805-1054
ekurtz@ford.com

12.1.5. Figure 3.34 Copyright Permission – Chris Green

Jaclyn Nesbitt

From: Chris Green <cagreen@mtu.edu>
Sent: Monday, July 18, 2011 7:59 AM
To: 'Jaclyn Nesbitt'
Subject: RE: Copyright Permission

Permission granted to use any of the drawings and models related to the Combustion Vessel.
-Chris Green

Christopher A. Green
Sr. Research Engineer I
Keweenaw Research Center
Michigan Technological University
(906) 487-2658
cagreen@mtu.edu

From: Jaclyn Nesbitt [mailto:jenesbit@mtu.edu]
Sent: Saturday, July 16, 2011 7:49 PM
To: cagreen
Subject: Copyright Permission

Hi Chris,

I am writing to ask your permission to reproduce the figure you created, the model of the cooled diesel injector window, in my dissertation. Please reply to this email to grant me permission to reproduce this figure in my dissertation, if this is okay with you.

Thanks,
Jaclyn

12.2. Supplements to Chapter 3 – Nozzle Hole Measurements

Scanning electron microscope (SEM) images were acquired of the eight holes in the injector nozzle to characterize variations in hole diameter as a potential explanation for plume-to-plume variations. SEM images were acquired at the Michigan Tech Applied Chemical and Morphological Analysis Laboratory (ACMAL, <http://mcff.mtu.edu/acmal/>), under the direction of Owen P. Mills. The SEM used was the JEOL JSM-6400. The procedure is as follows:

- Clean injector nozzle by sonication in acetone, run 5 cycles of cleaning.
- Sonicate for 5 minutes in isopropyl alcohol to remove the acetone residue left on the nozzle holes.
- Place nozzle (sample) on a sample holder, oriented such that one hole will be perpendicular to the electron beam. Apply conductive tape to the sample (to account for the lack of electricity conduction of the nozzle). Insert sample holder into the scanning electron microscope chamber.
- Align sample stage to the beam.
- Apply SEM beam at 20 kV.
- Acquire images:
 - 1000 pixels / line
 - IMS-1 -- Fast scan (50 Samples / second), save first image
 - 400X Resolution
 - 400 kHz Sample Rate
- Post process images in Matlab

These images of the nozzle hole were acquired twice to verify hole diameter measurements.

12.2.1. SEM Images – Test Set 1

Images from test set 1 are provided below, referenced to a hole number which corresponds to the referenced spray plumes discussed in the dissertation.

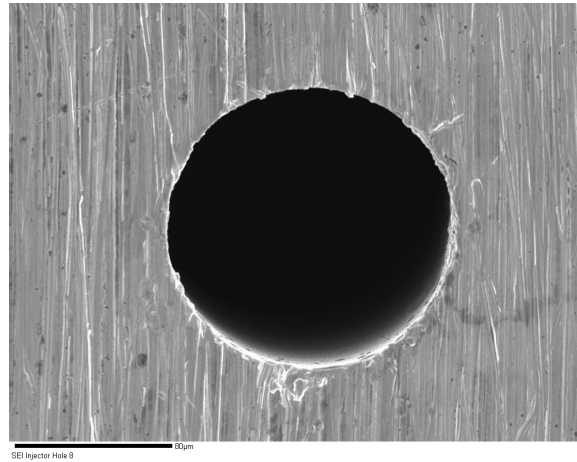


Figure 12.1: Hole number 1, test set 1.

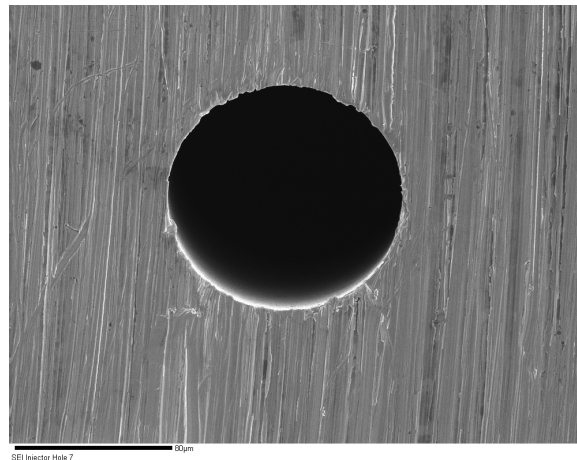


Figure 12.2: Hole number 2, test set 1.

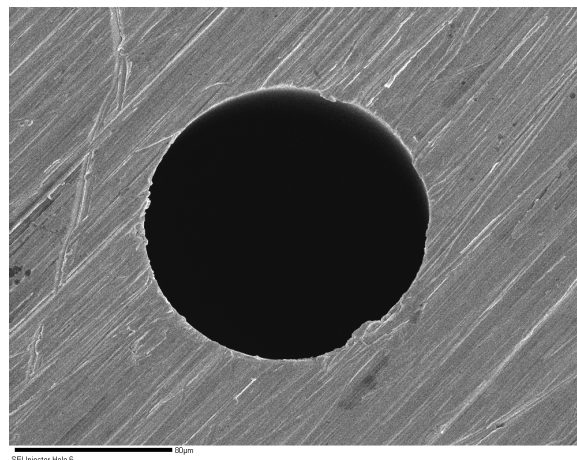


Figure 12.3: Hole number 3, test set 1.

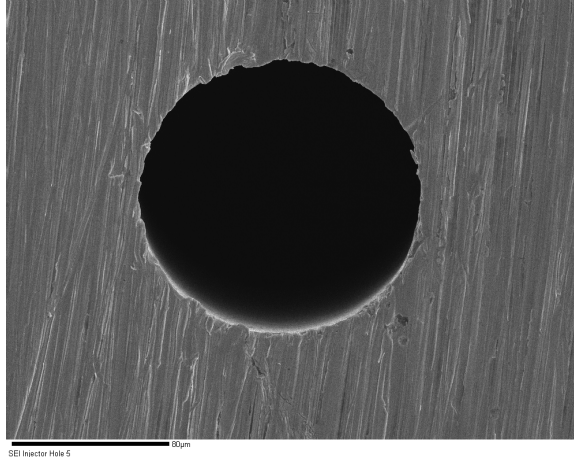


Figure 12.4: Hole number 4, test set 1.

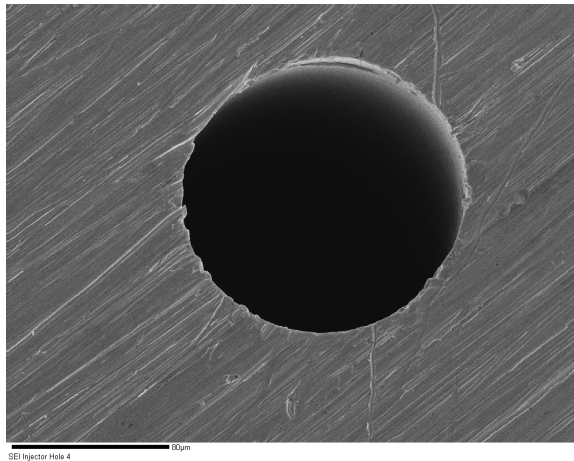


Figure 12.5: Hole number 5, test set 1.

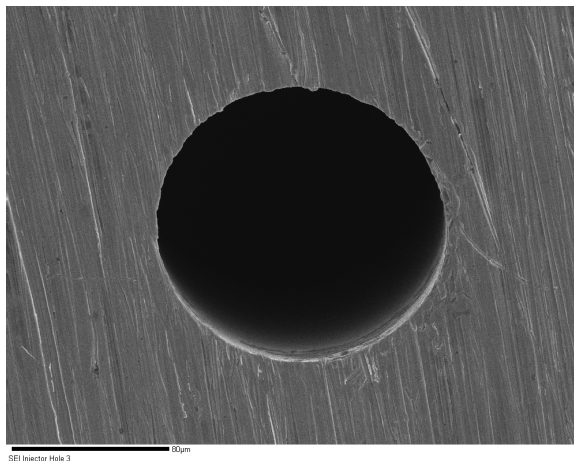


Figure 12.6: Hole number 6, test set 1.

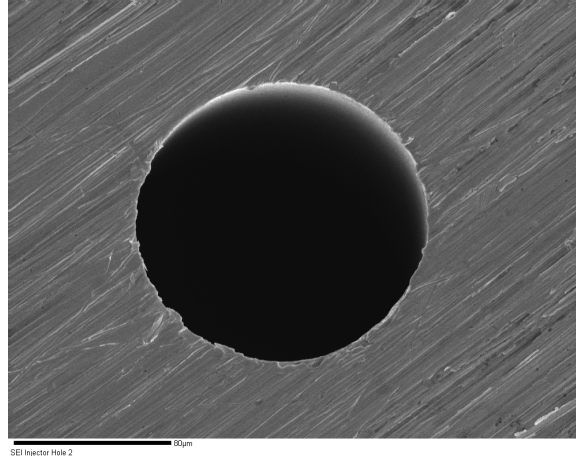


Figure 12.7: Hole number 7, test set 1.

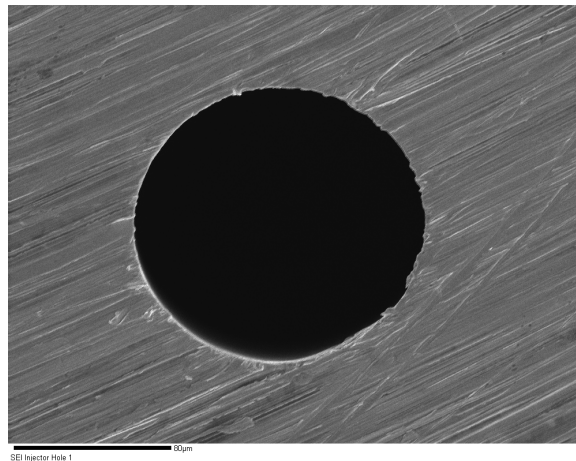


Figure 12.8: Hole number 8, test set 1.

For these SEM images, one obvious difference is hole number 2 being substantially smaller than the other 7 holes. This hole, however, does not yield a reduced liquid length as was discussed in Chapter 6.2. This led to the repeating of the SEM images to see if this significant difference in hole diameter was an artifact of setup or acquisition settings (i.e. magnification), or if it is a real observed phenomenon. Also of interest is differences in hole smoothness. Holes are not perfectly circular which is partially attributed to the non-normal nature of the scanning electron beam based on sample stage constraints in the SEM chamber, but is also a physical result of the nozzle, which can influence smoothness and hence fuel flow through the nozzle, which can translate to spray characteristics.

12.2.2. SEM Images – Test Set 2

In this second round of SEM tests, the same procedure and settings as Test Set 1 were used. SEM images for each hole of the 8-hole nozzle are shown in the figures below.

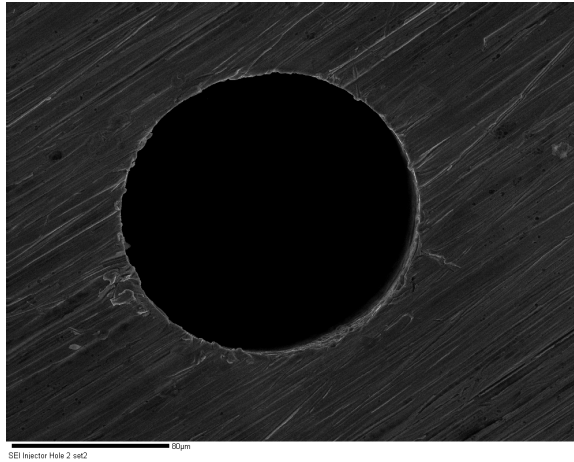


Figure 12.9: Hole number 1, test set 2.

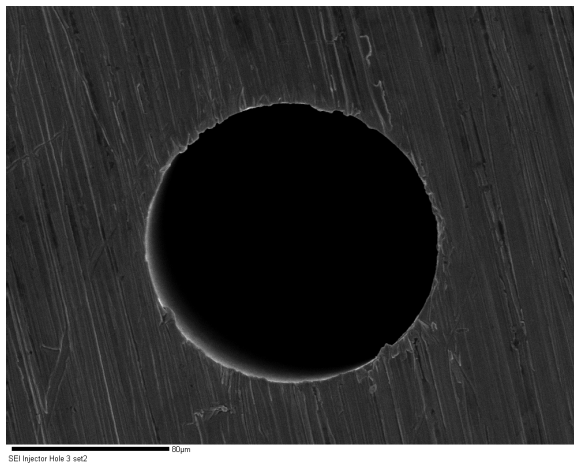


Figure 12.10: Hole number 2, test set 2.

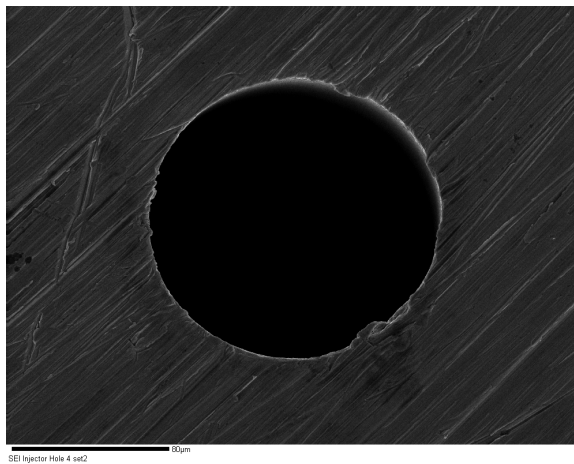


Figure 12.11: Hole number 3, test set 2.

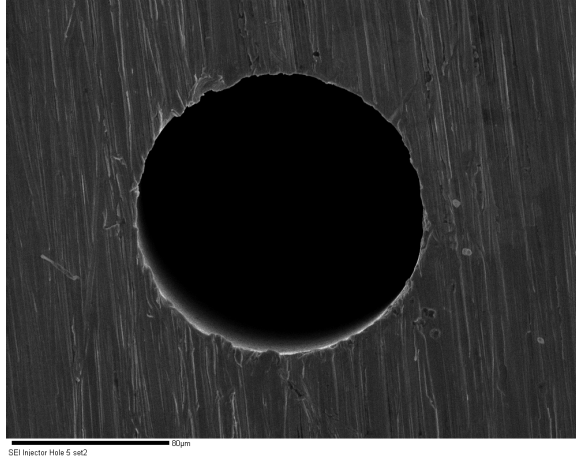


Figure 12.12: Hole number 4, test set 2.

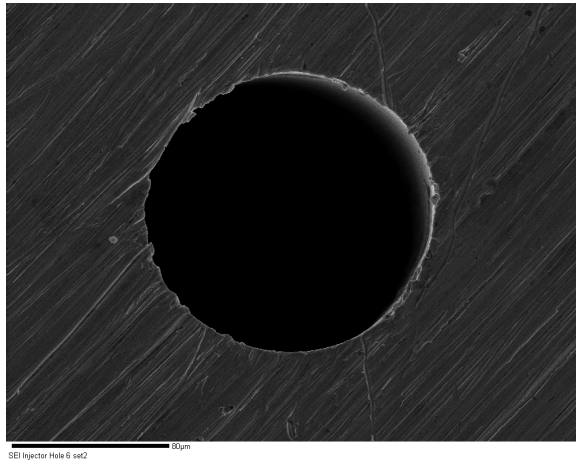


Figure 12.13: Hole number 5, test set 2.

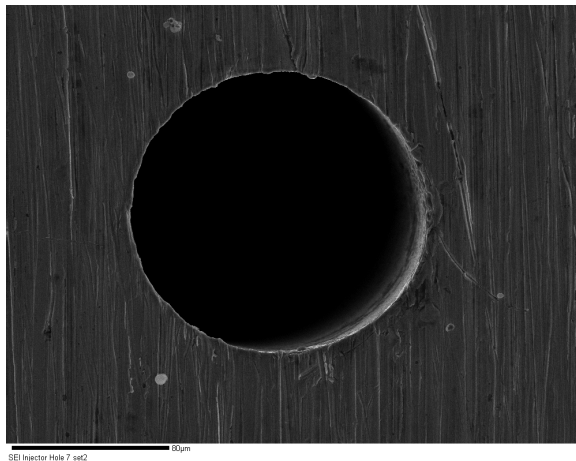


Figure 12.14: Hole number 6, test set 2.

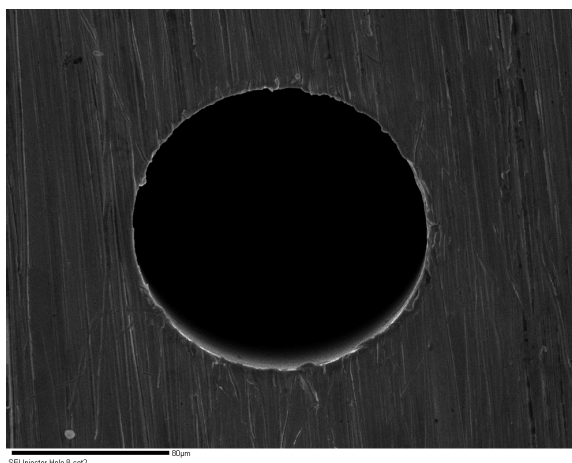


Figure 12.15: Hole number 7, test set 2.

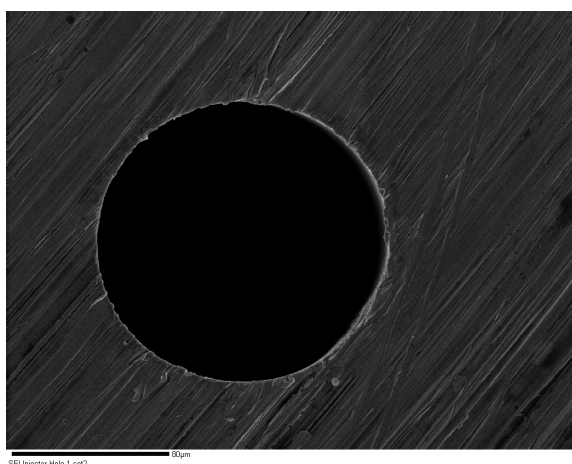


Figure 12.16: Hole number 8, test set 2.

The same scaling is used in all the images, and a direct comparison of the images by eye does not show any significant differences in hole diameter, as was seen in Hole 2 Test Set 1. Therefore, this reduced hole diameter was likely an artifact of scaling issue and is not a physical phenomenon. This is further confirmed since the expected small hole would have been hole 5 based on smallest liquid length, which was not the case here and hence it is not expected that hole two should be smallest, in fact, it should be one of the largest diameter holes based on liquid length trends.

12.3. Supplements to Chapter 4 - Chemical Kinetics Modeling

12.3.1. EES Extent of Reaction Initial Condition Determination

The Cantera chemical kinetics modeling steps for the preburn procedure are outlined below in Figure 12.17.

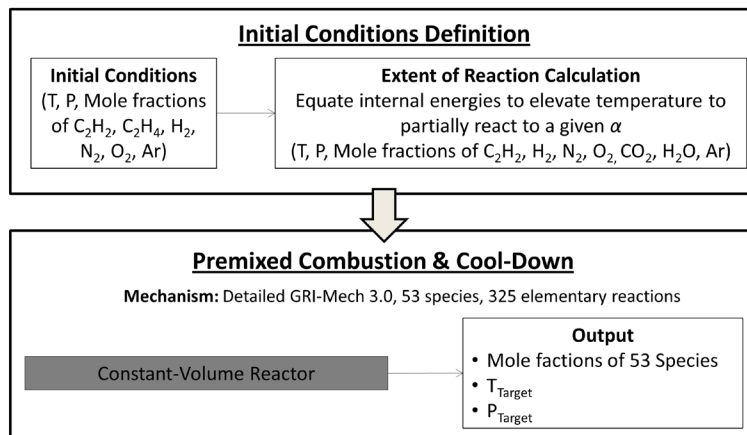


Figure 12.17: Preburn chemical kinetics modeling procedure.

This is a two-step process consisting of first computing the model initial conditions, and second modeling the chemical kinetics of the preburn and cool down procedure.

The first stage of the preburn modeling is discussed in detail below. An extent of reaction method was undertaken to determine the preburn modeling initial conditions which are input into the Cantera chemical kinetics model. These conditions include an elevated temperature, pressure, and partially reacted mole fractions, which are used to facilitate autoignition of the preburn mixture in the modeling. The extent of reaction method was undertaken using Engineering Equation Solver (EES)[®] software, with the procedure shown schematically in Figure 12.18.

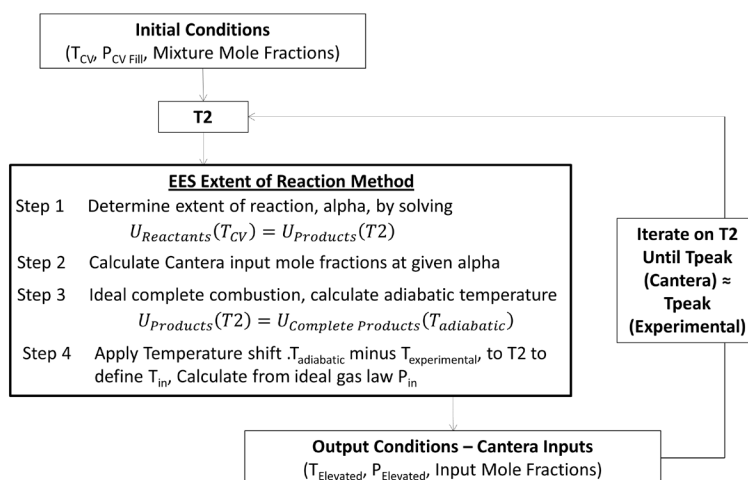


Figure 12.18: EES extent of reaction methodology.

This method requires EES inputs of initial temperature and pressure, which are defined based on the required ‘Spray A’ density and heated combustion vessel temperature, along with preburn mixture species mole fractions. An initial guess elevated temperature, T_2 , was also defined. This temperature will be iterated on until the Cantera model peak temperature matched the experimentally obtained peak temperature in the combustion vessel ‘Spray A’ experimental testing. With these inputs, combustion reaction stoichiometry was defined based on an arbitrary extent of reaction α such that the reaction was only partially completed (α is less than 1). This included ideal combustion product species of CO_2 , H_2O , O_2 , and N_2 . Conservation of energy was then

applied to determine this extent of reaction, alpha, such that the internal energy of the reactants at the starting temperature was equal to the internal energy of the products for a given extent of reaction at the elevated temperature T_2 . Internal energy of the products is the sum of the internal energy of all species in the products with the internal energy of a given species defined as the molar based internal energy of the species multiplied by the number of moles of that species in the products. The same definition was used for the internal energy of the reactants. This alpha value was then used to calculate the mole fractions of the Cantera input species at the elevated temperature and pressure conditions including reductions in mixture concentrations (due to partial combustion reactions) and the addition of CO_2 and H_2O due to a partial reaction from combustion products.

Finally, elevated pressure and temperature conditions must be defined for inputs to the Cantera modeling. The peak combustion temperature was calculated in EES based on an alpha of one, meaning 100% reaction completion as determined by equating the elevated reaction internal energy to the ideal product internal energy. The reaction at completion assumed ideal adiabatic combustion resulting in calculated peak temperature from combustion exceeding that achieved in the experimental preburn. The difference between the ideal peak combustion temperature and the actual experimentally achieved combustion temperature was determined and this temperature shift was applied to lower T_2 and defined as the input temperature to the Cantera modeling. Input pressure was calculated via the ideal gas law using the reactant mixture molecular weight. Therefore, the results of the EES extent of reaction method provided inputs of temperature, pressure and major species (N_2 , O_2 , CO_2 , H_2O , Ar, C_2H_2 and C_2H_4 , depending on initial gases in the preburn mixture) for the Cantera preburn modeling.

12.3.2. n-Heptane Autoignition Model

The n-heptane autoignition model is discussed here, including calculating the stoichiometric fuel – charge-gas mixture mole fractions, required as model inputs, along with full model implementation in Matlab interfaced with Cantera.

The following set of equations is used to calculate the stoichiometric fuel-charge gas mixture mole fractions. First, the total number of moles was calculated with the major species (minor species were not included), with one mole of fuel added into this mixture as defined in equation (106).

$$N_{\text{Total}} = 1 + \frac{\lambda * x * (1 + R/4)}{X_{\text{O}_2,0}} \quad (106)$$

The air-fuel mixture defines λ , which is 1 in this case for stoichiometric conditions, x is a property of the fuel representing the number of carbon atoms which is 7 for n-heptane, and R , which is defined as y/x is also a fuel property representing the ratio of hydrogen to carbon atoms in the fuel, which is 16/7 or 2.29 in this case. Finally $X_{\text{O}_2,0}$ is the mole fraction of oxygen atoms in the original mixture (before fuel addition).

With the total number of moles known, the individual species mole fractions for the n-heptane autoignition modeling was calculated using equation (107).

$$X_{\text{Species}} = \frac{\frac{X_{\text{Species},0}}{X_{\text{O}_2,0}} * \lambda * x * (1 + R/4)}{N_{\text{Total}}} \quad (107)$$

Where $X_{Species,o}$ is the initial mole fraction of each species before any fuel addition (designated by the 'o' (initial) in the subscript), where the *species* are CO₂, H₂O, N₂, O₂, and Argon, and $X_{O_2,o}$ is the initial oxygen mole fraction of the mixture before fuel addition. Mole fractions were calculated for each component in the mixture, with the fuel mole fraction calculated in equation (108).

$$X_{n\text{-heptane}} = \frac{1}{N_{\text{total}}} \quad (108)$$

The equation is valid since 1 mole of fuel was assumed in the mixture stoichiometry. The inputs computed here are used in the modeling, as will be discussed.

Modeling was undertaken using a constant pressure perfectly stirred reactor under constant pressure and enthalpy conditions using Cantera interfaced with MathworksTM Matlab. A flow diagram of the modeling is shown in Figure 12.19.

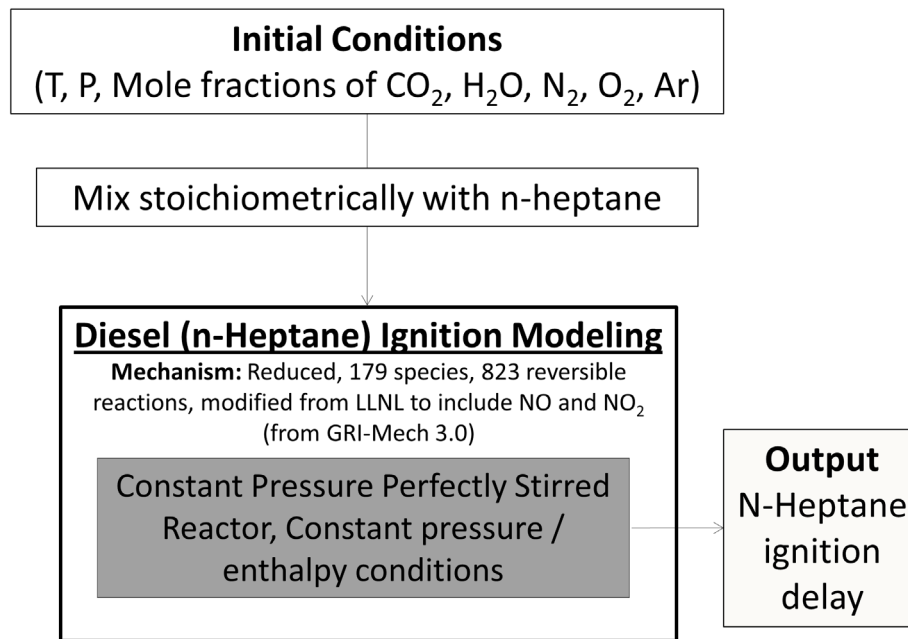


Figure 12.19: n-Heptane ignition delay modeling flow chart.

Constant pressure conditions are used since diesel mixing is typically a fast process and therefore there are minimal changes in pressure during this mixing process. Using the mole fraction of the ambient gas composition mixed with n-heptane at the initial pressure and temperature conditions as previously specified, the ignition delay of n-heptane was calculated along with the peak combustion temperature, compared amongst all ambient environments. The ignition delay is defined as the time at which the gradient in temperature reaches a maximum, as shown in Figure 12.20.

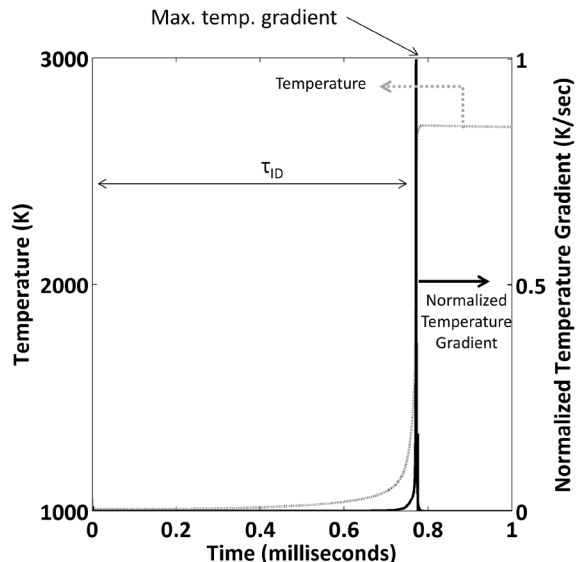


Figure 12.20: Ignition delay definition used in modeling.

12.3.3. Processing Files

There are several processing files used in the chemical kinetics modeling, however, not all are provided here. Rather, the files for the 21% oxygen analysis are included as being representative for all percent oxygen conditions investigated. Similar procedures are run for the differing oxygen levels, and also for the different institutions which are part of the ECN as was discussed in Chapter 4.

12.3.3.1. Extent of Reaction Calculation Using Engineering Equation Solver (EES)

Program inputs include initial temperature ($T1$), pressure ($P1$), guess elevated temperature ($T2$), density (ρ), expected temperature ($T_{expected}$), and volume fraction of the initial reactants. Outputs are input temperature (T_{input}), input pressure (P_{input}), and partially reacted mole fractions of species, CO_2 , H_2O , N_2 , O_2 , C_2H_2 , and H_2 , for input into the Cantera chemical kinetics model.

Cantera Starting Conditions 21.EES

```
//Run this program using a given volume fraction of initial reactants
(from Sandia's website), starting T1, P1 and a T2 which will be shifter
to determine the starting temperature of the kinetics. inputs to the
kinetics from the results of this program are YC2H2input, YH2input,
YN2input, YO2input, YH2Oinput and YCO2 input, as well as Tinput and
Pinput
```

```
"ASSUMING NO MINOR SPECIES"
```

```
"Initial Conditions - State 1"
```



```

T1=458; "K"
P1=2*10^3; "kPa"
T2=1150

//Volume fraction of initial reactants

C2H2_r=3.0
H2_r=0.5
N2_r=68.12
O2_r=28.38

//Convert to mole fractions

C2H2_reactant=C2H2_r/100;
H2_reactant=H2_r/100;
O2_reactant=O2_r/100;
N2_reactant=N2_r/100;

// Determine moles for stoichiometry

C2H2_reactant=a/(a+b+c+d)
H2_reactant=b/(a+b+c+d)
O2_reactant=c/(a+b+c+d)
N2_reactant=d/(a+b+c+d)

N_reactant=a+b+c+d

"Balance Reaction Assuming 100% Completion"

CO2_product=2*a
H2O_product=a+b
O2_product=(2*c-H2O_product-2*CO2_product)/2;
N2_product=d;

"Additional Concentrations Assuming Not Go to Completion"

O2_product_extent=c;
H2_product_extent=b
C2H2_product_extent=a;

//Considering the extent of reaction, alpha

N_product=alpha*(CO2_product+H2O_product+O2_product)+N2_product+(1-
alpha)*(O2_product_extent+C2H2_product_extent+H2_product_extent);
N_CO2_product=CO2_product*alpha;
N_H2O_product=H2O_product*alpha;
N_O2_product=O2_product*alpha;
N_N2_product=N2_product;

N_O2_product_extent=O2_product_extent*(1-alpha);
N_H2_product_extent=H2_product_extent*(1-alpha);
N_C2H2_product_extent=C2H2_product_extent*(1-alpha);

"Conservation of Energy"

```

```

U_Product=N_CO2_product*IntEnergy('CO2',T=T2)+N_H2O_product*IntEnergy('
H2O',T=T2)+N_O2_product*IntEnergy('O2',T=T2)+N_N2_product*IntEnergy('N2
',T=T2)+N_O2_product_ext*IntEnergy('O2',T=T2)+N_H2_product_ext*In
tEnergy('H2',T=T2)+N_C2H2_product_ext*IntEnergy('C2H2',T=T2);
U_Reactant=a*IntEnergy('C2H2',T=T1)+b*IntEnergy('H2',T=T1)+c*IntEnergy(
'O2',T=T1)+d*IntEnergy('N2',T=T1);

U_Reactant=U_Product;

//Mole fraction of initial reactants as inputs to the Cantera code

YC2H2input=N_C2H2_product_ext/N_product
YH2input=N_h2_product_ext/N_product
YO2input=(N_O2_product_ext+N_O2_product)/N_product
YN2input=N_N2_product/N_product
YH2Oinput=N_H2O_product/N_product
YCO2input=N_CO2_product/N_product

"Conservation of Mass to determine P2 for a given T2"

P2=P1*(N_product*T2)/(N_reactant*T1)

"Equilibrium Calculations - alpha =1 to determine peak pressure and
temperature"

N_C2H2=N_C2H2_product_ext
N_N2=N_N2_product
N_O2=N_O2_product_ext+N_O2_product
N_H2=N_H2_product_ext
N_CO2=N_CO2_product
N_H2O=N_H2O_product
N_reactant2=N_C2H2+N_N2+N_O2+N_H2+N_CO2+N_H2O

"Balance Reaction Assuming 100% Completion"

CO2_product2=2*N_C2H2+N_CO2;
H2O_product2=N_C2H2+N_H2+N_H2O;
O2_product2=(2*N_O2+2*N_CO2+N_H2O-H2O_product-2*CO2_product)/2;
N2_product2=N_N2;
N_product2=CO2_product+H2O_product+O2_product+N2_product

"Conservation of Energy"

U_Product2=CO2_product2*IntEnergy('CO2',T=TFinal)+H2O_product2*IntEnerg
y('H2O',T=TFinal)+O2_product2*IntEnergy('O2',T=TFinal)+N2_product2*IntE
nergy('N2',T=TFinal)
U_Reactant2=N_C2H2*IntEnergy('C2H2',T=T2)+N_H2*IntEnergy('H2',T=T2)+N_O
2*IntEnergy('O2',T=T2)+N_N2*IntEnergy('N2',T=T2)+N_CO2*IntEnergy('CO2',
T=T2)+N_H2O*IntEnergy('H2O',T=T2);

U_Reactant2=U_Product2;

"Conservation of Mass"

```

```

PFinal=P2*(N_product2*TFinal)/(N_reactant2*T2)
rho=14.8;
R=8.314;
MWCO2=MolarMass(CO2)
MWN2=MolarMass(N2)
MWH2O=MolarMass(H2O)
MWO2=MolarMass(O2)
MWC2H2=MolarMass(C2H2)
MWH2=MolarMass(H2)

MW=(N_CO2_product*MWCO2+N_H2O_product*MWH2O+N_N2_product*MWN2+(N_O2_pro
duct+N_O2_product_extent)*MWO2+N_H2_product_extent*MWH2+N_C2H2_product_
extent*MWC2H2)/N_product

//Expected from Sandia Data

Texpected=1752.154;
Pexpected=Texpected*(rho*R)/MW

//Apply temperature shift to account for heat transfer to match
Sandia's peak pressure and temperature in Cantera Kinetics

deltaT=TFinal-Texpected+16
Tinput=T2-deltaT;
Pinput=(rho*R*Tinput)/(MW)

```

12.3.3.2. Premixed Burn Phase Chemical Kinetics Model Using Cantera Interfaced with Matlab

This Matlab program takes the output from the EES program, and runs a 1-D chemical kinetics modeling to simulate the premixed burn phase including the preburn and cool-down stages. Output results are written into excel files to provide results for plotting and further analysis, and also provide the required inputs for the next modeling stage.

Reactor Ignition UV GRI21.m

```

function Reactor_Ignition_UV_GRI21
clear all
close all

%% USE THIS FOR 21% O2 Preburn Process GRI Mechanism

%Input YC2H2, YCO2, YH2O, YH2, YO2, YN2, T & P from EES Program
(Cantera
%Starting Conditions 21.EES

%Input Heat flux from Sandia P T Trace 21 perc O2.xls

%Verify that the heat flux tuning is correct, as well as indecies for
%maximum temperature. Also check that the time that the heat flux
starts is
%equivalent to the ignition delay time of the simulation.

```

```

%      Zero-dimensional kinetics: adiabatic, constant volume.
%      GRI 3.0 Reaction Mechanism - 53 species and 342 mechanisms
%
% H2      H      O      O2      OH      H2O      HO2      H2O2
% C       CH     CH2     CH2(S)  CH3     CH4      CO       CO2
% HCO     CH2O    CH2OH   CH3O    CH3OH   C2H     C2H2     C2H3
% C2H4    C2H5    C2H6    HCCO    CH2CO   HCCOH   N        NH
% NH2     NH3     NNH     NO      NO2     N2O     HNO      CN
% HCN     H2CN    HCNN    HCNO    HOCN    HNCO    NCO      N2
% AR      C3H7    C3H8    CH2CHO   CH3CHO
%
%      Inputs: Starting Pressure, Temperature and Mole Fractions
%      Heat Flux for given Pressure - Time Sandia Data
%      Make sure to define the heat flux function.

%Specify the GRI Mechanisms
gas = GRI30;
nsp = nSpecies(gas); % number of species

%Initial Conditions for Baseline conditions to match Sandia P, T data
for 21% O2
    To = 963; % temperature
    Po = 4061*1000; % pressure and oneatm is defined as 101325 N/m^2

%initial fuel-oxidizer mixture
ic2h2 = speciesIndex(gas, 'C2H2');
ih2 = speciesIndex(gas, 'H2');
io2 = speciesIndex(gas, 'O2');
in2 = speciesIndex(gas, 'N2');
ico2 = speciesIndex(gas, 'CO2');
ih2o = speciesIndex(gas, 'H2O');
xo = zeros(nsp,1); % mole fraction

% 21% O2 after preburn - Specify Mole Fractions of Reactants

xo(ic2h2) = 0.01697;
xo(ih2) = 0.002828;
xo(io2) = 0.2517;
xo(in2) = 0.6865;
xo(ih2o) = 0.01548;
xo(ico2) = 0.02653;

%Set the GRI Mechanism Starting Pressure, Temperature and Mole
Fractions.

set(gas, 'T', To, 'P', Po, 'X', xo);

y0 = (intEnergy_mass(gas) % Specific internal energy (J/kg)
      1.0/density(gas) % Mass density (kg/m^3)
      massFractions(gas)); % Mass fractions

options = odeset('RelTol',1.e-16,'AbsTol',1.e-16,'Stats','on');

t0 = cputime;

```

```

dt=1*10^-7;
t_max = 1.5; % maximum calculation time (sec)
time_interval=(0:dt:t_max);

%Solve the ODES
out =
ode15s(@reactor_ode,time_interval,y0,options,gas,@vdot,@area,@heatflux)
;

disp(['CPU time = ' num2str(cputime - t0)]);

plotdata = output(out,gas,To,Po, xo);

%%%%%%%%%%%%%%%%%%%%%%%%%%%%%%%%%%%%%%%%%%%%%%%%%%%%%%%%%%%%%%%%%%%%%%%%
% the functions below may be defined arbitrarily to set the reactor
% boundary conditions - the rate of change of volume, the heat
% flux, and the area.

% Rate of change of volume. Any arbitrary function may be implemented.
% Input arguments:
%   t      time
%   vol    volume
%   gas    ideal gas object

function v = vdot(t, vol, gas)
v=0.0; % Constant Volume

function q = heatflux(t, gas)

%Heat Flux (w/m^2)

q=0; %adiabatic before ignite premixed burn

%Include heat transfer after the premixed burn is completed.

if t>0.049237

% normalized heat flux
q=-1.0737*t^5+3.1999*t^4-3.2814*t^3+0.8166*t^2+1.1223*t-1.1717;

%Tuning the heat flux
q=2.6*10^7*q;

end

% surface area. Used only to compute heat transfer, in m^2

function a = area(t,vol)

a=0.048911614;

%%%%%%%%%%%%%%%%%%%%%%%%%%%%%%%%%%%%%%%%%%%%%%%%%%%%%%%%%%%%%%%%%%%%%%%%

% Since the solution variables used by the 'reactor' function are

```

```

% not necessarily those desired for output, this function is called
% after the integration is complete to generate the desired
% outputs.

function pv = output(s, gas, To, Po, xo)
times = s.x;
soln = s.y;
(m n) = size(times);
pv = zeros(nSpecies(gas) + 4, n);

for j = 1:n
    ss = soln(:,j);
    y = ss(3:end);           %ss(3:end): mass fraction
    mass = sum(y);
    u_mass = ss(1)/mass;    % ss(1): internal energy
    v_mass = ss(2)/mass;    % ss(2): volume
    setMassFractions(gas, y);
    setState_UV(gas, (u_mass v_mass));

    pv(1,j) = times(j); % second
    pv(2,j) = temperature(gas);
    tt(j) = times(j);
    tt0(j) = temperature(gas);
    pv(3,j) = density(gas);
    pv(4,j) = pressure(gas)/10^6;
    pv(5:end,j) = moleFractions(gas); % mole fraction
end

% calculate the ignition delay time
crit(1) = 0;
for j = 2:n
    crit(j) = (pv(2,j)-pv(2,j-1))/(pv(1,j)-pv(1,j-1));
end

(xmax,kig) = max(crit);
t_ign = pv(1,kig);
disp('Ignition Delay Time = ');
disp(t_ign);

% Read in Sandia experimental data to compare to the modeled pressure-
temperature
% time data
SandiaTemperature=xlsread('Sandia P T Trace 21Perc O2.xlsx', 'Sheet1',
'C1388:C9305');
SandiaIndex=length(SandiaTemperature);
SandiaPlotIndex=(1:SandiaIndex)*1*10^-4;

index = min(find(pv(1,:)>t_ign+1*10^-4))

% Plot experimental and modeled temperature - time data during the
cool down phase

figure

```

```

plot(pv(1,index:end)-t_ign, pv(2,index:end), SandiaPlotIndex,
SandiaTemperature)
legend('Simulation Results', 'Experimental Data')
title('21% O2')
xlabel('Time (Seconds)')
ylabel('Temperature (K)')

% define each species
ih = speciesIndex(gas, 'H');
ih2 = speciesIndex(gas, 'H2');
ioh = speciesIndex(gas, 'OH');
ih2o2 = speciesIndex(gas, 'H2O2');
ic=speciesIndex(gas, 'C');
ich2=speciesIndex(gas, 'CH2');
ich2s=speciesIndex(gas, 'CH2(S)');
ich3 = speciesIndex(gas, 'CH3');
ih2o = speciesIndex(gas, 'H2O');
iho2 = speciesIndex(gas, 'HO2');
ich = speciesIndex(gas, 'CH');
ich4=speciesIndex(gas, 'CH4');
ich2oh=speciesIndex(gas, 'CH2OH');
ich2oh=speciesIndex(gas, 'CH2O');
ich3oh=speciesIndex(gas, 'CH3OH');
ich3o=speciesIndex(gas, 'CH3O');
ic2h=speciesIndex(gas, 'C2H');
ico = speciesIndex(gas, 'CO');
ico2 = speciesIndex(gas, 'CO2');
ihco = speciesIndex(gas, 'HCO');
ic2h2 = speciesIndex(gas, 'C2H2');
ino = speciesIndex(gas, 'NO');
ino2 = speciesIndex(gas, 'NO2');
io2=speciesIndex(gas, 'O2');
in2=speciesIndex(gas, 'N2');
ic2h3=speciesIndex(gas, 'C2H3');
ic2h4=speciesIndex(gas, 'C2H4');
ic2h5=speciesIndex(gas, 'C2H5');
ic2h6=speciesIndex(gas, 'C2H6');
ihcco=speciesIndex(gas, 'HCCO');
ich2o=speciesIndex(gas, 'CH2O');
ich2co=speciesIndex(gas, 'CH2CO');
ihccoh=speciesIndex(gas, 'HCCOH');
in=speciesIndex(gas, 'N');
inh=speciesIndex(gas, 'NH');
inh2=speciesIndex(gas, 'NH2');
inh3=speciesIndex(gas, 'NH3');
innh=speciesIndex(gas, 'NNH');
in2o=speciesIndex(gas, 'N2O');
ihno=speciesIndex(gas, 'HNO');
icn=speciesIndex(gas, 'CN');
ihcn=speciesIndex(gas, 'HCN');
ih2cn=speciesIndex(gas, 'H2CN');
ihcnn=speciesIndex(gas, 'HCNN');
ihcno=speciesIndex(gas, 'HCNO');
ihocn=speciesIndex(gas, 'HOCN');
ihnco=speciesIndex(gas, 'HNCO');

```

```

inco=speciesIndex(gas,'NCO');
iar=speciesIndex(gas,'AR');
ic3h7=speciesIndex(gas,'C3H7');
ic3h8=speciesIndex(gas,'C3H8');
ich2cho=speciesIndex(gas,'CH2CHO');
ich3cho=speciesIndex(gas,'CH3CHO');
io=speciesIndex(gas,'O');

% plot the temperature, pressure and species mole fractions.

%plot Temperature as function of time
figure;
subplot(2,1,1);
plot(pv(1,:),pv(2,:));
xlabel('time (s)');
ylabel('Temperature');
title(('Final T = ' num2str(pv(2,end)) 'K; ', 'Max T = '
num2str(max(pv(2,:))) 'K; ', ' Ign Time = ',num2str(t_ign),'s'));

%Plot pressure as a function of time

subplot(2,1,2);
plot(pv(1,:),pv(4,:));
xlabel('time (s)');
ylabel('Pressure (MPa)');
title(('Final P = ' num2str(pv(4,end)) ' MPa; ', 'Max P = '
num2str(max(pv(4,:))) 'MPa',));

%Plot Species mole fractions as a function of time.

figure
semilogy(pv(1,:),pv(4+ioh,:),pv(1,:),pv(4+ino2,:),pv(1,:),pv(4+ino,:),
pv(1,:),pv(4+ic2h2,:),pv(1,:),pv(4+ih2,:));
xlabel('time (s)');
ylabel('Mole Fraction');
legend('OH', 'NO2', 'NO', 'C2H2','H2');
ylim((10^-9 1))

%Plot NO and NO2 only

figure
semilogy(pv(1,:),pv(4+ino,:),pv(1,:),pv(4+ino2,:))
legend('NO','NO2')
ylabel('Mole Fraction')
xlabel('Time (seconds)')
ylim((10^-9, 10^-3))

% find when temperature during cool-down reaches 1000 K

temperatureindex=min(find(pv(2,index:end)<1000))+index
temperaturenhep=pv(2,temperatureindex)

% save data - 53 species, temperature, and pressure at temperature of
interest (1000 K) for fuel injection

```



```

xlswrite('NHeptane Input Conditions 21%
02.xls',pv(2,temperatureindex),'sheet1', 'B1'); %Temperature
xlswrite('NHeptane Input Conditions 21%
02.xls',pv(4,temperatureindex),'sheet1', 'B2'); % Pressure
xlswrite('NHeptane Input Conditions 21%
02.xls',pv(4+ih2,temperatureindex),'sheet1', 'B3');
xlswrite('NHeptane Input Conditions 21%
02.xls',pv(4+ih,temperatureindex),'sheet1', 'B4');
xlswrite('NHeptane Input Conditions 21%
02.xls',pv(4+io,temperatureindex),'sheet1', 'B5');
xlswrite('NHeptane Input Conditions 21%
02.xls',pv(4+io2,temperatureindex),'sheet1', 'B6');
xlswrite('NHeptane Input Conditions 21%
02.xls',pv(4+ioh,temperatureindex),'sheet1', 'B53');
xlswrite('NHeptane Input Conditions 21%
02.xls',pv(4+ih2o,temperatureindex),'sheet1', 'B7');
xlswrite('NHeptane Input Conditions 21%
02.xls',pv(4+iho2,temperatureindex),'sheet1', 'B8');
xlswrite('NHeptane Input Conditions 21%
02.xls',pv(4+ih2o2,temperatureindex),'sheet1', 'B9');
xlswrite('NHeptane Input Conditions 21%
02.xls',pv(4+ic,temperatureindex),'sheet1', 'B10');
xlswrite('NHeptane Input Conditions 21%
02.xls',pv(4+ich,temperatureindex),'sheet1', 'B11');
xlswrite('NHeptane Input Conditions 21%
02.xls',pv(4+ich2,temperatureindex),'sheet1', 'B12');
xlswrite('NHeptane Input Conditions 21%
02.xls',pv(4+ich2s,temperatureindex),'sheet1', 'B13');
xlswrite('NHeptane Input Conditions 21%
02.xls',pv(4+ich3,temperatureindex),'sheet1', 'B14');
xlswrite('NHeptane Input Conditions 21%
02.xls',pv(4+ich4,temperatureindex),'sheet1', 'B15');
xlswrite('NHeptane Input Conditions 21%
02.xls',pv(4+ico,temperatureindex),'sheet1', 'B16');
xlswrite('NHeptane Input Conditions 21%
02.xls',pv(4+ico2,temperatureindex),'sheet1', 'B17');
xlswrite('NHeptane Input Conditions 21%
02.xls',pv(4+ihco,temperatureindex),'sheet1', 'B18');
xlswrite('NHeptane Input Conditions 21%
02.xls',pv(4+ich2o,temperatureindex),'sheet1', 'B19');
xlswrite('NHeptane Input Conditions 21%
02.xls',pv(4+ich2oh,temperatureindex),'sheet1', 'B20');
xlswrite('NHeptane Input Conditions 21%
02.xls',pv(4+ich3o,temperatureindex),'sheet1', 'B21');
xlswrite('NHeptane Input Conditions 21%
02.xls',pv(4+ich3oh,temperatureindex),'sheet1', 'B22');
xlswrite('NHeptane Input Conditions 21%
02.xls',pv(4+ic2h,temperatureindex),'sheet1', 'B23');
xlswrite('NHeptane Input Conditions 21%
02.xls',pv(4+ic2h2,temperatureindex),'sheet1', 'B24');
xlswrite('NHeptane Input Conditions 21%
02.xls',pv(4+ic2h3,temperatureindex),'sheet1', 'B25');
xlswrite('NHeptane Input Conditions 21%
02.xls',pv(4+ic2h4,temperatureindex),'sheet1', 'B26');

```

```

    xlswrite('NHeptane Input Conditions 21%
02.xls',pv(4+ic2h5,temperatureindex),'sheet1', 'B27');
    xlswrite('NHeptane Input Conditions 21%
02.xls',pv(4+ic2h6,temperatureindex),'sheet1', 'B28');
    xlswrite('NHeptane Input Conditions 21%
02.xls',pv(4+ihcco,temperatureindex),'sheet1', 'B29');
    xlswrite('NHeptane Input Conditions 21%
02.xls',pv(4+ich2co,temperatureindex),'sheet1', 'B30');
    xlswrite('NHeptane Input Conditions 21%
02.xls',pv(4+ihccoh,temperatureindex),'sheet1', 'B31');
    xlswrite('NHeptane Input Conditions 21%
02.xls',pv(4+in,temperatureindex),'sheet1', 'B32');
    xlswrite('NHeptane Input Conditions 21%
02.xls',pv(4+inh2,temperatureindex),'sheet1', 'B33');
    xlswrite('NHeptane Input Conditions 21%
02.xls',pv(4+inh3,temperatureindex),'sheet1', 'B34');
    xlswrite('NHeptane Input Conditions 21%
02.xls',pv(4+innh,temperatureindex),'sheet1', 'B35');
    xlswrite('NHeptane Input Conditions 21%
02.xls',pv(4+ino,temperatureindex),'sheet1', 'B36');
    xlswrite('NHeptane Input Conditions 21%
02.xls',pv(4+ino2,temperatureindex),'sheet1', 'B37');
    xlswrite('NHeptane Input Conditions 21%
02.xls',pv(4+in2o,temperatureindex),'sheet1', 'B38');
    xlswrite('NHeptane Input Conditions 21%
02.xls',pv(4+ihno,temperatureindex),'sheet1', 'B39');
    xlswrite('NHeptane Input Conditions 21%
02.xls',pv(4+icn,temperatureindex),'sheet1', 'B40');
    xlswrite('NHeptane Input Conditions 21%
02.xls',pv(4+ihcn,temperatureindex),'sheet1', 'B41');
    xlswrite('NHeptane Input Conditions 21%
02.xls',pv(4+ih2cn,temperatureindex),'sheet1', 'B42');
    xlswrite('NHeptane Input Conditions 21%
02.xls',pv(4+ihcnn,temperatureindex),'sheet1', 'B43');
    xlswrite('NHeptane Input Conditions 21%
02.xls',pv(4+ihcno,temperatureindex),'sheet1', 'B44');
    xlswrite('NHeptane Input Conditions 21%
02.xls',pv(4+ihocn,temperatureindex),'sheet1', 'B45');
    xlswrite('NHeptane Input Conditions 21%
02.xls',pv(4+ihnco,temperatureindex),'sheet1', 'B46');
    xlswrite('NHeptane Input Conditions 21%
02.xls',pv(4+inco,temperatureindex),'sheet1', 'B47');
    xlswrite('NHeptane Input Conditions 21%
02.xls',pv(4+iar,temperatureindex),'sheet1', 'B48');
    xlswrite('NHeptane Input Conditions 21%
02.xls',pv(4+ich2cho,temperatureindex),'sheet1', 'B51');
    xlswrite('NHeptane Input Conditions 21%
02.xls',pv(4+ic3h7,temperatureindex),'sheet1', 'B49');
    xlswrite('NHeptane Input Conditions 21%
02.xls',pv(4+ic3h8,temperatureindex),'sheet1', 'B50');
    xlswrite('NHeptane Input Conditions 21%
02.xls',pv(4+ich3cho,temperatureindex),'sheet1', 'B52');
    xlswrite('NHeptane Input Conditions 21%
02.xls',pv(4+in2,temperatureindex),'sheet1', 'B54');

```

```

    xlswrite('NHeptane Input Conditions 21%
O2.xls',temperatureindex,'sheet1','B56');

% Save time-dependent data during the entire modeling event -
temperature, time, pressure, no, no2 and oh
    xlswrite('NHeptane Input Conditions 21%
O2.xls',transpose(pv(2,:)),'sheet2','B2'); %Temperature
    xlswrite('NHeptane Input Conditions 21%
O2.xls',transpose(pv(1,:)),'sheet2','A2'); %Time
    xlswrite('NHeptane Input Conditions 21%
O2.xls',transpose(pv(4,:)),'sheet2','C2'); %Pressure
    xlswrite('NHeptane Input Conditions 21%
O2.xls',transpose(pv(4+ino,:)),'sheet2','D2'); %NO
    xlswrite('NHeptane Input Conditions 21%
O2.xls',transpose(pv(4+ino2,:)),'sheet2','E2'); %NO2
    xlswrite('NHeptane Input Conditions 21%
O2.xls',transpose(pv(4+ioh,:)),'sheet2','F2'); %OH

```

12.3.3.3. Cantera n-Heptane Ignition Delay Chemical Kinetics Model Using Matlab

This chemical kinetics model program takes outputs from the premixed burn phase of the program, mixing them stoichiometrically with n-heptane. Initial pressure and temperature are defined from the premixed burn program. The program outputs the ignition delay, along with peak temperature from combustion. Results are stored in an excel spreadsheet.

Reactor Ignition UV Heptane21.m

```

function Reactor_Ignition_UV_Heptane21 (gas)

% close all
% clear all

%% Use this program to combust the N_Heptane fuel in 21% O2 (from
premixed
%% combustion products). Determine the ignition delay of n-heptane.

% Take inputs from the results of the Reactor_Ignition_UV_GRI21.m file.

% This program uses the reduced n-heptane mechanism to determine the
% ignition delay.

%Generate N-heptane mechanism in cantera format.

f =
ck2cti('UC_hep_mod_chem.inp','UC_hep_mod_therm.dat','UC_hep_mod_trans.d
at');
g = importPhase('UC_hep_mod_chem.cti','UC_hep_mod_chem');
nsp=nSpecies(g)

% set the initial conditions
To = 840; %K
Po = xlsread('NHeptane 21% O2.xls','sheet2','G2'); % pressure

```

```

Po=Po*10^6; %Convert to Pascal

%initial fuel-oxidizer mixture - mole fractions - Without Fuel
ihcp = speciesIndex(g,'NC7H16');
ih = speciesIndex(g,'H');
ih2 = speciesIndex(g,'H2');
ioh = speciesIndex(g,'OH');
ih2o2 = speciesIndex(g,'H2O2');
ic=speciesIndex(g,'C');
ich2=speciesIndex(g,'CH2');
ich2s=speciesIndex(g,'CH2(S)');
ich3 = speciesIndex(g,'CH3');
ih2o = speciesIndex(g,'H2O');
iho2 = speciesIndex(g,'HO2');
ich = speciesIndex(g,'CH');
ich4=speciesIndex(g,'CH4');
ich2oh=speciesIndex(g,'CH2OH');
ich2oh=speciesIndex(g,'CH2O');
ich3oh=speciesIndex(g,'CH3OH');
ich3o=speciesIndex(g,'CH3O');
ic2h=speciesIndex(g,'C2H');
ico = speciesIndex(g,'CO');
ico2 = speciesIndex(g,'CO2');
ihco = speciesIndex(g,'HCO');
ic2h2 = speciesIndex(g,'C2H2');
ino = speciesIndex(g,'NO');
ino2 = speciesIndex(g,'NO2');
io2=speciesIndex(g,'O2');
in2=speciesIndex(g,'N2');
ic2h3=speciesIndex(g,'C2H3');
ic2h4=speciesIndex(g,'C2H4');
ic2h5=speciesIndex(g,'C2H5');
ic2h6=speciesIndex(g,'C2H6');
ihcco=speciesIndex(g,'HCCO');
ich2o=speciesIndex(g,'CH2O');
ich2co=speciesIndex(g,'CH2CO');
ihccoh=speciesIndex(g,'HCCOH');
in=speciesIndex(g,'N');
inh=speciesIndex(g,'NH');
inh2=speciesIndex(g,'NH2');
inh3=speciesIndex(g,'NH3');
innh=speciesIndex(g,'NNH');
in2o=speciesIndex(g,'N2O');
ihno=speciesIndex(g,'HNO');
icn=speciesIndex(g,'CN');
ihcn=speciesIndex(g,'HCN');
ih2cn=speciesIndex(g,'H2CN');
ihcnn=speciesIndex(g,'HCNN');
ihcno=speciesIndex(g,'HCNO');
ihocn=speciesIndex(g,'HOCN');
ihnco=speciesIndex(g,'HNCO');
inco=speciesIndex(g,'NCO');
iar=speciesIndex(g,'AR');
ic3h7=speciesIndex(g,'NC3H7');
ic3h8=speciesIndex(g,'C3H8');

```

```

ich2cho=speciesIndex(g,'CH2CHO');
ich3cho=speciesIndex(g,'CH3CHO');
io=speciesIndex(g,'O');

xo = zeros(nsp,1); % mole fraction

% Conversion from mole fraction without fuel to mole fraction
% with Fuel. The Fuel is n-heptane C7H16, the lambda is 1 for this
case,
% conversion only considers major species, O2, N2, CO2, H2O.

xo(io2)=xlsread('NHeptane 21% O2.xls','sheet2', 'G6');
yO2=xo(io2);

lambda=1;
y=16;
x=7;
R=y/x;
Ntotal=1+(lambda*x*(1+R/4))/yO2;

xo(ih2)=xlsread('NHeptane 21% O2.xls','sheet2', 'G3');
xo(ih)=xlsread('NHeptane 21% O2.xls','sheet2', 'G4');
xo(io)=xlsread('NHeptane 21% O2.xls','sheet2', 'G5');
xo(io2)=(xlsread('NHeptane 21% O2.xls','sheet2',
'G6')/yO2*lambda*x*(1+R/4))/Ntotal
xo(ih2o)=xlsread('NHeptane 21% O2.xls','sheet2', 'G53');
xo(ih2o)=(xlsread('NHeptane 21% O2.xls','sheet2',
'G7')/yO2*lambda*x*(1+R/4))/Ntotal
xo(iho2)=xlsread('NHeptane 21% O2.xls','sheet2', 'G8');
xo(ih2o2)=xlsread('NHeptane 21% O2.xls','sheet2', 'G9');
xo(ic)=xlsread('NHeptane 21% O2.xls','sheet2', 'G10');
xo(ich)=xlsread('NHeptane 21% O2.xls','sheet2', 'G11');
xo(ich2)=xlsread('NHeptane 21% O2.xls','sheet2', 'G12');
xo(ich2s)=xlsread('NHeptane 21% O2.xls','sheet2', 'G13');
xo(ich3)=xlsread('NHeptane 21% O2.xls','sheet2', 'G14');
xo(ich4)=xlsread('NHeptane 21% O2.xls','sheet2', 'G15');
xo(ico)=xlsread('NHeptane 21% O2.xls','sheet2', 'G16');
xo(ico2)=(xlsread('NHeptane 21% O2.xls','sheet2',
'G17')/yO2*lambda*x*(1+R/4))/Ntotal
xo(ihco)=xlsread('NHeptane 21% O2.xls','sheet2', 'G18');
xo(ich2o)=xlsread('NHeptane 21% O2.xls','sheet2', 'G19');
xo(ich2oh)=xlsread('NHeptane 21% O2.xls','sheet2', 'G20');
xo(ich3o)= xlsread('NHeptane 21% O2.xls','sheet2', 'G21');
xo(ich3oh)=xlsread('NHeptane 21% O2.xls','sheet2', 'G22');
xo(ic2h)=xlsread('NHeptane 21% O2.xls','sheet2', 'G23');
xo(ic2h2)=xlsread('NHeptane 21% O2.xls','sheet2', 'G24');
xo(ic2h3)=xlsread('NHeptane 21% O2.xls','sheet2', 'G25');
xo(ic2h4)=xlsread('NHeptane 21% O2.xls','sheet2', 'G26');
xo(ic2h5)=xlsread('NHeptane 21% O2.xls','sheet2', 'G27');
xo(ic2h6)=xlsread('NHeptane 21% O2.xls','sheet2', 'G28');
xo(ihcco)=xlsread('NHeptane 21% O2.xls','sheet2', 'G29');
xo(ich2co)=xlsread('NHeptane 21% O2.xls','sheet2', 'G30');
%xo(ihccoh)=xlsread('NHeptane 21% O2.xls','sheet2', 'G31');
xo(in)=xlsread('NHeptane 21% O2.xls','sheet2', 'G32');
xo(inh2)=xlsread('NHeptane 21% O2.xls','sheet2', 'G33');

```

```

xo(inh3)=xlsread('NHeptane 21% O2.xls','sheet2', 'G34');
xo(innh)=xlsread('NHeptane 21% O2.xls','sheet2', 'G35');
xo(ino)=xlsread('NHeptane 21% O2.xls','sheet2', 'G36');
xo(ino2)=xlsread('NHeptane 21% O2.xls','sheet2', 'G37');
xo(in2o)=xlsread('NHeptane 21% O2.xls','sheet2', 'G38');
xo(ihno)=xlsread('NHeptane 21% O2.xls','sheet2', 'G39');
xo(icn)=xlsread('NHeptane 21% O2.xls','sheet2', 'G40');
xo(ihcn)=xlsread('NHeptane 21% O2.xls','sheet2', 'G41');
xo(ih2cn)=xlsread('NHeptane 21% O2.xls','sheet2', 'G42');
xo(ihcnn)=xlsread('NHeptane 21% O2.xls','sheet2', 'G43');
xo(ihcno)=xlsread('NHeptane 21% O2.xls','sheet2', 'G44');
xo(ihocn)=xlsread('NHeptane 21% O2.xls','sheet2', 'G45');
xo(ihnco)=xlsread('NHeptane 21% O2.xls','sheet2', 'G46');
xo(inco)=xlsread('NHeptane 21% O2.xls','sheet2', 'G47');
xo(ic3h7)=xlsread('NHeptane 21% O2.xls','sheet2', 'G49');
xo(ic3h8)=xlsread('NHeptane 21% O2.xls','sheet2', 'G50');
xo(ich2cho)=xlsread('NHeptane 21% O2.xls','sheet2', 'G51');
xo(ich3cho)=xlsread('NHeptane 21% O2.xls','sheet2', 'G52');
xo(in2)=(xlsread('NHeptane 21%
O2.xls','sheet2','G54')/yO2*lambda*x*(1+R/4))/Ntotal
xo(ihep)=1/Ntotal %Mole Fraction of Fuel

% Write results for the initial composition (major species) to an excel
file.
xlswrite('NHeptane Results 21% O2.xls',Ntotal,'sheet3', 'I2'); %Mole
Total Input
xlswrite('NHeptane Results 21% O2.xls',yO2,'sheet3', 'I3'); %Mole
Fraction O2 Input
xlswrite('NHeptane Results 21% O2.xls',To,'sheet3', 'I4'); %Temperature
Input
xlswrite('NHeptane Results 21% O2.xls',Po,'sheet3', 'I5'); %Pressure
Input
xlswrite('NHeptane Results 21% O2.xls',xo(ihep),'sheet3', 'I6'); %Mole
Fraction Nhep
xlswrite('NHeptane Results 21% O2.xls',xo(in2),'sheet3', 'I7'); %Mole
Fraction N2
xlswrite('NHeptane Results 21% O2.xls',xo(ico2),'sheet3', 'I8'); %Mole
Fraction CO2
xlswrite('NHeptane Results 21% O2.xls',xo(ih2o),'sheet3', 'I9'); %Mole
Fraction H2O

%Set up the n-heptane mechnaism.
set(g,'T',To,'P',Po,'X',xo);

y0 = (enthalpy_mass(g) % Specific internal energy (J/kg)
      1.0/density(g) % Mass density (kg/m^3)
      massFractions(g)); % Mass fractions

options = odeset('RelTol',1.e-8,'AbsTol',1.e-8,'Stats','on');

t0 = cputime;

dt=1*10^-4;
t_max=.005;
time_interval=(0:dt:t_max);

```

```

out =
ode15s(@reactor_ode,time_interval,y0,options,g,@vdot,@area,@heatflux);

disp(['CPU time = ' num2str(cputime - t0)]);

plotdata = output(out,g,To,Po, xo);

%%%%%%%%%%%%%%%%%%%%%%%%%%%%%%%%%%%%%%%%%%%%%%%%%%%%%%%%%%%%%%%%%%%%%%%%%%%%%%
% the functions below may be defined arbitrarily to set the reactor
% boundary conditions - the rate of change of volume, the heat
% flux, and the area.

% Rate of change of volume. Any arbitrary function may be implemented.
% Input arguments:
%   t      time
%   vol    volume
%   gas    ideal gas object

function v = vdot(t, vol, g)

% Constant pressure reactor

v=1e5*(pressure(g)-4.175025*10^6);    % holds pressure close to Po

% heat flux (W/m^2).

function q = heatflux(t, g)

q=0;    % adiabatic

% surface area. Used only to compute heat transfer.

function a = area(t,vol)

a=0.048911614;

%%%%%%%%%%%%%%%%%%%%%%%%%%%%%%%%%%%%%%%%%%%%%%%%%%%%%%%%%%%%%%%%%%%%%%%%%%%%%%

% Since the solution variables used by the 'reactor' function are
% not necessarily those desired for output, this function is called
% after the integration is complete to generate the desired
% outputs.

function pv = output(s, g, To, Po, xo)
times = s.x;
soln = s.y;
(m n) = size(times);
pv = zeros(nSpecies(g) + 4, n);

set(g,'T',To,'P',Po);

for j = 1:n
    ss = soln(:,j);

```

```

y = ss(3:end);          %ss(3:end): mass fraction
mass = sum(y);
u_mass = ss(1)/mass;    % ss(1); internal energy
v_mass = ss(2)/mass;    % ss(2): volume
setMassFractions(g, y);
setState_UV(g, (u_mass v_mass));

pv(1,j) = times(j); % second
pv(2,j) = temperature(g);
tt(j) = times(j);
tt0(j) = temperature(g);
pv(3,j) = density(g);
pv(4,j) = pressure(g)/10^6;

pv(5:end,j) = moleFractions(g); % mole fraction
end
ttl=transpose(tt);
tt2=transpose(tt0);

% calculate the ignition delay time
crit(1) = 0;
for j = 2:n
    crit(j) = (pv(2,j)-pv(2,j-1))/(pv(1,j)-pv(1,j-1));
end
crit
(xmax,kig) = max(crit);
t_ign = pv(1,kig);
disp('Ignition Delay Time = ');
disp(t_ign);

% define species
ih = speciesIndex(g, 'H');
ih2 = speciesIndex(g, 'H2');
ioh = speciesIndex(g, 'OH');
io2=speciesIndex(g, 'O2');
ih2o = speciesIndex(g, 'H2O');
iho2 = speciesIndex(g, 'HO2');
ich = speciesIndex(g, 'CH');
ich3 = speciesIndex(g, 'CH3');
ico = speciesIndex(g, 'CO');
ico2 = speciesIndex(g, 'CO2');
ihco = speciesIndex(g, 'HCO');
ic2H2 = speciesIndex(g, 'C2H2');
ino = speciesIndex(g, 'NO');
ino2 = speciesIndex(g, 'NO2');
in2=speciesIndex(g, 'N2');
ihcp=speciesIndex(g, 'NC7H16');

% plot the temperature, pressure and species mole fractions

figure(3);
subplot(2,1,1);
plot(pv(1,:),pv(2,:));
xlabel('time (s)');
ylabel('Temperature (K)');

```



```

title(('Final T = ' num2str(pv(2,end)) 'K ', ' Ign Time = '
',num2str(t_ign*1000),'ms'));
subplot(2,1,2);
plot(pv(1,:),pv(4,:));
xlabel('time (s)');
ylabel('Pressure (MPa)');
title(('Final P = ' num2str(pv(4,end)) ' MPa'));

% subplot(2,2,3);

figure
semilogy(pv(1,:),pv(4+ioh,:), pv(1,:),pv(4+ino,:), pv(1,:),
pv(4+ino2,:), pv(1,:), pv(4+io2,:), pv(1,:), pv(4+ihep,:),pv(1,:),
pv(4+ico2,:), pv(1,:), pv(4+ih2o,:));
xlabel('time (s)');
ylabel('Mole Fraction');
title('Constituent Concentrations for 21% O2 in Premixed Combustion
Products - From Stoichiometric N-Heptane Combustion')
legend('OH', 'NO', 'NO2', 'Heptane', 'O2', 'CO2', 'H2O')
ylim((10^-9, 1))

% Plot no and no2 results
figure
semilogy(pv(1,:), pv(4+ino,:), pv(1,:), pv(4+ino2,:))
xlabel('time (s)');
ylabel('Mole Fraction');
legend('NO', 'NO2')
title('NO and NO2 Concentrations for 21% O2 in Premixed Combustion
Products - From Stoichiometric N-Heptane Combustion')
ylim((10^-9, 1))

% Write output results for temperature, time, pressure, NO, NO2, OH,
CO2, H2O, and Ignition Delay.

xlswrite('NHeptane Results 21% O2.xls',transpose(pv(2,:)), 'sheet3',
'B2'); %Temperature
xlswrite('NHeptane Results 21% O2.xls',transpose(pv(1,:)), 'sheet3',
'A2'); %Time
xlswrite('NHeptane Results 21% O2.xls',transpose(pv(4,:)), 'sheet3',
'C2'); %Pressure
xlswrite('NHeptane Results 21% O2.xls',transpose(pv(4+ino,:)), 'sheet3',
'D2'); %NO
xlswrite('NHeptane Results 21%
O2.xls',transpose(pv(4+ino2,:)), 'sheet3', 'E2'); %NO2
xlswrite('NHeptane Results 21% O2.xls',transpose(pv(4+ioh,:)), 'sheet3',
'F2'); %OH
xlswrite('NHeptane Results 21%
O2.xls',transpose(pv(4+ico2,:)), 'sheet3', 'G2'); %CO2
xlswrite('NHeptane Results 21%
O2.xls',transpose(pv(4+ih2o,:)), 'sheet3', 'H2'); %h2o
xlswrite('NHeptane Results 21% O2.xls',t_ign, 'sheet3', 'J2'); %Ignition
Delay

% Plot nitrogen results.

```

```
figure
plot(pv(1,:), pv(4+in2,:))
xlabel('Time (Seconds)')
ylabel('Mole Fraction N2')
```

12.3.3.4. ECN Modeling – Stoichiometric n-Heptane Mixtures with Major Species

This program determines the stoichiometric n-heptane ignition delay for various compositions (considering solely major species from the preburn). The mixtures from the differing institutions are all provided in the program, and must be uncommented to run for the different test conditions.

StoichNHeptane ECN.m

```
function Reactor_Ignition_UV_Heptane (gas)

close all
clear all

%% Use this program to combust the N_Heptane fuel in 15% O2 - ECN
Modeling

% This program uses the reduced n-heptane mechanism to determine the
% ignition delay.

%Generate N-heptane mechanism in cantera format.
% f = ck2cti

('UC_hep_mod_chem.inp','UC_hep_mod_therm.dat','UC_hep_mod_trans.dat');
g = importPhase('UC_hep_mod_chem.cti','UC_hep_mod_chem');
nsp=nSpecies(g)

% set the initial conditions

%To = 1000 K
% To=840;
% Po = 4.175025; % pressure
% Po=Po*10^6; %Convert to Pascal

%To=900 K
% To=735;
% Po=6*10^6;

%Based on Preburn
To = 740;
Po = 5.875*10^6;

%initial fuel-oxidizer mixture - mole fractions - Without Fuel
ihp = speciesIndex(g,'NC7H16')
io2=speciesIndex(g,'O2')
in2=speciesIndex(g,'N2')
ico2=speciesIndex(g,'CO2')
ih2o=speciesIndex(g,'H2O')
ino=speciesIndex(g,'NO')
```

```

ino2=speciesIndex(g,'NO2')
ioh=speciesIndex(g,'OH')
iar=speciesIndex(g,'AR')
xo = zeros(nsp,1); % mole fraction

%Conversion from mole fraction without fuel to mole fraction
%with Fuel. The Fuel is n-heptane C7H16, the lambda is 1 for this
%conversion only considers major species, O2, N2, CO2, H2O.

%% Standard 15% O2 Mixture - 38.3% EGR to match HC Ratio Diesel
%
% xo(io2) = 0.147982;
% xo(in2) = 0.766547;
% xo(ico2) = 0.037489;
% xo(ih2o) = 0.034529;
% xo(ihep) = 0.013452915;

%% Sandia 15% O2 Mixture
%
% xo(io2) = 0.147982;
% xo(in2) = 0.740897;
% xo(ico2) = 0.061166;
% xo(ih2o) = 0.035516;
% xo(ihep)= 0.013452915;

%% IFP 15% O2 mixture
%
% xo(io2) = 0.147982;
% xo(in2) = 0.70765;
% xo(ico2) = 0.01687;
% xo(ih2o) = 0.114045;
% xo(ihep) = 0.013452915;

%% Caterpillar 15% O2 Mixture

% xo(in2) = 0.838565;
% xo(io2) = 0.147982;
% xo(ihep) = 0.013452915;

%% Modified HCR - Diesel - 15% O2 (Kones)

% xo(in2) = 0.780063;
% xo(io2) = 0.147982;
% xo(ih2o) = 0.022691;
% xo(ico2) = 0.024466;
% xo(ihep) = 0.013452915;

%% Siebers SAE 96 15% O2 Mixture
% %
% xo(in2) = 0.743166;
% xo(ico2) = 0.060278;
% xo(ih2o) = 0.035121;
% xo(io2) = 0.147982;
% xo(ihep) = 0.013452915;

```

```

%% Eindhoven Mixture 15% O2

% xo(io2) = 0.147982;
% xo(ih2o) = 0.03157;
% xo(ihep) = 0.013452915;
% xo(ico2) = 0.063139;
% xo(iar) = 0.035811659;
% xo(in2) = 0.702422;

%% AIR

lambda=1;
y=16;
x=7;
R=y/x;
NFuel=1;
NRO2=lambda*(1+R/4);
NRN2=3.773*NRO2;
Ntotal=x*NRO2+x*NRN2+NFuel;
xo(io2)=x*NRO2/Ntotal;
xo(in2)=x*NRN2/Ntotal;
xo(ihep)=NFuel/Ntotal;

% 19.1 % o2 - partial EGR
% xo(io2)=.1912;
% xo(in2)=0.7727;
% xo(ih2o)=0.00986;
% xo(ico2)=.008628;
% xo(ihep)=0.01739;

%Set up the n-heptane mechnaism.
set(g,'T',To,'P',Po,'X',xo);

y0 = (enthalpy_mass(g)          % Specific internal energy (J/kg)
      1.0/density(g)            % Mass density (kg/m^3)
      massFractions(g));        % Mass fractions

options = odeset('RelTol',1.e-8,'AbsTol',1.e-8,'Stats','on');

t0 = cputime;

dt=1*10^-3;
t_max=.01;
time_interval=(0:dt:t_max);

out =
odel5s(@reactor_ode,time_interval,y0,options,g,@vdot,@area,@heatflux);

disp(('CPU time = ' num2str(cputime - t0)));

plotdata = output(out,g,To,Po, xo);

%%%%%%%%%%%%%%%%%%%%%%%%%%%%%%%%%%%%%%%%%%%%%%%%%%%%%%%%%%%%%%%%%%%%%%%%%%%%%%
% the functions below may be defined arbitrarily to set the reactor
% boundary conditions - the rate of change of volume, the heat

```

```

% flux, and the area.

% Rate of change of volume. Any arbitrary function may be implemented.
% Input arguments:
%   t      time
%   vol     volume
%   gas     ideal gas object

function v = vdot(t, vol, g)

% Choose constant volume or constant pressure

%constant pressure
%To=1000
%   v=1e5*(pressure(g)-4.175025*10^6);    % holds pressure close to Po

%To = 900
%   v=1e5*(pressure(g)-5.875*10^6);    % holds pressure close to Po

% heat flux (W/m^2).

function q = heatflux(t, g)

q=0;    % adiabatic

% surface area. Used only to compute heat transfer.
function a = area(t,vol)

a=0.048911614;

%%%%%%%%%%%%%%%%%%%%%%%%%%%%%%%%%%%%%%%%%%%%%%%%%%%%%%%%%%%%%%%%%%%%%%%%

% Since the solution variables used by the 'reactor' function are
% not necessarily those desired for output, this function is called
% after the integration is complete to generate the desired
% outputs.

function pv = output(s, g, To, Po, xo)
times = s.x;
soln = s.y;
(m n) = size(times);
pv = zeros(nSpecies(g) + 4, n);

set(g, 'T', To, 'P', Po);

for j = 1:n
    ss = soln(:,j);
    y = ss(3:end);          %ss(3:end): mass fraction
    mass = sum(y);
    u_mass = ss(1)/mass;    % ss(1): internal energy
    v_mass = ss(2)/mass;    % ss(2): volume
    setMassFractions(g, y);
    setState_UV(g, (u_mass v_mass));

```

```

    pv(1,j) = times(j); % second
    pv(2,j) = temperature(g);
    tt(j) = times(j);
    tt0(j) = temperature(g);
    pv(3,j) = density(g);
    pv(4,j) = pressure(g)/10^6;

    pv(5:end,j) = moleFractions(g); % mole fraction
end

ttl=transpose(tt);
tt2=transpose(tt0);

% calculate the ignition delay time
crit(1) = 0;
for j = 2:n
    crit(j) = (pv(2,j)-pv(2,j-1))/(pv(1,j)-pv(1,j-1));
end
crit
(xmax,kig) = max(crit);
t_ign = pv(1,kig);
%Displays ignition delay time in seconds
disp('Ignition Delay Time = ');
disp(t_ign);

% define each species
ih = speciesIndex(g, 'H');
ih2 = speciesIndex(g, 'H2');
ioh = speciesIndex(g, 'OH');
io2=speciesIndex(g, 'O2');
ih2o = speciesIndex(g, 'H2O');
iho2 = speciesIndex(g, 'HO2');
ich = speciesIndex(g, 'CH');
ich3 = speciesIndex(g, 'CH3');
ico = speciesIndex(g, 'CO');
ico2 = speciesIndex(g, 'CO2');
ihco = speciesIndex(g, 'HCO');
ic2H2 = speciesIndex(g, 'C2H2');
ino = speciesIndex(g, 'NO');
ino2 = speciesIndex(g, 'NO2');
in2=speciesIndex(g, 'N2');
ihcp=speciesIndex(g, 'NC7H16');

% plot the temperature, pressure and species mole fractions
figure(3);
subplot(2,1,1);
plot(pv(1,:),pv(2,:));
xlabel('time (s)');
ylabel('Temperature (K)');
title(('Final T = ' num2str(pv(2,end)) 'K ', ' Ign Time = ',num2str
(t_ign*1000), 'ms'));
subplot(2,1,2);
plot(pv(1,:),pv(4,:));
xlabel('time (s)');

```

```

ylabel('Pressure (MPa)');
title(('Final P = ' num2str(pv(4,end)) ' MPa'));

% Should match desired starting temperature (K)
Tmin=min(pv(2,:))

```

12.4. Image Processing & Data Analysis Programs

This appendix includes all processing used in the analysis of the experimental tests, including image processing programs along with data analysis programs. All programs are m-files which are run in Matlab to provide the necessary output results. These programs are commented to understand the steps taken.

12.4.1. Nonvaporizing (Nitrogen) Spray Image Processing Program

The nonvaporizing nitrogen sprays are processed using the following program to determine penetration and cone angle at both 60% penetration distance and 45 nozzle diameters, using a curve fit procedure.

N2ImageProcessing CH6.m

```

%% N2 Back Scattering (Liquid Phase) Image Processing Program
% Jaclyn Nesbitt
% January 17, 2011

% Use this program to determine penetration and cone angle of the
liquid
% phase sprays.
% Spray characteristics are calculated relative to the spray hole,
which
% is offset 1.5 mm from the injector tip.

%% Setup workspace

clear all;
close all;
clc;

%% Get information about test to process, change to correct directory.

DIRparent = ('\\mtucifs\dfshome\jenesbit\Desktop\\DieselSprayTesting -
Additional August 2010\');
Date = input('Enter Date in YYYYMMDD Format:', 's');
Time = input('Enter Test Time in HHMM Format:', 's');
NumPlumes = '8';
StartFrame = input('Enter First Frame to Process:', 's');
EndFrame = input('Enter Last Frame to Process:', 's');
Factor =1;
FolderName = strcat(Time, '_C001H001S0001');

```

```

dir_name = ((DIRparent Date '\\' FolderName));

filename = strcat(Time, '_C001H001S0001.avi');

cd (dir_name)

%% Read in Movie

mov = aviread(filename);

% Store Normalized Movie in NMOV
N = size(mov,2);
for i=1 : N;
    nmov( i).cdata = single( mov( i).cdata);
end

% Put orginial movie into single variable.
clear mov
mov = nmov;

%% Background Subtraction for Image Processing Preparation

Background = mov(1,1).cdata;

for i = 1:N-1;

Frame(i).cdata = imsubtract(Background, mov(1,i+1).cdata);

end

%% Find Injector Tip using Background Image

% Uncomment the below set of code to display background image.
% figure;
% imagesc(Background);
% colormap(gray);
% daspect([1 1 1])

% Scaled and adjust the background image to improve contrast.
BackgroundScaled = Background/max(max(Background));
BackgroundAdjusted = imadjust(BackgroundScaled);

% Apply multiplier to account for variations in SNR / contrast ratio
for
% different tests (due to not calibrating camera).

Multiplier = 1.75;

if strcmp(Date, '20100830') == 1
    Multiplier = 2;
end

% Convert the background image to Black and White, Apply Blob
Processing

```



```

BWBackground = im2bw(BackgroundAdjusted,
Multiplier*graythresh(BackgroundAdjusted));

BackgroundBlob = bwlabel(BWBackground,8);

ColoredBlobs = label2rgb(BackgroundBlob, 'hsv', 'k', 'shuffle');

%Uncomment to plot blobs from background resulting from blob analysis.
% figure
% imagesc(ColoredBlobs);
% daspect([1 1 1])

Stats1 = regionprops(BackgroundBlob, 'centroid', 'area', 'extrema');

Area1 = (Stats1.Area);
Centroid1 = (Stats1.Centroid);

% Use results of blob analysis to define injector tip location.

LargeAreas = find(Area1 > 100);
gg=LargeAreas(1);
for gg = 1: size(LargeAreas,2)
    LocX(gg) = Centroid1(LargeAreas(gg)*2-1)-size(Background,2)/2;
    LocY(gg) = Centroid1(LargeAreas(gg)*2)-size(Background,1)/2;
    DiffLoc(gg) = sqrt(LocX(gg)^2+LocY(gg)^2);
end
AreaIndex1 = LargeAreas(find(DiffLoc == min(DiffLoc)));
Extremal = (Stats1.Extrema);

CentroidIndexX = Centroid1(AreaIndex1*2-1);
CentroidIndexY = Centroid1(AreaIndex1*2);

DiffXX = abs(size(Background,2)/2-CentroidIndexX);
DiffYY = abs(size(Background,1)/2-CentroidIndexY);

AbsDiff = sqrt(DiffXX.^2+DiffYY.^2);

Index = find(AbsDiff == min(AbsDiff));

YTop = (Extremal(1, AreaIndex1(Index)*2)+Extremal(2,
AreaIndex1(Index)*2))/2;
YBottom =
(Extremal(5,AreaIndex1(Index)*2)+Extremal(6,AreaIndex1(Index)*2))/2;
TipIndexY = round((YTop+YBottom)/2);
XTop = (Extremal(1,AreaIndex1(Index)*2-
1)+Extremal(2,AreaIndex1(Index)*2-1))/2;
XBottom = (Extremal(5,AreaIndex1(Index)*2-
1)+Extremal(6,AreaIndex1(Index)*2-1))/2;
TipIndexX = round((XTop+XBottom)/2);

clear XBottom YBottom XTop YTop AbsDiff Index
clear DiffXX DiffYY CentroidIndexY Centroid1 AreaIndex1 CentroidIndexX
clear Extremal Stats1 AreaIndex1 LocX LocY gg DiffLoc LargeAreas Area1
clear BackgroundBlobs ColoredBlobs

```

```

clear Multiplier BackgroundScaled

%% Process Spray Images - frame by frame
% Determine penetration and cone angle (plume to plume and average
values)

xx = str2num(StartFrame)-1;

Total = size(mov,2);
PenetrationTotal = zeros(str2num(NumPlumes)+1, size(mov,2)-1);
AngleTotal = zeros(str2num(NumPlumes)+1, size(mov,2)-1);
DiffX(Total-1).Location = '';
DiffY(Total-1).Location = '';

for xx = str2num(StartFrame)-1:str2num(EndFrame)
Image = -Frame(xx).cdata;

    % Prepare Image for Rotation, Center Injector Tip
    ImageLarge = zeros(floor(1.3*size(Image,1)),
floor(1.3*size(Image,2)));
    IXCenter = floor(size(ImageLarge,2)/2);
    IYCenter = floor(size(ImageLarge,1)/2);
    DiffX(xx).Location = floor(TipIndexX - IXCenter);
    DiffY(xx).Location = floor(TipIndexY - IYCenter);

ImageLarge(abs(DiffY(xx).Location)+1:abs(DiffY(xx).Location)+size(Image
,1), abs(DiffX(xx).Location)+1:abs(DiffX(xx).Location)+1+size(Image,2)-
1) = Image;

    % Rotate image such that plumes travel left to right,
    % exiting horizontally from the injector.

AngleRotate = 360/str2num(NumPlumes);
if strcmp(NumPlumes, '8') == 1
    % Apply an offset to account for slight offset in injector
    % horizontal location even before rotation
    StartAngle = -3;
end

% Create a structure of data .... for the total number of plumes.

Plume(str2num(NumPlumes)).Intensity = '';
Plume(str2num(NumPlumes)).Shifted = '';
Plume(str2num(NumPlumes)).Scaled = '';
Plume(str2num(NumPlumes)).BW = '';
Plume(str2num(NumPlumes)).Blob = '';
Plume(str2num(NumPlumes)).Spray = '';
Plume(str2num(NumPlumes)).Boundary = '';
Plume(str2num(NumPlumes)).Penetration = '';
Plume(str2num(NumPlumes)).Theta = '';
Plume(str2num(NumPlumes)).AngleX = '';
Plume(str2num(NumPlumes)).AngleNegY = '';
Plume(str2num(NumPlumes)).AnglePosY = '';
Plume(str2num(NumPlumes)).EvaluationPositive = '';

```

```

Plume(str2num(NumPlumes)).EvaluationNegative = '';
Plume(str2num(NumPlumes)).AY = '';
Plume(str2num(NumPlumes)).AX = '';

% Process each spray plume of the given set of frames
ii = 1;
for ii = 1:str2num(NumPlumes);

    Plume(ii).Intensity =
imrotate(ImageLarge,StartAngle+AngleRotate*(ii-1));
    Offset = 40;

    Plume(ii).AX = round(size(Plume(ii).Intensity,2)/2);
    Plume(ii).AY = round(size(Plume(ii).Intensity,1)/2);

    Plume(ii).Shifted = Plume(ii).Intensity(Plume(ii).AY-
Offset:Plume(ii).AY+Offset, Plume(ii).AX:end);

    % Apply Mask to Isolate Adjacent Spray plumes
    VX = ceil((1 size(Plume(ii).Shifted,1)/(2*tand(AngleRotate
- 25)) size(Plume(ii).Shifted,2) size(Plume(ii).Shifted,2)
size(Plume(ii).Shifted,1)/(2*tand(AngleRotate - 25)))));
    VY = ceil((size(Plume(ii).Shifted,1)/2
size(Plume(ii).Shifted,1) size(Plume(ii).Shifted,1) 1 1));

    BW = roipoly(Plume(ii).Shifted,VX,VY);
    (I, J) = find(BW ==0);
    kk =1;

    for kk = 1:size(I,1)
        Plume(ii).Shifted(I(kk),J(kk)) = 0;
    end

    Plume(ii).Scaled = Plume(ii).Shifted /
max(max(Plume(ii).Shifted));

    % Threshold Image to Black and White and Apply Blob
Analysis.
    Threshold = 0.5*graythresh(Plume(ii).Scaled);
    Plume(ii).BW = im2bw(Plume(ii).Scaled, Factor*Threshold);
    Plume(ii).Blob = bwlabel(Plume(ii).BW,8);

    Stats = regionprops(Plume(ii).Blob, 'area', 'extrema',
'centroid');
    Area = (Stats.Area);
    Extrema= (Stats.Extrema);
    Centroid = (Stats.Centroid);
    AreaIndex = find(Area == max(Area));

    if size(AreaIndex,2) > 1
        CenterY = Centroid(AreaIndex*2);
        Differences = CenterY-size(Plume(ii).Spray,1)/2;
        CorrectIndex = find(abs(Differences) ==
min(abs(Differences)));
        AreaIndex = AreaIndex(1);

```

```

end

% Define the spray in black and white, removing noise and
all
% adjacent spray plumes.

Plume(ii).Spray = ismember(Plume(ii).Blob, AreaIndex);

Centerline(ii) = floor(Centroid(AreaIndex*2));
Lead = max(find(Plume(ii).Spray(Centerline(ii),:)==1));
TFLead = isempty(Lead);

% Determine spray boundary, use this to determine
penetration
% and cone angle.

if TFLead == 0
    Plume(ii).Boundary = bwtraceboundary(Plume(ii).Spray,
    (Centerline(ii), Lead), 'S');

%           Uncomment this set of code to plot the spray boundary
overlaid
%           on the original spray image
%           figure;
%           imagesc(Plume(ii).Shifted)
%           colormap(gray)
%           daspect([1 1 1])
%           hold on
%           plot(Plume(ii).Boundary(:,2), Plume(ii).Boundary(:,1), 'y-
')

%           Define Image Scaling - based on image size resolution and
scale
%           by cosine of 15 degrees to account for off-axis injector
spray
%           plume orientation

Scaling = 0.18/cosd(15); % mm/pixel

% Calculation penetration
OffsetHole = 1.5/(Scaling*cosd(15)); % Pixels - Distance
from injector tip center to inj hole.
Penetration = arrayfun(@(x) max(x.Boundary), Plume,
'UniformOutput', false); %
    Plume(ii).Penetration = Penetration(:,ii)(2)*Scaling - 1.5;
% Subtract off difference in penetration based on inj tip definition

%% Calculate Cone Angle

% First find spray width in xx*Do increments
Do = 0.14; % mm

% Determine spray edges based on spray boundary over the region of
interest

```

```

% for the cone angle processing (to maximum boundary location).

MaxKK = max(Plume(ii).Boundary(:,2));
MinKK = min(Plume(ii).Boundary(:,2));
kk = MinKK;
for kk = MinKK : MaxKK
    EdgeW = Plume(ii).Boundary(find(Plume(ii).Boundary(:,2) == kk),1);
    TopEdgeW(kk,ii) = max(EdgeW);
    BotEdgeW(kk,ii) = min(EdgeW);
    Widths(kk,ii) = abs(TopEdgeW(kk,ii) - BotEdgeW(kk,ii) );
end

MaxWidth(ii) = max(Widths(:,ii));
CorrespondMaxXDist(ii) = round(max(find(Widths(:,ii) == MaxWidth(ii)))-
OffsetHole); % Applied Offset to account for off center holes.
CorrespondMaxXDistReference(ii)=max(find(Widths(:,ii) ==
MaxWidth(ii)));
TopMaxWidth(ii) = TopEdgeW(max(find(Widths(:,ii) == MaxWidth(ii))),ii);
BotMaxWidth(ii) = BotEdgeW(max(find(Widths(:,ii) == MaxWidth(ii))),ii);
%% DEFINE CONE ANGLE METHODS

% Method 1 -- Calculate Cone Angle at 60% Pen, CF Method
DistanceCalcAtSixty(ii) =
round(0.6*Plume(ii).Penetration/(Scaling*cosd(15))); % Pixels
PenReferenceSixty(ii) = round(DistanceCalcAtSixty(ii)+
1.5/(Scaling*cosd(15)));

if PenReferenceSixty(ii) > MaxKK
    Plume(ii).ThetaM1Star = NaN;
else
    Plume(ii).AngleX1S = (MinKK:1:PenReferenceSixty(ii));
    Plume(ii).AngleY1STop =
(TopEdgeW(MinKK:1:PenReferenceSixty(ii),ii)');
    Plume(ii).AngleY1SBot =
(BotEdgeW(MinKK:1:PenReferenceSixty(ii),ii)');

    AngleXSixty = Plume(ii).AngleX1S(:);
    AngleNegYSixty = Plume(ii).AngleY1SBot(:);
    AnglePosYSixty = Plume(ii).AngleY1STop(:);

% Linear Curve Fit Spray Edge - Top and Bottom
% Force curve fit through Injector Origin

if size(AngleXSixty,1) >= 2
    ok6_ = isfinite(AngleXSixty) & isfinite(AngleNegYSixty);
    st6_ = (0.9746908242292236 );
    ft6_ = fittype('m*(x-8.333)+41',...
    'dependent',{'y'},'independent',{'x'},...
    'coefficients',{'m'});

% Fit this model using new data
cf6_ =
fit(AngleXSixty(ok6_),AngleNegYSixty(ok6_),ft6_,'Startpoint',st6_);

EvaluationNegativeSixty = feval(cf6_, (OffsetHole AngleXSixty'));

```

```

ok16_ = isfinite(AngleXSixty) & isfinite(AnglePosYSixty);

st16_ = (0.9746908242292236 );
ft16_ = fittype('m*(x-8.333)+41',...
    'dependent',{'y'}, 'independent',{'x'},...
    'coefficients',{'m'});

% Fit this model using new data
cf16_ =
fit(AngleXSixty(ok16_),AnglePosYSixty(ok16_),ft16_,'Startpoint',st16_);
EvaluationPositiveSixty = feval(cf16_,(OffsetHole AngleXSixty));

YNegPenSixty = feval(cf16_, round(PenReferenceSixty(ii)));
YPosPenSixty = feval(cf6_, round(PenReferenceSixty(ii)));

PositiveThetaSixty = atan((YPosPenSixty-
(Offset+1))/(DistanceCalcAtSixty(ii)))*180/pi;
NegativeThetaSixty = atan((YNegPenSixty-
(Offset+1))/(DistanceCalcAtSixty(ii)))*180/pi;

Plume(ii).ThetaM1Star =
abs(PositiveThetaSixty)+abs(NegativeThetaSixty);
else
    Plume(ii).ThetaM1Star = NaN;

end
end
%% Method 2 -- Calculate Cone Angle at 45*Do, CF Method
DistanceCalcAtFortyFive(ii) = round(45*Do/(Scaling*cosd(15))); % Pixels
PenReferenceFortyFive(ii) = round(DistanceCalcAtFortyFive(ii)+
1.5/(Scaling*cosd(15)));

if PenReferenceFortyFive(ii) > MaxKK
    Plume(ii).ThetaM2Star = NaN;
else
    Plume(ii).AngleX6S = (MinKK:1:PenReferenceFortyFive(ii));
    Plume(ii).AngleY6STop =
(TopEdgeW(MinKK:1:PenReferenceFortyFive(ii),ii)');
    Plume(ii).AngleY6SBot =
(BotEdgeW(MinKK:1:PenReferenceFortyFive(ii),ii)');

    AngleXFortyFive = Plume(ii).AngleX6S(:);
    AngleNegYFortyFive = Plume(ii).AngleY6SBot(:);
    AnglePosYFortyFive = Plume(ii).AngleY6STop(:);

% Linear Curve Fit Spray Edge - Top and Bottom
% Force curve fit through Injector Origin

if size(AngleXFortyFive,1) >= 2
ok_ = isfinite(AngleXFortyFive) & isfinite(AngleNegYFortyFive);
st_ = (0.9746908242292236 );
ft_ = fittype('m*(x-8.333)+41',...
    'dependent',{'y'}, 'independent',{'x'},...

```

```

        'coefficients',{'m'});

% Fit this model using new data
cf_ =
fit(AngleXFortyFive(ok_),AngleNegYFortyFive(ok_),ft_,'Startpoint',st_);

EvaluationNegativeFortyFive = feval(cf_, (OffsetHole
AngleXFortyFive'));
ok1_ = isfinite(AngleXFortyFive) & isfinite(AnglePosYFortyFive);

st1_ = (0.9746908242292236 );
ft1_ = fittype('m*(x-8.333)+41',...
'dependent',{'y'},'independent',{'x'},...
'coefficients',{'m'});

% Fit this model using new data
cf1_ =
fit(AngleXFortyFive(ok1_),AnglePosYFortyFive(ok1_),ft1_,'Startpoint',st
1_);
EvaluationPositiveFortyFive = feval(cf1_,(OffsetHole
AngleXFortyFive'));
YNegPenFortyFive = feval(cf1_, round(PenReferenceFortyFive(ii)));
YPosPenFortyFive = feval(cf_, round(PenReferenceFortyFive(ii)));

PositiveThetaFortyFive = atan((YPosPenFortyFive-
(Offset+1))/(DistanceCalcAtFortyFive(ii)))*180/pi;
NegativeThetaFortyFive = atan((YNegPenFortyFive-
(Offset+1))/(DistanceCalcAtFortyFive(ii)))*180/pi;

Plume(ii).ThetaM2Star =
abs(PositiveThetaFortyFive)+abs(NegativeThetaFortyFive);
else
    Plume(ii).ThetaM2Star = NaN;

end

end

subplot(4,2,ii);
drawnow
imagesc(Plume(ii).Shifted)
colormap(gray)
daspect([1 1 1])
hold on
plot((Plume(ii).Penetration+1.5)/Scaling, Offset+1, 'mo',
'MarkerFaceColor','m')
hold on
    if isnan(Plume(ii).ThetaM1Star) == 0
        plot(AngleXSixty, AnglePosYSixty, 'ro', (OffsetHole AngleXSixty'),
EvaluationPositiveSixty, 'r-')
        hold on
        plot(AngleXSixty, AngleNegYSixty, 'ro', (OffsetHole AngleXSixty'),
EvaluationNegativeSixty, 'r-')
        hold on

```

```

        plot((PenReferenceSixty(ii) PenReferenceSixty(ii)), (1
size(Plume(ii).Shifted,1)), 'r-');
    end
        if isnan(Plume(ii).ThetaM2Star) == 0
            hold on
                plot(AngleXFortyFive, AnglePosYFortyFive, 'go', (OffsetHole
AngleXFortyFive'), EvaluationPositiveFortyFive, 'g-')
            hold on
                plot(AngleXFortyFive, AngleNegYFortyFive, 'go', (OffsetHole
AngleXFortyFive'), EvaluationNegativeFortyFive, 'g-')
            hold on
                plot((PenReferenceFortyFive(ii) PenReferenceFortyFive(ii)), (1
size(Plume(ii).Shifted,1)), 'g-');
        end
            title({'Original Spray Image with Curve-Fitted Cone Angle
Edges Determined Via XX*Sigma'; 'Green - FiftyPercPen, Red - 45Do, Pink
Dot - Spray Penetration'})

% Calculate Cone Angles from the Curve Fit Results

end

        end

        %% Collect Results, Put into Single Array

PenetrationPlume = arrayfun(@(x) mean(x.Penetration), Plume);
AvgPenetration = mean(PenetrationPlume);
PenetrationSpray(:,xx) = (PenetrationPlume AvgPenetration);

% CA at 60% Pen
ThetaPlumeM1Star = arrayfun(@(x) mean(x.ThetaM1Star), Plume);
AvgThetaM1Star = mean(ThetaPlumeM1Star);
ThetaSprayM1Star(:,xx) = (ThetaPlumeM1Star AvgThetaM1Star);

% CA at 45 Do
ThetaPlumeM2Star = arrayfun(@(x) mean(x.ThetaM2Star), Plume);
AvgThetaM2Star = mean(ThetaPlumeM2Star);
ThetaSprayM2Star(:,xx) = (ThetaPlumeM2Star AvgThetaM2Star);

xx = xx+1;

clear ConeT ConeB SixtyPercPen
clear Plume
end

```

12.4.2. Vaporizing (0% Oxygen) Spray Image Processing Program

The vaporizing (0% oxygen) spray images are processed to determine liquid length, and cone angle at both 60% of the liquid length and 45 nozzle diameters. The cone angle results are not included in discussions here based on reduced resolution and small spray width, therefore limited accuracy in these measurements based on the current optical setup.

ZeroPercO2ImageProcessing CH6.m

```
%% 0% O2 Back Scattering (Liquid Phase) Image Processing Program
% Jaclyn Nesbitt
% January 14, 2011

% Use this program to determine penetration and cone angle of the
liquid
% phase sprays.
% Injector spray characteristics referenced relative to injector
nozzle
% hole, offset 1.5 mm from injector tip.
% CA method - at 60% Pen, CF and at 45Do - CF (constant location)

%% Setup workspace

clear all;
close all;
clc;

%% Get information about test, change to correct directory.

DIRparent = ('\\mtucifs\dfshome\jenesbit\Desktop\\DieselSprayTesting -
Additional August 2010\');

Date = input('Enter Date in YYYYMMDD Format:', 's');
Time = input('Enter Test Time in HHMM Format:', 's');
NumPlumes = '8';
StartFrame = input('Enter First Frame to Process:', 's');
EndFrame = input('Enter Last Frame to Process:', 's');

Factor = 1;

FolderName = strcat(Time, '_C001H001S0001');

dir_name = ((DIRparent Date '\\' FolderName));

filename = strcat(Time, '_C001H001S0001.avi');

cd (dir_name)

%% Read in Movie

mov = aviread(filename);

% Store Normalized Movie in NMOV
N = size(mov,2);
for i=1 : N;
    nmov( i).cdata = single( mov( i).cdata);
end

% Put orginial movie into single variable.
clear mov
mov = nmov;
```

```

%% Background Subtraction;

Background = mov(1,1).cdata;

for i = 1:N-1;

Frame(i).cdata = imsubtract(Background, mov(1,i+1).cdata);

end

%% Find Injector Tip using Background Image

% Uncomment the set of code below to display background image.
% figure;
% imagesc(Background);
% colormap(gray);
% daspect([1 1 1])

% Scale and adjust background image.
BackgroundScaled = Background/max(max(Background));
BackgroundAdjusted = imadjust(BackgroundScaled);

% Apply multiplier to account for variations in SNR / contrast ratio
% for different tests (due to not calibrating camera).
Multiplier = 1.75;

if strcmp(Time, '1657') == 1
    Multiplier = 2;
end

if strcmp(Time, '1741') == 1
    Background = mov(1,2).cdata;
    BackgroundScaled = Background/max(max(Background));
    BackgroundAdjusted = imadjust(BackgroundScaled);
    Multiplier = 1.55;
end

% Convert image to black and white, process with blob analysis
BWBackground = im2bw(BackgroundAdjusted,
Multiplier*graythresh(BackgroundAdjusted));
BackgroundBlob = bwlabel(BWBackground,8);
ColoredBlobs = label2rgb(BackgroundBlob, 'hsv', 'k', 'shuffle');

% Uncomment to plot blobs from background resulting from blob analysis.
% figure
% imagesc(ColoredBlobs);
% daspect([1 1 1])

Stats1 = regionprops(BackgroundBlob, 'centroid', 'area', 'extrema');

Area1 = (Stats1.Area);
Centroid1 = (Stats1.Centroid);

% Isolate spray ROI from background noise

```

```

LargeAreas = find(Areal > 100);
gg=LargeAreas(1);
for gg = 1: size(LargeAreas,2)
    LocX(gg) = Centroid1(LargeAreas(gg)*2-1)-size(Background,2)/2;
    LocY(gg) = Centroid1(LargeAreas(gg)*2)-size(Background,1)/2;
    DiffLoc(gg) = sqrt(LocX(gg)^2+LocY(gg)^2);
end
AreaIndex1 = LargeAreas(find(DiffLoc == min(DiffLoc)));
Extremal1 = (Stats1.Extrema);

CentroidIndexX = Centroid1(AreaIndex1*2-1);
CentroidIndexY = Centroid1(AreaIndex1*2);

DiffXX = abs(size(Background,2)/2-CentroidIndexX);
DiffYY = abs(size(Background,1)/2-CentroidIndexY);

AbsDiff = sqrt(DiffXX.^2+DiffYY.^2);

Index = find(AbsDiff == min(AbsDiff));

% Define the injector tip location.
YTop = (Extremal1(1, AreaIndex1(Index)*2)+Extremal1(2,
AreaIndex1(Index)*2))/2;
YBottom =
(Extremal1(5,AreaIndex1(Index)*2)+Extremal1(6,AreaIndex1(Index)*2))/2;
TipIndexY = round((YTop+YBottom)/2);
XTop = (Extremal1(1,AreaIndex1(Index)*2-
1)+Extremal1(2,AreaIndex1(Index)*2-1))/2;
XBottom = (Extremal1(5,AreaIndex1(Index)*2-
1)+Extremal1(6,AreaIndex1(Index)*2-1))/2;
TipIndexX = round((XTop+XBottom)/2);

clear XBottom YBottom XTop YTop AbsDiff Index
clear DiffXX DiffYY CentroidIndexY Centroid1 AreaIndex1 CentroidIndexX
clear Extremal1 Stats1 AreaIndex1 LocX LocY gg DiffLoc LargeAreas Areal
clear BackgroundBlobs ColoredBlobs
clear Multiplier BackgroundScaled

%% Process Spray Images - frame by frame
% Determine penetration and cone angle (plume to plume and average
values)

xx = str2num(StartFrame)-1;

Total = size(mov,2);
PenetrationTotal = zeros(str2num(NumPlumes)+1, size(mov,2)-1);
AngleTotal = zeros(str2num(NumPlumes)+1, size(mov,2)-1);
DiffX(Total-1).Location = '';
DiffY(Total-1).Location = '';

for xx = str2num(StartFrame)-1:str2num(EndFrame)

    % Prepare image frames for processing.
    Image = -Frame(xx).cdata;

```

```

    ImageLarge = zeros(floor(1.3*size(Image,1)),
    floor(1.3*size(Image,2)));
    IXCenter = floor(size(ImageLarge,2)/2);
    IYCenter = floor(size(ImageLarge,1)/2);
    DiffX(xx).Location = floor(TipIndexX - IXCenter);
    DiffY(xx).Location = floor(TipIndexY - IYCenter);

ImageLarge(abs(DiffY(xx).Location)+1:abs(DiffY(xx).Location)+size(Image
,1), abs(DiffX(xx).Location)+1:abs(DiffX(xx).Location)+1+size(Image,2)-
1) = Image;

    % Rotate image such that plumes travel left to right,
    % exiting horizontally from the injector.
    AngleRotate = 360/str2num(NumPlumes);
    if strcmp(NumPlumes, '8') == 1
        StartAngle = -3;
    end

    % Create a structure for data analysis.... for the total number of
    plumes.

    Plume(str2num(NumPlumes)).Intensity = '';
    Plume(str2num(NumPlumes)).Shifted = '';
    Plume(str2num(NumPlumes)).Scaled = '';
    Plume(str2num(NumPlumes)).BW = '';
    Plume(str2num(NumPlumes)).Blob = '';
    Plume(str2num(NumPlumes)).Spray = '';
    Plume(str2num(NumPlumes)).Boundary = '';
    Plume(str2num(NumPlumes)).Penetration = '';
    Plume(str2num(NumPlumes)).Theta = '';
    Plume(str2num(NumPlumes)).AngleX = '';
    Plume(str2num(NumPlumes)).AngleNegY = '';
    Plume(str2num(NumPlumes)).AnglePosY = '';
    Plume(str2num(NumPlumes)).EvaluationPositive = '';
    Plume(str2num(NumPlumes)).EvaluationNegative = '';
    Plume(str2num(NumPlumes)).AX = '';
    Plume(str2num(NumPlumes)).AY = '';

    ii = 1;
    for ii = 1:str2num(NumPlumes);

        % Rotate image
        Plume(ii).Intensity =
imrotate(ImageLarge,StartAngle+AngleRotate*(ii-1));
        Offset = 20;

        Plume(ii).AX = round(size(Plume(ii).Intensity,2)/2);
        Plume(ii).AY = round(size(Plume(ii).Intensity,1)/2);

        % Isolate spray plume of interest
        Plume(ii).Shifted = Plume(ii).Intensity(Plume(ii).AY-
Offset:Plume(ii).AY+Offset, Plume(ii).AX:end);

        % Apply mask to remove adjacent plumes.

```

```

        VX = ceil((1 size(Plume(ii).Shifted,1)/(2*tand(AngleRotate
- 25)) size(Plume(ii).Shifted,2) size(Plume(ii).Shifted,2)
size(Plume(ii).Shifted,1)/(2*tand(AngleRotate - 25)))));
        VY = ceil((size(Plume(ii).Shifted,1)/2
size(Plume(ii).Shifted,1) size(Plume(ii).Shifted,1) 1 1));

        BW = roipoly(Plume(ii).Shifted,VX,VY);
        (I, J) = find(BW ==0);
        kk =1;

        for kk = 1:size(I,1)
            Plume(ii).Shifted(I(kk),J(kk)) = 0;
        end

        % Convert Image to Black and White, Apply blob analysis on
the
        % image

        Plume(ii).IntensitySum = Plume(ii).Shifted;
        Plume(ii).Scaled = Plume(ii).Shifted /
max(max(Plume(ii).Shifted));
        Threshold = 0.5*graythresh(Plume(ii).Scaled);
        Plume(ii).BW = im2bw(Plume(ii).Scaled, Factor*Threshold);
        Plume(ii).Blob = bwlabel(Plume(ii).BW,4);

        Stats = regionprops(Plume(ii).Blob, 'area', 'extrema',
'centroid');
        Area = (Stats.Area);
        Extrema= (Stats.Extrema);
        Centroid = (Stats.Centroid);
        AreaIndex = find(Area == max(Area));

        if size(AreaIndex,2) > 1
            CenterY = Centroid(AreaIndex*2);
            Differences = CenterY-size(Plume(ii).Spray,1)/2;
            CorrectIndex = find(abs(Differences) ==
min(abs(Differences)));
            AreaIndex = AreaIndex(1);
        end

        % Prepare image with all background noise removed.
        Plume(ii).Spray = ismember(Plume(ii).Blob, AreaIndex);

        % Define scaling in mm/pixel, scaled by cosine of 15
degrees to
        % account for off-axis spray plume orientation
        Scaling = 0.18/cosd(15);

        OffsetHole = 1.5/(Scaling*cosd(15)); % Pixels - Distance
from injector tip center to inj hole.

        Centerline(ii) = round(Centroid(AreaIndex*2));
        Lead = max(find(Plume(ii).Spray(Centerline(ii),:)==1));
        TFLead = isempty(Lead);

```

```

        % Determine spray boundary, use this to determine penetration
and
        % cone angle.
        if TFLead == 0

            Plume(ii).Boundary = bwtraceboundary(Plume(ii).Spray,
(Centerline(ii), Lead), 'S');

            Penetration = arrayfun(@(x) max(x.Boundary), Plume,
'UniformOutput', false);
            Plume(ii).Penetration = Penetration(:,ii)(2)*Scaling -
1.5;% Subtract off difference in penetration based on inj tip
definition

%% Calculate Cone Angle

% First find spray width in xx*Do increments
Do = 0.14; % mm

MaxKK = max(Plume(ii).Boundary(:,2));
MinKK = 30; % Define starting region for considering spray cone angle -
>
% don't consider the region before the ceramic based on high noise.
if min(Plume(ii).Boundary(:,2)) > MinKK
    MinKK = min(Plume(ii).Boundary(:,2));
end
kk = MinKK;

if MinKK < MaxKK
% Define spray widths over ROI
for kk = MinKK : MaxKK

    EdgeW = Plume(ii).Boundary(find(Plume(ii).Boundary(:,2) == kk),1);
    TopEdgeW(kk,ii) = max(EdgeW);
    BotEdgeW(kk,ii) = min(EdgeW);
    Widths(kk,ii) = abs(TopEdgeW(kk,ii) -BotEdgeW(kk,ii) );
end

%% DEFINE CONE ANGLE METHODS

% Method 1 -- Calculate Cone Angle at 60% Pen, CF Method
DistanceCalcAtSixty(ii) =
round(0.6*Plume(ii).Penetration/(Scaling*cosd(15))); % Pixels
PenReferenceSixty(ii) = round(DistanceCalcAtSixty(ii)+
1.5/(Scaling*cosd(15)));

if PenReferenceSixty(ii) > MaxKK
    Plume(ii).ThetaM1Star = NaN;
else
    Plume(ii).AngleX1S = (MinKK:1:PenReferenceSixty(ii));
    Plume(ii).AngleY1STop =
(TopEdgeW(MinKK:1:PenReferenceSixty(ii),ii)');
    Plume(ii).AngleY1SBot =
(BotEdgeW(MinKK:1:PenReferenceSixty(ii),ii)');

```

```

    AngleXSixty = Plume(ii).AngleX1S(:);
    AngleNegYSixty = Plume(ii).AngleY1SBot(:);
    AnglePosYSixty = Plume(ii).AngleY1STop(:);

% Linear Curve Fit Spray Edge - Top and Bottom
% Force curve fit through Injector Origin

if size(AngleXSixty,1) >= 2
    ok6_ = isfinite(AngleXSixty) & isfinite(AngleNegYSixty);
    st6_ = (0.9746908242292236 );
    ft6_ = fittype('m*(x-8.333)+21',...
        'dependent',{'y'}, 'independent',{'x'},...
        'coefficients',{'m'});

% Fit this model using new data
cf6_ =
fit(AngleXSixty(ok6_),AngleNegYSixty(ok6_),ft6_,'Startpoint',st6_);

EvaluationNegativeSixty = feval(cf6_, (OffsetHole AngleXSixty'));
ok16_ = isfinite(AngleXSixty) & isfinite(AnglePosYSixty);

st16_ = (0.9746908242292236 );
ft16_ = fittype('m*(x-8.333)+21',...
    'dependent',{'y'}, 'independent',{'x'},...
    'coefficients',{'m'});

% Fit this model using new data
cf16_ =
fit(AngleXSixty(ok16_),AnglePosYSixty(ok16_),ft16_,'Startpoint',st16_);
EvaluationPositiveSixty = feval(cf16_, (OffsetHole AngleXSixty'));

YNegPenSixty = feval(cf16_, round(PenReferenceSixty(ii)));
YPosPenSixty = feval(cf6_, round(PenReferenceSixty(ii)));

PositiveThetaSixty = atan((YPosPenSixty-
    (Offset+1))/(DistanceCalcAtSixty(ii)))*180/pi;
NegativeThetaSixty = atan((YNegPenSixty-
    (Offset+1))/(DistanceCalcAtSixty(ii)))*180/pi;

Plume(ii).ThetaM1Star =
abs(PositiveThetaSixty)+abs(NegativeThetaSixty);
else
    Plume(ii).ThetaM1Star = NaN;
end
end

% Method 2 -- Calculate Cone Angle at 45*Do, CF Method
DistanceCalcAtFortyFive(ii) = round(45*Do/(Scaling*cosd(15))); % Pixels
PenReferenceFortyFive(ii) = round(DistanceCalcAtFortyFive(ii)+
1.5/(Scaling*cosd(15)));

if PenReferenceFortyFive(ii) > MaxKK
    Plume(ii).ThetaM2Star = NaN;
else

```

```

    Plume(ii).AngleX6S = (MinKK:1:PenReferenceFortyFive(ii));
    Plume(ii).AngleY6STop =
(TopEdgeW(MinKK:1:PenReferenceFortyFive(ii),ii)');
    Plume(ii).AngleY6SBot =
(BotEdgeW(MinKK:1:PenReferenceFortyFive(ii),ii)');

    AngleXFortyFive = Plume(ii).AngleX6S(:);
    AngleNegYFortyFive = Plume(ii).AngleY6SBot(:);
    AnglePosYFortyFive = Plume(ii).AngleY6STop(:);

% Linear Curve Fit Spray Edge - Top and Bottom
% Force curve fit through Injector Origin

if size(AngleXFortyFive,1) >= 2
ok_ = isfinite(AngleXFortyFive) & isfinite(AngleNegYFortyFive);
st_ = (0.9746908242292236 );
ft_ = fittype('m*(x-8.333)+21',...
'dependent',{'y'},'independent',{'x'},...
'coefficients',{'m'});

% Fit this model using new data
cf_ =
fit(AngleXFortyFive(ok_),AngleNegYFortyFive(ok_),ft_,'Startpoint',st_);

EvaluationNegativeFortyFive = feval(cf_, (OffsetHole
AngleXFortyFive'));
ok1_ = isfinite(AngleXFortyFive) & isfinite(AnglePosYFortyFive);

st1_ = (0.9746908242292236 );
ft1_ = fittype('m*(x-8.333)+21',...
'dependent',{'y'},'independent',{'x'},...
'coefficients',{'m'});

% Fit this model using new data
cf1_ =
fit(AngleXFortyFive(ok1_),AnglePosYFortyFive(ok1_),ft1_,'Startpoint',st
1_);
EvaluationPositiveFortyFive = feval(cf1_, (OffsetHole
AngleXFortyFive'));
YNegPenFortyFive = feval(cf1_, round(PenReferenceFortyFive(ii)));
YPosPenFortyFive = feval(cf_, round(PenReferenceFortyFive(ii)));

PositiveThetaFortyFive = atan((YPosPenFortyFive-
(Offset+1))/(DistanceCalcAtFortyFive(ii)))*180/pi;
NegativeThetaFortyFive = atan((YNegPenFortyFive-
(Offset+1))/(DistanceCalcAtFortyFive(ii)))*180/pi;

Plume(ii).ThetaM2Star =
abs(PositiveThetaFortyFive)+abs(NegativeThetaFortyFive);
else
    Plume(ii).ThetaM2Star = NaN;
end

end
end

```



```

drawnow
subplot(4,2,ii)
imagesc(Plume(ii).Shifted)
colormap(gray)
daspect([1 1 1])
hold on
plot((Plume(ii).Penetration+1.5)/Scaling, Offset+1, 'mo',
'MarkerFaceColor', 'm')
if isnan(Plume(ii).ThetaM1Star) == 0
    hold on
    plot(AngleXSixty, AnglePosYSixty, 'ro', (OffsetHole
AngleXSixty'), EvaluationPositiveSixty, 'r-')
    hold on
    plot(AngleXSixty, AngleNegYSixty, 'ro', (OffsetHole
AngleXSixty'), EvaluationNegativeSixty, 'r-')
end
if isnan(Plume(ii).ThetaM2Star) == 0
    hold on
    plot(AngleXFortyFive, AnglePosYFortyFive, 'go', (OffsetHole
AngleXFortyFive'), EvaluationPositiveFortyFive, 'g-')
    hold on
    plot(AngleXFortyFive, AngleNegYFortyFive, 'go', (OffsetHole
AngleXFortyFive'), EvaluationNegativeFortyFive, 'g-')
end
    hold on
    plot((round(PenReferenceSixty(ii)) round(PenReferenceSixty(ii))),
(1 size(Plume(ii).Shifted,1)), 'r-');
    hold on
    plot((PenReferenceFortyFive(ii) PenReferenceFortyFive(ii)), (1
size(Plume(ii).Shifted,1)), 'g-');
    title({'Original Spray Image with Curve-Fitted Cone Angle Edges
Determined Via XX*Sigma'; 'Green - FiftyPercPen, Red - 45Do, Pink Dot -
Spray Penetration'})
else
    Plume(ii).ThetaM1Star = NaN;
    Plume(ii).ThetaM2Star = NaN;
end

end

clear AngleXFortyFive AngleXSixty AnglePosYFortyFive AnglePosYSixty
clear AngleNegYFortyFive AngleNegYSixty
clear EvaluationPositiveFortyFive EvaluationNegativeFortyFive
clear EvaluationPositiveSixty EvaluationNegativeSixty
clear PositiveThetaSixty NegativeThetaSixty PositiveThetaFortyFive
NegativeThetaFortyFive
clear st1_cf1_ok1_ft1_
clear st16_cf16_ok16_ft16_
clear st_cf_ok_ft_
clear st6_cf6_ok6_ft6_
clear YPosPenFortyFive YNegPenFortyFive YPosPenSixty YNegPenSixty

end

% Put Data into Arrays that are Organized for Future Post-Processing

```

```

PenetrationPlume = arrayfun(@(x) mean(x.Penetration), Plume);
AvgPenetration = mean(PenetrationPlume);
PenetrationSpray(:,xx) = (PenetrationPlume AvgPenetration);

% Cone angle at 60% Penetration
ThetaPlumeM1Star = arrayfun(@(x) mean(x.ThetaM1Star), Plume);
AvgThetaM1Star = mean(ThetaPlumeM1Star);
ThetaSprayM1Star(:,xx) = (ThetaPlumeM1Star AvgThetaM1Star);

% Cone angle at 45Do
ThetaPlumeM2Star = arrayfun(@(x) mean(x.ThetaM2Star), Plume);
AvgThetaM2Star = mean(ThetaPlumeM2Star);
ThetaSprayM2Star(:,xx) = (ThetaPlumeM2Star AvgThetaM2Star);

xx = xx+1;

end

% Save data for penetration in an m-file
cd (strcat(DIRparent, 'Dissertation - ILASS Extension'))
SaveName=strcat(Time, 'ReducedCFData.mat');
Plume1P = PenetrationSpray(1,:);
Plume2P = PenetrationSpray(2,:);
Plume3P = PenetrationSpray(3,:);
Plume4P = PenetrationSpray(4,:);
Plume5P = PenetrationSpray(5,:);
Plume6P = PenetrationSpray(6,:);
Plume7P = PenetrationSpray(7,:);
Plume8P = PenetrationSpray(8,:);

save(SaveName, 'Plume1P', 'Plume2P', 'Plume3P', 'Plume4P', 'Plume5P',
'Plume6P', 'Plume7P', 'Plume8P')

```

12.4.3. Combusting (21% Oxygen) Spray Image Processing Program

The combusting oxygen images are processed to determine flame length, lift-off length, cone angle at 60% flame length, and total combusting spray plume intensity.

IP21PercO2 CH6.m

```

%% Use this program to process Back Scattering 21% O2 Spray Images.
% Calculate penetration, lift off length and cone angle of the
% combusting spray.
% Cone angle calculated at 60% of Flame Length. Cannot calculate at
45Do
% because 45Do is less than the lift off length location.
% Also calculate total intensity inside spray plume.

% Jaclyn Nesbitt
% January 25, 2011

%% Set up workspace.

```

```

clear all;
close all;
clc;

%% Get information about test, change to correct directory.
DIRparent = ('\\mtucifs\dfshome\jenesbit\Desktop\\DieselSprayTesting -
Additional August 2010\');
Date = input('Enter Date in YYYYMMDD Format:', 's');
Time = input('Enter Test Time in HHMM Format:', 's');
NumPlumes = '8';
StartFrame = input('Enter First Frame to Process:', 's');
EndFrame = input('Enter Last Frame to Process:', 's');

% Plume Display - plume number of results to show in figures
PlumeDisplay = 1;

Factor = 1;

FolderName = strcat(Time, '_C001H001S0001');

dir_name = ((DIRparent Date '\\' FolderName));

filename = strcat(Time, '_C001H001S0001.avi');

cd (dir_name)

% Define Image Scaling
Scaling = 0.18/cosd(15); % mm/pixel, scaled by cosine 15 degrees to
account
% for spray plume orientation relative to plane of the injector.
OffsetHole = 1.5/(Scaling*cosd(15)); % Pixels - Distance from injector
tip center to inj hole.

%% Read in Movie

mov = aviread(filename);

% Store Normalized Movie in NMOV
N = size(mov,2);
for i=1 : N;
    nmov( i).cdata = single( mov( i).cdata);
end

% Put orginial movie into single variable.

clear mov
mov = nmov;

%% Determine injector tip location.
% Find crossing point of the 8 plumes in the center -- look at a given
% frame in the image.

% Look at frame 14, convert to black and white, blob analysis.
% Injector tip is the crossing point of all 8 spray plume centroids.

```

```

Frame = mov(14).cdata;

BW = im2bw(Frame/max(max(Frame)),
0.25*graythresh(Frame/max(max(Frame))));

figure; imagesc(BW)

StatsComb = regionprops(BW, 'area', 'extrema', 'centroid',
'orientation');

    AreaComb = (StatsComb.Area);
    ExtremaComb= (StatsComb.Extrema);
    CentroidComb = (StatsComb.Centroid);
    OrientationComb= (StatsComb.Orientation);
    AreaIndexComb = find(AreaComb > 1000); %Should give 8 spray
plumes

    % For each plume, find centroid
    OrientationPlumes = OrientationComb(AreaIndexComb);
    CentroidX = (CentroidComb(AreaIndexComb*2-1));
    CentroidY = (CentroidComb(AreaIndexComb*2));

IndexA = find(OrientationPlumes <= 55 & OrientationPlumes >= 35);
Index8 = IndexA(find(CentroidY(IndexA) < size(BW,1)/2));
Index4 = IndexA(find(CentroidY(IndexA) > size(BW,1)/2));

PlumeX(8) = CentroidX(Index8);
PlumeY(8) = CentroidY(Index8);
PlumeX(4) = CentroidX(Index4);
PlumeY(4) = CentroidY(Index4);

IndexB = find(OrientationPlumes <= -35 & OrientationPlumes >=-55);
Index6 = IndexB(find(CentroidY(IndexB) < size(BW,1)/2));
Index2 = IndexB(find(CentroidY(IndexB) > size(BW,1)/2));

PlumeX(6) = CentroidX(Index6);
PlumeY(6) = CentroidY(Index6);
PlumeX(2) = CentroidX(Index2);
PlumeY(2) = CentroidY(Index2);

IndexC = find(OrientationPlumes <=10 & OrientationPlumes >=-10);
Index1 = IndexC(find(CentroidX(IndexC) > size(BW,2)/2));
Index5 = IndexC(find(CentroidX(IndexC) < size(BW,2)/2));

PlumeX(1) = CentroidX(Index1);
PlumeY(1) = CentroidY(Index1);
PlumeX(5) = CentroidX(Index5);
PlumeY(5) = CentroidY(Index5);

IndexD = find(abs(OrientationPlumes) <=100 & abs(OrientationPlumes)
>=80);
Index7 = IndexD(find(CentroidY(IndexD) < size(BW,1)/2));
Index3 = IndexD(find(CentroidY(IndexD) > size(BW,1)/2));
PlumeX(3) = CentroidX(Index3);
PlumeY(3) = CentroidY(Index3);

```

```

PlumeX(7) = CentroidX(Index7);
PlumeY(7) = CentroidY(Index7);

LineAX = (PlumeX(5) PlumeX(1));
LineAY = (PlumeY(5) PlumeY(1));

LineBX = (PlumeX(6) PlumeX(2));
LineBY = (PlumeY(6) PlumeY(2));

LineCX = (PlumeX(7) PlumeX(3));
LineCY = (PlumeY(7) PlumeY(3));

LineDX = (PlumeX(4) PlumeX(8));
LineDY = (PlumeY(4) PlumeY(8));

MidpointAX = mean((LineAX(1), LineAX(2)));
MidpointAY = mean((LineAY(1), LineAY(2)));
MidpointBX = mean((LineBX(1), LineBX(2)));
MidpointBY = mean((LineBY(1), LineBY(2)));
MidpointCX = mean((LineCX(1), LineCX(2)));
MidpointCY = mean((LineCY(1), LineCY(2)));
MidpointDX = mean((LineDX(1), LineDX(2)));
MidpointDY = mean((LineDY(1), LineDY(2)));

% X, Y coordinates of Injector Tip
TipIndexX = mean((MidpointAX MidpointBX MidpointCX MidpointDX));
TipIndexY = mean((MidpointAY MidpointBY MidpointCY MidpointDY));

% Plot results
figure; imagesc(Frame)
hold on;
plot(TipIndexX, TipIndexY, 'yo', 'MarkerFaceColor', 'y')
hold on
plot(LineAX, LineAY, 'b-')
hold on
plot(LineBX, LineBY, 'g-')
hold on
plot(LineCX, LineCY, 'r-')
hold on
plot(LineDX, LineDY, 'm-')
hold on
plot(MidpointAX, MidpointAY, 'bo')
hold on
plot(MidpointBX, MidpointBY, 'gs')
hold on
plot(MidpointCX, MidpointCY, 'rx')
hold on
plot(MidpointDX, MidpointDY, 'md')

%% PROCESS IMAGES - frame by frame

xx = str2num(StartFrame);

Total = size(mov,2);
PenetrationTotal = zeros(str2num(NumPlumes)+1, size(mov,2)-1);

```

```

AngleTotal = zeros(str2num(NumPlumes)+1, size(mov,2)-1);
DiffX(Total-1).Location = '';
DiffY(Total-1).Location = '';

for xx = str2num(StartFrame):str2num(EndFrame)

    % Prepare image for rotation.

    Image = mov(xx).cdata;

    ImageLarge = zeros(floor(1.3*size(Image,1)),
floor(1.3*size(Image,2)));
    IXCenter = floor(size(ImageLarge,2)/2);
    IYCenter = floor(size(ImageLarge,1)/2);
    DiffX(xx).Location = abs(floor(TipIndexX - IXCenter));
    DiffY(xx).Location = abs(floor(TipIndexY - IYCenter));

ImageLarge(abs(DiffY(xx).Location):abs(DiffY(xx).Location)+size(Image,1)
)-1, abs(DiffX(xx).Location):abs(DiffX(xx).Location)+size(Image,2)-1) =
Image;

    AngleRotate = 360/str2num(NumPlumes);

    StartAngle = -3;

    % Create a structure for data processing.... for the total number
of plumes.

    Plume(str2num(NumPlumes)).Intensity = '';
    Plume(str2num(NumPlumes)).Shifted = '';
    Plume(str2num(NumPlumes)).Scaled = '';
    Plume(str2num(NumPlumes)).BW = '';
    Plume(str2num(NumPlumes)).Blob = '';
    Plume(str2num(NumPlumes)).Spray = '';
    Plume(str2num(NumPlumes)).Boundary = '';
    Plume(str2num(NumPlumes)).Penetration = '';
    Plume(str2num(NumPlumes)).Theta = '';
    ii = 1;
    for ii = 1:str2num(NumPlumes);

        % Rotate images
        Plume(ii).Intensity =
imrotate(ImageLarge,StartAngle+AngleRotate*(ii-1));
        Offset = 50;

        Plume(ii).AX = floor(size(Plume(ii).Intensity,2)/2);
        Plume(ii).AY = floor(size(Plume(ii).Intensity,1)/2);

        % Isolate ROI of image
        Plume(ii).Shifted = Plume(ii).Intensity(Plume(ii).AY-
Offset:Plume(ii).AY+Offset, Plume(ii).AX:end);
        Plume(ii).IntensitySum = Plume(ii).Shifted;
        figure; imagesc(Plume(ii).Shifted); colormap(gray);
daspect([1 1 1]); axis off

```

```

        % Apply mask to remove adjacent spray plumes.
        VX = ceil((1 size(Plume(ii).Shifted,1)/(2*tand(AngleRotate
- 25)) size(Plume(ii).Shifted,2) size(Plume(ii).Shifted,2)
size(Plume(ii).Shifted,1)/(2*tand(AngleRotate - 25)))));
        VY = ceil((size(Plume(ii).Shifted,1)/2
size(Plume(ii).Shifted,1) size(Plume(ii).Shifted,1) 1 1));

        BW = roipoly(Plume(ii).Shifted,VX,VY);
        (I, J) = find(BW ==0);
        kk =1;

        for kk = 1:size(I,1)
            Plume(ii).Shifted(I(kk),J(kk)) = 0;
        end

        Plume(ii).Scaled = Plume(ii).Shifted /
max(max(Plume(ii).Shifted));

        % Threshold image and convert to black and white for blob
        % analysis.

        Threshold =0.15*graythresh(Plume(ii).Scaled);

        Plume(ii).BW = im2bw(Plume(ii).Scaled, Factor*Threshold);
        Plume(ii).Blob = bwlabel(Plume(ii).BW,8);

        StatsComb = regionprops(Plume(ii).Blob, 'area', 'extrema',
'centroid');
        AreaComb = (StatsComb.Area);
        ExtremaComb= (StatsComb.Extrema);
        CentroidComb = (StatsComb.Centroid);
        AreaIndexComb = find(AreaComb == max(AreaComb));

        % AreaComb will be empty - if there is no combusting plume
due
        % uneven start of combustion, so we won't process those
regions

        if isempty(AreaComb) == 0

            % Isolate combusting spray plume from the rest of the
            % image.
            Plume(ii).SprayComb = ismember(Plume(ii).Blob,
AreaIndexComb);

            CenterlineComb(ii) =
round(CentroidComb(AreaIndexComb*2));
            LeadComb(ii) =
max(find(Plume(ii).SprayComb(CenterlineComb(ii),:)==1));

            % Find boundary of combusting spray plume.
            Plume(ii).BoundaryComb =
bwtraceboundary(Plume(ii).SprayComb, (CenterlineComb(ii),
LeadComb(ii)), 'S');

```

```

X1=1;

% Determine flame length (penetration)
FlameLength = arrayfun(@(x) max(x.BoundaryComb), Plume,
'UniformOutput', false);
Plume(ii).FlameLength = FlameLength{:,ii}(2)*Scaling-
1.5; % Subtract off difference in penetration based on inj tip
definition

% Look at intensity distribution in the image - use to
% define an approximation for our liquid length.

(I1, J1) = find(Plume(ii).SprayComb ==0);
kk1 =1;

for kk1 = 1:size(I1,1)
    Plume(ii).IntensitySum(I1(kk1),J1(kk1)) = 0;
end

% Look at the intensity radially across the spray in 1
% pixel increments progressing downstream of the spray.

for X1 = 1 :
(Plume(ii).FlameLength/(Scaling*cosd(15))+1.5)+10;

    VertIntensity(X1) =
sum(improfile(Plume(ii).IntensitySum, (X1,X1),
(1,size(Plume(ii).IntensitySum,1)))));

end

% Define a threshold for liquid length 10% of the
maximum
% radial intensity.

MaxSumInt = max(VertIntensity);
ThresholdInt = 0.1*max(VertIntensity);
% Uncomment the below section of code to plot the vertical (radial)
% intensity distribution and show the threshold location, relative to
the
% combusting flame image.

% figure;
% subplot(2,1,1)
% plot(VertIntensity)
% hold on
% plot((1:size(VertIntensity,2)),
(ThresholdInt+zeros(size(VertIntensity,2),1)), 'r-')
% xlim((1 (Plume(ii).FlameLength/(Scaling*cosd(15))+1.5)+10))
% subplot(2,1,2);
% imagesc(Plume(ii).IntensitySum);
% xlim((1 (Plume(ii).FlameLength/(Scaling*cosd(15))+1.5)+10))
% hold on

```



```

% plot((min(find(VertIntensity >=ThresholdInt)) min(find(VertIntensity
>=ThresholdInt))), (1, size(Plume(ii).IntensitySum,1)), 'y-')
% axis off
% keyboard
% close all

% Determine LOL for plume.
Plume(ii).LOL = min(find(VertIntensity >= ThresholdInt));

%% Determine total intensity within combusting plume.
(I1, J1) = find(Plume(ii).SprayComb ==0);
    kk1 =1;

    for kk1 = 1:size(I1,1)
        Plume(ii).IntensitySum(I1(kk1),J1(kk1)) = 0;
    end

    Plume(ii).TotalPlumeIntensity
=sum(sum(Plume(ii).IntensitySum));

%% Calculate Cone Angle

clear VertIntensity

% First find spray width in xx*Do increments
Do = 0.14; % mm

% Determine spray width - based on combusting boundaries.
MaxKK = max(Plume(ii).BoundaryComb(:,2));
MinKK = min(Plume(ii).BoundaryComb(:,2));
kk = MinKK;
for kk = MinKK : MaxKK
    EdgeW = Plume(ii).BoundaryComb(find(Plume(ii).BoundaryComb(:,2) ==
kk),1);
    TopEdgeW(kk,ii) = max(EdgeW);
    BotEdgeW(kk,ii) = min(EdgeW);
    Widths(kk,ii) = abs(TopEdgeW(kk,ii) -BotEdgeW(kk,ii) );
end

% Calculate Cone angle at 60% Of Combusting Flame Length
SixtyPercPen(ii) = round(0.6*Plume(ii).FlameLength/(Scaling*cosd(15)));
% Pixels
SixtyPercPenReference(ii) = round(SixtyPercPen(ii)+
1.5/(Scaling*cosd(15)));

if SixtyPercPenReference(ii) > MaxKK
    Plume(ii).ThetaM1Star = NaN;
else
    Plume(ii).AngleX1S = (MinKK:1:SixtyPercPenReference(ii));
    Plume(ii).AngleY1STop =
(TopEdgeW(MinKK:1:SixtyPercPenReference(ii),ii)');
    Plume(ii).AngleY1SBot =
(BotEdgeW(MinKK:1:SixtyPercPenReference(ii),ii)');

    AngleXSixtyPerc = Plume(ii).AngleX1S(:);

```

```

        AngleNegYSixtyPerc = Plume(ii).AngleY1SBot(:);
        AnglePosYSixtyPerc = Plume(ii).AngleY1STop(:);

    if size(AngleXSixtyPerc,1) >= 2
        ok_ = isfinite(AngleXSixtyPerc) & isfinite(AngleNegYSixtyPerc);
        st_ = (0.9746908242292236 );
        ft_ = fittype('m*(x-8.333)+51',...
            'dependent',{'y'},'independent',{'x'},...
            'coefficients',{'m'});

        % Fit this model using new data
        cf_ =
        fit(AngleXSixtyPerc(ok_),AngleNegYSixtyPerc(ok_),ft_,'Startpoint',st_);

        EvaluationNegativeSixtyPerc = feval(cf_, (OffsetHole
        AngleXSixtyPerc'));
        ok1_ = isfinite(AngleXSixtyPerc) & isfinite(AnglePosYSixtyPerc);

        st1_ = (0.9746908242292236 );
        ft1_ = fittype('m*(x-8.333)+51',...
            'dependent',{'y'},'independent',{'x'},...
            'coefficients',{'m'});

        % Fit this model using new data
        cf1_ =
        fit(AngleXSixtyPerc(ok1_),AnglePosYSixtyPerc(ok1_),ft_,'Startpoint',st1_);
        EvaluationPositiveSixtyPerc = feval(cf1_, (OffsetHole
        AngleXSixtyPerc'));

        YNegPenSixtyPerc = feval(cf1_, round(SixtyPercPenReference(ii)));
        YPosPenSixtyPerc = feval(cf_, round(SixtyPercPenReference(ii)));

        PositiveThetaSixtyPerc = atan((YPosPenSixtyPerc-
        (Offset+1))/(SixtyPercPen(ii)))*180/pi;
        NegativeThetaSixtyPerc = atan((YNegPenSixtyPerc-
        (Offset+1))/(SixtyPercPen(ii)))*180/pi;

        Plume(ii).ThetaM1Star =
        abs(PositiveThetaSixtyPerc)+abs(NegativeThetaSixtyPerc);

    else
        Plume(ii).ThetaM1Star = NaN;
    end
end

% Plot Results - combusting image + boundary + cone angle + lift off
length
subplot(4,2,ii)
drawnow
imagesc(Plume(ii).Scaled(:, :))
colormap(gray)
daspect([1 1 1])
hold on
T = isempty(Plume(ii).BoundaryComb);

```

```

if T == 0
plot(Plume(ii).BoundaryComb(:,2), Plume(ii).BoundaryComb(:,1), 'y',
'LineWidth', 2);
end
% Plot Method 1
TestEmptyS = isnan(Plume(ii).ThetaM1Star);
if TestEmptyS == 0;
    hold on
plot((OffsetHole Plume(ii).AngleX1S), EvaluationPositiveSixtyPerc, 'w-
', 'LineWidth', 2)
hold on
plot((OffsetHole Plume(ii).AngleX1S), EvaluationNegativeSixtyPerc, 'w-
', 'LineWidth', 2)
end
hold on
plot((SixtyPercPenReference(ii) SixtyPercPenReference(ii)), (1
size(Plume(ii).Scaled,1)), 'w-', 'LineWidth', 2);
hold on
plot(OffsetHole, Offset+1, 'ro', 'MarkerFaceColor', 'r')
hold on
plot((Plume(ii).LOL Plume(ii).LOL), (1 size(Plume(ii).Scaled,1)), 'm-')
axis off
hold off
title({'Yellow-Boundary, White - 0.6S CF, White - 0.6S Line'; 'Red
Circle - Nozzle Hole Tip, Magenta - LOL'})

    end
end

% Organize results into arrays
FlameLengthPlume = arrayfun(@(x) mean(x.FlameLength), Plume);
AvgFlameLength = mean(FlameLengthPlume);
FlameLengthSpray(:,xx) = (FlameLengthPlume AvgFlameLength);

LOLPlume = arrayfun(@(x) mean(x.LOL), Plume);
AvgLiftOff = mean(LOLPlume);
LiftOffLength(:,xx) = (LOLPlume AvgLiftOff).*Scaling-1.5; % Shift by
actual tip nozzle location

ThetaPlumeM1Star = arrayfun(@(x) mean(x.ThetaM1Star), Plume);
AvgThetaM1Star = mean(ThetaPlumeM1Star);
ThetaSprayM1Star(:,xx) = (ThetaPlumeM1Star AvgThetaM1Star);

PlumeIntensityAll = arrayfun(@(x) mean(x.TotalPlumeIntensity), Plume);
AvgPlumeIntensity = mean(PlumeIntensityAll);
PlumeIntensitySpray(:,xx) = (PlumeIntensityAll AvgPlumeIntensity);

xx = xx+1;

clear ConeTComb ConeBComb SixtyPercPenComb
clear Plume

end

```

12.4.4. Gaussian Curve Fit Image Processing for Nonvaporizing Sprays

The m-file for processing the nitrogen sprays using a Gaussian curve fitting intensity distribution methodology is provided below, used to determine cone angle at 45 nozzle diameters. Penetration is also determined in this processing program.

IPN2 GaussianCAMethod.m

```
% N2 Back Scattering (Liquid Phase) Image Processing Program
% Gaussian Curve Fitting Method

% Jaclyn Nesbitt
% Febraury 28, 2011 -- Updated CF method.
% Using modified Gaussian CF Method.

% Use this program to determine penetration and cone angle of the
liquid
% phase sprays. Redefine injector tip location for each plume
individually
% - 1.5 mm offset (based on Ford information / drawing) - distance from
nozzle tip
% center to nozzle hole. Use 45 Do CF CA Methods, with Gaussian curve
fitting.

%% Setup workspace

clear all;
close all;
clc;

%% Get information about test, change to correct directory.
DIRparent = ('\\mtucifs\dfshome\jenesbit\Desktop\\DieselSprayTesting -
Additional August 2010\');

Date = input('Enter Date in YYYYMMDD Format:', 's');
Time = input('Enter Test Time in HHMM Format:', 's');

NumPlumes = '8';
StartFrame = input('Enter First Frame to Process:', 's');
EndFrame = input('Enter Last Frame to Process:', 's');

%Define which plume will be shown in the figures
PlumeDisplay = 1;

% Factor = 1;

FolderName = strcat(Time, '_C001H001S0001');

dir_name = ((DIRparent Date '\\' FolderName));

filename = strcat(Time, '_C001H001S0001.avi');

cd (dir_name)
```

```

% Define scaling and injector tip offset.

Scaling = 0.18/cosd(15);
OffsetHole = 1.5/(Scaling*cosd(15)); % Pixels - Distance from injector
tip center to inj hole.

%% Read in Movie

mov = aviread(filename);

% Store Normalized Movie in NMOV
N = size(mov,2);
for i=1 : N;
    nmov( i).cdata = single( mov( i).cdata);
end

% Put orginial movie into single variable.
clear mov
mov = nmov;

cd (DIRparent)

%% Background Subtraction;

Background = mov(1,1).cdata;

for i = 1:N-1;

Frame(i).cdata = imsubtract(Background, mov(1,i+1).cdata);

end

%% Find Injector Tip using Background Image

% Display background image - uncomment below.
% figure; imagesc(Background); colormap(gray); daspect((1 1 1))

BackgroundScaled = Background/max(max(Background));
BackgroundAdjusted = imadjust(BackgroundScaled);

% Apply multiplier to account for variations in SNR / contrast ratio
for different tests (due to not calibrating camera).
Multiplier = 1.75;

if strcmp(Date, '20100830') == 1
    Multiplier = 2;
end

BWBackground = im2bw(BackgroundAdjusted,
Multiplier*graythresh(BackgroundAdjusted));

BackgroundBlob = bwlabel(BWBackground,8);

ColoredBlobs = label2rgb(BackgroundBlob, 'hsv', 'k', 'shuffle');

```

```

%Uncomment to plot blobs from background resulting from blob analysis.
% figure
% imagesc(ColoredBlobs);
% daspect([1 1 1])

Stats1 = regionprops(BackgroundBlob, 'centroid', 'area', 'extrema');

Area1 = (Stats1.Area);
Centroid1 = (Stats1.Centroid);

LargeAreas = find(Area1 > 100);
gg=LargeAreas(1);
for gg = 1: size(LargeAreas,2)
    LocX(gg) = Centroid1(LargeAreas(gg)*2-1)-size(Background,2)/2;
    LocY(gg) = Centroid1(LargeAreas(gg)*2)-size(Background,1)/2;
    DiffLoc(gg) = sqrt(LocX(gg)^2+LocY(gg)^2);
end
AreaIndex1 = LargeAreas(find(DiffLoc == min(DiffLoc)));
Extremal = (Stats1.Extrema);

CentroidIndexX = Centroid1(AreaIndex1*2-1);
CentroidIndexY = Centroid1(AreaIndex1*2);

DiffXX = abs(size(Background,2)/2-CentroidIndexX);
DiffYY = abs(size(Background,1)/2-CentroidIndexY);

AbsDiff = sqrt(DiffXX.^2+DiffYY.^2);

Index = find(AbsDiff == min(AbsDiff));

YTop = (Extremal(1, AreaIndex1(Index)*2)+Extremal(2,
AreaIndex1(Index)*2))/2;
YBottom =
(Extremal(5,AreaIndex1(Index)*2)+Extremal(6,AreaIndex1(Index)*2))/2;
TipIndexY = round((YTop+YBottom)/2);
XTop = (Extremal(1,AreaIndex1(Index)*2-
1)+Extremal(2,AreaIndex1(Index)*2-1))/2;
XBottom = (Extremal(5,AreaIndex1(Index)*2-
1)+Extremal(6,AreaIndex1(Index)*2-1))/2;
TipIndexX = round((XTop+XBottom)/2);

clear MagDiff IndexTip DiffXX DiffYY ii HalfY HalfX Centroid1
clear Stats1 BackgroundBlob ColoredBlobs BWBackground
BackgroundAdjusted
clear Multiplier BackgroundScaled

%% Process Spray Images - frame by frame - to determine penetration and
cone angle (plume to plume and average values)

xx = str2num(StartFrame)-1;

Total = size(mov,2);
PenetrationTotal = zeros(str2num(NumPlumes)+1, size(mov,2)-1);
AngleTotal = zeros(str2num(NumPlumes)+1, size(mov,2)-1);

```

```

DiffX(Total-1).Location = '';
DiffY(Total-1).Location = '';

for xx = str2num(StartFrame)-1:str2num(EndFrame)

    Image = -Frame(xx).cdata;
    ImageLarge = zeros(floor(1.3*size(Image,1)),
floor(1.3*size(Image,2)));
    IXCenter = floor(size(ImageLarge,2)/2);
    IYCenter = floor(size(ImageLarge,1)/2);
    DiffX(xx).Location = floor(TipIndexX - IXCenter);
    DiffY(xx).Location = floor(TipIndexY - IYCenter);

ImageLarge(abs(DiffY(xx).Location)+1:abs(DiffY(xx).Location)+size(Image
,1), abs(DiffX(xx).Location)+1:abs(DiffX
(xx).Location)+1+size(Image,2)-1) = Image;

    % Rotate image such that plumes travel left to right, exiting
horizontal from the injector.
    AngleRotate = 360/str2num(NumPlumes);
    if strcmp(NumPlumes, '8') == 1
        StartAngle = -3;
    end

    % Create a structure.... for the total number of plumes.

    Plume(str2num(NumPlumes)).Intensity = '';
    Plume(str2num(NumPlumes)).Shifted = '';
    Plume(str2num(NumPlumes)).Scaled = '';
    Plume(str2num(NumPlumes)).BW = '';
    Plume(str2num(NumPlumes)).Blob = '';
    Plume(str2num(NumPlumes)).Spray = '';
    Plume(str2num(NumPlumes)).Boundary = '';
    Plume(str2num(NumPlumes)).Penetration = '';
    Plume(str2num(NumPlumes)).Theta = '';
    Plume(str2num(NumPlumes)).AngleX = '';
    Plume(str2num(NumPlumes)).AngleNegY = '';
    Plume(str2num(NumPlumes)).AnglePosY = '';
    Plume(str2num(NumPlumes)).EvaluationPositive = '';
    Plume(str2num(NumPlumes)).EvaluationNegative = '';
    Plume(str2num(NumPlumes)).LinearFitPositive = '';
    Plume(str2num(NumPlumes)).LinearFitNegative = '';
    SaveSigmaCF = zeros(27,8);
    SaveSigmaFactor = zeros(27,8);
    SavePointsUsed = zeros(27,8);
    SaveMeanCFUsed = zeros(27,8);

    ii = 1;

    % Process each spray plume of the 8 hole nozzle separately

    for ii = 1:str2num(NumPlumes);

```

```

        % Rotate the images, chose the desired ROI, ensure correct
horizontal plume orientation.
        Plume(ii).Intensity =
imrotate(ImageLarge,StartAngle+AngleRotate*(ii-1));
        Offset = 40;

        Plume(ii).AX = round(size(Plume(ii).Intensity,2)/2);
        Plume(ii).AY = round(size(Plume(ii).Intensity,1)/2);

        Plume(ii).Shifted = Plume(ii).Intensity(Plume(ii).AY-
Offset:Plume(ii).AY+Offset, Plume(ii).AX:end);

        VX = ceil((1 size(Plume(ii).Shifted,1)/(2*tand(AngleRotate
- 25)) size(Plume(ii).Shifted,2) size(Plume
(ii).Shifted,2) size(Plume(ii).Shifted,1)/(2*tand(AngleRotate - 25)))));
        VY = ceil((size(Plume(ii).Shifted,1)/2
size(Plume(ii).Shifted,1) size(Plume(ii).Shifted,1) 1 1));

        BW = roipoly(Plume(ii).Shifted,VX,VY);
        (I, J) = find(BW ==0);
        kk =1;

        for kk = 1:size(I,1)
            Plume(ii).Shifted(I(kk),J(kk)) = 0;
        end

        Plume(ii).Scaled = Plume(ii).Shifted /
max(max(Plume(ii).Shifted));

        % Find the intensity profile along the spray centerline, use
this to define the tip of the spray (penetration)
        XX1 = 1;
        XX2 = size(Plume(ii).Scaled, 2);
        YAxis = Offset+1;
        CCL = improfile(Plume(ii).Scaled,(XX1 XX2), (YAxis YAxis));
        Plume(ii).SprayTip = min(find(CCL(ceil(3*OffsetHole):end)
<= 0.1))+ceil(3*OffsetHole)-1;

        Plume(ii).Penetration = Plume(ii).SprayTip*Scaling-1.5; %
Account for 1.5 mm shift in injector tip location

        % Plot results of spray tip overlaid on origianl spray image

        if ii == PlumeDisplay
            figure;
            drawnow;
            subplot(2,1,1)
            imagesc(Plume(ii).Shifted)
            daspect([1 1 1])
            colormap(gray)
            hold on
            plot(Plume(ii).SprayTip,YAxis, 'go', 'MarkerFaceColor',
'g');

```



```

        title('Original Spray Image, Green Dot Shows Penetration
Tip')
        subplot(2,1,2)
        plot((1:1:size(CCL,1)), CCL);
        hold on
        plot(Plume(ii).SprayTip, CCL(Plume(ii).SprayTip), 'go',
'MarkerFaceColor', 'g');
        xlabel('Intensity Distribution')
        ylabel('Distance Along Profile')
        title('Penetration')
    end

%% Cone Angle Determination

% Define considered regions for CA calculation

Do = 0.14; % mm
FortyFiveDiameters = round(Do*45/(Scaling*cosd(15))); % Pixels
MaxKK = (FortyFiveDiameters);

% Add exception to max - if the forty five diameters is larger than the
% spray tip - then max KK is less -- and 0.5*Penetration because that
% is the only
% CA we can determine.

if FortyFiveDiameters >
round(1*Plume(ii).Penetration/(Scaling*cosd(15)))
    ProcessDo45 = 0;
else
    ProcessDo45 = 1;
end

MinKK = round(2*OffsetHole) ; %% Starting point of considering spray
widths in cone angle
MaxKK = round(MaxKK + OffsetHole); % Reference to Injector Tip
Increments = MaxKK - MinKK+1;

% Create a profile structure

C(Increments).Profile = '';
C(Increments).Offset = '';
C(Increments).OffsetProfile = '';
C(Increments).XVector = '';
C(Increments).MeanFit = '';
C(Increments).Sigma = '';
C(Increments).A = '';
C(Increments).YY1 = '';
C(Increments).YY2 = '';

kk = 1;
kkstar = MinKK;
Stepping=1;
Skips = ();

```

```

% Take intensity profiles across the spray in 1 pixel increments moving
downstream the spray.
% Find the data of interest - only decreasing data points are
considered.
for kk =1 : Increments
    C(kk).YY1 = 1;
    C(kk).YY2 = size(Plume(ii).Shifted,1);
    C(kk).Profile = improfile(Plume(ii).Shifted, (kkstar kkstar),
(C(kk).YY1 C(kk).YY2));
    C(kk).XVector = (1:1:size(C(kk).Profile,1))'+C(kk).YY1-1;

    global X Y

    MidPoint = round(max(C(kk).XVector)/2);

% Find decreasing data
IndexL = max(find(C(kk).Profile(1:MidPoint) <= 0));
IndexR = min(find(C(kk).Profile(MidPoint:end) <= 0))+MidPoint-1;

gg = MidPoint+2;
Difference = -1;
while Difference < 0
    Difference = C(kk).Profile(gg+1)-C(kk).Profile(gg);
    if gg >= IndexR
        gg = gg+1;
        break
    end
    gg = gg + 1;
end

RightEdge = gg - 2;

while C(kk).Profile(RightEdge) > 0.2*max(C(kk).Profile)
    % We Haven't identified the correct end point
    gg = RightEdge +2;
    Difference = -1;
    if gg >= IndexR
        gg = gg-2;
        break
    end
end
if Difference < 0
    Difference = C(kk).Profile(ii+1)-C(kk).Profile(ii);
    if ii >= IndexR
        gg = gg+1;
        break
    end
    gg = gg + 1;
end

RightEdge = gg - 2;
end

% Conside from midpoint to x = 0 -- need to reverse data.

jj = MidPoint-2;

```

```

Difference = -1;
while Difference < 0
    Difference = C(kk).Profile(jj) - C(kk).Profile(jj+1);
    if jj <= IndexL
        jj = jj-1;
        break
    end
    jj = jj - 1;
end

LeftEdge = jj + 2;

while C(kk).Profile(LeftEdge) > 0.2*max(C(kk).Profile)
    % We Haven't identified the correct end point
    jj = LeftEdge-2;
    Difference = -1;
    if jj <= IndexL
        jj = jj-1;
        break
    end
    while Difference < 0
        Difference = C(kk).Profile(jj) - C(kk).Profile(jj+1);
        if jj <= IndexL
            jj = jj-1;
            break
        end
        jj = jj - 1;
    end
    LeftEdge = jj + 2;
end

% Apply a gaussian curve fit to the intensity region of interest.
Output curve fit parameters.

C(kk).Y = C(kk).Profile(LeftEdge:1:RightEdge);
C(kk).X = C(kk).XVector(LeftEdge:1:RightEdge);

X = C(kk).X;
Y = C(kk).Y;

start = (max(Y) mean(X) size(Y(find(Y>0.5*max(Y))),1)/2.355
min(C(kk).Profile));

bestcoeffs = fminsearch(@OffsetGauss, start);

C(kk).A = bestcoeffs(1);
C(kk).MeanFit = bestcoeffs(2);
C(kk).Sigma = bestcoeffs(3);
C(kk).Offset = bestcoeffs(4);

C(kk).FittedData = C(kk).A*exp(-(C(kk).XVector-
C(kk).MeanFit).^2/(2* C(kk).Sigma^2))+C(kk).Offset;

% Define parameters using the curve fit values.

```

```

a = 1;
b = -2*(C(kk).MeanFit);
c = C(kk).MeanFit^2+2*C(kk).Sigma^2*log((-C(kk).Offset)/C(kk).A);

IntersectionL = (-b - sqrt(b^2-4*a*c))/(2*a);
IntersectionR = (-b + sqrt(b^2-4*a*c))/(2*a);

C(kk).SigmaL = (IntersectionR-IntersectionL)/C(kk).Sigma;
SigmaL(kk) = C(kk).SigmaL;

Imag = ~isreal(SigmaL(kk));

if Imag == 1
    Skips(Stepping) = kk;
    Stepping = Stepping+1;
end

FitOffset(kk) = C(kk).Offset;

C(kk).FittedShort = C(kk).A*exp(-(C(kk).X- C(kk).MeanFit).^2/(2*
C(kk).Sigma^2))+C(kk).Offset;

if kkstar == round(FortyFiveDiameters+OffsetHole)
    FortyFiveDiametersIndex = kk;
end

% Define results of curve fit - i.e. measures of goodness of fit (RMSE,
NRMSE, R2 etc...)

kkstar = kkstar+1;
Deviations = C(kk).Y - mean(C(kk).Y); %Measure of Spread
% Total sum of squares - proportional to sample variance
SST = sum(Deviations.^2); % Total Variation to be accounted for
Residuals = C(kk).Y - C(kk).FittedShort; %Measure of mismatch
SSE = sum(Residuals.^2); %Variation not accounted for
RSq(kk) = 1 - SSE/SST; %Percent of error explained - R^2 should be
close to 1
RMSE(kk) = (sum(Residuals.^2)/size(Residuals,1))^(1/2);
NRMSE(kk) = (RMSE(kk)/(max(C(kk).Y)-min(C(kk).Y)))*100;

% Plot results - gaussian curve fitting overlaid on intensity
distribution.
if ii == PlumeDisplay
    if kk == 1
        figure;
    end
    drawnow
    plot(C(kk).XVector, C(kk).FittedData);
    hold on
    plot(C(kk).XVector, C(kk).Profile, 'r');
    hold on
    plot(C(kk).X, C(kk).Y, 'kx')
    xlabel('Distance Along Profile')
    ylabel('Intensity (Counts)')

```

```

        legend('Gaussian Curve Fit', 'Profile Data', 'Data Used in
Curve Fit');
        title({strcat('Gaussian Fit: Intensity = ', num2str(C(kk).A),
'*exp(-(Distance-', num2str(C(kk).MeanFit), ')^2/

(2*', num2str(C(kk).Sigma), '^2))', '+', num2str(C(kk).Offset));...
        strcat('Rsqr:', num2str(RSq(kk)), '; NRMSE:',
num2str(NRMSE(kk)))));
        xlim((0 Offset*2))
        ylim((-20 160))

    end

end

% Plot results of NRMSE and threshold value of NRMSE to understand okay
(used CF's) and errors in CF's
if ii == PlumeDisplay

figure;

plot((MinKK:1:Increments+MinKK-1), zeros(Increments,1)'+5, 'k-')
hold on
plot((MinKK:1:Increments+MinKK-1), NRMSE, 'bo', 'MarkerFaceColor', 'b')
legend('Threshold NRMSE', 'NRMSE')
xlabel('Index - Corresponds to Radial Profile')
ylabel('NRMSE (%) of Gaussian Curve Fit')

end

% Define the indices of curve fits which are not included in defining
the spray edge to calculate cone angle.
Skipping = find(NRMSE >5 | isnan(RSq) | isinf(SigmaL));

if isempty(Skipping)
    SkipFits = Skipping;
else

SkipFits = unique((Skipping Skips));
end

aa =1;
bb =1;
Indexing = (1:1:Increments);
DistProfile = (MinKK:1:Increments+MinKK-1);
for aa = 1:size(Indexing,2)
Left = ismember(Indexing(aa), SkipFits);
if Left == 0;
    PointsUsed(bb) = DistProfile(Indexing(aa));
    SigmaCFUsed(bb) = C(aa).Sigma;
    SigmaFactorUsed(bb) = C(aa).SigmaL/2;
    MeanCFUsed(bb) = C(aa).MeanFit;
    bb = bb + 1;
end
end

```

```

end

%% Use gaussian curve fit to determine cone angle edges.

% Define edges as +- x* Sigma, relative to mean value (center
% point), x is some factor of sigma.

Index = 1;
IndexMoving = 1;
for Index = 1:Increments
    if ismember(Index,SkipFits)
    else
Factor = sqrt(log(1)/log(C(Index).A)+1);
EdgePos(IndexMoving) =
C(Index).MeanFit+C(Index).Sigma*C(Index).SigmaL/2*Factor;
EdgeNeg(IndexMoving) = C(Index).MeanFit-
C(Index).Sigma*C(Index).SigmaL/2*Factor;

clear Factor
if ProcessDo45 == 1
    if Index+MinKK-1 <= FortyFiveDiameters+OffsetHole
        AngleXFortyFive(IndexMoving) = Index+MinKK-1;
    end
end
IndexMoving = IndexMoving+1;

    end
end

SkipAngles = isequal(Increments,SkipFits);
SkipAngles2 = (size(SkipFits, 2) == Increments);
if SkipAngles == 0
    if SkipAngles2 == 0

        if ProcessDo45 == 1
AngleXFortyFive = (AngleXFortyFive);
AnglePosYFortyFive = (EdgePos(1:size(AngleXFortyFive,2)));
AngleNegYFortyFive = (EdgeNeg(1:size(AngleXFortyFive,2)));

AngleXFortyFive = AngleXFortyFive(:);
AngleNegYFortyFive = AngleNegYFortyFive(:);
AnglePosYFortyFive = AnglePosYFortyFive(:);

if size(AngleXFortyFive,1) >= 2
ok_ = isfinite(AngleXFortyFive) & isfinite(AngleNegYFortyFive);
st_ = (0.9746908242292236 );
ft_ = fittype('m*(x-8.333)+41',...
    'dependent',{'y'},'independent',{'x'},...
    'coefficients',{'m'});

% Fit this model using new data
cf_ =
fit(AngleXFortyFive(ok_),AngleNegYFortyFive(ok_),ft_,'Startpoint',st_);

```

```

EvaluationNegativeFortyFive = feval(cf_, (OffsetHole
AngleXFortyFive'));
ok_ = isfinite(AngleXFortyFive) & isfinite(AnglePosYFortyFive);

st1_ = (0.9746908242292236 );
ft1_ = fittype('m*(x-8.333)+41',...
    'dependent',{'y'}, 'independent',{'x'},...
    'coefficients',{'m'});

% Fit this model using new data
cfl_ =
fit(AngleXFortyFive(ok_),AnglePosYFortyFive(ok_),ft_,'Startpoint',st_);
EvaluationPositiveFortyFive = feval(cfl_,(OffsetHole
AngleXFortyFive'));

% Display linear fits, overlaid on original image pictures.
if ii == PlumeDisplay
    figure;
    drawnow
    imagesc(Plume(ii).Shifted)
    colormap(gray)
    daspect([1 1 1])
    hold on
    plot(Plume(ii).SprayTip, Offset+1, 'mo', 'MarkerFaceColor', 'm')

    if ProcessDo45 == 1
        hold on
        plot(AngleXFortyFive, AnglePosYFortyFive, 'go', (OffsetHole
AngleXFortyFive'), EvaluationPositiveFortyFive, 'g-')
        hold on
        plot(AngleXFortyFive, AngleNegYFortyFive, 'go', (OffsetHole
AngleXFortyFive'), EvaluationNegativeFortyFive, 'g-')
    end

    hold on
    plot((round(FortyFiveDiameters+OffsetHole)
round(FortyFiveDiameters+OffsetHole)), (1 size(Plume(ii).Shifted,1)),
'r-');
    title({'Original Spray Image with Curve-Fitted Cone Angle Edges
Determined Via XX*Sigma'; 'Green - FiftyPercPen, Red -
45Do, Pink Dot - Spray Penetration'})
end

YNegPenFortyFive = feval(cfl_, round(FortyFiveDiameters+OffsetHole));
YPosPenFortyFive = feval(cf_, round(FortyFiveDiameters+OffsetHole));

PositiveThetaFortyFive = atan((YPosPenFortyFive-
(Offset+1))/(FortyFiveDiameters))*180/pi;
NegativeThetaFortyFive = atan((YNegPenFortyFive-
(Offset+1))/(FortyFiveDiameters))*180/pi;

Plume(ii).ThetaTotalFortyFive =
abs(PositiveThetaFortyFive)+abs(NegativeThetaFortyFive);

```

```

else
    Plume(ii).ThetaTotalFortyFive = NaN;
end
else
    Plume(ii).ThetaTotalFortyFive = NaN;
end
else
    Plume(ii).ThetaTotalFortyFive = NaN;
end
else
    Plume(ii).ThetaTotalFortyFive = NaN;
end

clear AngleXFifty AnglePosYFifty AngleNegYFifty
clear AngleXFortyFive AnglePosYFortyFive AngleNegYFortyFive
clear PositiveThetaFifty NegativeThetaFifty YNegPenFifty YPosPenFifty
clear LinearFitPositiveFifty LinearFitNegativeFifty
clear EvaluationPositiveFifty EvaluationNegativeFifty
clear PositiveThetaFortyFive NegativeThetaFortyFive YNegPenFortyFive
clear YPosPenFortyFive
clear LinearFitPositiveFortyFive LinearFitNegativeFortyFive
clear EvaluationPositiveFortyFive EvaluationNegativeFortyFive
clear Index IndexMoving Increments
clear Deviations EdgeNeg EdgePos
clear FiftyPercPen MinKK MaxKK SkipFits kk kkstar
clear RSq Residuals SSE SST
clear C SkipAngles
clear SigmaCFUsed aa bb SigmaFactorUsed MeanCFUsed PointsUsed
clear Left Indexing DistProfile
clear MaxKK MinKK Increments Stepping X Y MidPoint
clear IndeL IndexR gg Difference
clear RightEdge jj LeftEdge start bestcoeffs a b c
clear IntersectionL IntersectionR Imag SigmaL Skips FitOffset
clear FortyFiveDiametersIndex Deviations RMSE NRMSE Skipping SkipFits
clear ProcessDo45
clear ok_ cf1_ cf_ st_ ft_ st1_ ft1_

    end

PenetrationPlume = arrayfun(@(x) mean(x.Penetration), Plume);
AvgPenetration = mean(PenetrationPlume);

PenetrationSpray(:,xx) = (PenetrationPlume AvgPenetration);

ThetaPlumeM45Do = arrayfun(@(x) mean(x.ThetaTotalFortyFive), Plume);
AvgThetaM45Do = mean(ThetaPlumeM45Do);

ThetaSprayM45Do(:,xx) = (ThetaPlumeM45Do AvgThetaM45Do);

xx = xx+1;

clear Plume
clear Penetrationplume AvgPenetration
clear ThetaPlumeM50Perc AvgThetaM50Perc

```



```
clear ThetaPlumeM45Do AvgThetaM45Do

close all
end
```

12.4.5. Data Analysis Program

Data analysis consists of reading in the BDF data file from the ADX into Matlab, and appropriately configuring the data. Based on the system design and data storage, every 5 ms, there is 0.2 ms of repeated data. Therefore, this data must be removed from the results to ensure the final results represent the actual test data. After the data is removed, the empty data channels are removed, and the desired data is stored in variables of interest, as defined using a text file, provided by the user, *TextFileDefinitions.txt*. The results (data in the channel variable names of interest) are written to a .mat file for easier retrieval in the future (*TestFileData.mat*), and the appropriate program is run to determine condition data, either vaporizing, non-vaporizing or combusting sprays. Required inputs for this processing program are the total number of analog data channels (8), sampling frequency (100 kHz), tests date (YYYYMMDD format), test time (HHMM), and the test type (combusting, vaporizing, or non-vaporizing). To run the program, run *BDFConversion_RUN_ME.m*. This program calls the sub-routines, of *BDFConversion_TextReadIn_8CH_100kHz.m*, and *TEXTFILEREADIN.m*. Finally, the data processing sub-routine is run for the specified test type, either non-vaporizing (*DataAnalysisN2.m*), vaporizing (*DataAnalysisZeroPercO2.m*), or combusting (*DataAnalysis21PercO2.m*). These files are provided in this, and the subsequent sections.

BDFConversion_RUN_ME.m

```
% BDF Conversion
% Run this program to convert the BDF data from the ADX into data
accessible
% in Matlab. This program calls subprograms that actually run the
% conversion routines.

% Jaclyn Nesbitt
% May 2009

%% Setup Workspace

clear all
close all
clc

%%%%%%%%%%%%%% User Inputs %%%%%%%%%%%%%%%

% Channel Number
NumAnalogChannels = input ('Enter Number of Analog Channels (8 or
16): ');
if NumAnalogChannels ~= 8 && NumAnalogChannels ~= 16
```

```

        error ('Invalid Entry for Number of Analog Channels, must be 8 or
16');
end

% Sampling Frequency
SampleFrequencykHz = input ('Enter Sampling Frequency in kHz (5 or
100):');
if SampleFrequencykHz ~= 5 && SampleFrequencykHz~=100
    error ('Invalid Entry for Sampling Frequency in kHz, must be 5 or
100');
end

YYYYMMDD = input('Enter Test Date in format YYYYMMDD:', 's');
HHMM = input('Enter Test Time in format HHMM:', 's');
TestType = input('Enter Test Type (N2, 0PercO2, 21PercO2):', 's');
% Directory Pathname Designation

DIRparent=('\\mtucifs\dfshome\jenesbit\Desktop\DieselSprayTesting -
Additional August 2010\');
home_dir = DIRparent;
dir_name = ((DIRparent YYYYMMDD '\' HHMM));
processing_file =
('\\mtucifs\dfshome\jenesbit\Desktop\Dissertation\MFILES');

%%%%%%%%%%%%%%%%%%%%%%%%%%%%%%%%%%%%%%%%%%%%%%%%%%%%%%%%%%%%%%%%%%%%%%%%
if SampleFrequencykHz == 100 && NumAnalogChannels == 8
    run BDFConversion_TextReadIN_8CH_100kHz
end

if SampleFrequencykHz == 100 && NumAnalogChannels == 16
    run BDFConversion_TextReadIN_16CH_100kHz
end

if SampleFrequencykHz == 5 && NumAnalogChannels == 16
    run BDonversion_TextReadIN_16CH_5kHz
end

if SampleFrequencykHz == 5 && NumAnalogChannels == 8
    run BDFConversion_TextReadIN_8CH_5kHz
end

date = date;

```

BDFConversion TextReadIN 8CH 100kHz.m

```

%% BDF File Read Into Matlab - 8 Channels, 100 kHz.

% Jaclyn Nesbitt
% May 3, 2009

% Revised further by Sam Johnson for user inputs and automated pathname
% designations
% May 5, 2009

% Revised Further July 27 2009 by Jaclyn Nesbitt

```

```

% Incorporating necessary fix for bug in ADX:
% every 5 ms it repeats 0.2 ms of data.

% This file reads in the high speed data from the ADX in two analog
data
% files (two for the 16 channel solution, 1 for the 8 channel
solution).
% The analog data files also contain all necessary PWM data. The
% PWM data is interpolated to match the sampling frequency of the
% analog data. The user must change the filename of the data file to
match
% the desired file. This file can be modified if desired to write the
data
% to a CSV file.

% The format of the binary file is as follows:
% First 4 bytes is the number of channels saved as long
% Second 4 bytes is the number of saved data per channel
% After that the data is saved in 4 bytes floating point real numbers
% (IEEE standard format)
% We can ignore the first 8 bytes and then start reading the data as 4
% byte floating point numbers.

% User must specify the number of channels which were sampled and
stored on
% the Analog card - 8 or 16, along with the sampling frequency in kHz
(5 or 100).

%% Set up Matlab for Data Read

clc;
cd (dir_name)

%% Read ADX binary Data -- in BDF Format (Directly from ADX).

% If number of analog channels is 8 - there is only one analog data
file.

    fid = fopen ((dir_name '\AnalogData1.bdf'), 'r');

%%%%%%%%%%%%%%%%%%%%%%%%%%%%%%%%%%%%%%%%%%%%%%%%%%%%%%%%%%%%%%%%%%%%%%%%

% N_CHN and N_DATA - based on data storage - this first 8 bytes can be
% ignored. This corresponds to data in the first Analog card.

N_CHN = fread (fid, 1, 'integer*4');
N_DATA = fread (fid, 1, 'integer*4');

% READ IN ACTUAL DATA - from both analog cards and PWM
% Reading data from card 1
numelem=N_CHN*N_DATA;
EndIndex = floor(numelem/5200);
X = fread (fid, 'float32');
X2 = reshape (X, N_CHN, N_DATA);

```

```

X3(:,1:25) = X2(:,1:25); % Read in first 25 sets - each set has 20 data
points
                                % sampled at 100 kHz - this represents the
first
                                % 500 good data points
j = 25;

% Sort through data, deleting 20 sample (0.2ms) of data every 5 ms (500
% samples)
for i =1:EndIndex-1;
X3(:,25*i+1:(i+1)*25) = X2(:,j+2:j+26);
j = 26+j;
i = i + 1;
end

% Get the last bit of data.

if size(X2,2) > j(end)
    Difference = size(X2,2)-j(end);
    X3(:, 25*i(end)+1:25*i(end)+1+Difference-2) =
X2(:,j(end)+2:j(end)+Difference);
end

% Format all data channels with the corrected data.
Dimension = size(X3,1)*size(X3,2)/10;
PWMDimension = size(X3,2);
Channel1 = reshape (X3 ((1:20),:), Dimension, 1); % CV Dynamic
pressure
Channel2 = reshape (X3 ((21:40),:), Dimension, 1);
Channel3 = reshape (X3 ((41:60),:), Dimension, 1);
Channel4 = reshape (X3 ((61:80),:), Dimension, 1);
Channel5 = reshape (X3 ((81:100),:), Dimension, 1);
Channel6 = reshape (X3 ((101:120),:), Dimension, 1);
Channel7 = reshape (X3 ((121:140),:), Dimension, 1);
Channel8 = reshape (X3 ((141:160),:), Dimension, 1);
Time = reshape(X3 ((181:200),:), Dimension, 1); % Relative to ADX Clock

% PWM Data -- correctly align the data from the PWM card into
individual
% channels.
Channel9 = reshape (X3 ((161:161),:), PWMDimension, 1);
Channel10 = reshape (X3 ((162:162),:), PWMDimension, 1);
Channel11 = reshape (X3 ((163:163),:), PWMDimension, 1);
Channel12 = reshape (X3 ((164:164),:), PWMDimension, 1);
Channel13 = reshape (X3 ((165:165),:), PWMDimension, 1);
Channel14 = reshape (X3 ((166:166),:), PWMDimension, 1);
Channel15 = reshape (X3 ((167:167),:), PWMDimension, 1);
Channel16 = reshape (X3 ((168:168),:), PWMDimension, 1);
Channel17 = reshape (X3 ((169:169),:), PWMDimension, 1);
Channel18 = reshape (X3 ((170:170),:), PWMDimension, 1);
Channel19 = reshape (X3 ((171:171),:), PWMDimension, 1);
Channel20 = reshape (X3 ((172:172),:), PWMDimension, 1);
Channel21 = reshape (X3 ((173:173),:), PWMDimension, 1);
Channel22 = reshape (X3 ((174:174),:), PWMDimension, 1);

```

```

Channel23 = reshape (X3 ((175:175),:), PWMDimension, 1);
Channel24 = reshape (X3 ((176:176),:), PWMDimension, 1);
Channel25 = reshape (X3 ((177:177),:), PWMDimension, 1);
Channel26 = reshape (X3 ((178:178),:), PWMDimension, 1);
Channel27 = reshape (X3 ((179:179),:), PWMDimension, 1); % Injection
trigger
Channel28 = reshape (X3 ((180:180),:), PWMDimension, 1); % Ignition
trigger

% Interpolate PWM Data to Match Data Sampling Rate of Analog Cards.

% Scale represents the frequency ratio of the increased frequency
% requirement to the current frequency of the PWM data
scale=20;

Channel9 = interp (Channel9, scale, 1, 0.008);
Channel10 = interp (Channel10, scale, 1, 0.008);
Channel11 = interp (Channel11, scale, 1, 0.008);
Channel12 = interp (Channel12, scale, 1, 0.008);
Channel13 = interp (Channel13, scale, 1, 0.008);
Channel14 = interp (Channel14, scale, 1, 0.008);
Channel15 = interp (Channel15, scale, 1, 0.008);
Channel16 = interp (Channel16, scale, 1, 0.008);
Channel17 = interp (Channel17, scale, 1, 0.008);
Channel18 = interp (Channel18, scale, 1, 0.008);
Channel19 = interp (Channel19, scale, 1, 0.008);
Channel20 = interp (Channel20, scale, 1, 0.008);
Channel21 = interp (Channel21, scale, 1, 0.008);
Channel22 = interp (Channel22, scale, 1, 0.008);
Channel23 = interp (Channel23, scale, 1, 0.008);
Channel24 = interp (Channel24, scale, 1, 0.008);
Channel25 = interp (Channel25, scale, 1, 0.008);
Channel26 = interp (Channel26, scale, 1, 0.008);
Channel27 = interp (Channel27, scale, 1, 0.008);
Channel28 = interp (Channel28, scale, 1, 0.008);

% Close Files
fclose (fid);

%% Clear up workspace

clear scale
clear numelem2
clear numelem
clear fid2
clear fid
clear X_2
clear X3_2
clear X3
clear X
clear N_DATA2
clear N_DATA
clear N_CHN2
clear N_CHN

```

```

%% Run Subsequent Processing Routines

cd (processing_file)

run TEXTFILEREADIN;

cd (processing_file)

if strcmp(TestType, 'N2') == 1
    run DataAnalysisN2;
end

if strcmp(TestType, '0PercO2') == 1
    run DataAnalysisZeroPercO2;
end

if strcmp(TestType, '21PercO2') == 1
    run DataAnalysis21PercO2;
end

```

TEXTFILEREADIN.m

```

%% Text File Read-In and Data Variable Updates

% Jaclyn Nesbitt
% June 1 2009

% This file reads in a text file of definitions - including variable
names
% - to convert the BDF generic file names into those used for the given
% test.

%% Read in Text File with Variable Names corresponding to hardware
channels

(card, channel, BDFFilename, Signal, Units) = textread((dir_name
'\TextFileDefinitions.txt'), '%s %s %s %s %s', 'headerlines', 1);

% Determine which Channels are not used, and delete this data from the
BDF
% conversion file.

TF = strcmp('n/a', Signal);

indices = find(TF==1);

NoData=BDFFilename(indices);

trial(:,1)=strcmp('Channel1', NoData);
trial(:,2)=strcmp('Channel2', NoData);
trial(:,3)=strcmp('Channel3', NoData);
trial(:,4)=strcmp('Channel4', NoData);
trial(:,5)=strcmp('Channel5', NoData);
trial(:,6)=strcmp('Channel6', NoData);

```

```

trial(:,7)=strcmp('Channel7', NoData);
trial(:,8)=strcmp('Channel8', NoData);

if NumAnalogChannels == 16

trial(:,9)=strcmp('Channel1_2', NoData);
trial(:,10)=strcmp('Channel2_2', NoData);
trial(:,11)=strcmp('Channel3_2', NoData);
trial(:,12)=strcmp('Channel4_2', NoData);
trial(:,13)=strcmp('Channel5_2', NoData);
trial(:,14)=strcmp('Channel6_2', NoData);
trial(:,15)=strcmp('Channel7_2', NoData);
trial(:,16)=strcmp('Channel8_2', NoData);

end

trial(:,17)=strcmp('Channel27', NoData);
trial(:,18)=strcmp('Channel28', NoData);
trial(:,19)=strcmp('Channel15', NoData);
trial(:,20)=strcmp('Channel16', NoData);
trial(:,21)=strcmp('Channel17', NoData);
trial(:,22)=strcmp('Channel18', NoData);
trial(:,23)=strcmp('Channel19', NoData);
trial(:,24)=strcmp('Channel20', NoData);
trial(:,25)=strcmp('Channel21', NoData);
trial(:,26)=strcmp('Channel22', NoData);
trial(:,27)=strcmp('Channel23', NoData);
trial(:,28)=strcmp('Channel24', NoData);
trial(:,29)=strcmp('Channel25', NoData);
trial(:,30)=strcmp('Channel26', NoData);
trial(:,31)=strcmp('Channel9', NoData);
trial(:,32)=strcmp('Channel10', NoData);
trial(:,33)=strcmp('Channel11', NoData);
trial(:,34)=strcmp('Channel12', NoData);
trial(:,35)=strcmp('Channel13', NoData);
trial(:,36)=strcmp('Channel14', NoData);

i=1;

for i=1:36
    IndexOfInterest = find(trial(:,i)==1);

    if IndexOfInterest ~= NaN;
        if i==1
            clear Channel1
        elseif i==2
            clear Channel2
        elseif i==3
            clear Channel3
        elseif i==4
            clear Channel4
        elseif i==5
            clear Channel5
        elseif i==6
            clear Channel6

```

```

elseif i==7
    clear Channel7
elseif i==8
    clear Channel8
elseif i==9
    clear Channel1_2
elseif i==10
    clear Channel2_2
elseif i==11
    clear Channel3_2
elseif i==12
    clear Channel4_2
elseif i==13
    clear Channel5_2
elseif i==14
    clear Channel6_2
elseif i==15
    clear Channel7_2
elseif i==16
    clear Channel8_2
elseif i==17
    clear Channel27
elseif i==18
    clear Channel28
elseif i==19
    clear Channel15
elseif i==20
    clear Channel16
elseif i==21
    clear Channel17
elseif i==22
    clear Channel18
elseif i==23
    clear Channel19
elseif i==24
    clear Channel20
elseif i==25
    clear Channel21
elseif i==26
    clear Channel22
elseif i==27
    clear Channel23
elseif i==28
    clear Channel24
elseif i==29
    clear Channel25
elseif i==30
    clear Channel26
elseif i==31
    clear Channel9
elseif i==32
    clear Channel10
elseif i==33
    clear Channel11
elseif i==34

```



```

        clear Channel12
    elseif i==35
        clear Channel13
    elseif i==36
        clear Channel14
    end
end

i=i+1;

end

% Redefine variable names to correspond to those defined in the text
file
% to use in the plotting routines.

dataindices = find(TF==0);

j=1;

for j=1:36

    DataIndexOfInterest = find(dataindices==j);

    if DataIndexOfInterest ~= NaN

        if j==1
            assignin('base', char(Signal(j)), Channel1);
            clear Channel1
        elseif j==2
            assignin('base', char(Signal(j)), Channel2);
            clear Channel2
        elseif j==3
            assignin('base', char(Signal(j)), Channel3);
            clear Channel3
        elseif j==4
            assignin('base', char(Signal(j)), Channel4);
            clear Channel4
        elseif j==5
            assignin('base', char(Signal(j)), Channel5);
            clear Channel5
        elseif j==6
            assignin('base', char(Signal(j)), Channel6);
            clear Channel6
        elseif j==7
            assignin('base', char(Signal(j)), Channel7);
            clear Channel7
        elseif j==8
            assignin('base', char(Signal(j)), Channel8);
            clear Channel8
        elseif j==17
            assignin('base', char(Signal(j)), Channel27);
            clear Channel27
        elseif j==18
            assignin('base', char(Signal(j)), Channel28);

```

```

        clear Channel28
elseif j==19
    assignin('base', char(Signal(j)), Channel15);
    clear Channel15
elseif j==20
    assignin('base', char(Signal(j)), Channel16);
    clear Channel16
elseif j==21
    assignin('base', char(Signal(j)), Channel17);
    clear Channel17
elseif j==22
    assignin('base', char(Signal(j)), Channel18);
    clear Channel18
elseif j==23
    assignin('base', char(Signal(j)), Channel19);
    clear Channel19
elseif j==24
    assignin('base', char(Signal(j)), Channel20);
    clear Channel20
elseif j==25
    assignin('base', char(Signal(j)), Channel21);
    clear Channel21
elseif j==26
    assignin('base', char(Signal(j)), Channel22);
    clear Channel22
elseif j==27
    assignin('base', char(Signal(j)), Channel23);
    clear Channel23
elseif j==28
    assignin('base', char(Signal(j)), Channel24);
    clear Channel24
elseif j==29
    assignin('base', char(Signal(j)), Channel25);
    clear Channel25
elseif j==30
    assignin('base', char(Signal(j)), Channel26);
    clear Channel26
elseif j==31
    assignin('base', char(Signal(j)), Channel19);
    clear Channel19
elseif j==32
    assignin('base', char(Signal(j)), Channel10);
    clear Channel10
elseif j==33
    assignin('base', char(Signal(j)), Channel11);
    clear Channel11
elseif j==34
    assignin('base', char(Signal(j)), Channel12);
    clear Channel12
elseif j==35
    assignin('base', char(Signal(j)), Channel13);
    clear Channel13
elseif j==36
    assignin('base', char(Signal(j)), Channel14);
    clear Channel14

```

```

end
if NumAnalogChannels == 16
if j==9
    assignin('base', char(Signal(j)), Channel1_2);
    clear Channel1_2
elseif j==10
    assignin('base', char(Signal(j)), Channel2_2);
    clear Channel2_2
elseif j==11
    assignin('base', char(Signal(j)), Channel3_2);
    clear Channel3_2
elseif j==12
    assignin('base', char(Signal(j)), Channel4_2);
    clear Channel4_2
elseif j==13
    assignin('base', char(Signal(j)), Channel5_2);
    clear Channel5_2
elseif j==14
    assignin('base', char(Signal(j)), Channel6_2);
    clear Channel6_2
elseif j==15
    assignin('base', char(Signal(j)), Channel7_2);
    clear Channel7_2
elseif j==16
    assignin('base', char(Signal(j)), Channel8_2);
    clear Channel8_2
end
end
end

% Create Time Vector
% The length of this vector must match the length of the log duration
as
% taken by the ADx where "time" equals the log duration in seconds
Fs = 100000; % Set sample rate of ADx (Samples/sec)
% Note: When sampling frequency of ADx
is set % at 5 kHz, data is interpolated to 100
kHz % so timevector will still match

N = size(Pressure,1); % Create data point vector
t = (1:N)/Fs*1000; % milliseconds
t = t'; % Convert t into a column vector
logdur = max(t)/1000; % Data log time duration (seconds)
endtime = max(t); % End timestamp in ms

%% Clear up workspace

clear DataIndexOfInterest
clear IndexOfInterest
clear NoData
clear TF
clear dataindices

```

```

clear i
clear j
clear trial
clear indices
clear N
clear logdur
clear Fs

%% Save Data into a Matfile for further post processing
cd (dir_name)

save TestFileData;

```

TextFileDefinitions.txt

Card	Channel	BDFFilename	Signal	Units
Analog1	1	Channel1	Pressure	psia
Analog1	2	Channel2	n/a	n/a
Analog1	3	Channel3	n/a	n/a
Analog1	4	Channel4	FuelPressure	Bar
Analog1	5	Channel5	SparkCurrent	A
Analog1	6	Channel6	n/a	n/a
Analog1	7	Channel7	PulseGenerator	V
Analog1	8	Channel8	Inhibit	V
Analog2	1	Channel1_2	n/a	n/a
Analog2	2	Channel2_2	n/a	n/a
Analog2	3	Channel3_2	n/a	n/a
Analog2	4	Channel4_2	n/a	n/a
Analog2	5	Channel5_2	n/a	n/a
Analog2	6	Channel6_2	n/a	n/a
Analog2	7	Channel7_2	n/a	n/a
Analog2	8	Channel8_2	n/a	n/a
PWMOutput	2	Channel27	Ignition	V
PWMOutput	1	Channel28	Injection	V
PWMOutput	3	Channel15	n/a	n/a
PWMOutput	4	Channel16	n/a	n/a
PWMOutput	5	Channel17	n/a	n/a
PWMOutput	6	Channel18	n/a	n/a
PWMOutput	7	Channel19	n/a	n/a
PWMOutput	8	Channel20	n/a	n/a
PWMOutput	9	Channel21	n/a	n/a
PWMOutput	10	Channel22	n/a	n/a
PWMOutput	11	Channel23	n/a	n/a
PWMOutput	12	Channel24	n/a	n/a
PWMOutput	13	Channel25	n/a	n/a
PWMOutput	14	Channel26	n/a	n/a
None	9	Channel9	n/a	n/a
None	10	Channel10	n/a	n/a
None	11	Channel11	n/a	n/a
None	12	Channel12	n/a	n/a
None	13	Channel13	n/a	n/a
None	14	Channel14	n/a	n/a

12.4.5.1. Nonvaporizing (Nitrogen) Tests

This program determines the relevant nitrogen test parameters, including fuel injection pressure at injection, and the actual density condition, calculated using the ideal gas law using fill pressure measured with the dynamic pressure transducer.

DataAnalysisN2.m

```
%% Analyze Nitrogen Data
% Analyze Data to Determine Fuel Pressure, Density, and Pressure at
% Injection

% Jaclyn Nesbitt

cd (dir_name)

FuelPressureBar = (FuelPressure*7500-15000)*0.06895;

% Determine relative Timings
InjectionPWM = min(find(Injection > 0));
PGStart = min(find(PulseGenerator > 0.5))-1;

% Record Important parameters including pressure at fuel injection and
% injection pressure

    PressureInjectionkPa = Pressure(PGStart)*6.89475729;

% Output fuel pressure at Injection
FuelPInjection = FuelPressureBar(PGStart) %Bar

R = 8.314; % m3*Pa / (K*mol)
T = 100+273.15; % K -- CV Heated to 100 C for Tests

MW_Mix = 2*14; %N2

% Output Density (Based on P and T), and Pressure at Injection
Density = (PressureInjectionkPa*1000*MW_Mix)/(R*T)*1/1000 %kg/m3
PressureInjectionBar = PressureInjectionkPa*0.01
```

12.4.5.2. Vaporizing (0% Oxygen) Tests

The vaporizing oxygen test processing file computes both bulk and core gas temperature and density at injection using the measurements from the dynamic pressure transducer and fuel injection pressure at injection.

DataAnalysisZeroPercO2.m

```
%% Analyze 0% O2 Data

% Jaclyn Nesbitt

% Analyze Data to Determine Fuel Pressure, Core Temperature and
Density,
% and Bulk Density and Temperature
```

```

cd (dir_name)

FuelPressureBar = (FuelPressure*7500-15000)*0.06895;

% Define Relative Timings

InjectionPWM = min(find(Injection > 0));
PGStart = min(find(PulseGenerator > 0.5))-1;

% Record Important parameters
% Parameters include pressure at injection, Fuel pressure at injection,
and
% CV Fill pressure

PressureInjectionkPa = Pressure(PGStart)*6.89475729;
FuelPInjection = FuelPressureBar(PGStart) %Bar
FillPressurekPa = Pressure(100*1000)*6.89475729;

R = 8.314; % m3*Pa / (K*mol)
T = 180+273.15; % K - CV Heated to 180 C

% Calculate Mixture Molecular Weight
P_C2H2 = 24.527;
P_H2 = 12.299;
P_N2Bal = 574.212;
P_O2N2 = 179.148;

P_Total = P_C2H2+P_H2 + P_N2Bal + P_O2N2; % Psi

PercO2N2 = 40; % O2/N2 Mixture, 40% O2, 60% N2

MW_C2H2 = 2*12+2*1;
MW_H2 = 2*1;
MW_O2 = 2*16;
MW_N2 = 2*14;
MW_O2N2 = PercO2N2/100*MW_O2 + (100-PercO2N2)/100*MW_N2;

MW_Mix =
P_C2H2/P_Total*MW_C2H2+P_H2/P_Total*MW_H2+P_N2Bal/P_Total*MW_N2 +
P_O2N2/P_Total*MW_O2N2;

%Calculate Bulk Gas Conditions (based on measured values)

BulkDensity = (FillPressurekPa*1000*MW_Mix)/(R*T)*1/1000 %kg/m3

BulkTempInjection =
(PressureInjectionkPa*1000*MW_Mix)/(BulkDensity*1000*R)

% Calculate core gas conditions - based on Sandia ECN - Lyle
Pickett
a = 0.0406*BulkDensity/20.28;
b = 0.026;

```

```

CoreTempInjection = BulkTempInjection*(1+a*(1-
T/BulkTempInjection)+b*(BulkTempInjection/T - 1))
CoreDensity =
(MW_Mix*PressureInjectionkPa*1000)/(R*CoreTempInjection)*1/1000 % kg/m3

```

12.4.5.3. Combusting (21% Oxygen) Tests

The combusting tests are processed using the following m-file, and parameters of bulk and core density and temperature based on dynamic pressure transducer measurements and fuel injection pressure. Additionally, ignition delay and heat release are calculated from the pressure data.

DataAnalysis21PercO2.m

```

%% Analyze 21% O2 Data

% Jaclyn Nesbitt

% Analyze Data to Determine Fuel Pressure, Core Temperature and
Density,
% and Bulk Density and Temperature

cd (dir_name)

FuelPressureBar = (FuelPressure*7500-15000)*0.06895;

% Define Relative Timings

InjectionPWM = min(find(Injection > 0));
PGStart = min(find(PulseGenerator > 0.5))-1;

% Record Important parameters - pressure at injection, fuel pressure,
and
% fill pressure of the CV

PressureInjectionkPa = Pressure(PGStart)*6.89475729;
FuelPInjection = FuelPressureBar(PGStart) %Bar
FillPressurekPa = Pressure(50*1000)*6.89475729;

R = 8.314; % m3*Pa / (K*mol)
T = 180+273.15; % K - 180 C heated CV

% Compute the bulk and core gas conditions
MW_Mix = 28.83;

% Bulk gas conditions from pressure trace
BulkDensity = (FillPressurekPa*1000*MW_Mix)/(R*T)*1/1000 %kg/m3

BulkTempInjection =
(PressureInjectionkPa*1000*MW_Mix)/(BulkDensity*1000*R)

% Core gas relationship - Lyle Pickett
a = 0.0406*BulkDensity/20.28;
b = 0.026;

```

```

    CoreTempInjection = BulkTempInjection*(1+a*(1-
T/BulkTempInjection)+b*(BulkTempInjection/T - 1))

    CoreDensity =
(MW_Mix*PressureInjectionkPa*1000)/(R*CoreTempInjection)*1/1000 % kg/m3

%% Ignition Delay Determination

% Isolate pressure region of interest - relative to injection trigger
InjectionTrig = min(find(Injection > 0));

% Read in oscilloscope data -> from injector driver
    Filename = strcat(HHMM, '.csv');
    Vector = csvread(Filename,16,1);
    Trigger = Vector(:,1);
    Voltage = Vector(:,2)*20;
    Current = Vector(:,3)*2;
    TimeOscope = (0:2/2500:2-2/2500);

%Reference Oscope and ADX Data to Same Timings

PGStartOscope = min(find(Trigger > 0.5))-1;
PGStart = min(find(PulseGenerator > 0.5))-1;
VoltageStart = min(find(Voltage>12))-1;

Delay = (VoltageStart - PGStartOscope)*2/2500; %ms

PGTrig = min(find(PulseGenerator > 0.05))-1;

PressureInterest = Pressure(PGTrig:PGTrig+2000);

TimeInterest = t(PGTrig:PGTrig+2000)-t(PGTrig);

%Filter Data
Fs = 100*1000;
Fn = Fs/2;

% Low pass filter at 2000 Hz
(d,c) = butter(2, 2000/Fn, 'low');
fmfp = filtfilt(d, c, PressureInterest);
figure;
plot(TimeInterest, PressureInterest, TimeInterest, fmfp, 'r');
xlabel('Time (ms)')
ylabel('Pressure (psia)')
legend('Pressure Trace', 'Filtered Pressure Trace')

% Look at cool-down ROI
Index = max(find(Pressure == max(Pressure)));

% Filter Cool Down Pressure Data with 2000 Hz LP Filter
PressureCD = Pressure(Index:PGTrig);
TimeCD = t(Index:PGTrig);

```



```

figure; plot(PressureCD)

(dd,cd2) = butter(2, 2000/Fn, 'low');
fmfpCD = filtfilt(dd, cd2, PressureCD);
figure;
plot(TimeCD, PressureCD, TimeCD, fmfpCD, 'r');
xlabel('Time (ms)')
ylabel('Pressure (psia)')
legend('Pressure Trace', 'Filtered Pressure Trace')

PDecay = fmfpCD - Pressure(end);
TDecay = TimeCD;

%% Fit an exponential function as linear using curve fit by applying
the
%% logarirthm to the Decay

fit1=polyfit(TDecay, log(PDecay), 1);

%Plot original data and the curve fitted results.
figure
plot(TDecay, PDecay, TDecay, exp(fit1(2)).*exp(fit1(1)*TDecay))
xlabel('Time (milliseconds)')
ylabel('Pressure (psia)')
legend('Data', 'MTU Polyfit Curve Fit')

% Output Cool Down Time Constant

Tau = -fit1(1); %ms

Fitted = exp(fit1(2)).*exp(fit1(1)*t(Index:end))+Pressure(end);

(dda,cda) = butter(2, 2000/Fn, 'low');
T2 = t(Index:end)-t(PGTrig);

PFiltered = filtfilt(dda, cda, Pressure(Index:end));
figure;
plot(T2, Pressure(Index:end), T2, PFiltered, 'r');
xlabel('Time (ms)')
ylabel('Pressure (psia)')
legend('Pressure Trace', 'Filtered Pressure Trace')
SubP = PFiltered - Fitted;

figure; plot(t(Index:end)-t(PGTrig), SubP)
xlabel('Time (ms)')
ylabel('Filtered and Subtracted Data for Ign Delay Determination')
grid on

IndexA = min(find(T2>0));
IgnDelay_2 = T2(min(find(SubP(IndexA:end) > 0))+IndexA-1)-Delay-.245;

% Plot Ignition Delay with Pressure Trace
figure;
plot(TimeInterest, fmfp);
hold on

```

```

plot(IgnDelay_2+0.245, fmf(min(find(TimeInterest > IgnDelay_2+0.245))-
1), 'ro', 'MarkerFaceColor', 'r', 'MarkerEdgeColor', 'r')
xlabel('Time (ms) - Relative to Start of Trigger')
ylabel('Pressure (psia)')
grid on
title(strcat('Ign Delay = ', num2str(IgnDelay_2), ' ms Relative to
Start of Fuel'))

%% HRR Analysis
Index_Injection = PGStart;
t_injection = t(Index_Injection);
p_injection = Pressure(Index_Injection);

figure;
subplot(2,1,1)
plot(t,Pressure)
xlabel('Time (ms)')
ylabel('Pressure (psia)')
hold on
plot(t,PulseGenerator*450, 'r-')
subplot(2,1,2)
plot(t,Pressure)
xlabel('Time (ms)')
ylabel('Pressure (psia) or Scaled Signal (V)')
hold on
plot(t,PulseGenerator*450, 'r-')
xlim((t_injection-50 t_injection+100))
ylim((p_injection-50 p_injection+250))
legend('Pressure', 'Injection Trigger from PG')

%% Consider region of 2nd stage HR

% First we have to smooth the pressure data
% HR analysis - relative to SOFUEL

PSecond = Pressure(Index_Injection+25:end);
TSecond = t(Index_Injection+25:end);
PGSecond = PulseGenerator(Index_Injection+25:end);

PeakPressureSecondInd = max(find(PSecond == max(PSecond)))-10;
PeakPressureSecond = PSecond(PeakPressureSecondInd);
PSecondCropped = PSecond(1:PeakPressureSecondInd);
TSecondCropped = TSecond(1:PeakPressureSecondInd);
PGSecondCropped = PGSecond(1:PeakPressureSecondInd);
IndexSecond = max(find(PSecondCropped == min(PSecondCropped)));
MinPressure = PSecondCropped(IndexSecond);

PSecondCroppedSmoothed = smooth(PSecondCropped, 100);

dt = TSecondCropped(2)-TSecondCropped(1);

kk = 1;

for i = 1 : size(PSecondCropped,1)-1

```

```

dPdt(kk) = (PSecondCroppedSmoothed(i+1)-PSecondCroppedSmoothed(i))/dt;
% psi/ms
kk = kk + 1;
end

gamma = 1.35;
V = 1.1; % L
dqdt = 1/(gamma-1)*V/1000*dPdt*6894.75729*1000/1000; %kW

tASOI = TSecondCropped(1:end-1) - min(TSecondCropped);
PASOI = PSecondCropped(1:end-1);
PGASOI = PGSecondCropped(1:end-1);
figure;
subplot(2,1,1)
plot(tASOI, dqdt)
xlabel('Time ASOI (ms), Injection Trigger at 0 ms')
grid on
ylabel('Heat Release Rate, kJ/s (kW)')
ylim([-100 350])
% ylim([-100 max(dqdt)+50])
subplot(2,1,2)
plot(tASOI, PASOI*101.325/14.7);
hold on;
plot(tASOI, PSecondCroppedSmoothed(1:end-1)*101.325/14.7, 'r-')
legend('Pressure Trace', 'Smoothed Trace', 'Location', 'SouthEast')
xlabel('Time ASOI (ms), Injection Trigger at 0 ms')
ylabel('Pressure (kPa)')

%% OSCOPE DATA

Filename = strcat(HHMM, '.csv');

Vector = csvread(Filename,16,1);
Trigger = Vector(:,1);
Voltage = Vector(:,2)*20;
Current = Vector(:,3)*2;
TimeOscope = (0:2/2500:2-2/2500);

OScopeIndex = min(find(Trigger > 0.5))-1;

SOC = min(find(Current > 1))-1;

tOscope = TimeOscope(SOC-100:end)-TimeOscope(SOC);
CurrentInt = Current(SOC-100:end);
VoltageInt = Voltage(SOC-100:end);

figure
(AX, H1, H2) = plotyy(tOscope, CurrentInt, tOscope, VoltageInt);
set(AX(1),'XColor','k','YColor','k','FontSize',10,'YTick',(-20:5:20),'XTick',-0.20:.2:2);
set(AX(2),'XColor','k','YColor','k','FontSize',10,'YTick',(-30:25:170),'XTick',-0.20:.2:2);
set(get(AX(1),'Ylabel'),'String','Current (A)','Color','k','FontSize',10);

```

```

set(get(AX(2), 'Ylabel'), 'String', 'Voltage (V)', 'Color', 'k',
'FontSize', 10);
set(H1, 'LineStyle', '-', 'LineWidth', 1);
set(H2, 'LineStyle', '-', 'LineWidth', 1);
set(H1, 'Color', 'b');
set(H2, 'Color', 'r');
xlabel('Time (ms)')
    grid on
axis(AX(1), (-0.20 2 -20 20));
axis(AX(2), (-0.20 2 -30 170));
legend((H1; H2), 'Current', 'Voltage', 'Location', 'South');

tt = (-0.2 0 0.244 0.245 0.5 1 1.0625 1.0635 10);
INJ = (0 0 0 100 100 100 100 0 0);

figure
subplot(2,1,1)
(AX, H1, H2) = plotyy(tOscope, CurrentInt, tOscope, VoltageInt);
set(AX(1), 'XColor', 'k', 'YColor', 'k', 'FontSize', 10, 'YTick', (-
20:5:20), 'XTick', -0.20:.2:2);
set(AX(2), 'XColor', 'k', 'YColor', 'k', 'FontSize', 10, 'YTick', (-
30:25:170), 'XTick', -0.20:.2:2);
set(get(AX(1), 'Ylabel'), 'String', 'Current (A)', 'Color', 'k',
'FontSize', 10);
set(get(AX(2), 'Ylabel'), 'String', 'Voltage (V)', 'Color', 'k',
'FontSize', 10);
set(H1, 'LineStyle', '-', 'LineWidth', 1);
set(H2, 'LineStyle', '-', 'LineWidth', 1);
set(H1, 'Color', 'b');
set(H2, 'Color', 'r');
xlabel('Time After Start of Current (ms)')
    grid on
axis(AX(1), (-0.20 2 -20 20));
axis(AX(2), (-0.20 2 -30 170));
legend((H1; H2), 'Current', 'Voltage', 'Location', 'South');
subplot(2,1,2)
(BX, I1, I2) = plotyy(tASOI+0.245, dqdt, tASOI+0.245,
PASOI*101.325/14.7);
set(BX(1), 'XColor', 'k', 'YColor', 'k', 'FontSize', 10, 'YTick', (-
100:75:350), 'XTick', -0.20:2:10);
set(BX(2), 'XColor', 'k', 'YColor', 'k', 'FontSize', 10, 'YTick',
(11000:250:12500), 'XTick', -0.20:2:10);
set(get(BX(1), 'Ylabel'), 'String', 'Heat Release Rate kJ/s (kW)',
'Color', 'k', 'FontSize', 10);
set(get(BX(2), 'Ylabel'), 'String', 'Pressure (kPa)', 'Color', 'k',
'FontSize', 10);
set(I1, 'LineStyle', '-', 'LineWidth', 1);
set(I2, 'LineStyle', '-', 'LineWidth', 1);
set(I1, 'Color', 'b');
set(I2, 'Color', 'r');
xlabel('Time After Start of Current (ms)')
    grid on
axis(BX(1), (-0.20 10 -100 350));
axis(BX(2), (-0.20 10 11000 12500));
hold on;

```

```

I3 = plot(tASOI-0.006, PGASOI*5, 'g-');
hold on;
I4 = plot(tt, INJ, 'k-');
legend((I1; I2; I3; I4), 'dQ/dt', 'Pressure', 'PG Trigger to Driver',
'Fuel Injection', 'Location', 'SouthEast');

dqdtROI = dqdt(1:end-10);

QTotal = sum(dqdtROI)*dt/1000; %kJ

QLHVDiesel = 44; %MJ/kg

MdotFuel = 49; %mg

QTotalEnergy = MdotFuel/1000/1000*43*1000; %Kj

cd ((DIRparent, 'Data Processing Results'))

Name = strcat(HHMM, 'TestData21PercO2.txt');
fid = fopen(Name, 'w');
fprintf(fid, '%g \r\n', FillPressurekPa);
fprintf(fid, '%g \r\n', FuelPInjection);
fprintf(fid, '%g \r\n', BulkDensity);
fprintf(fid, '%g \r\n', BulkTempInjection);
fprintf(fid, '%g \r\n', CoreDensity);
fprintf(fid, '%g \r\n', CoreTempInjection);
fprintf(fid, '%g \r\n', PressureInjectionkPa);
fprintf(fid, '%g \r\n', IgnDelay_2);
fprintf(fid, '%g \r\n', QTotal);
fprintf(fid, '%g \r\n', QTotalEnergy);
fprintf(fid, '%g \r\n', Tau);
fclose(fid);

```

12.5. Supplements to Chapter 5 – Optical Setup and Processing Method Influence

Additional results from the investigation into the effect of image setup and processing methodology on the spray results, as discussed in Chapter 5.3, are presented here.

12.5.1. Case B: 34.8 kg/m³ Ambient Density, 1700 Bar Injection Pressure.

For the 34.8 kg/m³ ambient density case the CV is heated to 373 K and pressurized with nitrogen to 39 bar. The average experimental fill pressure for the Baseline A case was 39.3 bar with a fuel injection pressure of 1786 bar, with that of the Baseline B case having a fill pressure of 39.2 bar and injection pressure of 1682 bar. Back scattering images for this test condition, under the two setups, are shown in Figure 12.21. Scaling and intensity are not preserved in the images.

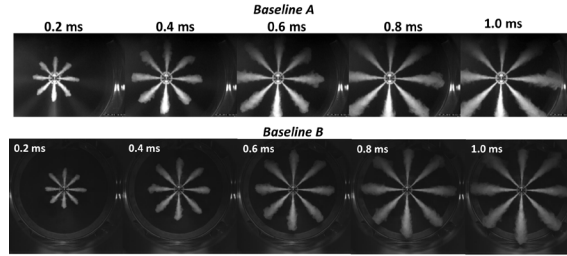


Figure 12.21: Back scattering images for Baseline A setup (Top) and Baseline B setup (bottom) for the 34.8 kg/m³ density case, 1700 bar injection pressure.

The results for penetration and cone angle are presented in Figure 12.22 for the three image processing methods and two imaging setups. These results are presented using the optimum threshold factors including a 40% increase in threshold for Baseline A Image Processing 1 Method (Gaussian Filter, 0.5 Threshold Black and White), 20% decrease in threshold for Baseline A Image Processing 2 Method (Gaussian Filter, Graythresh Threshold Black and White), and the baseline, 1.0, threshold factor for Baseline B (No Filter, Graythresh Threshold Black and White).

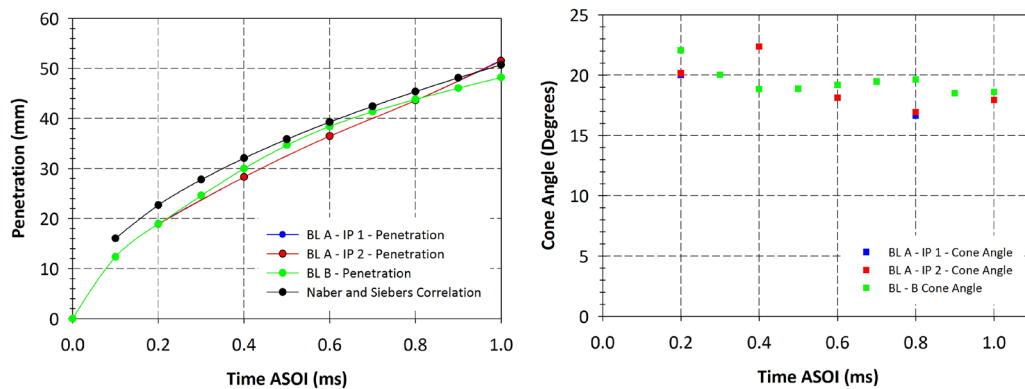


Figure 12.22: Image processing results for penetration (left) and cone angle (right) as a function of time ASOI for the three result sets, for 34.8 kg/m³ ambient density, 1700 bar injection pressure. Penetration correlation of the Naber and Siebers (1996) is also included in the figure.

Penetration increased as a function of time ASOI with that for the Baseline B case exceeding that of the other two cases slightly. Cone angle started at a large value and decreased as a function of time ASOI for the Baseline B case with more fluctuations seen under the Baseline A cases. The correlation over-predicted penetration in the short times ASOI agreeing best with the trend from the Baseline B results from 0.4 ms ASOI on. In the short time scales, the correlation is not valid as the dominant trend is injected liquid behavior, not entrained gas, which was the theory used to develop the correlation and may explain this over-prediction trend. However, relative to the lower injection pressure / charge-gas density case, agreement in early times ASOI for the correlation relative to the experimental results improved, which is attributed to the decreased break-up or transition time from linear to square-root time dependence for the elevated injection pressure and charge gas density (refer to equation (5)).

12.5.1.1. Baseline A – IP 1

First, the threshold for the BL A IP 1 case was increased and decreased by 0 to 50% in increments of 10% to understand changes in penetration and cone angle. This threshold was applied in defining the Gaussian filter that was applied to the image before the image was converted to black and white using a 0.5 threshold. Plots were developed to understand the influence of threshold on penetration and cone angle to quantify the optimal choice in threshold, as shown in Figure 12.23.

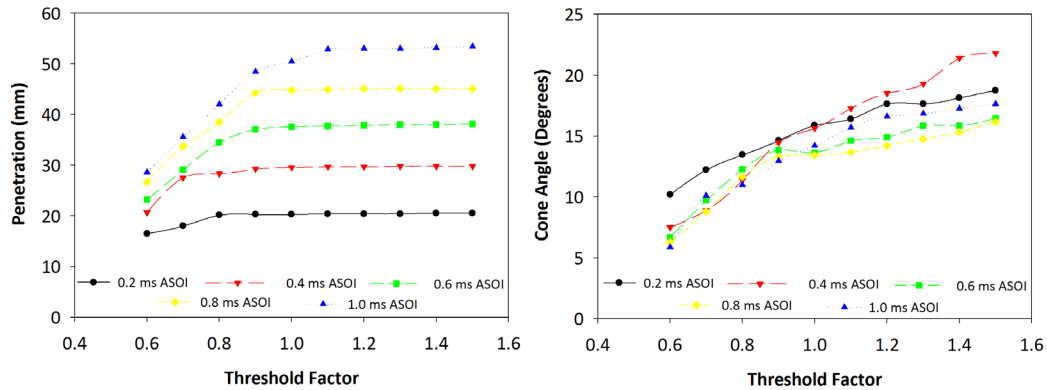


Figure 12.23: Penetration (left) and cone angle (right) as a function of threshold factor for Baseline A image processing method 1 results.

The influence of threshold factor on penetration levels off as threshold factor was increased above 1.1. For cone angle, the results did not level off until even larger threshold factors between 1.4 to 1.5. The optimum choice of threshold factor for these conditions is defined as 1.4 or a 40% increase to provide results which were minimally influenced by choice of threshold. This optimum choice of threshold is further confirmed by the images (Figure 12.24) showing spray boundary and cone angle edge points for the case of 0.6 ms ASOI.

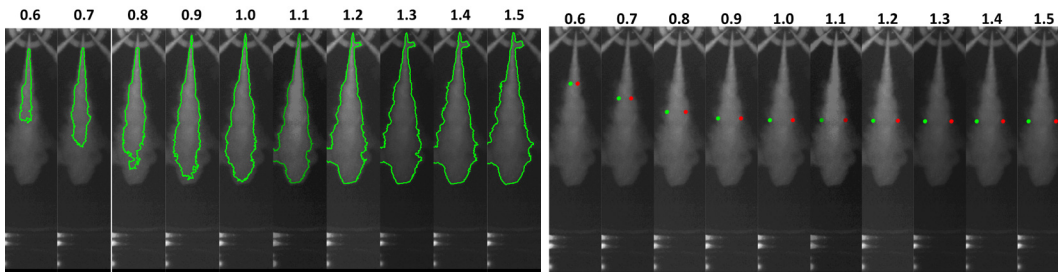


Figure 12.24: Spray images showing threshold influence on penetration (left) and cone angle (right) results for BL A IP 1.

The images confirmed that threshold factors less than 1 miss portions of the spray edge and were not effective processing methods, rather, the threshold factors from 1.3 and up captured the entire spray region providing more accurate results. This setup and processing method combination is clearly not optimum as threshold factor largely governs the results for cone angle.

12.5.1.2. Baseline A – IP 2

BL A IP 2 involved a similar method as IP 1, with the exception of thresholding to black and white which used Matlab's graythresh function to define the threshold for

converting the image to black and white as opposed to a constant, with results shown in Figure 12.25.

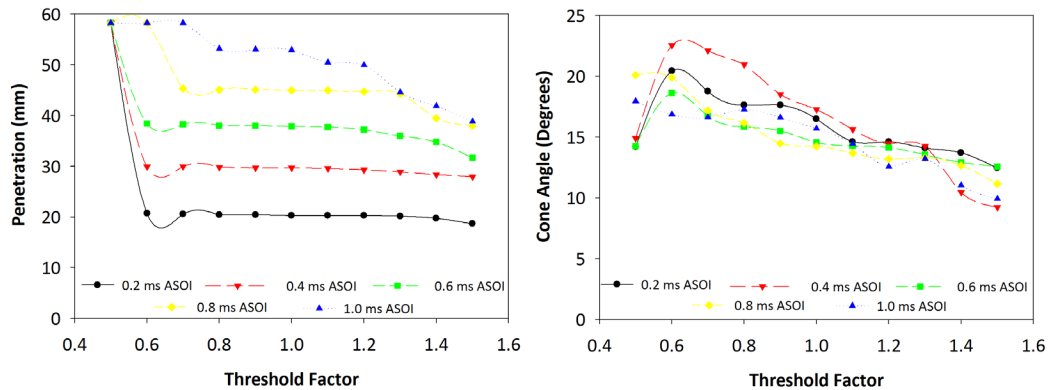


Figure 12.25: Penetration (left) and cone angle (right) as a function of threshold factor for BL A IP 2 results.

In this instance the optimum threshold factor occurred in the range from 0.8 to 1.2, as evidenced by penetration being flat as a function of threshold. Images marked with geometric spray characteristics were a final confirmation of the optimum threshold value, as shown in Figure 12.26.

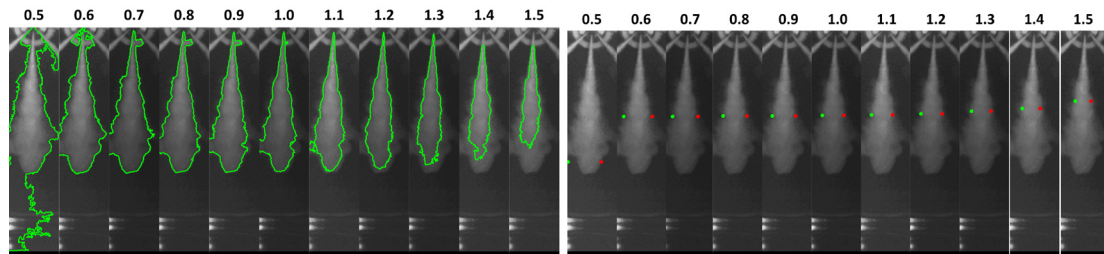


Figure 12.26: Spray images showing threshold influence on penetration (Top) and cone angle (Bottom) results for baseline A IP 2.

As seen from the threshold factor plots, threshold factors in the range of 0.8 to 1.0 provide optimum values for thresholding without missing any of the spray edge. Even under these optimum conditions, some of the spray edge was overlooked as evident in the above images, attributed to the low SNR produced from this imaging setup. This leads to the choice of a 20% decrease in threshold factor.

12.5.1.3. Baseline B

The influence of threshold factor on the image setup and processing method used for Baseline B is characterized in Figure 12.27. The threshold factor was applied to the Matlab function `graythresh` which was used to determine the threshold value of intensity relative to the image intensity distribution for converting to black and white.

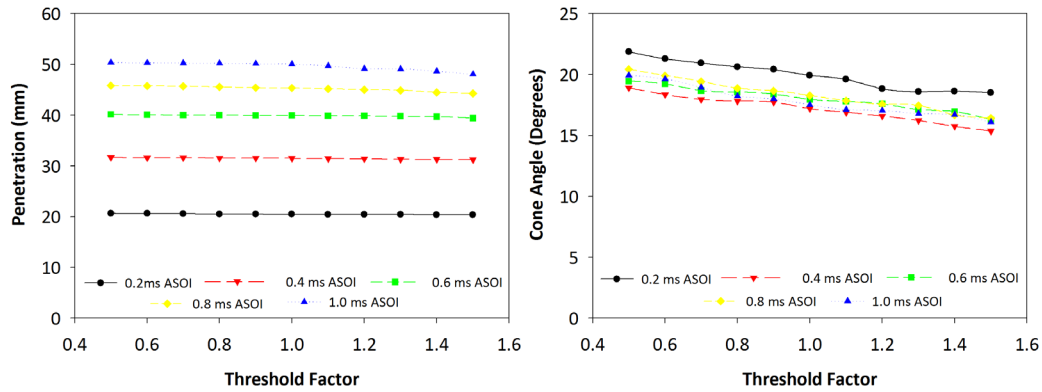


Figure 12.27: Penetration (left) and cone angle (right) as a function of threshold factor for Baseline B image setup & processing method.

Penetration was only influenced by threshold factor minimally for the 1.0 ms time ASOI case with larger threshold factors in excess of 1.0. For all other conditions, penetration was constant as a function of threshold factor showing the minimal influence of threshold factor on penetration for this image setup and processing method. Cone angle has slightly more variation, but, less spread between the data then under other conditions. On average, cone angle decreased as a function of threshold value, however, looking closely the change in cone angle as a function of threshold factor was minimal for the middle threshold factors (0.9 – 1.1). For times 0.4 ms ASOI and larger, cone angle was on average constant at each threshold factor which was expected since cone angle goes through a development period (less than 0.4 ms ASOI in this case, refer to Figure 12.22) before reaching steady state. The observations of optimal threshold factor in the images further confirm the above conclusions, as shown in Figure 12.28.

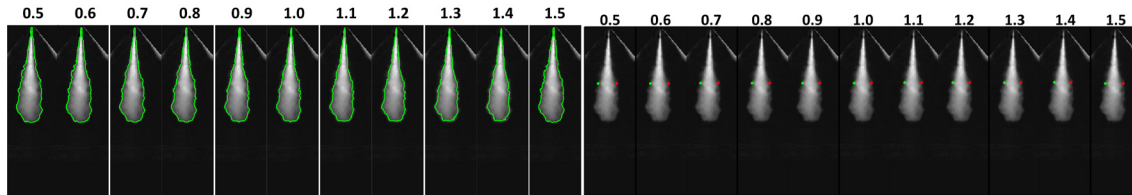


Figure 12.28: Spray images showing threshold influence on penetration (top) and cone angle (bottom) results for Baseline B.

There are insignificant changes in the penetration boundary, with significant trends seen for cone angle with there being no noticeable under- or over- estimation of the spray in the images. Therefore, the baseline 1.0 threshold factor was chosen to provide robust results.

12.6. Supplements to Chapter 6 – Experimental Results

12.6.1. Non-Vaporizing Results

12.6.1.1. Repeat Tests - Chiller Off – Fuel Temperature 328 K

Test conditions for the first set of repeat tests are summarized in Table 12.1, with the fuel-injection chiller off (Refer to Chapter 3.4.2.3 for chiller details). Injection was at 0.8 ms trigger duration (1.4 ms fuel injection duration).

Table 12.1
Repeatability test conditions, chiller off.

	Injection Pressure (Bar)	Density (kg/m ³)	Ambient Pressure (Bar)
Test 1	1975	34.8	38.6
Test 2	1970	34.7	38.5
Test 3	1990	34.9	38.7

Test conditions show small variations which will not impact macroscopic spray characteristics. Images are shown for the three repeat tests in Figure 12.29.

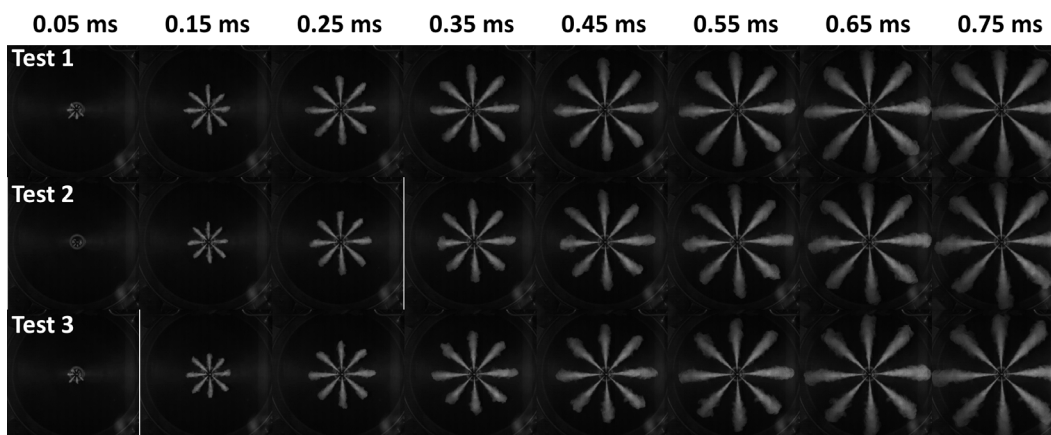


Figure 12.29: Spray images from repeat tests, 34.8 kg/m³ Nitrogen, 2000 bar injection pressure, chiller off.

The images show no significant variations in macroscopic spray characteristics in regards to penetration or spray spreading (cone angle) which was further confirmed by image processing results. Shown in Figure 12.30 are the Median penetration over eight spray plumes is characterized as a function of time ASOI.

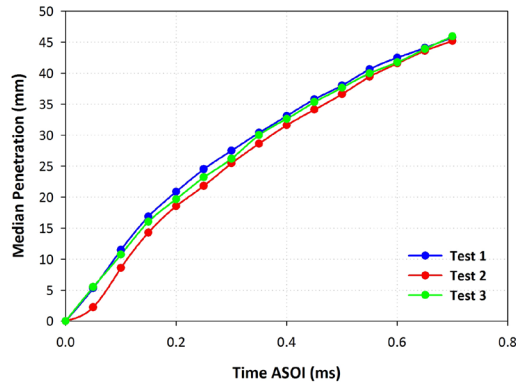


Figure 12.30: Median penetration as a function of time ASOI for the three repeatability tests with the chiller off, 34.8 kg/m³ density, 2000 bar injection pressure.

As time after start of injection increased, the fuel continued to penetrate across the combustion vessel. Test 1 and Test 3 had similar median penetrations, with Test 2 being slightly less. This is attributed to the delay in start of injection of the fuel as shown in Figure 12.29. There could be jitter in the camera timing and applying a 0.05 ms time shift to Test 2 would align Test 1 and Test 3 within expected repeatability and also have the expected linear trend through the origin at SOI (Naber and Siebers 1996). Overall, the median penetration exhibited the expected spray trend, with penetration being linear with time after start of injection during the start of injection before transitioning to square root time dependence during the remainder of the injection period (Naber and Siebers 1996). The difference in time dependent penetration is the result of a transition from injected fuel dependent spray behavior to entrained gas dependent behavior in longer times ASOI (Naber and Siebers 1996).

Results are shown in Figure 12.31 to repeatability in the median cone angle for these test conditions calculated at 60% penetration using the linear curve fit methodology as discussed in Chapter 5.4.1. As time ASOI increased, cone angle started large, and subsequently reduced to a steady state value around 18 degrees.

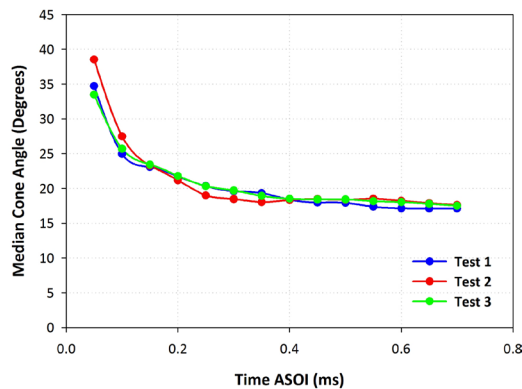


Figure 12.31: Median cone angle as a function of time ASOI for repeat tests, chiller off.

Individual plume behavior was compared during the injection event for tests 1, 2 and 3, in Figure 12.32, Figure 12.33, and Figure 12.34, respectively including both penetration and cone angle at 60% penetration.

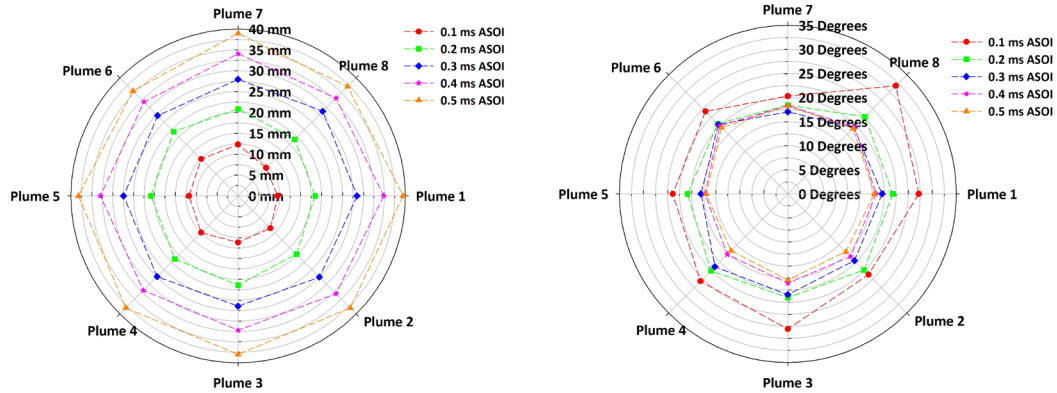


Figure 12.32: Repeat tests, chiller off, nitrogen spray penetration (left) and cone angle at 60% penetration (right) as a function of time ASOI for all 8 spray plumes, Test 1.

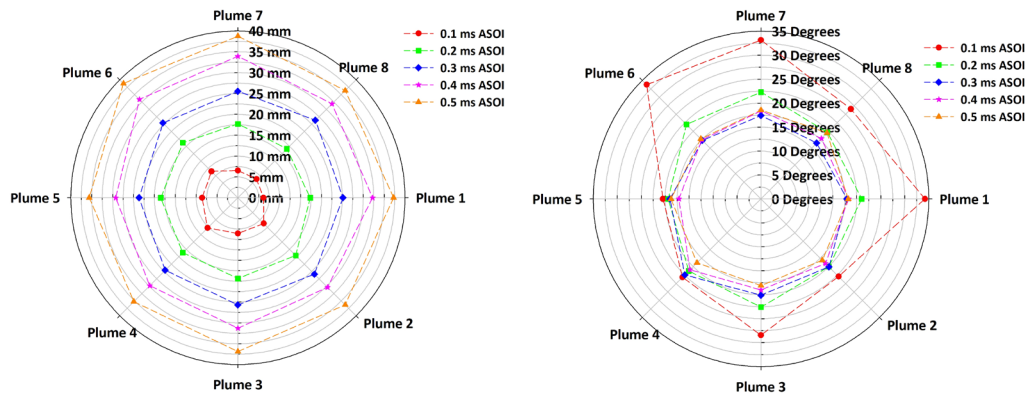


Figure 12.33: Repeat tests, chiller off, nitrogen spray penetration (left) and cone angle at 60% penetration (right) as a function of time ASOI for all 8 spray plumes, Test 2.

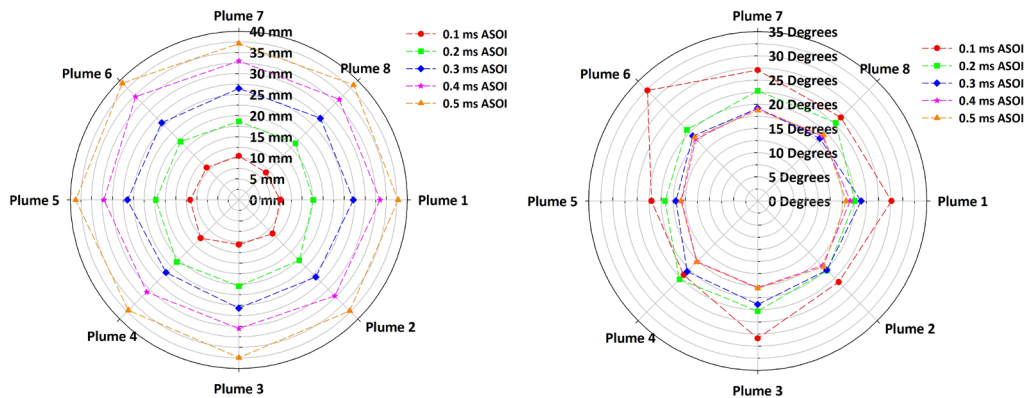


Figure 12.34: Repeat tests, chiller off, nitrogen spray penetration (left) and cone angle at 60% penetration (right) as a function of time ASOI for all 8 spray plumes, Test 3.

All plots show more variations at the start of injection, 0.1 ms ASOI, for both cone angle and penetration. This was attributed to eccentric needle lift as seen in the

images for 0.05 ms ASOI. Cone angle reached a median steady state value by 0.5 ms ASOI, but there was a degree span in cone angle even at this steady state when comparing the plumes.

Plume trends were compared to the mean penetration value over all 8 spray plumes at two different times, 0.1 ms ASOI and 0.5 ms ASOI, in Figure 12.35, to understand trends in plume behavior, along with repeatability. The mean value used for comparison was that over all 8 spray plumes, just considering tests 1 and 3 as will be discussed.

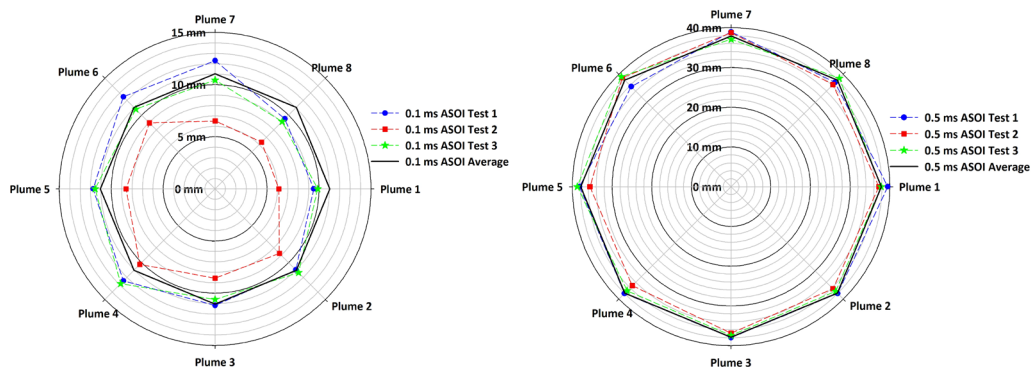


Figure 12.35: Repeat tests, chiller off, diesel spray penetration compared to the average value over all eight plumes for tests 1 and 3, 0.1 ms ASOI left figure; 0.5 ms ASOI right figure.

The first key observation in both figures was that test 2 typically had reduced penetration values relative to the other tests as expected based on the trends in Figure 12.30. Secondly, the test to test variations are amplified during the 0.1 ms ASOI case due to transient needle lift behavior and characteristics. Taking into consideration only Tests 1 and 3 to understand plume trends at 0.5 ms ASOI (after the transient opening stage of injection is complete), the following conclusions could be made. Trends were different for both Test 1 and Test 3 in regards to plume behavior. For plumes 2, 3, 4, and 5, Test 1 liquid penetration matched the mean value, whereas for plumes 1 and 3 and 6 the liquid penetration matched the mean value. For test 1 plumes 1 and 7 were greater than the mean, and plumes 6 and 8 less than the mean. For test 3, plumes 2, 4, and 7 were less than the mean, and plumes 5, 6, and 8 greater than the mean value. There were no consistent plume trends over the three repeat tests.

12.6.1.2. Repeat Tests - Chiller On – Fuel Temperature 321 K

Test conditions for the repeatability tests with the chiller on (reduced fuel temperature) are summarized in Table 12.2. Injection was at 0.8 ms trigger duration (1.4 ms fuel injection duration).

Table 12.2
Repeatability test conditions, chiller on.

	Injection Pressure (Bar)	Density (kg/m ³)	Ambient Pressure (Bar)
Test 1	1990	34.9	38.6
Test 2	1985	34.9	38.6
Test 3	1980	35.2	39.0

Variation in test conditions of ambient pressure, injection pressure, and density were minimal and the images and results showed differences as a result of system repeatability and shot-to-shot injection variability. Images are shown for the three repeat tests in Figure 12.36.

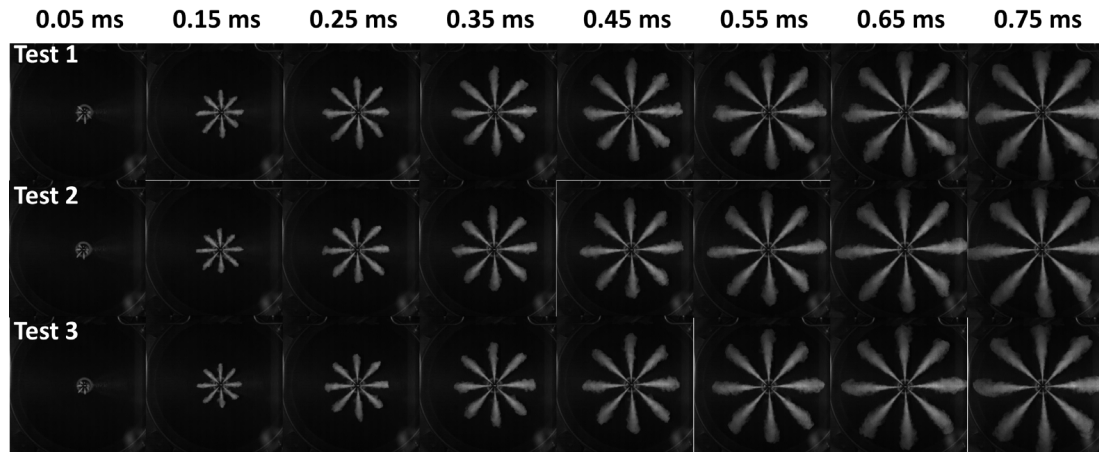


Figure 12.36: Diesel spray images from repeatability tests, 34.8 kg/m³ nitrogen, 2000 bar injection pressure, chiller on (reduced fuel temperature).

There are no noticeable differences in macroscopic spray images showing high system repeatability and minimal test to test variation. The magnitude of test repeatability was quantified via image processing with results for median penetration shown in Figure 12.37.

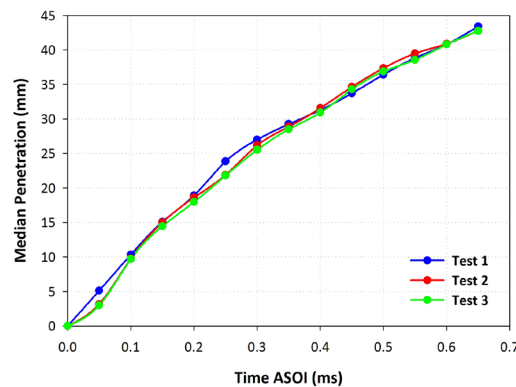


Figure 12.37: Median penetration as a function of time ASOI for the three repeat tests, chiller on.

Results for all three tests for median penetration were similar. A few deviations of Test 1 relative to Tests 2 and 3 existed, however, these were not significant, which shows the

test to test repeatability. Also compared was median cone angle calculated at 60% penetration, shown in Figure 12.38.

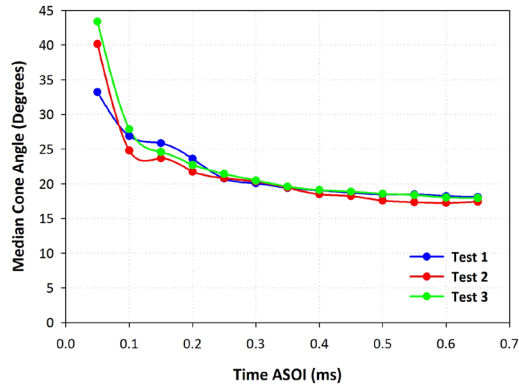


Figure 12.38: Median cone angle as a function of time ASOI for three repeat tests, chiller on.

Cone angle was similar over the three tests with the most variation occurring during the transient spray development phase before reaching steady state. Cone angle at steady state for test 2 was slightly narrower than test 1 and test 3.

Plume to plume variations were compared for each repeat test with the chiller on at different times after start of injection for both penetration and cone angle as shown in Figure 12.39, Figure 12.40, and Figure 12.41 for tests 1, 2, and 3 respectively.

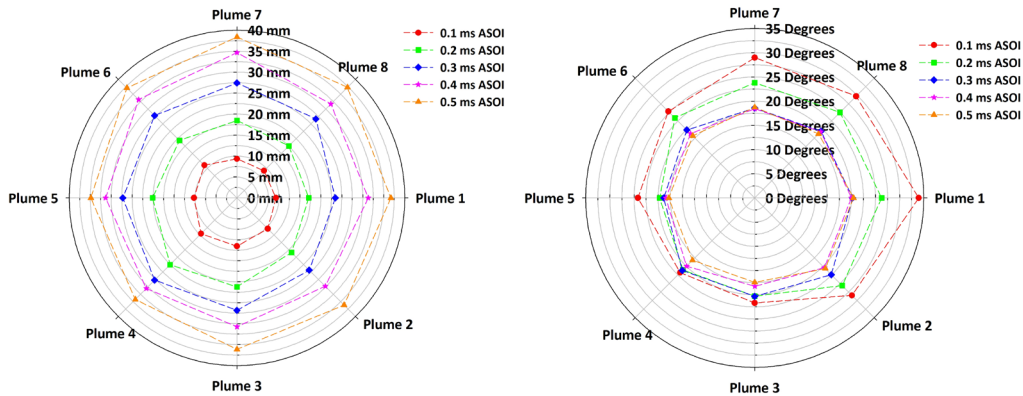


Figure 12.39: Repeat tests, chiller on, nitrogen spray penetration (left) and cone angle at 60% penetration (right) as a function of time ASOI for all 8 spray plumes, Test 1.

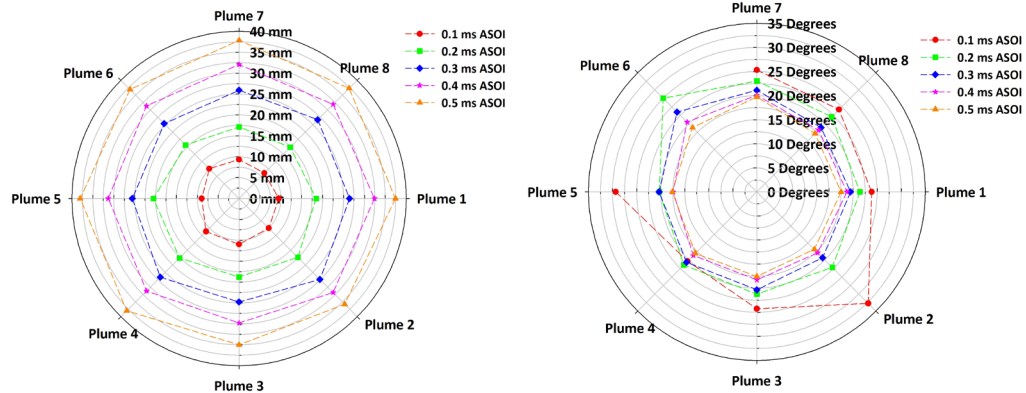


Figure 12.40: Repeat tests, chiller on, nitrogen spray penetration (left) and cone angle at 60% penetration (right) as a function of time ASOI for all 8 spray plumes, Test 2.

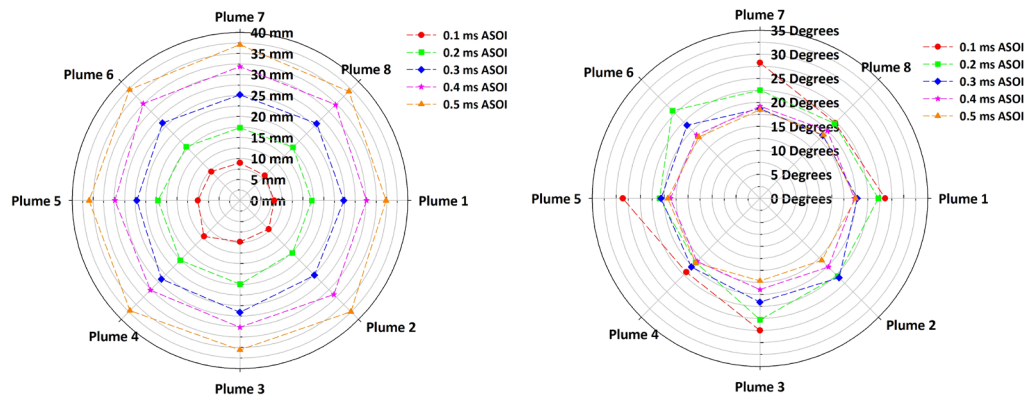


Figure 12.41: Repeat tests, chiller on, nitrogen spray penetration (left) and cone angle at 60% penetration (right) as a function of time ASOI for all 8 spray plumes, Test 3.

As a consistent trend, there were the largest variations 0.1 ms ASOI during the transient spray development with reduced variations in longer times ASOI. However, plume-to-plume variations did not yield consistent trends as a function of time ASOI.

A comparison of the plume to plume trends relative to the mean value over all 8 plumes for all three tests at both 0.1 ms ASOI and 0.5 ms ASOI in Figure 12.42.

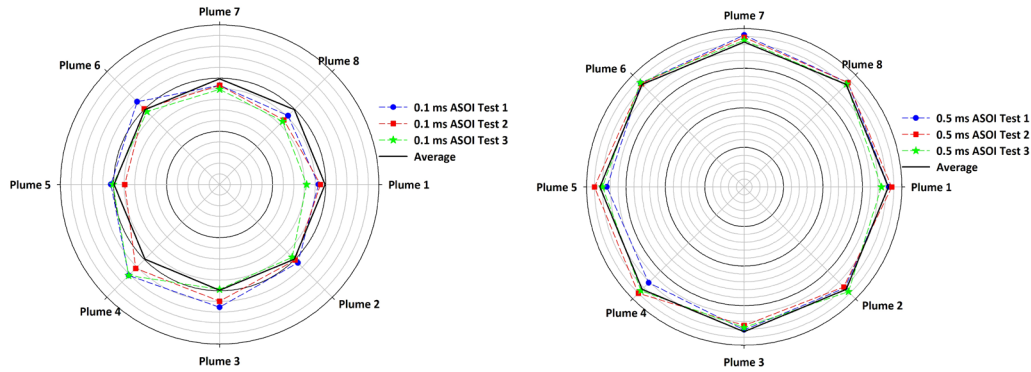


Figure 12.42: Repeat tests, chiller off, diesel spray penetration compared to the average value over all eight plumes for tests 1 through 3, 0.1 ms ASOI in left figure; 0.5 ms ASOI in right figure.

The 0.1 ms ASOI figure shows the transient start of injection behavior with the eccentric needle lift showing plumes 1, 7 and 8 having reduced liquid penetration at the start of injection relative to the other plumes. For the case of 0.5 ms ASOI, some consistent trends in regards to plume behavior were noted. There was good agreement for plumes 3, 6, 7 and 8 in regards to consistency between tests. Plume 6, 7, and 8 were consistently penetrating larger than the mean value, with plumes 1, 2, 4 and 5 having inconsistent trends meaning some plumes penetrated further than the mean, whereas others penetrated shorter. Plume 3 was without fail penetrating shorter than the mean liquid phase penetration. This could be attributed to various factors. There could be small time variations, and since penetration is proportional to the square root of time (Naber and Siebesr 1996), a jitter of 0.05 ms in time could cause a change of $\pm 2.5\%$ in penetration values which would minimize observation of these trends. This time jitter will be removed from the vaporizing spray images, as will be discussed, since comparison was of the mean liquid length which was considered over a 1 ms steady state time period resulting in more pronounced plume-to-plume trends.

To remove the time-dependent nature of the comparison, the 0.5 ms ASOI case was considered, with each test being compared to the mean value for the given test over the eight plumes, as opposed to the one common mean value shown in Figure 12.43.

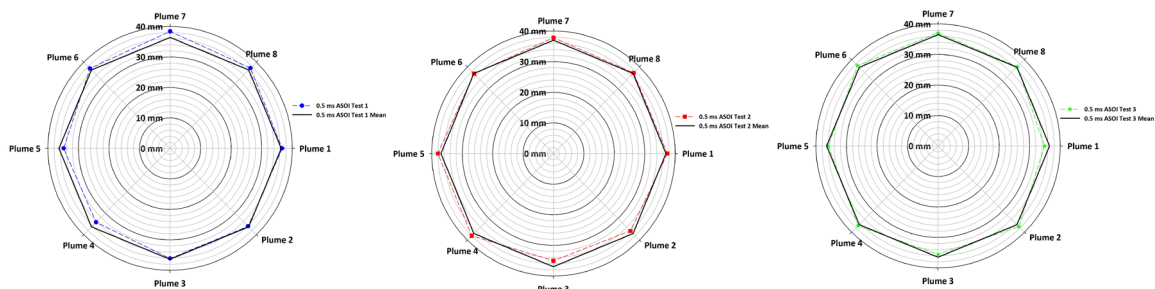


Figure 12.43: Test 1, 2, and 3 at 0.5 ms ASOI comparing the individual plume values to the mean value over all eight plumes for the given test, chiller on repeat tests.

Although the time jitter had been removed by comparing the test data to the mean for that test, the trends were still not consistent test to test. More specifically, in test 1, plumes 4 and 5 were less than the mean, plumes 1, 2, and 3 approximated the mean value, and plumes 6, 7 and 8 larger were than the mean. Conversely in test 2, plumes 2 and 3 were

less than the mean, plumes 6 and 8 approximated the mean value, and plumes 1, 4, 6 and 7 were larger than the mean. Finally, test 3 had even different trends with plume 1 and 3 being less than the mean, plumes 4, 5 and 8 being approximately the mean value, and plumes 2, 6 and 7 being larger than the mean. These observations show the transient nature of the plume trends.

As discussed (section 6.2), there were consistent plume to plume trends under the vaporizing sprays, however, the plume to plume trends during these non-vaporizing repeat tests have not been consistent. This could be attributed to the vaporizing spray test results being averaged during the steady state period with 67 data points for each plume value for the mean liquid length compared to the one value shown here for the non-vaporizing test conditions. Averaging over a set of data points helps to minimize the transient spray behavior during an injection event to provide more representative data.

12.6.1.3. Combined Repeat Results

A comparison of the repeat results at the two different fuel temperatures is shown in Figure 12.44 for median penetration and median cone angle.

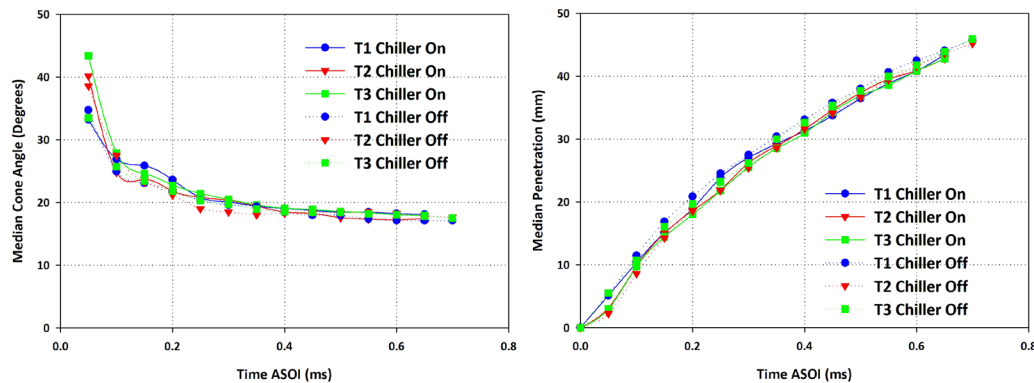


Figure 12.44: Repeat tests, chiller on and chiller off median penetration comparison on left, median cone angle comparison on right.

Based on the results in the above figure for both median penetration and median cone angle, fuel temperature had no significant impact on the penetration or cone angle at these conditions for the non-vaporizing spray tests. Penetration increased about 4% for the fuel temperature increase from 321 to 328 K, which is negligible relative to the 4% spread in the penetration results for the repeat tests. There is a 5% spread in cone angle over the repeat test conditions, with a negligible 3% decrease in cone angle for the fuel temperature increase.

12.6.1.4. Injection Pressure Sweep – Chiller Off – 328 K Fuel Temperature

These tests are for an injection pressure sweep with the chiller off, at 373 K ambient nitrogen gas temperature, and 34.8 kg/m³ charge-gas density. Polar plots showing penetration and cone angle for each plume as a function of time ASOI is shown in Figure 12.45, Figure 12.46, and Figure 12.47 for 1034, 1379 and 2000 bar injection pressure cases.

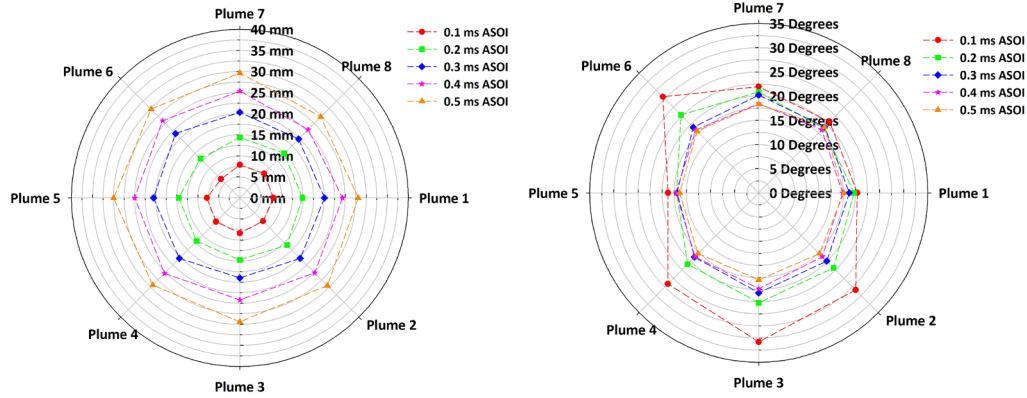


Figure 12.45: Chiller off, nitrogen spray penetration(left) and cone angle at 60% penetration (right) as a function of time ASOI for all 8 spray plumes, 1034 bar.

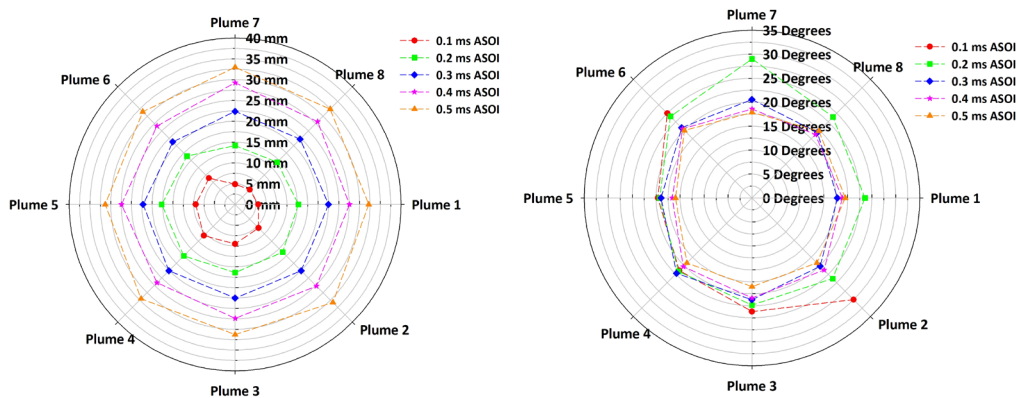


Figure 12.46: Chiller off, nitrogen spray penetration (left) and cone angle at 60% penetration (right) as a function of time ASOI for all 8 spray plumes, 1379 bar.

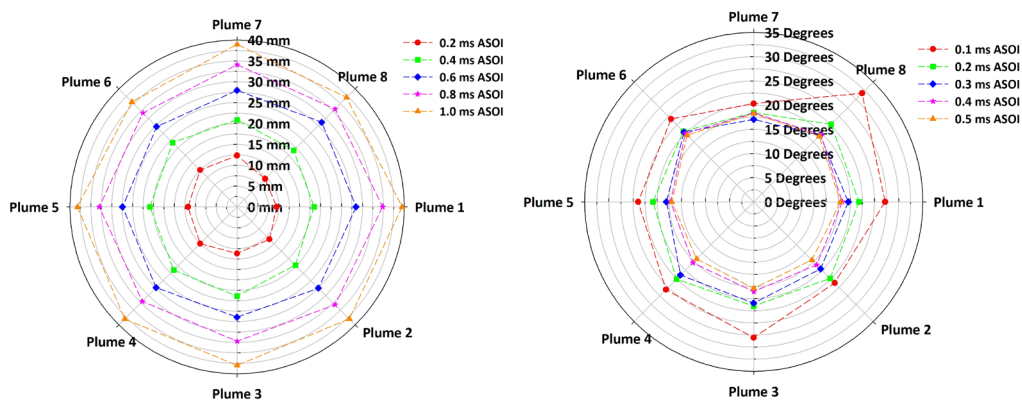


Figure 12.47: Chiller off, nitrogen spray penetration(left) and cone angle at 60% penetration (right) as a function of time ASOI for all 8 spray plumes, 2000 bar.

Shown in the above polar plots is the radial expansion of the penetration circles as time ASOI increased, and also as injection pressure increased at a set time ASOI. Repeatability in regards to minimization of plume to plume variations improved for all test cases as time ASOI increased due to the reduction of transient spray effects. Cone

angle showed significant variation at 0.1 and 0.2 ms ASOI with this variation reducing as the spray continued to penetrate.

12.6.1.5. Injection Pressure Sweep – Chiller On – 321 K Fuel Temperature

Test conditions for the injection pressure sweep tests with the chiller on (reduced fuel temperature) are summarized in Table 12.3. Injection was for a 0.8 ms trigger duration (1.4 ms fuel injection duration).

Table 12.3
Injection pressure sweep test conditions – chiller on, 373 K Nitrogen charge-gas conditions.

	Injection Pressure (Bar)	Density (kg/m ³)	Ambient Pressure (Bar)
1034 Bar	1045	34.6	38.3
1379 Bar	1399	35.0	38.7
2000 Bar	1991	34.9	38.6

Variation in test conditions of ambient pressure and density are minimal, and hence the images and results will show differences as a result of injection pressure. Images are shown for the three repeat tests in Figure 12.48.

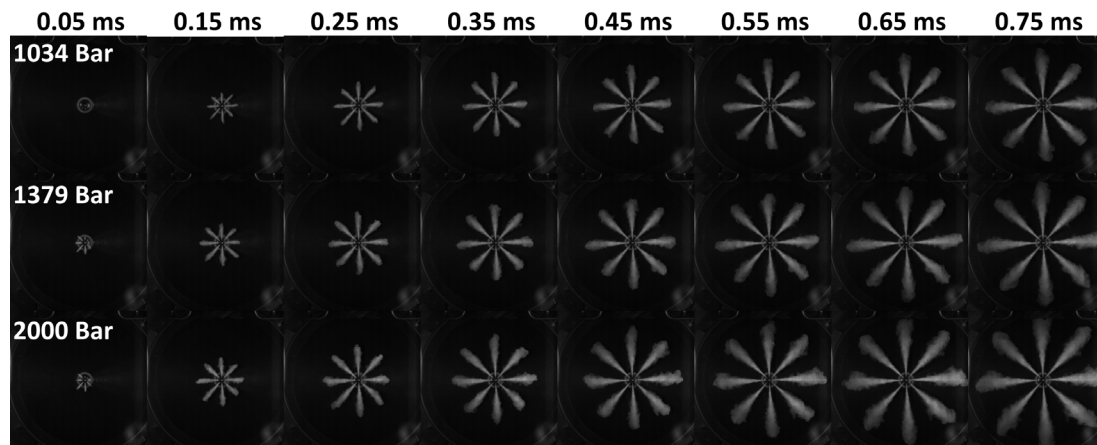


Figure 12.48: Diesel spray images from injection pressure sweep tests, 34.8 kg/m³ and 373 K Nitrogen, 1034, 1379 and 2000 bar injection pressures, chiller on (reduced fuel temperature).

As injection pressure increased, spray penetration increased, with trends in cone angle being difficult to discern from the images. The magnitude of the influence of injection pressure on penetration and cone angle (Figure 12.49) was quantified by image processing of the spray images.

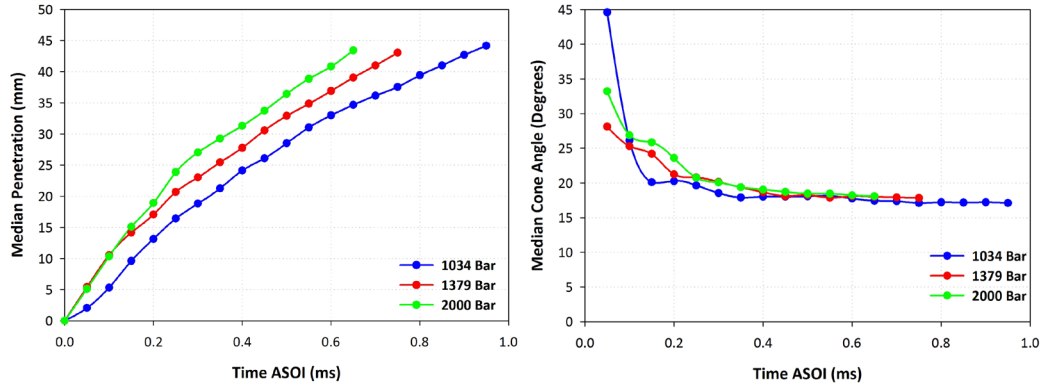


Figure 12.49: Median penetration in left figure, cone angle in right figure, as a function of time ASOI for three different injection pressures, chiller on.

An increase in injection pressure at the fuel temperature of 321 K resulted in similar increases in penetration of 40% for injection pressure increasing from 1034 to 2000 bar, however, for the smaller increase in injection pressure from 1034 to 1379 bar, penetration increased an average of 25%. Cone angle showed a 4% increase from 1034 to 1379 bar and a 7% increase from 1034 to 2000 bar, which is seen at the SOI, with levels after development showing no relative change between injection pressures.

The plume to plume variations are compared for both penetration and cone angle as a function of time ASOI as shown in Figure 12.50, Figure 12.51, and Figure 12.52.

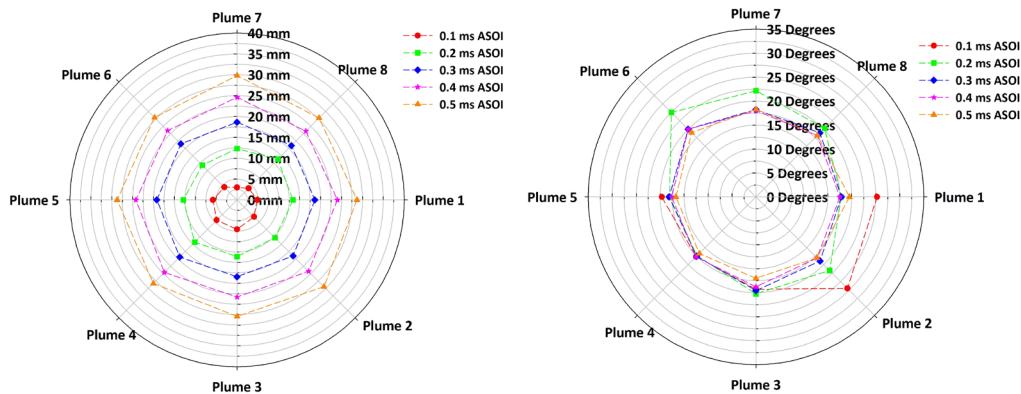


Figure 12.50: Chiller on, nitrogen spray penetration (left) and cone angle at 60% penetration (right) as a function of time ASOI for all 8 spray plumes, 1034 bar.

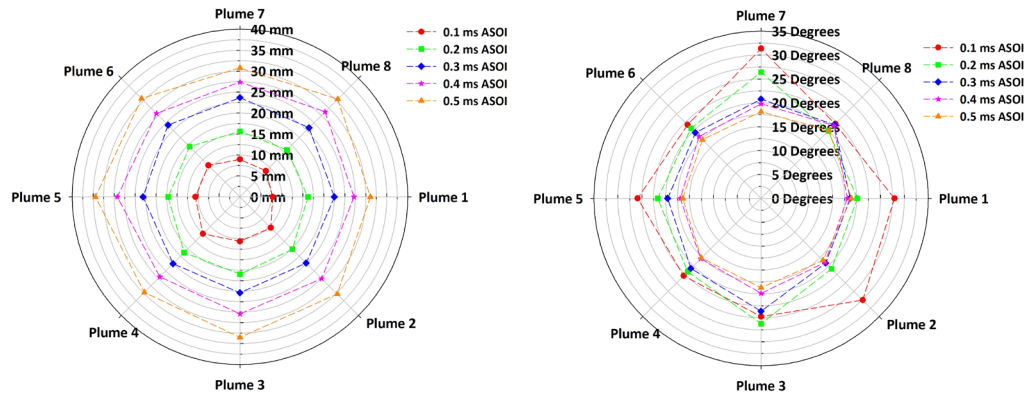


Figure 12.51: Chiller on, nitrogen spray penetration (left) and cone angle at 60% penetration (right) as a function of time ASOI for all 8 spray plumes, 1379 bar.

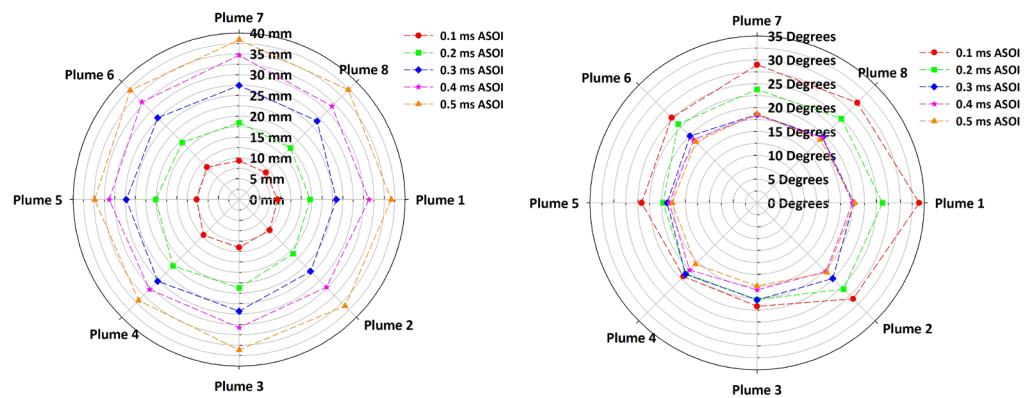


Figure 12.52: Chiller on, nitrogen spray penetration (left) and cone angle at 60% penetration (right) as a function of time ASOI for all 8 spray plumes, 2000 bar.

As a function of time ASOI, penetration increased and cone angle decreased. Both penetration and cone angle showed significant variation during the transient SOI for example at 0.1 ms ASOI.

Plume-to-plume variations can be best understood by the plots shown in Figure 12.53 which consider 0.1 and 0.5 ms ASOI penetration relative to the mean value over the 8 spray plumes.

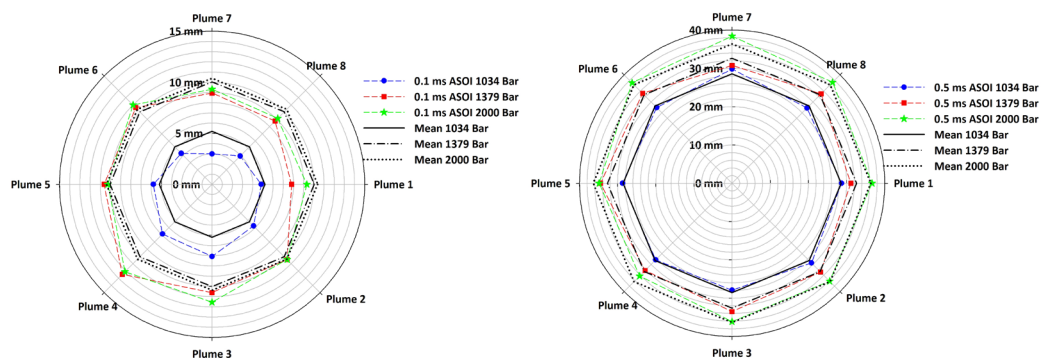


Figure 12.53: Penetration at 0.1 ms ASOI (left) and 0.5 ms ASOI (right) for the injection pressure sweep with the chiller on.

At 0.1 ms ASOI, the actual penetration was shorter than the mean for plumes 1, 7, and 8, showing the eccentric nature of the initial injection event. In the case of 0.5 ms ASOI, trends for plume variations were not consistent over the three injection pressures investigated. For the 1034 bar injection pressure, the penetration was equal to the mean for plumes 1, 4, and 5, less than the mean for plumes 3, 6, and 8, and greater than the mean for plumes 2 & 7. For 1379 bar injection pressure, plumes 1, 4, and 7 were less than the mean, plumes 3, 5, 6, and 8 greater than the mean, and plume 2 is equal to the mean. For the 2000 bar injection pressure case plumes 1, 2, and 3 were equal to the mean, plumes 4 and 5 less than the mean, and plumes 6, 7, and 8 greater than the mean. Trends with injection pressure vary for the different spray plumes. It has been hypothesized that the plume to plume variations could be attributed to differences in internal flow geometries. This geometry could be impacted by injection pressure variations as flow characteristics will be altered by different injection pressures and therefore injection velocities.

12.6.1.6. Combined Injection Pressure Sweep Results

A comparison of the influence of fuel temperature (for the two chiller settings) is provided in Figure 12.54 for median penetration and for median cone angle.

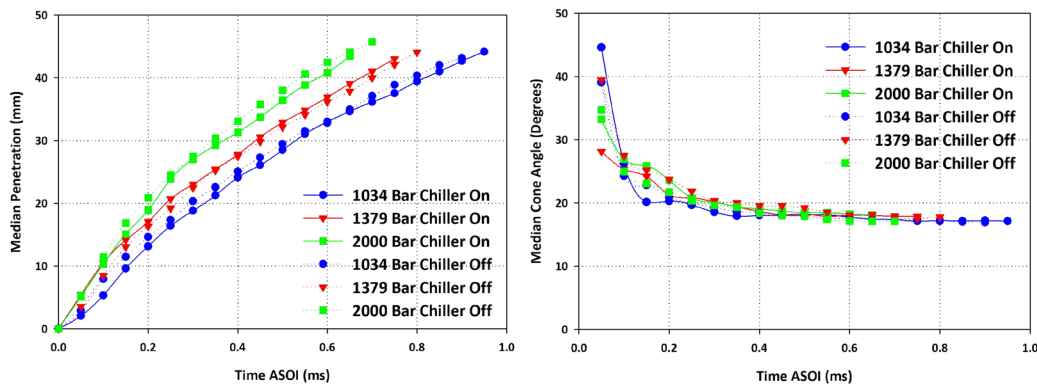


Figure 12.54: Median penetration as a function of time ASOI for the injection pressure sweeps, with chiller on and chiller off.

As injection pressure increased, the spray penetration increased as expected. Also, as fuel temperature increased (i.e. chiller off), the penetration increased slightly with the exception of the 1379 bar case which could be attributed to jitter in the camera timing. For a fuel temperature increase of 321 to 328 K, penetration increased 9% for the 1034 bar case and 5% for the 2000 bar case. For the 1379 bar case, however, penetration decreased by 5% for this fuel temperature increase, which is unexpected and likely due to camera jitter. Overall, the magnitude of the influence of fuel temperature on penetration was minimal for the small change in fuel temperature considered here. Cone angle showed no variation as fuel pressure was changed, at a constant fuel temperature. As fuel temperature increased from 321 to 328 K, there was a 4% decrease in cone angle at 1034 bar, no change at 1379 bar, and a 10% decrease in cone angle at 2000 bar.

12.6.1.7. Density Variation

These tests are for a charge-gas density variation with the chiller off, at 373 K ambient nitrogen gas temperature, and 2000 bar injection pressure. Polar plots showing penetration and cone angle for each plume as a function of time ASOI are shown in

Figure 12.55 and Figure 12.56, for 17.4 and 34.8 kg/m³ density, respectively, to understand the plume to plume trends.

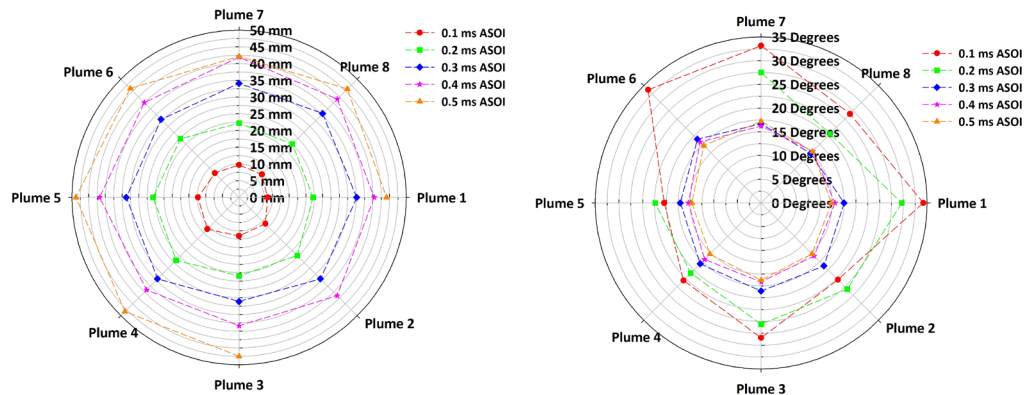


Figure 12.55: Chiller off, nitrogen spray penetration as a function of time ASOI for all 8 spray plumes, 17.4 kg/m³, 2000 bar injection pressure.

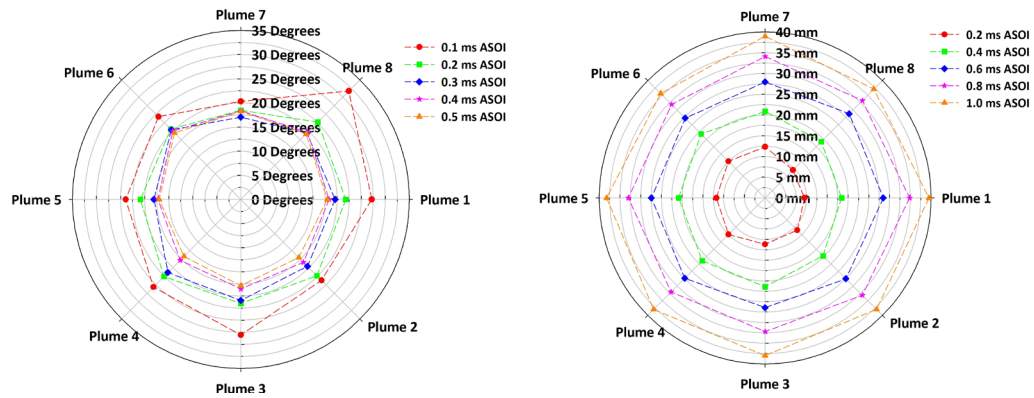


Figure 12.56: Chiller off, nitrogen spray penetration as a function of time ASOI for all 8 spray plumes, 34.8 kg/m³, 2000 bar injection pressure.

Consistent with prior tests were the large variations in both penetration and cone angle during the transient start of injection. Plume to plume variations were larger for cone angle during the transient portion of the injection event, however, once the cone angle was approaching a steady state value, these plume to plume variations were reduced.

12.6.2. Vaporizing Results

Plume to plume variation results are provided in these sections as polar plots for all vaporizing (0% Oxygen) spray tests.

12.6.2.1. Repeat Tests – Chiller On – 355 K Fuel Temperature

Three repeat tests were undertaken with the chiller on to enable study of a reduced fuel temperature, from 90°C with the chiller off reduced to 355 K with the chiller on. These tests were undertaken at a charge gas temperature of 1100 K, 34.8 kg/m³ ambient density 0% O₂ environment, 2000 bar fuel injection pressure, and 1.6 ms injection trigger duration. Test conditions are provided in Table 12.4, as determined from the acquired data.

Table 12.4
Ambient conditions at injection.

Test Set	ρ_{Bulk} (kg/m ³)	ρ_{Core} (kg/m ³)	T _{Bulk} at Inj. (K)	T _{Core} at Inj. (K)	P _{Inj.} (Bar)
Repeat 1	34.5	32.0	1110	1190	2000
Repeat 2	34.9	32.4	1100	1180	2010
Repeat 3	34.8	32.3	1100	1180	2000

There were minimal variations in conditions for each test of the repeat sets, and these variations are small enough in magnitude so they will not have any significant impact on overall spray parameters.

Looking at background subtracted images during steady state, variations between liquid penetration were not apparent as shown in Figure 12.57.

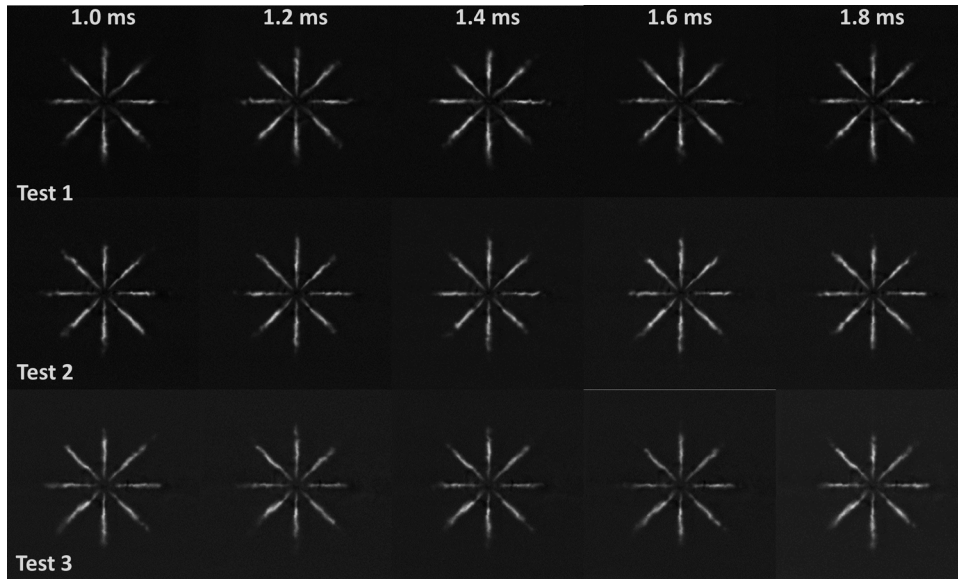


Figure 12.57: Background subtracted spray images. Repeat tests: 34.8 kg/m³ density, 0% O₂, 1100 K, 2000 bar injection pressure, chiller on. Scaling is preserved between images.

Looking at the background subtracted spray images there are no large variations between test runs during steady state. There were shot to shot variations which were a result of system repeatability and are also attributed to fluctuations about the mean steady state liquid length.

Median liquid penetration for all three tests was calculated from the back scattered images with results shown in Figure 12.58.

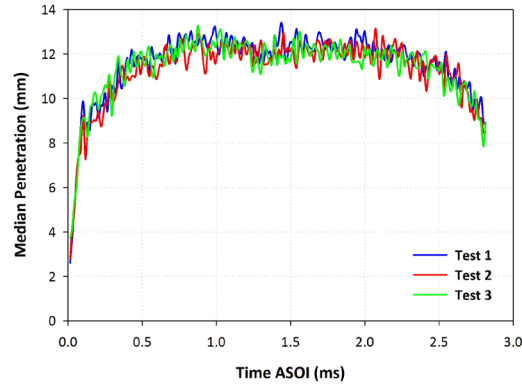


Figure 12.58: Median liquid penetration versus time ASOI for the three repeat tests at reduced fuel temperature, chiller on. 34.8 kg/m^3 , 0% O_2 , 1100 K temperature, 2000 bar injection pressure.

For the repeat tests, there was test-to-test consistency in median liquid phase fuel penetration with minimal variation even in the transient SOI. Liquid penetration reached a steady state around 0.75 ms ASOI, falling off after 2.2 ms ASOI due to the transient end of injection. The mean steady state liquid length (from 1 to 2 ms ASOI) varies by at most 0.3 mm over the three repeat tests. Although median penetration was shown to be consistent, of interest is any consistency in the plume to plume variations evident in the repeat tests with the chiller off.

Shown in Figure 12.59, Figure 12.60, and Figure 12.61 are individual polar plots for results from the repeat tests, 1, 2 and 3 respectively. These plots include a time during the transient SOI, along with several results during the steady state time interval.

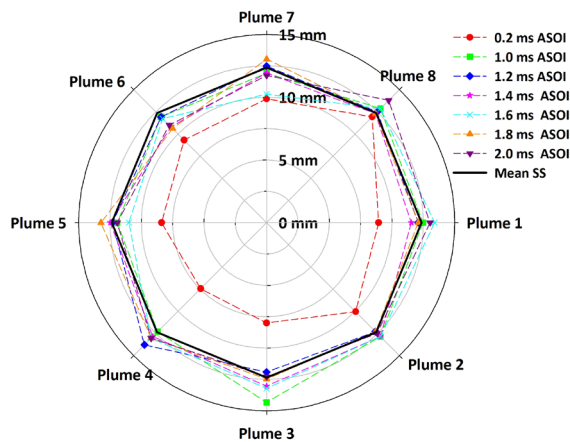


Figure 12.59: Polar plot of liquid penetration as a function of various times ASOI, 34.8 kg/m^3 , 0% O_2 , 2000 bar injection pressure, 1100 K, Test 1.

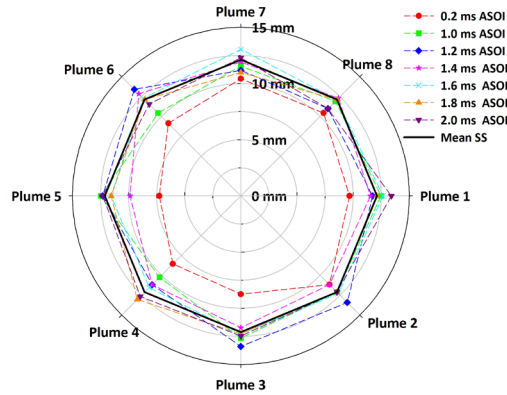


Figure 12.60: Polar plot of liquid penetration as a function of various times ASOI, 34.8 kg/m^3 , 0% O_2 , 2000 bar injection pressure, 1100 K, Test 2.

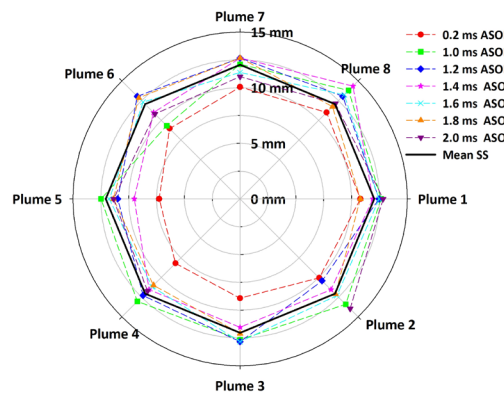


Figure 12.61: Polar plot of liquid penetration as a function of various times ASOI, 34.8 kg/m^3 , 0% O_2 , 2000 bar injection pressure, 1100 K, Test 3.

With identical conditions it was expected that all plumes would exhibit the same spray behavior. However, as seen in the above polar plots, there was extensive variation. During the transient SOI (0.2 ms ASOI), this variation between plumes and between tests was quite large due to the developing nature of the spray. Even during the steady state portion there was extensive fluctuations not only at different times ASOI, but also for each plume. This was likely attributed to the fluctuation of a spray plume about a mean liquid length evidenced in images and high speed movies which could be attributed to various factors, as discussed in Chapter 2.3.5 and Chapter 3.4.2.1. Additionally, gradients or non-uniformities in temperature may exist within the CV influencing vaporization and liquid length trends.

Considering the steady state liquid length from 1 to 2 ms ASOI for each plume from each test relative to the mean value over all three tests (mean SS LL) trends in the plume variation became more evident as shown in Figure 12.62.

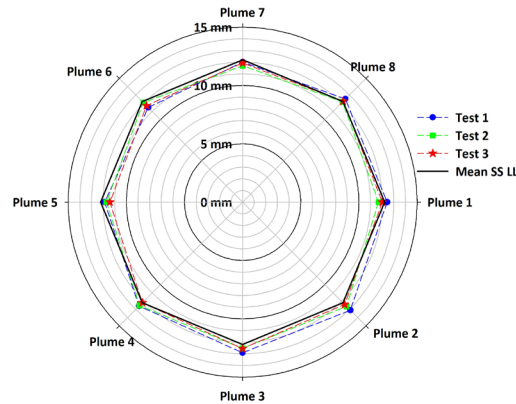


Figure 12.62: Polar plot of normalized liquid length during steady state (1 to 2 ms ASOI), 34.8 kg/m³, 0% O₂, 1100 K, Repeat Tests, Chiller On.

Plumes 5, 6, and 7 have liquid lengths shorter than the mean by an average of 0.5 mm, whereas plumes 1 and 4 typically have a LL the same as the mean, within 0.1 mm, with some exceptions. Plumes 2, 3 and 8 had liquid lengths longer than the mean value by an average of 0.5 mm. These repeat trends were consistent with the plume-to-plume variations seen under other conditions discussed earlier with these variations being likely attributed to physical injector phenomenon based on their consistent appearance over a wide range of conditions.

12.6.2.2. Combined Repeat Results

Combined results from the repeat tests with both the chiller on and chiller off for median liquid length over all eight plumes are shown in Figure 12.63.

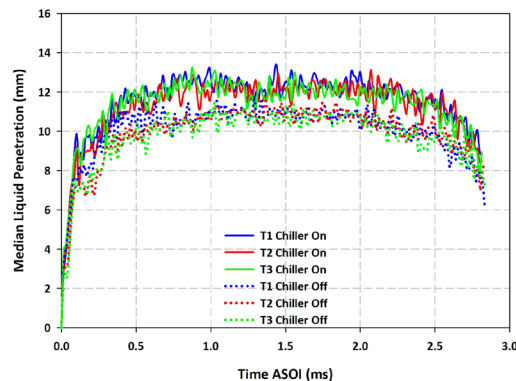


Figure 12.63: Combined vaporizing spray repeat results, chiller on (355 K injector temperature) and chiller off (363 K injector temperature).

With the chiller on, fuel temperature is reduced, and the median liquid length increased 14% relative to the elevated fuel temperature case. This trend was expected as additional energy was required (air entrained) to fully vaporize all fuel at the lower temperature resulting in a liquid length increase.

12.6.2.3. Injection Pressure Sweep – Chiller Off – 363 K Fuel Temperature

These tests are an injection pressure sweep with the chiller off, at 1100 K ambient zero percent oxygen gas temperature and 34.8 kg/m³ charge-gas density. Polar plots were prepared to understand the plume to plume variations under these conditions, as shown in

Figure 12.64, Figure 12.65, and Figure 12.66 for injection pressures of 1034, 1379, and 2000 bar respectively.

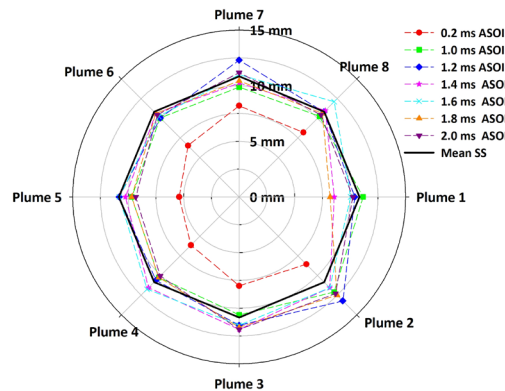


Figure 12.64: Polar plot of liquid penetration as a function of various times ASOI, 34.8 kg/m³ 0% O₂, 1034 bar injection pressure, 1100 K, chiller off.

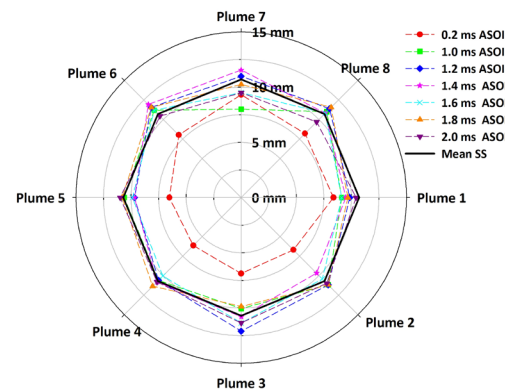


Figure 12.65: Polar plot of liquid penetration as a function of various times ASOI, 34.8 kg/m³ 0% O₂, 1379 bar injection pressure, 1100 K, chiller off.

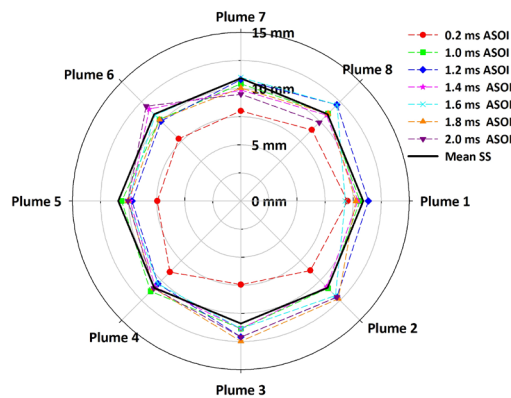


Figure 12.66: Polar plot of liquid penetration as a function of various times ASOI, 34.8 kg/m³ 0% O₂, 2000 bar injection pressure, 1100 K, chiller off.

As expected there was the most variation during the transient start of injection (0.2 ms), before the liquid phase penetration reached steady state. At steady state, the variation was smaller between plumes and also as a function of time.

12.6.2.4. Injection Pressure Sweep – Chiller On – 355 K Fuel Temperature

An injection pressure sweep was also undertaken at a reduced fuel temperature of 82°C, with actual test conditions summarized in Table 12.5.

Table 12.5
Ambient conditions at injection – injection pressure sweep – chiller on.

Test Set	ρ_{Bulk} (kg/m ³)	ρ_{Core} (kg/m ³)	T _{Bulk} at Inj. (K)	T _{Core} at Inj. (K)	P _{Inj.} (Bar)
1034 Bar	34.7	32.2	1100	1190	1070
1379 Bar	34.8	32.2	1100	1190	1370
2000 Bar	34.5	32.0	1100	1190	2000

With the chiller on, injection pressure sweep ambient conditions were similar with no significant variations. Again, all figures and discussion refer to the desired injection pressure. Background subtracted spray images are shown in Figure 12.67.

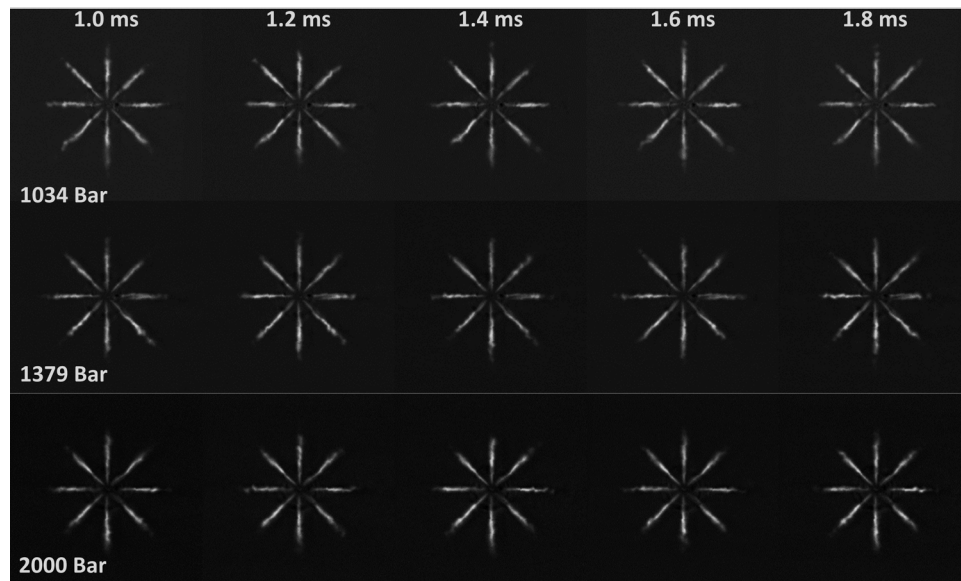


Figure 12.67: Background subtracted spray images. Injection pressure sweep test: 34.8 kg/m³ density, 0% O₂, 1100 K, chiller on.

Injection pressure had a negligible influence on spray characteristics. This was further confirmed from the image processing results, with results for median liquid penetration as a function of time ASOI shown in Figure 12.68.

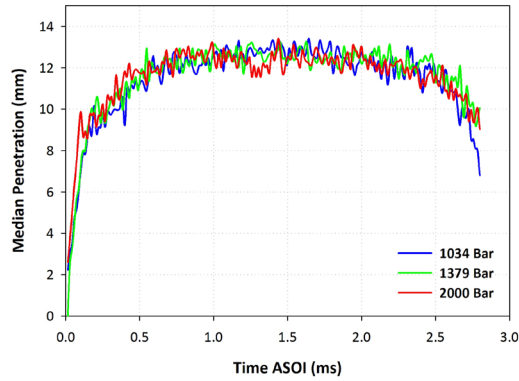


Figure 12.68: Median penetration (liquid) as a function of time ASOI for the injection pressure sweep at 34.8 kg/m^3 density, 1100 K, 0% O_2 , fuel chiller on.

During start of injection the 2000 bar fuel pressure injection case reached steady state earlier, but again liquid length was not influenced by injection pressure with less than a 1% change in mean steady state liquid length over these conditions.

The plume trends as a function of these three injection pressures with the fuel chiller on is of interest, as shown in Figure 12.69, Figure 12.70, and Figure 12.71 for the injection pressures of 1034, 1379, and 2000 bar.

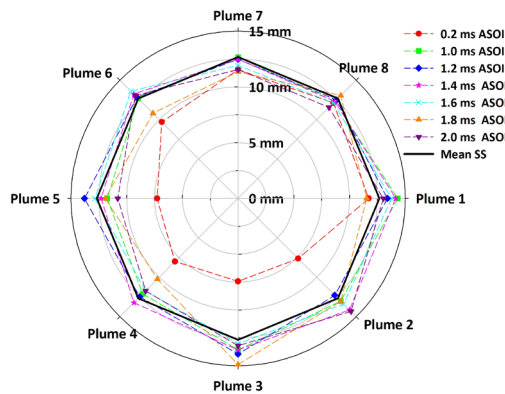


Figure 12.69: Polar plot of liquid penetration as a function of various times ASOI, 34.8 kg/m^3 0% O_2 , 1034 bar injection pressure, 1100 K, chiller on.

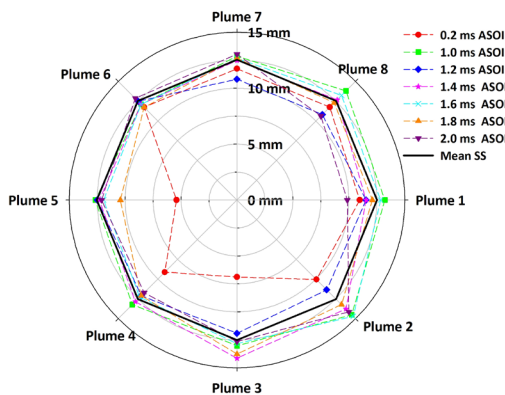


Figure 12.70: Polar plot of liquid penetration as a function of various times ASOI, 34.8 kg/m^3 0% O_2 , 1379 bar injection pressure, 1100 K, chiller on.

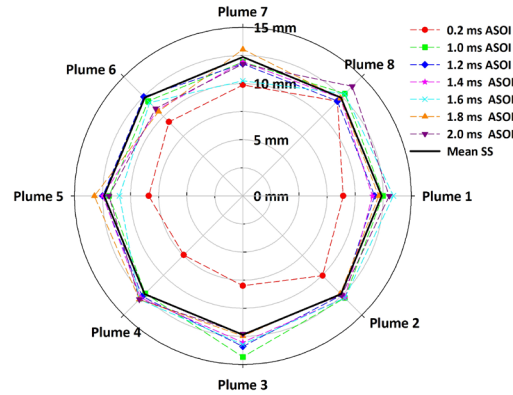


Figure 12.71: Polar plot of liquid penetration as a function of various times ASOI, 34.8 kg/m³ 0% O₂, 2000 bar injection pressure, 1100 K, chiller on.

Consistent with previous tests, there was the most variation during the transient start of injection phase at 0.2 ms. There was also plume to plume variation as a function of time ASOI and for each injection pressure which were difficult to compare in the above polar plots.

Looking at the steady state (1 to 2 ms ASOI) liquid length of each plume normalized by the mean steady state liquid length over all eight plumes, enabled an easier comparison of the plume to plume variations by removing the injection pressure influence, as shown in Figure 12.72.

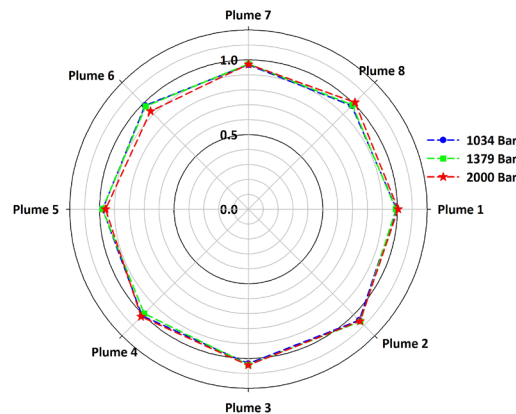


Figure 12.72: Polar plot of normalized liquid length during steady state (1 to 2 ms ASOI), 34.8 kg/m³ 0% O₂, 1100 K, chiller on.

Plumes 1, 5, 6, and 7 consistently had normalized liquid lengths less than one, or less than the mean value by above 4%, agreeing with past trends. Plumes 2 and 3 also had liquid lengths consistently larger than one, or greater than the mean by at least 4%, over the injection pressure sweep, again, agreeing with past trends. Under these conditions, plume 8 had a normalized liquid length less than one for all conditions except for 2000 bar, which was opposite to what was previously observed, however, this deviation is less than 1%. Plume 4 had a mean liquid length approximately the same as the mean value.

12.6.2.5. Combined Results – Fuel Pressure Sweep

There were consistencies in plume trends in regards to plumes 1, 5, 6, and 7 being constantly less than the mean, and plumes 2 and 3 being larger than the mean for these injection pressure sweeps at high and low fuel temperatures. Also of interest was a

general comparison of the influence of fuel temperature on the liquid length, for the three injection pressures investigated, as shown in Figure 12.73.

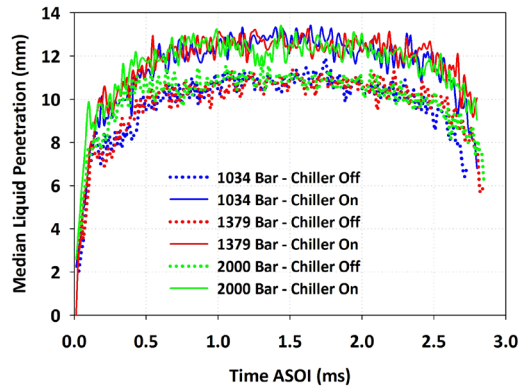


Figure 12.73: Median liquid penetration as a function of time ASOI for the injection pressure sweep with both the chiller off and chiller on. 0% O₂, 1100 K, 34.8 kg/m³ density

With the chiller off the fuel temperature increased with the liquid penetration reduced relative to that of the chiller being on by 12%. Based on literature, liquid length increases linearly with a reduction in fuel temperature (Siebers 1998). At the higher fuel temperature (chiller off) it takes less energy to heat up and vaporize the fuel which reduces the required spray length to entrain sufficient energy to vaporize the fuel, thereby reducing the liquid length

12.6.2.6. Charge Gas Density Variation

These tests are for a charge-gas density variation with the chiller off at 1100 K ambient zero percent oxygen gas temperature and 2000 bar injection pressure. It is of interest to understand the plume to plume variations of mean steady state liquid length under these conditions, as shown in Figure 12.74 and Figure 12.75, for the 17.4 and 34.8 kg/m³ density cases, respectively.

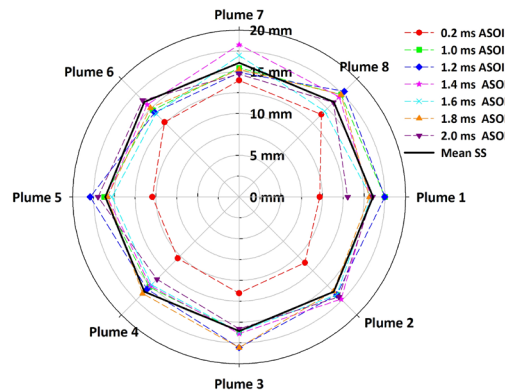


Figure 12.74: Polar plot of liquid penetration as a function of various times ASOI, 17.4 kg/m³ 0% O₂, 2000 bar injection pressure, 1100 K, chiller off.

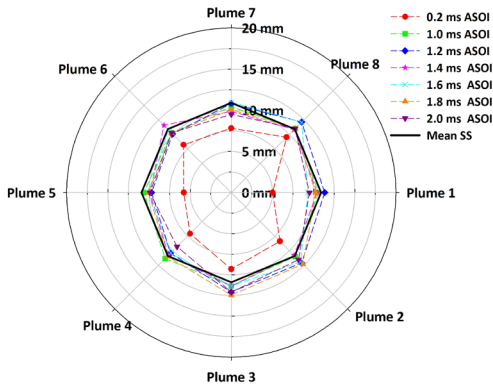


Figure 12.75: Polar plot of liquid penetration as a function of various times ASOI, 34.8 kg/m³ 0% O₂, 2000 bar injection pressure, 1100 K, chiller off.

In agreement with prior results, there was the most variation between plumes during the transient SOI as evidenced by the 0.2 ms ASOI condition. There were still plume to plume variations in the longer times ASOI during steady state. These variations become more evident in the lower density case which could potentially be attributed to temperature gradients existing across the chamber. These gradients would have a larger influence on the spray characteristics as the spray penetrates further across the chamber.

12.6.2.7. Charge Gas Temperature Sweep at 1379 Bar

A charge temperature sweep was previously discussed at 2000 bar injection pressure; however, a restricted charge temperature sweep was undertaken at a reduced injection pressure of 1379 bar to further understand the influence with test conditions summarized in Table 12.6.

Table 12.6
Ambient conditions at injection – charge temperature sweep at 1379 Bar.

Test Set	ρ_{Bulk} (kg/m ³)	ρ_{Core} (kg/m ³)	T_{Bulk} at Inj. (K)	T_{Core} at Inj. (K)	$P_{\text{Inj.}}$ (Bar)
950 K	34.6	32.5	950	1015	1380
1100 K	34.7	32.1	1100	1190	1380
1200 K	34.8	32.0	1200	1300	1370

Injection pressure and density were consistent, with a variation in bulk gas temperature as desired. Background subtracted spray images for these test conditions are provided in Figure 12.76.

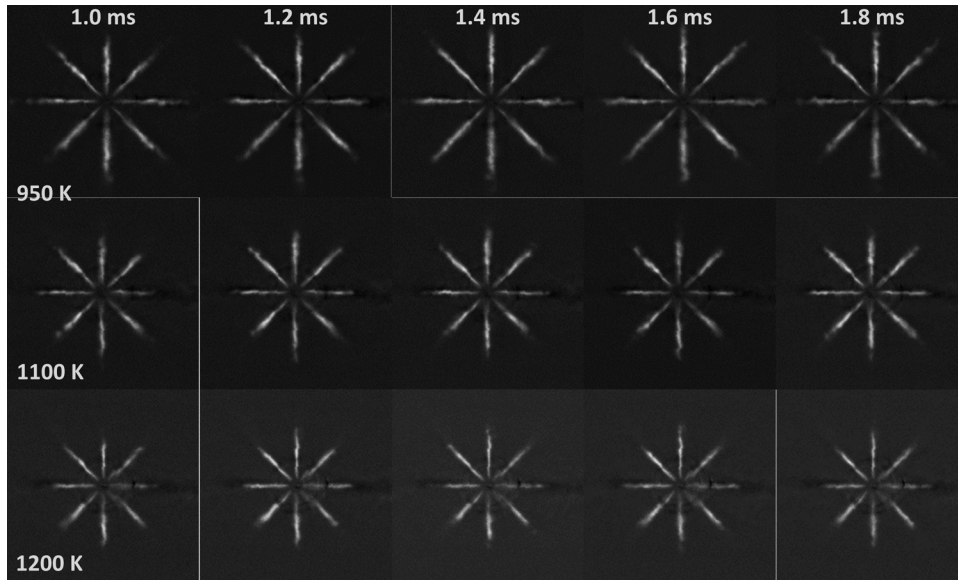


Figure 12.76: Background subtracted spray images. Charge temperature sweep, 0% O₂, 1379 bar injection pressure, 34.8 kg/m³ density.

As charge gas temperature increased liquid phase penetration reduced due to increased vaporization. This was quantified by image processing with results for median penetration as a function of time ASOI shown in Figure 12.77.

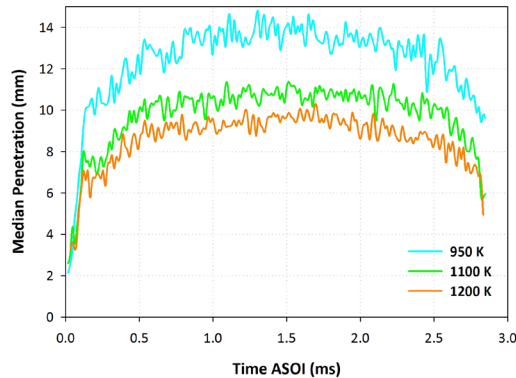


Figure 12.77: Median liquid penetration as a function of time ASOI for the temperature sweep, 950 to 1200 K, 0% O₂, 34.8 kg/m³, 1379 bar injection pressure.

When temperature increased, liquid length decreased nonlinearly with temperature which was also evidenced in the increased injection pressure case. The reduction in liquid length is 30% for a 250 K charge gas temperature increase (from 950 to 1200 K). Steady state liquid length was reached by 1.0 ms ASOI for all cases.

Of interest are the plume to plume variations over this charge temperature sweep, defined by polar plot comparisons shown in Figure 12.78, Figure 12.79, and Figure 12.80 for charge temperatures of 950, 1100 and 1200 K, respectively.

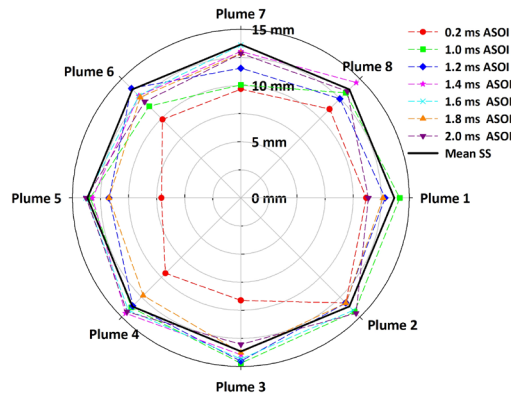


Figure 12.78: Polar plot of liquid penetration as a function of various times ASOI, 34.8 kg/m^3 0% O_2 , 1379 bar injection pressure, 950 K, chiller off.

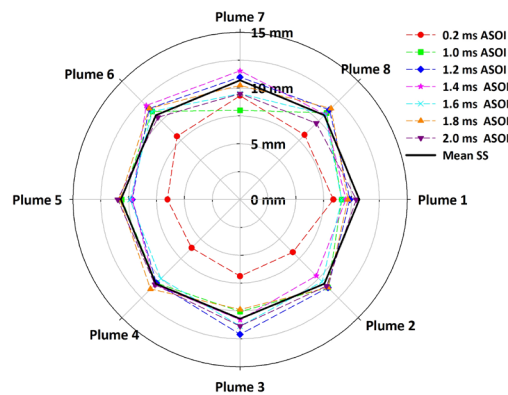


Figure 12.79: Polar plot of liquid penetration as a function of various times ASOI, 34.8 kg/m^3 0% O_2 , 1379 bar injection pressure, 1100 K, chiller off.

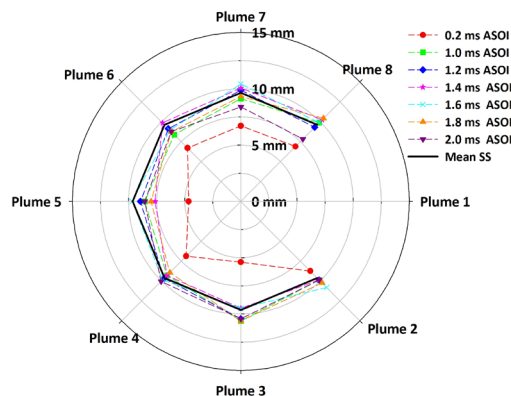


Figure 12.80: Polar plot of liquid penetration as a function of various times ASOI, 34.8 kg/m^3 0% O_2 , 1379 bar injection pressure, 1200 K, chiller off.

At the 1200 K charge gas temperature, there were no results for Plume 1 due to background interference. In all cases there existed plume to plume variation and fluctuations in liquid length about the mean value evidenced in the spray movies.

Plume trends can be better understood looking at the normalized mean liquid length for the three charge temperatures as shown in Figure 12.81.

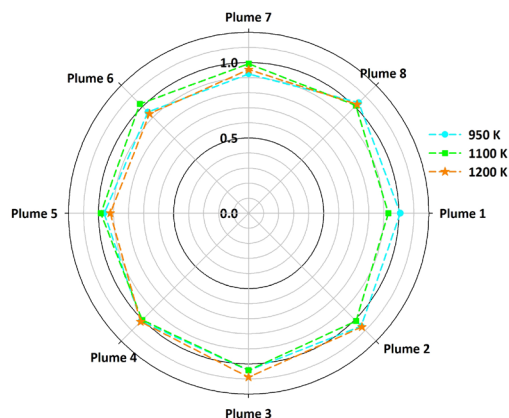


Figure 12.81: Polar plot of normalized liquid length during steady state (1 to 2 ms ASOI), 34.8 kg/m³ charge-gas density, 0% O₂, charge gas temperature sweep, chiller off, 1379 bar injection pressure.

The normalized mean liquid length was determined for each plume by taking the mean liquid length of the spray plume, from 1 to 2 ms ASOI, and normalizing it by the mean steady state liquid length over all eight plumes. Plumes 1, 5, and 7 had normalized mean liquid lengths less than the mean by 3 to 5%. Plume 6 was also less than the mean with the exception of the 1100 K case. Plumes 2, 3, and 8 had mean liquid lengths which exceeded the normalized mean value by 2 to 6%, agreeing with trends over different ambient conditions. Plume 4 has a liquid length very close to the mean, within 1%.

12.6.3. Combusting Results – Plume to Plume Variations

Plume to plume variation results are provided in these sections as polar plots for all combusting (21% Oxygen) spray tests.

12.6.3.1. Repeat Tests – Chiller Off

Test conditions for the two repeat tests with the chiller off are summarized in Table 12.7. Injection was at 0.6 ms trigger duration which corresponds to 1.1 ms fuel duration. Tests were conducted at 34.8 kg/m³ charge gas density, 1100 K bulk gas temperature, and 2000 bar injection pressure.

Table 12.7
Combusting repeat tests.

	Injection Pressure (Bar)	Bulk Gas Density (kg/m ³)	Bulk Gas Temperature (K)	Core Gas Density (kg/m ³)	Core Gas Temperature (K)	Ignition Delay (ms)	Net Heat Release (kJ)
Test 1	2000	33.9	1100	31.5	1190	0.52	1.52
Test 2	2030	33.9	1100	31.5	1190	0.50	1.52

Images are shown for these repeat tests in Figure 12.82.

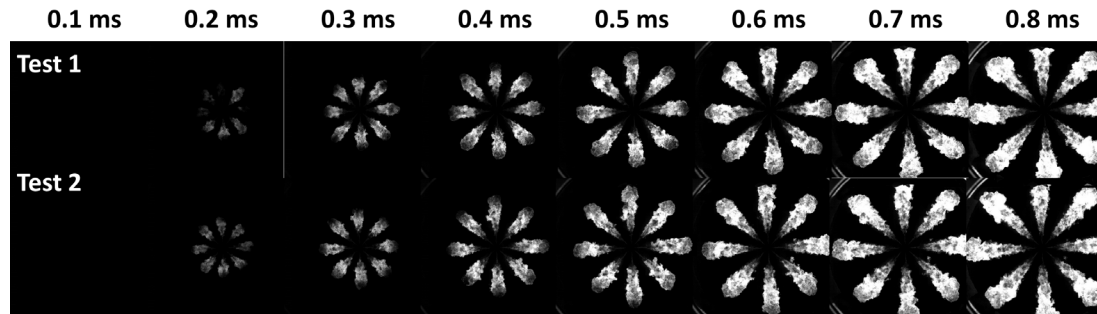


Figure 12.82: Combusting spray images from repeat tests, 2000 bar injection pressures, 1100 K bulk gas temperature, 34.8 kg/m³ density.

Similarities exist between the two repeat tests in regards to ignition delay and flame growth. Lift off length was also similar between the two sets of tests as shown in the images. Quantified median spray parameters of flame length, cone angle at 60% flame length, lift-off length, and total combustive plume intensity are provided in, Figure 12.83, Figure 12.84, Figure 12.85, and Figure 12.86, respectively.

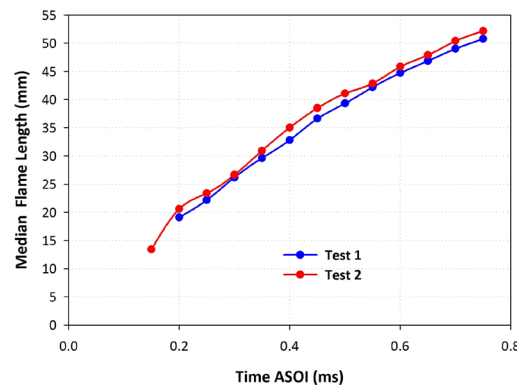


Figure 12.83: Median flame length versus time ASOI for combustive spray repeat tests, 2000 bar injection pressure, 1100 K bulk gas temperature, 34.8 kg/m³ density. Computed ignition delay from pressure was an average 0.51 ms.

As time ASOI increased, the flame length increased. The initial gap between 0 ms to the first location of flame length was due to the ignition delay and the minimal combustion luminosity during the start of combustion and because of this flame length does not exist. Test 1 and Test 2 exhibit very similar flame lengths, within 5%, with small differences likely attributed to camera timing jitter.

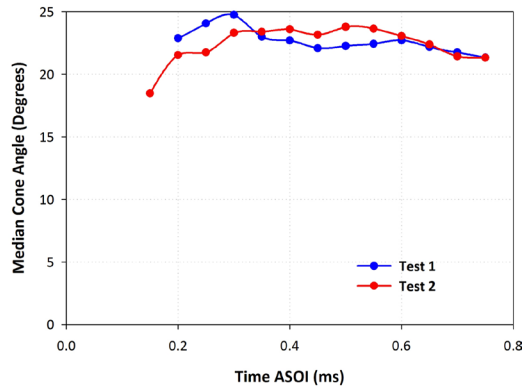


Figure 12.84: Median cone angle versus time ASOI for combustng spray repeat tests, 2000 bar injection pressure, 1100 K bulk gas temperature, 34.8 kg/m³ density.

Cone angle was relatively constant during combustion with small fluctuations around a nominal value of 22 degrees. The test to test variations were not significant at 1%.

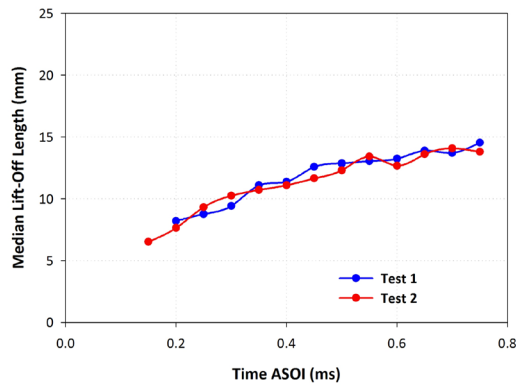


Figure 12.85: Median lift-off length versus time ASOI for combustng spray repeat tests, 2000 bar injection pressure, 1100 K bulk gas temperature, 34.8 kg/m³ density.

Lift-off length slowly increased as a function of time ASOI, being very similar between the two tests eventually reaching 12 mm, with less than 6% average variation.

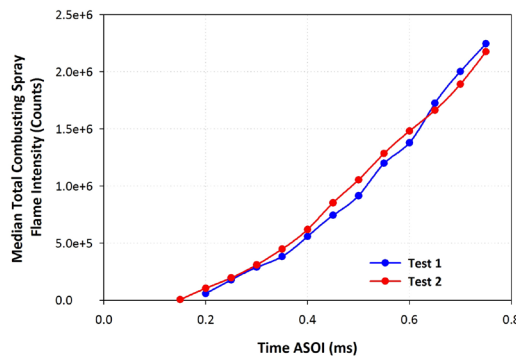


Figure 12.86: Median combustng plume intensity versus time ASOI for combustng spray repeat tests, 2000 bar injection pressure, 1100 K bulk gas temperature, 34.8 kg/m³ density.

Total combustng plume intensity was similar between the two test conditions exponentially increasing as the flame propagates across the chamber. Variation can reach

24% between the two tests, but this could be attributed to comparing the median value and hence different spray combusting plumes. Overall, repeat tests confirmed agreement in all parameters analyzed.

A comparison of individual plume characteristics is undertaken to understand any additional variations, shown in Figure 12.87 and Figure 12.88 for Test 1 and Test 2 respectively.

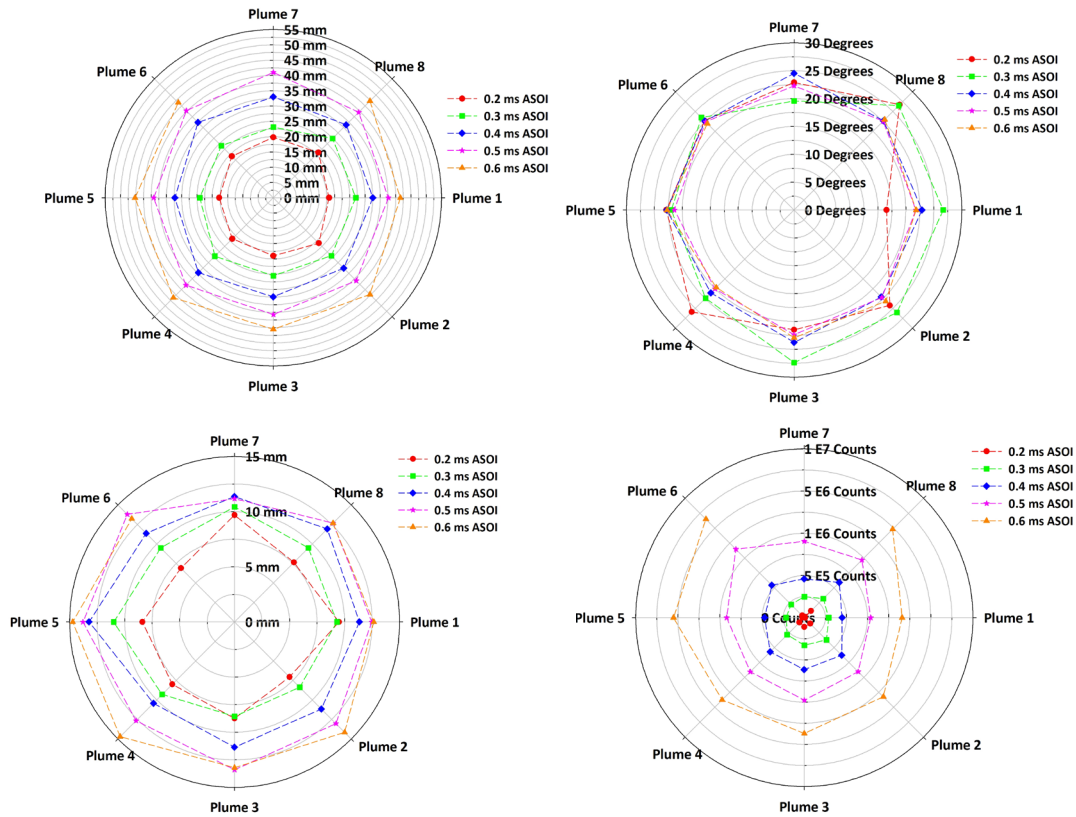


Figure 12.87: Polar plots for Test 1 of the repeats considering plume to plume variations in flame length, cone angle, lift-off length, and total combust intensity for 2000 bar injection pressure, 1100 K bulk gas temperature, 34.8 kg/m³ density.

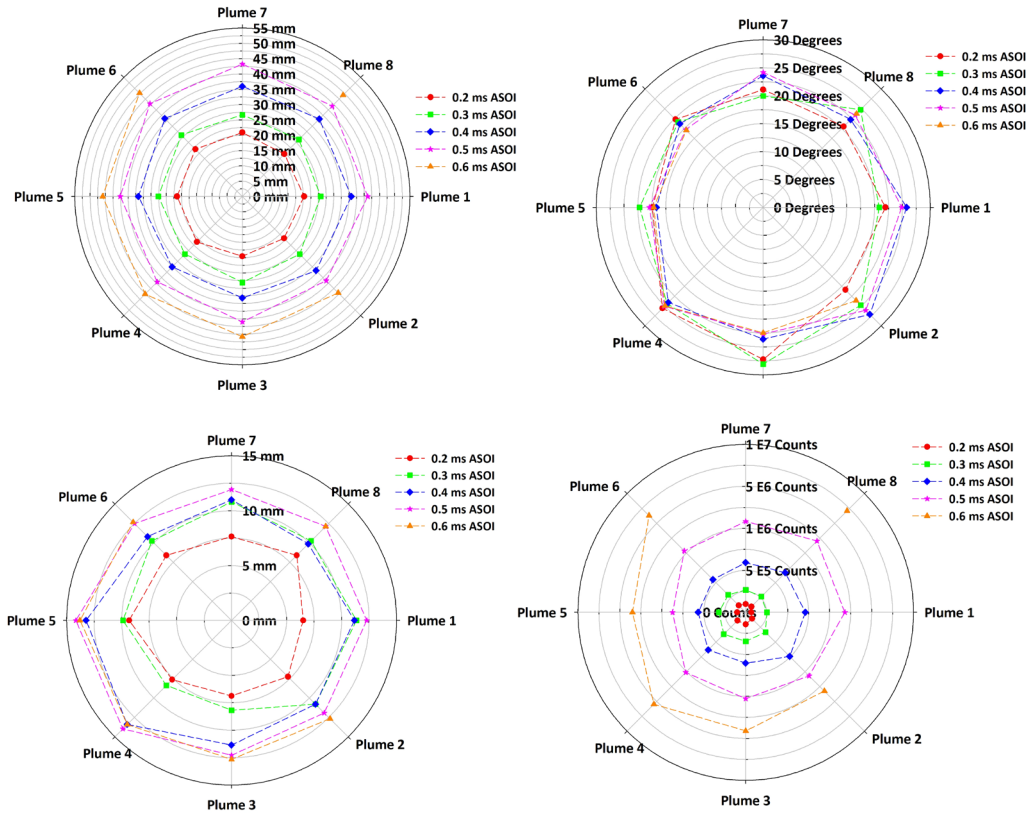


Figure 12.88: Polar plots for Test 2 of the repeats considering plume to plume variations in flame length, cone angle, lift-off length, and total combusting intensity for 2000 bar injection pressure, 1100 K bulk gas temperature, 34.8 kg/m³ density.

Plume to plume variations in flame length were not well pronounced for test 1 or test 2, although, they were evident at certain conditions for example test 2, plume 1 at 0.6 ms ASOI had a noticeably reduced flame length. Plume-to-plume variations in cone angle were apparent for all times ASOI, with cone angle being widest for plumes 1, 2, 3 and 8, more noticeably in the long times ASOI. Trends in lift-off length were also prevalent, with plumes 3, 4, 5 and 6 showing noticeably longer lift-off lengths relative to the other plumes. There were also plume to plume variations in combusting intensity, however, these were not consistent test to test.

12.6.3.2. Injection Pressure Variation at 950 K

The 950 K bulk gas temperature injection pressure variation was undertaken at both 1379 and 2000 bar, for an ambient charge gas density of 34.8 kg/m³, with actual test conditions defined in Table 12.8.

Table 12.8
Combusting test conditions for injection pressure variation at 950 K bulk gas temperature.

	Injection Pressure (Bar)	Bulk Gas Density (kg/m ³)	Bulk Gas Temperature (K)	Core Gas Density (kg/m ³)	Core Gas Temperature (K)	Ignition Delay (ms)	Net Heat Release (kJ)
1379 Bar	1380	33.9	950	31.8	1010	0.93	1.12
2000 Bar	2030	33.7	960	31.7	1020	0.81	1.61

There were small variations in gas density and temperatures, but these were negligible relative to the change in injection pressure which is currently of interest. Ignition delay was reduced by about 14% with the increase in injection pressure as the spray penetrated across the chamber faster and at higher velocity enhancing fuel-air mixing and the resulting combustion, agreeing with literature (Kobori et al. 2000). Heat release was also larger by over 40% for the higher injection pressure case which was expected since the injection duration was kept constant so at the higher injection pressure, more fuel will be injected providing more energy for heat release. Images of the combustng spray from these tests are shown in Figure 12.89.

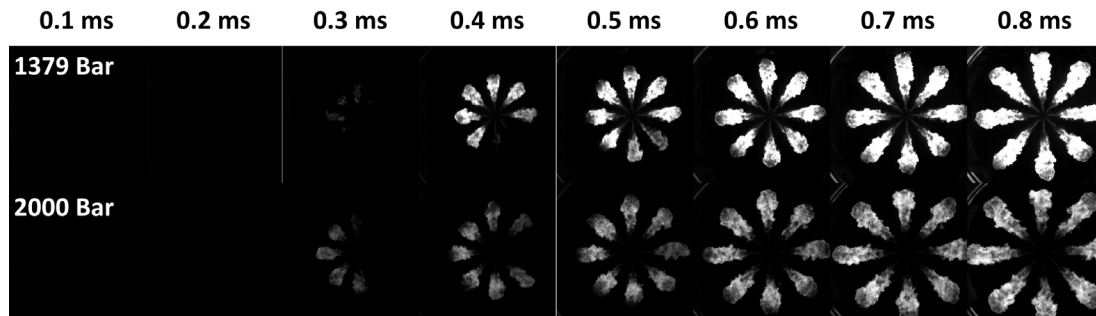


Figure 12.89: Combusting spray images from injection pressure variation, 950 K bulk gas temperature, 34.8 kg/m³ density. Computed ignition delay from pressure was 0.93 ms at 1379 bar, and 0.81 ms at 2000 bar.

Some notable differences were apparent in the images in the above figure. Intensity of the 1379 bar test case was higher than that of the higher injection pressure condition. The 2000 bar injection pressure condition showed a shorter ignition delay and faster flame development. These differences were quantified in the following set of figures for flame length (Figure 12.90), cone angle (Figure 12.91), lift-off length (Figure 12.92) and combustng plume intensity (Figure 12.93).

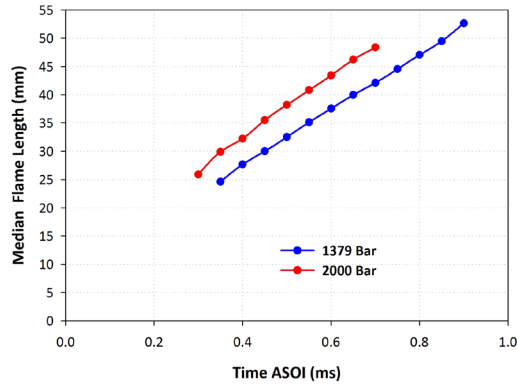


Figure 12.90: Median flame length versus time ASOI for combustng spray tests, 950 K bulk gas temperature, 34.8 kg/m³ density.

As injection pressure increased spray momentum increased enabling it to travel farther under the same conditions relative to that of a lower injection pressure spray, as shown by the increased flame length of the higher density spray. The magnitude of this increase is close to 17%.

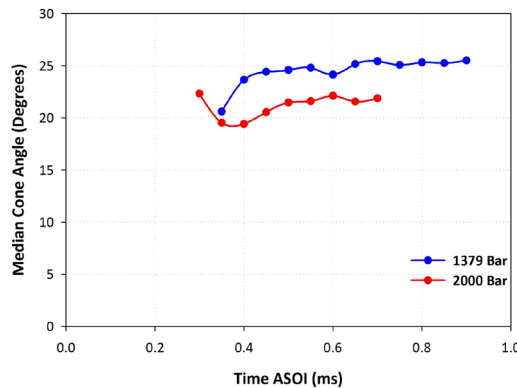


Figure 12.91: Median cone angle versus time ASOI for combustng spray tests, 950 K bulk gas temperature, 34.8 kg/m³ density.

Cone angle, a measure of the combustng spray flames spreading and air entrainment, was a quasi-steady value and larger for the 1379 bar injection pressure case by an average of 3 degrees. Therefore cone angle decreases by about 13% over this injection pressure increase. This could be attributed to the cone angle definition, with cone angle being calculated at 60% flame length and therefore cone angle was calculated at different distances for the two injection pressures based on the differences in flame length, however, the relative location in the spray would be consistent.

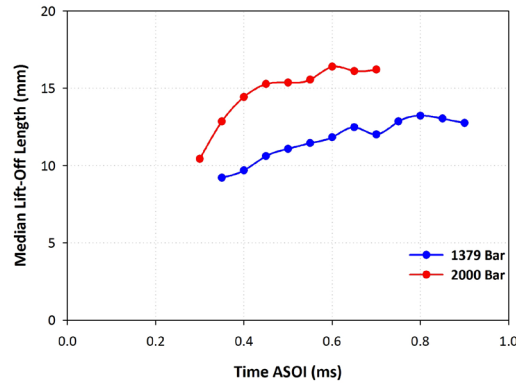


Figure 12.92: Median lift-off length versus time ASOI for combustng spray tests, 950 K bulk gas temperature, 34.8 kg/m³ density.

Lift-off length was larger by close to 40% for the 2000 bar injection pressure case. As injection pressure increased, the spray had a faster injection velocity and could then travel further in a given amount of time. The spray would have traveled further across the chamber before sufficient mixing occurred for the correct stoichiometry for the onset of combustion, as denoted by the increase in liquid length, agreeing with literature (Siebers and Higgins 2001).

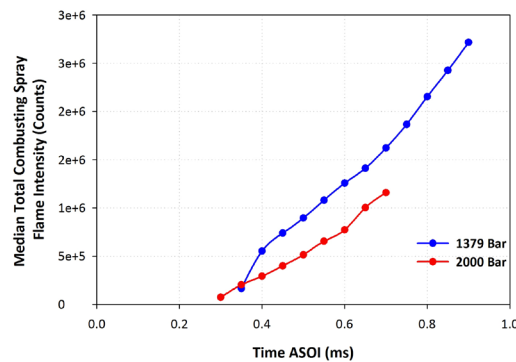


Figure 12.93: Median combustng plume intensity versus time ASOI for combustng spray tests, 950 K bulk gas temperature, 34.8 kg/m³ density.

Agreeing with the images, there was higher total combustng spray luminosity for the 1379 bar case relative to the 2000 bar case by close to 50%. This higher total luminosity indicates that higher soot will be formed in the lower injection pressure condition. This was expected as increased injection pressures provide improved atomization and fuel-air mixing reducing levels of emissions, especially under this low-temperature combustion conditions.

A comparison of the plume-to-plume trends as a function of various times ASOI is shown in Figure 12.94 for the 1379 bar case, and Figure 12.95 for the 2000 bar case.

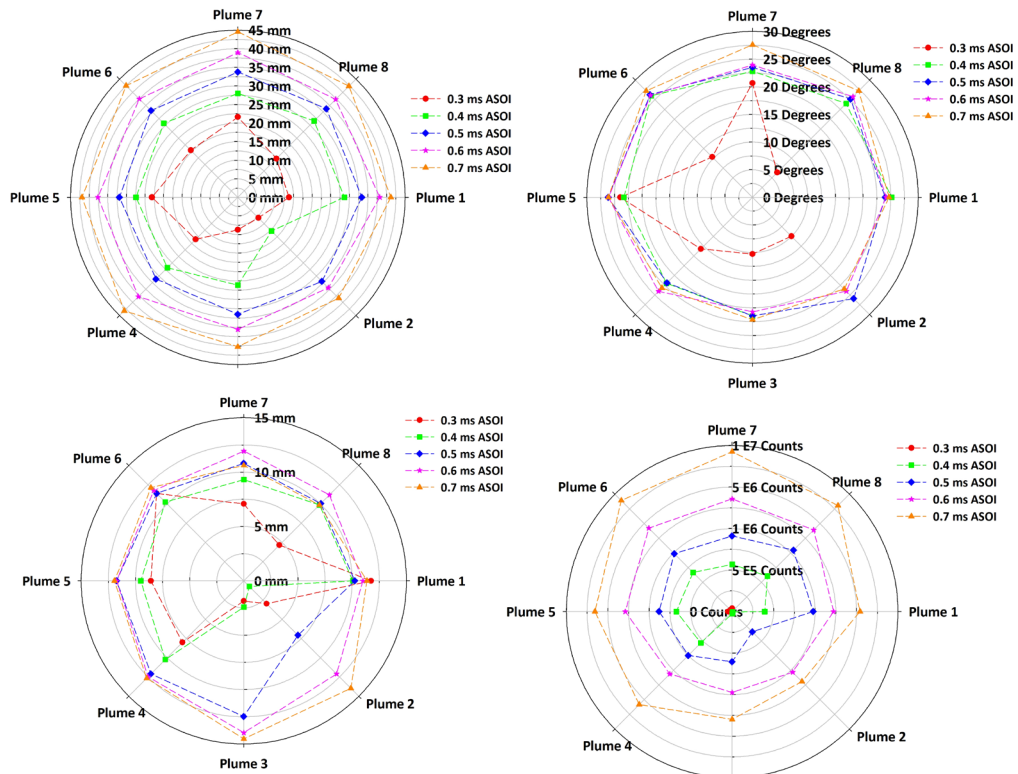


Figure 12.94: Polar plots for 1379 bar injection pressure considering plume to plume variations in flame length, cone angle, lift-off length, and total combusting intensity for 950 K bulk gas temperature, 34.8 kg/m³ density.

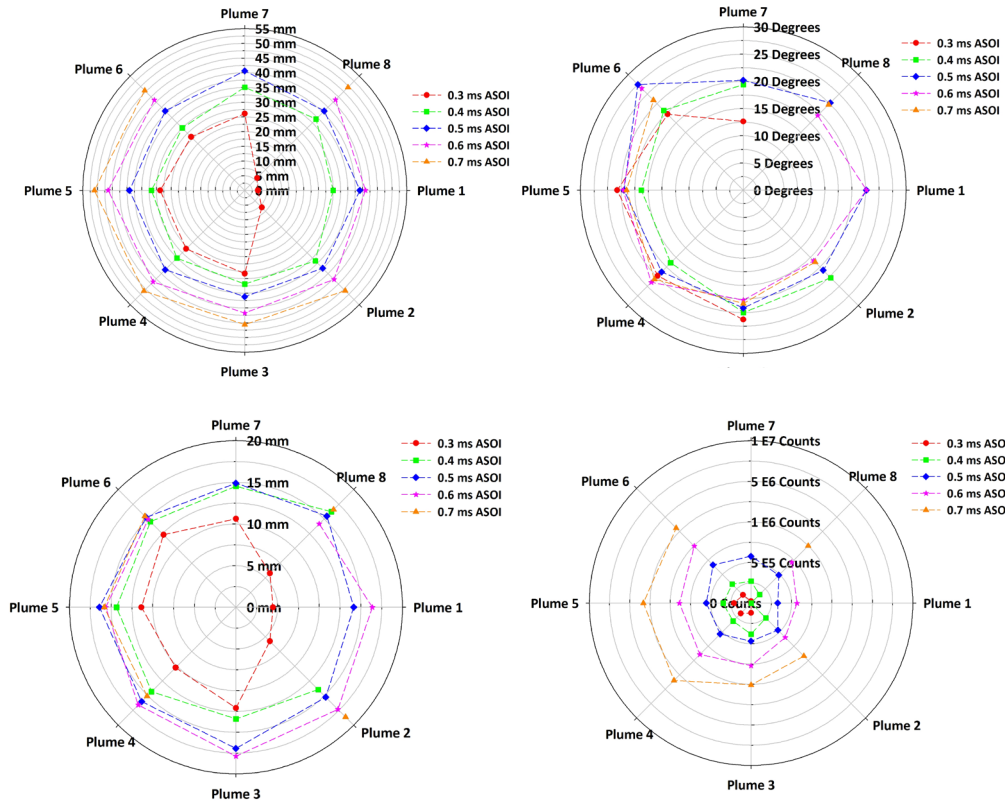


Figure 12.95: Polar plots for 2000 bar injection pressure considering plume to plume variations in flame length, cone angle, lift-off length, and total combust intensity for 950 K bulk gas temperature, 34.8 kg/m³ density.

Plume to plume variations in flame length were most apparent early times ASOI after which the plume variations were reduced. There were similar trends for cone angle, with the exception of plume 6, which had consistently larger cone angle than other plumes. Variations in lift-off length were much more pronounced, being largest for plumes 2, 3, and 4. Intensity was not consistent for the different spray plumes, especially as the time after start of injection increased.

12.6.3.3. Injection Pressure Variation at 1100 K

These tests are for an injection pressure variation at 1100 K ambient 21 percent oxygen gas temperature, 34.8 kg/m³ charge-gas density, and chiller off. A comparison of the plume-to-plume trends as a function of various times ASOI is shown in Figure 12.96 for the 1034 bar case, Figure 12.97 for the 1379 bar case, and were presented in Figure 12.87 for the 2000 bar case.

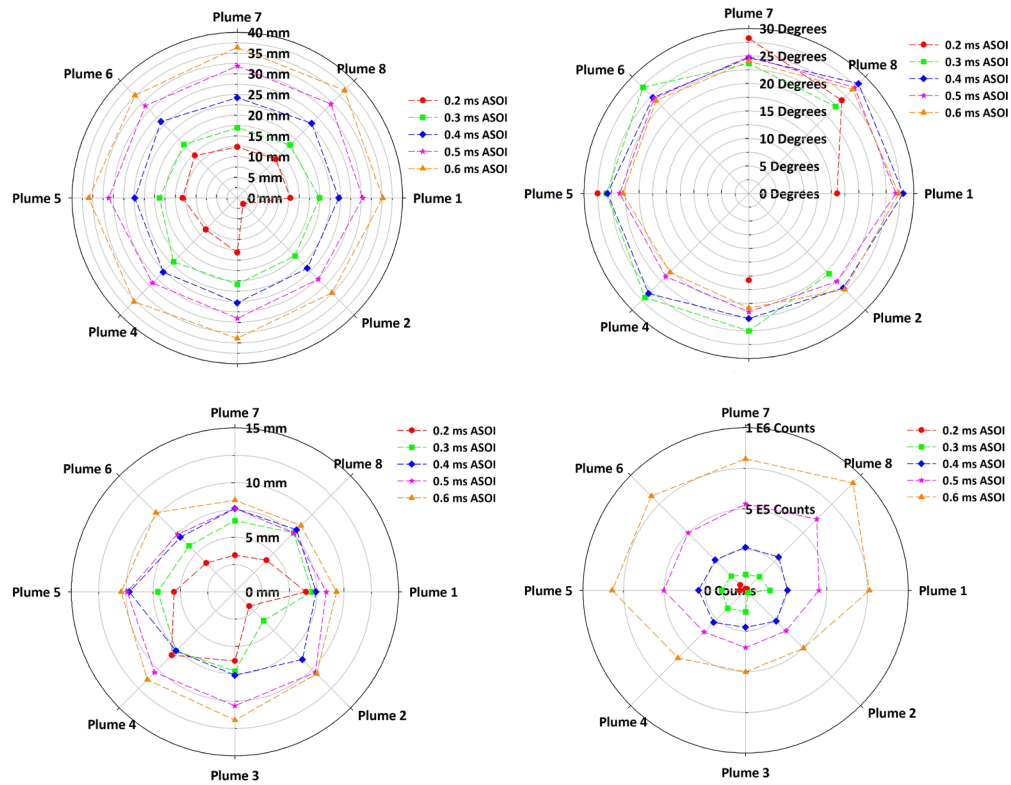


Figure 12.96: Polar plots for 1034 bar injection pressure considering plume to plume variations in flame length, cone angle, lift-off length, and total combusting intensity for 1100 K bulk gas temperature, 34.8 kg/m³ density.

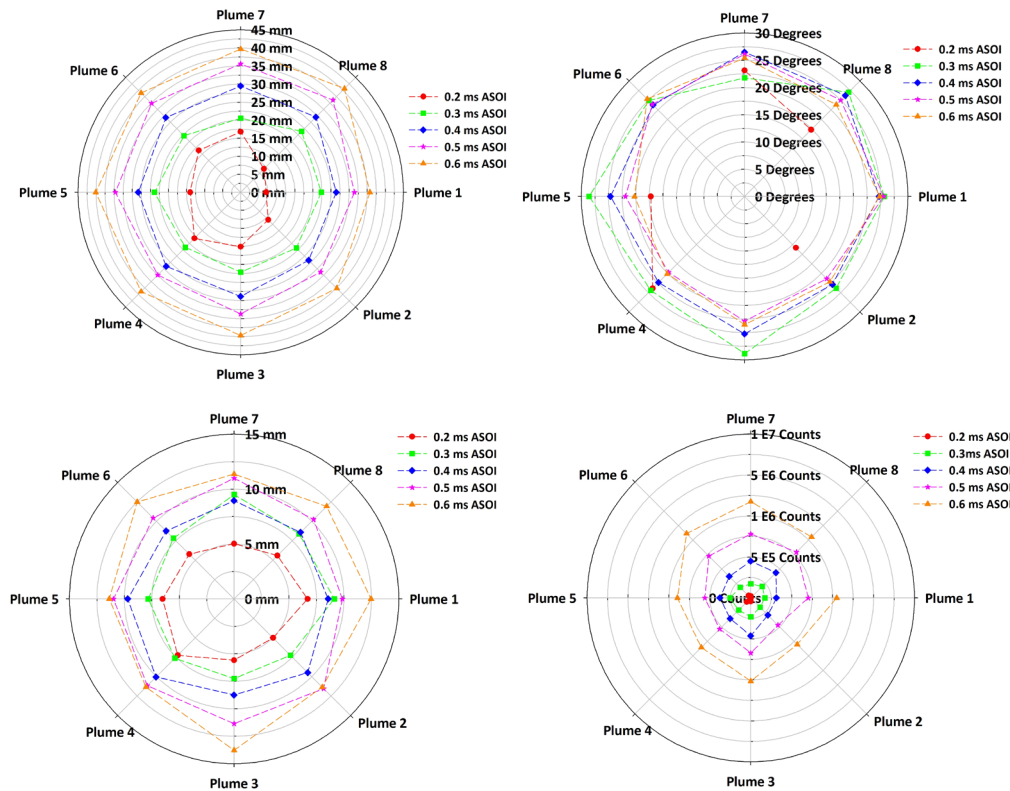


Figure 12.97: Polar plots for 1379 bar injection pressure considering plume to plume variations in flame length, cone angle, lift-off length, and total combust intensity for 1100 K bulk gas temperature, 34.8 kg/m³ density.

During the early phase ASOI flame length was largely asymmetric, with this asymmetry reducing as time ASOI increased. Cone angle showed large asymmetries, however, these asymmetries were inconsistent between test conditions. Lift-off length was largely asymmetric in early times ASOI, and still exhibited noticeable fluctuations at longer times ASOI. Plume total intensity was also largely asymmetric when comparing different plumes; however, again as was the case with other parameters, variations were not consistent over the differing injection pressures considered.

12.6.3.4. Charge Gas Density Variation

These tests are for charge-gas density variation at 1100 K ambient 21 percent oxygen gas temperature, and chiller off. Of interest is a comparison of the plume-to-plume trends as a function of various times ASOI shown in Figure 12.98 for the 17.4 kg/m³ density case, and were presented in Figure 12.87 for the 34.8 kg/m³ density case.

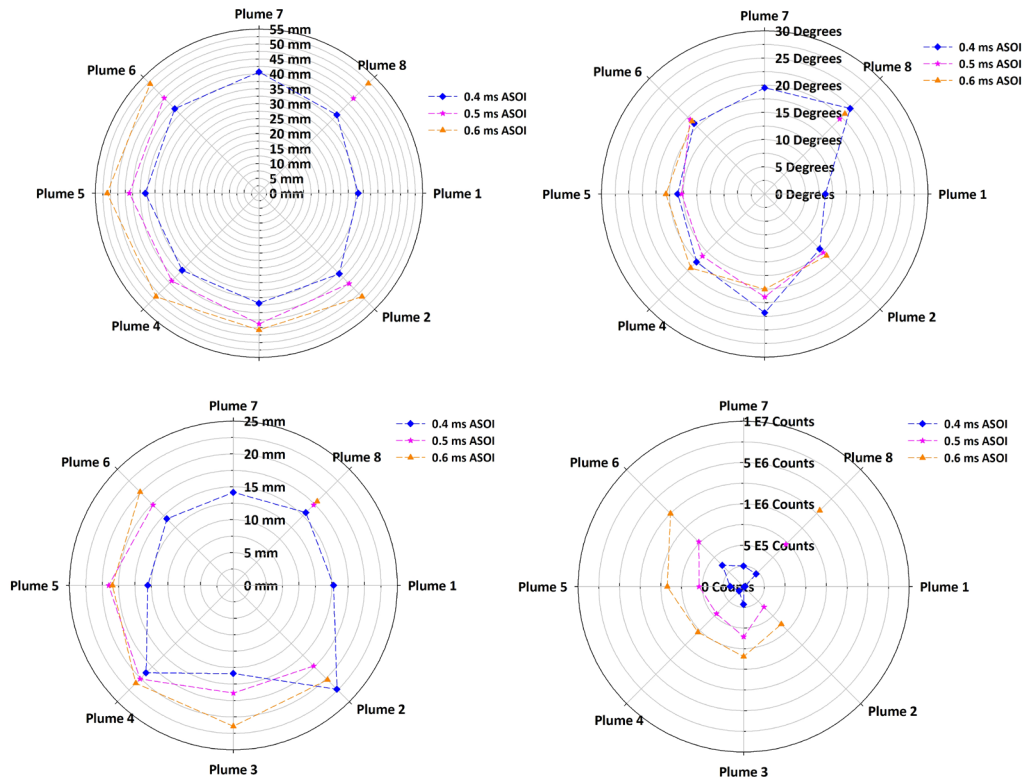


Figure 12.98: Polar plots for 2000 bar injection pressure considering plume to plume variations in flame length, cone angle, lift-off length, and total combust intensity for 1100 K bulk gas temperature, 17.4 kg/m³ density.

As the time ASOI increased, there were reductions in the plume to plume variations for the differing spray parameters. Although the magnitude of these plume to plume variations were significant, they were not consistent for the two different density cases.

12.6.3.5. Charge Gas Temperature Variation – 1379 Bar Injection Pressure

The influence of charge gas temperature on combust spray flame characteristics is also of interest. First, tests at the reduced, 1379 bar, injection pressure were considered. These were undertaken at 34.8 kg/m³ charge-gas density with actual test conditions provided in Table 12.9.

Table 12.9
Combusting test conditions for charge gas temperature variation at 1379 bar injection pressure and 34.8 kg/m³ charge gas bulk density.

	Injection Pressure (Bar)	Bulk Gas Density (kg/m ³)	Bulk Gas Temperature (K)	Core Gas Density (kg/m ³)	Core Gas Temperature (K)	Ignition Delay (ms)	Net Heat Release (kJ)
950 K	1380	33.9	950	31.8	1010	0.93	1.12
1100 K	1370	33.9	1100	31.4	1190	0.59	1.09

Test conditions relative to the set-points were comparable and therefore the results will be influenced only by the bulk gas temperature. Ignition delay was reduced by close to

40% for the higher temperature as expected (Kobori et al. 2000). Heat release was similar for the two tests (less than 3% variation) as the injection pressure was the same with comparable amounts of fuel being injected. Images from these tests are shown in Figure 12.99.

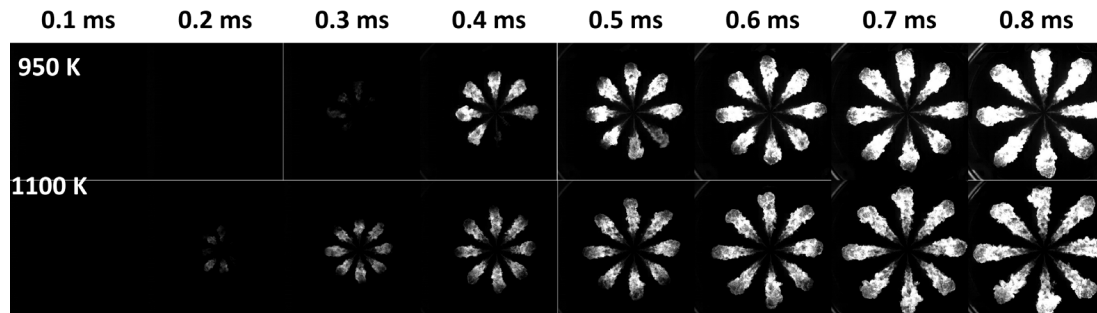


Figure 12.99: Combusting spray images from tests at 1379 bar injection pressure, 34.8 kg/m³ Density, Charge gas temperature variation.

The total combusting plume intensity was reduced and ignition delay decreased as charge gas temperature increased. Parameter comparison is best understood from the image processing results as shown in Figure 12.100, Figure 12.101, Figure 12.102, and Figure 12.103 for flame length, cone angle, lift-off length, and total combusting spray plume intensity, respectively.

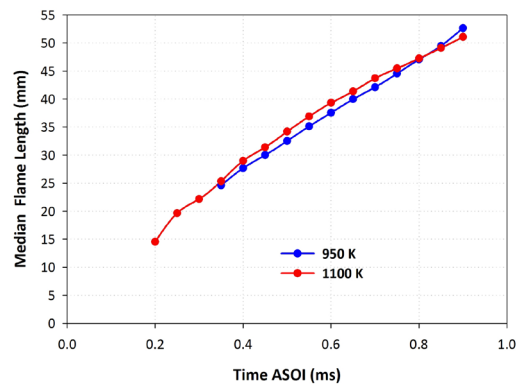


Figure 12.100: Median flame length versus time ASOI for combusting spray tests, 34.8 kg/m³ density, 1379 bar injection pressure. Computed ignition delay from pressure measurements of 0.93 ms and 0.59 ms for 950 and 1100 K charge-gas temperatures, respectively.

As charge-gas temperature increased, there were negligible variations in median flame length, less than 2%. This indicates that charge-gas temperature is not the governing factor in flame length; rather, injection pressure was more influential and the governing parameter as it controls the momentum of the spray.

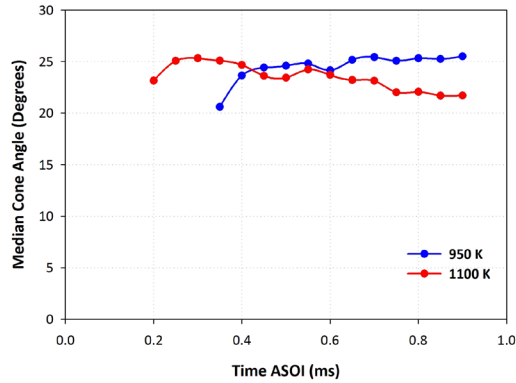


Figure 12.101: Median cone angle versus time ASOI for combustng spray tests, 34.8 kg/m³ density, 1379 bar injection pressure.

Cone angle was similar for both charge-gas temperatures, until later into the injection event at which the 950 K charge gas temperature had a larger cone angle by about 3 degrees relative to 1100 K.

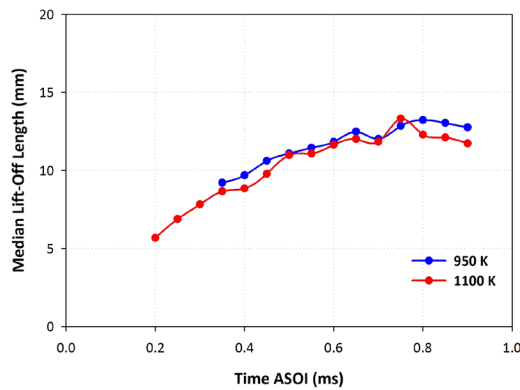


Figure 12.102: Median lift-off length versus time ASOI for combustng spray tests, 34.8 kg/m³ density, 1379 bar injection pressure.

Lift-off length was similar for both charge gas temperatures at the 1379 bar injection pressure, being about 1 mm longer for the 950 K temperature condition. It was expected that as temperature decreased, lift-off length would increase (Higgins and Siebers 2001, Siebers and Higgins 2001), these trends were not significant here.

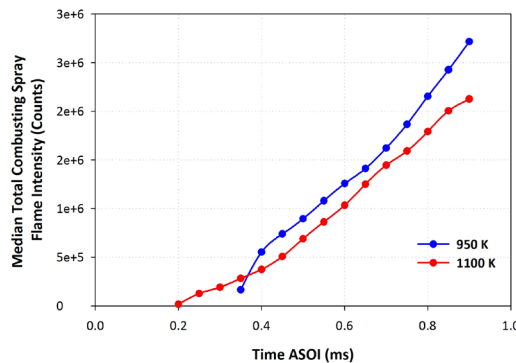


Figure 12.103: Median combustng plume intensity versus time ASOI for combustng spray tests, 34.8 kg/m³ density, 1379 bar injection pressure.

At the 1379 bar injection pressure, as charge-gas temperature increased, the combusting spray flame intensity decreased.

Polar plots comparing the plume to plume variations were presented in Figure 12.94 and Figure 12.97 for the 950 and 1100 K charge gas temperatures, respectively. Both conditions showed significant plume-to-plume variations without any consistency in trends for these variations.

12.6.3.6. Charge Gas Temperature Variation – 2000 Bar Injection Pressure

These tests are for a charge-gas temperature variation in an ambient 21 percent oxygen environment, 34.8 kg/m³ charge-gas density, 2000 bar injection pressure, and chiller off. Polar plots comparing the plume to plume variations were presented in Figure 12.95 and Figure 12.87 for the 950 and 1100 K charge gas temperatures, respectively. Again, no consistent trends in plume variations were evidenced.

12.7. Supplements to Chapter 7

12.7.1. Liquid Length Modeling Programs & Property Constants

This appendix includes processing programs used in EES for liquid length determination, including both tabulated thermodynamic property relations, and the programs for the developed equation of state methodology.

12.7.1.1. Tabulated Thermodynamic Property Relationships

Tabulated thermodynamic property relationships were obtained from Schihr et al. 2006. Units for enthalpies are in kJ/kg, temperature in °R, saturation pressure in Psia, and saturation density in lbm/ft³. Conversions are applied to reach SI units. Equations are provided for the needed thermophysical properties for liquid length application, and constants are provided for cetane as the single-component surrogate, for application in chapter 7.2 (Schihr et al. 2006).

Saturated Fuel Enthalpy (T_s , P_s)

$$\begin{aligned} P_{r,s} < 0.2 \quad h_f(T_s) &= AT_{r,s} - B \\ P_{r,s} \geq 0.2 \quad h_f(T_s) &= -CT_{r,s}^2 + DT_{r,s} - E \end{aligned}$$

Constants	Cetane
A	1869.7
B	550.15
C	929.51
D	3520.3
E	1283.4

Fuel Saturation Pressure (Ts)

$$\ln(P_s) = C1 - \frac{C2}{T_s} - C3 \cdot \ln(T_s) + C4T_s^2 + \frac{C5}{T_s^2}$$

Constants	Cetane
C1	174.2
C2	28534
C3	21.09
C4	2.5228E-6
C5	88111

Fuel Enthalpy (Tf, Pa)

$$h_f(T_f, P_a) = 1.0429 \cdot P_{a,r} + 320.95$$

Fuel Compressibility (Ts)

$$Z_f(T_s, P_s) = -aT_{r,s}^3 + bT_{r,s}^2 - cT_{r,s} + d$$

Constants	Cetane
a	16.587
b	34.594
c	24.531
d	6.689

Saturated Liquid Rho Fuel (Tf) -> Rackett Equation

$$\frac{1}{\rho_s} = \left(\frac{RT_c}{P_c} \right) \cdot Z_{ra}^{(1+(1-T_{f,r})^{2/7})}$$

$$Z_{ra} = 0.2386$$

12.7.1.2. Liquid Length Modeling Program Using Tabulated Thermodynamic Property Relations

The liquid length is calculated using tabulated thermodynamic property relationships in EES, provided in the file below. This requires inputs of ambient temperature and density (core conditions). The program below is for the chiller off case and fuel temperature is defined as 363 K, for the chiller on case the program is identical but fuel temperature is defined as 355 K. The EES program is solved using a parametric table approach, which includes definition of ambient core gas temperature and pressure for solution of the liquid length.

LL Correlation – CetaneAmbient0PercO2_ChillerOff.EES

"Run this program to calculate LL using Siebers Model with Tabulated Thermodynamic Property Relationships, Using Cetane as the Representative Fuel"

"Input conditions are temperature and density (ambient, core conditions), and fuel temperature"

"Functions for Calculating Thermodynamic Properties"

"Schihi et al. 2006"

"Function to calculate Saturated Fuel Enthalpy as function of reduced saturation pressure and temperature"

function SaturatedFuelEnthalpy(Prs, Trs)

"Saturated Fuel Enthalpy Constants"

Ahfs:= 1869.7

Bhfs:= 550.15

Chfs:= 929.51

Dhfs:= 3520.3

Ehfs:= 1283.4

if (Prs < 0.2) Then SaturatedFuelEnthalpy:= Ahfs*Trs-Bhfs else
SaturatedFuelEnthalpy:=-Chfs*Trs^2+Dhfs*Trs-Ehfs

end

"Function to calculate the fuel saturation pressure as a function of the saturation temperature"

function FuelSaturationPressure(Ts)

"Fuel Saturation Pressure Constants"

C1 := 174.2;

C2 := 28534;

C3 := 21.09;

C4 := 2.5228e-6;

C5 := 88111;

Ts_Rankine = ConvertTemp('K', 'R', Ts);

FuelSaturationPressure := exp(C1-C2/(Ts_Rankine)-
C3*ln(Ts_Rankine)+C4*(Ts_Rankine)^2+C5/(Ts_Rankine)^2)*0.0689475749;

end

"Function to calculate the Liquid Fuel Enthalpy as a function of the fuel temperature and reduced ambient pressure"

function FuelEnthalpy(Tf, Par)

CetaneC1 = 1.0429;

CetaneC2 = 320.95;

FuelEnthalpy := CetaneC1*Par + CetaneC2;

end

```
"Function to calculate the fuel compressibility as a function of the
reduced saturation temperature"
function FuelCompressibility(Trs)
```

```
AZf = 16.587
BZf = 34.594
CZf = 24.531
DZf = 6.869
```

```
FuelCompressibility := -AZf*Trs^3 + BZf*Trs^2-CZf*Trs+DZf
```

```
end
```

```
"Function to calculate the ambient enthalpy -- for 0%O2 Post Preburn"
function N2Enthalpy(Ta, R)
```

```
if (Ta < 1000) then
```

```
a1N2 = 0.02926640E+02
a2N2 = 0.14879768E-02
a3N2 = -0.05684760E-05
a4N2 = 0.10097038E-09
a5N2 = -0.06753351E-13
a6N2 = -0.09227977E+04
```

```
N2Enthalpy =
R*Ta*(a1N2+a2N2*Ta/2+a3N2*Ta^2/3+a4N2*Ta^3/4+a5N2*Ta^4/5+a6N2/Ta)
```

```
endif
```

```
if (Ta >=1000) then
```

```
a1N2 =0.03298677E+02
a2N2 =0.14082404E-02
a3N2 = -0.03963222E-04
a4N2 =0.05641515E-07
a5N2 =-0.02444854E-10
a6N2 =-0.10208999E+04
```

```
N2Enthalpy =
R*Ta*(a1N2+a2N2*Ta/2+a3N2*Ta^2/3+a4N2*Ta^3/4+a5N2*Ta^4/5+a6N2/Ta)
```

```
endif
```

```
end
```

```
function H2OEnthalpy(Ta, R)
```

```
if (Ta < 1000) then
```

```
a1H2O = 3.03399249E+00
a2H2O = 2.17691804E-03
a3H2O = -1.64072518E-07
a4H2O = -9.70419870E-11
a5H2O = 1.68200992E-14
```

```

a6H2O = -3.00042971E+04

H2OEnthalpy =
R*Ta*(a1H2O+a2H2O*Ta/2+a3H2O*Ta^2/3+a4H2O*Ta^3/4+a5H2O*Ta^4/5+a6H2O/Ta)

endif

if (Ta >=1000) then

a1H2O = 4.19864056E+00
a2H2O =-2.03643410E-03
a3H2O = 6.52040211E-06
a4H2O =-5.48797062E-09
a5H2O =1.77197817E-12
a6H2O =-3.02937267E+04

H2OEnthalpy =
R*Ta*(a1H2O+a2H2O*Ta/2+a3H2O*Ta^2/3+a4H2O*Ta^3/4+a5H2O*Ta^4/5+a6H2O/Ta)

endif
end

function CO2Enthalpy(Ta, R)

if (Ta < 1000) then

a1CO2 = 3.85746029E+00
a2CO2 =4.41437026E-03
a3CO2 = -2.21481404E-06
a4CO2 = 5.23490188E-10
a5CO2 = -4.72084164E-14
a6CO2 = -4.87591660E+04

CO2Enthalpy =
R*Ta*(a1CO2+a2CO2*Ta/2+a3CO2*Ta^2/3+a4CO2*Ta^3/4+a5CO2*Ta^4/5+a6CO2/Ta)

endif

if (Ta >=1000) then

a1CO2 = 2.35677352E+00
a2CO2 =8.98459677E-03
a3CO2 = -7.12356269E-06
a4CO2 = 2.45919022E-09
a5CO2 = -1.43699548E-13
a6CO2 = -4.83719697E+04

CO2Enthalpy =
R*Ta*(a1CO2+a2CO2*Ta/2+a3CO2*Ta^2/3+a4CO2*Ta^3/4+a5CO2*Ta^4/5+a6CO2/Ta)

endif
end

"Define Cetane Parameters"

```



```

"Tcr = Critical Temperature - Cetane as Diesel Surrogate"
Tcr = 722; "K"

"Pcr = Critical Pressure - Cetane as Diesel Surrogate"
Pcr = 14.1; "Bar"
PcrkPa = Pcr*convert(bar, kPa)

"Molecular Weight - Cetane"
Mf = 226.44; "kg/kmol"

"Rackett Parameter - Cetane"
ZraCetane = 0.2386;

"Define Experimental Conditions"

"Ideal Gas Constant"
R = 8.314; "kJ/kmol-K"

"Liquid Fuel Temperature"
Tf = 363; "K"

"Ta = Ambient Temperature - Defined for Test Conditions in 0% O2
Environment, Core Gas"

"Nozzle Orifice Diameter"
d = 0.145; "mm"

"Tfr = Reduced Fuel Temperature - Definition"
Tfr = Tf/Tcr; "Unitless"

"Define Ambient Parameters -- 0% O2 Mixture"

"Ambient Compressibility -- Assume 1 based on pressures and
temperatures used in this study"
Za = 1;

"Pcra = Critical Ambient Pressure - Use Modified Prausnitz and Gunn
Rule"
$Constant YCO2# = 0.0632
$Constant YN2# = 0.8852
$Constant YH2O# = 0.0475

$Constant MWCO2# = 44 (kg/kmol)
$Constant MWH2O# = 18 (kg/kmol)
$Constant MWN2# = 28 (kg/kmol)

$Constant Tc_CO2# = 304.1 (K)
$Constant Tc_N2# = 126.2 (K)
$Constant Tc_H2O# = 647.3 (K)

$Constant Vc_CO2# = 93.9E-3 (m^3/kmol)
$Constant Vc_N2# = 89.8E-3 (m^3/kmol)
$Constant Vc_H2O# = 57.1E-3 (m^3/kmol)

$Constant Zc_CO2# = 0.274

```

```

$Constant Zc_N2# = 0.290
$Constant Zc_H2O# = 0.235

"Calculate critical mixture temperature based on Kays Rule"
TcMix = YCO2#*Tc_CO2#+YH2O#*Tc_H2O#+YN2#*Tc_N2#;
Pcra =
R*TcMix*(YCO2#*Zc_CO2#+YH2O#*Zc_H2O#+YN2#*Zc_N2#)/(YCO2#*Vc_CO2#+YN2#*V
c_N2#+YH2O#*Vc_H2O#) *convert(kPa,Bar)

"Par = Reduced Ambient Pressure"
Par = Pa/Pcra;

"Molecular Weight - Ambient"

MWMix = (YCO2#*MWCO2#+YH2O#*MWH2O#+YN2#*MWN2#)
Ma = MWMix; "kg/kmol "

"Ambient Density - Defined for Test Conditions in 0% O2 Environment,
Core Gas"

"Pa = Ambient Pressure"
"Calculate from Density / Temperature Ambient; MWMix (0% O2)= 27.89
kg/kmol"
Pa = RhoA*R*Ta/MWMix*convert(kPa,bar)

"Calculate Saturated Liquid Fuel Density at Fuel Injection Temperature"

RhoF = 1/((R*Tcr/(PcrkPa*Mf))*ZraCetane^(1+(1-Tfr)^(2/7)))

"Trs = Reduced Saturation Temperature - Definition"
Trs = Ts/Tcr; "Unitless"

"Evaluate Functions"

"Fuel Saturation Pressure"
Ps = FuelSaturationPressure(Ts)

"Prs = Reduced Saturation Pressure - Definition"
Prs = Ps/Pcr; "Unitless"

"Fuel saturated enthalpy"
Hfs = SaturatedFuelEnthalpy(Prs, Trs);

"Fuel Enthalpy at Injection Temperature"
Hf = FuelEnthalpy(Tf, Par)

"Fuel Compressibility"
Zf = FuelCompressibility(Trs);

"Ambient Enthalpy at Ambient Temperature"

HN2 = N2Enthalpy(Ta, R)
HH2O = H2OEnthalpy(Ta,R)
HCO2 = CO2Enthalpy(Ta,R)

```

```

HaMolar = HN2*YN2#+HH2O*YH2O#+HCO2*YCO2#;
Ha = HaMolar/MWMix;

"Ambient Enthalpy at Saturation Temperature"

HN2Ts = N2Enthalpy(Ts, R)
HH2OTs = H2OEnthalpy(Ts,R)
HCO2Ts = CO2Enthalpy(Ts,R)

HasMolar = HN2Ts*YN2#+HH2OTs*YH2O#+HCO2Ts*YCO2#
Has = HasMolar/MWMix;

"Evaluate Vapor Coefficient for Iterative Solution for Ts"
LHS = (Za*Mf)
RHS = ((Ha-Has)/(Hfs-Hf))*(Zf*(Pa-Ps)*Ma)/Ps
LHS = RHS;

"Calculate LL using Correlation"

"Evaluate Evaporation Coefficient"
B = ((Ha-Has)/(Hfs-Hf))

"Calculate TanTheta/2 Using Siebers 1999-01-0528 Correlation"
"Assume constant 0.2640 per literature"
TanTheta2 = 0.2640*((RhoA/RhoF)^0.19-0.0043*sqrt(RhoF/RhoA));
"Tan(Theta/2)"
Theta2 = arctan(TanTheta2); "Degrees"

"LL Correlation Constants - Siebers 1999-01-0528"
aLL = 0.66
bLL = 0.41

"Guess for Ca -- per Literature"
Ca = 0.8

"Evaluate LL"
LL = bLL/aLL*sqrt(RhoF/RhoA)*(sqrt(Ca)*d)/(TanTheta2)*sqrt((2/B+1)^2-1)

```

Table 12.10
Variable guesses, units, and lower and upper limits for the LL model evaluation,
using tabulated thermodynamic properties.

Variable	Guess	Lower Limit	Upper Limit	Units
aLL	0.66	-Infinity	Infinity	
B	1	-Infinity	Infinity	
bLL	0.41	-Infinity	Infinity	
Ca	0.8	-Infinity	Infinity	
d	0.145	-Infinity	Infinity	mm
Ha	1	-Infinity	Infinity	kJ/kg
HaMolar	1	-Infinity	Infinity	kJ/kmol
Has	1	-Infinity	Infinity	kJ/kg
HasMolar	1	-Infinity	Infinity	kJ/kmol
HCO2	1	-Infinity	Infinity	kJ/kmol
HCO2Ts	1	-Infinity	Infinity	kJ/kmol
Hf	1	-Infinity	Infinity	kJ/kg
Hfs	1	-Infinity	Infinity	kJ/kg
HH2O	1	-Infinity	Infinity	kJ/kmol
HH2OTs	1	-Infinity	Infinity	kJ/kmol
HN2	1	-Infinity	Infinity	kJ/kmol
HN2Ts	1	-Infinity	Infinity	kJ/kmol
LHS	226.4	-Infinity	Infinity	
LL	1	-Infinity	Infinity	mm
Ma	28.42	-Infinity	Infinity	kg/kmol
Mf	226.4	-Infinity	Infinity	kg/kmol
MWMix	28.42	-Infinity	Infinity	kg/kmol
Pa	1	-Infinity	Infinity	Bar
Par		-Infinity	Infinity	
Pcr	14.1	-Infinity	Infinity	Bar
Pcra	43.49	-Infinity	Infinity	Bar
PerkPa	1410	-Infinity	Infinity	kPa
Prs	1	-Infinity	Infinity	
Ps	1	-Infinity	Infinity	
R	8.314	-Infinity	Infinity	kJ/kmol-K
RhoA	1	-Infinity	Infinity	kg/m ³
RhoF	720.9	-Infinity	Infinity	kg/m ³
RHS	226.4	-Infinity	Infinity	kg/kmol
Ta	1	-Infinity	Infinity	K
TanTheta2	1	-Infinity	Infinity	
TcMix	161.7	-Infinity	Infinity	K
Tcr	722	-Infinity	Infinity	K
Tf	363	-Infinity	Infinity	K
Tfr	0.5028	-Infinity	Infinity	
Theta2	1	-Infinity	Infinity	Degrees
Trs	1	-Infinity	Infinity	
Ts	500	453	760	K
Za	1	-Infinity	Infinity	
Zf	1	-Infinity	Infinity	
ZraCetane	0.2386	-Infinity	Infinity	

12.7.1.3. Equation of State Approach – Liquid Length

Liquid length is calculated using the Siebers 1999 model via an equation of state approach, for single component fuels. Inputs are ambient temperature and pressure and fuel temperature (experimental test conditions), fuel properties of critical pressure and temperature, acentric factor, Rackett parameter, molecular weight of the fuel, and ideal gas constant pressure specific heat capacity coefficients for the fuel. The program outputs the fuel spray liquid length by solving for the saturation temperature, and evaluating the model equation.

ComboEOSMethodology.EES

```
"Evaluate Liquid Length for Cetane as a single-component Surrogate"
"Nasa "

"http://www.me.berkeley.edu/gri_mech/data/nasa_plnm.html"

"GRI 3.0 mechanism coefficients"

"Ambient Mixture"

"Function to calculate the ambient enthalpy Ideal Gas -- for 0%O2 Post
Preburn"

function HN2 (Ta)

if (Ta < 1000) then

a1N2 = 0.02926640E+02
a2N2 = 0.14879768E-02
a3N2 = -0.05684760E-05
a4N2 = 0.10097038E-09
a5N2 = -0.06753351E-13

HN2 =
GasConstant#*(a1N2*Ta+a2N2*Ta^2/2+a3N2*Ta^3/3+a4N2*Ta^4/4+a5N2*Ta^5/5 -
(a1N2*TRef#+a2N2*TRef#^2/2+a3N2*TRef#^3/3+a4N2*TRef#^4/4+a5N2*TRef#^5/5
))
endif

if (Ta >=1000) then

a1N2 =0.03298677E+02
a2N2 =0.14082404E-02
a3N2 = -0.03963222E-04
a4N2 =0.05641515E-07
a5N2 =-0.02444854E-10

a1N2r = 0.02926640E+02
a2N2r = 0.14879768E-02
a3N2r = -0.05684760E-05
a4N2r = 0.10097038E-09
a5N2r = -0.06753351E-13
```

```

HN2 =
GasConstant#*(a1N2*Ta+a2N2*Ta^2/2+a3N2*Ta^3/3+a4N2*Ta^4/4+a5N2*Ta^5/5 -
(a1N2r*TRef#+a2N2r*TRef#^2/2+a3N2r*TRef#^3/3+a4N2r*TRef#^4/4+a5N2r*TRef
#^5/5 ))

endif
end

function HH2O(Ta)

if (Ta < 1000) then

a1H2O = 3.03399249E+00
a2H2O = 2.17691804E-03
a3H2O = -1.64072518E-07
a4H2O = -9.70419870E-11
a5H2O = 1.68200992E-14

HH2O =
GasConstant#*(a1H2O*Ta+a2H2O*Ta^2/2+a3H2O*Ta^3/3+a4H2O*Ta^4/4+a5H2O*Ta^
5/5 -
(a1H2O*TRef#+a2H2O*TRef#^2/2+a3H2O*TRef#^3/3+a4H2O*TRef#^4/4+a5H2O*TRef
#^5/5 ))
endif

if (Ta >=1000) then

a1H2O = 4.19864056E+00
a2H2O = -2.03643410E-03
a3H2O = 6.52040211E-06
a4H2O = -5.48797062E-09
a5H2O = 1.77197817E-12

a1H2Or = 3.03399249E+00
a2H2Or = 2.17691804E-03
a3H2Or = -1.64072518E-07
a4H2Or = -9.70419870E-11
a5H2Or = 1.68200992E-14

HH2O =
GasConstant#*(a1H2O*Ta+a2H2O*Ta^2/2+a3H2O*Ta^3/3+a4H2O*Ta^4/4+a5H2O*Ta^
5/5 -
(a1H2Or*TRef#+a2H2Or*TRef#^2/2+a3H2Or*TRef#^3/3+a4H2Or*TRef#^4/4+a5H2Or
*TRef#^5/5 ))

endif

end

function HCO2(Ta)

if (Ta < 1000) then

a1CO2 = 3.85746029E+00

```

```

a2CO2 =4.41437026E-03
a3CO2 = -2.21481404E-06
a4CO2 = 5.23490188E-10
a5CO2 = -4.72084164E-14

HCO2 =
GasConstant#*(a1CO2*Ta+a2CO2*Ta^2/2+a3CO2*Ta^3/3+a4CO2*Ta^4/4+a5CO2*Ta^
5/5 -
(a1CO2*TRef#+a2CO2*TRef#^2/2+a3CO2*TRef#^3/3+a4CO2*TRef#^4/4+a5CO2*TRef
#^5/5 ))

endif

if (Ta >=1000) then

a1CO2 = 2.35677352E+00
a2CO2 =8.98459677E-03
a3CO2 = -7.12356269E-06
a4CO2 = 2.45919022E-09
a5CO2 = -1.43699548E-13

a1CO2r = 3.85746029E+00
a2CO2r =4.41437026E-03
a3CO2r = -2.21481404E-06
a4CO2r = 5.23490188E-10
a5CO2r = -4.72084164E-14

HCO2 =
GasConstant#*(a1CO2*Ta+a2CO2*Ta^2/2+a3CO2*Ta^3/3+a4CO2*Ta^4/4+a5CO2*Ta^
5/5 -
(a1CO2r*TRef#+a2CO2r*TRef#^2/2+a3CO2r*TRef#^3/3+a4CO2r*TRef#^4/4+a5CO2r
*TRef#^5/5 ))
endif

end

function HaN2(Ta)

if (Ta <=1000) then

a1N2 = 0.02926640E+02
a2N2 = 0.14879768E-02
a3N2 = -0.05684760E-05
a4N2 = 0.10097038E-09
a5N2 = -0.06753351E-13

HaN2 =
GasConstant#*(a1N2*Ta+a2N2*Ta^2/2+a3N2*Ta^3/3+a4N2*Ta^4/4+a5N2*Ta^5/5 -
(a1N2*TRef#+a2N2*TRef#^2/2+a3N2*TRef#^3/3+a4N2*TRef#^4/4+a5N2*TRef#^5/5
))
endif

if (Ta >1000) then

```

```

a1N2 =0.03298677E+02
a2N2 =0.14082404E-02
a3N2 = -0.03963222E-04
a4N2 =0.05641515E-07
a5N2 =-0.02444854E-10

a1N2r = 0.02926640E+02
a2N2r = 0.14879768E-02
a3N2r = -0.05684760E-05
a4N2r = 0.10097038E-09
a5N2r = -0.06753351E-13

HaN2Ref =
GasConstant#*(a1N2r*TMid#+a2N2r*TMid#^2/2+a3N2r*TMid#^3/3+a4N2r*TMid#^4
/4+a5N2r*TMid#^5/5 -
(a1N2r*TRef#+a2N2r*TRef#^2/2+a3N2r*TRef#^3/3+a4N2r*TRef#^4/4+a5N2r*TRef
#^5/5 ))
HaN2Up =
GasConstant#*(a1N2*Ta+a2N2*Ta^2/2+a3N2*Ta^3/3+a4N2*Ta^4/4+a5N2*Ta^5/5 -
(a1N2*TMid#+a2N2*TMid#^2/2+a3N2*TMid#^3/3+a4N2*TMid#^4/4+a5N2*TMid#^5/5
))
HaN2 = HaN2Ref+HaN2Up

endif
end

function HaH2O(Ta)

if (Ta <= 1000) then

a1H2O = 3.03399249E+00
a2H2O = 2.17691804E-03
a3H2O = -1.64072518E-07
a4H2O = -9.70419870E-11
a5H2O = 1.68200992E-14

HaH2O =
GasConstant#*(a1H2O*Ta+a2H2O*Ta^2/2+a3H2O*Ta^3/3+a4H2O*Ta^4/4+a5H2O*Ta^
5/5 -
(a1H2O*TRef#+a2H2O*TRef#^2/2+a3H2O*TRef#^3/3+a4H2O*TRef#^4/4+a5H2O*TRef
#^5/5 ))
endif

if (Ta >1000) then

a1H2O = 4.19864056E+00
a2H2O =-2.03643410E-03
a3H2O = 6.52040211E-06
a4H2O =-5.48797062E-09
a5H2O =1.77197817E-12

a1H2Or = 3.03399249E+00

```



```

a2H2Or = 2.17691804E-03
a3H2Or = -1.64072518E-07
a4H2Or = -9.70419870E-11
a5H2Or = 1.68200992E-14

HaH2ORef =
GasConstant#*(a1H2Or*TMid#+a2H2Or*TMid#^2/2+a3H2Or*TMid#^3/3+a4H2Or*TMi
d#^4/4+a5H2Or*TMid#^5/5 -
(a1H2Or*TRef#+a2H2Or*TRef#^2/2+a3H2Or*TRef#^3/3+a4H2Or*TRef#^4/4+a5H2Or
*TRef#^5/5 ))
HaH2OUp =
GasConstant#*(a1H2O*Ta+a2H2O*Ta^2/2+a3H2O*Ta^3/3+a4H2O*Ta^4/4+a5H2O*Ta^
5/5 -
(a1H2O*TMid#+a2H2O*TMid#^2/2+a3H2O*TMid#^3/3+a4H2O*TMid#^4/4+a5H2O*TMid
#^5/5 ))

HaH2O = HaH2ORef+HaH2OUp
endif

end

function HaCO2(Ta)

if (Ta <= 1000) then

a1CO2 = 3.85746029E+00
a2CO2 =4.41437026E-03
a3CO2 = -2.21481404E-06
a4CO2 = 5.23490188E-10
a5CO2 = -4.72084164E-14

HaCO2 =
GasConstant#*(a1CO2*Ta+a2CO2*Ta^2/2+a3CO2*Ta^3/3+a4CO2*Ta^4/4+a5CO2*Ta^
5/5 -
(a1CO2*TRef#+a2CO2*TRef#^2/2+a3CO2*TRef#^3/3+a4CO2*TRef#^4/4+a5CO2*TRef
#^5/5 ))

endif

if (Ta >1000) then

a1CO2 = 2.35677352E+00
a2CO2 =8.98459677E-03
a3CO2 = -7.12356269E-06
a4CO2 = 2.45919022E-09
a5CO2 = -1.43699548E-13

a1CO2r = 2.35677352E+00
a2CO2r =8.98459677E-03
a3CO2r = -7.12356269E-06
a4CO2r = 2.45919022E-09
a5CO2r = -1.43699548E-13

HaCO2Ref =
GasConstant#*(a1CO2r*TMid#+a2CO2r*TMid#^2/2+a3CO2r*TMid#^3/3+a4CO2r*TMi

```

```

d#^4/4+a5CO2r*Tmid#^5/5 -
(alCO2r*TRef#+a2CO2r*TRef#^2/2+a3CO2r*TRef#^3/3+a4CO2r*TRef#^4/4+a5CO2r
*TRef#^5/5 ))
HaCO2Up =
GasConstant#*(a1CO2*Ta+a2CO2*Ta^2/2+a3CO2*Ta^3/3+a4CO2*Ta^4/4+a5CO2*Ta^
5/5 -
(a1CO2*Tmid#+a2CO2*Tmid#^2/2+a3CO2*Tmid#^3/3+a4CO2*Tmid#^4/4+a5CO2*Tmid
#^5/5 ))
HaCO2 = HaCO2Ref+HaCO2Up
endif

end

function HFuelS(Ts)

A = -1.302E1
B = 1.529E0
C = -8.537E-4
D = 1.85E-7

HFuelS= (A*Ts+B*Ts^2/2+C*Ts^3/3+D*Ts^4/4 -
(A*TRef#+B*TRef#^2/2+C*TRef#^3/3+D*TRef#^4/4))

end

function HFuel(Tf)

A = -1.302E1
B = 1.529E0
C = -8.537E-4
D = 1.85E-7

HFuel = (A*Tf+B*Tf^2/2+C*Tf^3/3+D*Tf^4/4 -
(A*TRef#+B*TRef#^2/2+C*TRef#^3/3+D*TRef#^4/4))

end

function RootFinder(AConstant, BConstant)

"Solve Cubic Equation"

"Z^3 - (1-B)Z^2 + (A-2B-3B^2)Z - (AB-B^2-B^3) = 0"

a_2 = -(1-BConstant)
a_1 = (AConstant-2*BConstant-3*BConstant^2)
a_0 = -(AConstant*BConstant-BConstant^2-BConstant^3)

call RealCubicRoots(a_2, a_1, a_0:z_1, z_2, z_3)

Z = max(z_1, z_2, z_3)

RootFinder= (Z)

end

```

```

"Determine liquid compressibility root"
function RootFinderL(AConstant, BConstant)

"Solve Cubic Equation"


$$Z^3 - (1-B)Z^2 + (A-2B-3B^2)Z - (AB-B^2-B^3) = 0$$


a_2 = -(1-BConstant)
a_1 = (AConstant-2*BConstant-3*BConstant^2)
a_0 = -(AConstant*BConstant-BConstant^2-BConstant^3)

call RealCubicRoots(a_2, a_1, a_0:z_1, z_2, z_3)

Zl = min(z_1, z_2, z_3)

RootFinderL = (Zl)

end

"Determine fugacity"
function FugacityEval(Zl, AConstant, BConstant, Pressure)

FugacityEval= Pressure*exp(Zl-1-ln(Zl-BConstant)-
AConstant/(2*sqrt(2)*BConstant)*ln((Zl+(1+sqrt(2))*BConstant)/(Zl+(1-
sqrt(2))*BConstant)))

end

"Define Constants"
$Constant GasConstant# = 8.314 (kJ/kmol-K)
$Constant TRef# = 298.15 (K)
$Constant d# = 0.145 (mm)
$Constant Ca# = 0.8

"LL Correlation Constants - Siebers 1999-01-0528"
$Constant aLL# = 0.66
$Constant bLL# = 0.41

"Fuel Properties"
Tc = 722 (K)
Pc = 1410 (kPa)
$Constant w# = 0.742
$Constant MWFuel# = 226.41 (kg/kmol)

"Ambient Properties"

$Constant MWCO2# = 44 (kg/kmol)
$Constant MWN2# = 28 (kg/kmol)
$Constant MWH2O# = 18 (kg/kmol)

$Constant YCO2# = 0.0632
$Constant YN2# = 0.8852
$Constant YH2O# = 0.0475

$Constant Pc_CO2# = 7380 (kPa)

```

```

$Constant Pc_N2# = 3390 (kPa)
$Constant Pc_H2O# = 22120 (kPa)

$Constant Tc_CO2# = 304.1 (K)
$Constant Tc_N2# = 126.2 (K)
$Constant Tc_H2O# = 647.3 (K)

$Constant Vc_CO2# = 93.9E-3 (m^3/kmol)
$Constant Vc_N2# = 89.8E-3 (m^3/kmol)
$Constant Vc_H2O# = 57.1E-3 (m^3/kmol)

$Constant Zc_CO2# = 0.274
$Constant Zc_N2# = 0.290
$Constant Zc_H2O# = 0.235

$Constant w_CO2# = 0.239
$Constant w_H2O# = 0.344
$Constant w_N2# = 0.039

TcMix = YCO2#*Tc_CO2#+YH2O#*Tc_H2O#+YN2#*Tc_N2#;
Wmix = YCO2#*w_CO2#+YH2O#*w_H2O#+YN2#*w_N2#
PcMix =
GasConstant#*TcMix*(YCO2#*Zc_CO2#+YH2O#*Zc_H2O#+YN2#*Zc_N2#) / (YCO2#*Vc_
CO2#+YN2#*Vc_N2#+YH2O#*Vc_H2O#)
MWMix = YCO2#*MWCO2#+YH2O#*MWH2O#+YN2#*MWN2#

"Fuel temperature"
Tf = 363 (K)
Tfr = Tf/Tc

"Density - Fuel"

ZraFuel = 0.2388
RhoF = 1/((GasConstant#*Tc/Pc)*ZraFuel^(1+(1-Tfr)^(2/7)))*MWFuel#

"Corresponding saturation pressure at the fuel temperature"
Zlfps = RootFinderL(AConstantF, BConstantF)
Zgfps = RootFinder(AConstantF, BConstantF)

flfps = FugacityEval(Zlfps, AConstantF, BConstantF, Pfs)
fgfps = FugacityEval(Zgfps, AConstantF, BConstantF, Pfs)

"Equate fugacities to determine saturation pressure for given
temperature"
flfps = fgfps

"Saturation Temperature"

"Ps = 662.6 (kPa)"

"Corresponding saturation pressure at the saturation temperature"
Zlfs = RootFinderL(AConstantFS, BConstantFS)
Zgfs = RootFinder(AConstantFS, BConstantFS)

flfs = FugacityEval(Zlfs, AConstantFS, BConstantFS, Ps)

```

```

fgfs = FugacityEval(Zgfs, AConstantFS, BConstantFS, Ps)

"Equate fugacities to determine saturation pressure for given
temperature"
flfs = fgfs

"Reduced Fuel Temperature"
Trf = Tf/Tc
Trs= Ts/Tc

"Ambient Conditions"
Ta = 1300 (K)
Pa = 12170 (kPa)
PDelta = Pa-Ps
RhoA = MWMix*Pa/(GasConstant#*Ta)

Tra = Ta/TcMix
Tras = Ts/TcMix

"EOS Parameters"

"Fuel"
a = 0.4572*GasConstant#^2*Tc^2/Pc
b = 0.0778*GasConstant#*Tc/Pc
Kappa = 0.37464+1.54226*w#-0.26992*w#^2

"Fuel at Fuel Temperature"
alphaF = (1+(Kappa)*(1-Trf^0.5))^2
BConstantF = b*Pfs/(GasConstant#*Tf)
AConstantF= a*alphaF*Pfs/(GasConstant#^2*Tf^2)
dadTf =-a*Kappa*sqrt(alphaF/(Tf*Tc))

"Fuel at Saturation Temperature"
alphaFS = (1+(Kappa)*(1-Trs^0.5))^2
BConstantFS = b*Ps/(GasConstant#*Ts)
AConstantFS = a*alphaFS*Ps/(GasConstant#^2*Ts^2)
dadTfs = -a*Kappa*sqrt(alphaFS/(Ts*Tc))

"Charge Gas"
a_amb = 0.4572*GasConstant#^2*TcMix^2/PcMix
b_amb = 0.0778*GasConstant#*TcMix/PcMix
Kappa_amb = 0.37464+1.54226*wMix-0.26992*wMix^2

"Charge Gas at Ambient Temperature"
alphaA = (1+(Kappa_amb)*(1-Tra^0.5))^2
BConstantA = b_amb*Pa/(GasConstant#*Ta)
AConstantA = a_amb*alphaA*Pa/(GasConstant#^2*Ta^2)
dadTa = -a_amb*Kappa_amb*sqrt(alphaA/(Ta*TcMix))

"Charge Gas at Saturation Temperature"
alphaAS = (1+(Kappa_amb)*(1-Tras^0.5))^2
BConstantAs = b_amb*PDelta/(GasConstant#*Ts)
AConstantAs = a_amb*alphaAS*PDelta/(GasConstant#^2*Ts^2)
dadTAs = -a_amb*Kappa_amb*sqrt(alphaAS/(Ts*TcMix))

```

```

"Determine Fuel Enthalpy at Tf"
"Saturated vapor compressibility at Tf, Pfs"
Zvf = RootFinder(AConstantF, BConstantF)
HDepSVF = (GasConstant#*Tf*(Zvf-1)+(Tf*(dadTf)-
a)/(2*sqrt(2)*b)*ln((Zvf+(1+sqrt(2))*BConstantF)/(Zvf+(1-
sqrt(2))*BConstantF)))

"Calculate enthalpy of vaporization - Pitzer + Watson method"
"Calculated for the temperature of the liquid fuel"

TrFake = 0.8
EnthalpyVapFake = GasConstant#*Tc*(7.08*(1-TrFake)^0.354+10.95*w#*(1-
TrFake)^0.456)
EnthalpyVapF = EnthalpyVapFake*((1-Trf)/(1-TrFake))^0.38

HStarF = HFuel(Tf)

EnthalpyFuelTf = -EnthalpyVapF+HDepSVF+HStarF

Hf_Tf = EnthalpyFuelTf/MWFuel#

"Determine Fuel Enthalpy at Ts"
Zvfs = RootFinder(AConstantFS, BConstantFS)

HDepFS = (GasConstant#*Ts*(Zvfs-1)+(Ts*(dadTfs)-
a)/(2*sqrt(2)*b)*ln((Zvfs+(1+sqrt(2))*BConstantFS)/(Zvfs+(1-
sqrt(2))*BConstantFS)))

HStarFS = HFuels(Ts)

EnthalpyFuelTs = HDepFS + HStarFS

Hf_Ts = EnthalpyFuelTs/MWFuel#

Denominator = Hf_Ts-Hf_Tf

"Determine Ambient Enthalpy at Ta"
Za = RootFinder(AConstantA, BConstantA)

HDepA = (GasConstant#*Ta*(Za-1)+(Ta*(dadTA)-
a_amb)/(2*sqrt(2)*b_amb)*ln((Za+(1+sqrt(2))*BConstantA)/(Za+(1-
sqrt(2))*BConstantA)))

$Constant TMid# = 1000 (K)
HCO2_A = HaCO2(Ta)
HN2_A = HaN2(Ta)
HH2O_A = HaH2O(Ta)

HStarA = (HCO2_A)*YCO2#+(HH2O_A)*YH2O#+(HN2_A)*YN2#

Ha = HDepA+HStarA

Ha_Ta = Ha/MWMix;

"Determine Ambient Enthalpy at Ts"

```

```

Zas = RootFinder(AConstantAS, BConstantAS)

HDepAS = (GasConstant#*Ts*(Zas-1)+(Ts*(dadTas)-
a_amb)/(2*sqrt(2)*b_amb)*ln((Zas+(1+sqrt(2))*BConstantAS)/(Zas+(1-
sqrt(2))*BConstantAS)))

HCO2_AS = HCO2(Ts)
HN2_AS = HN2(Ts)
HH2O_AS = HH2O(Ts)

HStarAS = HCO2_AS*YCO2#+HH2O_AS*YH2O#+HN2_AS*YN2#

HaS = HDepAS+HStarAS

Ha_Ts = HaS/MWMix;

Numerator = Ha-Ta-Ha_Ts

BRHS = Numerator / Denominator

BLHS = (Ps*MWFuel#*Zas)/(Zvfs*(Pa-Ps)*MWMix)

"Equate evaporation coefficient to determine saturation temperature"
BRHS = BLHS

"Calculate TanTheta/2 Using Siebers 1999-01-0528 Correlation"
"Assume constant 0.2640 per literature"
TanTheta2 = 0.2640*((RhoA/RhoF)^0.19-0.0043*sqrt(RhoF/RhoA));
"Tan(Theta/2)"
Theta2 = arctan(TanTheta2); "Degrees"

"Evaluate LL"
LL =
bLL#/aLL#*sqrt(RhoF/RhoA)*(sqrt(Ca#)*d#)/(TanTheta2)*sqrt((2/BLHS+1)^2-
1)

```

Table 12.11
Variable guesses, units, and lower and upper limits for the LL model evaluation,
using tabulated thermodynamic properties.

Variable	Guess	Lower Limit	Upper Limit	Units
a	1	0	Infinity	$\text{m}^6 \cdot \text{kPa} / (\text{kmol}^2)$
AConstantA	1	0	1	
AConstantAS	0.09	0	10	
AConstantF	0.00016	1E-6	1	
AConstantFS	0.3	0	10	
alphaA	1	0	1	
alphaAS	0.5	0	10	
alphaF	1	0	10	
alphaFS	1.8	0	10	
a_amb	1	0	Infinity	$\text{m}^6 \cdot \text{kPa} / (\text{kmol}^2)$
B	1	0	1	m^3 / kmol
BConstantA	1	0	Infinity	
BConstantAS	0.08	0	Infinity	
BConstantF	0.0000067	0	AConstantF	
BConstantFS	0.04	0	AConstantFS	
BLHS	0.7	0	Infinity	
BRHS	0.7	0	Infinity	
b_amb	1	0	Infinity	m^3 / kmol
dadTa	1	-Infinity	Infinity	$\text{m}^6 \cdot \text{kPa} / (\text{kmol}^2 \cdot \text{K})$
dadTAs	1	-Infinity	Infinity	$\text{m}^6 \cdot \text{kPa} / (\text{kmol}^2 \cdot \text{K})$
dadTf	1	-Infinity	Infinity	$\text{m}^6 \cdot \text{kPa} / (\text{kmol}^2 \cdot \text{K})$
dadTfs	1	-Infinity	Infinity	$\text{m}^6 \cdot \text{kPa} / (\text{kmol}^2 \cdot \text{K})$
Denominator	1	-Infinity	Infinity	kJ / kg
EnthalpyFuelTf	1	-Infinity	Infinity	kJ / kmol
EnthalpyFuelTs	1	-Infinity	Infinity	kJ / kmol
EnthalpyVapF	1	-Infinity	Infinity	kJ / kmol
EnthalpyVapFake	1	-Infinity	Infinity	kJ / kmol
fgfps	0.06	0	Infinity	kPa
Fgfs	440	0	Infinity	kPa
flfps	0.06	0	Infinity	kPa
flfs	440	0	Infinity	kPa
Ha	28964	-Infinity	Infinity	kJ / kmol
HaS	1	-Infinity	Infinity	kJ / kmol
Ha_Ta	1019	-Infinity	Infinity	kJ / kg
Ha_Ts	1	-Infinity	Infinity	kJ / kg
HCO2_A	43940	-Infinity	Infinity	kJ / kmol
HCO2_AS	1	-Infinity	Infinity	kJ / kmol
HDepA	9.93	-Infinity	Infinity	kJ / kmol
HDepAS	1	-Infinity	Infinity	kJ / kmol
HDepFS	1	-Infinity	Infinity	kJ / kmol
HDepSVF	1	-Infinity	Infinity	kJ / kmol
Hf_Tf	1	-Infinity	Infinity	kJ / kg
Hf_Ts	1	-Infinity	Infinity	kJ / kg
HH2O_A	34109	-Infinity	Infinity	kJ / kmol
HH2O_AS	1	-Infinity	Infinity	kJ / kmol
HN2_A	27741	-Infinity	Infinity	kJ / kmol
HN2_AS	1	-Infinity	Infinity	kJ / kmol
HStarA	28954	-Infinity	Infinity	kJ / kmol

Table 12.11, Continued

HStarAS	1	-Infinity	Infinity	kJ/kmol
HStarF	26302	-Infinity	Infinity	kJ/kmol
HStarFS	1	-Infinity	Infinity	kJ/kmol
Kappa	1	-Infinity	Infinity	
Kappa_amb	1	-Infinity	Infinity	
LL	1	-Infinity	Infinity	mm
MWMix	1	-Infinity	Infinity	kg/kmol
Numerator	1	-Infinity	Infinity	kJ/kg
Pa	1	-Infinity	Infinity	kPa
Pc	1	-Infinity	Infinity	kPa
PcMix	1	-Infinity	Infinity	kPa
PDelta	1	-Infinity	Infinity	kPa
Pfs	0.06	1E-2	10	kPa
Ps	600	2E2	Pc	kPa
RhoA	1	-Infinity	Infinity	kg/m ³
RhoF	1	-Infinity	Infinity	kg/m ³
Ta	1	-Infinity	Infinity	K
TanTheta2	1	-Infinity	Infinity	
Tc	1	-Infinity	Infinity	K
TcMix	1	0	Infinity	K
Tf	1	0	Infinity	K
Tfr	1	-Infinity	Infinity	
Theta2	1	-Infinity	Infinity	Degrees
Tra	1	0	Infinity	
Tras	1	0	Infinity	
Trf	1	0	Infinity	
TrFake	1	0	Infinity	
Trs	0.9	0	Infinity	
Ts	600	Tf	Tc	K
Wmix	1	0	Infinity	
Za	1	BConstantA	2	
Zas	1	BConstantAS	2	
Zgfps	1	BConstantF	1	
Zgfs	0.7	BConstantFS	1	
Zlfps	0.000007	BConstantF	Zgfps	
Zlfs	0.06	BConstantFS	Zgfs	
ZraFuel	1	-Infinity	Infinity	
Zvf	1	BConstantF	2	
Zvfs	0.7	BConstantFS	2	

12.7.1.4. Single-Component Fuel Properties

General fuel properties of molecular weight and boiling point for various single-component fuels are provided in Table 12.12.

Table 12.12
General fuel properties (Reid et al. 1987). *Data from Poling et al. 2001. Diesel fuel properties from AFDC 2010a.

Fuel	Formula	Molecular Weight (kg/kmol)	Boiling Point (K)
Cetane	C16H34	226.448	560
n-Heptane	C7H16	100.205	372
n-Heptadecane	C17H36	240.475	575
n-Decane	C10H22	142.286	447
1-Methylnapthalene	C11H10	142.201	518
Iso-octane	C8H18	114.232	372
Methylcyclohexane	C7H14	98.189	374
Toulene	C7H8	92.141	384
n-Dodecane	C12H26	170.34	490
n-Octadecane	C18H38	254.504	590
n-Tetradecane	C14H30	198.394	527
Heptamethylnonane*	C16H34	226.446	520
Diesel	C8 to C25	~200	453-613 K

12.7.1.5. Fuel Properties - Equation of State Evaluation

Fuel properties required for the equation of state evaluation are critical temperature and pressure, molecular weight, acentric factor (omega), and the Rackett parameter. Properties are readily available in Reid et al. (1987) and are reproduced here for fuels typically used in representing diesels, in Table 12.13.

Table 12.13
Fuel properties for Equation of State Modeling (Reid et al. 1987). n/a signifies data not available / tabulated. *Data from Poling et al. 2001. ^ Data from Schihr et al. 2006.

Fuel	Formula	Molecular Weight (kg/kmol)	Tc (K)	Pc (Bar)	Omega	Zra
Cetane	C16H34	226.448	722.0	14.1	0.742	0.2388
n-Heptane	C7H16	100.205	540.3	27.4	0.349	0.2604
n-Heptadecane	C17H36	240.475	722.0	13.0	0.770	0.2343
n-Decane	C10H22	142.286	617.7	21.2	0.489	0.2507
1-Methylnapthalene	C11H10	142.201	772.0	36.0	0.310	n/a
Iso-octane	C8H18	114.232	544.0	25.7	0.266	0.2684
Methylcyclohexane	C7H14	98.189	572.2	34.7	0.268	0.2704
Toulene	C7H8	92.141	591.8	41.0	0.263	0.2644
n-Dodecane	C12H26	170.34	658.2	18.2	0.575	0.2466
n-Octadecane	C18H38	254.504	748.0	12.0	0.790	0.2275
n-Tetradecane	C14H30	198.394	693.0	14.4	0.581	0.238^
Heptamethylnonane*	C16H34	226.446	693.0	15.7	0.548	n/a

12.7.1.6. Ideal Gas Ambient Charge Gas Specific Heat Constants

Constant pressure specific heat capacity is used to calculate the enthalpy of the ambient charge gas as an ideal gas, using equation (109).

$$C_p^*(T) = R \cdot (a_1 + a_2T + a_3T^2 + a_4T^3 + a_5T^4) \quad (109)$$

Constants for the a_i values for the three species comprising the charge-gas mixture are provided in Table 12.14. For cases where the ambient temperature is greater than the mid-point of the temperature validity range (1000 K), the integral is evaluated in two phases, first from the reference temperature to 1000 K using the a_i constants for the lower temperature range, and second from 1000 K to the ambient temperature, using the a_i constants for the upper temperature range.

Table 12.14
Ideal gas constant pressure specific heat capacity polynomial constants (McBride et al. 1993, Smith 1999).

	Valid Temperature Range (K)	a1 (-)	a2 (1/k)	a3 (1/K ²)	a4 (1/K ³)	a5 (1/K ⁴)
CO ₂	200 - 1000	3.85746E0	4.41437E-3	-2.21481E-6	5.23490E-10	-4.7208E-14
	1000 - 3500	2.35677E0	8.98459E-3	-7.12356E-6	2.45919E-9	-1.43699E-13
N ₂	300 -1000	0.0292E2	0.14879E-2	-0.05684E-5	0.10097E-9	-0.06753E-13
	1000-5000	0.03298E2	0.14082E-2	-0.03963E-4	0.05641E-7	-0.02444E-10
H ₂ O	200 - 1000	3.03399E0	2.17691E-3	-1.64072E-7	-9.7041E-11	1.68200E-14
	1000 - 3500	4.19864E0	-2.03643E-3	6.52040E-6	-5.48797E-9	1.77197E-12
O ₂	200 - 1000	3.28253E0	1.48308E-3	-7.57966E-7	2.09470E-10	-2.16717E-14
	1000 - 3500	3.78245E0	-2.99673E-3	9.84730E-6	-9.68129E-9	3.24372E-12

12.7.1.7. Ideal Gas Fuel Specific Heat Constants

Constant pressure specific heat capacity is used to calculate the enthalpy of the fuel as an ideal gas, using equation (110).

$$C_{p,\text{fuel}}^*(T) = A_{Cpf} + B_{Cpf} \cdot T + C_{Cpf} \cdot T^2 + D_{Cpf} \cdot T^3 \quad (110)$$

Constants of A_{Cpf} , B_{Cpf} , C_{Cpf} , and D_{Cpf} are tabulated in Reid et al. (1987), with values listed in Table 12.15, for several hydrocarbon fuels of interest.

Table 12.15
Ideal gas constant pressure specific heat capacity polynomial constants for fuels (Reid et al. 1987). *Data from LLNL heptamethylnonane mechanism.

Fuel	A_{Cpf} (kJ/kmol-K)	B_{Cpf} (kJ/kmol-K ²)	C_{Cpf} (kJ/kmol-K ³)	D_{Cpf} (kJ/kmol-K ⁴)
Cetane	-1.302E1	1.529E0	-8.537E-4	1.85E-7
n-Heptane	-5.146E0	6.762E-1	-3.651E-4	7.658E-8
n-Heptadecane	-1.397E1	1.624E0	-9.081E-4	1.972E-7
n-Decane	-7.037E1	1.232E0	-8.646E-4	2.455E-7
1-Methylnapthalene	-6.482E1	9.387E-1	-6.942E-4	2.016E-7
Iso-octane	-7.461E0	-7.779E-1	-4.287E-4	9.173E-8
Methylcyclohexane	-6.192E1	7.842E-1	-4.438E-4	9.366E-8
Toulene	-2.435E1	5.125E-1	-2.765E-4	4.911E-8
n-Dodecane	-9.28E0	1.149E0	-6.347E-4	1.359E-7
n-Octadecane	-1.447E1	1.717E0	-9.592E-4	2.078E-7
n-Tetradecane	-1.098E1	1.338E0	-7.423E-4	1.598E-7
Heptamethylnonane	5.1559E1	7.3606E-2	-2.4989E-5	3.8609E-9

12.7.1.8. Multi-Component Surrogate Fuel Liquid Length Methodology

To determine the liquid length using the equation of state approach for a multi-component surrogate, the Mean Evaporation Coefficient methodology is used. This requires applying the generic equation of state program, defined in section 0 to determine the evaporation coefficient for each of the single component fuels. The results are then combined for all of the fuel components to enable determination of the multi-component fuel surrogate, using the program provided below. Required inputs are ambient pressure and temperature conditions, fuel component properties including critical temperature and pressure, acentric factor, molecular weight, and Rackett parameter, along with each evaporation coefficient and mole fraction of the individual fuel species defining properties of the multi-component surrogate.

MultiComponentLL MECMethod.EES

"MEC Method"

"Determine Liquid Length of Multi-Component Fuel"

"Results from single component runs of Evaporation Coefficient"

\$Constant B1# = 1.238

\$Constant B2# = 1.14

"Define Constants"

\$Constant Tf# = 363 (K)

\$Constant aLL# = 0.66

\$Constant bLL# = 0.41

\$Constant Ca# = 0.8

\$Constant d# = 0.145 (mm)

\$Constant GasConstant# = 8.314 (kJ/kmol-K)

"Define Ambient Conditions"

\$Constant Ta# = 1430 (K)

\$Constant Pa# = 13260 (kPa)

\$Constant MWCO2# = 44 (kg/kmol)

\$Constant MWN2# = 28 (kg/kmol)

\$Constant MWH2O# = 18 (kg/kmol)

\$Constant YCO2# = 0.0632

\$Constant YN2# = 0.8852

\$Constant YH2O# = 0.0475

MWMix = YCO2#*MWCO2#+YH2O#*MWH2O#+YN2#*MWN2#

RhoA = MWMix*Pa#/(GasConstant#*Ta#)

"Fuel 1 - n-decane"

\$Constant Ra1# = 0.2507

\$Constant MW1# = 142.286 (kg/kmol)

```

$Constant Pc1# = 2120 (kPa)
$Constant Tc1# = 617.7 (K)
$Constant w1# = 0.489

"Fuel 2 - methylnaphthalene"

$Constant w2# = 0.310
$Constant MW2# = 142.201 (kg/kmol)
$Constant Pc2# = 3600 (kPa)
$Constant Tc2# = 772 (K)

Ra2 = 0.29056 - 0.08775*w2#

"Mixture Composition - Volume (Mole Fraction)"

$Constant Y1# = 0.70
$Constant Y2# = 0.30

"Mixture Critical Temperature - Kays Rule"

TcMix = Y1#*Tc1# + Y2#*Tc2#

"Convert mixture composition to mass fraction Basis"

MWMixF = Y1#*MW1#+Y2#*MW2#

X1 = Y1#*MW1#/MWMixF
X2 = Y2#*MW2#/MWMixF

"Mixture Fuel Density"

ZraMix = X1*Ra1#+X2*Ra2

Tfr = Tf#/TcMix

Vmix = GasConstant#*(X1*Tc1#/Pc1#+X2*Tc2#/Pc2#)*ZraMix^(1+(1-
Tfr)^(2/7))

RhoFMix = 1/(VMix/MWMixF)

"Evaluate Spray Angle for LL Determination"
TanTheta2 = 0.2640*((RhoA/RhoFMix)^0.19-0.0043*sqrt(RhoFMix/RhoA));
"Tan(Theta/2)"

"Evaluate Mean Evaporation Coefficient"

BMix = X1*B1# + X2*B2#

"Evaluate LL"
LL =
bLL#/aLL#*sqrt(RhoFMix/RhoA)*(sqrt(Ca#)*d#)/(TanTheta2)*sqrt((2/BMix+1)
^2-1)

```

12.8. Supplements to Chapter 8

12.8.1. Frequency Analysis Matlab Programs

Two matlab files were used in the frequency analysis of the liquid length fluctuations and fuel pressure fluctuations, as provided below.

12.8.1.1. Frequency Analysis of Liquid Length Fluctuations

Frequency analysis of the liquid length fluctuations is characterized using the following .m File. This program loads in the liquid length data saved as a result of image processing, and applies frequency analysis including an FFT, autopower, and PSD to the quasi-steady region of interest, 1 to 2 ms ASOI. To determine the frequency peaks it calls an existing .m file, *Extrema.m*, provided in the Matlab Central File Exchange (Aguilera 2006).

FrequencyAnalysis_VaporizingSprays.m

```
%% Frequency analysis of Liquid Length Fluctuations (0% O2)

%% Setup Workspace
clear all
close all
clc

% Define time vector in ms during steady state, based on camera framing
rate.
Time = (-0.1+74*1/67500*1000:1/67500*1000:1/67500*1000*141-0.1);

% Input desired test for processing. Open liquid length results (as
determined from image processing)
TimeProcess = input('Enter Test Time in HHMM Format:', 's');
filename = strcat(TimeProcess, 'LLData.mat');
load(filename)

% Plot Combined Liquid Length Results
figure;
plot(Time, PenetrationSpray(1,:), 'ro-', 'MarkerFaceColor', 'r')
hold on
plot(Time, PenetrationSpray(2,:), 'go-', 'MarkerFaceColor', 'g')
hold on
plot(Time, PenetrationSpray(3,:), 'bo-', 'MarkerFaceColor', 'b')
hold on
plot(Time, PenetrationSpray(4,:), 'mo-', 'MarkerFaceColor', 'm')
hold on
plot(Time, PenetrationSpray(5,:), 'co-', 'MarkerFaceColor', 'c')
hold on
plot(Time, PenetrationSpray(6,:), 'yo-', 'MarkerFaceColor', 'y')
hold on
plot(Time, PenetrationSpray(7,:), 'o-', 'Color', (0.5 0 0.5),
'MarkerFaceColor', (0.5 0 0.5))
hold on
```

```

plot(Time, PenetrationSpray(8,:), 'o-', 'Color', (0 0.5 0.5),
'MarkerFaceColor', (0 0.5 0.5))
hold on
h = plot(Time, mean(PenetrationSpray(:,:)), 'k-', 'LineWidth', 2);
set(gca, 'FontName', 'Calibri', 'FontSize', 14, 'FontWeight', 'Bold');
grid on
xlabel('Time ASOI (ms)', 'FontName', 'Calibri', 'FontSize', 14,
'FontWeight', 'Bold')
ylabel('Quasi-Steady Liquid Penetration (mm)', 'FontName', 'Calibri',
'FontSize', 14, 'FontWeight', 'Bold')
grid on
xlim((1 2))
ylim((0 15))
hleg = legend('Plume 1', 'Plume 2', 'Plume 3', 'Plume 4', 'Plume 5',
'Plume 6', 'Plume 7', 'Plume 8', 'Mean', 'Location',
'South');
set(hleg, 'FontName', 'Calibri', 'FontSize', 12, 'FontWeight', 'Bold')
%% ANALYSIS for 8 PLUMES

PeakFrequency = zeros(8, 5);
PeakTimes = zeros(8, 5);
PeakAmps = zeros(8, 5);

% Process each plume independently.

PlumeNum = 1;

for PlumeNum = 1:8

PenPlume = PenetrationSpray(PlumeNum,:);

%% Apply offset to plume (mean SS LL) to remove dc frequency
MeanSSL = mean(PenPlume);
PenPlumeOffset = PenPlume - MeanSSL;

%% Plot Pen of Plume Relative to Mean SS LL, And Offset plume
figure;
plot(Time, PenPlume, 'b-', 'LineWidth', 2)
hold on
plot(Time, zeros(size(Time))+MeanSSL, 'g-', 'LineWidth', 2)
hold on
plot(Time, PenPlumeOffset, 'r-', 'LineWidth', 2)
legend('Plume Penetration Data', 'Mean SS Liquid Length', 'Plume
Penetration Offset by Mean SS LL', 'Location', 'South')
hold off
ylabel('Liquid Penetration (mm)')
xlabel('Time ASOI (ms)')
title(strcat('Plume ', num2str(PlumeNum)))
xlim((0.9 2.1))
grid on

%% Define Sampling Parameters

Fsample = 67500; % Framing Rate

```

```

N = size((PenPlume),2); %Blocksize - Take of Penetration

F_Nyquist = Fsample/2;

delta_T = 1/Fsample; %Seconds

T_meas = N*delta_T; %Seconds

delta_f = 1/T_meas; %Hz

frequency = (0:delta_f:delta_f*N/2);

%% Apply WINDOW - Tukey Window

% r <= 0 gives rectangular window -- no window
% r>= 1 gives Hann Window
% Default r = 0.5
% L = number of points for window.

% Setup window function Using r = 0.5
L = size(PenPlumeOffset,2);
r = 0.5;

w = tukeywin(L,r)';

% Apply window to data
TukeyData = PenPlumeOffset.*w;

% Uncomment to plot results of windowed data, compared to original
data.
% figure;
% grid on
% xlabel('Time (ms)')
% ylabel('Shifted and Windowed Penetration (mm)')
% plot(Time,TukeyData, 'b-', 'LineWidth', 2)
% hold on
% plot(Time, PenPlumeOffset, 'r-', 'LineWidth', 2)
% legend('Windowed Data', 'Data')
% title('Tukey Window, R = 0.5')
% hold off

%% Frequency Analysis -> FFT, PSD, Autopower

fft_result_tukey = transpose(fft(TukeyData))./(sum(w.^2)/N); % Apply
ECF
fft_final_tukey = (fft_result_tukey(1) 2*fft_result_tukey(2:N/2+1)');

AutoPower_tukey = fft_final_tukey.*conj(fft_final_tukey);

PSD_tukey = AutoPower_tukey / delta_f;

% Uncomment to plot PSD results of frequency analysis.
% figure;
% plot(frequency, PSD_tukey, 'b-', 'LineWidth', 2)

```



```

% title('PSD of Offset Penetration Data with Tukey Window')
% grid on
% xlabel('Frequency (Hz)')
% ylabel('Power -- Magnitude^2 per unit Frequency (Hz)')

%% Find Extrema

(ymax,imax,ymin,imin) = extrema(PSD_tukey);

% Look at first 5 maximum spikes in PSD - their frequency is of
interest.

MaxFreqs = frequency(imax(1:5)); %Hz
MaxTimes = 1./MaxFreqs*1000; %us
MaxAmps = ymax(1:5);

%% Save Data
PeakFrequency(PlumeNum, :) = MaxFreqs;
PeakTimes(PlumeNum, :) = MaxTimes;
PeakAmps(PlumeNum, :) = MaxAmps;
PSDResults(PlumeNum, :) = PSD_tukey;
FrequencyResults(PlumeNum, :) = frequency;

%% Set up workspace for next iteration
clear PenPlume PenPlumeOffset
clear FSample N L r w delta_T delta_F F_Nyquist T_meas frequency
clear TukeyData
clear fft_result_tukey fft_final_tukey AutoPower_tukey
AutoPowerScaling_tukey
clear PSD_tukey
clear ymax imax ymin imin MaxFreqs MaxTimes MaxAmps
clear MeanSSL
end

% Plot combined PSD results for all 8 plumes
figure;
plot(FrequencyResults(1,:)./1000, PSDResults(1,:), 'r-')
hold on
plot(FrequencyResults(2,:)./1000, PSDResults(2,:), 'g-')
hold on
plot(FrequencyResults(3,:)./1000, PSDResults(3,:), 'b-')
hold on
plot(FrequencyResults(4,:)./1000, PSDResults(4,:), 'm-')
hold on
plot(FrequencyResults(5,:)./1000, PSDResults(5,:), 'c-')
hold on
plot(FrequencyResults(6,:)./1000, PSDResults(6,:), '-', 'Color', (0.5
0.5 0))
hold on
plot(FrequencyResults(7,:)./1000, PSDResults(7,:), '-', 'Color', (0.5 0
0.5))
hold on
plot(FrequencyResults(8,:)./1000, PSDResults(8,:), '-', 'Color', (0 0.5
0.5))
set(gca, 'FontName', 'Calibri', 'FontSize', 14, 'FontWeight', 'Bold');

```

```

grid on
xlabel('Frequency (kHz)', 'FontName', 'Calibri', 'FontSize', 14,
'FontWeight', 'Bold')
ylabel('PSD - Power Magnitude^2 per unit Frequency (Hz)', 'FontName',
'Calibri', 'FontSize', 14, 'FontWeight', 'Bold')
grid on
hleg = legend('Plume 1', 'Plume 2', 'Plume 3', 'Plume 4', 'Plume 5',
'Plume 6', 'Plume 7', 'Plume 8', 'Location',
'NorthEast');
set(hleg, 'FontName', 'Calibri', 'FontSize', 12, 'FontWeight', 'Bold')

```

12.8.1.2. Frequency Analysis of Fuel Pressure Fluctuations

The frequency of the fuel pressure fluctuations is characterized by applying an FFT to the fuel pressure data during the region of interest, surrounding the injection event, focused on the fluctuations in the data as a result of injection. This is accomplished using the following m-file, *FFT_FuelPressure.m*.

FFT_FuelPressure.m

```

%% Run this program to characterize fuel pressure fluctuations -
frequency

% First run data processing (BDF Conversion file) through the 0% O2
data processing, to provide
% fuel pressure data, as well as information on timings.

% Define start and end of injection (Sample Numbers)

InjectionStart = 2.140*10^5;
EndInjection = 2.200*10^5;

% Plot Fuel Pressure ROI - Injection
figure;
plot(t(InjectionStart:EndInjection),
FuelPressureBar(InjectionStart:EndInjection))
xlabel('Time (ms)')
ylabel('Fuel Pressure (bar)')

% Define fuel pressure ROI
FuelPressureInterest = FuelPressureBar(InjectionStart:EndInjection);

% Define sampling parameters, based on 100 kHz sampling rate.
Fsample = 100000;

N = size(FuelPressureInterest,1); %Blocksize

F_Nyquist = Fsample/2;

delta_T = 1/Fsample; %Seconds

T_meas = N*delta_T; %Seconds

```

```

delta_f = 1/T_meas; %Hz
time = (0:N-1)*delta_T; %Seconds
frequency = (0:delta_f:delta_f*N/2);

%% Take an FFT of the fuel pressure ROI
fft_result = transpose(fft(FuelPressureInterest));
fft_final = (fft_result(1) 2*fft_result(2:N/2+1))./N;

% Plot FFT Results
figure;
plot(frequency, abs(fft_final));
xlabel('Frequency (Hz)');
ylabel('FFT Amplitude');
% Determine the spikes in frequency based on the above figure

```

12.8.2. Magnitude of Liquid Length Fluctuations

The magnitude of liquid length fluctuations were determined, both the maximum and average extent relative to the mean value, as detailed below. The average extent of the fluctuations was determined to mitigate the influence of outlier points on understanding these fluctuations. Key observations from the liquid length fluctuations were that the positive fluctuations typically exceeded that of the negative fluctuations, with the overall magnitude of the fluctuations, both average and maximum extent, being very similar over all test conditions investigated. These results are discussed in detail in Chapter 8.3, with the figures here providing supporting information.

12.8.2.1. Maximum Extent of Fluctuations

The magnitude of the liquid length fluctuations are determined over the quasi-steady time period by defining the maximum and minimum values of the liquid length during this interval, relative to the mean value. This section provides results for mean liquid length for each plume of the multi-hole injector along with the average value in the bar charts, with error bars representing the fluctuation magnitude. The positive error bar magnitude is the difference between the maximum liquid length to the mean value, with the negative error bar magnitude being the difference between the minimum liquid length to the mean value, over the 1 to 2 ms ASOI period.

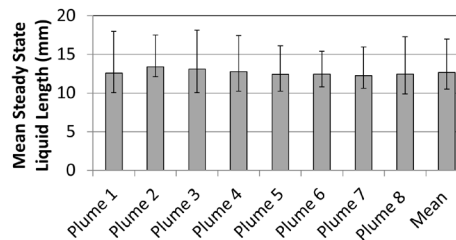


Figure 12.104: Mean quasi-steady liquid length with error bars showing the maximum magnitude of the fluctuations in liquid length, for 34.8 kg/m³ density, 0% oxygen, 1034 bar injection pressure, 355 K fuel temperature, 1100 K charge gas temperature.

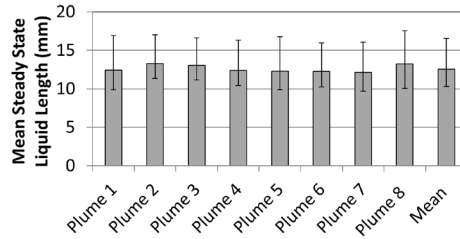


Figure 12.105: Mean quasi-steady liquid length with error bars showing the maximum magnitude of the fluctuations in liquid length, for 34.8 kg/m³ density, 0% oxygen, 1379 bar injection pressure, 355 K fuel temperature, 1100 K charge gas temperature.

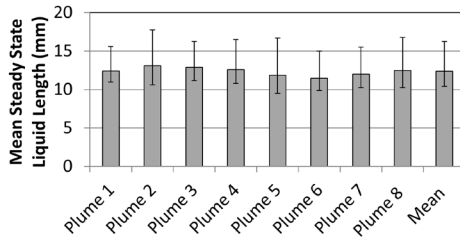


Figure 12.106: Mean quasi-steady liquid length with error bars showing the maximum magnitude of the fluctuations in liquid length, for 34.8 kg/m³ density, 0% oxygen, 2000 bar injection pressure, 355 K fuel temperature, 1100 K charge gas temperature, repeat test 1.

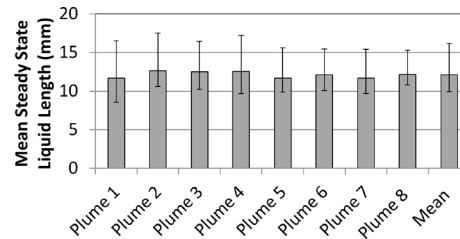


Figure 12.107: Mean quasi-steady liquid length with error bars showing the maximum magnitude of the fluctuations in liquid length, for 34.8 kg/m³ density, 0% oxygen, 1034 bar injection pressure, 355 K fuel temperature, 1100 K charge gas temperature, repeat test 2.

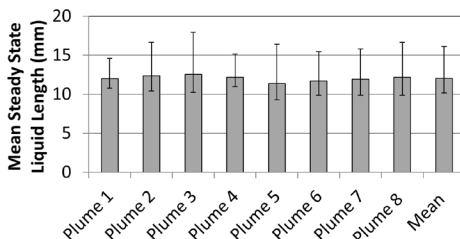


Figure 12.108: Mean quasi-steady liquid length with error bars showing the maximum magnitude of the fluctuations in liquid length, for 34.8 kg/m³ density, 0% oxygen, 1034 bar injection pressure, 355 K fuel temperature, 1100 K charge gas temperature, repeat test 3.

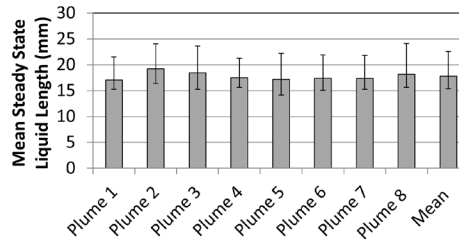


Figure 12.109: Mean quasi-steady liquid length with error bars showing the maximum magnitude of the fluctuations in liquid length, for 34.8 kg/m³ density, 0% oxygen, 2000 bar injection pressure, 363 K fuel temperature, 800 K charge gas temperature.

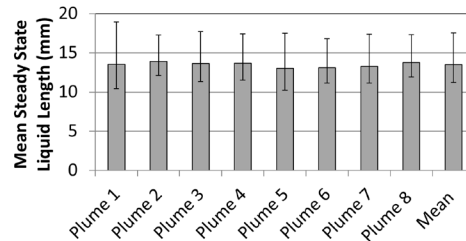


Figure 12.110: Mean quasi-steady liquid length with error bars showing the maximum magnitude of the fluctuations in liquid length, for 34.8 kg/m³ density, 0% oxygen, 2000 bar injection pressure, 363 K fuel temperature, 950 K charge gas temperature.

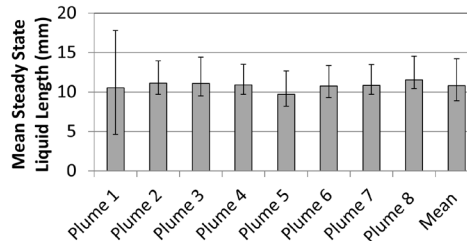


Figure 12.111: Mean quasi-steady liquid length with error bars showing the maximum magnitude of the fluctuations in liquid length, for 34.8 kg/m³ density, 0% oxygen, 2000 bar injection pressure, 363 K fuel temperature, 1100 K charge gas temperature, repeat test 2.

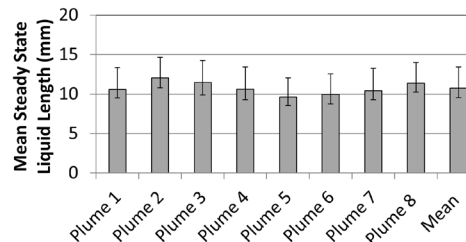


Figure 12.112: Mean quasi-steady liquid length with error bars showing the maximum magnitude of the fluctuations in liquid length, for 34.8 kg/m³ density, 0% oxygen, 2000 bar injection pressure, 363 K fuel temperature, 1100 K charge gas temperature, repeat test 3.

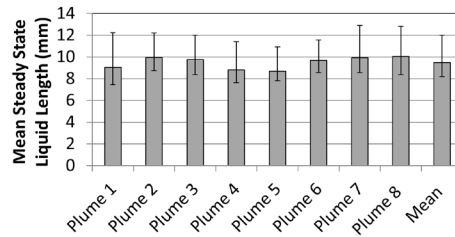


Figure 12.113: Mean quasi-steady liquid length with error bars showing the maximum magnitude of the fluctuations in liquid length, for 34.8 kg/m³ density, 0% oxygen, 2000 bar injection pressure, 363 K fuel temperature, 1200 K charge gas temperature.

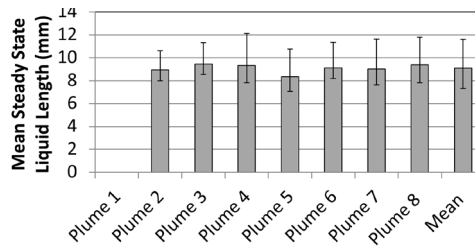


Figure 12.114: Mean quasi-steady liquid length with error bars showing the maximum magnitude of the fluctuations in liquid length, for 34.8 kg/m³ density, 0% oxygen, 2000 bar injection pressure, 363 K fuel temperature, 1300 K charge gas temperature.

As the determined liquid length results were not representative of the actual spray behavior based on interference in image processing, no results are provided for plume 1.

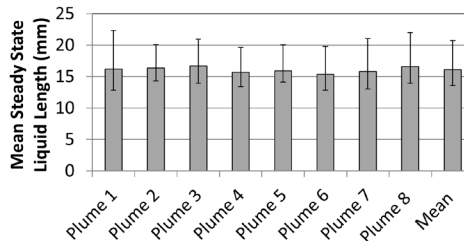


Figure 12.115: Mean quasi-steady liquid length with error bars showing the maximum magnitude of the fluctuations in liquid length, for 17.4 kg/m³ density, 0% oxygen, 2000 bar injection pressure, 363 K fuel temperature, 1100 K charge gas temperature.

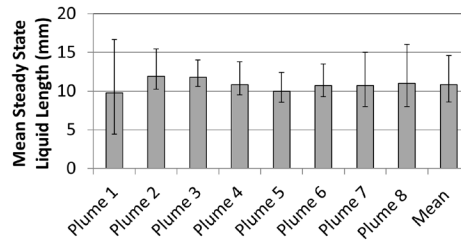


Figure 12.116: Mean quasi-steady liquid length with error bars showing the maximum magnitude of the fluctuations in liquid length, for 34.8 kg/m³ density, 0% oxygen, 1034 bar injection pressure, 363 K fuel temperature, 1100 K charge gas temperature.

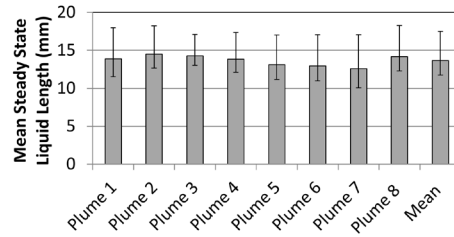


Figure 12.117: Mean quasi-steady liquid length with error bars showing the maximum magnitude of the fluctuations in liquid length, for 34.8 kg/m³ density, 0% oxygen, 1379 bar injection pressure, 363 K fuel temperature, 950 K charge gas temperature.

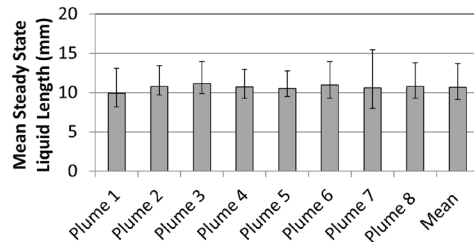


Figure 12.118: Mean quasi-steady liquid length with error bars showing the maximum magnitude of the fluctuations in liquid length, for 34.8 kg/m³ density, 0% oxygen, 1379 bar injection pressure, 363 K fuel temperature, 1100 K charge gas temperature.

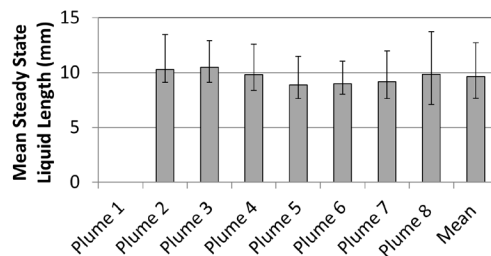


Figure 12.119: Mean quasi-steady liquid length with error bars showing the maximum magnitude of the fluctuations in liquid length, for 34.8 kg/m³ density, 0% oxygen, 1379 bar injection pressure, 363 K fuel temperature, 1200 K charge gas temperature.

No results are provided for plume 1 due to errors in image processing based on interference from the ceramic surrounding the injector, therefore, the determined liquid length results are not representative of the actual spray behavior.

12.8.2.2. Average Extent of Fluctuations

The average magnitude of the liquid length fluctuations were determined over the quasi-steady value by finding the values of liquid length exceeding the mean value (positive value), and those falling below the mean value (negative value). The average of these positive and negative liquid lengths, relative to the mean, was determined. The average value defined the fluctuations, relative to the mean value. This section provides results for mean liquid length for each plume of the multi-hole injector, along with the average value in the bar charts with error bars representing the fluctuation average magnitude. The positive error bar magnitude is the difference between the average liquid lengths exceeding the mean value, with the negative error bar magnitude being the difference between the average liquid lengths being less than the mean value, over the 1 to 2 ms ASOI period.

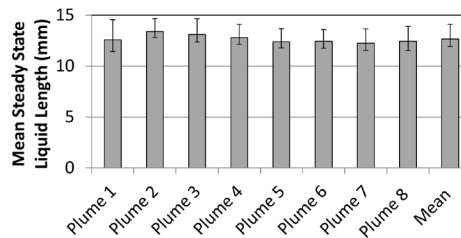


Figure 12.120: Mean quasi-steady liquid length with error bars showing the average magnitude of the fluctuations in liquid length, for 34.8 kg/m³ density, 0% oxygen, 1034 bar injection pressure, 355 K fuel temperature, 1100 K charge gas temperature.

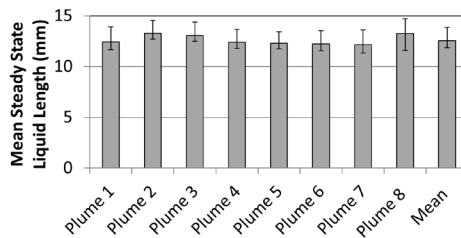


Figure 12.121: Mean quasi-steady liquid length with error bars showing the average magnitude of the fluctuations in liquid length, for 34.8 kg/m³ density, 0% oxygen, 1379 bar injection pressure, 355 K fuel temperature, 1100 K charge gas temperature.

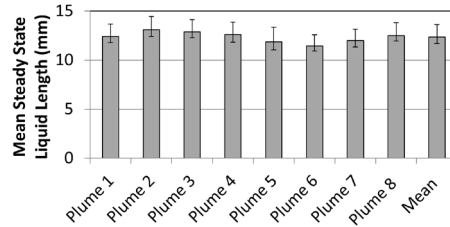


Figure 12.122: Mean quasi-steady liquid length with error bars showing the average magnitude of the fluctuations in liquid length, for 34.8 kg/m³ density, 0% oxygen, 2000 bar injection pressure, 355 K fuel temperature, 1100 K charge gas temperature, repeat test 1.

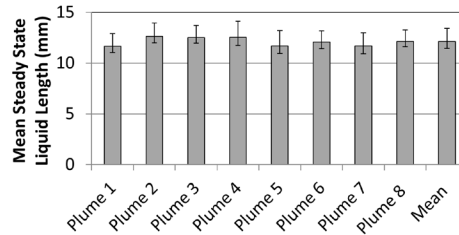


Figure 12.123: Mean quasi-steady liquid length with error bars showing the average magnitude of the fluctuations in liquid length, for 34.8 kg/m³ density, 0% oxygen, 1034 bar injection pressure, 355 K fuel temperature, 1100 K charge gas temperature, repeat test 2.

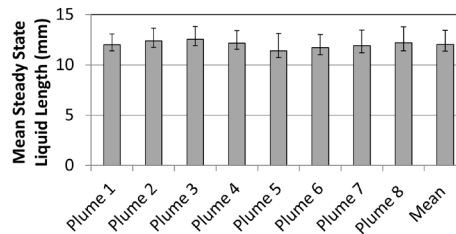


Figure 12.124: Mean quasi-steady liquid length with error bars showing the average magnitude of the fluctuations in liquid length, for 34.8 kg/m³ density, 0% oxygen, 1034 bar injection pressure, 355 K fuel temperature, 1100 K charge gas temperature, repeat test 3.

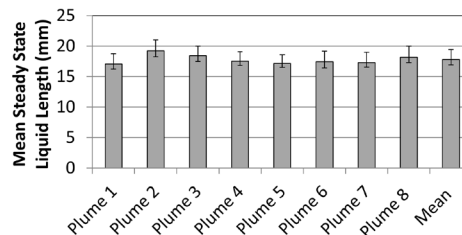


Figure 12.125: Mean quasi-steady liquid length with error bars showing the average magnitude of the fluctuations in liquid length, for 34.8 kg/m³ density, 0% oxygen, 2000 bar injection pressure, 363 K fuel temperature, 800 K charge gas temperature.

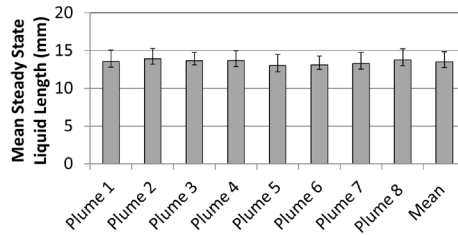


Figure 12.126: Mean quasi-steady liquid length with error bars showing the average magnitude of the fluctuations in liquid length, for 34.8 kg/m³ density, 0% oxygen, 2000 bar injection pressure, 363 K fuel temperature, 950 K charge gas temperature.

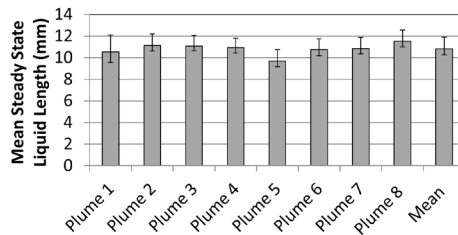


Figure 12.127: Mean quasi-steady liquid length with error bars showing the average magnitude of the fluctuations in liquid length, for 34.8 kg/m³ density, 0% oxygen, 2000 bar injection pressure, 363 K fuel temperature, 1100 K charge gas temperature, repeat test 2.

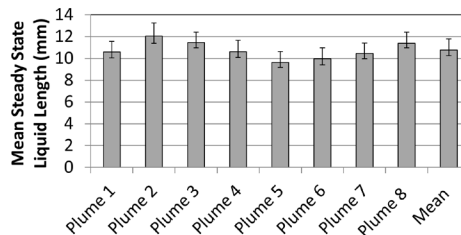


Figure 12.128: Mean quasi-steady liquid length with error bars showing the average magnitude of the fluctuations in liquid length, for 34.8 kg/m³ density, 0% oxygen, 2000 bar injection pressure, 363 K fuel temperature, 1100 K charge gas temperature, repeat test 3.

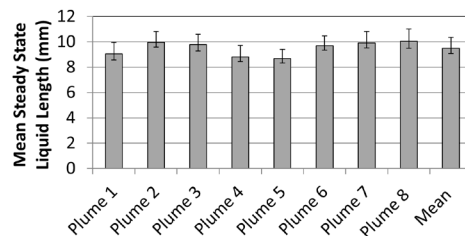


Figure 12.129: Mean quasi-steady liquid length with error bars showing the average magnitude of the fluctuations in liquid length, for 34.8 kg/m³ density, 0% oxygen, 2000 bar injection pressure, 363 K fuel temperature, 1200 K charge gas temperature.

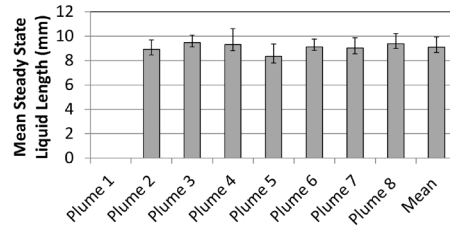


Figure 12.130: Mean quasi-steady liquid length with error bars showing the average magnitude of the fluctuations in liquid length, for 34.8 kg/m³ density, 0% oxygen, 2000 bar injection pressure, 363 K fuel temperature, 1300 K charge gas temperature.

No results were provided for plume 1 based on interference with the spray signal from the ceramic surrounding the injector, thereby providing errors in image processing and therefore the determined liquid length results are not representative of the actual spray behavior.

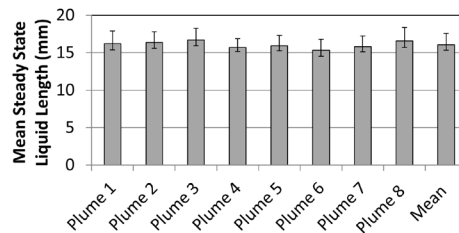


Figure 12.131: Mean quasi-steady liquid length with error bars showing the average magnitude of the fluctuations in liquid length, for 17.4 kg/m³ density, 0% oxygen, 2000 bar injection pressure, 363 K fuel temperature, 1100 K charge gas temperature.

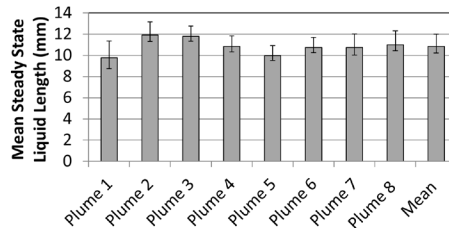


Figure 12.132: Mean quasi-steady liquid length with error bars showing the average magnitude of the fluctuations in liquid length, for 34.8 kg/m³ density, 0% oxygen, 1034 bar injection pressure, 363 K fuel temperature, 1100 K charge gas temperature.

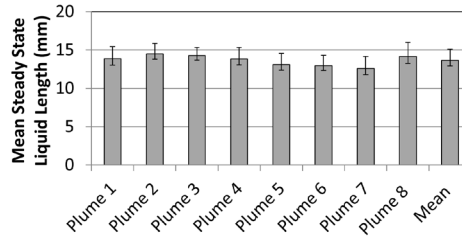


Figure 12.133: Mean quasi-steady liquid length with error bars showing the average magnitude of the fluctuations in liquid length, for 34.8 kg/m³ density, 0% oxygen, 1379 bar injection pressure, 363 K fuel temperature, 950 K charge gas temperature.

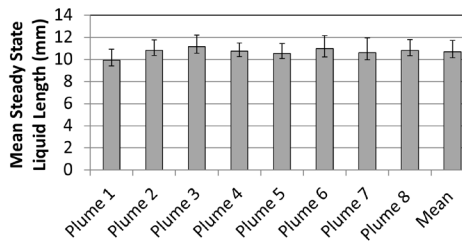


Figure 12.134: Mean quasi-steady liquid length with error bars showing the average magnitude of the fluctuations in liquid length, for 34.8 kg/m³ density, 0% oxygen, 1379 bar injection pressure, 363 K fuel temperature, 1100 K charge gas temperature.

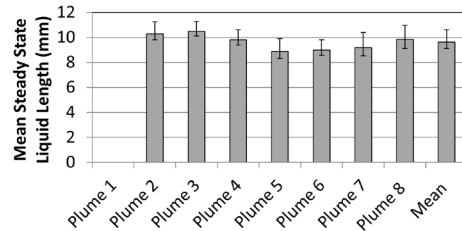


Figure 12.135: Mean quasi-steady liquid length with error bars showing the average magnitude of the fluctuations in liquid length, for 34.8 kg/m³ density, 0% oxygen, 1379 bar injection pressure, 363 K fuel temperature, 1200 K charge gas temperature.

No results were provided for plume 1 due to errors in image processing based on interference from the ceramic surrounding the injector, therefore, the determined liquid length results were not representative of the actual spray behavior.

12.8.3. Penetration and PSD Results

Plots for liquid penetration as a function of time ASOI, during the quasi-steady liquid length period (1 to 2 ms ASOI), are included in this section for each of the vaporizing spray tests, along with the corresponding PSD results from the frequency analysis. These plots include data for each of the eight plumes from the multi-hole injector for comparison.

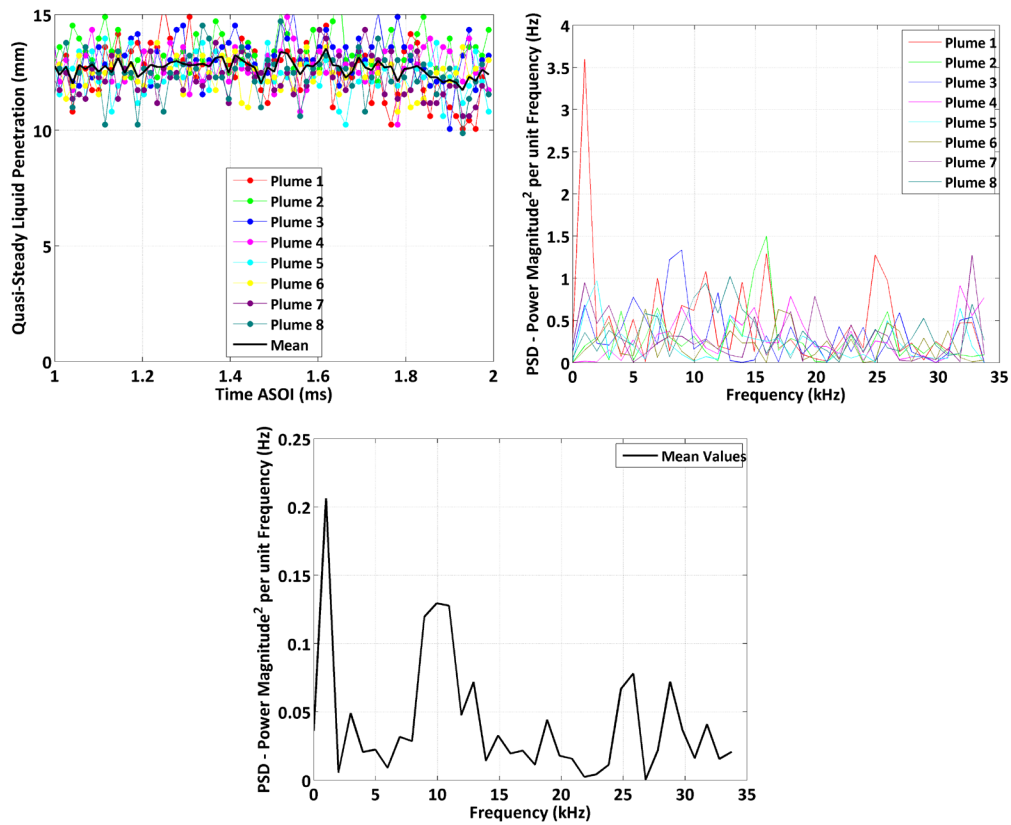


Figure 12.136: Quasi-steady penetration versus time ASOI (Left) for all eight spray plumes, PSD versus frequency (Right) for all eight sprays plumes. Test conditions of 1034 Bar, 355 K fuel temperature, 34.8 kg/m³, 1100 K 0% O₂ environment. Bottom figure provides information on the dominant mean frequencies for the mean liquid length fluctuations.

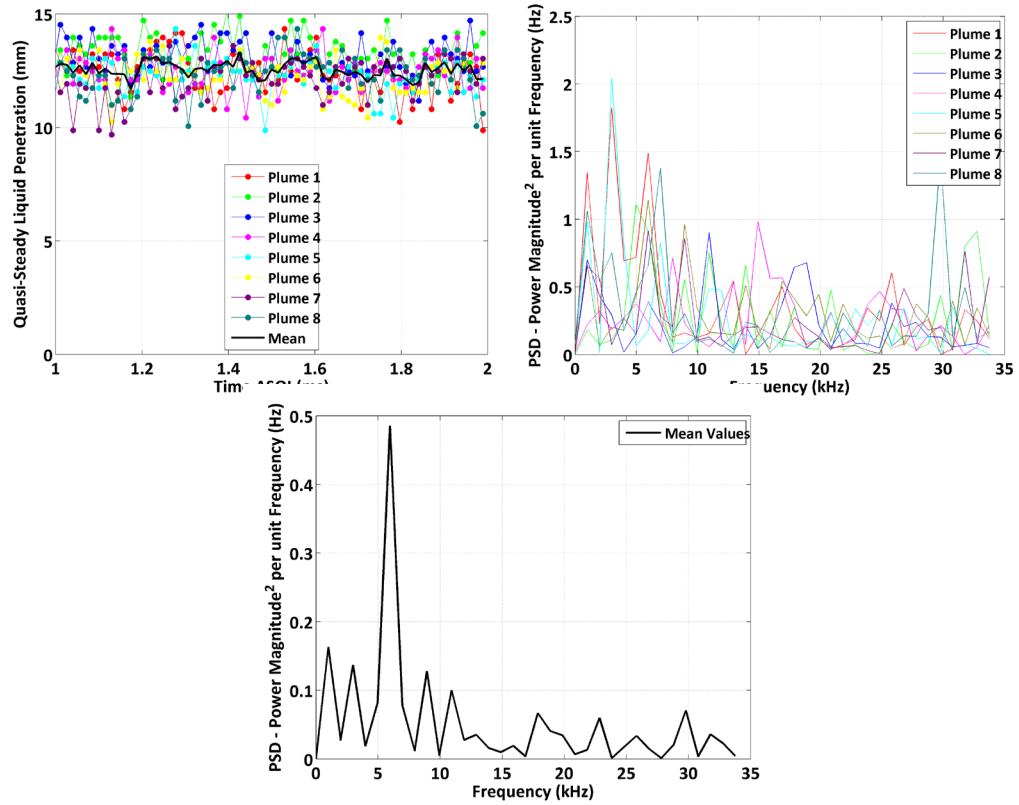


Figure 12.137: Quasi-steady penetration versus time ASOI (Left) for all eight spray plumes, PSD versus frequency (Right) for all eight sprays plumes. Test conditions of 1379 Bar, 355 K fuel temperature, 34.8 kg/m³, 1100 K 0% O₂ environment. Bottom figure provides information on the dominant mean frequencies for the mean liquid length fluctuations.

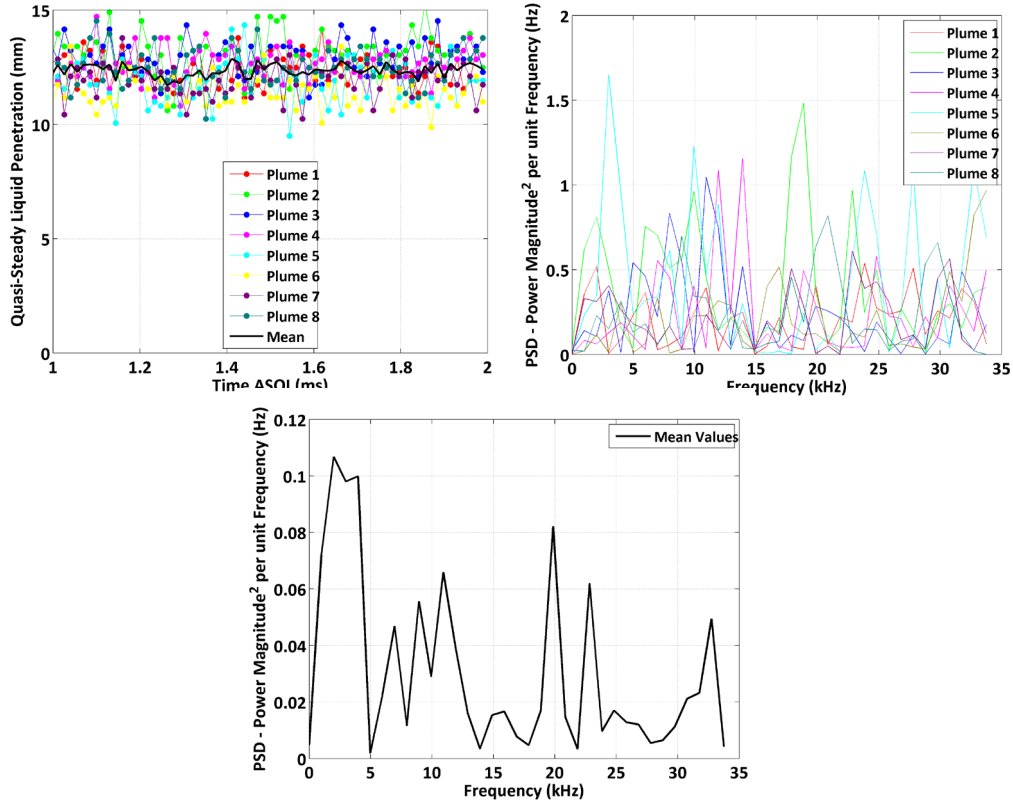


Figure 12.138: Quasi-steady penetration versus time ASOI (Left) for all eight spray plumes, PSD versus frequency (Right) for all eight sprays plumes. Test conditions of 2000 Bar, 355 K fuel temperature, 34.8 kg/m^3 , 1100 K 0% O_2 environment, Repeat test 1. Bottom figure provides information on the dominant mean frequencies for the mean liquid length fluctuations.

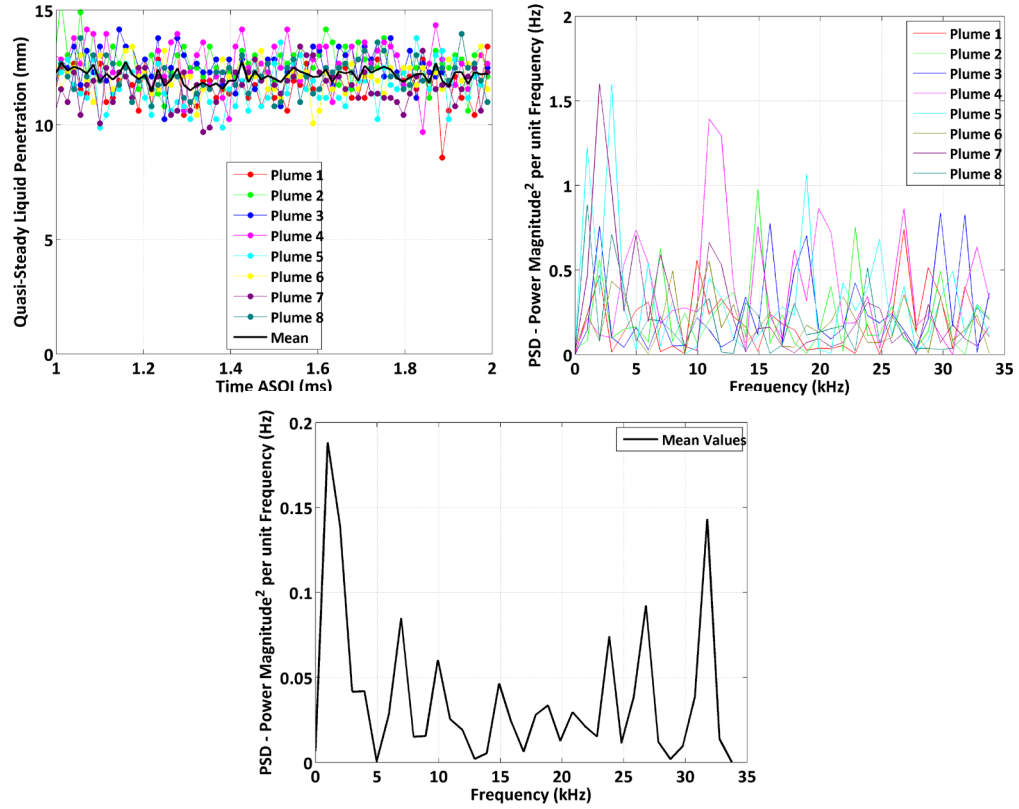


Figure 12.139: Quasi-steady penetration versus time ASOI (Left) for all eight spray plumes, PSD versus frequency (Right) for all eight sprays plumes. Test conditions of 2000 Bar, 355 K fuel temperature, 34.8 kg/m³, 1100 K 0% O₂ environment, Repeat test 2. Bottom figure provides information on the dominant mean frequencies for the mean liquid length fluctuations.

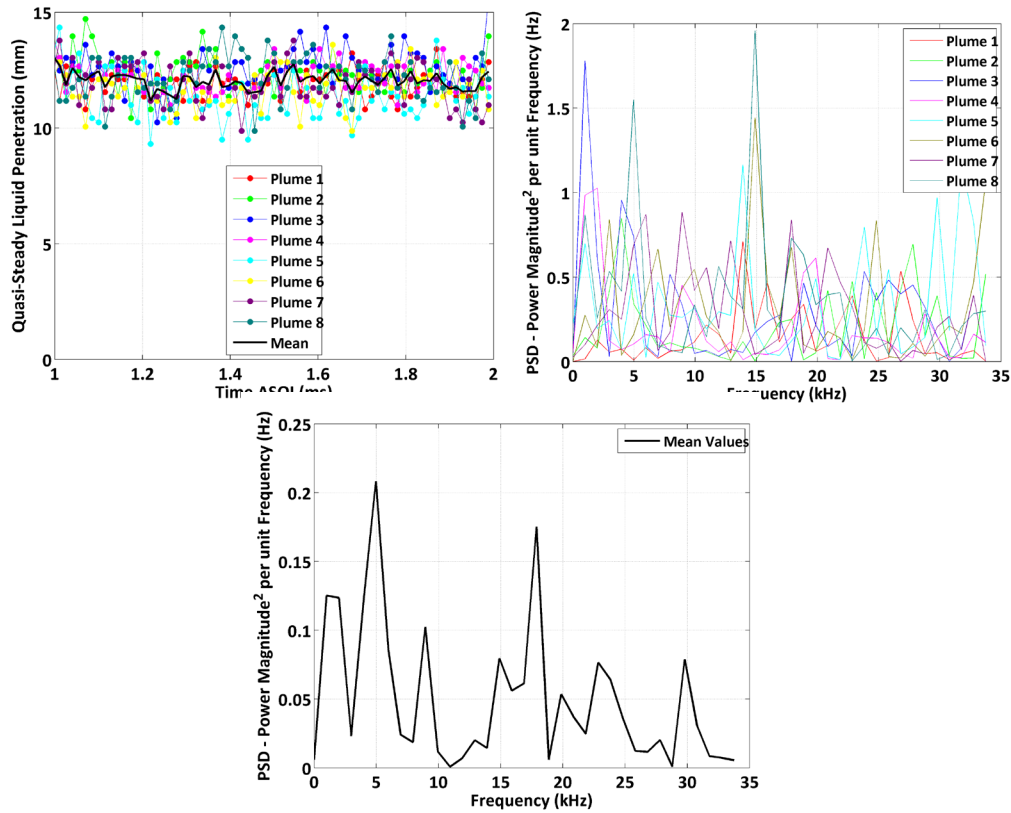


Figure 12.140: Quasi-steady penetration versus time ASOI (Left) for all eight spray plumes, PSD versus frequency (Right) for all eight sprays plumes. Test conditions of 2000 Bar, 355 K fuel temperature, 34.8 kg/m^3 , 1100 K 0% O_2 environment, Repeat test 3. Bottom figure provides information on the dominant mean frequencies for the mean liquid length fluctuations.

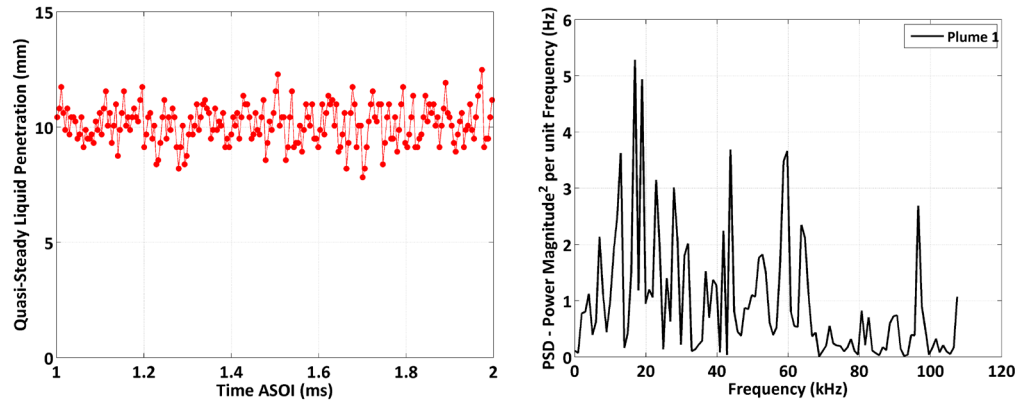


Figure 12.141: Quasi-steady penetration versus time ASOI (Left) for all eight spray plumes, PSD versus frequency (Right) for the first spray plume. Test conditions of 2000 Bar, 355K fuel temperature, 34.8 kg/m³, 1100 K 0% O₂ environment, high frame rate (216,000 fps frame rate).

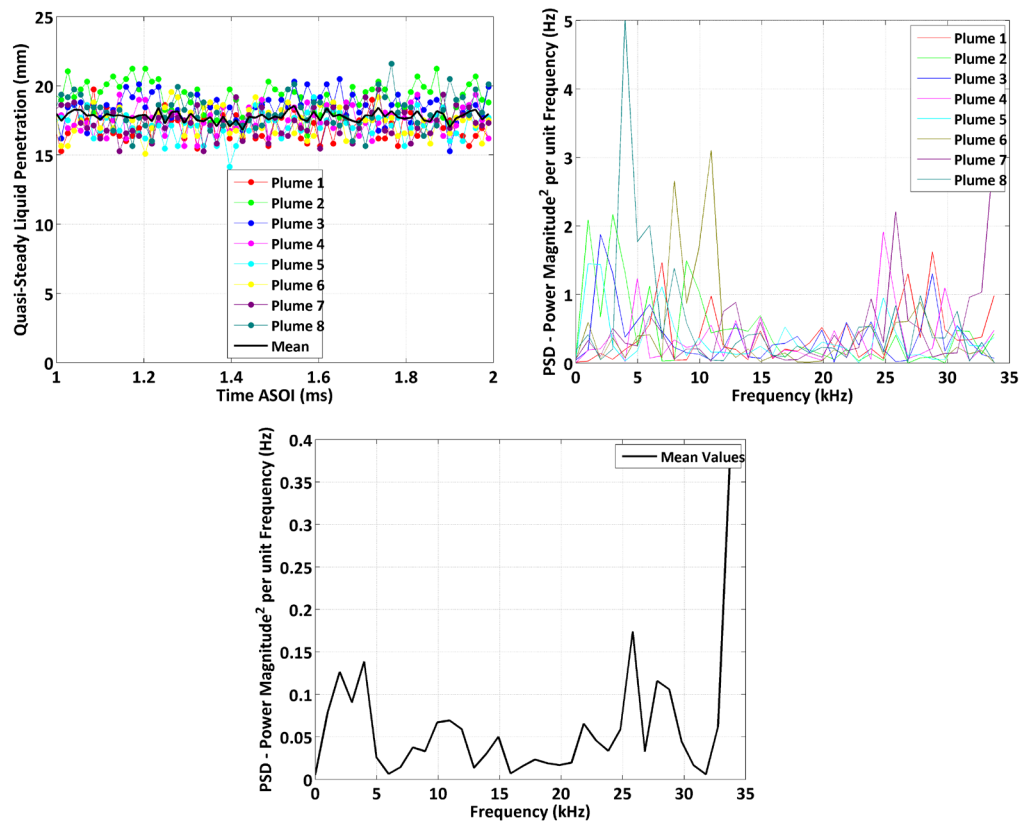


Figure 12.142: Quasi-steady penetration versus time ASOI (Left) for all eight spray plumes, PSD versus frequency (Right) for all eight sprays plumes. Test conditions of 2000 Bar, 363 K fuel temperature, 34.8 kg/m³, 800 K 0% O₂ environment. Bottom figure provides information on the dominant mean frequencies for the mean liquid length fluctuations.

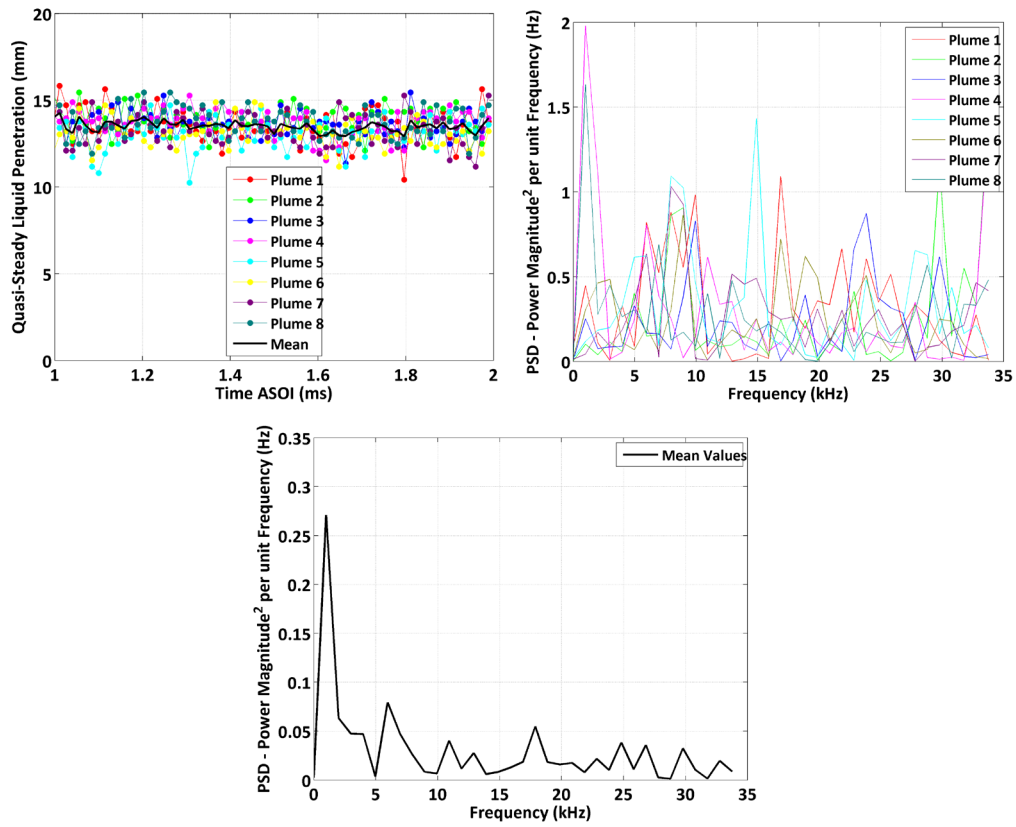


Figure 12.143: Quasi-steady penetration versus time ASOI (Left) for all eight spray plumes, PSD versus frequency (Right) for all eight sprays plumes. Test conditions of 2000 Bar, 363 K fuel temperature, 34.8 kg/m^3 , 950 K 0% O_2 environment. Bottom figure provides information on the dominant mean frequencies for the mean liquid length fluctuations.

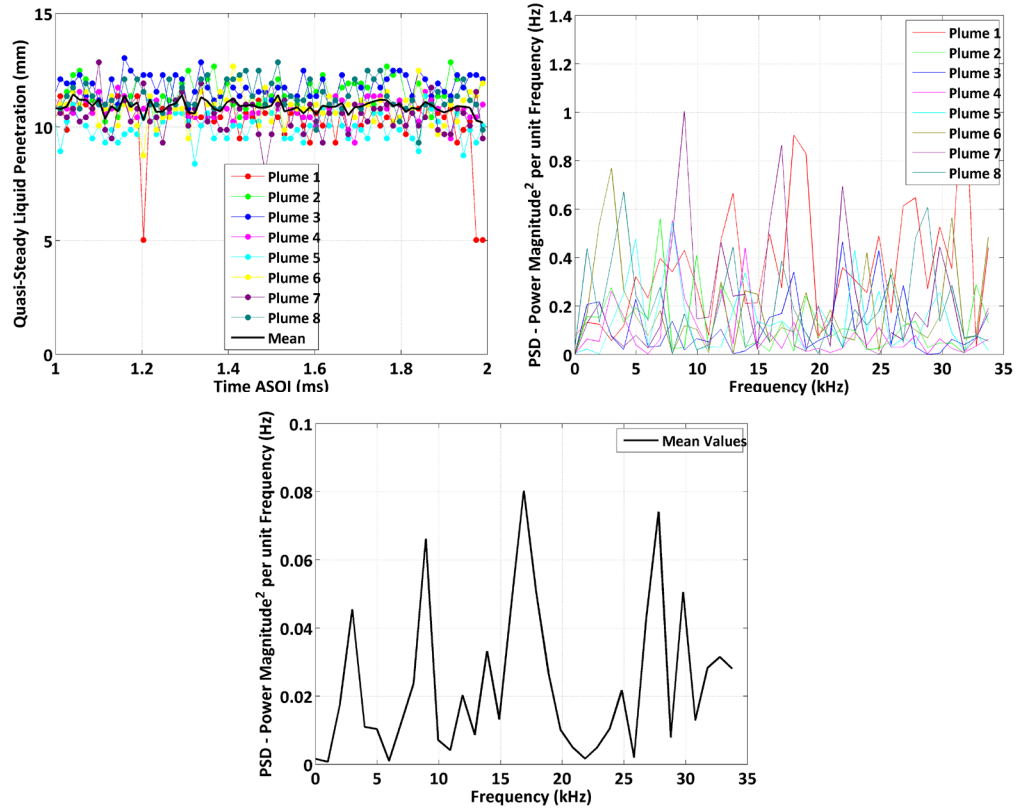


Figure 12.144: Quasi-steady penetration versus time ASOI (Left) for all eight spray plumes, PSD versus frequency (Right) for all eight sprays plumes. Test conditions of 2000 Bar, 363 K fuel temperature, 34.8 kg/m³, 1100 K 0% O₂ environment, Repeat test 1. Bottom figure provides information on the dominant mean frequencies for the mean liquid length fluctuations.

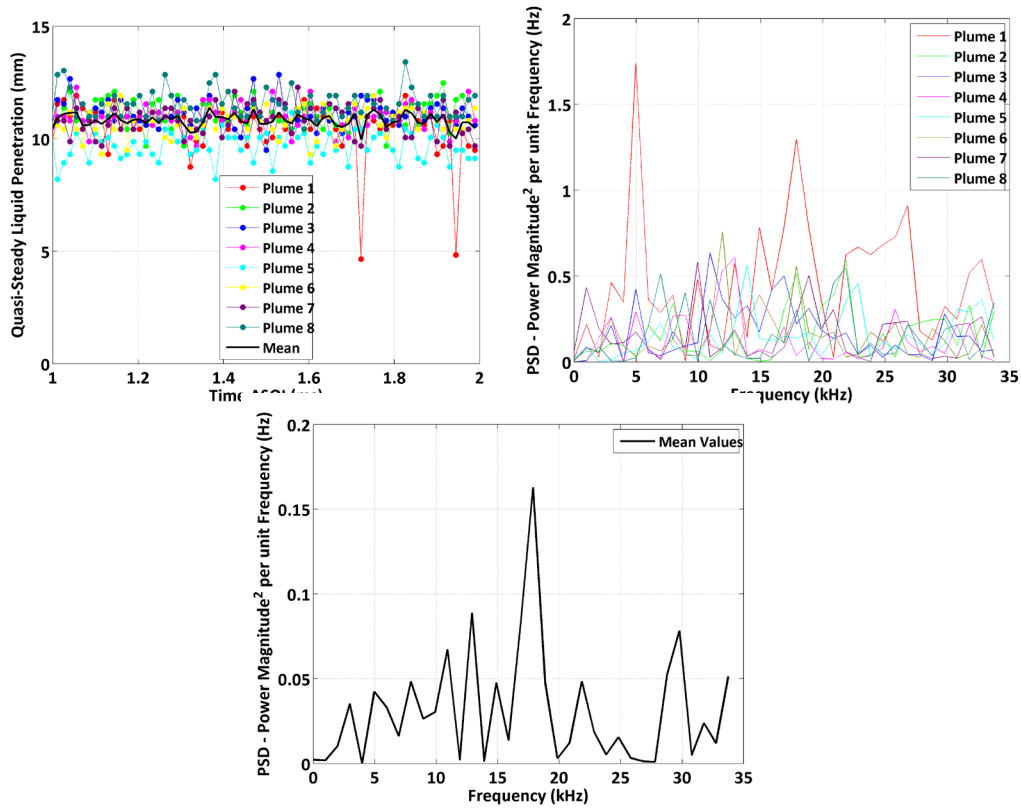


Figure 12.145: Quasi-steady penetration versus time ASOI (Left) for all eight spray plumes, PSD versus frequency (Right) for all eight sprays plumes. Test conditions of 2000 Bar, 363 K fuel temperature, 34.8 kg/m^3 , 1100 K 0% O_2 environment, Repeat test 2. Bottom figure provides information on the dominant mean frequencies for the mean liquid length fluctuations.

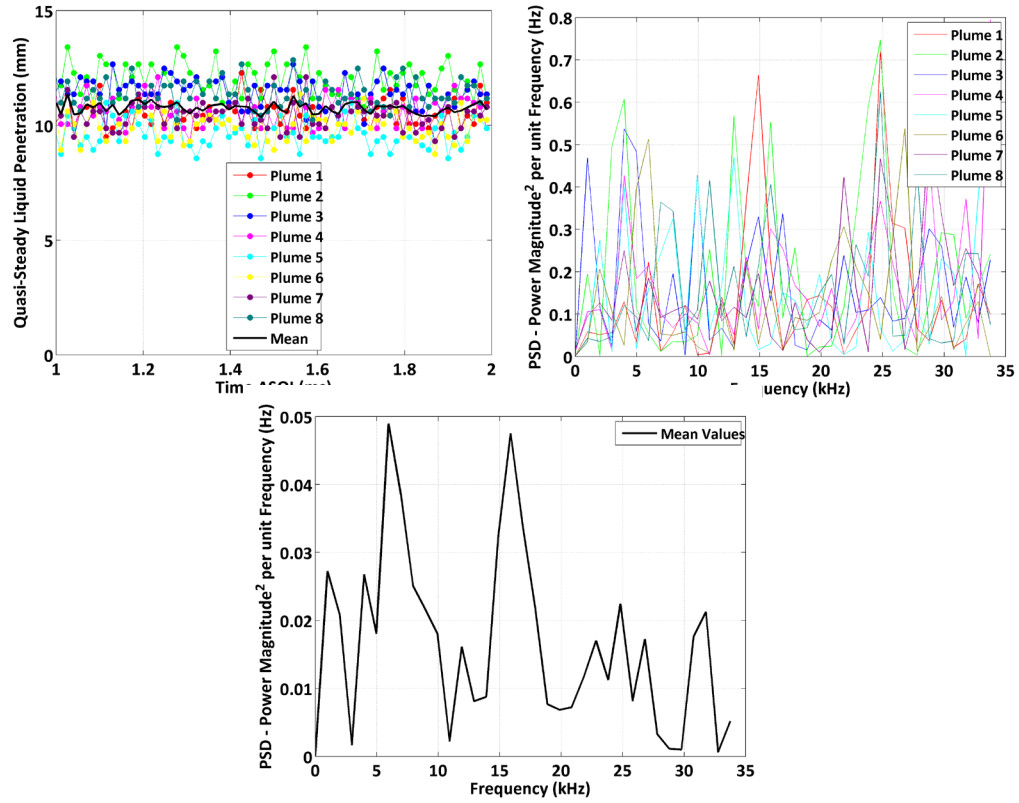


Figure 12.146: Quasi-steady penetration versus time ASOI (Left) for all eight spray plumes, PSD versus frequency (Right) for all eight sprays plumes. Test conditions of 2000 Bar, 363 K fuel temperature, 34.8 kg/m^3 , 1100 K 0% O_2 environment, Repeat test 3. Bottom figure provides information on the dominant mean frequencies for the mean liquid length fluctuations.

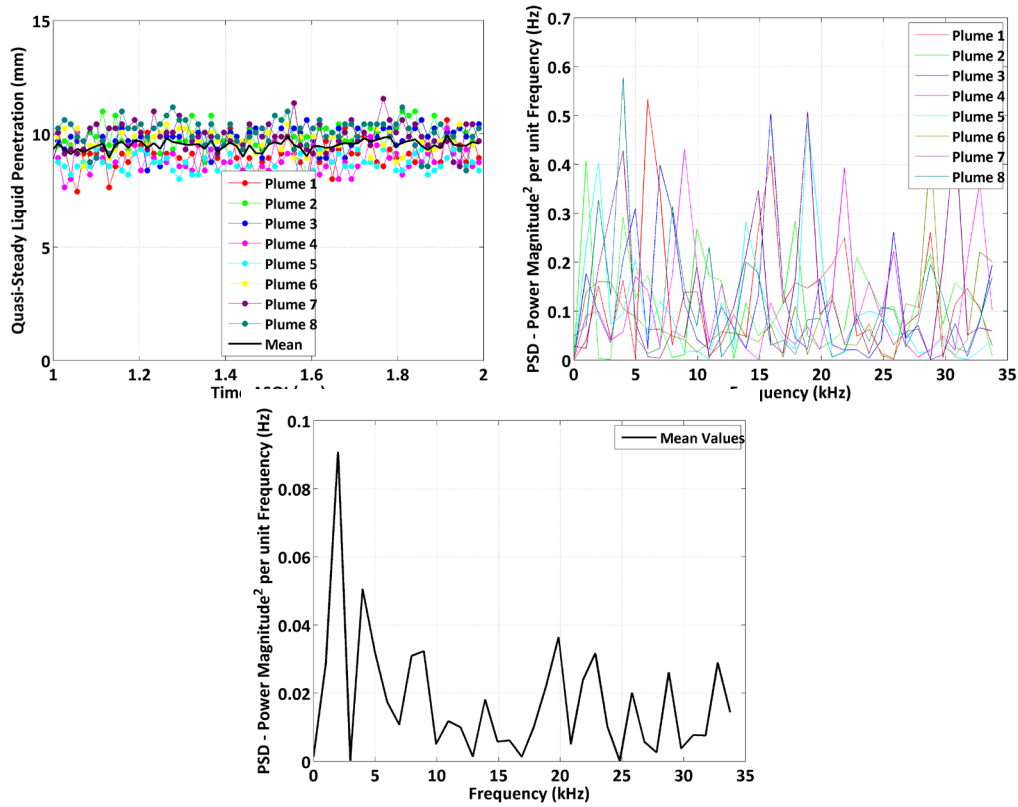


Figure 12.147: Quasi-steady penetration versus time ASOI (Left) for all eight spray plumes, PSD versus frequency (Right) for all eight sprays plumes. Test conditions of 2000 Bar, 363 K fuel temperature, 34.8 kg/m^3 , 1200 K 0% O_2 environment. Bottom figure provides information on the dominant mean frequencies for the mean liquid length fluctuations.

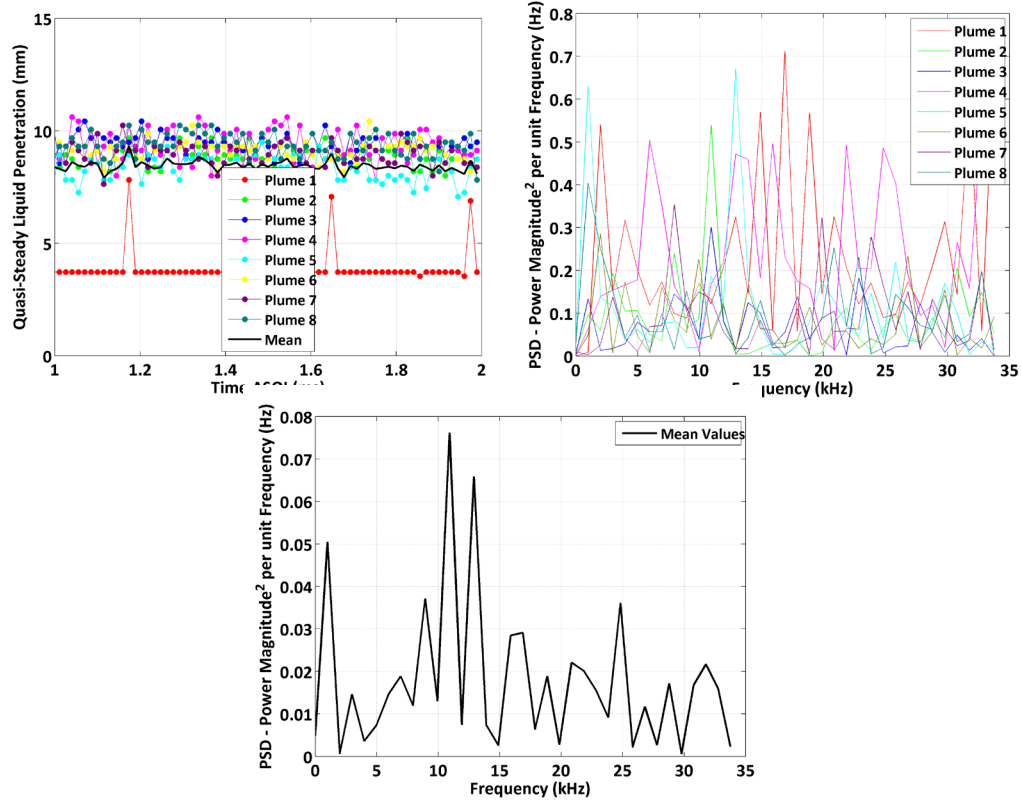


Figure 12.148: Quasi-steady penetration versus time ASOI (Left) for all eight spray plumes, PSD versus frequency (Right) for all eight sprays plumes. Test conditions of 2000 Bar, 363 K fuel temperature, 34.8 kg/m^3 , 1300 K 0% O_2 environment. Bottom figure provides information on the dominant mean frequencies for the mean liquid length fluctuations.

The reduced liquid length for this high temperature condition made accurate detection of the spray region difficult and more sensitive to reductions in signal to noise ratio. This error was evident in plume 1 results where the liquid penetration was mostly constant, at a penetration slightly less than 4 mm, signifying that the liquid spray region was being misidentified as the ceramic insulator surrounding the injector tip (seen in images in Chapter 6) based on the reduced signal to noise ratio in this area, amplified by the reducing liquid length under these higher temperature conditions.

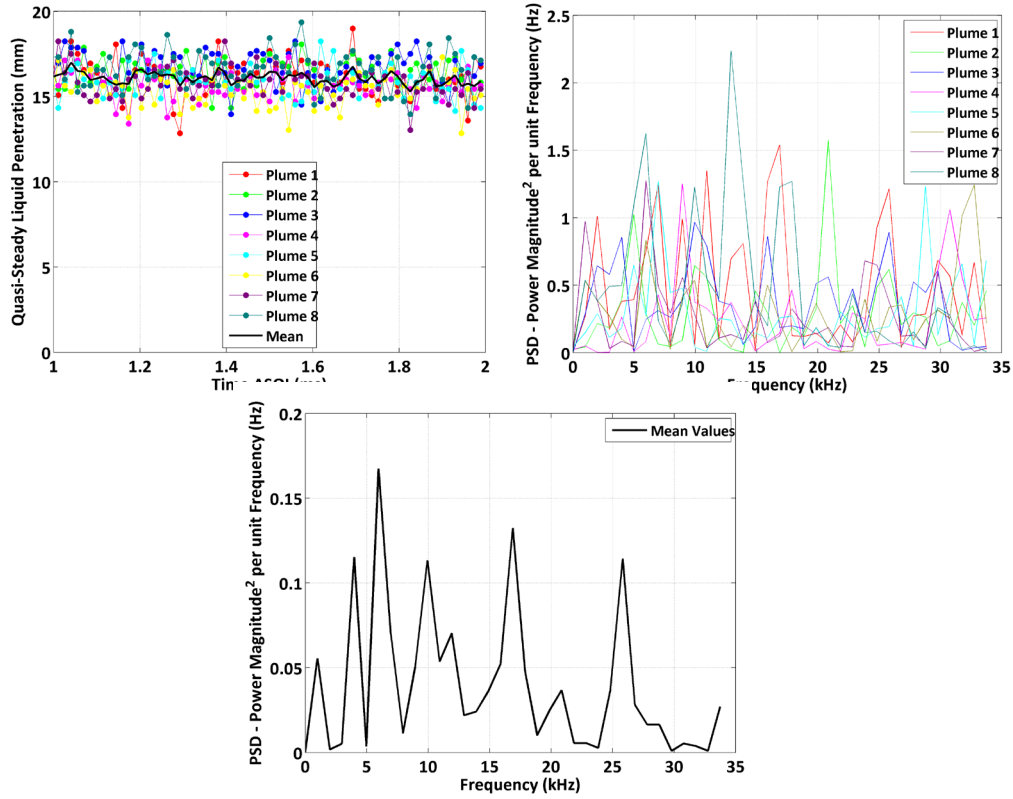


Figure 12.149: Quasi-steady penetration versus time ASOI (Left) for all eight spray plumes, PSD versus frequency (Right) for all eight sprays plumes. Test conditions of 2000 Bar, 363 K fuel temperature, 17.4 kg/m³, 1100 K 0% O₂ environment.

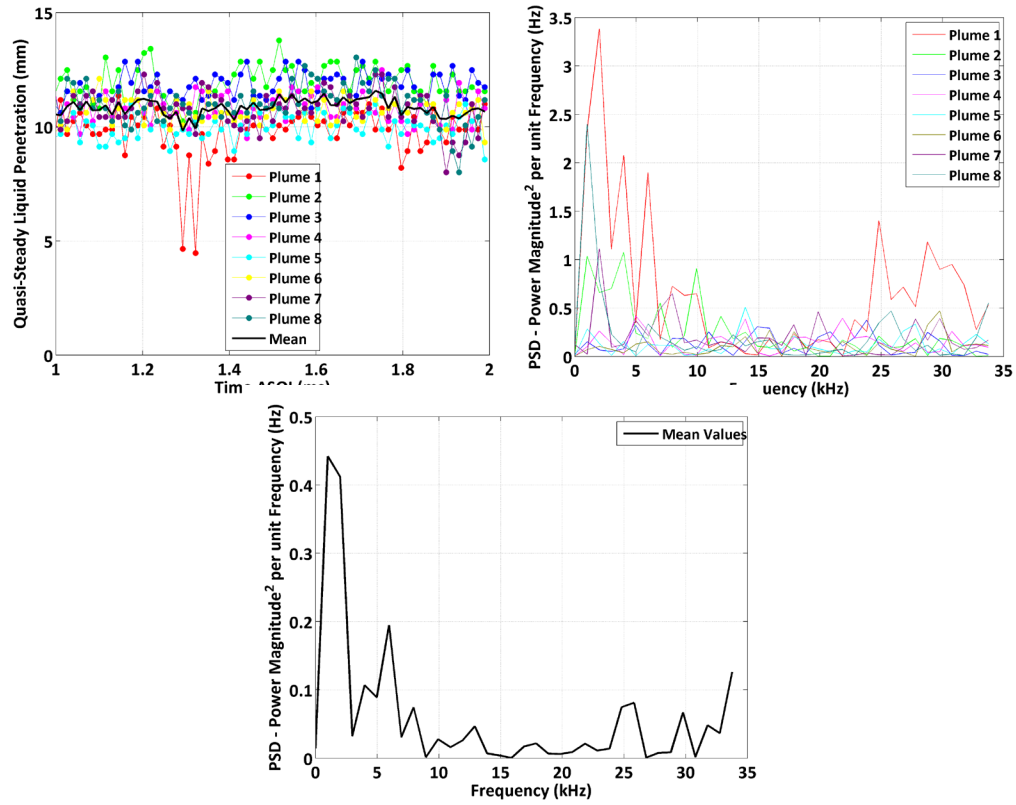


Figure 12.150: Quasi-steady penetration versus time ASOI (Left) for all eight spray plumes, PSD versus frequency (Right) for all eight sprays plumes. Test conditions of 1034 Bar, 363 K fuel temperature, 34.8 kg/m³, 1100 K 0% O₂ environment.

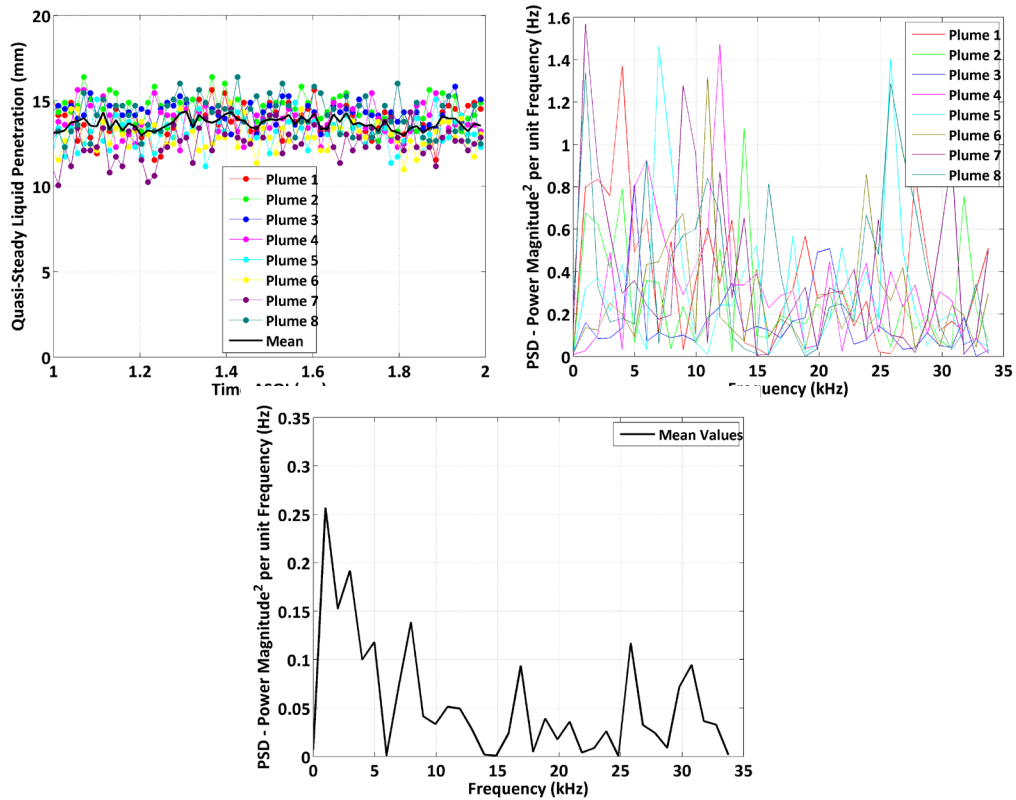


Figure 12.151: Quasi-steady penetration versus time ASOI (Left) for all eight spray plumes, PSD versus frequency (Right) for all eight sprays plumes. Test conditions of 1379 Bar, 363 K fuel temperature, 34.8 kg/m³, 950 K 0% O₂ environment.

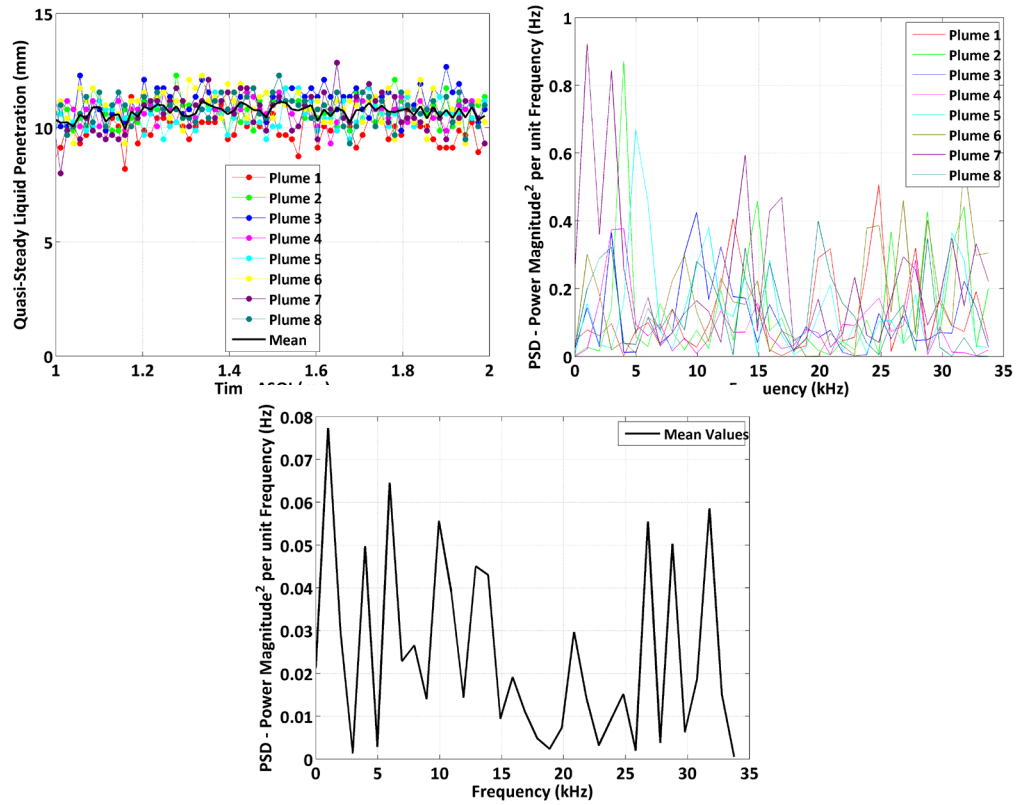


Figure 12.152: Quasi-steady penetration versus time ASOI (Left) for all eight spray plumes, PSD versus frequency (Right) for all eight sprays plumes. Test conditions of 1379 Bar, 363 K fuel temperature, 34.8 kg/m³, 1100 K 0% O₂ environment.

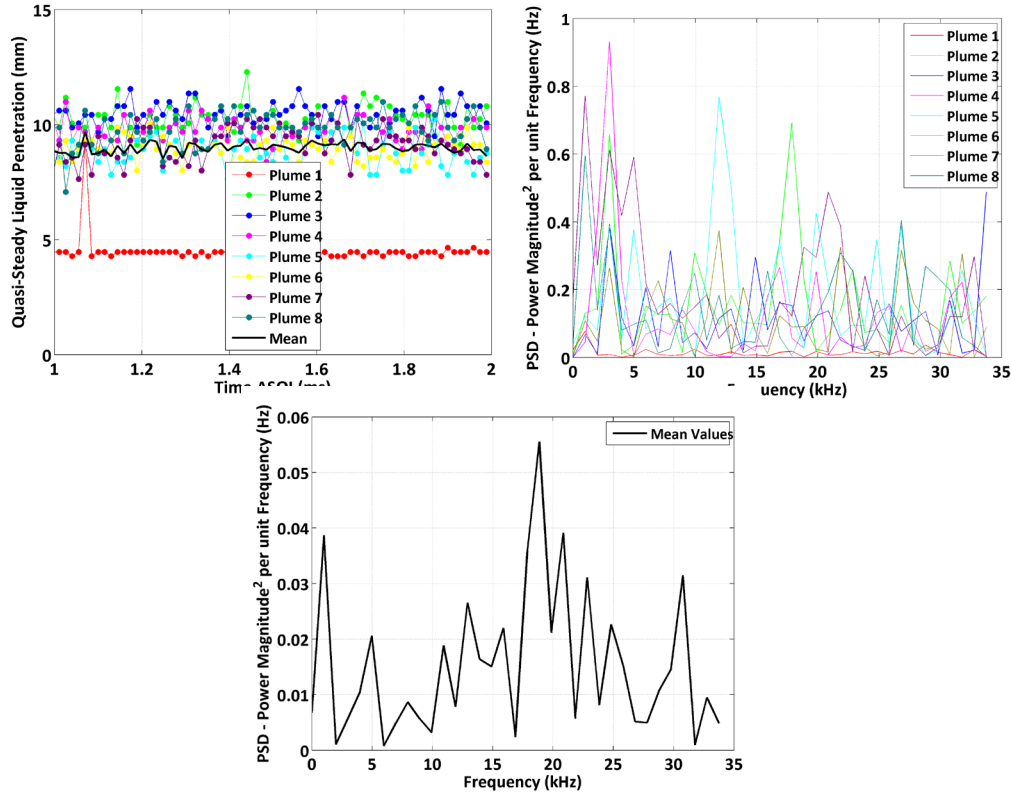


Figure 12.153: Quasi-steady penetration versus time ASOI (Left) for all eight spray plumes, PSD versus frequency (Right) for all eight sprays plumes. Test conditions of 1379 Bar, 363 K fuel temperature, 34.8 kg/m^3 , 1200 K 0% O_2 environment.

There are errors in the liquid penetration of plume 1, similar to the 1300 K case at 2000 bar injection pressure, attributed to reduced signal to noise ratio for the shorter penetrations, and the subsequent error in image processing with the ceramic shield for the injector being mistaken as the spray region. This data and the corresponding frequency analysis for this spray plume were not considered in the results.

The dominant frequencies as determined from the PSD frequency analysis are presented in the following set of tables for each of the 8 spray plumes from the multi-hole injector, over all test conditions. There exist some repeats in frequency, however, the presence of individual dominant frequencies is not evidenced over this range of test conditions.

Table 12.16
Dominant frequency components resulting from PSD analysis, Plume 1.

Ambient Density (kg/m ³)	Fuel Press. (bar)	Fuel Temperature (K)	Temp. at Injection (K)	1 st Freq. (Hz)	2 nd Freq. (Hz)	3 rd Freq. (Hz)	4 th Freq. (Hz)	5 th Freq. (Hz)
34.8	1034	355	1100	993	15882	24816	10919	6949
34.8	1379	355	1100	2978	5956	993	25809	12904
34.8	2000	355	1100 (R1)	23824	1985	27794	19853	10919
34.8	2000	355	1100 (R2)	26801	9926	28787	1985	31765
34.8	2000	355	1100 (R3)	13897	26801	15882	22831	18860
34.8	2000	363	800	28787	6949	26801	33750	10919
34.8	2000	363	950	16875	9926	7941	5956	21838
34.8	2000	363	1100 (R1)	31765	17868	12904	27794	29779
34.8	2000	363	1100 (R2)	4963	17868	26801	14890	22831
34.8	2000	363	1100 (R3)	24816	14890	5956	32757	19853
34.8	2000	363	1200	5956	15882	28787	21838	3971
34.8	2000	363	1300	n/a	n/a	n/a	n/a	n/a
17.4	2000	363	1100	16875	10919	6949	25809	1985
34.8	1034	363	1100	1985	3971	5956	24816	28787
34.8	1379	363	950	3971	27794	1985	5956	12904
34.8	1379	363	1100	24816	12904	27794	20846	32757
34.8	1379	363	1200	n/a	n/a	n/a	n/a	n/a

Table 12.17
Dominant frequency components resulting from PSD analysis, Plume 2.

Ambient Density (kg/m ³)	Fuel Press. (bar)	Fuel Temperature (K)	Temp. at Injection (K)	1 st Freq. (Hz)	2 nd Freq. (Hz)	3 rd Freq. (Hz)	4 th Freq. (Hz)	5 th Freq. (Hz)
34.8	1034	355	1100	15882	6949	3971	25809	12904
34.8	1379	355	1100	4963	32757	10919	13897	8934
34.8	2000	355	1100 (R1)	18860	22831	9926	1985	5956
34.8	2000	355	1100 (R2)	14890	22831	6949	1985	29779
34.8	2000	355	1100 (R3)	3971	27794	33750	22831	20846
34.8	2000	363	800	2978	993	8934	5956	14890
34.8	2000	363	950	33750	29779	8934	31765	22831
34.8	2000	363	1100 (R1)	6949	9926	11912	32757	2978
34.8	2000	363	1100 (R2)	21838	17868	7941	31765	33750
34.8	2000	363	1100 (R3)	24816	3971	12904	15882	29779
34.8	2000	363	1200	993	3971	17868	9926	28787
34.8	2000	363	1300	10919	7941	30772	2978	32757
17.4	2000	363	1100	20846	4963	9926	25809	33750
34.8	1034	363	1100	3971	993	9926	6949	11912
34.8	1379	363	950	13897	3971	31765	993	11912
34.8	1379	363	1100	3971	14890	31765	28787	25809
34.8	1379	363	1200	17868	2978	9926	30772	22831

Table 12.18
Dominant frequency components resulting from PSD analysis, Plume 3.

Ambient Density (kg/m ³)	Fuel Press. (bar)	Fuel Temperature (K)	Temp. at Injection (K)	1 st Freq. (Hz)	2 nd Freq. (Hz)	3 rd Freq. (Hz)	4 th Freq. (Hz)	5 th Freq. (Hz)
34.8	1034	355	1100	8934	11912	4963	993	26801
34.8	1379	355	1100	10919	993	18860	5956	25809
34.8	2000	355	1100 (R1)	10919	7941	4963	13897	31765
34.8	2000	355	1100 (R2)	29779	31765	15882	1985	18860
34.8	2000	355	1100 (R3)	993	3971	23824	7941	25809
34.8	2000	363	800	1985	28787	5956	23824	21838
34.8	2000	363	950	23824	9926	29779	18860	4963
34.8	2000	363	1100 (R1)	21838	24816	17868	26801	4963
34.8	2000	363	1100 (R2)	10919	16875	4963	13897	18860
34.8	2000	363	1100 (R3)	3971	993	9926	16875	14890
34.8	2000	363	1200	15882	6949	4963	25809	33750
34.8	2000	363	1300	10919	22831	7941	17868	993
17.4	2000	363	1100	9926	25809	15882	3971	1985
34.8	1034	363	1100	23824	4963	14890	20846	10919
34.8	1379	363	950	4963	20846	12904	31765	993
34.8	1379	363	1100	9926	2978	11912	31765	15882
34.8	1379	363	1200	33750	2978	7941	14890	5956

Table 12.19
Dominant frequency components resulting from PSD analysis, Plume 4.

Ambient Density (kg/m ³)	Fuel Press. (bar)	Fuel Temperature (K)	Temp. at Injection (K)	1 st Freq. (Hz)	2 nd Freq. (Hz)	3 rd Freq. (Hz)	4 th Freq. (Hz)	5 th Freq. (Hz)
34.8	1034	355	1100	31765	17868	33750	8934	14890
34.8	1379	355	1100	14890	7941	16875	12904	24816
34.8	2000	355	1100 (R1)	13897	11912	24816	6949	33750
34.8	2000	355	1100 (R2)	10919	19853	26801	14890	4963
34.8	2000	355	1100 (R3)	1985	19853	8934	28787	32757
34.8	2000	363	800	24816	4963	29779	14890	12904
34.8	2000	363	950	993	33750	5956	10919	12904
34.8	2000	363	1100 (R1)	7941	13897	11912	2978	17868
34.8	2000	363	1100 (R2)	12904	25809	4963	8934	2978
34.8	2000	363	1100 (R3)	33750	28787	3971	31765	24816
34.8	2000	363	1200	8934	21838	32757	25809	4963
34.8	2000	363	1300	32757	5956	15882	21838	24816
17.4	2000	363	1100	8934	30772	17868	6949	12904
34.8	1034	363	1100	4963	21838	13897	1985	30772
34.8	1379	363	950	11912	5956	2978	20846	23824
34.8	1379	363	1100	3971	27794	24816	14890	11912
34.8	1379	363	1200	2978	16875	19853	31765	25809

Table 12.20
Dominant frequency components resulting from PSD analysis, Plume 5.

Ambient Density (kg/m ³)	Fuel Press. (bar)	Fuel Temperature (K)	Temp. at Injection (K)	1 st Freq. (Hz)	2 nd Freq. (Hz)	3 rd Freq. (Hz)	4 th Freq. (Hz)	5 th Freq. (Hz)
34.8	1034	355	1100	1985	31765	6949	12904	25809
34.8	1379	355	1100	2978	993	6949	10919	30772
34.8	2000	355	1100 (R1)	2978	9926	32757	27794	23824
34.8	2000	355	1100 (R2)	2978	993	18860	24816	5956
34.8	2000	355	1100 (R3)	31765	13897	29779	23824	993
34.8	2000	363	800	993	6949	24816	30772	16875
34.8	2000	363	950	14890	7941	27794	5956	23824
34.8	2000	363	1100 (R1)	7941	4963	22831	13897	24816
34.8	2000	363	1100 (R2)	13897	22831	32757	30772	6949
34.8	2000	363	1100 (R3)	33750	12904	9926	3971	7941
34.8	2000	363	1200	18860	1985	13897	4963	6949
34.8	2000	363	1300	12904	993	25809	10919	19853
17.4	2000	363	1100	6949	28787	33750	31765	4963
34.8	1034	363	1100	13897	27794	993	32757	17868
34.8	1379	363	950	6949	25809	17868	14890	21838
34.8	1379	363	1100	4963	10919	30772	15882	13897
34.8	1379	363	1200	11912	19853	2978	26801	4963

Table 12.21
Dominant frequency components resulting from PSD analysis, Plume 6.

Ambient Density (kg/m ³)	Fuel Press. (bar)	Fuel Temperature (K)	Temp. at Injection (K)	1 st Freq. (Hz)	2 nd Freq. (Hz)	3 rd Freq. (Hz)	4 th Freq. (Hz)	5 th Freq. (Hz)
34.8	1034	355	1100	5956	16875	2978	25809	30772
34.8	1379	355	1100	5956	8934	993	16875	13897
34.8	2000	355	1100 (R1)	33750	16875	30772	6949	11912
34.8	2000	355	1100 (R2)	10919	7941	2978	26801	21838
34.8	2000	355	1100 (R3)	14890	33750	2978	24816	17868
34.8	2000	363	800	10919	7941	27794	993	23824
34.8	2000	363	950	8934	16875	18860	23824	2978
34.8	2000	363	1100 (R1)	2978	30772	33750	23824	25809
34.8	2000	363	1100 (R2)	11912	17868	14890	2978	25809
34.8	2000	363	1100 (R3)	26801	5956	21838	13897	1985
34.8	2000	363	1200	28787	32757	1985	20846	26801
34.8	2000	363	1300	1985	26801	9926	3971	6949
17.4	2000	363	1100	32757	5956	9926	993	15882
34.8	1034	363	1100	29779	15882	17868	13897	21838
34.8	1379	363	950	10919	23824	8934	26801	14890
34.8	1379	363	1100	31765	26801	28787	24816	33750
34.8	1379	363	1200	11912	21838	26801	31765	2978

Table 12.22
Dominant frequency components resulting from PSD analysis, Plume 7.

Ambient Density (kg/m ³)	Fuel Press. (bar)	Fuel Temperature (K)	Temp. at Injection (K)	1 st Freq. (Hz)	2 nd Freq. (Hz)	3 rd Freq. (Hz)	4 th Freq. (Hz)	5 th Freq. (Hz)
34.8	1034	355	1100	32757	993	19853	2978	17868
34.8	1379	355	1100	5956	8934	31765	993	33750
34.8	2000	355	1100 (R1)	22831	30772	17868	24816	2978
34.8	2000	355	1100 (R2)	1985	4963	10919	6949	23824
34.8	2000	355	1100 (R3)	8934	5956	17868	12904	20846
34.8	2000	363	800	33750	25809	23824	12904	5956
34.8	2000	363	950	7941	5956	12904	14890	32757
34.8	2000	363	1100 (R1)	8934	16875	21838	11912	29779
34.8	2000	363	1100 (R2)	9926	18860	993	20846	32757
34.8	2000	363	1100 (R3)	28787	24816	21838	31765	3971
34.8	2000	363	1200	18860	30772	3971	14890	9926
34.8	2000	363	1300	7941	19853	23824	32757	26801
17.4	2000	363	1100	5956	993	23824	29779	8934
34.8	1034	363	1100	1985	7941	19853	29779	27794
34.8	1379	363	950	993	8934	30772	11912	13897
34.8	1379	363	1100	993	2978	13897	16875	30772
34.8	1379	363	1200	993	2978	4963	20846	18860

Table 12.23
Dominant frequency components resulting from PSD analysis, Plume 7.

Ambient Density (kg/m ³)	Fuel Press. (bar)	Fuel Temperature (K)	Temp. at Injection (K)	1 st Freq. (Hz)	2 nd Freq. (Hz)	3 rd Freq. (Hz)	4 th Freq. (Hz)	5 th Freq. (Hz)
34.8	1034	355	1100	12904	10919	32757	5956	28787
34.8	1379	355	1100	29779	6949	993	2978	31765
34.8	2000	355	1100 (R1)	20846	8934	29779	17868	3971
34.8	2000	355	1100 (R2)	993	2978	23824	10919	13897
34.8	2000	355	1100 (R3)	14890	4963	993	17868	11912
34.8	2000	363	800	3971	5956	7941	27794	25809
34.8	2000	363	950	993	6949	28787	33750	12904
34.8	2000	363	1100 (R1)	3971	28787	12904	993	16875
34.8	2000	363	1100 (R2)	21838	6949	8934	10919	33750
34.8	2000	363	1100 (R3)	24816	27794	10919	15882	6949
34.8	2000	363	1200	3971	1985	7941	10919	13897
34.8	2000	363	1300	993	20846	22831	32757	8934
17.4	2000	363	1100	12904	5956	17868	9926	993
34.8	1034	363	1100	993	33750	25809	5956	12904
34.8	1379	363	950	993	25809	5956	10919	15882
34.8	1379	363	1100	19853	28787	2978	13897	9926
34.8	1379	363	1200	993	26801	2978	21838	28787